THE UNIVERSITY *of* EDINBURGH

Fire performance of unprotected and protected concrete filled steel hollow structural sections

David Rush

PhD – The University of Edinburgh – 2013

Declaration

I, David Rush, declare that this thesis and the work presented in it are my own and that it has been generated by me as the result of my own original research. I confirm that:

1. this work was done wholly or mainly while in candidature for a research degree at this University;
2. where any part of this thesis has previously been submitted for a degree or any other qualification at this University or any other institution, this has been clearly stated;
3. where I have consulted the published work of others, this is always clearly attributed;
4. where I have quoted from the work of others, the source is always given. With the exception of such quotations, this thesis is entirely my own work;
5. I have acknowledged all main sources of help; and
6. where the thesis is based on work done by myself jointly with others, I have made clear exactly what was done by others and what I have contributed myself.

Signed: ……

Date: ……

List of related publications:

- Journal Paper:
    - Rush, D., Bisby, L., Lane, B., and Melandinos, A. (2012). *Structural performance of unprotected concrete-filled steel hollow sections in fire: A review and meta-analysis of available test data*. Steel and Composite Structures, 12(4), 325–352.
- Conference Papers:
    - Rush, D., O'Loughlin, E., and Bisby, L. (2012). *Concrete-filled stuctural hollow sections in fire: accounting for heat transfer across a gap.* 15th International conference on Experimental Mechanics, Porto, Portugal, 22nd-27th July (paper 2677).
    - Rush, D., Bisby, L., Melandinos, A., and Lane, B. (2011). *Fire Resistance Design of Unprotected Concrete Filled Steel Hollow Sections: Meta-Analysis of Available Furnace Test Data*. 10th International Symposium on Fire Safety Science, Maryland, USA. 19th-24th June, pp. 1549–1562.
    - Rush, D., Bisby, L., Lane, B., and Jowsey, A. (2010). *Structural Fire Performance of CFS Sections: State-of-the-Art and Knowledge Gaps.* 12th International Interflam Conference, Nottingham, UK, 5th-7th July, pp. 57–70.

Acknowledgements

I have had the great pleasure of working with, becoming friends with, and in one case marrying, so many wonderful people during my time on this project. I would have been thoroughly lost without their love, kindness, support, wisdom and care for my wellbeing.

First and foremost I must thank my Lord and God for the opportunity to be able to conduct this research and the positions and conditions that I have favourably found myself in. I also have to thank God for my wife, who loves and supports me, encourages me when I question myself and who has been the highlight of my life for the past two years, and without whom I cannot function.

I would also like to thank, from the bottom of my heart, my supervisor, colleague and friend Professor Luke Bisby, and all those who support him. He is a constant source of encouragement, friendship and, most importantly, inspiration. I have learnt a lot about the nature of research and what it takes to be a world-leading academic, but also what it is to lead people. I would also thank my second supervisor Dr. Martin Gillie for the emotional support and numerical modelling advice he gave me to conduct this research.

The research could not have been conducted without the technical and fiscal support of my sponsor companies. For all those at Arup, thank you for inviting me into the creative and technically gifted environment that drives and inspires your work. For those at International Paint Ltd, I thank you for your patience with me, for the tests that you helped me so much to complete, and for making me feel at home when I tested at your facilities. I would like to say a special thanks to Dr. Allan Jowsey, who has been a massive help on this project from start to finish.

I would like to thank all of those with any association at the BRE Centre for Fire Safety Engineering based at the University of Edinburgh, for their daily encouragements and friendships. In particular, but in no particular order, thanks are due to Michal Krajcovic, Jim Hutchinson, Derek Jardine, Dr. Tim Stratford, Dr. Stephen Welch, Cristian Maluk, Zafiris Triantafyllidis, Dr. Angus Law, Dr. Rory

Hadden, Dr. Kate Anderson, Dr. Susan Deeny, Dr. Nicolas Bal, Dr. John Gales, Steffen Kahrmann, Dr. Joanne Knox, Dr. Adam Ervine, Sam Grindrod, Emma McIntyre, Holly Smith, Eoin O'Loughlin and Michael Woodrow.

I would like to thank my friends and family for the love, prayers and support over the past four years. I pray a special prayer of thanks for my parents for the time and effort in raising me and supporting me and their continual encouragement of my education and inquiry. I'd like to thank my church family and all those I have prayed with, and prayed for by, over the past four years. I'd like to thank my best men at my wedding who make my life so rich and enjoyable, and I'd like to thank my friend Jesically Milker, for their love and support and helping me relax whilst I have been writing up.

This work was financially supported by the ESPRC Cooperative Awards in Science and Engineering, Ove Arup and Partners Limited, International Paint Limited, The University of Edinburgh, and the BRE Centre for Fire Safety Engineering.

Abstract

Concrete filled steel hollow structural (CFS) sections are increasingly used to support large compressive loads in buildings, with the concrete infill and the steel tube working together to yield several benefits both at ambient temperature and during a fire. These members are now widely applied in the design of highly optimized multi-storey and high rise buildings where fire resistance ratings of two or more hours may be required. Whilst the response and design of these sections at ambient temperatures is reasonably well understood, their response in fire, and thus their fire resistance design, is less well established. Structural fire resistance design guidance is available but has been developed based on tests of predominantly short, concentrically-loaded, small-diameter columns in braced frames using normal strength concrete. The current prescriptive guidance is limited and the design of CFS columns is thus often based on a detailed performance based approach, which can be time consuming and expensive and which is generally not well supported by a deep understanding of CFS columns' behaviour in real fires. This thesis aims to understand the fundamental thermal and mechanical factors at play within these sections so as to provide guidance on how to improve their design for fire resistance when applied either as unprotected or protected sections. A meta-analysis of available furnace test data is used to demonstrate that current guidance fails to capture the relevant mechanics and thus poorly predicts fire resistance. It is also demonstrated that the predictive abilities of the available design standards vary with physical characteristics of the CFS section such as shape and size. A factor which has been observed in furnace tests on CFS sections but which is not accounted for in available guidance is the formation of an air gap between the steel tube and the concrete core due to differential expansion; this affects their structural response in fire. The insulating effect of air gap formation has not previously been addressed in literature and an experimental program is presented to systematically assess the effects of a gap on the heat transfer through the section; showing that the presence of even a 1 mm gap is important.

To explicitly assess the heat transfer response within both unprotected and fire protected (i.e. insulated) CFS sections, 34 large scale standard furnace tests were performed in partnership with an industry sponsor. Fourteen tests on large scale

unloaded unprotected CFS sections are presented to assess current capability to predict the thermal response and to assess the effects of different sectional and material parameters on heating. New best practice thermal modelling guidance is suggested based on comparison between the models and observed temperatures from the tests. Twenty CFS specimens of varying size and shape, protected with different types and thicknesses of intumescent paint fire insulation, were also tested unloaded in a furnace to understand the thermal evolution within protected CFS sections and to develop design guidance to support application of intumescent coatings in performance based fire resistance design of CFS sections. These tests demonstrate that the intumescent coatings were far more effective than expected when applied to CFS sections, and that current methods of designing the coatings' thickness are overly conservative. The reason for this appears to be that the calculation of effective section factor which is used in the prescription of intumescent coating thicknesses is based on the thermal response of unprotected CFS sections which display fundamentally different heating characteristics from protected sections due to the development of a thermal gradient in the concrete core. It is also demonstrated (by calculation supported by the testing presented herein) that the steel failure temperature (i.e. limiting temperature) of an unprotected CFS column in fire is significantly higher than one which is protected; procedures to determine the limiting temperature of protected sections are suggested. Finally, the residual strength of fire-exposed CFS columns is examined through structural testing of 19 of the 34 fire tested columns along with unheated control specimens. The results provide insights into the residual response of unprotected and protected CFS section exposed to fire, and demonstrate a reasonable ability to calculate their residual structural capacity.

The work presented in this thesis has shed light on the ability of available guidance to rationally predict the thermal and structural response to fire of CFS columns, has improved the understanding of the thermal evolution within protected and unprotected CFS sections in fire, has provided best-practice guidance and material input parameters for both thermal and structural modelling of CFS sections, and has improved understanding of the residual capacity of CFS sections after a fire.

Contents

List of figures

List of tables

List of notation

Acronyms

CFS	Concrete filled structural hollow section
DFT	Dry film thickness
EC4	Eurocode 4
F.R.	Fire resistance
FF	Fixed-fixed
FIB	Fibre reinforced concrete
FNA	French national annex
HSC	High strength concrete
ME	Mean error
MPE	Mean percentage error
PC	Plain concrete
PF	Pinned-fixed
PP	Pinned-pinned
RC	Reinforced concrete
RSI	Residual strength index
TC	Thermocouple

Subscripts

air	air
a	steel tube
c	concrete
eff	effective
fi	fire
g	gas
gap	gap
int	intumescent
p	protection
s	reinforcement
t	time
θ	temperature

Latin letters

A_i	Area of material *i* (mm^2)
$A_{i,\theta}$	Area of material *i* at temperature (mm^2)
b_i	Internal breadth of CFS column (mm)
$c_{i,\theta}$	Specific heat capacity of material *i* at temperature (J/kg^oC)
d	Outer diameter of CFS column (mm)
d_p	Dry film thickness (DFT, mm)
e	Eccentricity (mm)
$E_{a,\theta}$	Elastic modulus at temperature (N/mm^2)
$E_{c,sec,\theta}$	Secant modulus of elasticity for structural concrete at temperature (N/mm^2)
E_{cfs}	Residual elastic modulus of CFS column (N/mm^2)
E_{cm}	Secant modulus of elasticity for structural concrete (N/mm^2)
E_i	Elastic modulus (N/mm^2)
$E_{i,\theta}$	Elastic modulus of material *i* at temperature (N/mm^2)
$E_{Ti,\theta,\sigma}$	Elastic tangent modulus of material *i* at temperature and stress (N/mm^2)
f	Empirical modification factor
$f_{ap,\theta}$	Proportional limit at temperature (N/mm^2)
$f_{ay,\theta}$	Yield strength of steel at temperature (N/mm^2)
f_{cd}	Design strength of concrete (N/mm^2)
f_{ck}	Characteristic strength of concrete (N/mm^2)
$f_{i,\theta}$	Yield strength of material I at temperature (N/mm^2)
f_{sd}	Design strength of reinforcement (N/mm^2)
f_{yd}	Design yield strength of steel (N/mm^2)
Gr_w	Grashof number for the air gap
h_{gap}	Width dependent gap conductivity ($W/m^{2o}C$)
h_j	Gap conductance (W/m^oC) (Ghojel, 2004)
$\dot{h}_{net}$	Net heat flux (W/m^2)
$\dot{h}_{net,c}$	Net convective heat flux (W/m^2)
$\dot{h}_{net,r}$	Net radiative heat flux (W/m^2)
H_p	Heated perimeter (mm)
H_p/A	Section factor (m^{-1})
$H_p/A_{eff}\,(Exp)$	Experimental effective sections factor (m^{-1})

$H_p/A_{eff}\,(Th)$	Current effective section factor (m^{-1}) (Hicks et al., 2002)
$(H_p/A_{eff})'$	Instantaneous effective section factor (m^{-1})
$(H_p/A_{eff})'_{t,ave}$	Time averaged effective section factor (m^{-1})
$I_{i,\theta}$	Second moment of area at temperature (mm^4)
$k_{ay,\theta}$	Yield strength reduction factors at temperature
$k_{Ea,\theta}$	Elastic modulus reduction factors at temperature
$k_{py,\theta}$	Proportional limit reduction factors at temperature
l_{eff}	Effective length (m) (KL in NRCC fire resistance design equation (Kodur, 2007))
$l_{eff,\theta}$	Effective length of member at temperature (m)
$N_{fi,Rd}$	Design resistance to axial compression in fire
N_{cr}	Ambient Euler buckling load (kN)
$N_{fi,cr}$	Design plastic resistance to compression (kN)
$N_{fi,pl,Rd}$	Plastic resistance to compression in fire (kN)
$N_{fi,Rd}$	Design resistance to axial compression in fire (kN)
$N_{fi,Sd}$	Applied load in fire (kN)
$N_{pl,R}$	Ambient plastic resistance to compression (kN)
$N_{pl,Rd}$	Ambient design plastic resistance to compression (kN) (Nu in RSI design by (Han and Huo, 2003)
N_{Rd}	Ambient design resistance to axial compression
N_{Sd}	Applied load (kN) (C in NRCC fire resistance design equation (Kodur, 2007))
$Nu(t)$	Residual load capacity (kN)
Nu_{gap}	Nusselt number for the air gap
R	Fire resistance in NRCC design equation (Kodur, 2007) (F.R., mins)
t	Time (seconds)
$t_{a,eff}$	Effective steel thickness (mm)
$t_{c,eff}$	Effective concrete thickness (mm)
t_{FR}	Fire resistance time (mins)
t_{furn}	Time in furnace (mins)
t_i	Thickness (mm)
w	Gap width (mm)

Greek Letters

α	Buckling curve imperfection factor
α_c	Concrete utilisation factor
α_{con}	Coefficient of heat transfer by convection (W/m^{2o}C)
β	Non-dimensional parameter (FNA fire resistance design approach (CEN,2007))
γ	Non-dimensional parameter (FNA fire resistance design approach (CEN,2007))
$\gamma_{m,i}$	Material safety reduction factor
δ	Steel contribution factor
δ_{x2}	Mid-height deflection (mm)
δ_y	Axial deflection (mm)
$\varepsilon_{c1,\theta}$	Strain corresponding to $f_{c,\theta}$
$\varepsilon_{cu1,\theta}$	Ultimate concrete strain in fire
ε_i	Strain of material *i*
$\varepsilon_{i,\theta}$	Strain in material *i* at temperature
$\varepsilon_{m,i}$	Emissivity of material *i*
$\varepsilon_{p,\theta}$	Proportional strain limit for steel
$\varepsilon_{t,\theta}$	Limiting stain for yield strength
$\varepsilon_{u,\theta}$	Ultimate strain limit for steel
$\varepsilon_{y,\theta}$	Yield strain for steel
η	Concrete core efficiency factor
$\theta_{a,cr}$	Limiting temperature of steel (^{o}C)
θ_i	Temperature of material *i* (^{o}C)
λ_{Han}	Slenderness according to Han (Han and Huo, 2003)
$\lambda_{i,\theta}$	Thermal conductivity of material *i* (temperature dependent) (W/m^{o}C)
$\lambda_{p,t}$	Thermal conductivity of protection (time dependent) (W/m^{o}C)
$\overline{\lambda_\theta}$	Relative slenderness at temperature (= $\sqrt{N_{fi,pl,Rd}/N_{fi,cr}}$)
$\overline{\lambda_\theta}_{transitional}$	Transitional relative slenderness
μ	Mean of data
μ_o	Utilisation factor (N_{Sd}/N_{Rd})
ξ	Confinement factor
σ	Standard deviation of the errors
σ	Stefan Boltzmann constant (= 5.67x10^{-8} W/m^{2}K^4)

$\sigma_{i,\theta}$	Stress of material *i* at temperature (N/mm^2)
Φ	Configuration factor
χ	Buckling curve reduction factor
$\chi(\overline{\lambda_\theta})$	Buckling reduction factor dependent on relative slenderness
φ_d	Empirically derived reduction coefficient for eccentrically loading
φ_{ecc}	Empirically derived reduction coefficient for eccentrically loading (FNA fire resistance design approach (CEN,2007))
$\varphi_{i,\theta}$	Reduction coefficient to material *i* at temperature
φ_s	Empirically derived reduction coefficient for reinforcement

Chapter 1: Introduction

1.1 General

Concrete filled steel hollow structural (CFS) section columns are an efficient, cost-effective, and aesthetically pleasing means by which to support large compressive loads in buildings. These structural members consist of a hollow steel tube which is in-filled with concrete and, through composite action, superior load carrying capacity and structural fire resistance can be achieved as compared with unfilled steel tubes. The concrete infill and the steel tube work together to give several key benefits, both at ambient temperature and during fire. The steel tube acts as stay-in-place formwork during casting of the concrete, thus reducing forming and stripping costs, it provides lateral confinement to the infill concrete which can enhance the concrete's compressive strength and axial deformability, and it provides a smooth, rugged, and robust architectural surface finish; these types of members are now widely specified by engineers and architects, particularly for use in the design and construction of multi-storey buildings for which structural fire resistance ratings of two hours or more may be required (Communities and Local Government, 2007).

The composite action that is observed in CFS columns during fire means that adequate fire resistance can sometimes be achieved without the need for applied fire protection to the steel. Structural fire design guidance (ANSI/AISC, 2005; CEN, 2005, 2007; Kodur, 2007; Lennon et al., 2007) is available for many shapes, sizes, and configurations of unprotected CFS columns. In cases where calculations show that an unprotected CFS column cannot achieve adequate fire resistance, external fire protection must be applied to the steel tube, and in such cases spray applied intumescent coatings are the preferred method of fire protection in the UK (Hicks et al., 2002). However, much of the available fire resistance design guidance was developed for conventional applications based predominantly on large-scale standard fire tests of short, concentrically loaded, small-diameter columns envisioned for use in braced frames using normal strength concrete (compressive strength of 40 MPa or less). The structural performance of realistic, modern CFS columns, which may incorporate high strength and/or fibre reinforced concrete without any internal steel

bar reinforcement or externally applied fire protection, under realistic thermal and loading scenarios as would be expected for a structural frame in a real building fire, is not well known. Current fire-resistance design guidance is therefore rather limited in scope, and this makes the design of CFS columns using performance-based approaches difficult to defend to approving authorities, particularly given the inherent complexities in modelling both the thermal and structural response of CFS sections during heating.

1.2 Motivation for research

Due to the popularity of CFS columns and the paucity of available information on (or rational design guidance for) their fire performance, it has been identified that a better understanding of their thermal and mechanical response to fire is needed. Available empirically based guidance is insufficient to support performance based design. Specifically, a fundamental understanding of CFS sections' thermal and structural behaviour in fire, for both protected and unprotected sections, is needed to develop safe, economical and practical models and modelling approaches so that performance-based designs can be defensibly and rationally made. Current codified design approaches and protection design procedures are limited in scope and are therefore barriers to the widespread implementation of CFS columns in construction.

1.3 Statement of problem

Current codified design approaches are either purely empirical or limited in scope, or both. Relatively little guidance is available on the appropriate selection of the numerous design inputs required to rationally assess the performance CFS columns in fire. This limits their use in design, as engineers are forced to apply greater caution in the conservative assumptions they adopt to try to mitigate their uncertainties in the application of current fire resistant design guidance (e.g. CEN, 2005, 2007). There is considerable uncertainty in the ability of the available design guidance for the fire performance of CFS sections to accurately predict fire resistance, even in standard heating scenarios let alone natural design fires. Best practice computational modelling guidance for performance based design of CFS sections is therefore needed.

Intumescent paint fire protection systems are typically ‘designed’, or rather ‘specified’, to protect CFS sections to a prescribed limiting steel tube temperature at some predefined period of standard fire exposure (both the limiting temperature and the required period will vary from jurisdiction to jurisdiction). This is a difficult task, firstly due to a paucity of test data on the performance of intumescent coatings for protecting CFS sections in fire, secondly due to difficulties in measuring their comparatively complex thermal response in fire tests, and thirdly due to the fundamental differences in evolution of thermal gradients within protected, as opposed to unprotected, CFS sections. This results in design guidance (e.g. Hicks et al., 2002) that is extremely limited, not fully understood, and which can be empirically shown to be overly conservative for most fire protection materials.

When the conservatisms of the structural design and the design of intumescent protection systems are applied to an entire structure containing CFS columns, the costs of construction can be significantly higher compared to the same structure if it were designed with unprotected (or plain) steel or concrete elements. This results in buildings not making best use of the environmental, economic and aesthetic advantages of CFS columns, thus negatively impacting on sustainability and economic drivers. A more complete understanding of the behaviour of protected CFS columns in fire is needed.

Another area of concern is the post fire response of CFS columns, since relatively little research in this area has been conducted. The reductions in strength properties due to fire for the component steel and concrete elements that constitute a CFS column are reasonably well known; however, due to the lack of available research design tools (e.g. Han and Huo, 2003) are limited in scope. This results in the assessment of the post-fire residual capacity of CFS columns being under-predicted to ensure conservatism in the face of uncertainties, and thus designs for repair and re-use programs of structures with CFS columns after a fire will also be overly conservative. An ability to rationally predict the remaining load carrying capacity of fire-exposed CFS columns is needed.

1.4 Research objectives

The experimental and analytical studies presented in this thesis aim to analyse the available design methods, thermal and post-fire structural response of protected and unprotected CFS columns subjected to cellulosic and smouldering fires. To achieve this objective, an exhaustive literature review and meta-analysis have been conducted; numerical models have been developed and critically assessed; and small- and medium-scale thermal tests on idealised, representative CFS columns have been conducted at the University of Edinburgh and at the Worldwide Fire Protection Laboratories of an industrial partner, International Paint Ltd, Gateshead, UK. The primary objectives of the research project were:

- to statistically assess the predictive ability of current design guidance for unprotected CFS sections in fire, in light of the available experimental data;
- to develop and validate against experimental data, best-practice numerical modelling approaches to accurately and rationally predict the thermal profiles within CFS sections accounting for all necessary factors;
- to experimentally investigate, at realistic scale, the thermal response of both unprotected and protected CFS columns of various shapes and sizes under exposure to standard cellulosic and smouldering fires; and
- to investigate, both numerically and experimentally, the cause(s) of the widely known conservatism which is seen in the prescription of required thicknesses of intumescent paint protection for CFS sections, and to provide improved, rational guidance for use by designers who wish to apply protected CFS columns in real projects.

The secondary objectives of this research were:

- to perform an exhaustive survey of the existing literature, available test data, and international design information on CFS columns at ambient temperature, in fire, and residually after a fire;
- to develop an exhaustive database of available tests on CFS sections in the literature which can be used for model development and validation;

- to perform a small-scale experimental program and analytical assessment of the effect that the size of an air gap that may form between the steel tube and concrete core, due to differential thermal expansion, might have on the heat transfer across it and thus to assess its potential impacts for fire-safe design and analysis of CFS columns; and
- to perform a medium-scale experimental program and numerical assessment of the ability to predict the residual strength of both protected and unprotected CFS columns after exposure to fire.

1.5 Scope of project

The work presented in this thesis involved both small and medium-scale experimental studies as well as thermal and structural numerical analyses. The small scale experimental program consisted of tests on 15 idealised CFS heat transfer sections, fabricated from a steel plate backed by a mass of concrete, to assess the effect of air gap formation at the steel-concrete interface on heat transfer in CFS columns. The medium-scale experimental program included furnace tests on 34 unloaded, unprotected and protected, fully instrumented, full-size, short (1000 – 1400 mm) steel tubes filled with plain or hybrid steel and polypropylene fibre-reinforced concrete; assessments of the thermal response of the protected and unprotected columns were made. Nineteen of these 34 thermal test specimens, along with an additional six unheated control CFS columns were used to assess the residual structural capacity of the CFS columns after exposure to fire. Small-scale tests were performed within the Rushbrook Fire Laboratory at the University of Edinburgh, furnace tests were performed at International Paint's fire testing laboratory in Gateshead, UK, and residual structural tests were performed within the Large Structures test hall at the University of Edinburgh.

Numerical analyses involved the development and validation of structural and thermal modelling approaches to predict both the temperatures within and the structural response of (1) the small- and (2) medium-scale test specimens tested within this project; and (3) of specimens described within the literature. The

numerical work was conducted using both the finite element analysis computer program ABAQUS and various spreadsheet analyses coded by the author.

1.6 Outline of thesis

This thesis contains eight chapters. Chapter 2 presents a review of the development and design of CFS columns at ambient temperatures, in fire, and residually after a fire. The chapter begins with a history of CFS columns and how they are designed for ambient conditions. It then summarizes the numerous large scale structural fire tests conducted around the world since the 1950's and available in the literature. More than 380 tests are noted, and an in-depth analysis of the parameters and constructional detail variables under which they were tested is presented. The discussion then assesses the different thermal and structural modelling approaches which have been adopted by various researchers and design codes to analyse and predict the response of these types of elements in fire, with particular attention given to the rationality and realism of the assumptions made. The means by which different regulatory authorities allow the application and design of concrete filled steel hollow sections in fire is also discussed. The final topic treated is available information on the residual strength capacity of the columns and the testing, modelling and design recommendations that are provided in literature.

Chapter 3 presents a comprehensive statistical meta-analysis of fire resistance design approaches for CFS columns from North America (Kodur, 2007), the Eurocode 4 Annex H approach (CEN, 2005), and the French National Annex to Eurocode 4 – Annexe PCRB approach (CEN, 2007) to assess the accuracy and precision of the respective approaches. A large database of furnace test results is assembled and used to provide a statistical confidence measure for the various design approaches used for CFS sections in fire. The Eurocode design approaches in their implementation require assumed thermal profiles, which can be modelled in several ways by making a range of choices regarding modelling and material input parameters. Chapter 3 presents statistical assessments of different thermal modelling choices and approaches that are within and outside code restrictions on permissible values, in an effort to develop best-practice modelling guidance for use by practicing engineers.

Chapter 4 presents details and results of small-scale thermal tests used to assess the impact of the formation of an air gap between the steel tube and concrete core of a CFS section during fire, and the subsequent development of thermal modelling approaches based on the observed temperatures.

Chapter 5 presents the results and observations of 34 medium-scale furnace tests on CFS columns; it does this in two parts. First, tests on 14 unprotected CFS sections are presented and discussed. The results of these tests are predicted using the best-practice thermal modelling approaches derived from the meta-analysis presented in Chapter 3, and the predictions are compared to the observed thermal responses of the unprotected CFS cross-sections. Second, the results of 20 medium-scale furnace tests on protected CFS sections are presented to better understand the influence of intumescent fire protection on the thermal profiles within CFS sections.

Chapter 6 presents numerical thermal modelling of the unprotected CFS sections tests presented in Chapter 5, so that improved thermal modelling guidance for use in the structural modelling of CFS columns can be provided. Chapter 6 also assess the thermal response of the protected CFS columns presented in Chapter 5, and provides design guidance for the parameters required to prescribe the thickness of intumescent paint coatings based on a desired fire resistance and steel tube limiting temperature.

Chapter 7 presents the results and observations of the medium-scale residual strength tests to demonstrate the ability to predict the post fire structural capacity of CFS sections, and to better understand the effects that the maximum temperatures experienced within CFS sections have on the failure of thermally damaged CFS sections.

Chapter 8 presents conclusions from the experimental and numerical studies, as well as recommendations for future work and best practice guidance for the design of CFS columns both during and after fire.

Chapter 2: Review of the literature

2.1 A brief history of CFS columns

Concrete filled steel hollow sections (CFSs) have been used and researched since the early 20th century. A comprehensive historical review is given by Eggemann (2006). In 1908 William H. Burr first applied these columns successfully when constructing the McGraw Building in New York. These elements are now being used in construction around the world and for all types of buildings including: Auckland Airport in New Zealand, Fleet Place House in London, UK, the WaMu Centre/Seattle Art Museum Expansion in USA, the Shenxigou Bridge, Sichuan, and the Canton Tower, in Guangzhou, China, which is 600 m tall.

Dedicated research on CFSs started in the USA initially in 1912 by Burr, but the first rigorous results came from Swain and Holmes in 1915 (in Eggemann, 2006) who first documented systematic research and produced design formulae to determine the allowable design loads. This was followed in the 1920's by guidance from the American Concrete Institute (ACI) where limits on the allowable stress in the steel section were introduced. In the mid 1930's, sectional analysis methods to predict the "squash" load of the CFS columns, accomplished by adding the allowable loads that can be carried by the steel tube and the concrete core together, with appropriate safety factors, could be found in the available codes (e.g. DIN 1045-1943 (in Eggemann, 2006)).

At the same time, in Europe development and research into CFSs started in Germany around 1934 with work by Memmler, Bierett and Gruning (in Eggemann, 2006). Research was slowed by the Second World War but in post-war Europe the economic advantages of using a concrete infill to enhance the structural capacity of steel columns was widely utilised, most notably by the Swiss in the "Motor-Columbus" overhead power line systems (Eggemann, 2006). The concept of the 'effective slenderness' for composite columns was introduced in Germany in 1953, in which the stiffness of both the concrete infill and the steel were considered to act simultaneously (in Eggemann, 2006) and the design of concrete steel filled tubes was provided in codes (e.g. VDE 0210, 1953 (in Eggemann, 2006)). The design of CFS

columns at this point was limited to those with an effective slenderness less than 50, which in many common applications was so small as to be impractical. In 1957, Kloppel and Goder (in Eggemann, 2006) derived formulae and diagrams that aided (by comparing the radius of gyration of a composite column with that of a bare steel column) in the design of CFSs.

In the 1960s and 1970s work focused on understanding in more detail how CFS columns react under different loading conditions, including combined axial-flexural loading. Neogi et al. (1969) considered the effects of eccentric loading on the columns and Knowles and Park (1969, 1970) studied in greater detail the strength of CFS columns under pure axial loading (in Eggemann, 2006). In the mid-1970s, design rules for composite columns were drafted and made available in a specific German code based on the work of Roik, Bergmann, Bode and Wagenknecht (in Eggemann, 2006); these are used now as the basis for the simplified design methods for CFSs given in EC4 (CEN, 2004).

2.2 CFS columns at ambient temperature

2.2.1 Experiments on CFS columns at ambient temperature

The structural response and prediction of capacity at ambient temperatures of CFS columns is reasonably well understood. Goode and Lam (2008) compare the 1,819 available tests on concrete-filled sections against Eurocode 4 (EC4)'s (CEN, 2004a) failure load predictions and show that the test/prediction ratio for all the tests is 1.11. Of the 1,819 tests available, only 970 fall within the limiting criteria stated within EC4, and the authors suggest that an expansion of the limits in concrete strength should be considered, from C50/60 to C75/95 for circular columns and C60/75 for rectangular columns, without sacrificing the predictive qualities of the method. Shanmugam and Lakshmi's (2001) state-of-the-art review of composite columns comments on 580 of these test specimens and give a detailed analysis of the analytical research conducted on them. Through the available analysis and experimentation, several key aspects of the columns response are noted; these are briefly described in the following sections.

2.2.1.1 Advantages of CFS columns

The axial and flexural load carrying capacity of a CFS section is increased as compared with a hollow section. The steel hollow section confines the concrete, increasing its strength and deformability, and the load carrying capacity of the column is thus greater than the sum of its parts. There is no appreciable difference in the load carrying capacity of a CFS column if the load is applied to the whole section or solely to the concrete core. The concrete also restrains the steel tube, delaying local buckling of the steel tube wall. The steel tube acts as permanent formwork, thus increasing construction speed and efficiency and improving the sustainability of the construction technique. The capital and construction costs are reduced as well since a smaller footprint for the columns in the architectural floor plan create more useable floor area and allow smaller foundations to be used.

2.2.1.2 Failure modes of CFS columns

The failure mode of short CFS columns is dominated by compression and thus characterized by concrete crushing and local buckling of the steel tube. Slender columns tend toward failure by global buckling without visible signs of local buckling until post-peak deflections become very large. Intermediate slenderness columns fail by a combination of local buckling and yielding of the steel tube, crushing of concrete in the compressive zone and tensile cracking in the tension zone (Shanmugam and Lakshmi, 2001).

When eccentricity is applied to CFS columns, the yield strain is typically reached in the compressive zones at loads varying between 80% and 90% of the final failure load. After failure the tensile strains reach yield as the column undergoes large lateral displacements and consequently high secondary bending moments (Shanmugam and Lakshmi, 2001).

Circular cross-sections exhibit greater deformability and ductility as compared with rectangular cross-sections, a consideration which can be important in seismic areas, and a method of introducing two skins (one inner and one outer) of steel has also been developed (e.g. Tao et al., 2004) which can significantly improve the axial load and ductility of the columns. Interestingly, the ductility of single walled CFS

columns is not affected based on whether there are any mechanical connectors between the steel and the concrete (Shanmugam and Lakshmi, 2001).

2.2.1.3 Materials and sectional characteristics

The use of mechanical connectors may be necessary in some circumstances where large shear loads are present within a CFS column, or if there is a requirement to accommodate dynamic behaviour as in seismic regions. Load is transferred from the internal face of the steel tube into the concrete via friction and the interface pressure is vitally important to the efficiency of load transfer where no mechanical means are present. When loaded in shear, confined concrete has the ability to act as a diagonal compression strut within a CFS column, with the steel wall acting as a tension strut, and this can significantly improve the shear capacity of a CFS section as compared to a steel tube alone. The bond strength between the concrete and steel is dependent on the surface roughness of the inside of the tube and the variation in shape of the cross section. The bond strength has been shown to be greater in circular sections than in rectangular ones (Shanmugam and Lakshmi, 2001).

A concrete filled steel tube has a local buckling capacity about 50% more than that of an unfilled tube due to the restraint to inward buckling provided by the concrete infill. The effect of local buckling on the overall axial capacity of the column is a function of the steel plate diameter to wall thickness ratio, and most design standards account for this using an effective diameter or area (e.g. CEN, 2009a). The steel tube also limits the effects of shrinkage of the concrete as the continuously humid conditions within the tube reduce the rate of contraction during the early stages of curing.

Creep under load occurs in composite columns, and this can lower the flexural stiffness of the column over the long term, an issue which is more significant in eccentrically loaded columns, and can also cause increased lateral deflections of composite columns (Shanmugam and Lakshmi, 2001); however the extent of these effects are not well quantified in the literature.

Circular hollow sections provide considerable confinement to the concrete core which can increase its compressive resistance by up to 15% (Hicks et al., 2002), whilst rectangular sections only experience confinement in the corner regions and overall the confinement effect on the concrete is negligible. The compressive strength of concrete is increased by confinement due to the steel wall restraining the lateral dilation of the concrete core during compressive loading, and thus increases the core's plastic resistance; however, confinement does not improve the Young's modulus of concrete or the second moment of area over which they act, and so does not improve the buckling strength of a CFS column (Morino and Tsuda, 2002). The confinement effect is reduced when bending moments are applied to a CFS column, since the mean compressive strain is reduced in the concrete in these cases (Shanmugam and Lakshmi, 2001); however the bending resistance remains greater than the sum of the strengths of the steel tube and concrete due to the confinement still present (Morino and Tsuda, 2002). The effect is also reduced with increasing slenderness, since greater lateral deflections increase the secondary bending moments (Shanmugam and Lakshmi, 2001). Local buckling, if present, also reduces the effectiveness of steel confinement of the concrete core due to a loss in confining hoop stresses; this is more prevalent in square CFSs (Morino and Tsuda, 2002) due to stress concentrations at the corners.

2.2.2 Numerical studies of CFS columns at ambient temperatures

Numerous computational and analytical studies on CFS columns have been reported in the literature. Shanmugam and Lakshmi's (2001) state-of-the-art review into CFS columns notes several such studies. Also noted is the fact that a considerable amount of rigorous study is still needed to clearly identify and account for the effects of parameters such as slenderness, confinement, internal reinforcement, and sectional and material imperfections. These parameters are under increasing consideration around the world as new forms and designs of buildings are being proposed with new and novel materials specified. Research in the ambient design of CFS columns is therefore allowing more complex buildings. For example Tao et al. (2009) have experimentally analysed the behaviour of stiffened CFS columns and found that

stiffeners delay local buckling and improve confinement which increases the load capacity of the CFS columns; Liang et al. (2006) looked at the strength and ductility of high strength slender CFS columns and developed computer models, validated by experiments, to predict the ultimate strengths and axial load deflection response, allowing slender columns to be assessed rationally for design; and Mouli and Khelafi (2007) studied the use of lightweight concrete in CFS column stubs, and showed that the lightweight aggregate concrete offered higher bond strengths than normal weight concrete, so that this material could be defensibly used.

2.2.3 Design of CFS columns at ambient temperatures

Various regulatory bodies (e.g. ACI, American Institute of Steel Construction (AISC), Architectural Institute of Japan (AIJ)) provide design guidance and recommendations for the application of CFS columns in the built environment. The current thesis focuses predominantly on European design approaches, since these are the approaches which currently govern the design of CFS columns in the UK. The ambient temperature design of CFS columns in Europe is described in EC4 Part 1-1 (CEN, 2004a), giving two distinct allowable design methods for composite columns based on similar mechanics principals to those given in EC2 and EC3 (CEN, 2009a, 2010a) for steel and concrete structural design, respectively. EC4 Part 1-1 gives both a ‘simplified’ design method with fairly strict limits of applicability, and a ‘general’ design method which is comprehensive and allows for designing columns outside of the applicability limits of the simplified method. Hicks et al. (2002) provide a detailed design guide for CFS columns under ambient conditions based on the EC4 design approaches.

The EC4 simplified design method is as follows (after Hicks et al., 2002):

1. Check that the limits of the simplified design method are satisfied (described below).
2. Calculate the plastic resistance to compression, Euler buckling load, and relative slenderness of the cross-section.
3. Calculate the buckling resistance of the column.
4. Check whether second-order effects should be considered.

5. Calculate the effect of interaction between axial load and bending.
6. Calculate the longitudinal and traverse shear.

The first three of these parts form the basis of design at ambient temperature for CFS columns. The limits and restrictions referred to in Step 1 are (Hicks et al., 2002):

a) the column is doubly-symmetrical and of uniform cross-section over its height;
b) the steel contribution ratio δ ($= A_a f_{yd}/N_{pl,Rd}$) must satisfy the following conditions:
   $0.2 \leq \delta \leq 0.9$
   if δ is less than 0.2 then the column may be designed according to EC2-1-1 (CEN, 2010a), if δ is greater than 0.9, the concrete is ignored in the calculations and the column is designed as a bare steel section;
c) the maximum non-dimensional slenderness ratio of the composite column $\bar{\lambda}$ ($= \sqrt{N_{pl,R}/N_{cr}}$) is limited to 2.0; and
d) the maximum amount of internal steel reinforcement in the concrete that can be considered in the analysis is 6% of the concrete area. However, if design for fire resistance is not needed, according to EC4-1-1 (CEN, 2004a), no minimum amount of reinforcement is required, meaning that:
   $0\% \leq A_s/A_c \leq 6.0\%$.

If the column satisfies the above criteria the next step is to calculate the plastic resistance of the cross-section and its resistance to buckling. The plastic resistance is calculated by summing the resistance of the component parts (assuming that local buckling of the steel tube will not occur) as;

$$N_{pl,Rd} = A_a f_{yd} + A_s f_{sd} + A_c f_{cd} \quad (2\text{-}1)$$

where:

A_a, A_s and A_c are the areas of the steel section, the reinforcement and the concrete, respectively; and

f_{yd}, f_{sd} and f_{cd} are the design strengths of the steel, the reinforcement and the concrete, respectively.

The above equation is applicable to rectangular hollow sections filled with concrete, and does not allow for an increase in concrete strength due to confinement from the steel section acting in hoop tension. For circular hollow sections filled with concrete an enhancement of the concrete strength is allowed due to tri-axial confinement, which can increase the compressive resistance by up to 15% (Hicks et al., 2002). The enhancement depends on the slenderness of the column, and for non-dimensional slenderness of $\bar{\lambda} > 0.5$ the effect of confinement is neglected. The strength enhancement is also dependant on the level of effective load eccentricity, *e*, and should not exceed a limit of *d/10*, where *d* is the outer diameter of the section. If the element being designed is outside either of these limits the column should be designed neglecting confinement (Equation 2-1); otherwise the section can be designed using:

$$N_{pl,Rd} = A_a \eta_2 f_{yd} + A_s f_{sd} + A_c f_{cd} \left[1 + \eta_1 \, {t_a . f_y}/{d . f_{ck}} \right] \qquad (2\text{-}2)$$

where:

t_a is the wall thickness of the steel hollow section

f_y is the steel yield strength

f_{ck} is the characteristic concrete strength

$$\eta_1 = \eta_{10}\left(1 - \frac{10e}{d}\right)$$

$$\eta_2 = \eta_{20} + (1 - \eta_{20})\frac{10e}{d}$$

$$\eta_{10} = 4.9 - 18.5\bar{\lambda} + 17\overline{\lambda^2}$$

$$\eta_{20} = 0.25\left(3 + 2\bar{\lambda}\right)$$

$$e = \frac{M_{Sd}}{N_{Sd}} = \frac{\text{maximum design moment}}{\text{design applied load}}$$

To determine the plastic resistance to load, the effective flexural stiffness of the column is obtained by summing the flexural stiffnesses of each of the component parts as shown below, along with an empirical factor on the concrete calibrated from test results:

$$(EI)_{eff} = E_a I_a + E_s I_s + 0.6 E_{cm} I_c \quad (2\text{-}3)$$

where:

I_a, I_s and I_c are the second moment of area for the steel section, the reinforcement and the concrete respectively;

E_a and E_s are the initial elastic moduli for the steel section and the reinforcement respectively; and

E_{cm} is the secant modulus of elasticity for structural concrete and is equal to $[22 \cdot [(f_{ck} + 8)/10]^{0.3}]$ (CEN, 2010a)

Modifiers for long term loading conditions (i.e. to account for creep) are applicable and limits are given by Hicks et al. (2002).

The column buckling resistance is calculated using a reduction coefficient, χ, obtained from buckling curves in EC3-1-1 (CEN, 2009a) and based on the design plastic resistance. Thus:

$$N_{Rd} = \chi . N_{pl,Rd} \quad (2\text{-}4)$$

where:

$$\chi = \frac{1}{\phi + \left[\phi^2 - \bar{\lambda}^2\right]^{0.5}}$$

$$\phi = 0.5\left[1 + \alpha\left(\bar{\lambda} - 0.2\right) + \bar{\lambda}^2\right]$$

α is an imperfection parameter dependant on the buckling curve considered which for CFS elements is buckling curve "*a*" (CEN, 2004a) defined in EC3 (CEN, 2009a).

The non-dimensional slenderness is defined as:

$$\bar{\lambda} = \sqrt{N_{pl,R}/N_{cr}} \tag{2-5}$$

$N_{pl,R}$ is the plastic resistance of the composite cross section using the characteristic strengths of the materials rather than the design strengths.

The Euler buckling load is defined as:

$$N_{cr} = \pi^2 (EI)_{eff} / {l_{eff}}^2 \tag{2-6}$$

where l_{eff} is the effective buckling length of the column.

The effect of second order moments due to imperfections can be assessed and a reduction in the effective flexural stiffness obtained; there are also design methods for combined bending and compression, both of which can be found in EC4-1-1 (CEN, 2004a). The code also provides guidance on how to determine shear resistance.

2.3 CFS columns at high temperatures

2.3.1 Experimental studies of CFS columns in fire

2.3.1.1 Column furnace tests

Beginning in the mid 1950's and continuing to the present day, more than 380 large scale standard fire tests have been carried out on CFS columns of various types in fire testing furnaces. A comprehensive summary of the available test data and relevant test parameters is given in Table 2-1 to Table 2-4. These tables divide the available data into tests on (1) concentrically loaded unprotected columns (Table 2-1), (2) eccentrically loaded unprotected columns (Table 2-2), (3) concentrically loaded protected columns (Table 2-3), and (4) eccentrically loaded protected columns (Table 2-4). In all cases the thermal exposure was based on a *standard* fire (i.e. temperature versus time curve) and all thermal exposures were similar or identical to the ISO 834 fire (ISO, 1999). The main contributors to the available test

database for concrete-filled SHS are the National Research Council of Canada (NRCC) and the Comité International pour le Dévelopment et l'Etude de la Construction Tubulaire (CIDECT). In some cases, when populating the database, all of the pertinent data were not available, most notably with respect to the specific details of the observed failure modes for many of the earlier tests. A key criticism of the available data is that they all imposed uniform heating in standard furnace tests, which have numerous well-documented shortcomings (see for example Beyler et al., 2007). The key parameters noted in Tables 1 to 4 are discussed below.

Steel tube characteristics

The dimensions and strength of the steel tube section with respect to the concrete core play central roles in the fire performance of CFS columns. These parameters dictate the relative contributions of the steel tube and the infill concrete to the overall load carrying capacity of the column, both at ambient temperature and during fire. In general, unprotected columns, which rely more heavily on the steel tube, will tend to be more critical in fire since they lose a greater proportion of their strength due to heating of the external steel tube. However, various competing factors should also be considered, such as the fact that thinner walled tubes are more likely to buckle locally and this may affect both the effective length of a column during fire and its axial crushing strength. Interestingly, it appears that the specific factors leading to, and the consequences of, local buckling of the steel tube on the fire performance of CFS columns have received only limited direct research attention to date (Ding and Wang, 2008).

Standard fire tests performed to date have considered steel tube thicknesses ranging from 3.6-16 mm, with tube-to-infill cross-sectional area ratios as low as 0.9% and as high as 5.1%. Data from tests on circular sections from 121-600 mm in diameter are available in the literature, and on square sections ranging from 100-350 mm in minimum side length. However, the vast majority of tests (≈85%) have been on columns with a largest minimum dimension of less than 300 mm, and only a single test has ever been performed on a column over 478 mm in largest minimum dimension; in this case the load ratio (i.e. the ratio of the applied forces in fire conditions to the design load capacity of the member at room temperature) during

testing was unrealistically low (about 0.2). Despite the obvious practical difficulties in performing realistic fire tests on members larger than 600 mm in diameter, the lack of fire test data for very large columns is currently a limiting factor in applying available design procedures (Kodur, 2007). This is somewhat puzzling, since it seems reasonable to assume that once the fundamental mechanics of CFS columns are understood and appropriately modelled, there is no obvious reason that larger sections should not be designed using available analysis tools. Steel strengths represented in the available fire test data range from 240 to 510 MPa.

The cross-sectional shape (circular or square) of the steel SHS plays two interrelated roles in the response of CFS columns during fire; one structural and one thermal. First, as previously noted at ambient temperatures circular tubes are effective at uniformly confining the concrete core as axial loads are increased, so that the concrete is placed in a state of tri-axial stress which increases both its strength and its axial-flexural deformability; square or rectangular columns provide less effective and non-uniform confinement with only minimal increases in strength but considerable enhancements in deformability. Loss of confinement due to excessive heating of the steel tube during a fire, which in addition to reductions in the strength and stiffness of the tube may also cause separation from the core due to differential thermal expansion, will result in a greater proportional loss of strength for a circular column than for a rectangular one. Second, circular sections exposed to uniform heating will heat up uniformly, whereas square sections will heat more rapidly at the corners, potentially inducing additional thermal stresses within the cross-section which could affect the structural response to heating. Both circular and square/rectangular concrete-filled SHS have been extensively studied through furnace testing in the available literature, with over a hundred standard furnace tests performed on each shape. However, the potential influence(s) of cross-sectional shape on the issues noted above, the observed failure modes, or the performance of applied fire protection have received little direct attention.

Table 2-1: Historical furnace test data for unprotected concentrically loaded CFS columns

Researchers		Specimen details				Steel Tube					Concrete						Failure				
Name[Ref]	Date	Length	End Conditions		Load Ratio	Section Shape		Section Size	Wall Thickness	Steel Strength	Concrete Type		Strength		A_s/A_c Ratio	Cover	Time		Mode		
													28 - Day	Test			C	S	LB	GB	Cr
		m						*mm*	*mm*	*MPa*			*MPa*	*MPa*		*mm*	*min*	*min*			
NRCC[a]	1982-95	3.81	PP	5	<0.3	40	C	51	141 - 406	4.8 - 12.7	300 - 350	PC	45	24 - 91	12 - 107	-	-	48-294	62-131		24	21
			PF	-	<0.6	28	S	22	150 - 305	5 - 12.7	300 - 419	RC	12	38 - 82	38 - 93	2.1 - 2.5%	40	43-188	39-212		6	6
			FF	68	>0.6	4						FIB	16	41 - 90	39 - 100	1.77%	-	65-259	60-128		7	9
CIDECT[# b]	1954-76	3.6 to 4.8	PP	7	<0.3	7	C	17	121 - 600	3.6 - 16	240-420	PC	16	21-46	30-52	-	-	36	24-165	??		
			PF	-	<0.6	32	S	35	140 - 300	3.6 - 8	300-429	RC	33	7-95	7-95	1.3-3.7%	25-50	12-198	16-192			
			FF	45	>0.6	5						FIB	3	47-52	50-56	4.30%	-	-	19-80			
CIDECT[c]	1977-2000	0.8 to 5.8	PP	7	<0.3	34	C	19	159 - 324	3.6 - 8	286-410	PC	38	31-96	34-96	-	-	28-102	15-134	??		
			PF	4	<0.6	20	S	33	150 - 350	4 - 10	243-550	RC	12	32-99	38-99	1 - 2.9%	35-43	65-134	51-135			
			FF	41	>0.6	-						FIB	4	40-98	48-98	2.8 - 4.3%	-	77	55-81			
Han[d]	2003	3.81	PP	6	>0.6	6	C	4	150-478	4.6-8	259-381	PC	6	40-69	49	-	-	20-29	16-21	1	4	1
							S	2	150-200¢	8	341										
Suzuki[e]	1990	1.32 – 2.99	PP	9	<0.3	9	S	16	200-300	4.5-9	293-349	PC	13	28-30	28-32.6	-		-	76-152	??		
			PF	7	<0.6	7						RC	3	30	32.6	1.53%	17.5	-	78-147			
Sakumoto[f]	1993	3.5	PP	1	<0.3	1	S	1	300	9	358	PC	1	??	37.5	-	-	-	33	1*		1*
Romero[g]	2011	3	PP	1	<0.3	6	C	15	159	6	334 - 341	PC	6	??	29 - 71	-	-	11-42	-	??		
			PF	14	<0.6	9						RC	5	??	24 - 77	2.50%	16	13-65	-			
												FIB	4	??	27 - 94	1.70%	-	16-36	-			
Kim[h]	2005	3.5	PP	20	<0.6	20	C	10	319-406	7-9	304-311	PC	20	28 - 38	??	-	-	28-150	44-160	??		
							S	10	300-350	9	363										
Lu[i]	1993	0.76	FF	4	<0.3	2	S	4	150-200	5-6	467-486	PC	4	90-99	??	-	-	-	26-92	4*		4*
					<0.6	2																

Table notations : *¢ - rectangular (300 x ¢);* ** local buckling occurred first followed by crushing of the concrete; # Specimen details not fully known*

Table 2-1 references: a) Kodur and Latour 2005; Myllymaki et al., 1994; Kodur and Lie 1995; Chabot and Lie 1992; Kodur and Lie 1996b; Lie and Chabot 1992; b) Stanke 1975; CIDECT 1976; Grandjean et al., 1981a; Grandjean et al., 1981b; c) Hass et al., 2001; CIDECT 1976; d) Han et al., 2003a; Han et al., 2003b; e) Suzuki et al., 1985; Kimura et al., 1990 f) Sakumoto et al., 1994; g) DK Kim et al., 2005; h) Lu et al., 2009; i) Romero et al., 2011

Table 2-2: Historical furnace test data for unprotected eccentrically loaded CFS columns

Researchers		Specimen details					Steel Tube					Concrete							Failure					
Name[Ref]	Date	Length	End Conditions		Load Ratio		Section Shape		Section Size	Wall Thickness	Steel Strength	Concrete Type		Strength		A_s/A_c Ratio	Cover		Time		Mode		
														28 - Day	Test				C	S	LB	GB	Cr
		m							*mm*	*mm*	*MPa*			*MPa*	*MPa*		*mm*		*min*	*min*			
NRCC[j]	1990-94	3.81	PP	3	<0.3	2	C	1	219	8.2	350	PC	1	24.3	31.9	-	-		33	-	-	1	-
					<0.6	1	S	2	300	8	394	RC	2	40.7	43.8	5.07%	40		-	58-126	-	2	-
		Eccentricity ratio 15-40%																						
CIDECT[# k]	1977-82 & 2001	3.03	PP	2	<0.3	2	C	5	133-356	4-6	235-383	PC	10	30-64	30-64	-	-		33-69	22-112	??		
		to	PF	37	<0.6	24	S	35	100-300	4-12.5	234-550	RC	30	27-75	27-75	0.9-4.4%	15-43		45-56	23-92			
		5.2	FF	1	>0.6	6																		
		Eccentricity ratio 2.5-150%																						
Han[l]	2003	3.81	PP	6	>0.6	6	C	4	219-478	4.6-8	293-381	PC	6	40-69	49	-	-		7-32	20-24	-	4	2
							S	2	150-200¢	8	341													
		Eccentricity ratio 15-30%																						
Lu[m]	2003	0.76	FF	2	<0.6	2	S	2	150-200	467-486	394	PC	2	90-99	??	-	-		-	43-55	2*	-	2*
		Eccentricity ratio 12.5-17%																						

Table notations : *¢ - rectangular (300 x ¢);* ** local buckling occurred first followed by crushing of the concrete; # Specimen details not fully known*

Table 2-2 references: j) Myllymaki et al., 1994; Lie and Chabot 1992; k) CIDECT 1976; Kordina and Klingsch 1983; Klingsch and Wittbecker 1988; Renaud and Joyeux 2001 ; l) Han et al., 2003a; Han et al., 2003b; m) Lu et al., 2009.

Table 2-3: Historical furnace test data for protected concentrically loaded CFS columns

Researchers		Specimen details					Steel Tube					Concrete							Failure				
Name[Ref]	Date	Length	End Conditions		Load Ratio		Section Shape		Section Size	Wall Thickness	Steel Strength	Concrete Type		Strength		A_s/A_c Ratio	Cover		Time		Mode		
														28 - Day	Test				C	S	LB	GB	Cr
		m							*mm*	*mm*	*MPa*			*MPa*	*MPa*		*mm*		*min*	*min*			
CIDECT[n #]	1971-75	3.6	PP	2	<0.3	3	C	5	168-219	3.6-12.5	300-360	PC	33	18-51	??	-	-		-	46-290	??		
			FF	43	<0.6	12	S	40	140-330	3.6-8	355-388	RC	12	45-47	41-55	1.1-3.7%	25-33		64-90	35-130			
					>0.6	30																	
		Intumescent Paint - 15 (1 - 2 kg/m^2), 6 - Rock Wool, 2 - Liquid Stone[¥], 9 - Vermiculite Boards, 4 - Plaster, 3 - Plaster Shells, 2 - Alphapan[§], 4 - Asbestos Cement																					
Suzuki[o]	1990	2.99	PP	4	<0.3	2	S	4	200-300	6-9	313-327	PC	4	28	28	-	-		-	120[$]	??		
					<0.6	2																	
		Rock Wool (30mm thick) – 4																					
Sakumoto[p]	1993	3.5	PP	4	<0.3	4	S	4	300	9	358-361	PC	4	??	38	-	-		-	166-194	4*		4*
		Ceramic Board – 3 Intumescent Paint -1 (1.25 kg/m2)																					
Han[q]	2003	3.81	PP	11	>0.6	11	C	5	150-478	4.6-8	259-381	PC	11	18-69	19-49	-	-		120-196	78-169		10	1
							S	6	150-350¢	5.3-8	246-341												
		Intumescent Paint - 11 (4.4 - 10 kg/m^2)																					
Edwards[r]	1997	3.6	FF	6	<0.6	5	C	2	168-324	6.3	306-321	PC	6	34-43	43-48	-	-		115-166	102-146	??		
					>0.6	1	S	4	150-300	6.3-16	331-375												
		Intumescent Paint - 6 (0.8 - 1.1 kg/m^2)																					

¢ - 4 rectangular, 2 square *; * local buckling occurred first followed by crushing of the concrete # Specimen details not fully know*

¥ - Liquid Stone protection consisted of vermiculite particles mixed with a synthetic stone produced by a reaction of calcite and portlandite

§ - Alphapan is a form of protection consisting of panels cut from plates made of agglomerated rock fibres

Table 2-3 references: n) CIDECT 1976; o) Suzuki et al., 1985 p) Sakumoto et al., 1994; q) Han et al., 2003a; Han et al.,2003b; r) Edwards 2000.

Table 2-4: Historical furnace test data for protected eccentrically loaded CFS columns

Researchers		Specimen details					Steel Tube				Concrete						Failure				
Name[Ref]	Date	Length	End Conditions		Load Ratio		Section Shape	Section Size	Wall Thickness	Steel Strength	Concrete Type		Strength		A_s/A_c Ratio	Cover	Time		Mode		
		m						*mm*	*mm*	*MPa*			28 - Day *MPa*	Test *MPa*		*mm*	C *min*	S *Min*	LB	GB	Cr
Sakumoto[s]	1993	3.5	PP	4	<0.3	3	S	4	300	9	358-361	PC	4	??	38	-	-	-	88-148	-	4	-
					<0.6	1															
		Ceramic Board – 3					Intumescent Paint -1 (1.25 kg/m^2)					Eccentricity ratio		10%							
Han[t]	2003	3.81	PP	1	>0.6	1	S	1	350	8	284	PC	1	18	19	-	-	-	108	-	-	1
		Intumescent Paint -1 (2.8 kg/m^2)										Eccentricity ratio		30%							

Table 2-4 references: s) Sakumoto et al., 1994; t) Han et al., 2003a; Han et al., 2003b

Abbreviations used in Tables 1 - 4 : PP – Pinned-pined, PF – Pinned-fixed, FF – Fixed-fixed , C – Circular, S – Square, PC – Plain concrete, RC – Reinforced concrete, FIB – Fibre reinforced concrete, As – Cross-sectional area of steel, Ac – Cross-sectional area of concrete, LB – Local buckling, GB – Global buckling, Cr – Crushing.

Concrete infill material

The type of concrete infill within the CFS column (plain concrete (PC), rebar reinforced concrete (RC), or fibre reinforced concrete (FIB)) drastically affects its fire performance. Unprotected PC filled CFS columns fail at comparatively low loads when exposed to fire. Rapid loss of strength and stiffness of the fire exposed steel tube as temperatures increase cause loads to be shed to the concrete and, depending on the level of axial and flexural loads in the section, eventually lead to excessive local stresses in the concrete which cause failure as the concrete absorbs energy, the micro structure starts to deteriorate, creating micro cracks, and the concrete loses its continuity and thus its capacity to carry load (Kodur, 2007). PC filled CFS columns have particularly low fire resistance when load eccentricity, flexural loads, or second order effects play significant roles. PC infill has been used in the majority of tests available in the literature (≈68%), whereas RC and FIB infill have been used in 25% and 7% of the tests, respectively.

Of the available fire tests on CFS columns, 79% have used concrete with $f_c' < 50$ MPa and only 8% have used $f_c' > 70$ MPa. This tendency toward lower concrete strengths reflects the fact that the bulk of the tests (≈63%) were performed prior to 1980, so that the tested concrete strengths were representative of mixes being used in construction at that time; these are not, however, reflective of current practice. Concrete specified in CFS columns in current multi-storey building designs tends toward 70 MPa or higher; this is clearly reflected in the literature by the recent emergence of studies focused specifically on the response to fire of CFS columns with f_c' up to 100 MPa (Han et al., 2003; Hass et al., 2000; Kodur and Latour, 2005; Lu et al., 2009).

Not surprisingly, the introduction of internal steel reinforcement within the concrete core considerably increases the fire resistance of a CFS column, in particular when flexural effects are present. In addition to carrying a portion of the total loads on the column once the steel tube is heated, the internal steel reinforcement also acts to decrease the propagation and localization of cracks within the concrete and slows the loss of strength on further heating (Myllymaki et al., 1994). As is the case for conventional RC columns, the increase in fire performance depends on many factors,

although the reinforcement ratio and amount of concrete cover to the internal reinforcement within the concrete core are key factors.

Core steel reinforcement ratios between 1.0-5.1% have been tested, although the vast majority (> 80%) have used between 1.0-3.0% with various internal layouts, typically using between four and eight longitudinal bars with square ties or steel spirals This is comparable to (perhaps slightly lower than) that which would typically be found in conventional concrete columns. Reinforcement ratios above 3.0% have been shown to provide comparatively little benefit for improved fire resistance (Stanke, 1975).

While RC filled SHS columns perform well in fire and can typically be designed without any need for applied fire protection, there are many practical concerns associated with the placement of the internal steel cages which can be difficult, costly, and time consuming. Thus, RC infill is not favoured in modern CFS column designs. There is a clear trend toward the use of PC infill which, although the least costly option and the most easily placed, considerably reduces fire resistance and can force the use of applied fire protection (bringing additional costs and construction issues). One possible means to avoid having to use applied fire protection, first examined in the late 1970s (CIDECT, 1976) with limited success, but subsequently studied in additional detail with increased success (Kodur and Lie, 1995), is to use FIB infill. The advantage of FIB over PC infill is that suitably proportioned steel fibres within the concrete arrest the propagation of micro cracks and improve the continuity of the concrete core and its ability to carry load. Furthermore, the fibres enhance the tensile strength of the infill concrete, potentially allowing it to carry tensile forces due to small flexural effects (although this has yet to be experimental confirmed). The fibres also slightly increase the compressive strength of the infill (Kodur, 2007). Research studies at NRCC have shown that FIB infill can provide fire resistance values which are comparable to those of RC filled SHS columns (Kodur and Lie, 1996a), although this has only actually been demonstrated for concentric loading for a single steel fibre type and volume content (1.8% by mass). FIB infill reduces the likelihood of internal concrete spalling and separation and thus alleviates the potential problems of lack of continuity in the concrete. Hybrid fibre reinforced

concrete (incorporating both polypropylene (PP) and steel fibres) may further enhance performance in fire, based on anecdotal evidence from PP fibre suppliers. The mechanics of FIB infill CFS columns in fire remain poorly understood, and additional research is needed.

The type of aggregate used in the concrete also plays a role during fire. Different aggregates may result in an order of magnitude difference in the coefficient of thermal expansion of the core. This may impact heat transfer within the section and the formation and size of the air gap at the steel-concrete interface. It may also affect the transfer of load from the steel tube to the concrete core, and hence the column's deformation and ultimate failure mode. Only limited research has considered the possible effect(s) of aggregate type on CFS columns. For instance, an NRCC study (Chabot and Lie, 1992) showed that a siliceous aggregate RC in-filled CFS column tested at a load ratio of 0.58 had half the fire endurance of an equivalent CFS column with carbonate aggregate infill tested at the same load ratio. Considerations around aggregate types may become important in the future as sustainability concerns force contractors to use locally sourced materials.

Spalling of the core concrete of CFS columns has not been commonly observed within the reported tests, due to the reduced heating rates applied to the concrete as a result of the steel tube acting as a protective and homogenizing layer. The steam pressure that builds up within a CFS section as a result of water vaporisation is allowed to egress through 20 mm diameter vent holes which are typically positioned at the top and bottom of the section in question. Without these vent holes there is a possibility of the section rupturing violently under the influence of high temperatures.

Slenderness and rotational restraint

The relative slenderness and end fixity of the tested specimens is crucial when considering their response to fire, particularly in terms of their observed failure modes since slender columns are more likely to fail by *global* buckling whereas short columns will fail by *local* buckling and/or crushing of the core. Column lengths between 760-5800 mm are represented in the literature, although the vast majority

(≈83%) are between 3030 and 3810 mm (i.e. a single storey height). This is due to the reasonably consistent size of available standard fire testing facilities globally. The lack of data from realistic fire tests of slender CFS columns is currently claimed to limit their application in many applications (Kodur, 2007). However, the most slender CFS columns reported in the literature have non-dimensional slenderness (calculated according to Eurocode procedures (CEN, 2005, 2008a; Lennon et al., 2007)) of about 1.3. This slenderness is well within the practical range for CFS columns that are likely to be considered in all but a small minority of practical design situations.

Several column end fixity combinations are represented in the literature and are given as: fixed-fixed (FF), pinned-fixed (PF), and pinned-pinned (PP). The majority of tests (≈64%) have been on FF members, although it is worth noting that the true fixity achieved during furnace testing is never perfect and is probably not known. It should also be noted that columns are rarely heated over their entire height during furnace testing (for instance, in the NRCC testing furnace columns are heated over 80% of their total length (Chabot and Lie, 1992; Kodur and Lie, 1995, 1996a) with the ends insulated). This has potentially important implications, particularly for FF and PF columns when relating the non-dimensional slenderness at ambient conditions to the effective slenderness of the column during a fire test. Unheated regions will maintain their full flexural stiffness during a fire test, which artificially reduces the assumed effective slenderness during the test as compared with a column in a real building. Furthermore, there is compelling evidence from non-standard furnace tests performed on CFS columns which included load introduction regions with beams framing into the columns during the tests, that end fixity, load introduction, axial load ratio, and steel tube thickness all influence both the likelihood and location of local buckling of the steel tube during fire – the location of the local buckle dictating plastic hinge formation and being the primary factor determining the effective length of the column during a fire (Wang and Davies, 2003). Thus, FF and PF furnace tests may be unconservative with respect to the true effective length of CFS columns during fire, unless the true end fixities of the tested columns are accounted for in considerable detail.

This effective length issue is particularly noteworthy given that Eurocode (CEN, 2005) provisions permit the effective lengths of columns in non-sway frames to be taken as 0.5 during fire if the columns are continuous across multiple floors, whereas certain test data suggest that local buckling of the steel tube, typically at the top of the heated length, may lead (unconservatively) to an effective length of about 1.0 times the storey height, regardless of the end fixity condition or vertical continuity (Wang and Davies, 2003).

Load eccentricity and bending

The relative importance of load eccentricity and bending depends predominantly on the type of concrete infill. The majority of available tests (>80%) have been on CFS columns under concentric load. Intentionally applied load eccentricity ratios between 2.5% and 150% are present in the literature. However, the only rational way to test the specific impacts of load eccentricity for various types of concrete infill would be to test identical CFS columns with different initial load eccentricities but at the same load ratio; such comparative data do not exist.

The available data clearly show that CFS columns filled with PC are highly sensitive to load eccentricity, and that they suffer major reductions in fire resistance under loads of increasing eccentricity (all other factors being equal). This is clearly due to the fact that PC infill is severely limited in its ability to carry flexural loads once the steel tube heats and sheds its load to the concrete core. Unprotected CFS columns with PC infill are generally not used where load eccentricity or bending (including slenderness effects) are expected during a fire. When identical CFS columns with PC infill are tested under different initial load eccentricities but at the same fire test load ratio, the specific impact of eccentricity is less severe, although the available data are highly contradictory. For unprotected PC filled CFS columns with identical load ratios the available data (Han et al., 2003; Lu et al., 2009) suggest that initial eccentricity ratios as high as 30% may have no obvious detrimental effect on fire resistance (albeit with fire resistances of less than 30 min in all cases). For fire protected PC filled CFS columns, however, limited data (Sakumoto et al., 1994) show that eccentricity ratios of only 10% may cause reductions in fire resistance of up to 40% (with a fire resistance of 166-188 minutes for concentric loading). For

unprotected CFS columns with RC infill, no negative influence of eccentricity or bending is expected within the practical range of internal steel reinforcement ratios for columns with the same load ratio (Kordina and Klingsch, 1983).

While research has suggested that use of FIB infill can improve the fire performance of concentrically loaded CFS columns with unreinforced concrete infill, the benefits of FIB infill for columns with eccentric loads and/or bending have not been properly investigated to date.

Load ratio

In practice, the load ratio for a structural member typically lies somewhere in the range of 0.3 to 0.5 (Buchanan, 2002); in some cases up to 0.6 depending on a multitude of ambient temperature design considerations. The fire resistance of any type of column is explicitly linked to the sustained load applied during testing, with higher load ratios leading to lower fire resistance ratings. Load ratios of less than 0.3 (≈30% of available tests) are likely to be unrealistically low, and greater than 0.6 (≈21% of available tests) unrealistically high for most typical applications. Furthermore, it is important to consider the eccentricity of the applied load and the resulting reduction in nominal strength at ambient (due to axial-flexural interaction) when quoting the load ratio imposed during a fire test.

Failure modes

The four typical stages of deformation of a concentrically loaded CFS column in fire are well documented in the literature (see Wang and Orton, 2008). In Stage I, the steel tube heats up and expands both in the horizontal (radial) and vertical (longitudinal) directions. The steel, having a higher coefficient of thermal expansion and heating more rapidly than the concrete core, expands at a faster rate than the concrete infill and this can create an air gap between the steel tube and the infill and allow the steel to expand unrestrained. The precise consequences of this expansion in the hoop direction are not well known, although it appears that there are both thermal effects (i.e. reduction of heat transfer to the concrete and effective insulation of the back face of the steel tube) and structural effects (i.e. removal of support against local buckling of the tube side-wall). In the axial direction thermal expansion of the

tube causes it to carry more of the gravity loads as it expands but is restrained by the floors above. This longitudinal expansion continues until the tube takes so much of the load that it yields locally in compression and rapidly shortens and transfers load back to the core (Stage II). Provided that the column remains stable during this contraction (which is notably *not* assured) the load will continue to be carried by the cooler concrete core with only minor changes in column length as the fire continues (Stage III). In the best case, the core continues to carry the load until there is sufficient degradation of the concrete that the load can no longer be supported, and the column fails (Stage IV).

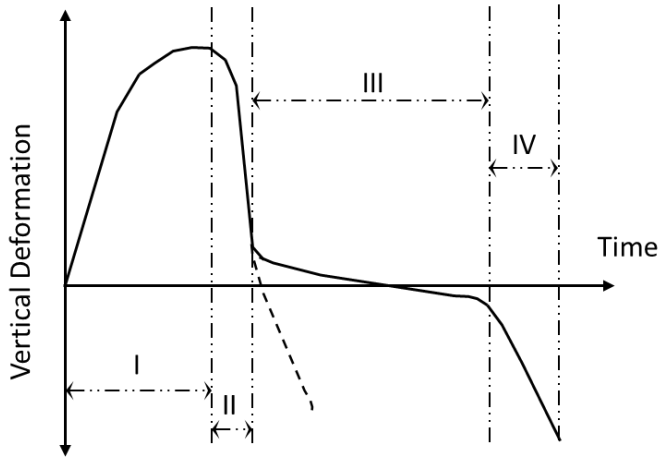

Figure 2-1: Stages of deformation of CFS columns in fire (after Wang and Orton, 2008)

It is unfortunate (although not surprising) that many of the available testing reports from furnace tests on CFS columns devote relatively little attention to describing the observed failure modes in any significant detail, since this information is of fundamental importance in understanding the mechanics at play during fire. Tests have generally been grouped into two broad categories: buckling and crushing (shown in Figure 2-2). *Global* buckling failures occur when three locations of little to no rotational restraint (hinges) develop a collapse mechanism in a column and large lateral deflection of the column occurs. The hinge locations are invariably associated with areas of *local* buckling of the steel tube, and it should be noted that the factors influencing the formation of these hinge regions (including load introduction,

rotational restraint, inter-storey effects, localized heating) remain poorly understood (Wang and Davies, 2003). As expected, buckling failures are more prevalent in slender columns with eccentrically applied loads. Crushing failures occur where the degradation of the core concrete's compressive strength and integrity is sufficient that the load can no longer be supported. Such failures are typically accompanied by *local* 'elephant's foot' buckling of the steel tube at the crushing location. This local buckling has apparently been observed coincident with the majority of crushing failures; however the location of these local buckles is not consistent from test to test. Clearly, the buckle location will impact the crushing and global buckling capacities and should be clearly reported in future tests. Of the available tests for which failure modes are clearly quoted (≈96 tests), 47% are stated as global buckling and 53% as crushing/local buckling

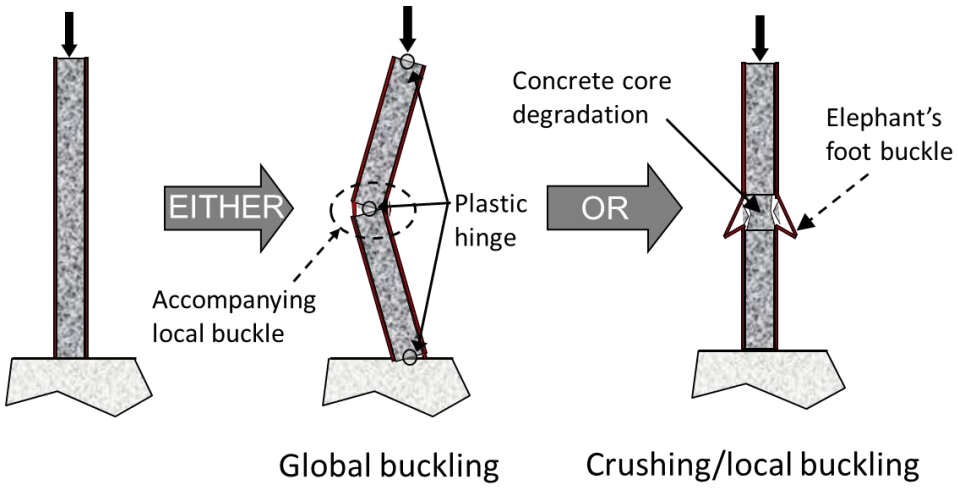

Figure 2-2: Possible failure modes of CFS columns in fire

Finally, it must be noted that not all CFS columns are able to transition from Stage II to Stage III, and some CFS columns fail shortly after first yielding or local buckling of the SHS tube. As discussed by Wang and Orton (2008), whether a CFS column is able to pass through all four stages of deformation depends on many factors, although risk factors include slenderness, low internal reinforcement ratio, high applied load, load eccentricity, and (for reasons unknown) stiff rotational restraint 'at the top'. Wang and Orton (2008) state that there is currently no simple method to identify CFS columns that are *not* able to go through all four stages; clear evidence

of a fundamentally incomplete understanding of the mechanics and interactions leading to failure.

Small-scale sectional tests

Huo et al. (2009) tested 3 stub column specimens in an electric furnace. Two of the specimens were instrumented to measure the temperature during a heating and cooling regime, whilst the third test was loaded to 20% of its axial load capacity at ambient and was heated up to a sustained temperature of 800^{o}C until it failed. The tests showed that the temperature of the steel decreased as soon as the furnace temperature started to enter the cooling phase, whilst the temperature at the centre of the concrete continued to increase past this point and peaked shortly afterwards. The temperatures then started to converge as the furnace continued to cool.

Han et al. (2003) also looked at the temperature field within rectangular CFS columns with and without fire protection subjected to the ISO 834 standard fire. They surmised that the effect of the tube dimension had a greater impact on the concrete core temperature than on the steel temperature and that this effect decreased in severity as the dimension exceeded 400 mm and three hours of heating. They also showed that a thickness of 5 mm of fire protection material was equivalent to 25 mm of concrete protective cover. They attempted a finite element heat transfer prediction of the internal temperatures, but with considerable variability and a lack of consistency and repeatability.

Ghojel (2004) is one of few authors to present work on the interface thermal conductance across the air gap which typically forms between the steel section and the concrete core in CFS columns. In this testing, specimens were circular concrete filled galvanised steel sections filled with plain (i.e. unreinforced) concrete. The CFS sections were heated in an electric furnace. The mean furnace temperature reached a maximum of 900^{o}C.

Ghojel (2004) suggests that the interface conductance, (h_j), can be considered as the sum of the contact conductance, (h_c), and the gap conductance, (h_g). The results of the testing showed that as the steel temperature increased the conductance at the

interface decreased and, assuming that the contact conductance remained uniform with steel temperature, the determining factor became the gap conductance, which was determined by the thermal conductivity of the gap material and the gap width. When the steel temperature rises above 200^{o}C, the water within the concrete near the interface has mostly evaporated into steam and as a result the interface conductance begins to plateau. This could be due to two countering actions, (1) the increasing gap dimension reducing conductance and (2) increased thermal conductivity of superheated steam within the gap, thus increasing the conductivity.

Ghojel (2004) proposed a correlation to determine the interface conductance (h_j) between the temperature of 25-700^{o}C for unloaded columns:

$$h_j = 1926 - 765.8 \cdot \exp(-339.9 \cdot \theta_a^{-1.4}) \quad (2\text{-}7)$$

where θ_a is the steel temperature.

For loaded columns, Ghojel (2004) calibrated the above correlation against a test reported in the literature by Lie (1994), which reduced the effect by a factor of 12 to:

$$h_j = 160.5 - 63.8 \cdot \exp(-339.9 \cdot \theta_a^{-1.4}) \quad (2\text{-}8)$$

The reason for this is thought to be the increase in load due to the axial thermal expansion of the steel being restrained by the support conditions and thus increasing lateral expansion potentially increasing the gap size and reducing the gap conductance.

2.3.1.2 Fire protection using intumescent paint

One of the most popular forms of protecting steel from the effects of fire is to use an intumescent paint (reactive coating). An intumescent coating is one that is unobtrusive at room temperature but under the influence of heat, expands up to a hundred times its original thickness and produces a multi-cellular char layer which acts as a thermal barrier between the fire and the steel. The thermal properties of the char are variable with time and temperature and dependent on how the char forms, which is directly dependant on the heating exposure. The vast majority of the

available fire testing on intumescents used in the built environment was conducted under standard fire conditions (e.g. ISO 834 (ISO, 1999)), which is not necessarily representative of many real fire scenarios.

Intumescents generally have three active ingredients; an acid source, a carbon or charring source and a blowing agent, bound together in a binding polymer (Duquesne et al., 2004). When the intumescent coating is heated, several reactions occur and to form a good insulative layer these reactions have to take place in the correct order and timing. Under heating the coating initially melts and forms a viscous material; at the same time the acid source breaks down to yield a mineral acid as a catalyst. This catalyst reacts with the charring source to yield the carbon char, whilst the blowing agent decomposes to release gases (Zhang et al., 2012). These gases, in part, get trapped in the viscous fluid layer causing the coating to swell rapidly. As the temperature increases the viscous fluid layer hardens and the carbon char oxidises leaving a protective insulating layer (Zhang et al., 2012). After the char has formed it begins to degrade with increasing temperature and will gradually reduce in volume and effectiveness. If the above reactions occur out of order the intumescent char does not form correctly and the protection is less effective.

For intumescents applied to columns, the testing standards prescribe (CEN, 2002, 2010b) a set minimum number of tests that need to be reported and used to calculate the required thickness of fire protection to ensure that a prescribed limiting temperature is not reached for the required duration of exposure to the standard fire. Tests are conducted on loaded and unloaded columns to measure the temperature within the steel sections and the efficiency and robustness of the intumescent coating under exposure to a standard fire in a furnace. The coatings are also sometimes tested under different (more or less ‘severe’) heating regimes to ensure that they are able to react properly in all credible thermal and mechanical loading situations. This is due to intumescent being comparatively expensive to test and apply, so the optimisation of an intumescent’s insulation properties for a range of temperatures and sections is practically very important to manufacturers.

The thickness of the intumescent film coating applied to protect a structural element is prescribed in its so-called dry film state, commonly reported in tabulated form and based on the limiting temperature of the steel, the required fire resistance duration, and the structural element's 'section factor'. The section factor, H_p/A, of a structural member is the ratio of the heated surface area of the section to its volume, which, if the element has a uniform cross section over its length, is equivalent to the heated perimeter, H_p, divided by the cross-sectional area, A. The tables will be for a specific time period for which the element in question has to resist the fire insult (Communities and Local Government, 2007).

For steel sections the resistance is usually found by calculating the 'critical temperature' at which the element will fail in the standard fire scenario and can range from 350-700^{o}C. The limiting temperature calculation for a steel section in Europe is given by EC3 (CEN, 2009b) as:

$$\theta_{a,cr} = 39.19 \cdot \ln\left[\frac{1}{0.9674 \cdot \mu_0^{3.833}} - 1\right] + 482 \qquad (2\text{-}9)$$

where μ_0 is the utilisation factor (the ratio of the design load in the fire situation to the design resistance of the member at ambient conditions)

The required dry film thickness (DFT) of the intumescent is then tabulated using empirical data from furnace tests for different DFTs, critical temperatures and fire resistance times, with reference to the section factor of the element, H_p/A. For hollow steel tubes the section factor is taken as equivalent to $1/t_a$ where t_a is the steel wall thickness.

2.3.1.3 Intumescent fire protection of CFS columns

As noted in Section 2.3.1.1, PC in-filled CFS columns may require some kind of applied fire protection to achieve required fire resistance ratings in some applications. While spray-applied and board systems of fire protection have been applied to CFS columns, intumescent coatings are the preferred method of fire protection for these types of members. Many different, proprietary intumescent paints are available, and it is impossible to make generalizations regarding their thermal insulation characteristics. While many hundreds of certification tests have

been performed in furnaces on hollow SHS tubes protected with intumescent paints, relatively few such tests are available on CFS columns (particularly under load).

Approximately 24 furnace tests are available in the literature that report on the use of intumescent fire protection during structural fire tests of CFS columns. These tests show that the coatings dramatically improve fire performance and are particularly of interest for achieving fire resistances of more than 30 minutes, although the evolution of thermal protection and its influence on the temperature profile across the section remain poorly understood. For instance, the temperature gradient along the developing char, which will be directly related to the heat input as a result of the substrate's thermal response, can affect the evolution of an optimum insulating char layer, and most currently available intumescent paints have been carefully optimized to perform on unfilled steel sections or profiles rather than on CFS columns. For any intumescent coating to function optimally in a fire, the substrate needs to heat up at the 'correct' rate, which demands conformance tests specific to CFS columns; these exist only rarely and for specific products (Edwards, 2000). The heat sink effect of infill concrete can possibly be translated to a lower "effective" section factor, as suggested by Edwards (2000). The main criterion for any intumescent formulation in this application is to be able to cover section factors of about 300 m^{-1} as well as a lower range of section factors that could include CFS columns. However, it should be noted that at very low section factors certain intumescent products may crack and de-bond prior to intumescing. There is a paucity of reliable thermal property data for intumescent systems (Wang and Orton, 2008) and very little is known about the influence of the heat sink effects of the concrete infill, or the formation of a gap between the steel and the concrete, on the evolution or "stickability" of the intumescent char.

The specification of intumescent fire protection for CFS sections cannot be the same as that of plain steel due to the concrete core's ability to provide structural strength but also to its property of a means of heat transfer away from the steel, so that the temperature of the steel is no longer the only critical structural component in the element. One of the methods currently used to account for the concrete core's effect is to increase the "effective" steel wall thickness and calculate an "effective" section

factor to account for the presence of the concrete core. The effective wall thickness under this treatment is given by (Hicks et al., 2002):

$$t_{a,eff} = t_a + t_{c,eff} \tag{2-10}$$

with:

$$t_{c,eff} = \begin{cases} 0.15 b_i, & b_i < 12\sqrt{t_{FR}} \\ 1.8\sqrt{t_{FR}}, & b_i \geq 12\sqrt{t_{FR}} \end{cases} \tag{2-11}$$

where t_a is the steel wall thickness, $t_{c,eff}$ is the effective increase in wall thickness due to the concrete, b_i is the minimum cross sectional dimension of the concrete core, and t_{FR} is the fire resistance time. The section factor is then calculated using the surface area of the steel and the effective area of the steel based on $t_{a,eff}$, and the fire protection thickness can be determined in the conventional manner (i.e. by the use of tabulated empirical data from furnace tests on plain steel sections).

Only limited data are available on the appropriate critical temperatures for use when designing CFS columns. One of the only contributors in this area is Edwards (2000), who through experimental testing derived the following purely empirical adjustment to the limiting temperature of the steel for protected sections:

$$\frac{\theta_f}{\theta_l} = 0.988 + 0.643 \cdot \alpha_c \tag{2-12}$$

where θ_f is the limiting temperature of the steel component of a CFS column to be used in defining the required fire protection, θ_l is the limiting temperature of the steel based on an unfilled section (Equation 2-9) and α_c is the concrete contribution factor, which is taken as $(0.6 \cdot f_{cu} \cdot A_c/\gamma_c)/\left[(0.6 \cdot f_{cu} \cdot A_c/\gamma_c) + \left(f_y \cdot A_s/\gamma_s\right)\right]$. Edwards' tests, however, were conducted with only one type of intumescent coating and only on six individual specimens, and more tests need to be conducted with a larger variety of coating types in order to verify its applicability for loaded columns.

2.4 Structural materials at elevated temperature

2.4.1 Steel in fire

Steel when heated undergoes several thermal and mechanical changes. The mechanical and thermal properties of steel at high temperature are reasonably well understood and tests around the world seem to show good correlations and repeatability, such that there is confidence in the material models currently being used in design.

2.4.1.1 Mechanical properties

The stress-strain response of steel changes significantly at high temperature. Tests by Kirby and Preston (1988) on S275 steel ("*S*" referring to the steel as structural, "*275*" refers to the yield strength of the material (i.e. 275 N/mm^2)) showed that strain hardening at elevated temperatures occurs all the way through the plastic range, leading to the replacement of a yield plateau with a gradual increase of strength when the strain increases.

In ambient temperature design the steel yield plateau is critical as it defines the design yield strength of the material at a given strain. This approach cannot strictly be used at high temperature. Beam tests by Kirby and Preston, (1988), showed strains in excess of 3%, which included the thermally induced strains. The stress related strains in the steel were in the order of 2-3%. So for steel members in bending a conservative limit of 1.5% strain for yield strength has been introduced.

The Eurocodes (CEN, 2005, 2009b) for steel and composite members appear to use the results from Kirby and Preston (1988) to derive reduction factors for the effective yield strength, $f_{ay,\theta}$, (related to a 2% strain limit), the proportional limit, $f_{ap,\theta}$, and the slope of linear elastic range, $E_{a,\theta}$. Figure 2-3 illustrates the variation of the EC mechanical property reduction factors for steel with temperature. It can be seen that the stiffness of steel reduces earlier and more rapidly than its strength; this can have important effects on failure mode.

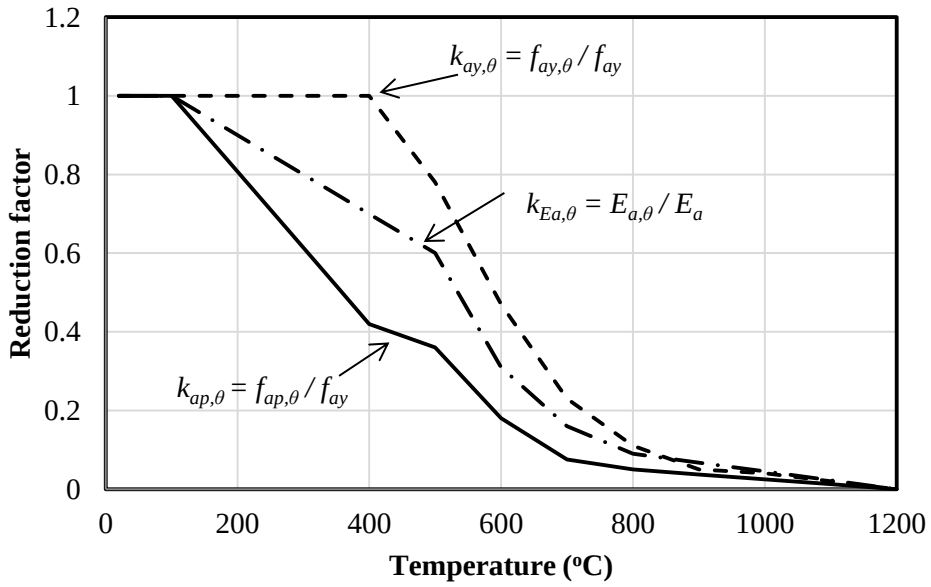

Figure 2-3: Reduction factors for mechanical properties of structural steel suggested in EC3 (CEN, 2009b)

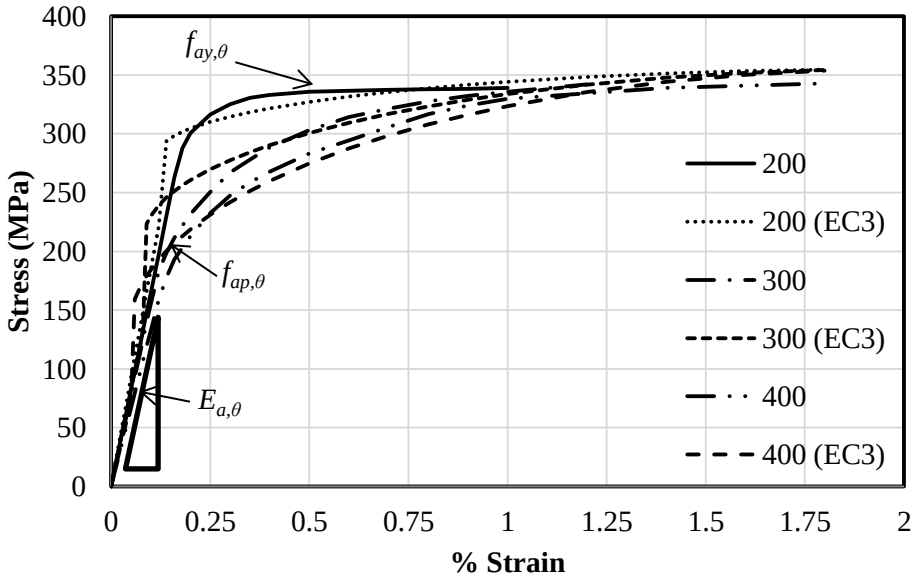

Figure 2-4: Comparison of stress versus strain curves suggested by Kirby and Preston (1988) and EC3 (CEN, 2009b) at temperatures of 200, 300 and 400°C

The stress-strain relationship of steel at any given temperature, shown in Figure 2-4 according to the Eurocodes, defines the reduction factors shown in Figure 2-3. The initial stage is a linear progression up to the proportional limit, $f_{ap,\theta}$, with a slope equal to the elastic modulus, $E_{a,\theta}$. The second stage is an elliptical progression from the elastic to the plastic range of the curve, from the proportional limit, $f_{ap,\theta}$, to the effective yield strength, $f_{ay,\theta}$. The third stage is characterised by a plateau at yield stress up to a limiting strain of 15% (CEN, 2009b). The Eurocodes "implicitly" consider the effect of creep in its material model; in EC3 (CEN, 2009b) a method to incorporate strain hardening is introduced.

2.4.1.2 Thermal properties

Thermal conductivity and specific heat capacity

The thermal conductivity of steel decreases in an almost linear fashion with increasing temperature up to about 800^{o}C, after which point it remains fairly constant. Kodur et al. (2010) review the thermal conductivity of steel as well as its specific heat capacity, as shown in Figure 2-5 and Figure 2-6, respectively. The Specific heat capacity of steel slowly increases with temperature up to a point around 750^{o}C where a large spike occurs. This is due to an endothermic molecular phase change within the material that consumes energy. There are discrepancies in various design codes as to the severity of the energy required to facilitate the phase change, and Kodur et al. (2010) state that this is due to a paucity of test data.

Thermal expansion

Kodur et al. (2010) also present a summary of tests on the thermal elongation of steel. The results show that as the temperature increases the thermal expansion increases up to nearly 750^{o}C. At this point, where the phase change in the metal occurs, a shallow decreasing curve to 800^{o}C is apparent. After this the thermal strain begins to increase again at essentially the original rate.

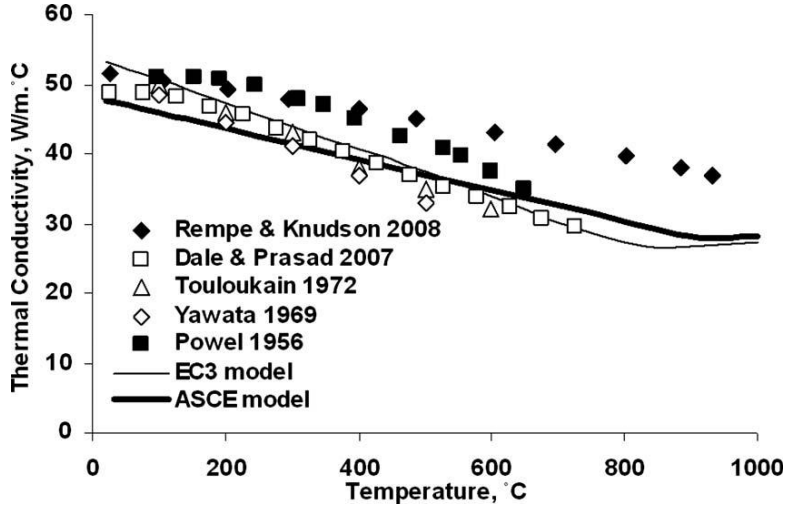

Figure 2-5: Comparison of design models and experimental data for thermal conductivity of steel (reproduced from Kodur et al., 2010)

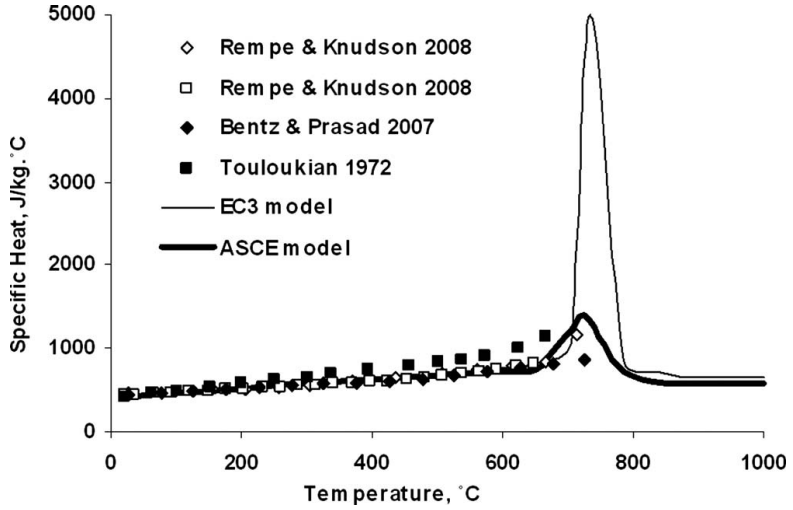

Figure 2-6: Comparison of design models and experimental data on the specific heat capacity of steel (reproduced from Kodur et al., 2010)

Emissivity

The emissivity of steel, $\varepsilon_{m,a}$, is difficult to measure during fire tests or real fires and has been under regular reassessment during the past few decades. Kay et al. (1996) summarise testing on the emissivity of oxidised mild steel, making the conclusion that for the temperature range 20-800^{o}C the emissivity varies between 0.79 and 0.93. This variability is because as the steel heats to around 650^{o}C an oxide film on the surface begins to form and the steel begins to act as a black body. Above 650^{o}C, the

steelwork glows and its emissivity drops. The authors note that modern steelwork is usually protected with paint which chars and similarly act like a black body.

Contrary to the above, Paloposki and Liedquist (2005) studied the emissivity of steel and found that between 150^{o}C and 385^{o}C the emissivity was about 0.2, after which it sharply increased to about 0.65 at 550^{o}C and then became independent of temperature at about 0.65. A similar trend was found by Bentz et al., (2009) where the steelwork was blasted. The authors found that the room temperature emissivity of the blasted steelwork was 0.32, increasing rapidly to 0.8 between 200 and 400^{o}C and then slowly increasing toward about 0.95 at 800^{o}C. Other sources in the literature (e.g. Drysdale, 2011) report the emissivity of polished steel being 0.14-0.32 for the temperature range between 425 and 1025^{o}C.

Figure 2-7 shows the reported data for the emissivity of steel in either the oxidised state (Kay et al., 1996) or in the blasted state (Bentz et al., 2009; Paloposki and Liedquist, 2005). Eurocode 4's (CEN, 2005) prescribed value of 0.7 for the entire temperature range and the value reported in Drysdale (2011) are also shown.

As Figure 2-7 shows, there is considerable variability in the reported emissivity of steel with regard to temperature which can vary between 0.14 and 0.95. The EC4 value for emissivity across all temperatures is 0.7, and can thus be said to be conservative at low temperature and unconservative at high temperatures. The variability in the reported data means that the selection of an appropriate set of values is difficult in practice (this is discussed in considerable detail later in this thesis).

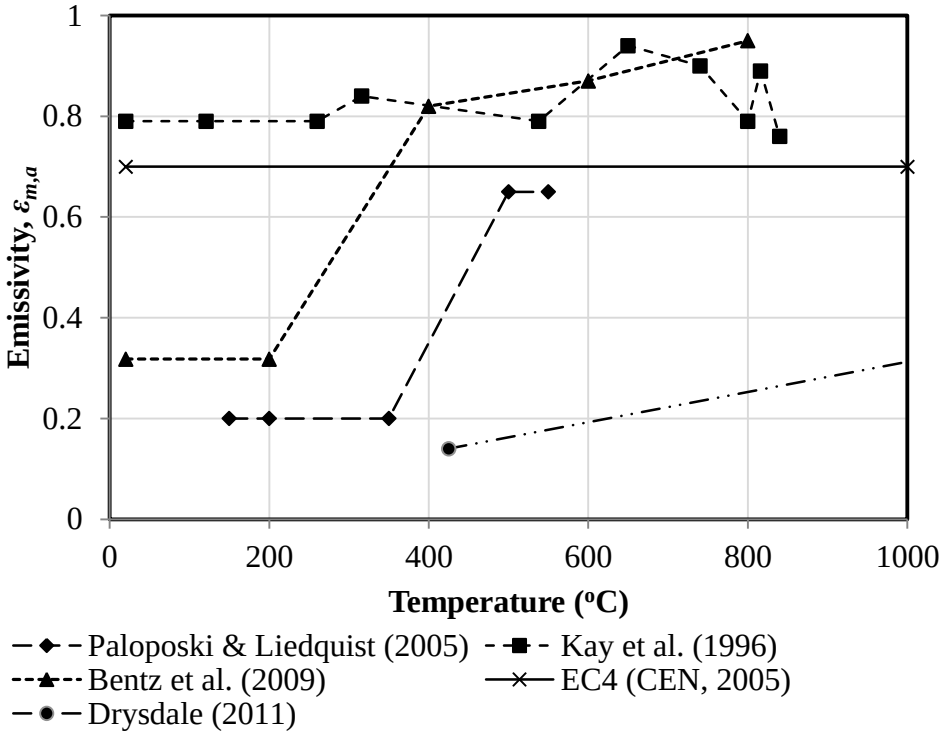

Figure 2-7: Variability of emissivity of steel at different temperatures from various sources available in the literature

2.4.2 Concrete in fire

The relative homogeneity of steel is one of the reasons that its material properties are reasonably well understood. This cannot be said for concrete, whose high temperature performance is dependent on the type of aggregate, cement, strength, reinforcement, heating rate, water content, and how long it has been cured for, among other factors. The physical and chemical transformation of concrete at high temperature has been studied for many years but unfortunately there has been a tendency to assess and analyse the material under standard fire curves which are not necessarily representative of actual fires, and as such the real chemical and physical response to fire in relation to thermal gradients, which can be significant, to the integrity of the material, are not fully captured.

The three main types of infill used in CFS columns are plain unreinforced concrete infill, reinforced concrete infill, and fibre reinforced concrete infill, all of which are usually made with normal-strength concrete (NSC) or high-strength concrete (HSC).

Both of these will react differently in fire and will again react differently with reinforcement. The reactions differ not only physically with different mechanical and thermal reactions, but they will also differ in their chemical reactions. Some of these reactions will be reversible on cooling (e.g. strength rebound below 600^{o}C according to Bazant and Kaplan (1996)) whilst others will not (e.g. the evaporation of pore water in the concrete).

2.4.2.1 Chemical properties

All concrete contains a certain amount of pore water which has not been fixed to cement during the curing process. This water will usually vaporize on heating when the temperature exceeds 100-140^{o}C; which may be above the normal boiling point of water due to the pressurization of water vapour within the pores. This pressure build up can also contribute to a spalling phenomenon due to the vapour not having enough space to dissipate into. One theory of spalling says that the pressure escapes by cracking the concrete in tension and causing it to physically break apart (Fletcher et al., 2006).

When the temperature of concrete reaches about 400^{o}C the cement paste begins to degrade and the calcium hydroxide releases water which reduces the strength of the concrete. Some aggregates may also chemically degrade under heating; for example quartz based aggregates undergo a mineral transformation at about 575^{o}C and limestone aggregates decompose at about 800^{o}C. The differential thermal expansion between the aggregates and the cement can also lead to a reduction in strength due to cracking of the cement paste and in extreme cases spalling. In general however concrete will maintain approximately 60 to 75% (CEN, 2008b) of its strength up to a certain temperature dependent on its aggregate type; about 660^{o}C for carbonate and 430^{o}C for siliceous aggregates (Fletcher et al., 2007), respectively, after which it will rapidly lose compressive strength (retaining only 10 to 15% of its ambient strength at 800-900^{o}C) (CEN, 2008b; Fletcher et al., 2006).

2.4.2.2 Mechanical properties

The mechanical response of concrete at elevated temperature has been reasonably well documented, but as the development of new concrete mixes continues the need

to continue the analysis of the mechanical and thermal response of concrete remains. Schneider (1988) provides an overview of the state-of-the-art at that time and presents the problems in assessing material properties for concrete that can vary so greatly under testing situations that are not necessarily the same between studies.

Schneider (1988) reports the mechanical strength, elastic modulus and stress-strain relationship of concrete at high temperatures, noting that aggregate-cement ratio, type of aggregate and stress level significantly influence the response. Schneider also reports on analytical models for strength and stress-strain response that are the basis for the models in EC2-1-2 (CEN, 2008b). These were developed for normal and lightweight concretes. There is a tendency in modern construction to use high strength concrete for which the normal strength models are no longer appropriate and have been shown to be un-conservative by up to 25% (Phan, 1996).

Phan (1996) reports on the fire performance of HSC (with compressive strengths greater than 45 MPa) and whilst the test data vary greatly some common trends can be observed. High strength concrete's mechanical response varies due to temperature differently than for normal strength concrete, and these differences are more pronounced up to 400^{o}C with stronger concretes exhibiting greater strength loss than lower strength concretes. At about 800^{o}C, HSC loses about 30% of its ambient strength. This loss of strength is characterised by three stages: (1) an initial stage of strength loss (up to 100^{o}C), (2) a period of strength stabilization and possible strength recovery (between 100 and 400^{o}C), and (3) a linear decrease in strength with temperature (see Figure 2-9 on Page 53). The addition of silica fume to concrete mixes has two effects: (1) more strength loss compared to similar mixes without silica fume; and (2) more susceptibility to spalling due to a denser cement paste.

One of the problems with high strength concrete is its propensity for spalling. To overcome this, the addition of polypropylene fibres has been used as a way to contain cracking and encourage moisture movement by creating more micro-pores within the substrate (Fletcher et al., 2007).

The addition of fibres to concrete also has other benefits at ambient temperatures and in fire. The compressive strength of concrete with steel fibre-reinforcement can be higher than that of plain concrete and can increase by up to 25% up to temperatures of 400^{o}C, whereas plain concrete declines continuously with increasing temperature (Lie and Kodur, 1995a). The presence of steel fibres increases the ductility and ultimate strain of the concrete and can develop up to 20% higher restraint stresses caused by thermal expansion than plain concrete (Lie and Kodur, 1995a).

2.4.2.3 Thermal properties

The conductivity, specific heat and density of concrete were studied in depth by Harmathy (1970) who used the addition of the component parts to formulate a bulk characterisation for each of the thermal properties. Through testing he provided the first set of thermal properties for concrete. Since Harmathy's early work there has been constant research and refinement into the thermal properties of concrete, and design codes have been created to model the thermal properties of concrete (e.g. EC2-1-2 (CEN, 2008b)).

The effect of temperature on the thermal properties of high strength concrete has been characterised by Kodur and Sultan (2003). The thermal conductivity of HSC decreases with temperature, with siliceous aggregates having a slightly higher thermal conductivity due to the higher crystallinity of the siliceous aggregate. For fibre reinforced concrete the thermal conductivity plateaus between 400-1000^{o}C, which is suggested by Kodur and Sultan (2003) to be due to the steel fibres limiting the crack width growth and propagation. The specific heat capacity of the HSC is similar to that of normal strength concrete and is similarly dependent on the aggregate type. The specific heat capacity of carbonate aggregate concretes is elevated, especially above 600^{o}C where the aggregates decarbonise releasing CO_2. The addition of steel fibres to the concrete has only minor impacts on specific heat.

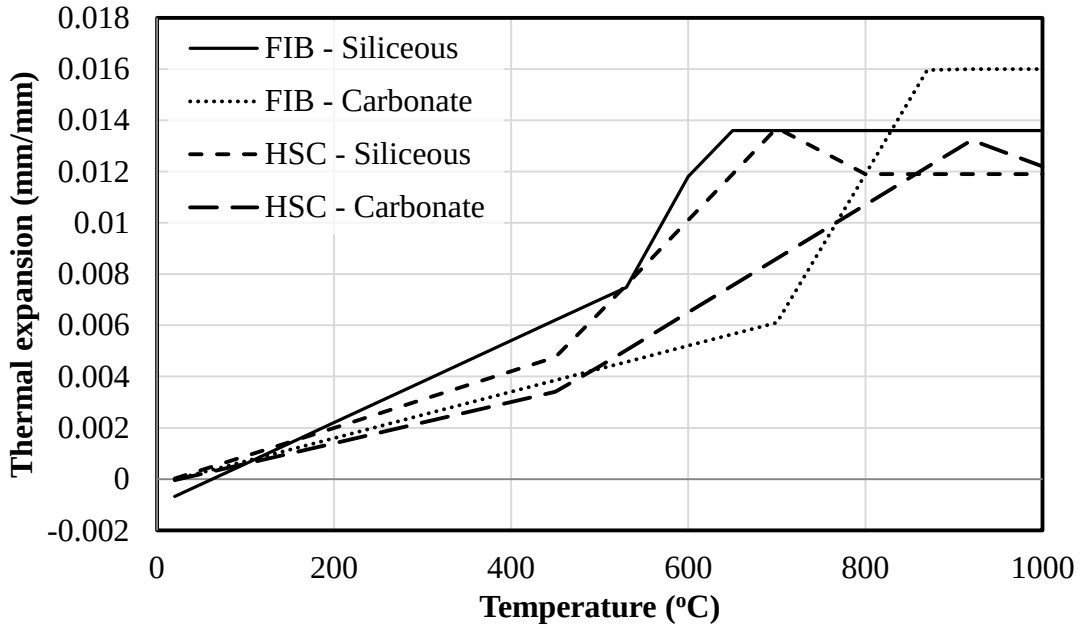

Figure 2-8: Variation of thermal expansion of different concrete types with increasing temperature (from Kodur and Sultan, 2003)

The thermal expansion of fibre-reinforced concrete is not significantly affected by the presence of steel fibres in the mix below 800°C, as compared to HSC (Lie and Kodur, 1995b); expansion being dependant primarily on aggregate type. Siliceous concretes expand with an increase of temperature up to around 700°C, after which the expansion remains constant. Above 800°C the thermal expansion of plain HSC declines but for steel fibre reinforced concrete it can increase as seen in Figure 2-8. Kodur and Sultan (2003) also provide thermal material models for HSC and fibre-reinforced concretes.

2.4.2.4 Trends and concerns for concrete at high temperature

The use of high strength concretes is on the increase and it is widely expected that HSC will gradually replace normal strength concrete in structural design (Pliya et al., 2011). Higher than normal strength concretes have lower permeability as compared with NSC, and this is thought to lead to it being more susceptible to spalling on heating. One way that spalling can be overcome is with the addition of polypropylene fibres, which melt at relatively low temperature (160°C) and can create pores which water vapour at high pressure can safely occupy. The extra

porosity could lead to a reduction in mechanical performance (Pliya et al., 2011), however this is rarely a problem for the fibre volume contents typically used for spalling mitigation. Contrary to this, it has been suggested that polypropylene fibres act as a barrier to the movement of moisture and that they encourage the cracking of concrete deeper within the element (Fletcher et al., 2006). There needs to be a greater attempt to characterise concretes for the use in design as there is a greater variety of products available to the designer (Fletcher et al., 2006).

Steel fibres can also be added to a concrete mix to reduce crack propagation and increase the concrete ductility, particularly in tension, both at ambient temperatures and in the fire load situation.

2.4.3 Computational studies of CFS columns in fire

2.4.3.1 Structural modelling approaches for CFS columns in fire

Many modelling approaches have been used in an attempt to predict the fire resistance of CFS columns. The motivation for these models is twofold. First and foremost, a suitably validated model can be used to perform parametric studies on various column parameters and develop simple analytical formulae and procedures for column design, without the need to test large numbers of specimens. Second, suitably validated 3D finite element (FE) models can be used to study (with limited verifiability in many cases) the specific impacts of key issues (e.g. non-standard heating regimes, air gap formation, local buckling, longitudinal slip between the concrete and the steel tube, etc.) which cannot be easily captured using simple sectional analysis models. It is noteworthy that all of the computational modelling approaches discussed below depend on user inputs for a wide variety of parameters for which limited guidance is available (for instance, the resultant emissivity in fire is taken anywhere between 0.32 and 1.0 in the quoted studies, typically with little or no obvious justification), and have been validated by comparison against ‘selected’ test data. Full statistical comparisons of the respective modelling approaches against the full database of available test results are not available (see Chapter 3).

Simple crushing analyses

The simplest models presented in the literature predict only the crushing strength of CFS columns (Chung et al., 2008; Yin et al., 2006). These models simply apply stress-strain curves for the columns' constituent materials at elevated temperature (taken from any number of available sources) and assume that the thermal and structural behaviour of the member is uncoupled, that there is perfect bond between the steel tube and the infill, that no gaps form between the tube and the concrete, that no slip occurs between the tube and the concrete, and that neither local nor global buckling need be considered; all of these assumptions are known to be false, but the degree to which they influence the models' predictive ability is not clearly known. Such an analysis is only ever potentially appropriate for stocky columns, and based on the most-observed failure modes in experiments it would seem that such approaches are indefensible in most cases. Indeed, in a study by Chung et al. (2008) using this approach the model over-predicted both the temperatures and the failure times in every comparison against tests.

Cross-sectional equilibrium approaches

Several models in the literature have taken an approach based on a cross-sectional equilibrium analysis (Han et al., 2003; Kodur and Lie, 1996b). The column's cross-section is divided into annular or square elements and sectional equilibrium at mid height is used through an iterative analysis to develop curves of capacity versus time of fire exposure. These models assume that the concrete has no tensile strength, plane sections remain plane, there is perfect bond between steel and concrete (and thus no slip, air gap, or local buckling), and there is no composite action between the steel and the concrete, and no concrete confinement due to the steel tube. It is further assumed that effective length of the fixed-fixed column remains uniform throughout the heating at $0.7L_{cr}$ (*chosen* to match test data from the NRCC column furnace). The deflected shape of the column is assumed as sinusoidal – therefore prescribing the failure mechanism for the column as one with a single hinge at mid-height. Comparison against results from *selected* NRCC tests has shown this approach to conservatively predict fire resistance.

Custom finite element packages

Several custom finite element (FE) software packages, developed specifically for structural fire analysis and incorporating varying degrees of complexity, have been applied to CFS columns. This includes independent work by Schaumann et al. (2009), Kodur and Fike (2009), and Renaud (2004). These analyses all differ in many subtle respects which are not important for the current discussion. Neither Schaumann et al. (2009) nor Kodur and Fike (2009) included the effects of gap formation, slip between the SHS tube and the concrete, confinement, or local buckling, despite the fact that the authors highlighted their potential importance.

Renaud's (2004) comprehensive analysis considers the thermal impacts of gap formation (albeit by *imposing* a predefined thermal resistance so as to match test observations) as well as the structural impacts of slip between the steel tube and the infill concrete (using a special connection element), although it appears not to consider local buckling of the steel tube. Renaud's analysis is validated against 33 tests, yet 300+ tests are available. It is not clear why these specific tests were chosen. A notable conclusion of Renaud's study was that slip appears to play an important role, particularly within the first 30 minutes of a standard fire test with PC infill or for columns with eccentric load, bending, or high slenderness.

General purpose finite element models

Several studies have used general purpose FE packages to perform structural fire analyses of CFS columns. Zha (2003) presents a 3D FE model of a circular CFS column exposed to a standard fire using DYNA3D, apparently neglecting gap formation, slip, concrete confinement, and local buckling. This is validated *only* against the highly conservative tabular design approach given in Eurocode 4 (CEN, 2005) rather than against real experimental data. Hong and Varma (2009) used ABAQUS to model the standard fire behaviour of CFS columns and, while ignoring the influence of gap formation, included slip and local buckling in their analysis by *manually* de-bonding the steel tube over a prescribed length near the column mid height. The model was validated against 15 tests selected from the literature; again it

is unclear why these specific tests were chosen. This study confirmed that the effects of local buckling and slip are more important for columns which experience bending. Espinós et al. (2009) also used ABAQUS, neglecting gap formation, confinement, slip, and local buckling, and verified their model against only eight experimental results, none of which had load ratios above 0.3.

The most advanced 3D FE modelling presented to date is by Ding and Wang (2009) using the commercial FE code ANSYS. This study considered the potential thermal and structural impacts of gap formation and slip between the steel tube and the infill concrete, as well as local buckling of the steel tube. The thermal influence of an air gap was modelled by assuming a constant air gap of 1 mm with an assumed associated thermal resistance *chosen* to match selected tests available in the literature. The resulting thermal analysis indicated that the accuracy of temperature prediction in CFS columns in fire can be noticeably improved by accounting for the formation of an air gap. Given the number of parameters upon which the formation of an air gap depends, research is needed to understand and model this process for the range of steel sections and concrete infill materials currently used in practice. Slip was considered using 3D surface-to-surface contact elements and a Coulomb friction model. The results of parametric studies to investigate the potential effects of slip on lateral deflection response and time to failure indicated that the effects were minor. On the basis of their work, Ding and Wang (2009) concluded that it was not absolutely essential to include slip in the analysis, although slightly better results were obtained when slip was included, that the specific properties of the bond-slip response were of little significance as long as slip was included, and that introducing an air gap improved the accuracy of the thermal analysis and hence the structural performance predictions.

Other models reported in the literature include neural network (Al-khaleefi et al., 2002) and Rankine (Tan and Tang, 2004) approaches. However, these methods are not expected to capture important subtleties of the mechanics of CFS columns in fire.

2.4.3.2 Models for thermal and mechanical response of materials in fire

Later in this thesis a number of different mechanical and thermal property models are considered for use in the analysis and design of CFS columns for fire resistance. All of the models considered later in this thesis are reviewed in the following sections, including models from the Eurocodes (CEN, 2005, 2008b, 2009b) and Lie and Irwin (1995).

Eurocodes

EC2 – concrete

Section 3 of EC2-1-2 (CEN, 2008b) presents suggested thermal and mechanical property models for concrete for use in modelling their response to fire.

Mechanical properties

The reduction in the maximum compressive strengths and corresponding strain at a given temperature for the concrete is defined by the reduction factors given in Table 2-5 for normal strength and high strength concretes at different temperatures and aggregate types. The suggested reduction in strength with temperature for various concrete types is given in Figure 2-9.

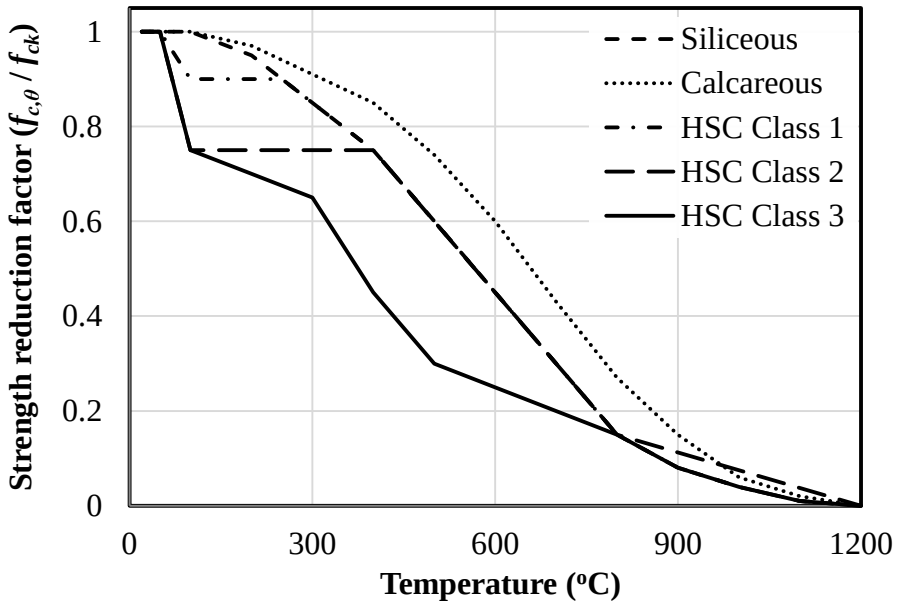

Figure 2-9: EC2-1-2 concrete strength reduction factors with respect to temperature (CEN, 2008b)

Table 2-5: Concrete reduction factors (CEN, 2008b)

	Normal Weight Concrete						HSC		
	Siliceous			Calcareous			Class 1	Class 2	Class 3
Temp							C55/67 - C60/75	C70/85 - C80/95	C90/105
(°C)	$f_{c,\theta}/f_{ck}$	$\varepsilon_{c1,\theta}$	$\varepsilon_{cu1,\theta}$	$f_{c,\theta}/f_{ck}$	$\varepsilon_{c1,\theta}$	$\varepsilon_{cu1,\theta}$	$f_{c,\theta}/f_{ck}$	$f_{c,\theta}/f_{ck}$	$f_{c,\theta}/f_{ck}$
20	1	0.0025	0.02	1	0.0025	0.02	1	1	1
50	--	--	--	--	--	--	1	1	1
100	1	0.004	0.0225	1	0.004	0.0225	0.9	0.75	0.75
200	0.95	0.0055	0.025	0.97	0.0055	0.025	--	--	0.7
250	--	--	--	--	--	--	0.9	--	--
300	0.85	0.007	0.0275	0.91	0.007	0.0275	0.85	--	0.65
400	0.75	0.01	0.03	0.85	0.01	0.03	0.75	0.75	0.45
500	0.6	0.015	0.0325	0.74	0.015	0.0325	--	--	0.3
600	0.45	0.025	0.035	0.6	0.025	0.035	--	--	0.25
700	0.3	0.025	0.0375	0.43	0.025	0.0375	--	--	--
800	0.15	0.025	0.04	0.27	0.025	0.04	0.15	0.15	0.15
900	0.08	0.025	0.0425	0.15	0.025	0.0425	0.08	--	0.08
1000	0.04	0.025	0.045	0.06	0.025	0.045	0.04	--	0.04
1100	0.01	0.025	0.0475	0.02	0.025	0.0475	0.01	--	0.01
1200	0	0	0	0	0	0	0	0	0

The corresponding stress-strain relationship is:

$$\sigma_{c,\theta} = \begin{cases} \dfrac{3\varepsilon_c f_{c,\theta}}{\varepsilon_{c1,\theta}\left(2+\left(\dfrac{\varepsilon}{\varepsilon_{c1,\theta}}\right)^3\right)}, & \varepsilon_c \le \varepsilon_{c1,\theta} \\ \text{Linear or non}-\text{linear models are permitted, } \varepsilon_{c1,\theta} < \varepsilon_c \le \varepsilon_{cu1,\theta} \end{cases} \quad (2\text{-}13)$$

which produces the stress versus strain relationships shown in Figure 2-10. EC2 (CEN, 2008b) also provides guidance on "non-standard" situations, for instance that during the use of natural fire situations, the descending branch of the stress-strain relationship should be modified, possible strength gain in the cooling phase of a fire should be ignored, and tensile strength can conservatively be ignored (if it is necessary to include tensile strength a linear reduction of strength can be prescribed, as in Section 3.2.2.2 of EC2 (CEN, 2008b)).

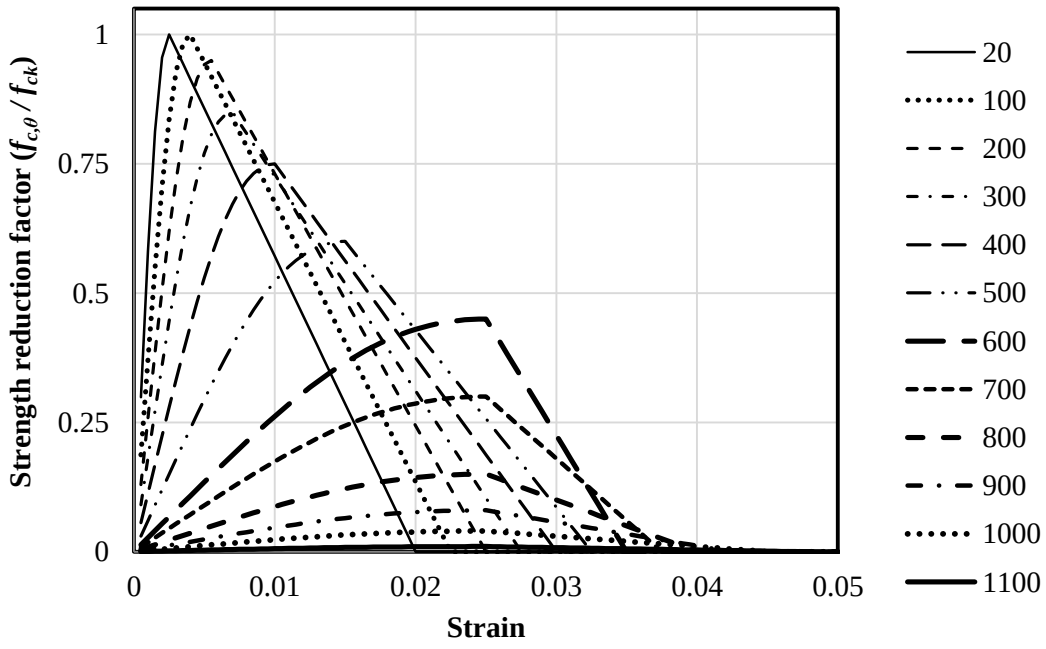

Figure 2-10: Representative relative stress–strain curves for concrete at different temperatures (CEN, 2008b)

The thermal elongation (thermal strain) of concrete is primarily dependent on the type of aggregate used. For siliceous aggregates:

$$\varepsilon_{c,\theta} = \begin{cases} -1.8\,\text{x}10^{-4} + 9\,\text{x}10^{-6}\theta_c + 2.3\,\text{x}10^{-11}\theta_c^3, & 20^oC \le \theta_c \le 700^oC \\ 14\,\text{x}\,10^{-3}, & 700^oC < \theta_c \le 1200^oC \end{cases} \quad (2\text{-}14)$$

For calcareous aggregates:

$$\varepsilon_{c,\theta} = \begin{cases} -1.2\,\text{x}10^{-4} + 6\,\text{x}10^{-6}\theta_c + 1.4\,\text{x}10^{-11}\theta_c^3, & 20^oC \le \theta_c \le 805^oC \\ 12\,\text{x}\,10^{-3}, & 805^oC < \theta_c \le 1200^oC \end{cases} \quad (2\text{-}15)$$

Thermal properties

The thermal properties for normal and high strength concretes are the same according to EC2 (CEN, 2008b)

Specific heat capacity (J/kg·^{o}C) of dry concrete (moisture content is equal to zero) is defined for both siliceous and calcareous concrete as:

$$c_{p,c,\theta} = \begin{cases} 900 & 20^oC \le \theta_c \le 100^oC \\ 900 + (\theta_c - 100) & 100^oC < \theta_c \le 200^oC \\ 1000 + (\theta_c - 200)/2 & 200^oC < \theta_c \le 400^oC \\ 1100 & 400^oC < \theta_c \le 1200^oC \end{cases} \quad (2\text{-}16)$$

When the moisture is not explicitly considered in the calculation method used (which would occur only very rarely), the specific heat of concrete can be adjusted to account for the extra energy required to vaporise the moisture with differing peak values depending on the mass of water within the concrete. The assumed peak is constant between 100^{o}C and 115^{o}C and decreases linearly between 115^{o}C and 200^{o}C. For example the peak for 3% moisture content by mass is 2020 J/kg·^{o}C and a specific heat capacity relationship would be as shown in Figure 2-11.

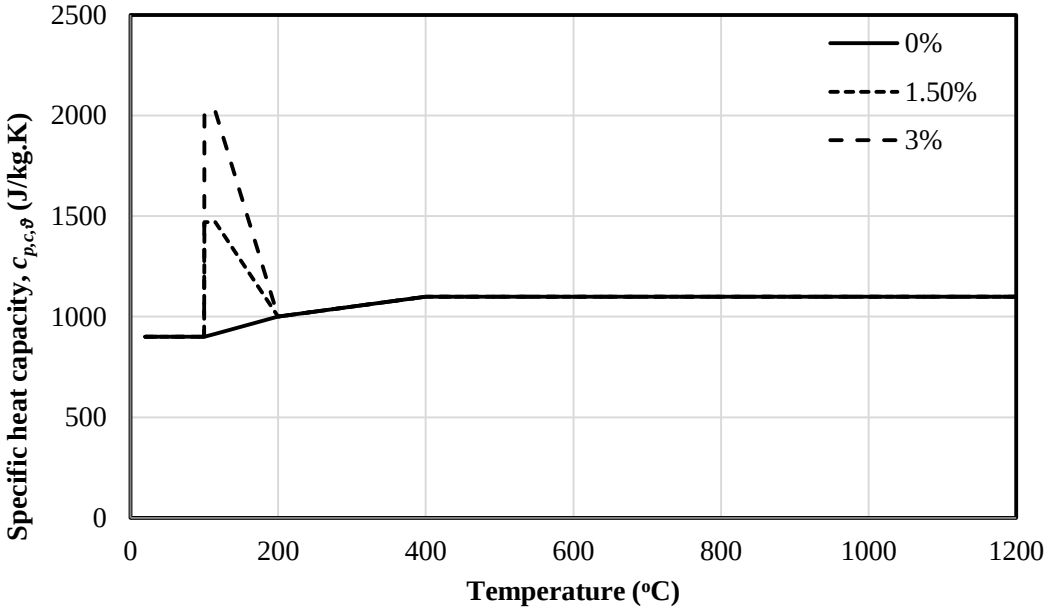

Figure 2-11: Assumed specific heat of concrete with 0%, 1.5% and 3% (by mass) moisture content according to EC2-1-2 (CEN, 2008b)

Thermal conductivity (W/m^{o}C) is defined by upper and lower limits for normal weight and high strength concrete according to the UK National annex to EC2 (CEN, 2004b) for temperatures ranging from 20^{o}C to 1200^{o}C:

$$\lambda_{c,\theta} = \begin{cases} 2 - 0.2451\left(\frac{\theta_c}{100}\right) + 0.0107\left(\frac{\theta_c}{100}\right)^2, & Upper\ limit \\ 1.36 - 0.136\left(\frac{\theta_c}{100}\right) + 0.0057\left(\frac{\theta_c}{100}\right)^2, & Lower\ limit \end{cases} \quad (2\text{-}17)$$

The density of concrete (kg/m^3) is influenced by moisture loss and is defined in EC2 as follows:

$$\rho_{c,\theta} = \begin{cases} \rho(\theta_{20}) & 20^oC \le \theta_c \le 115^oC \\ \rho(\theta_{20}) \cdot (1 - 0.02(\theta_c - 115)/85) & 115^oC < \theta_c \le 200^oC \\ \rho(\theta_{20}) \cdot (0.98 - 0.03(\theta_c - 200)/200) & 200^oC < \theta_c \le 400^oC \\ \rho(\theta_{20}) \cdot (0.95 - 0.07(\theta_c - 400)/800) & 400^oC < \theta_c \le 1200^oC \end{cases} \quad (2\text{-}18)$$

EC3 – steel

EC3-1-2 (CEN, 2009b) describes the mechanical and thermal responses of structural steel, whilst EC2 (CEN, 2008b) describes the response of reinforcing and prestressing steels.

Mechanical properties

The codified reduction factors for mechanical properties of structural steel and common reinforcing steels are given in Table 2-6. The relationship between stress and strain for various temperatures is given by the equations in Table 2-7.

The thermal elongation of steel is defined by:

$$\frac{\Delta l}{l} = \begin{cases} 1.2\,\text{x}10^{-5}\theta_a + 0.4\,\text{x}10^{-8}\theta_a^2 - 2.416\,\text{x}10^{-4} & 20^oC \le \theta_a < 750^oC \\ 1.1\,\text{x}10^{-2} & 750^oC \le \theta_a < 860^oC \\ 2\,\text{x}10^{-5}\theta_a - 6.2\,\text{x}10^{-3} & 860^oC \le \theta_a < 1200^oC \end{cases} \quad (2\text{-}19)$$

Table 2-6: Reduction factors for structural (from EC3 (CEN, 2009b)) and reinforcing steel (from EC2 (CEN, 2008b))

Steel temp.	Reduction factors at temperature θ_a relative to the value of f_y or E_a at 20°C					
	Effective yield strength		Proportional limit		Linear elastic range	
	Struct.	*Rein.*	*Struct.*	*Rein.*	*Struct.*	*Rein.*
θ	$k_{ay,\theta} = f_{ay,\theta} / f_{ay}$	$k_{sy,\theta} = f_{sy,\theta} / f_{sy}$	$k_{ap,\theta} = f_{ap,\theta} / f_{ay}$	$k_{sp,\theta} = f_{sp,\theta} / f_{sy}$	$k_{Ea,\theta} = E_{a,\theta} / E_a$	$k_{Es,\theta} = E_{s,\theta} / E_s$
20 °C	1	1	1	1.00	1	1.00
100 °C	1	1	1	0.96	1	1.00
200 °C	1	1	0.807	0.92	0.9	0.87
300 °C	1	1	0.613	0.81	0.8	0.72
350 °C	1	0.97	0.517	0.72	0.75	0.64
400 °C	1	0.94	0.42	0.63	0.7	0.56
500 °C	0.78	0.67	0.36	0.44	0.6	0.40
600 °C	0.47	0.40	0.18	0.26	0.31	0.24
700 °C	0.23	0.12	0.075	0.08	0.16	0.08
800 °C	0.11	0.11	0.05	0.06	0.09	0.06
900 °C	0.05	0.08	0.0375	0.05	0.0675	0.05
1000 °C	0.04	0.05	0.025	0.03	0.045	0.03
1100 °C	0.02	0.03	0.0125	0.02	0.0225	0.02
1200 °C	0	0.00	0	0.00	0	0.00

Table 2-7: Stress strain relationships suggested for structural steel at elevated temperatures according to EC3 (CEN, 2009b)

Strain Range	Stress σ_a	Tangent Modulus
$\varepsilon_a \leq \varepsilon_{p,\theta}$	$\varepsilon_a \cdot E_{a,\theta}$	$E_{a,\theta}$
$\varepsilon_a \leq \varepsilon_{p,\theta}$	$f_{p,\theta} - c + \left(\frac{b}{a}\right)\left[a^2 - \left(\varepsilon_{y,\theta} - \varepsilon_a\right)^2\right]^{0.5}$	$\frac{b\left(\varepsilon_{y,\theta} - \varepsilon_a\right)}{a\left[a^2 - \left(\varepsilon_{y,\theta} - \varepsilon_a\right)^2\right]^{0.5}}$
$\varepsilon_a \leq \varepsilon_{p,\theta}$	$f_{y,\theta}$	0
$\varepsilon_a \leq \varepsilon_{p,\theta}$	$f_{y,\theta}\left[1 - \frac{\varepsilon - \varepsilon_{t,\theta}}{\varepsilon_{u,\theta} - \varepsilon_{t,\theta}}\right]$	-
$\varepsilon_a = \varepsilon_{u,\theta}$	0.00	-
Parameters	$\varepsilon_{p,\theta} = f_{p,\theta}/E_{a,\theta}$ $\varepsilon_{y,\theta} = 0.02$ $\varepsilon_{t,\theta} = 0.15$ $\varepsilon_{u,\theta} = 0.20$	
Functions	$a^2 = \left(\varepsilon_{y,\theta} - \varepsilon_{p,\theta}\right)\left(\varepsilon_{y,\theta} - \varepsilon_{p,\theta} + c/E_{a,\theta}\right)$ $b^2 = c\left(\varepsilon_{y,\theta} - \varepsilon_{p,\theta}\right)E_{a,\theta} + c^2$ $c = \frac{\left(f_{y,\theta} - f_{p,\theta}\right)^2}{\left(\varepsilon_{y,\theta} - \varepsilon_{p,\theta}\right)E_{a,\theta} - 2\left(f_{y,\theta} - f_{p,\theta}\right)}$	

Annex A of EC3 (CEN, 2009b) provides a method to include strain hardening in the stress strain relationship for steel at high temperature using the assumption that this only occurs below 400°C. The relationship, shown in Figure 2-12, is as follows:

$$f_{u,\theta} = \begin{cases} 1.25 f_{y,\theta} & \theta_a < 300^o C \\ f_{y,\theta}(2 - 0.0025 \cdot \theta_a) & 300^o C \le \theta_a < 400^o C \\ f_{y,\theta} & \theta_a \ge 400^o C \end{cases} \quad (2\text{-}20)$$

$$\sigma_a = \begin{cases} 50\left(f_{u,\theta} - f_{y,\theta}\right)\varepsilon_a + 2f_{y,\theta} - f_{u,\theta} & 0.02 < \varepsilon_a < 0.04 \\ f_{u,\theta} & 0.04 \le \varepsilon_a \le 0.15 \\ f_{u,\theta}\left(1 - 20(\varepsilon_a - 0.15)\right) & 0.15 < \varepsilon_a \le 0.20 \\ 0.00 & 0.15 < \varepsilon_a \le 0.20 \end{cases} \quad (2\text{-}21)$$

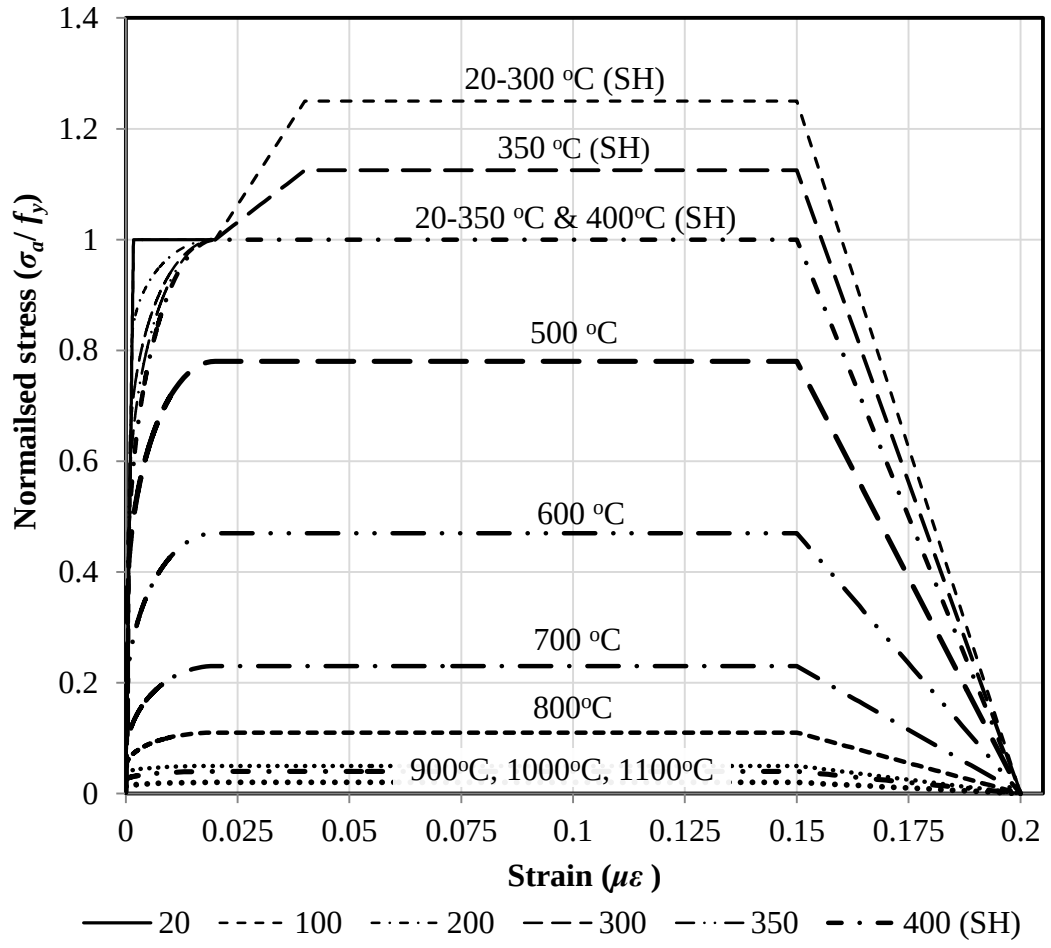

Figure 2-12: Normalised stress-strain relationships for structural steel at different temperatures, including strain hardening (CEN, 2009b)

The suggested stress strain relationships are shown in Figure 2-12. At 400°C it is the same regardless of whether strain hardening (SH) has been included. The maximum stress in the steel, without stain hardening, between 20 and 400°C is the yield stress (i.e. a normalised stress of 1.0). The maximum stress when including stain hardening is 1.25 times the yield stress and this occurs at strains between 0.04 and 0.15, and only at temperatures below 300°C (20-300°C, (SH) in Figure 2-12).

Thermal properties

The specific heat of carbon steel, $c_{p,a,\theta}$, in J/kg·°C is given in EC3 as:

$$c_{p,a,\theta} = \begin{cases} 425 + 0.773\theta_a - 0.00169\theta_a^2 + 2.22\,\text{x}10^{-6}\theta_a^3\,, & 20^oC \le \theta_a < 600^oC \\ 666 + \dfrac{13002}{738 - \theta_a} & 600^oC \le \theta_a < 735^oC \\ 545 + \dfrac{17820}{\theta_a - 731} & 735^oC \le \theta_a < 900^oC \\ 650 & 900^oC \le \theta_a < 1200^oC \end{cases} \quad (2\text{-}22)$$

The thermal conductivity, $\lambda_{a,\theta}$, in W/m°C is defined by:

$$\lambda_{a,\theta} = \begin{cases} 54 - 0.033\theta_a & 20^oC \le \theta_a < 800^oC \\ 27.3 & 800^oC \le \theta_a < 1200^oC \end{cases} \quad (2\text{-}23)$$

The density of steel is assumed to remain constant and to be independent of temperature, taken as:

$$\rho_a = 7850\ kg/m^3 \quad (2\text{-}24)$$

EC4 – steel-concrete composite sections

EC4 (CEN, 2005) for steel-concrete composite construction presents the same material and thermal models for steel as EC2 and EC3, including accounting for strain hardening. For the EC4 concrete models the more conservative models for siliceous concrete and steel reinforcement are assumed, however if more precise models are required then the provisions described in EC2 for calcareous concrete can

be used, and for hot-rolled steel reinforcement the structural steel material models can be used with a limit of 1.1 (instead of 1.25) to account for strain hardening.

Eurocode 4 (CEN, 2005) also provides simplified approximations of material properties for steel and concrete. This is to provide an easier analytical process and therefore reduce computational time for the specific case of steel-concrete composite sections. In EC4 the density of steel is assumed to be uniform and independent of temperature whilst the simplified model for concrete density accounts for the reduction in mass due to water evaporation:

$$\rho_i = \begin{cases} 7850 & steel \\ 2354 - 23.47(\theta_c/100) & concrete \end{cases} \quad (2\text{-}25)$$

In EC4 the thermal elongation for both steel and concrete can be conservatively assumed to be linear with regards to temperature:

$$\frac{\Delta l}{l} = \begin{cases} 14\,\text{x}10^{-6}(\theta_a - 20) & steel \\ 18\,\text{x}10^{-6}(\theta_c - 20) & concrete \end{cases} \quad (2\text{-}26)$$

The specific heat capacity (J/kg^{o}C) of steel and concrete can be conservatively assumed to be constant and independent of temperature, or, for concrete, a simplified temperature dependent model is also given.

$$c_{p,i} = \begin{cases} 600 & steel \\ 890 + 56.2(\theta_c/100) - 3.4(\theta_c/100)^2 & concrete \\ 1000 & concrete \end{cases} \quad (2\text{-}27)$$

As in EC2, EC4 (CEN, 2005) provides guidance on a peak specific heat capacity for the concrete to account for the energy required to vaporise the pore moisture. The specification of where the presumed peak in specific heat occurs is less stringent than in EC2. Eurocode 4 (CEN, 2005) states that the peak value is "situated between 100 and 200^{o}C, such as 115^{o}C." The graphical representation provided in EC4 shows that

the start of the ascent in specific heat is at 100°C and the end of the descent is at 200°C. The peak magnitude is also increased, with a value of 5600 J/kg·°C at a 10% moisture content prescribed as a possible situation that might occur in a CFS section.

The thermal conductivity of steel and concrete are also given as independent of temperature for simplified analysis according to EC4:

$$\lambda_i = \begin{cases} 45 & steel \\ 1.60 & concrete \end{cases} \quad (2\text{-}28)$$

Lie and Irwin's (1995) material models

Lie and Irwin (1995) present high temperature material models for both steel and concrete which have been specifically developed to treat CFS columns in fire. These were apparently verified against tests.

Steel properties

The mechanical response of steel is defined by:

$$f_y = \begin{cases} \dfrac{f(\theta_a, 0.001)}{0.001} \cdot \varepsilon_a & \varepsilon_a \le \varepsilon_p \\ \dfrac{f(\theta_a, 0.001)}{0.001} \cdot \varepsilon_p + f\left(\theta_a, \left(\varepsilon_a - \varepsilon_p + 0.001\right)\right) - f(T, 0.001) & \varepsilon_a > \varepsilon_p \end{cases} \quad (2\text{-}29)$$

where $\varepsilon_p = 4\text{x}10^{-6} \cdot f_{yo}$ and

$$f(\theta_a, \varepsilon_i) = (50 - 0.04\theta_a) \cdot \left[1 - \exp\left((-30 + 0.03T) \cdot \sqrt{\varepsilon_i}\right)\right] \cdot 6.9$$

Thermal conductivity for steel is given by:

$$\lambda_{a,\theta} = \begin{cases} -0.022\theta_a + 48 & 0 \le \theta_a \le 900^o C \\ 28.2 & \theta_a > 900^o C \end{cases} \quad (2\text{-}30)$$

Thermal expansion is given by:

$$\frac{\Delta l}{l} = \begin{cases} (0.004\theta_a + 12)\ \text{x}10^{-6} & 0 \le \theta_a \le 1000^o C \\ 16\ \text{x}10^{-6} & \theta_a > 1000^o C \end{cases} \quad (2\text{-}31)$$

Thermal capacity is defined by:

$$\rho_a c_{p,a,\theta} = \begin{cases} (0.004\theta_a + 3.3)\ \text{x}10^6 & 0 < \theta_a \leq 650^o C \\ (0.068\theta_a + 38.3)\ \text{x}10^6 & 650 < \theta_a \leq 725^o C \\ (-0.086\theta_a + 73.35)\ \text{x}10^6 & 725 < \theta_a \leq 800^o C \\ 4.55\ \text{x}10^6 & \theta_a > 800^o C \end{cases} \quad (2\text{-}32)$$

Concrete properties

The mechanical response of concrete is defined:

$$f_c = \begin{cases} f_c' \left[1 - \left(\frac{\varepsilon_{max} - \varepsilon_c}{\varepsilon_{max}}\right)^2\right] & \varepsilon_c \leq \varepsilon_{max} \\ f_c' \left[1 - \left(\frac{\varepsilon_c - \varepsilon_{max}}{3\varepsilon_{max}}\right)^2\right] & \varepsilon_c > \varepsilon_{max} \end{cases} \quad (2\text{-}33)$$

where

$$\varepsilon_{max} = 0.0025 + \left(6.0\theta_c + 0.04{\theta_c}^2\right) \text{x}\ 10^{-6}$$

and

$$f_c' = \begin{cases} f_{co}' & 0 < \theta_c < 450^o C \\ f_{co}' \left[2.011 - 2.353\left(\theta_c - \frac{20}{1000}\right)\right] & 450 \leq \theta_c \leq 874^o C \\ 0 & \theta_c > 874^o C \end{cases}$$

Thermal conductivity is given by:

$$\lambda_{c,\theta} = \begin{cases} 1.355 & 0 \leq \theta_c \leq 293^o C \\ -0.001241\theta_c + 1.7162 & \theta_c > 293^o C \end{cases} \quad (2\text{-}34)$$

Thermal expansion is given by:

$$\frac{\Delta l}{l} = (0.008\theta_c + 6)\ \text{x}10^{-6} \quad (2\text{-}35)$$

Thermal capacity is defined by:

$$\rho_{c,\theta}c_{p,c,\theta} = \begin{cases} 2.566\,\text{x}10^6 & 0 < \theta_c \leq 400^oC \\ (0.1756\theta_c - 68.034)\,\text{x}10^6 & 400 < \theta_c \leq 410^oC \\ (-0.05043\theta_c + 25.00671)\,\text{x}10^6 & 410 < \theta_c \leq 445^oC \\ 2.566\,\text{x}10^6 & 445 < \theta_c \leq 500^oC \\ (0.01603\theta_c - 5.44881)\,\text{x}10^6 & 500 < \theta_c \leq 635^oC \\ (0.16635\theta_c - 100.90225)\,\text{x}10^6 & 635 < \theta_c \leq 715^oC \\ (-0.22103\theta_c + 176.07343)\,\text{x}10^6 & 715 < \theta_c \leq 785^oC \\ 2.566\,\text{x}10^6 & \theta_c > 785^oC \end{cases} \quad (2\text{-}36)$$

The effects of moisture within the concrete are accounted for by a uniform thermal capacity of $\rho_w c_w = 4.2\text{x}10^6$ J/m^3 and a heat of vaporisation of 2.3x10^6 J/kg. The models assume that the moisture starts to evaporate in any given layer of concrete when the temperature of the layer reaches 100^{o}C, and all the energy from the fire is used to evaporate water until all the moisture in the layer has evaporated.

2.4.3.3 Fire modelling

Modelling fire is difficult. Cox (1994) notes that the "underlying physical and chemical processes are extremely difficult to model (e.g. turbulent buoyant convection, radiative heat transfer, combustion, finite rate kinetics), but uncertainties in, for example, the location of the fire within the enclosure, the very nature of the fuel involved, the configuration of ventilation openings, and the external wind conditions will all affect the outcome." The complexities of fire, coupled with the fact that modern buildings are becoming increasingly complex in architectural design, with many having large floor plates and non-standard compartment shapes, the standard fire models being used are becoming less and less applicable. Nonetheless, this work considers predominantly the use of standard fires (e.g. ASTM, 2007) for assessment and design of CFS columns at elevated temperature.

The standard time temperature curve that is predominantly used in testing and modelling in Europe is based on the ISO 834 (ISO, 1999) fire curve:

$$\theta_g = 345\log_{10}(8t + 1) + 20 \quad (2\text{-}37)$$

This simple standard fire curve in Equation 2-37 allows engineers to simplify the true complexity of real fires and expedite the design process. Other standardised time versus temperature curves, such as hydrocarbon fire curves, external fire curves, and slow growth 'smouldering' curves can be used in design and testing for specific purposes, where applicable. The slow heating smouldering fire curve is sometimes used in the testing of reactive coatings and intumescent paints, since these protective coatings are activated by heat flux and their performance needs to be assessed under various possible heating regimes. The Eurocode smouldering curve (CEN, 2010c) is given by:

$$\theta_g = \begin{cases} 154t^{0.25} + 20 & 0 < t \leq 21 \\ 345\log_{10}(8(t-20)+1) + 20 & t > 21 \end{cases} \quad (2\text{-}38)$$

As shown in Figure 2-13, for example, neither of the time-temperature curves shown is an accurate representation of how a real fire evolves in a real situation (see Figure 2-13) where localised heating, the cooling phase of the fire, and fire movement around a compartment may occur, amongst others.

The annexes of EC1 (CEN, 2009c) allow the prescription of different design fires that are more tailored to a "real" situations than those prescribed by the ISO 834 (ISO, 1999) cellulosic fire or smouldering curve (CEN, 2010c). Annex A of EC1 provides a method of calculating the time history of compartment fire temperatures based on fire load densities, compartment linings, and ventilation factors, and predicts a cooling phase. Annex C of EC1 also suggests a model for treating localised fires in compartments where flashover is unlikely to occur. Annex D of EC1 is an informative annex for advanced fire models, where the application of one-zone, two- zone or CFD models is explained.

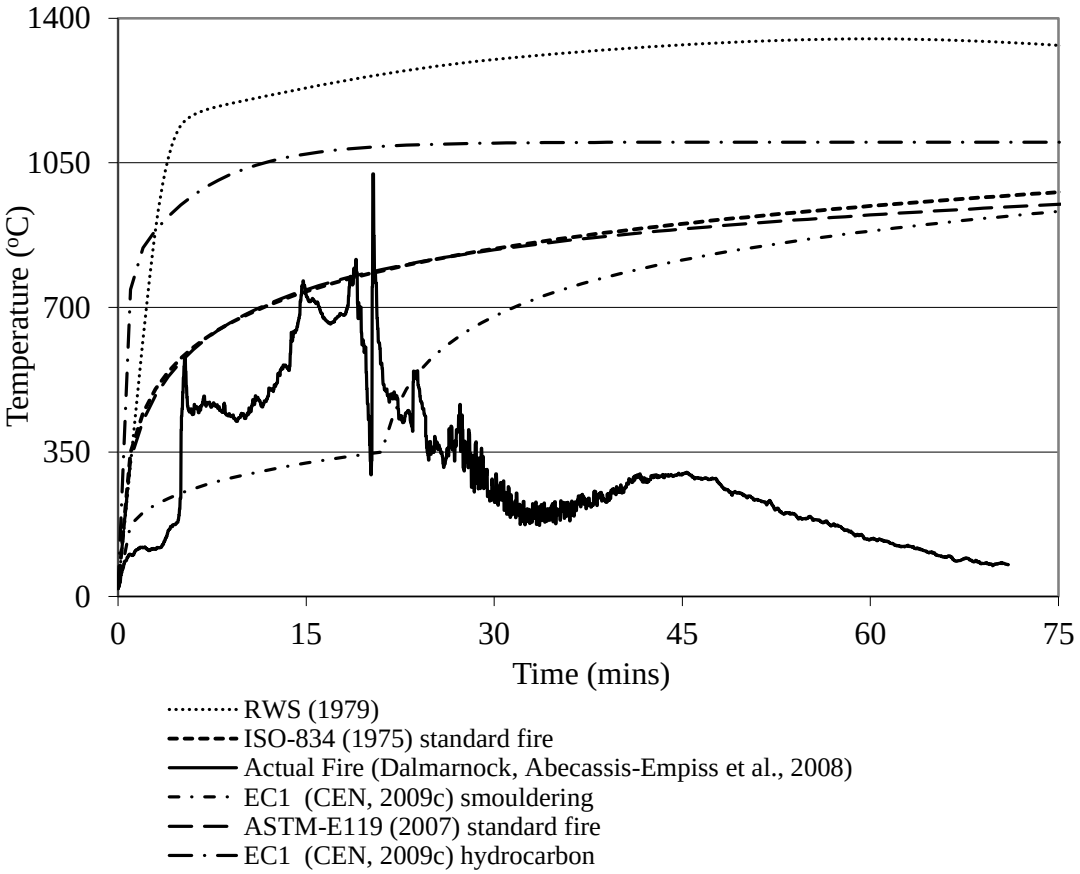

Figure 2-13: Comparison of one real compartment fire (Abecassis-Empis et al., 2008) and a variety of possible standard fires

Essentially all of the models developed have been largely based on tests from standard sized and shaped compartments of reasonably small dimensions. With modern construction forms and larger open plan office spaces with large areas of possible ventilation (glazing), the appropriateness of the code prescribed models may be difficult to defend. A new performance-based methodology which attempts to quantifiably account for travelling fires in large open-plan compartments has been proposed by (Stern-Gottfried et al., 2010) where the fire within a large compartment travels from one point to another.

2.4.3.4 Modelling of intumescents

Modelling of intumescents is a very complex problem. The critical parameter that is required when modelling intumescent coatings for use in heat transfer analyses is the

'effective thermal conductivity' of the protective char layer which forms on heating. EN 13381-8:2010 (CEN, 2010b) gives two possible methods to calculate the effective thermal conductivity: (1) the variable approach and (2) the constant approach. In both of these approaches the density and specific heat of the material (as well as its volume) are assumed fixed at 1000 J/(kg·^{o}C) and 100 kg/m^{3}, respectively. Both approaches use the same basic equation form which is essentially a time-discretized difference calculation based on a simple energy balance:

$$\Delta\theta_{\alpha,t} = \frac{\lambda_{p,t}}{d_p} \times \frac{H_p}{A} \times \frac{1}{c_{p,a,\theta} \times \rho_a} \times \left(\theta_g - \theta_{a,t}\right) \times \Delta t \qquad (2\text{-}39)$$

where $\Delta\theta_{\alpha,t}$ is the steel temperature rise over a time step Δt (which has a specified maximum value of 30s to ensure numerical stability), θ_g is the furnace temperature during that time step, d_p is the dry film thickness of the reactive coating (which is unphysically assumed to remain constant), H_p/A is the section factor of the element, $c_{p,a,\theta}$ and ρ_a are the specific heat and density of steel respectively, and $\lambda_{p,t}$ is the effective thermal conductivity of the protective material at that specific time and for a specific thickness,d_p.

Using this approach a variable thermal conductivity for the intumescent, based on the temperature of the steel measured during a furnace test, can be calculated from tests for an intumescent protection material. This process is presented and applied in Chapter 6 of the current thesis.

Zhang et al. (2012) present a much more complicated, comprehensive finite difference model of an intumescent coating that makes several assumptions including: (1) that the heat and mass transfer is one-dimensional, (2) that the coating is made of three component parts; being acid source, blowing agent and charring material, and following three independent reactions; being melting of the substrate, swelling of the viscous material and charring and degradation of the intumesced material, (3) that the internal pressure of the gases produced during the swelling and charring process remains at one atmosphere so that the expansion rate can be calculated by the ideal gas law, (4) that the char degradation and shrinkage is assumed to be linear with the depletion of charring material, (5) that the mean bubble

size is proportional to the conversion of the blowing agent and inversely proportional to the conversion of the charring materials, (6) that the expansion of the coating only occurs between the temperature of the substrate melting and char forming, and (7) that not all the gases released to create the bubbles are retained in the char, and the amount of gas trapped is assumed to be constant fraction based on a trial and error approach (Zhang et al., 2012).

Zhang et al. (2012) note that their assumptions do not accurately capture the observed reactions but that they are a 'good approximation' and are validated against thermogravimetric and cone calorimeter tests which show good agreement with the model. Using their model, Zhang et al. (2012) are able predict the mass loss rate, the temperature of the substrate, and the expansion thickness of the intumescent char. The major contribution of this model is the trapped gas ratio, which is a function of the local temperature and the mass loss rate. The predictive method was also found not to be sensitive to the calibrated input parameters, strangely suggesting that large inaccuracies in input parameters would not harm the predictive qualities of the model. Whilst the authors show the ability to model the performance of intumescent coatings, this process is complex and difficult to implement in practice.

2.4.4 Fire resistance design guidance for CFS columns

Various design approaches are available for fire-safe design of CFS columns. The following sections describe the most popular of the available approaches used both in Europe and North America.

2.4.4.1 NRCC design guidance

Current North American procedures for the fire resistance design of CFS columns are based on work performed at NRCC. Kodur's (2007) state-of-the-art review notes that the National Building Code of Canada (NBCC, 2005), ASCE-29 (ASCE, 1999), ACI 216 (ACI, 2007) and AISC Fire Guide (Ruddy et al., 2003) all use a semi-empirical design equation developed at NRCC which is expressed as:

$$R = f.\left(\frac{f_c' + 20}{KL - 1000}\right) d^2 \sqrt{\frac{d}{C}} \qquad (2\text{-}40)$$

This equation was developed using a computer analysis program developed at NRCC (Kodur, 2007) which was validated/calibrated against tests conducted by NRCC and CIDECT (Kodur, 1999). In this equation the fire resistance, *R*, is a function of the concrete compressive strength, f'_c, the column's effective length, *KL*, the diameter or width of the column, *d*, the applied load, *C*, and an empirical modification factor, *f* (calibrated using NRCC's sectional analysis computer program (Kodur , 1999)). Table 2-8 provides the recommended values of the *f* factor for PC, RC and FIB concrete.

Table 2-8: Possible values of the empirical parameter *f* in Equation 2-40 (from Kodur, 1999)

Filling type	**PC**		**RC**								**FIB**	
Aggregate type	S[a]	C[b]	S[a]				C[b]				S[a]	C[b]
% of steel reinf.	N/A		< 3		≥ 3		< 3		≥ 3		<1.77[c]	≥1.77[c]
Cover to reinf. (mm)	N/A		< 25	≥ 25	< 25	≥ 25	< 25	≥ 25	< 25	≥ 25	-	-
f – Circular HSS ($x10^{-2}$)	7.0	8.0	7.5	8.0	8.0	8.5	8.5	9.0	9.0	9.5	7.5	8.5
f – Square HSS ($x10^{-2}$)	6.0	7.0	6.5	7.0	7.0	7.5	7.5	8.0	8.0	8.5	6.5	7.5

[a] siliceous aggregate, [b] carbonate aggregate, [c] % of steel fibres by mass.

A unique feature of this approach is that it was developed also to account for the beneficial effects of including steel fibre reinforcement within the infill concrete. Equation 2-40 was developed from tests/modelling that explicitly used the ASTM-E119 (ASTM, 2007) standard fire and it therefore does not allow for other fire scenarios. This somewhat restricts its usefulness for performance-based structural fire design. As seen in Figure 2-13, the ASTM-E119 standard fire time-temperature curve is similar to the ISO 834 (ISO, 1999) curve. Table 2-9 shows the limits of applicability of the NRCC approach.

Table 2-9: Restrictions on application of NRCC approach (Kodur, 2007)

	NRCC		
	PC	*RC*	*FIB*
Fire resistance (mins)	≤ 120	≤ 180	≤ 180
Axial load	≤ 1×	≤ 1.7×	≤ 1.1×
	Factored compressive resistance of the core according to Ref.(CSA, 1994)		
Eccentric loads	Not considered		
Concrete strength (MPa)	20-40	20-55	
HSS size (mm) Circular (*d*) Square (*b*)	 140-410 140-305	 165-410 175-305	 140-410 100-305
% of steel reinf.	N/A	1.5-5	1.75
Concrete cover to reinf. (mm)	N/A	20-50	N/A
Effective length (m)	2-4	2-4.5	

2.4.4.2 EC4 design guidance

EC4 (CEN, 2005) presents three alternative approaches for fire resistance design of CFS columns: (1) a tabulated approach, (2) simple calculation models, and (3) advanced analysis. All three are discussed in the following sections.

Tabulated approach

The simplest approach given in EC4 is to apply prescriptive requirements that are given in Table 4.7 of EC4 (CEN, 2005) which gives minimum sectional properties for a given load ratio (the ratio of the applied load during fire to the nominal load capacity of the element at ambient temperature) and required fire resistance. This is given in Table 2-10. No calculations are required in using the EC4 tabulated approach. The simplicity of this approach makes it highly conservative in its evaluation of the likely fire resistance of a given design. This is partly because the analysis performed in developing the tabulated requirements assumed twice the design buckling length when calculating the resistance to buckling at ambient temperature, and then used this number to calibrate the load ratios. Obviously, this affects the results and ensures their safety by accounting for column imperfections

and load eccentricity or deliberately introduced moments. The approach assigns fire resistance ratings in 30 minute intervals, making it inherently conservative by up to half an hour.

Table 2-10: Minimum cross-sectional dimensions for CFS columns in fire according to the EC4 tabulated approach (CEN, 2005)

Load Level		Minimum cross sectional dimensions at specific standard fire resistance				
		R30	**R60**	**R90**	**R120**	**R180**
≤ 0.28	Diameter (d) of breadth (b or h) [mm]	160	200	220	260	400
	reinforcement ratio ($A_s/(A_c+A_s)$) in %	0	1.5	3	6	6
	Cover (u_s) [mm]	-	30	40	50	60
≤ 0.47	Diameter (d) of breadth (b or h) [mm]	260	260	400	450	500
	reinforcement ratio ($A_s/(A_c+A_s)$) in %	0	3	6	6	6
	Cover (u_s) [mm]	-	30	40	50	60
≤ 0.66	Diameter (d) of breadth (b or h) [mm]	260	450	550	-	-
	reinforcement ratio ($A_s/(A_c+A_s)$) in %	3	6	6	-	-
	Cover (u_s) [mm]	25	30	40	-	-

EC4 simple calculation models

The second suggested approach is to use a relatively simple calculation model, of which there are two alternative methods suggested by EC4, one given in the main text of EC4 and the other given in Annex H (CEN, 2005). Both approaches use a simplified sectional analysis technique which has two distinct steps: first, a temperature distribution over the cross-section is determined (using one of a number of applicable methods) for a given duration of fire exposure, and second, from this thermal analysis a calculation of the design axial buckling/crushing capacity of the column is made. The first steps of both approaches are identical, but the approaches differ in calculating the design resistance to axial compression, $N_{fi,Rd}$.

Step 1: Several methods can be used to calculate the temperature field within the section after a given duration of fire, ranging from detailed finite element analysis to a more simplified one-dimensional (1D) heat transfer analysis based on EC1 (CEN, 2009c) and EC4 (CEN, 2005), in which material thermal properties can be assumed as code-specified constant values or temperature dependant values. Guidance on how

to calculate the temperature profile within a section is widely available (e.g. Lennon et al., 2007). It is noteworthy that EC4 Annex H states that the thermal resistance between the steel wall and the concrete may be neglected, presumably because this is assumed to be a conservative omission.

EC1 (CEN, 2009c) provides guidance on the modelling of the net heat flux, $\dot{h}_{net}$, transferred to elements by the net radiative heat flux, $\dot{h}_{net,r}$, and the net convective heat flux, $\dot{h}_{net,c}$.

$$\dot{h}_{net} = \dot{h}_{net,r} + \dot{h}_{net,c} \quad (2\text{-}41)$$

where

$$\dot{h}_{net,c} = \alpha_{con} \cdot (\theta_g - \theta_m) \quad (2\text{-}42)$$

with α_{con} being the coefficient of heat transfer by convection (taken as 25 W/m^{2o}C for the standard time-temperature curve), θ_g being the temperature of the gas near the member and θ_m being the temperature of the exposed surface of the member.

$$\dot{h}_{net,r} = \Phi \cdot \varepsilon_m \varepsilon_f \sigma[(\theta_r + 273)^4 - (\theta_m + 273)^4] \quad (2\text{-}43)$$

where Φ is the configuration factor, ε_m is the emissivity of the member, ε_f is the emissivity of the fire, σ is the Stephan Boltzmann constant with EC1 prescribing the values as 1.0, 0.7 (for steel and concrete), 1.0 and 5.67 x10^{-8} W/m^{2}K^4, respectively. θ_r is the effective radiation temperature of the fire environment which can be assumed to be the gas phase temperature, θ_g, for a fully engulfed member.

Step 2: Once the temperature profile within the section at a given time of fire exposure has been established, the cross-section is discretized into elements in which the temperature is assumed to be uniform, and, using a simple spreadsheet analysis, relatively simple equations can be used to check that the design resistance of the column, $N_{fi,Rd}$, at the given time (and temperature profile) is greater than the design load in fire, $N_{fi,Sd}$. The calculation of the design resistance is different depending on which approach is adopted (see below).

General design approach: This design approach can be used for all composite columns including concrete filled hollow sections. The design resistance of the column to axial compression is determined by Clause 4.3.5.1 of EC4 (CEN, 2005):

$$N_{fi,Rd} = \chi N_{fi,pl,Rd} \tag{2-44}$$

where χ is a reduction coefficient found from Buckling Curve 'c' of EC3 (CEN, 2009a) and is dependent on the relative slenderness, $\bar{\lambda}_\theta$, of the column at the given time and temperature. $N_{fi,pl,Rd}$ is the design value of plastic resistance to crushing and is given by:

$$N_{fi,pl,Rd} = \sum_j \frac{A_{a,\theta} f_{ay,\theta}}{\gamma_{M,fi,a}} + \sum_k \frac{A_{s,\theta} f_{sy,\theta}}{\gamma_{M,fi,s}} + \sum_m \frac{A_{c,\theta} f_{c,\theta}}{\gamma_{M,fi,c}} \tag{2-45}$$

where $A_{i,\theta}$ is the area of the element at a given temperature, $f_{i,\theta}$ is the strength of the material at a given temperature and $\gamma_{M,fi,i}$ is the material safety factor. The cross section is divided into its constituent parts, with the steel tube (subscript *a*), the concrete (subscript *c*), and any internal steel reinforcement (subscript *s*), and these parts may be discretized further into thinner layers. The relative slenderness, $\bar{\lambda}_\theta$, is given by:

$$\bar{\lambda}_\theta = \sqrt{\frac{N_{fi,pl,R}}{N_{fi,cr}}} \tag{2-46}$$

where $N_{fi,pl,R}$ is the value of $N_{fi,pl,Rd}$ when all the material safety factors $\gamma_{M,fi,i}$ are equal to unity. The Euler buckling load is given by:

$$N_{fi,cr} = \frac{\pi^2 . (EI)_{fi,eff}}{l^2_{eff,\theta}} \tag{2-47}$$

where $l_{eff,\theta}$ is the buckling length of the column in the fire situation and the $(EI)_{fi,eff}$ is the effective flexural rigidity given by:

$$(EI)_{fi,eff} = \sum_j \left(\varphi_{a,\theta} E_{a,\theta} I_{a,\theta}\right) + \sum_k \left(\varphi_{s,\theta} E_{s,\theta} I_{s,\theta}\right) + \sum_m \left(\varphi_{c,\theta} E_{c,sec,\theta} I_{c,\theta}\right) \tag{2-48}$$

where $I_{i,\theta}$ is the second moment of area, $E_{i,\theta}$ is the Young's modulus of the material at a given temperature, $E_{c,sec,\theta}$ is the characteristic value for the secant modulus of

concrete at a given temperature, determined by $f_{c,\theta}/\varepsilon_{cu,\theta}$, and $\varphi_{i,\theta}$ is a reduction coefficient depending on the effect of thermal stresses.

The introduction of the thermal stress reduction coefficient, $\varphi_{i,\theta}$, is to account for the non-uniform temperature profile within a composite section and thus the unequal thermal stresses and strains caused by different material and sectional thermal expansions. The general design approach does not give specific values for these reduction coefficients for concrete filled hollow sections, potentially rendering the method moot for CFS columns. Lennon et al. (2007) offer two solutions to overcome this, the first being the use of the reduction coefficients for partially encased columns in Annex G of EC4, or the second assuming that due to the lack of coefficients presented in Annex H, values of unity can therefore be applied.

The effective length of the column in the fire situation is dependent on where the column exposed is in relation to the building. If the column is on the top floor, then the effective length, $l_{eff,}$ in fire may be considered to be 0.7 times the system length, l, of the column, whereas the intermediate floors have a recommended value of 0.5. The effective length of the lowest floor column subjected to fire is dependent on the rotational rigidity of the connection at the column base.

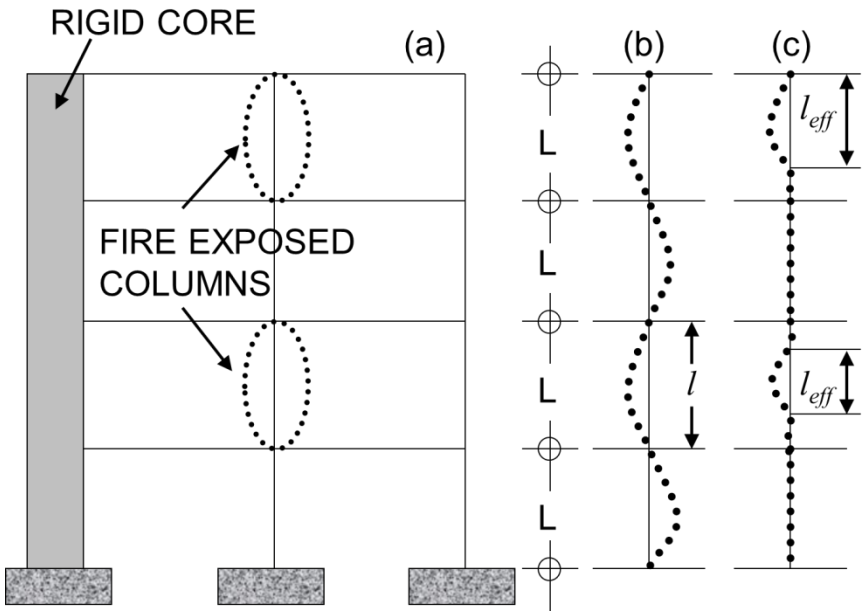

Figure 2-14: Effective length of columns in fire according to EC4 (CEN, 2005)

Annex H approach: This approach is specifically for concrete filled hollow sections and in this approach the design resistance of the column, $N_{fi,Rd}$, is determined directly from the design axial buckling load of the column during fire. This is found by assuming that all materials experience the same strain at a given time and temperature and then determining the strain at which the elastic critical or Euler buckling load, $N_{fi,cr,}$ is equal to the plastic (crushing) resistance to compression of the cross section, $N_{fi,pl,Rd}$ (CEN, 2005):

$$N_{fi,Rd} = N_{fi,cr} = N_{fi,pl,Rd} \tag{2-49}$$

$N_{fi,cr}$ is determined in the same manner as in Equation 2-6 but where the tangent elastic modulus, $E_{Ti,\theta,\sigma}$, is used and is dependent on the temperature and the strain within the discretized layer tangential, rather than, secant modulus.

$$N_{fi,cr} = \frac{\pi^2\left[\sum_j E_{Ta,\theta,\sigma} I_a + \sum_k E_{Tc,\theta,\sigma} I_c + \sum_m E_{Ts,\theta,\sigma} I_s\right]}{{l_\theta}^2} \tag{2-50}$$

$N_{fi,pl,Rd}$ is the summation of the crushing strength contributions of the respective materials at a given temperature and strain:

$$N_{fi,pl,Rd} = \sum_j \left(\frac{A_a \sigma_{a,\theta}}{\gamma_{M,fi,a}}\right) + \sum_k \left(\frac{A_c \sigma_{c,\theta}}{\gamma_{M,fi,c}}\right) + \sum_m \left(\frac{A_s \sigma_{s,\theta}}{\gamma_{M,fi,s}}\right) \tag{2-51}$$

Material models are provided in EC4 (CEN, 2005) to account for temperature induced reductions in mechanical properties of the respective materials (as discussed previously). Load eccentricity is accounted for in this analysis method by replacing the design axial load in fire, $N_{fi,Sd}$, with an equivalent concentric load to the column, N_{equ}, which is increased to reflect the detrimental effects of load eccentricity on fire resistance. The maximum permissible eccentricity is restricted and the following equation is used:

$$N_{equ} = \frac{N_{fi,sd}}{(\varphi_s \varphi_d)} \quad (2\text{-}52)$$

in which φ_s and φ_d are empirically-derived parameters to account for the steel reinforcement ratio and the load eccentricity; these are given graphically in EC4 Annex H.

Neither of these approaches are limited to the standard fire and so by calculating the resistance to load at consecutive instants of fire exposure, a wide variety of fire scenarios can be analysed. This makes this method applicable for performance-based design. The restrictions on the use of the approaches are shown in Table 2-11.

Table 2-11: EC4 Annex H (CEN, 2005) design restrictions

	buckling length l_θ	≤ 4.5 m
140 mm ≤	depth b or diameter d of the cross section	≤ 400
C20/25 ≤	concrete grades	≤ C40/50
0 % ≤	percentage of reinforcing steel	≤ 5 %
	standard fire resistance	≤ 120
	Load eccentricity $\delta = M/N$ (ratio of moment and axial force)	≤ 0.5 *b (or d)*

Advanced calculation models

The most advanced approach permitted by EC4 (CEN, 2005) is the suite of approaches termed ‘advanced calculation’ methods, in which detailed analyses (i.e. finite element models) of structures based on fundamental physical behaviour is permitted. The calculations in these models are complex, and these approaches are therefore not generally applicable to simple structural designs and are not considered in detail in the current discussion. Eurocode 4 (CEN, 2005) stipulates a number of requirements for such detailed modelling approaches. For instance, the thermal actions are to be as specified by EN 1991-1-2 (CEN, 2009c), and the thermal properties of the materials of these steel and concrete composites should be based on those given in EC4 (CEN, 2005). The advanced calculation approaches allow for non-linearity in both thermal and mechanical properties and responses (e.g. local buckling and stress concentrations). In theory, this permits a more realistic analysis,

provided that the true mechanics involved are properly understood and modelled and that appropriate assumptions and inputs (which are often unknown) are used.

The current UK National Annex (CEN, 2008a) prohibits the use of EC4 Annex H. The French national annex (CEN, 2007) provides an alternative design method for concrete-filled hollow sections, as discussed in the following section.

2.4.4.3 French National Annex – Annexe PCRB

Aribert, Renaud and Zhao (2008) have presented a simplified design approach for composite hollow section columns to be used in place of the EC4 Annex H approach. This approach has already been introduced into the French National Annex – Annexe PCRB (CEN, 2007) as it is stated that there are major shortcomings to the current Annex H approach. These can be summarised as follows (after Aribert et al., 2008):

1. The use of Engesser's concept tangent modulus has been extended to composite columns where the component parts of the column experience different temperatures but the same axial strain. This method obviously cannot take into account structural imperfections, self-equilibrated thermal stresses and geometrical second-order local behaviours (like the axial expansion of the steel compared to the concrete during the early stages of heating).
2. The method in Annex H for the determination of the axial buckling load is rather simplistic and is limited to the geometrical first order, thus for columns with relative slenderness above 0.4 the method can over predict the column capacity by up to 2.5 times.
3. The two factors that help to assess the columns' fire resistance under eccentric loading (one a function of the percentage of reinforcement and the other a function that is linked to the relative eccentricity imposed) are strongly coupled and both depend on the relative slenderness of the column in the fire situation.
4. The field of application (Table 2-11) of Annex H is limited and prohibits the design method of realistically sized (i.e. larger) columns in fire.
5. The Annex H method does not follow the same general flow chart for other types of composite columns, where familiar design concepts are used (reduction coefficients $\varphi_{a,\theta}, \varphi_{s,\theta}$ and $\varphi_{c,\theta}$, and buckling curve reduction factors $\chi(\bar{\lambda}_{\theta})$.

The authors set out a method based around the general flow chart as laid out in Clause 4.3.5.1.1 of EC4 (CEN, 2005). As noted above the value of the stiffness reduction coefficients ($\varphi_{a,\theta}, \varphi_{s,\theta}$ and $\varphi_{c,\theta}$) for CFSs are not set in EC4. In the new method Aribert et al. (2008) not only set these but also provide a new method for the calculation of the buckling curve reduction factor.

Stiffness reduction factors were found from numerical calibration against 33 test specimens (why these specific tests were chosen is not clear). Table 2-12 shows the stiffness reduction coefficients for the concrete core, steel reinforcement and steel tube.

Table 2-12: Values of the concrete, steel reinforcement and steel tube stiffness reduction coefficients $\varphi_{c,\theta}$, $\varphi_{s,\theta}$ and $\varphi_{a,\theta}$, according to the French National Annex PCRB approach (CEN, 2007)

Concrete	$\varphi_{c,\theta}$ =	1.2				
Reinforcement	u_s (cover); mm	30	40	50	60	
	$\varphi_{s,\theta}$ =	0.8	0.9	1.0	1.0	
Steel Tube	$\varphi_{a,\theta}$ =	*b* or *d* ; mm				
		100	150	200	250	350 to 610
	R30	0.30	0.23	0.15	0.15	0.15
	R60	-	0.30	0.23	0.15	0.15
	R90	-	-	0.30	0.20	0.15
	R120	-	-	0.30	0.20	0.20

Only the steel tube reduction factor has any time-temperature dependency attributed to it. Table 2-12 shows that as the size of the cross-section increases for a given fire resistance the overall contribution to the flexural stiffness of the steel hollow section decreases, whilst conversely for a given size of cross-section as the fire resistance increases the contribution of the steel hollow section to the overall flexural stiffness increases. This makes sense as the contribution of the concrete in larger sections will be more important at a given fire resistance, and as the fire resistance increases the

concrete's flexural stiffness will decrease, causing the steel hollow section to provide a greater proportion of rigidity to the overall stiffness.

The next change from the general method is the idea of a transitional relative slenderness where there is a discontinuity in the buckling resistance, where a sudden drop in buckling resistance occurs due to the differential thermal elongation between the steel hollow section and the concrete core. During the early stages of heating, the steel hollow section experiences considerable thermal elongation and compressive thermal stress whilst the concrete core (apart from a peripheral compressive zone) experiences tension (Aribert et al., 2008). This can cause rapid cracking in the concrete if the percentage of reinforcing steel is low or zero, and a reduction in stiffness. This behaviour ends when the steel reaches its yield strength and axial shortening of the entire column occurs. The next phase of behaviour is dependent on the column slenderness, $\bar{\lambda}_\theta$. When $\bar{\lambda}_\theta$ is small (i.e. $\bar{\lambda}_\theta < \bar{\lambda}_{\theta,transition}$) the bending of the column is sufficiently limited so that the whole cross-section experiences compressive stresses allowing for limit point instability, where an increase in load causes large deformations but into stable configurations. When $\bar{\lambda}_\theta$ exceeds $\bar{\lambda}_{\theta,transition}$ the flexural bending of the column is more pronounced. This causes a large zone of concrete in the column to be in tension, reducing the moment resistance at mid-height, and causing a steep drop in the stability of the column. This discontinuity reduces as the level of longitudinal reinforcement increases, and at low percentages of reinforcement there is a marked scatter dependent on the size of the section in the analytical data when comparing the relative slenderness to the buckling reduction factor.

To incorporate this transitional stage of buckling, Aribert et al. (2008) propose values for unreinforced composite columns and a graphical method for reinforced columns. For unreinforced columns the values of $\bar{\lambda}_{\theta,transition}$ proposed are as follows (assuming that a fire resistance of greater than 60 minutes is not realistic for unprotected PC infill CFS sections):

$$\bar{\lambda}_{\theta,transition} = \begin{cases} 1.0 \text{ for R30} \\ 1.35 \text{ for R60} \end{cases} \quad (2\text{-}53)$$

For RC infill columns $\bar{\lambda}_{\theta,transition}$ is determined by coupling two types of curves through a non-dimensional parameter, γ. The first curve provides γ as a function of the percentage of reinforcement and the size of the hollow section dependant on the fire resistance rating; they can be found in the French National Annex. Table 2-13 shows the values of γ derived from the figures in the French National Annex where any of the lines can be defined by a minimum and maximum value. The second curve, Figure 2-15, provides a correlation between the function γ and $\bar{\lambda}_{\theta,transition}$.

Table 2-13: Values of α_θ, β and γ (derived from figures 2 to 4 in the French National Annex PCRB (CEN, 2007)) for RC infill columns

	α_θ	β	γ						
			b* or *d (mm)		**Percentage reinforcement**				
					1%	**1.50%**	**2%**	**3%**	**5%**
R30	0.21	0.80	min	150	2.86	2.56	2.25	2.1	1.9
			max	610	5.62	4.71	3.83	3.02	2.31
R60	0.27	0.75	min	150	2.15	2.025	1.9	1.8	-
			max	610	4.26	3.62	2.96	2.33	
R90 & R120	0.34	0.70	min	200	2.1	1.95	1.8	1.75	-
			max	610	3.82	3.16	2.49	2.27	

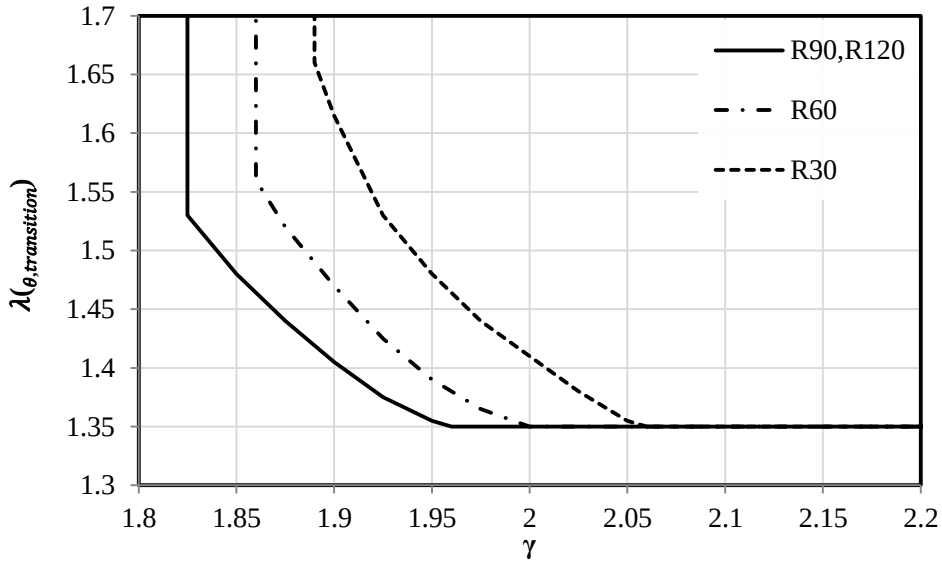

Figure 2-15: Correlation curves of γ and $\lambda_{\theta,transitional}$ for fire resistance ratings up to R120 according to the French National Annex PCRB (CEN, 2007)

The buckling curve reduction coefficient, $\chi(\bar{\lambda}_\theta)$, determination is dependent on whether the relative slenderness is greater or lesser than the transitional relative slenderness.

If $\bar{\lambda}_\theta < \bar{\lambda}_{\theta,transition}$, the buckling curve is expressed by the relationship:

$$\chi(\bar{\lambda}_\theta) = \frac{1}{\phi_\theta + \left[\phi_\theta^2 - \bar{\lambda}_\theta^2\right]^{0.5}} \quad (2\text{-}54)$$

where:

$\phi_\theta = 0.5\left[1 + \alpha_\theta \bar{\lambda}_\theta + \bar{\lambda}_\theta^2\right]$

α_θ is an imperfection parameter given in Table 2-13 and is dependent on the fire resistance rating.

If $\bar{\lambda}_\theta > \bar{\lambda}_{\theta,transition}$, the buckling curve is expressed by the relationship:

$$\chi(\bar{\lambda}_\theta) = \beta\left(\bar{\lambda}_\theta\right)^{-\gamma} \quad (2\text{-}55)$$

For reinforced columns the parameter γ is the same value as introduced for the determination of $\bar{\lambda}_{\theta,transition}$, whilst β depends solely on the fire resistance, as shown in Table 2-14.

For unreinforced columns β and γ are found in tabulated form as a function of the breadth (or depth) squared divided by the wall thickness of the hollow section as shown in Table 2-14.

Table 2-14: Values for β and γ for unreinforced columns in the French National Annex PCRB (CEN, 2007)

(b or d)^2 / e (mm)	2.5 x10^3	5 x10^3	7.5 x10^3	10 x10^3	12.5 x10^3	15 x10^3	20 x10^3	25 x10^3	30 x10^3	40 x10^3	50 x10^3
β =	0.78	0.69	0.60	0.51	0.43	0.40	0.36	0.32	0.25	0.20	0.12
γ =	2.49	2.68	2.87	3.03	3.16	3.20	3.27	3.35	3.42	3.57	3.72

The determination of the load capacity of the column is then determined using the same equation, Equation 2-44, as used in the general method of EC4.

This method also provides a correction factor to be applied to the axial buckling resistance, which depends on the relative slenderness, for eccentric loading:

$$N_{fi,Rd,\delta} = \varphi_{ecc} N_{fi,Rd} \tag{2-56}$$

where:

$$\varphi_{ecc} = \begin{matrix} a_1 + b_1\left(\bar{\lambda}_\theta - 1.35\right) & \bar{\lambda}_\theta < 1.35 \\ a_2 + b_2\left(\bar{\lambda}_\theta - 1.35\right) & \bar{\lambda}_\theta \geq 1.35 \end{matrix}$$

where: a_1 and b_1 are dependent on the percentage reinforcement (A_s/A_c) and the relative eccentricity, whilst a_2 and b_2 are dependent on the percentage reinforcement, the relative eccentricity and the fire resistance time (and in the case of b_2, also linearly on the hollow section size b (or d)). The coefficient b_2 is obtained by the linear relationship:

$$b_2 = \omega_0 + \omega_1 \cdot b(or\ d)$$

where ω_0 and ω_1 are based on the percentage reinforcement, as shown in Table 2-15.

This new approach laid out in the French National Annex allows for a greater range of sizes to be treated, as well as stronger infill concretes. The field of application of this method is greater than that of the Annex H approach and is shown in Table 2-16.

The method described has been calibrated by Aribert et al. (2008) against a numerical model which was calibrated against 33 tests from France, Germany and Canada. The consistency of the new simplified approach to the model was shown to be good, with the vast majority of predictions made by the simplified method being within 10% of the model. A more detailed analysis of the simplified method's ability to predict a much larger database of tests is performed in Chapter 3.

Table 2-15: Coefficients; a_1 & b_1; a_2 and ω_0 & ω_1, for the calculation of b_2, for eccentrically loaded columns in the French National Annex PCRB approach

	Relative eccentricity	Percentage of reinforcement A%							
		Coefficient a_1				**Coefficient b_1**			
		1%	2%	3%	5%	1%	2%	3%	5%
a_1 & b_1	0.125	0.33	0.46	0.55	0.59	-0.41	-0.25	-0.12	-0.07
	0.250	0.25	0.33	0.37	0.45	-0.19	-0.13	-0.09	-0.03
	0.500	0.19	0.23	0.26	0.30	-0.07	0.00	0.02	0.06
	1.000		0.15	0.18	0.19		0.04	0.06	0.05
	Relative eccentricity	Percentage of reinforcement A%							
		Coefficient a_2 (R30)				**Coefficient a_2** (R60, R90, R120)			
		1%	2%	3%	5%	1%	2%	3%	5%
a_2	0.125	0.61	0.62	0.63	0.64	0.48	0.54	0.59	0.63
	0.250	0.48	0.46	0.46	0.49	0.37	0.41	0.44	0.49
	0.500	0.34	0.32	0.32	0.32	0.23	0.28	0.30	0.33
	1.000		0.21	0.22	0.22		0.16	0.18	0.19
	fire resistance	Percentage of reinforcement A%							
		1%		2%		3%		5%	
		ω_0	ω_1	ω_0	ω_1	ω_0	ω_1	ω_0	ω_1
b_2	R30	-0.23	4.69	-0.02	1.43	0.08	0.57	0.13	0.29
	R60	0.00	1.37	0.02	0.74	0.06	0.43	0.05	0.69
	R90			0.06	0.37	0.07	0.30	0.05	0.50
	R120			0.10	0.27	0.07	0.30	0.08	0.43

Table 2-16: Aribert et al. (2008) field of application for the French National Annex PCRB approach

Type of Concrete		**Unreinforced concrete ($e = 0$)**		**Reinforced concrete**	
Strength Class (MPa)		C20/25 – C60-75			
Buckling length		$l_{eff}/(b \text{ or } d) \leq 30$			
Fire resistance		R30	R60	R30, R60	R90,R120
Min dimension (mm)		100	150	150	200
Max dimension (mm)		610			
Min A_s/A_c (%)	$e = 0$	N/A		1	
	$0.125 \leq e \leq 0.5$			1	2
	$0.5 \leq e \leq 1.0$			2	
Max A_s/A_c (%)	$e = 0$			5	
	$0.125 \leq e \leq 1.0$				

2.5 Residual strength of CFS sections after fire

Chapter 7 of this thesis presents a series of structural tests to failure of fire-damaged protected and unprotected CFS columns. The following sections provide a summary of the relatively sparse available knowledge on the residual mechanical properties of relevant materials after heating.

2.5.1 Steel residual properties

It is commonly understood that during a fire, that a structural steel element will retain approximately 60% of its ambient temperature strength at about 550^{o}C and this is widely considered to be an appropriate simplification of the failure temperature of structural steel. This is not the case when we consider the residual strength of a steel element which, from a residual (i.e. post-heating) perspective, loses little of its strength regardless of the temperature experienced.

Most structural steel rolled sections are formed at temperatures between 810 and 920^{o}C (Tide, 1998) where the material is mainly austenite, with small amounts of carbon and other alloying materials. As the material cools to below 770^{o}C the austenite changes form to its ambient temperature structure of cementite, pearlite and ferrite. This phase change is reversible, so an element heated up to 920^{o}C will only experience a minimal amount of residual strength loss and below the phase change

temperature it will regain close to 100% of its ambient properties (Tide, 1998). Kirby et al. (1986) report no strength loss below 600^{o}C and a linear strength decreases to losses of 15% and 30% for S275 and S355 steel, respectively, at 1000^{o}C.

2.5.2 Concrete residual properties

The residual strength of concrete is highly dependent on the level of temperature exposure. When concrete is heated a progressive series of physical and mineralogical changes occur and continue to occur during cooling. There is a continual degradation of the microstructure under the influence of high temperature, and the longer the concrete is exposed to heat the greater the degradation, leading to a lower residual strength (The Concrete Society, 2008). Not only is the residual strength of a concrete dependent on the duration of heating and the temperatures achieved but also on the type of aggregate, loading conditions and stress level during heating and cooling, and the concrete mix proportions (cement type, cement blend, additives and binders, water) (The Concrete Society, 2008). Figure 2-16 shows a comparison of test data assessing the high temperature residual strength of concrete.

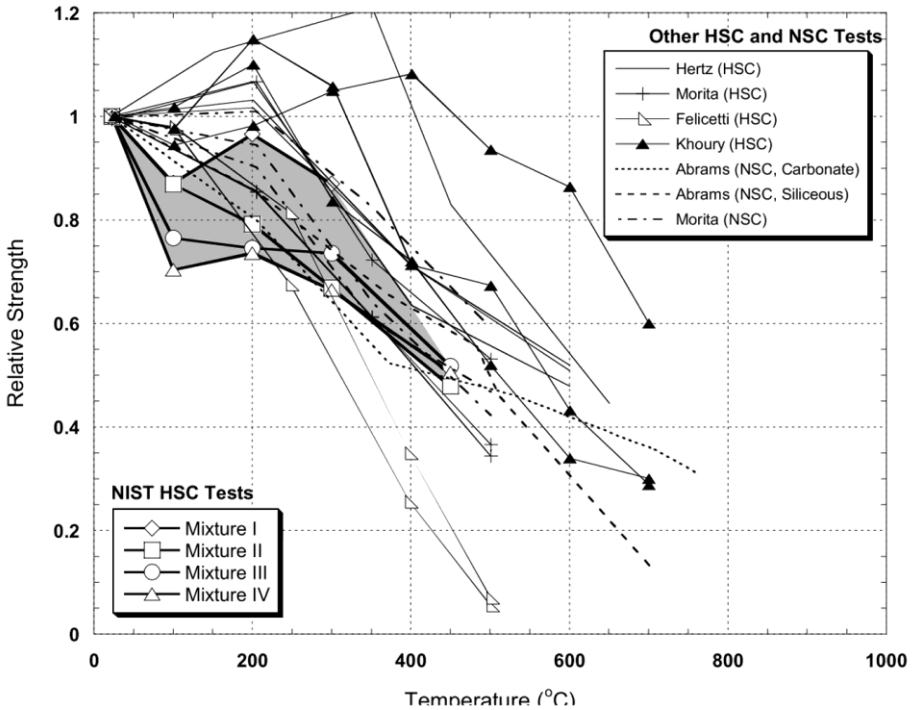

Figure 2-16: Comparison of high temperature residual strength tests of normal (NSC) and high strength concrete (HSC) (from Phan, 2002)

Table 2-17 summarises the main changes in concrete mineralogy on heating and their effects on residual strength. The first major change is the vaporisation of water physically bound in the cement matrix and aggregates. The high pressure water vapour fills the micro-pores in the concrete and can cause minor micro-cracking as the pressure increases past the tensile stress of the concrete (The Concrete Society, 2008). When the concrete temperature reaches 250 to 350^{o}C the chemically bound water in the cement starts to disassociate and significant strength loss starts to occur. This coincides with iron oxidisation within the aggregate causing a pink/red discoloration of the concrete which is more evident in siliceous concrete that have higher iron content (The Concrete Society, 2008). Once the temperature of the concrete exceeds 600^{o}C it has little to no residual value structurally due to the degradation of the cement matrix and aggregates and micro-cracks.

The degradation of concrete is similar between normal and high strength concrete (Anand and Arulraj, 2011), and is seen in most testing (e.g. Netinger et al. (2011) and Chen and Liu (2004)). The residual strength of concrete after it has experienced temperatures of 600^{o}C is between 35-50% of the ambient strength; at 800^{o}C this drops to between 10-40% and at 1000^{o}C to 5-30% depending on the mix design (Netinger et al., 2011). Test have also shown that using steel fibre within the concrete mix can increase the residual strength by 5-15% (Lau and Anson, 2006).

Table 2-17: Concrete mineralogical and strength changes due to heating (after The Concrete Society, 2008)

Heating temperature (^oC)	Changes caused by heating	
	Mineralogical changes	**Residual strength changes**
105 -140	Loss of physically bound water in cement and aggregates. Increase in capillary porosity and minor micro-cracking	Minor loss of strength possible (< 10%)
250-350	Pink/red discoloration of aggregate caused by oxidation of iron compounds. Bound water in cement matrix and associated degradation increases.	Significant strength loss from 300^oC
450-500	Dehydroxylation of portlandite. Continued discoloration of aggregates (deeper red) and cement matrix (yellow/beige in cross-polarised light).	
573	Transition of quartz from α- to β- phase, causing an increase in volume of about 5% and cracking of the aggregates.	Complete loss of structural integrity in temperatures in excess of 550-600^oC
600-800	Decarbonation of carbonates. Significant in calcareous concretes where contraction can be considerable due to the release of CO_2. This can cause severe micro-cracking of the remaining cement matric.	
800-1200	Complete disintegration of calcareous constituents of the aggregates and cement. Severe micro-cracking and discoloration (whitish grey)	
1200		Concrete starts to melt

2.5.3 Residual strength experiments on CFS column

The residual strength of CFS columns and ultimately the ability of a framing system to continue to carry load after a fire is an ever increasing economic and environmental driver in design. Lin-Hai Han (e.g. Han et al., 2002) is currently the only serious contributor to the analysis of CFS columns after fire. Table 2-18 gives a summary of Han's experimental programs on CFS columns. All of the specimens were subjected to the ISO 834 fire curve in Han's research.

Table 2-18: Residual Strength Tests (Han et al., 2005, 2002; Han and Huo, 2003)

	Specimen			Steel				Concrete			Test				Failure load
	Shape	Fixity	l	d *or* b	t_a	E_a	f_{sy}	$f_{cu,28}$	$f_{cu,test}$	E_c	T_{min}	a	e	λ_{Han}	N_{ue}
			mm	mm	mm	GPa	MPa	MPa	MPa	GPa	min	mm	mm	C = $4l/d$ S/R = $2\sqrt{3}l/d$	kN
Concentric Unprotected	C 4	PP 4	400-1200	108-133	4.32-4.8	190-201	340-356	47-70	53 - 71	30 - 31	90	0	0	12 - 44	362-632
	S/R 6	PP 6	380-1200	80-120	2.9-2.93	195-201	294-330	34 - 47	35 - 53	27 - 30	90	0	0	11 - 42	214-416
Eccentric Unprotected	C 2	PP 2	600-1200	108	4.32	201	356	70	72	31	90	0	15	22 - 44	227-387
	S/R 4	PP 4	600-1200	80-120	2.93	195	294	34	35 - 36	27	90	0	15-18	21 - 42	148-259
Concentric Protected	C 1	PP 1	900	108	4.32	201	356	70	72	31	180	25	0	33	779
	S/R 3	PP 3	900	80-120	2.93	195	330-294	34	35 - 36	27.44	180	25	0	26 - 32	358-455
Eccentric Protected	C 1	PP 1	900	108	4.32	201	356	70	72	31	180	25	15	33	485
	S/R 1	PP 1	900	100	2.93	195	294	34	35	27	180	25	15	31	302

C = circle, S/R = square/rectangular, PP = pin-pinned, l = length, d *or* b = depth or breadth, t_a = wall thickness, E_a = steel modulus of elasticity, f_{sy} = steel yield strength, $f_{cu,28}$ = 28-day concrete strength, $f_{cu,test}$ = test-day concrete strength, E_c = concrete modulus of elasticity, T_{min} = fire duration, a = protection thickness, e = eccentricity, λ_{Han} = slenderness according to Han and Huo (2003), and N_{ue} = ultimate failure load in the experiment.

The residual mechanical behaviour of fire exposed CFS columns under axial load was found to be ductile and it was seen that the composite enhancement of the concrete core was still present (Han et al., 2005). The columns failed in either global buckling ($l > 3d$) or local buckling with accompanying concrete core crushing ($l < 3d$). The global buckling failure can be considered to have three steps:

1. when the load is small, the lateral deflection at mid-height is small and approximately proportional to the axial load;
2. when the load reaches 60-70% of the failure load, the lateral deflection increases significantly; and
3. the failure of the specimens is seen by rupture of the steel after substantial cracking of the concrete, both in the tension zone, and a buckling of the steel in the compression zone.

The fire duration, column section size and the slenderness ratio have significant effects on the residual strength of the columns, whereas the other major parameters (steel ratio, concrete strength, steel strength, and steel ratio) have only a moderate effect. The fire exposure increases deflections and decreases the strength of CFS columns above 10 minutes of fire exposure time. Below this time there is deterioration of strength (Han et al., 2003). The testing also considered the effects on the residual strength of the columns if they were protected, unsurprisingly finding that the loss of strength was less for the protected situation (Han et al., 2002). An interesting phenomenon noted in the testing was that the effect of load eccentricity on the residual strength index of the column appeared to be important**.**

Huo et al. (2009) tested 15 stub columns to assess the effects of sustained pre-load and cooling phase on the residual strength and stiffness of CFS columns. The tubes were very short ($l < 330$ mm) and heated by a non-standard regime and so were not included in Table 2-18. Similar results to those by Han were obtained, in fact that the failure mechanism was local elephant's foot buckling. Huo et al. (2009) tests showed that pre-load in the columns had a remarkable effect on the mechanical behaviour of the column, and that the higher the pre-load level and the higher the exposed temperature, the greater the residual deformations within the columns. If the column

was exposed to a maximum of 400^{o}C then there was no obvious strength loss suffered. Above this temperature, considerable strength losses were observed. The temperatures that the concrete experiences during heating will also affect the bond behaviour. The higher the temperatures in the concrete, the lower the strength and therefore the load that can be applied through the concrete, through friction and shear at the surface, is reduced. Conversely, the higher the concrete temperature reached the easier the material will dilate (because of the greater presence of micro- and macro-cracks), thus creating contact with the steel tube (Tao et al., 2011).

2.5.4 Computational and analytical studies on high temperature residual performance of CFS sections

2.5.4.1 Structural modelling

High temperature residual strength finite element modelling analysis has been presented by Huo et al. (2009), in which both the residual strength of CFS columns and the thermal modelling of CFS with both a heating and cooling phase were considered. In their thermal model, Huo et al. (2009) used the material model proposed by Irwin and Lie (1990) discussed. The model also used a thermal contact conductance between the steel and the concrete of 100 W/m^2·K as proposed by Ding and Wang (2009). It was found that in the thermal modelling the effect of the vent holes could be neglected. No local buckling occurred and the columns failed residually due to elephants foot buckling.

Han and Huo (2003) have also modelled the residual strength of composite columns using a modified material model applied to the design method stated in GJB4142-2000 (GJB, 2001). The modified model showed good agreement with test data. From this refined material model the authors were able to create a set of formulae to predict the residual strength of CFS columns exposed to the ISO 834 fire.

2.5.4.2 Material modelling

The residual material mechanics of the steel and the concrete are described in Han and Huo (2003). For steel, a bi-linear stress-strain curve, shown in Figure 2-17, is given:

$$\sigma = \begin{cases} E_a(\theta_{a,max}) \cdot \varepsilon_a & \varepsilon_a \le \varepsilon_{sy}(T) \\ f_{sy}(\theta_{a,max}) + E_1(\theta_{a,max}) \cdot [\varepsilon - \varepsilon_{sy}(\theta_{a,max})] & \varepsilon_a > \varepsilon_{sy}(T) \end{cases} \quad (2\text{-}57)$$

in which $E_a(\theta_{a,max})$ = Young's modulus of steel;

$\varepsilon_{sy}(\theta_{a,max}) = f_{sy}(\theta_{a,max})/E_s(\theta_{a,max})$; $E_1(\theta_{a,max}) = 0.01E_s(\theta_{a,max})$;

$f_{sy}(\theta_{a,max})$ = the yield strength of steel after exposure to high temperature, $\theta_{a,max}$, and is expressed as:

$$f_{sy}(\theta_{a,max}) = \begin{cases} f_{sy} & \theta_{a,max} \le 400^oC \\ f_{sy}.[1 + 2.33\text{x}10^{-4} \cdot (\theta_{a,max} - 20) - 5.88\text{x}10^{-7} \cdot (\theta_{a,max} - 20)^2] & \theta_{a,max} > 400^oC \end{cases}$$

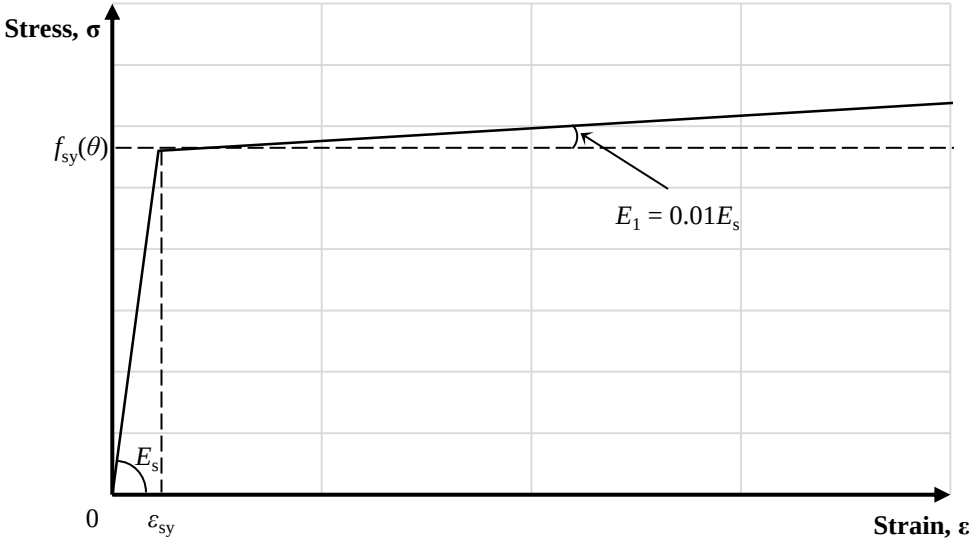

Figure 2-17: Bi-linear stress-strain relationship for the residual strength of steel (from Han and Huo, 2003)

The stress-strain relationship for the concrete is slightly more complex where confinement, ξ, of the concrete core plays an important role. The model used by Han and Huo (2003) is a modification of an ambient model where a reduction in the yield stress and strains due to temperature are introduced and are as follows. The stress-strain relationship for square sections is:

$$y = \begin{cases} (2.0 - 0.1 \cdot \xi^{0.745}) \cdot x - (1.0 - 0.1 \cdot \xi^{0.745}) \cdot x^2 & x \le 1 \\ \dfrac{x}{\beta_s x^{\eta} + x} & x > 1 \end{cases} \quad (2\text{-}58)$$

whereas for circular sections it is:

$$y = \begin{cases} (2.0 - 0.1 \cdot \xi^{0.745}) \cdot x - (1.0 - 0.1 \cdot \xi^{0.745}) \cdot x^2 & x \le 1 \\ 1 + \left(\dfrac{\xi^{0.745}}{2 + \xi}\right) \cdot (x^{0.1\xi} - 1) & (\xi \ge 1.12) \\ \dfrac{x}{\beta_c \cdot (x-1)^2 + x} & (\xi < 1.12) \end{cases} \quad x > 1 \quad (2\text{-}59)$$

where:

$$\beta_s = \begin{cases} \dfrac{0.75 \cdot {f_{ck}}^{0.1}}{\sqrt{1+\xi}}, & \xi \le 3.0 \\ \dfrac{0.75 \cdot {f_{ck}}^{0.1}}{\sqrt{1+\xi} \cdot (\xi - 2)^2}, & \xi > 3.0 \end{cases} ;$$

$$\beta_c = (2.36\text{x}10^{-5})^{[0.25 + (\xi - 0.5)^7]} \cdot f_{ck}^2 \cdot (5\text{x}10^{-4}) \ ;$$

$$\eta = 1.60 + 1.5 \cdot \left(\frac{\varepsilon_{0p}(\theta_{c,max})}{\varepsilon}\right) \ ;$$

$$\xi = \frac{A_s f_{sy}(\theta_{a,max})}{A_c f_{ck}} \ ; \text{and}$$

$$y = \sigma / \sigma_{0p}(\theta_{c,max}), \qquad x = \varepsilon / \varepsilon_{0p}(\theta_{c,max})$$

The residual compressive peak strength ($\sigma_{0p}(\theta_{c,max})$) and corresponding strain ($\varepsilon_{0p}(\theta_{c,max})$) of the confined concrete heated to a maximum temperature, $\theta_{c,max}$, and having cooled down to ambient temperature is given by Yang et al. (2008). Figure 2-18 shows the stress strain relationship of the concrete core when applying equations 2-58 to 2-65 with f_{ck} = 41 MPa, f_y = 345 MPa, and ξ = 1.0.

For square sections this is given as:

$$\sigma_{0\mathrm{p}}(\theta_{c,max}) = f_{cp}(\theta_{c,max}) \cdot \left[1 + (-0.0135\xi^2 + 0.1\xi) \cdot \left(\frac{24}{f_c'}\right)^{0.45} \cdot \left(1 - \frac{\theta_{c,max}}{1000}\right)^{9.55}\right] \quad (2\text{-}60)$$

$$\varepsilon_{0\mathrm{p}}(\theta_{c,max}) = \varepsilon_{ccp}(\theta_{c,max}) + \left[1330 + 760 \cdot \left(\frac{f_c'}{24} - 1\right)\right] \quad (2\text{-}61)$$

whereas for circular sections it is:

$$\sigma_{0\mathrm{p}}(\theta_{c,max}) = f_{cp}(\theta_{c,max}) \cdot \left[1 + (-0.054\xi^2 + 0.4\xi) \cdot \left(\frac{24}{f_c'}\right)^{0.45} \cdot \left(1 - \frac{\theta_{c,max}}{1000}\right)^{9.55}\right] \quad (2\text{-}62)$$

$$\varepsilon_{0\mathrm{p}}(\theta_{c,max}) = \varepsilon_{ccp}(\theta_{c,max}) + \left[1400 + 800 \cdot \left(\frac{f_c'}{24} - 1\right)\right] \quad (2\text{-}63)$$

where:

$$f_{cp}(\theta_{c,max}) = \frac{f_c'}{1 + 2.4 \cdot (\theta_{c,max} - 20)^6 \mathrm{x} 10^{-17}} \quad (2\text{-}64)$$

$$\varepsilon_{ccp}(\theta_{c,max}) = \left[1 + \left(1500 \cdot \theta_{c,max} + 5 \cdot {\theta_{c,max}}^2\right)\mathrm{x}10^{-6}\right] \cdot (1300 + 12.5 \cdot f_c') \quad (2\text{-}65)$$

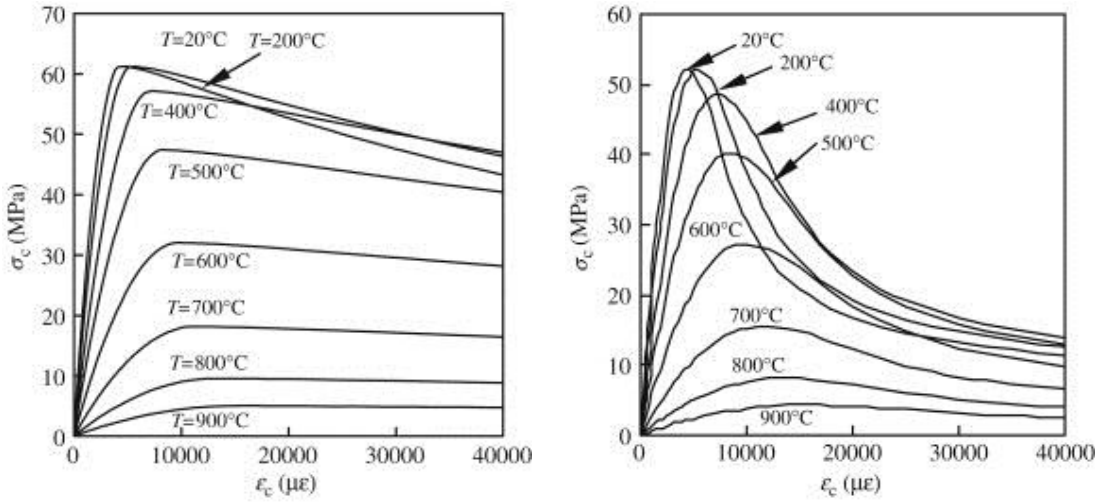

Figure 2-18: High temperature residual stress-strain curves of concrete within (a) circular and (b) square CFS sections at various temperatures for columns subjected to the ISO 834 fire (from Yang et al., 2008)

2.5.5 Residual strength design

Residual Strength Index (*RSI*) formulas for composite columns without fire protection exposed to the ISO 834 fire curve have been developed by Han and Huo (2003). The *RSI* was calculated using the relationships laid out in the previous section for each individual section, and then a parametric regression analysis was performed to obtain simplified *RSI* relationships for circular and square sections. For circular columns the *RSI* is given as:

$$RSI = \frac{N_u(t)}{N_u} = \begin{cases} (1 + 0.15t_0 - 2t_0^2 + 2t_0^3).f(D_0).f(\lambda_0) & t_0 \le 0.6 \\ (1 - 0.39t_0 + 0.095t_0^2).f(D_0).f(\lambda_0) & t_0 > 0.6 \end{cases} \quad (2\text{-}66)$$

whereas for rectangular sections the *RSI* is:

$$RSI = \frac{N_u(t)}{N_u} = \begin{cases} (1 - 0.036t_0 - 0.59t_0^2).f(D_0).f(\lambda_0) & t_0 \le 0.6 \\ (1 - 0.46t_0 + 0.117t_0^2).f(D_0).f(\lambda_0) & t_0 > 0.6 \end{cases} \quad (2\text{-}67)$$

where:

$$f(D_0) = \begin{cases} a.D_0^2 + b.D_0 + c, & D_0 \le 1 \\ d.(D_0 - 1) + 1, & D_0 > 1 \end{cases}$$

in which: $a = -0.73t_0 + 0.087$; $b = 1.41t_0 - 0.14$; $c = -0.68t_0 + 1.05$; and $d = 0.039 \ln t_0 + 0.09$; and

$$f(\lambda_0) = \begin{cases} e.\lambda_0 + f, & \lambda_0 \le 1.875 \\ g.\lambda_0 + h, & \lambda_0 > 1.875 \end{cases}$$

in which: $e = 0.05t_0^2 - 0.17t_0 + 0.018$; $f = -0.05t_0^2 + 0.17t_0 + 0.98$; $g = -0.06t_0^2 + 0.25t_0 - 0.039$; and $h = 0.1t_0^2 - 0.58t_0 + 1.09$; and

$$t_0 = \frac{t}{100}, \qquad D_0 = \frac{d}{600}, \qquad \lambda_0 = \frac{\lambda_{Han}}{40}$$

The units for time, *t*, are minutes and the sectional dimension, *d*, is in mm. The limits of applicability of these formulas are given by: $t \le 180$ min; $d = 200 -$

2000 mm; $A_s/A_c = 0.04 - 0.2$; $\lambda = 15 - 80$; $f_{sy} = 200 - 500$ MPa; $f_{ck} = 20 - 60$ MPa; and $e/d = 0 - 1.5$.

These equations are relevant only to unprotected sections subjected to standard fires, and therefore their applicability for real fires in real buildings is extremely limited

2.6 Knowledge gaps for the fire performance of CFS columns

2.6.1 Fire scenario

Current fire design procedures for CFS columns are based almost uniformly on standard furnace testing which has used standard fires. This is clearly inaccurate to model real fires (Beyler et al., 2007), and advanced structural fire engineering solutions thus typically impose parametric design fires in a performance-based environment. Data on the performance of CFS columns in real fire scenarios, which notably include a cooling phase, are not currently available. Assumptions made in modelling of the emissivity of fire environment within a furnace, and thus the heat transfer to the elements, vary greatly. Real fires (localized or travelling) may also impose non-uniform heating which may induce column curvatures and the formation of plastic hinges or thermal curvatures leading to secondary moments in real structures. This may also be important for CFS columns forming part of a compartment wall or building façade, where one-sided heating may occur.

2.6.2 Materials of construction

Most testing and modelling to date has focused on normal strength concrete infill whereas current practice is to use higher strengths. High strength concrete is known to be prone to spalling, to suffer proportionally greater losses in compressive strength on heating, and to display lower dilatency on loading, all of which may affect its response to loading in fire. Few tests have been performed on such columns (either constitutive, thermo-mechanical, or full-scale). Research (Kodur and Lie, 1995, 1996a) has suggested that FIB infill (whether normal strength or high strength) can provide similar fire resistance as RC infill (under concentric loading) although only limited data are available and the mechanisms of the improved response are neither confirmed nor understood, particularly when flexural effects are present. The thermal

and mechanical properties of steel are generally well established; however the reported values of the emissivity of steel in the literature vary considerably.

2.6.3 Sectional properties and response

The effects of differential thermal expansion and gap formation on the heat transfer within, and structural response of, CFS columns needs to be better understood, both for protected and unprotected columns. The size and timing of gap formation has been shown to affect heat transfer calculations for CFS columns and may affect the evolution and effectiveness of applied intumescent fire protection, when present. Both of these issues are treated later in this thesis. The cross-sectional size of a CFS column may influence the mechanical and thermal response of the column, particularly when intumescents are used (smaller sections tend to experience 'stickability' reductions). Column sizes being used commonly in high rise buildings are typically in excess of 600 mm in minimum dimension and can exceed 1600 mm, with plate thickness of 25 mm or more. No realistic testing has been done (or is foreseeable) on columns of this size, so a fundamental understanding of the underlying mechanics is needed to extend models and develop defensible designs. The bond-slip between infill concrete and steel tube has also received relatively little attention but clearly has relevance for load introduction or when bending is present.

2.6.4 Mechanical loading during fire (full structure response)

While a few tests with eccentric loading have been reported in the literature, little information is available for the most practically interesting cases of unprotected FIB infill and protected FIB and PC infill columns. For perimeter/edge elements in steel frames and 'diagrid' frames, the potential effects of bending moments on CFS columns and the formation and location of plastic hinges in the fire limit state need to be rationally assessed, particularly for un-braced structures. The appropriate effective length of CFS columns in fire has received considerable research attention (e.g. Wang, 2005), yet available guidance (which is based almost entirely on computational modelling) may be unconservative as discussed previously. How, why, and where local buckling might occur and how this might affects global failure

of a CFS column remains unclear (Wang, 2005), and the ability to accurately predict column failure modes appears to be marginal at present.

2.6.5 Applied fire protection

Very little research is available on the use of intumescent coatings, which are by far the preferred method of fire protection, for CFS members. Well-validated models are not yet available to predict the evolution of material/thermal properties in the intumescent process. Such models are needed for rational, performance-based design of these systems. Current interim guidance is therefore necessarily prescriptive (e.g. Wang and Orton, 2008). Questions remain as to the consistency and uniformity of protection provided by intumescent systems that were developed for hollow or profiled sections on CFS columns and the consequences for structural performance in real fires where non-standard, localised, or non-uniform heating (and cooling) may occur. This issue is treated later in this thesis.

2.6.6 Connections and load introduction

It is critically important in buildings incorporating CFS columns to ensure that loads from beams and floor plates can be transferred into the CFS concrete core, both during ambient design and in design for fire. Various methods to accomplish load transfer in these members are available, including internal shear connectors or through plates. Very few studies are available, however, on the heat transfer or structural performance of beam and floor plate connections to CFS columns during fire (Ding and Wang, 2009) and additional research is needed to identify robust, convenient, and economical beam-to-CFS column connections.

2.6.7 Residual strength of columns

The residual strength of CFS elements after fire is an area that has had little attention to date. The rehabilitation and safe re-entry into buildings using this design element is based on the work of a few authors and more information is needed. This is also critical as the columns may not fail during a fire but during the cooling phase or when they have returned to ambient temperature; the response during these times is dependent on the specific heating and loading histories (Yang et al., 2008).

2.7 Chapter summary

This chapter has presented an extensive state-of-the-art review of the development, design and assessment of the fire performance of CFS columns. It has shown that the ambient design of CFS columns has received extensive attention with over 1900 specimens being tested and many analytical studies conducted to understand and improve design. The structural fire resistance of CFS columns has received less attention with 380 specimens tested within furnaces; however little research has been devoted to the protection of CFS columns with intumescent protection. Similarly little experimentation has occurred on the characterisation and understanding of cross-sectional effects that are observed during the furnace tests, such as the formation of an air gap between the steel and the concrete. Many of the experimental studies reported steel tube failure temperatures; however the full cross-sectional thermal profile is less widely reported. The application and thermal effects of intumescent fire protection on CFS columns has received little attention in the literature with only 24 loaded furnace tests having occurred. This inhibits the ability to accurately check whether thermal modelling approaches are capturing the thermal profiles accurately and the subsequent ability to predict the structural fire resistance of CFS columns is not well understood. It has also been shown that the post-fire residual structural capacity of CFS columns has received very little attention with only 22 experiments reported in the literature, and simplistic design models are based on these tests. In the following chapters some of the issues and knowledge gaps presented in this chapter are studied and recommendations for future design are provided.

Chapter 3: Meta-analysis of available furnace test data

This chapter presents an empirical statistical assessment of code-based fire resistance design approaches for CFS columns in North America (Kodur, 2007) and Europe (CEN, 2005, 2007) by comparing code-predicted fire resistance times against observed fire resistance times from standard fire resistance tests carried out worldwide during the past 60 years. The chapter also assesses the ability to predict the failure temperatures of steel tubes in a CFS column, which is necessary for the accurate specification of fire protection systems (particularly intumescents). More than 300 furnace tests have been performed on CFS columns, as already highlighted in Section 2.3.1.1. To fairly assess the each of the available design approaches only applicable sections, defined by the limits of each approach, are used in each case.

As noted in Chapter 2 there are many uncertainties associated with CFS sections in fire. The meta-analysis presented in this chapter is an attempt to determine how accurately existing design codes and other calculation methods can predict the thermal and structural response, temperatures at failure, and most importantly the failure time of the specimens. The chapter focuses on the assumptions made in, and the uncertainties associated with, available research (whether experimental or numerical) and design approaches, and aims to provide a statistical assessment of the design processes, showing the extent to which the available approaches are appropriate, defensible, and most importantly ‘safe’.

3.1 Means of statistical comparison

The comparison between predicted results and results reported from tests available in the literature is made based on statistical measures of (1) conservatism, and (2) precision. These measures are also used to assess the possible influences of various potentially important modelling assumptions, approaches and parameters on the predicted fire resistance of unprotected CFS columns. Protected columns are not considered in the current chapter as no guidance is currently available for the prediction of temperatures and fire resistance of protected CFS columns exposed to fire.

The mean percentage error, *MPE*, and mean error, *ME*, are used herein to give indications of a model's conservatism (and, to a certain extent, its accuracy of prediction) and is calculated by taking the average percentage error (*MPE*) or the average error (*ME*) between the model prediction and the experimentally observed value for each result in the database for each respective design approach. Positive *MPEs* and *MEs* represent over-predictions, which for fire resistance assessment is unconservative (unsafe). The ideal is for values close to zero, meaning that on average the predictions are accurate. The standard deviation of the percentage errors, σ_{pe}, or actual errors, σ, of prediction provides an indication of a model's precision. The analysis assumes that the errors of prediction are normally distributed about their mean; the standard deviation can therefore be used to judge the statistical confidence in a model's predictive ability. Values of standard deviation closer to zero imply higher precision.

3.2 The NRCC fire resistance design approach

The NRCC approach (Kodur, 2007) was previously described in Section 2.4.4.1, and is used by several North American codes and design guides (e.g. ACI, 2007; ASCE, 1999; NBCC, 2005). The approach is based on the application of Equation 2-40 on Page 68 incorporating tabulated semi-empirical parameters (Table 2-8). The application is relatively straightforward to implement for columns of known materials and dimensions, making the NRCC approach easy and expedient to use.

3.2.1 Limits of design and applicable database

To fairly assess the NRCC approach, the limits given by Kodur (2007) need to be applied to the full database of test results reported in tables 2-1 to 2-4. The limits of the approach are given in Table 2-9. In applying these limits the resulting database includes 78 tests with a reasonably good distribution between shape, load ratio, wall thickness, and concrete strength. The data are limited in terms of end restraint conditions, effective length, and concrete type. The breakdown of the applicable specimens for the NRCC approach is given in Table 3-1.

Table 3-1: Details of specimens used in the evaluation of the NRCC (Kodur , 2007) design approach

Specimen details								Steel Tube						Concrete							
Lengths				End conditions[b]		Load ratio[c]		Section shape[d]		Section size (mm)		Wall thickness (mm)		Concrete type[e]		28 day strength (MPa)				A_s/A_c ratio[f]	
	Actual	Effective length[a]																			
		Design	*Furnace*																		
<2.2 m	-	-	23	P-P	10	0-0.2	25	C	20	<200	16	<4	13	PC	36	20-25	8	35-40	20	<1.5 %	4
2.2-3.0 m	-	68	43	P-F	2	0.2-0.4	31	S	58	200-250	27	4.1-5.99	16	RC	28	25-30	9	40-45	21	1.5-2.5 %	26
3.0-3.8 m	51	6	8	F-F	66	0.4-0.6	19			250-300	19	6-7.1	31	FIB	14	30-35	14	45-50	6	2.5-3.5 %	6
>3.8 m	27	4	4			0.6+	3			300+	16	7.11+	18							>3.5 %	6

[a] The design effective length is the code-specified effective length for the stated column end-conditions, whereas the furnace effective length is the effective length calibrated by the various testing facilities and stated in the original source references.
[b] P = pinned end condition, F = fixed end condition.
[c] Ratio of applied load on the column during the test to the columns nominal strength at ambient temperature.
[d] C – Circular section, S – Square section
[e] PC – plain concrete, RC – steel bar reinforced concrete, FIB – steel fibre reinforced concrete
[f] A_s – area of steel bar reinforcement, A_c – area of concrete.

3.2.2 Assessment of the NRCC design approach

Figure 3-1 shows the fire resistance predictions of the NRCC approach (Kodur, 2007) versus the observed (tested) fire resistance times for each applicable column in the reduced database. This figure includes a diagonal line representing a one-to-one (1:1) prediction (i.e. a perfect prediction). Points that fall above the 1:1 line represent over-predictions (unconservative), whereas points below the line are under-predictions (conservative). The dashed line in the figure represents the mean error of prediction.

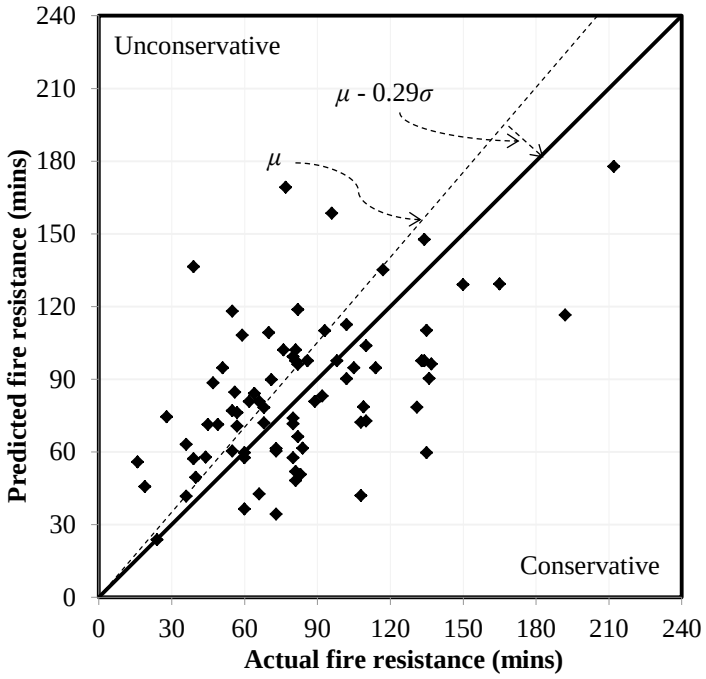

Figure 3-1: Predicted versus observed fire resistance based on the NRCC approach (Kodur, 2007)

The *MPE* of prediction for the NRCC approach is +17%, meaning that on average this approach over-predicts the fire resistance by 17%; the approach is thus unconservative on average. The standard deviation of the percentage error, σ_{pe}, of prediction is 59%, meaning that the NRCC approach's mean error of prediction is 0.29 standard deviations above the 1:1 line (i.e. on the unconservative side). The statistical confidence in the model is therefore relatively low and, assuming for

illustrative purposes that the error of prediction is normally distributed, only about 40% of the model predictions will lie on the conservative side of the 1:1 line.

3.2.2.1 Parameters affecting performance of the NRCC design approach

In an attempt to better understand the factors leading to the variability in the predictions, a more detailed statistical analysis was performed wherein the database was partitioned based on a number of different physical parameters, and the ability of the design approach to deal with these more specific data sets was explored.

Column cross-sectional size

Figure 3-2 shows the effect of column diameter on the accuracy and precision of fire resistance prediction for the NRCC approach (Kodur, 2007). This figure shows that the NRCC approach (Kodur, 2007) is generally less conservative for columns of larger diameters, for which it considerably over estimates fire resistance on average.

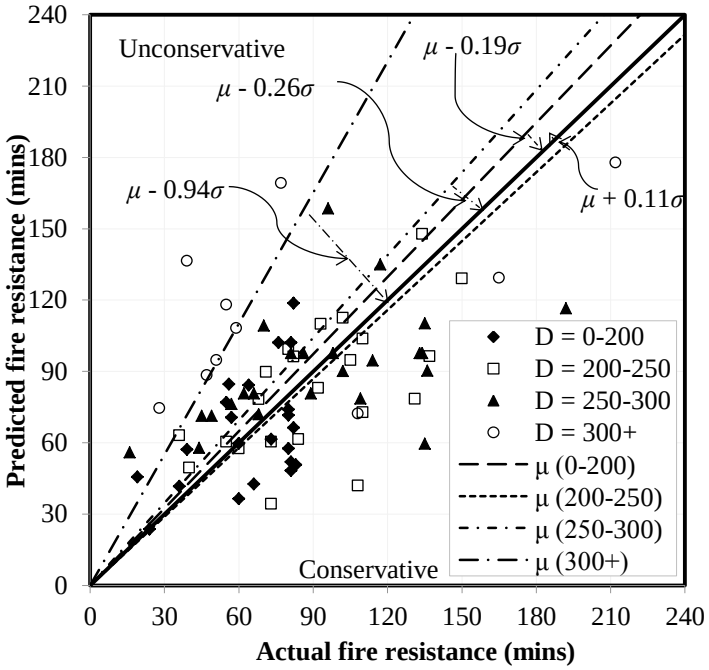

Figure 3-2: Predicted versus observed fire resistance partitioned by cross-sectional size based on the NRCC approach (Kodur, 2007)

The statistical confidence in prediction for columns with diameters greater than 300 mm is dramatically reduced (although this is partly because relatively few test results are available). The mean error of prediction for the columns with diameters above

300 mm is 0.94 standard deviations above the 1:1 line; i.e. only 19 % of the predictions for section sizes greater than 300 mm are likely to be conservatively predicted based on the available data. This is an important observation because columns in real buildings tend to fall at the larger end of the spectrum of possible column sizes, suggesting that this approach is a poor predictor of real-scale columns.

Effective length and fire test load ratio

A key parameter in the calculation of predicted fire resistance is the assumed effective (buckling) length of the column. In a real building, the effective length for design would be defined by the respective codes on the basis of the rotational restraint conditions acting at a column's extremities. This poses a problem for the comparative analyses presented herein, since some of the available test reports quote only idealised end conditions (i.e. pinned-pinned, pinned-fixed, fixed-fixed) (e.g. Kodur, 1999), whereas others give both the idealized column end conditions and 'calibrated' effective lengths based on the specific testing furnace used and the judgement of the researchers (e.g. Stanke, 1975). Furthermore, the available design codes give column effective lengths which are to be used for fire resistant design of columns in non-sway frames (CEN, 2005; CSA, 1994), and in many cases these do not match up with the effective length values quoted by researchers for furnace tests using these same end conditions. To reconcile this, the effective lengths quoted in test reports have been used when applying the respective design approaches, rather than using the design values that would be imposed by the codes (CEN, 2005; CSA, 1994) for these same columns. This is appropriate since it allows a better comparison of whether the respective approaches capture the true mechanics of CFS columns' response to fire, or whether they are more empirical in nature.

Figure 3-3 shows a comparison of the NRCC (Kodur , 2007) design approach in terms of the conservatism, *ME*, and the precision or standard deviation, σ, of the error of prediction when using the quoted furnace effective length. In this figure the databases have been partitioned on the basis of the fire test load ratio (the ratio of the applied load during the fire test to the ambient capacity of the column). It is noteworthy that the comparisons for load ratios greater than 0.6 should be treated

with caution, since the number of tests (3 tests) is too few to be considered statistically rigorous.

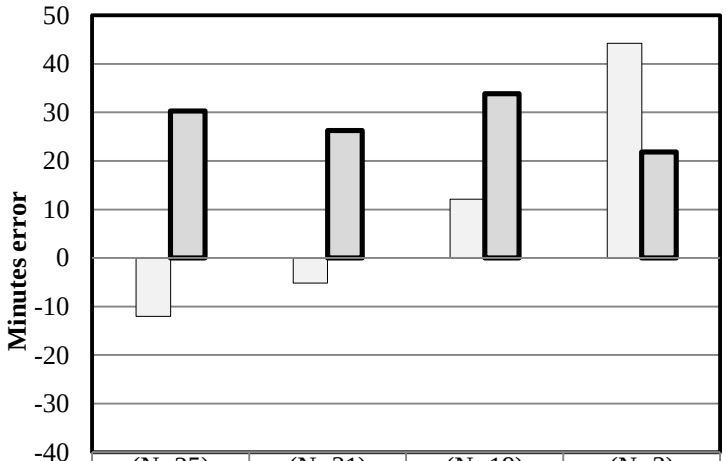

	(N=25) 0 - 0.2	(N=31) 0.2 - 0.4	(N=19) 0.4 - 0.6	(N=3) 0.6 +
□ ME	-12.0	-5.2	12.1	44.2
◘ σ	30.3	26.3	33.9	21.9

Figure 3-3: Comparison of *ME* and *σ* for the NRCC approach (Kodur , 2007) partitioned by load ratio

It is apparent in Figure 3-3 that the NRCC (Kodur, 2007) approach is most conservative for columns with low applied loads during fire, and it becomes less conservative, less accurate, and less precise as the load ratios increase. While the reasons for this are not clear, due in part to the mechanics used in the NRCC approach not being clear, this again suggests that the approach fails to capture the mechanics of CFS columns' response and/or failure during fire. This is important since load ratios in design typically range from 0.4 to 0.6 (Lennon et al., 2007).

Effect of cross-sectional shape (circular versus square)

The NRCC approach accounts for column shape and concrete fill type using the aforementioned, semi-empirical modification factor, *f* (given in Table 2-8). Figure 3-4 shows the effect of the fill type and shape of the column on the predictive performance of the NRCC approach (Kodur, 2007).

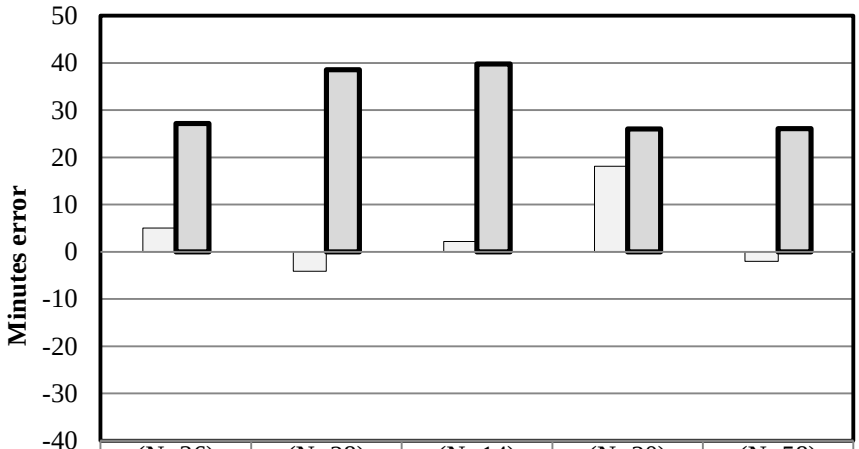

	(N=36) PC	(N=28) RC	(N=14) FIB	(N=20) Circle	(N=58) Square
	Fill			Shape	
□ ME	5.0	-4.1	2.2	18.1	-2.0
■ σ	27.2	38.6	39.8	26.0	26.1

Figure 3-4: Comparison of *ME* and *σ* for the NRCC approach (Kodur, 2007) partitioned by (a) fill type and (b) specimen shape

The approach is consistent with its fire resistance predictions across the different forms of concrete infill but over-predicts the fire resistance of the circular columns on average, whilst slightly under-predicting the fire resistance for square columns. On the basis of the analysis presented herein, the *f* factor appears not to properly account for column shape. Again, it appears that the NRCC (Kodur, 2007) approach fails to properly capture the mechanics of CFS columns' response in fire.

Effect of testing laboratory

Standard fire test furnaces globally are known to be different from one another in a host of potentially important respects (mostly with respect to the heat flux applied to the tested element resulting from different fuel sources, furnace linings, technique for measurement of gas phase temperature, control of the furnace, etc., but also in terms of the ratio of heated length to total length, loading configuration, rotational fixity, etc.). The NRCC (Kodur, 2007) model is affected by the differing testing laboratory conditions and furnaces as shown in Figure 3-5, which shows the variation in *ME* and *σ* for four different testing locations, each with five or more tests: NRCC (Canada), CSTB (France), CTICM (France), and Monash University (Australia).

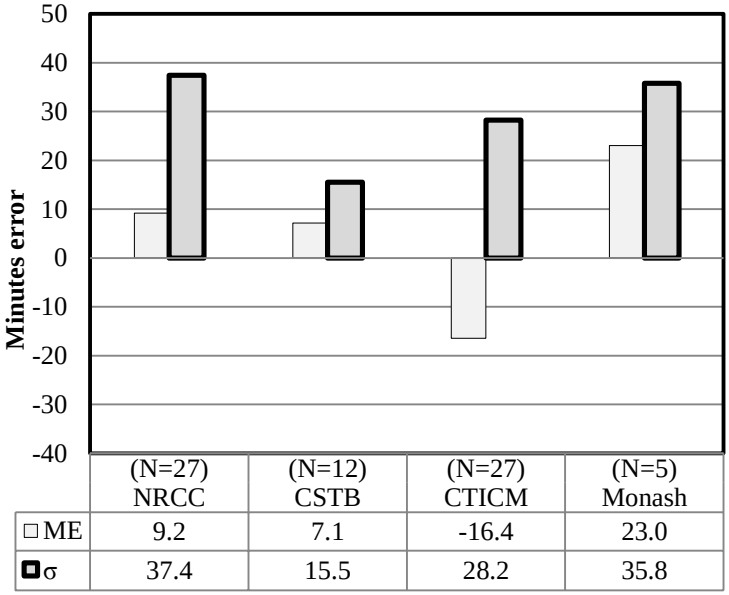

	(N=27) NRCC	(N=12) CSTB	(N=27) CTICM	(N=5) Monash
□ ME	9.2	7.1	-16.4	23.0
◘ σ	37.4	15.5	28.2	35.8

Figure 3-5: Comparison of *ME* and *σ* for the NRCC approach predictions (Kodur, 2007) partitioned by testing laboratory

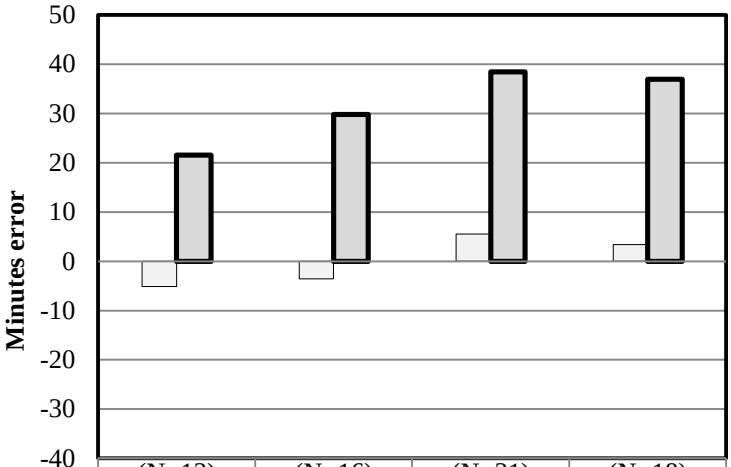

	(N=13) < 4 mm	(N=16) 4 - 6.0 mm	(N=31) 6.0 - 7.1 mm	(N=18) 7.11 + mm
□ ME	-5.1	-3.6	5.5	3.4
◘ σ	21.6	29.8	38.5	37.0

Figure 3-6: Comparison of *ME* and *σ* for the NRCC approach (Kodur, 2007) partitioned by steel wall thickness

Effect of steel tube wall thickness

Figure 3-6 shows a comparison of the *ME* and *σ* for the NRCC (Kodur, 2007) design approach, in this case with the data partitioned based on steel wall thickness. The

NRCC (Kodur, 2007) approach does not explicitly use steel wall thickness as a variable in determining the fire resistance of CFS columns, and its fire resistance predictions become less precise as the wall thickness increases.

The above observation again suggests that the NRCC approach fails to capture the relevant mechanics during fire. The trends appear to indicate that the behaviour of the steel tube is more important than assumed by this approach, since the conservatism generally reduces when the steel tube plays a more prominent structural role. This could be due to the impacts of gap formation and/or slip between the concrete and the steel tube, or to local buckling of the steel tube wall, all of which are commonly observed during testing of CFS columns in fire (see Rush et al., 2010); and none of which are explicitly accounted for in the NRCC approach.

3.2.3 Concluding remarks on the NRCC approach

The NRCC approach is an easy to use formula using empirically based parameters to account for fire's interaction with a CFS; this limits the applicability of the approach and its practical usefulness in performance based design. The formula is also, on average, an un-conservative predictor and has a large standard deviation such that only 40% of the predictions are conservative. The NRCC approach also struggles to properly account for load ratio, wall thickness, shape and the diameter of the section. The formula is a particularly poor predictor for circular specimens with diameters greater than 300 mm, larger wall thicknesses, and load ratios exceeding 0.4. The formula does attempt to account for different types of concrete infill; however, it struggles for consistency when different concrete strength ranges are compared.

3.3 Eurocode 4 – EN 1994-1-2

Eurocode 4 (EC4) (CEN, 2005) is the most commonly used design guidance for CFS columns in fire in Europe, and as already noted it presents three alternative approaches for the fire resistance design of CFS columns. The simplest approach is to apply the prescriptive requirements given in Table 4.7 of EC4 (CEN, 2005). The second approach is the simple calculation model given in Annex H of EC4 (CEN, 2005). The most advanced approach permitted by EC4 (CEN, 2005) is the suite of

approaches termed ‘Advanced Calculation’ methods used on fundamental physical behaviour; these advanced approaches are not considered in the current discussion.

In this section, assessments of the EC4 tabulated and Annex H approaches are made, with specific attention to the engineering decisions possible for use with the Annex H approach and how these might affect the predictions.

3.3.1 EC4 – tabulated approach

No calculations whatsoever are required to use the EC4 tabulated approach (Table 2-10) and, due to the simplicity of this prescriptive approach, it is not surprising that it is highly conservative in its evaluation of the likely fire resistance of a given CFS design. Figure 3-7 shows a comparison of the prescribed fire resistance for all applicable column tests in the test database, and confirms that the tabulated resistance in EC4 (CEN, 2005) is in general highly conservative. This approach is over-simplified and conservative in most cases, and it is therefore not discussed any further.

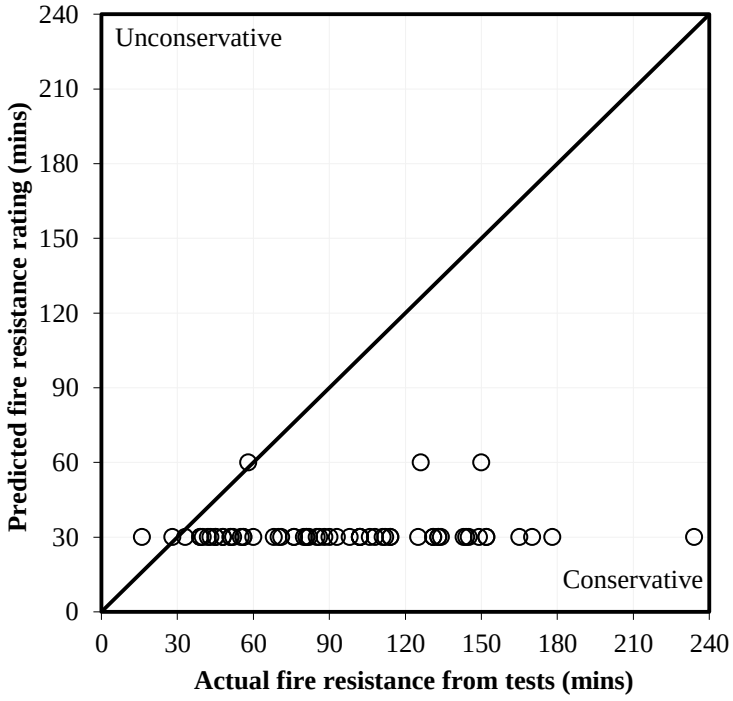

Figure 3-7: EC4 (CEN, 2005) tabulated fire resistance (EC4 Table 4.7) versus actual (observed) fire resistance

3.3.2 EC4 – Annex H approach

As already discussed, Annex H of EC4 (CEN, 2005) presents a simplified sectional analysis technique which calculates a temperature distribution over the cross-section using one of a number of applicable methods for a given duration of fire exposure, and calculates the design axial buckling/crushing capacity of the column. Several methods can be used to calculate the temperature field within the section after a given duration of any applicable fire, ranging from detailed finite element analysis to a more simplified 1D heat transfer, based on EC1 (CEN, 2009c) and EC4 (CEN, 2005) in which material thermal properties can be assumed as code-specified constant values or as temperature dependant values. Guidance on how to calculate the temperature profile within a section is widely available (e.g. Lennon et al., 2007). It is noteworthy that EC4 states that the thermal resistance between the steel wall and the concrete may be neglected, presumably because this is assumed to be a conservative omission. Once the temperature profile within the section at a given time of fire exposure has been established, the cross-section is discretized into elements in which the temperature is assumed to be uniform, and, using a simple spreadsheet analysis, relatively straightforward equations can be used to check that the design resistance of the column, $N_{fi,Rd}$, at the given time (and temperature profile) is greater than the design load in fire, $N_{fi,Sd}$. The calculation of $N_{fi,Rd}$ is made by employing equations 2-49 to 2-52 on Page 75.

The aim of the current analysis is to determine whether the assumptions and code-specified values for material and structural relationships are valid, and which combinations of design decisions provide the most accurate and precise predictions when compared to the database of furnace test results.

3.3.2.1 Limits of the Annex H design and applicable database

To fairly assess the EC4 Annex H approach, the limits on applicability need to be applied to the full database of furnace tests results as reported in tables 2-1 to 2-4 on in Chapter 2 on pages 21 to 24. The limits of the approach are detailed in Table 2-11 on Page 76. In applying the limits to the furnace tests, the resulting database includes 76 tests, with a reasonably good distribution between shape, load ratio, wall

thickness, and concrete strength but is limited in terms of end restraint conditions, effective length, and concrete type. The applicable specimens are given in Table 3-2.

3.3.2.2 Application of the Annex H design approach

As described previously, the first stage required to predict the columns fire resistance is to determine a temperature distribution over the column's cross-section for a given duration of exposure to fire, then the capacity is determined using equations 2-49 to 2-52, and this capacity is compared against the applied load in the fire limit state. In a design situation, the prescribed (required) fire resistance of the element would normally be known and a temperature profile and load capacity would need to be determined for this duration of fire exposure only. For the purposes of the current analysis, however, the goal was to *predict* the fire resistance of a given column, and the temperature distribution and column capacity are needed for essentially every instant during the entire duration of fire.

While a number of techniques exist to determine the temperature distribution in a circular or square CFS column during fire, finite element heat transfer analysis using ABAQUS finite element software was used in this study to predict the temperature distribution for each and every individual section type and size in the test database at one-minute intervals. The input parameters to the analysis, apart from the cross-sectional dimensions, were the thermal properties of steel and concrete, and the thermal insult (fire exposure). The thermal insults used in the vast majority of the tests were ISO 834 (ISO, 1999) standard fires (or similar).

Table 3-2: Details of specimens used in the evaluation of the EC4 Annex H approach (CEN, 2005)

Specimen details										**Steel Tube**						**Concrete**					
Lengths				End conditions[b]		Load ratio[c]		Eccentricity		Section shape[d]		Section size (mm)		Wall thickness (mm)		Concrete type[e]		28 day strength (MPa)		A_s/A_c ratio[f]	
	Actual	Effective length[a]																			
		Design	*Furnace*																		
<2.2 m	5	5	21	PP	9	0-0.2	19	zero	61	C	24	<200	16	≤4	15	PC	45	20-25	9	<1.5%	3
2.2-3.0 m	-	45	34	PF	17	0.2-0.4	32	<15%	7	S	52	200-250	33	4.0-6.0	16	RC	31	25-30	14	1.5-2.5%	21
3.0-3.8 m	38	14	9	FF	50	0.4-0.6	21	15-30%	6			250-300	17	6.0-7.0	27	FIB		30-35	28	2.5-3.5%	3
>3.8 m	33	12	12			0.6+	4	>30%	2			300+	10	≥7.0	17			35-40	25	>3.5%	4

[a] the design effective length is the code-specified effective length for the stated column end-conditions, whereas the furnace effective length is the effective length calibrated by the various testing facilities and stated in the original source references.
[b] P = pinned end condition, F = fixed end condition.
[c] the ratio of the applied load on the column during the test to the nominal strength of the column at ambient temperature.
[d] PC – plain concrete, RC – steel bar reinforced concrete, FIB – steel fibre reinforced concrete
[e] A_s – area of steel bar reinforcement, A_c – area of concrete.

Once the temperature distributions were obtained, the load capacities of the sections were determined. Guidance on how to calculate the load capacity according to the EC4 Annex H approach is available in a number of publications (e.g. Lennon et al., 2007; Aribert et al., 2008). Typically, the steel tube is assumed to have uniform temperature and the concrete cross-section is divided into ringed segments of equal thickness. This is shown schematically in Figure 3-8, where six concrete layers have been chosen. Clearly, the more layers that are taken the more refined the prediction, however between five (Aribert et al., 2008) and ten (Lennon et al., 2007) layers have been suggested in the literature; in the current analysis seven layers was assumed. A verification of this assumption was performed using the scheme set out in verification procedures SP Report 1999:36 (Wickström and Pålsson, 1999).

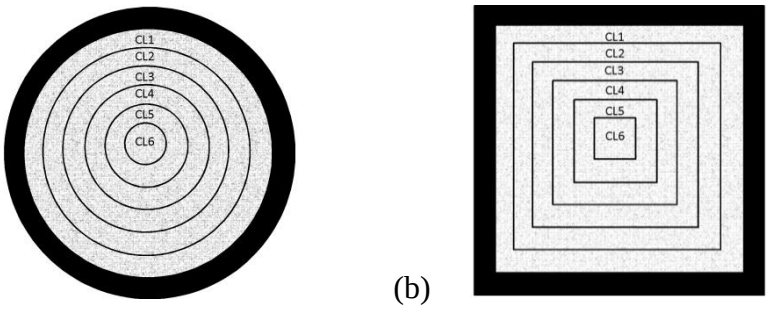

Figure 3-8: (a) Circular and (b) square segmentation used in EC4 Annex H (CEN, 2005) analysis (CLi = concrete layer i)

Each of the concrete rings is assumed to have a uniform temperature at any given instant in time, based on heat transfer analysis. The determination of the midpoint temperature for the concrete layers in circular sections is straightforward due to axisymmetry. The situation in a square section is more complicated; in a square section the temperature at the corners is higher than at the middle of the flat faces. However precedence exists (Aribert et al., 2008) to assume an equivalent uniform temperature in each concrete layer in the square section, provided that the uniform temperature chosen for the layer leads to the same (or smaller) contribution to either the plastic resistance in compression or the cross-section's flexural stiffness as would a more complete summation of a 2D grid of concrete elements. A heat transfer analysis was therefore performed (again using ABAQUS) for the square sections assuming a 2D square element mesh and the average temperature in each element

was determined. The average of all of the element temperatures within a given square ring was then determined and taken as the equivalent constant temperature for that concrete layer. An analysis of the mechanical response of the layer using the average temperature versus the response using a rigorous summation of the mechanical properties of each square element in the layer showed that the average temperature for the layer provides an accurate estimate for the load capacity analysis. Thus a full two dimensional discretization of square sections was not required.

The temperatures of the reinforcing steel within the cross section were taken to be the same as the temperature of the concrete layer in which it resides. A thermal model was also developed to assess whether the reinforcement has an effect on the temperature profile within a CFS section, and it was found not to have an effect on the concrete layer temperatures.

After the temperature of each layer was determined, the layer mechanical properties were found by interpolation of tables 3.1 through 3.4 of EC4 (CEN, 2005), and these properties were then applied within equations 2-49 to 2-52. The true levels of fixity, and therefore effective lengths of the columns, are difficult to determine with different heated lengths of specimens (e.g. Kodur, 1999) and various methods of creating the idealised end-conditions. The effective lengths that are employed in Equation 2-50 are, where available, those quoted in the respective test reports; otherwise the design values imposed by the codes (CEN, 2005; CSA, 1994) are used.

3.3.2.3 Meta-analysis iterative process

The process used to understand the EC4 Annex H approach is in four stages as outlined in Figure 3-9, which provides a development process from a conservative benchmark model to models that are statistically shown to be appropriate for use by a practicing structural engineer. The benchmark model, called *Base*, is a conservative and simple approach thought to be comparable to the initial design assumptions and decisions that a non-specialist practicing structural engineer would make in applying Annex H, from which the single parametric variations can be compared.

The single parametric variations stage interrogates individual assumptions and decisions made in the *Base* model by varying a single parameter, allowing an

assessment of the magnitude and effect of the individual modelling assumptions and decisions that are within and outwith EC4. From this, parametric variation combinations can be assessed rationally. From the combinations of various parameters the major interactions that affect the prediction accuracy and precision of the approach can be assessed, from which best practice modelling guidance can be given.

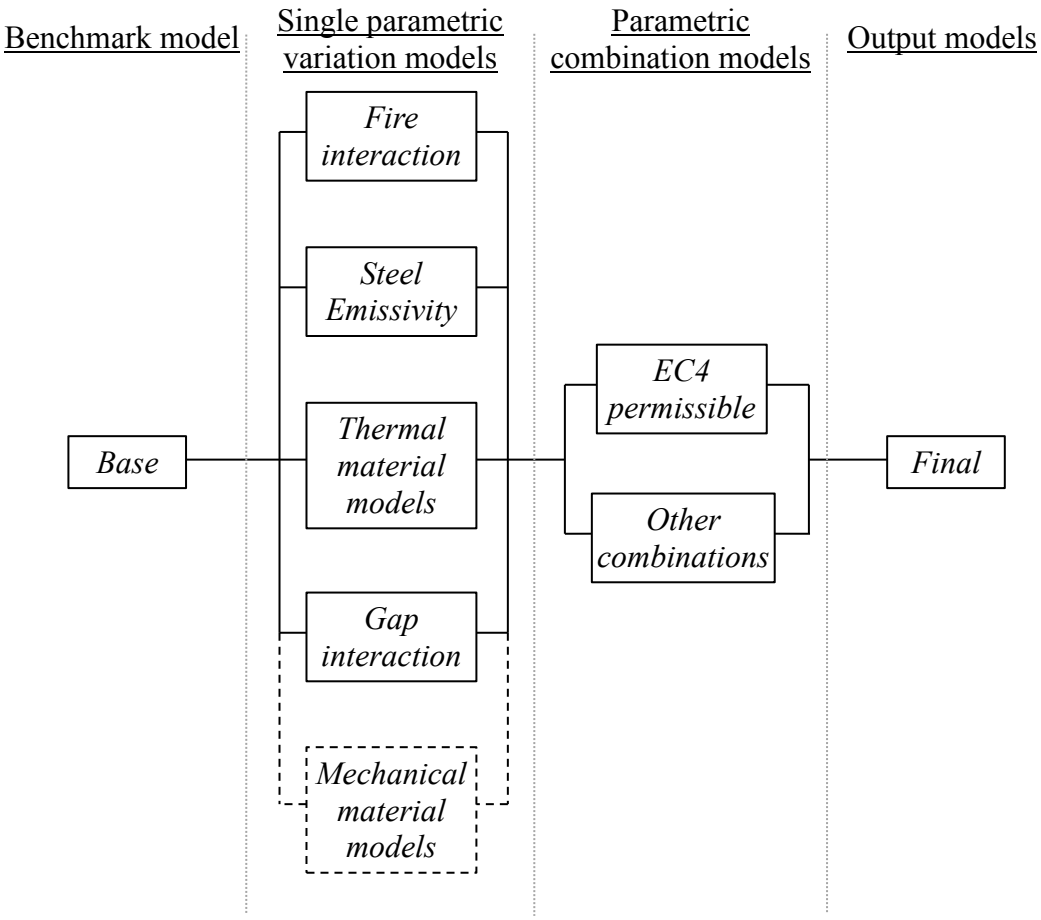

Figure 3-9: Iterative process flow chart showing the model variations used during the meta-analysis

3.3.2.4 Benchmark modelling

The *Base* modelling approach assumes:

1. the surface temperature of the unprotected CFS column is the same as that of the fire ($\theta_a = \theta_g$);
2. the emissivity of the steel is not important ($\varepsilon_{m,a}$ = N/A);

3. constant values for thermal conductivity, λ, and heat capacity, c, (equations 2-25, 2-27 and 2-28);
4. perfect contact at the steel tube-concrete core interface; and
5. the EC4 code defined mechanical material models for concrete (Table 2-5 and Equation 2-13) and for steel (tables 2-6 and 2-7).

The first assumption (i.e. $\theta_a = \theta_g$) is common in the analysis of unprotected steel elements in practice and is reasonably consistent with steel temperatures measured in tests (Kodur, 1999). This assumption is assumed to be conservative for uniformly heated columns, since in reality the temperature of the fire will be slightly higher than the steel surface temperature during the heating phase of a fire. This also provides the second assumption, ($\varepsilon_{m,a}$ = N/A), as the fire temperature can be applied to the steel surface in the ABAQUS models.

The third assumption in the *Base* model analysis is that constant values for thermal conductivity, λ, and heat capacity, c, can be used. The specific heat capacity for steel and concrete were therefore taken as c_a = 600 J/kg and c_c = 1000 J/kg respectively, and the thermal conductivities were taken as λ_a = 45 W/m and λ_c = 1.6 W/m, as recommended for simple calculation models in EC4 Annex H (CEN, 2005). This approach will also increase the conservatism of fire resistance prediction because the constant values suggested are an upper bound to the actual values. The fourth assumption is that there is perfect contact at the steel tube-concrete core interface, which is assumed to be a conservative as it increases the heat transfer into the concrete core. This assumption may not hold in reality if the steel is more structurally dominant. The fifth assumption is that the use of the EC4 code-specified mechanical models for steel and concrete is appropriate, which is commonly used in the application of the EC4 Annex H approach.

Results of benchmark model

The *Base* model was applied to the applicable sections in Table 3-2 and a predicted fire resistance was obtained for each section using the process outlined in Section 3.3.2.2. This value was then compared against the actual tested fire resistance for each specimen. Figure 3-10 shows the predicted versus observed fire resistances.

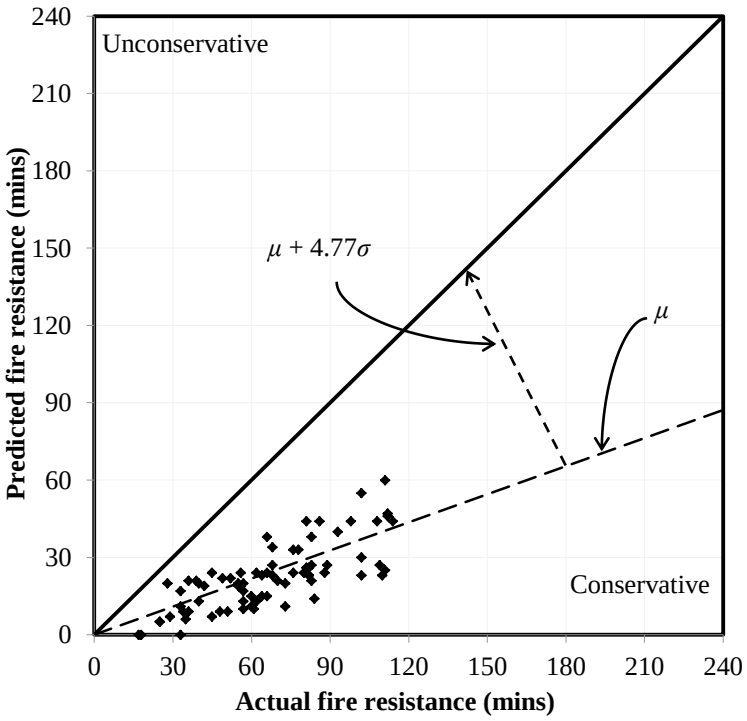

Figure 3-10: Predicted versus observed fire resistance based on the EC4 Annex H approach (CEN, 2005) using the *Base* modelling assumptions

Figure 3-10 shows that the predictions of the EC4 Annex H (CEN, 2005) approach, using the *Base* modelling assumptions, is highly conservative with a *MPE* of -67%, meaning this approach is 67% conservative, on average. The standard deviation of the error of prediction is 14% in this case, such that the mean error of prediction is 4.77 standard deviations *below* the 1:1 line; 99.9% of all predictions are statistically expected to be conservative. The actual mean error, *ME*, obtained using this method is -44 minutes (i.e. a 44 minute under prediction of fire resistance) with a standard deviation of 18 minutes.

The lack of accuracy could be because the data provided by the testing reports omit key pieces of information (true effective length, for instance) or due to the model not properly capturing the possible mechanics of CFS columns in fire, or missing other key aspects of behaviour observed in tests (alternative failure modes, local buckling, etc.). For the *Base* case, it is likely that the input parameters are also conservative.

The EC4 Annex H (CEN, 2005) approach considers eccentric loads, if present, using modification factors applied to the loads to create an *effective* concentric design load. When test results were partitioned based on eccentric or concentric loading, the conservatism increased for the eccentric loading cases. The *MPE*s for concentric and eccentric loading are -64% and -78%, respectively, and standard deviations are 13% and 13%, respectively. The reasons for this are not known, although it may be that the additional conservatism arises due to the conservative assumptions required to account for eccentric load effects in a simplified way.

3.3.2.5 Initial parametric study

The benchmark model, *Base*, for the thermal properties produces conservative predictions when compared to observed furnace test results, as would be assumed due to the numerous conservative assumptions that it makes. Using the same process, design assumptions are now critiqued individually by changing one assumed variable in the *Base* model and assessing the impact on the predictive quality.

Effect of fire interaction and steel emissivity

The conservative assumption that the steel temperature is equal to the gas phase temperature is unrealistic, and it over-predicts the steel temperatures and thus the section temperatures, causing under-predictions of fire resistance. EC1-1-2 (CEN, 2009c) provides guidance on modelling heat transfer using a net heat flux, $\dot{h}_{net}$ (Equation 2-41) transferred to elements during fire which is the sum of the net convective heat flux, $\dot{h}_{net,c}$ (Equation 2-42), and the net radiative heat flux, $\dot{h}_{net,r}$ (Equation 2-43).

The net radiative heat flux is significantly affected by the assumed values for the emissivity of the steel, $\varepsilon_{m,a}$, and the emissivity of the fire, $\varepsilon_{m,fi}$. The emissivity of the fire assumed in the Eurocodes (CEN, 2009c) is 1.0. Whilst this assumption is conservative, it is clearly not physically realistic. The National Research Centre Canada (NRCC) suggest adopting a lower value for the emissivity of their testing furnace ($\varepsilon_{m,fi}$ = 0.75) for the vast majority of their modelling of CFS sections in fire (e.g. Kodur and Lie, 1997; Lie et al., 1992).

The emissivity of the steel, $\varepsilon_{m,a}$, is similarly important in the determination of heat flux to the steel tube, Figure 2-5 on Page 42 shows the values for steel emissivity, $\varepsilon_{m,a}$, available within literature. In addition to these variable empirically based values from the literature, NRCC take a constant steel emissivity of 0.8 (Irwin and Lie, 1992) in most of their analysis of CFS's in fire, whilst EC4 specifies a value of 0.7. Figure 3-11 shows a comparison of the *Base* model ($\theta_a = \theta_g$) against different fire interaction and steel emissivity assumption approaches using equations 2-41 to 2-43. The following combinations are used:

- Model: *EC1-2* - $\varepsilon_{m,fi} = 1.0$, $\varepsilon_{m,a} = 0.7$;
- Model: *NRCCa* - $\varepsilon_{m,fi} = 0.75$, $\varepsilon_{m,a} = 0.7$;
- Model: *Drysdale* - $\varepsilon_{m,fi} = 1.0$, $\varepsilon_{m,a} = 0.2$ (approximation of Drysdale (2011);
- Model: *NRCCb* - $\varepsilon_{m,fi} = 1.0$, $\varepsilon_{m,a} = 0.8$; and
- Model: *NIST* - $\varepsilon_{m,fi} = 1.0$, (Bentz et al., 2009) described below by:
  - $\varepsilon_{m,a} = \begin{cases} 0.32, & \theta_a = 20 \\ 0.32, & \theta_a = 200 \\ 0.85, & \theta_a = 400 \\ 0.95, & \theta_a = 800 \\ 0.95, & \theta_a = 1200 \end{cases}$

The overall accuracy of the predictions made in the *Base* model, with the assumption that the steel face temperature is equal to the gas phase temperature ($\theta_a = \theta_g$), has a mean error, *ME*, of -44 minutes. The *EC1-2* modelling approach using code suggested values improves the *ME* by 14 minutes to -29 minutes, whilst further improvements are shown with the *NRCCa* adopted fire emissivity value of 0.75 to a ME of -27 minutes. Comparing the *Drysdale* modelling approach to the *EC1-2* improvements in *ME* of 20 minutes to -10 minutes are seen, unlike the *NRCCb* and *NIST* modelling approaches, where little difference is seen. The standard deviations of the errors (σ) remain around 18 minutes regardless of the modelling approach taken. Clearly, if the column heats up more quickly as a consequence of higher assumed emissivities, the conservatism of the modelling increases. By introducing a more realistic boundary between the fire and the steel face of a CFS the predictive quality of the design method is improved, however the conservatism remains.

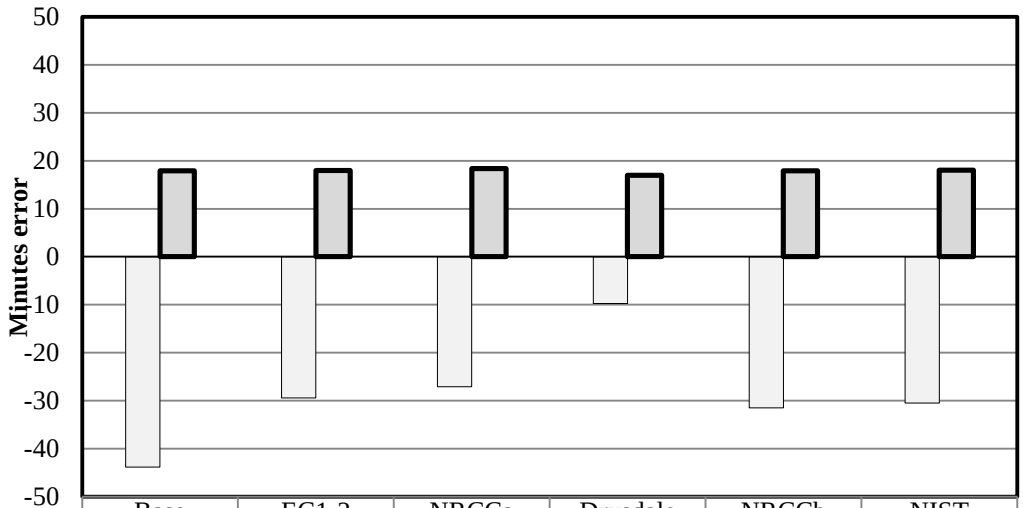

	Base	EC1-2	NRCCa	Drysdale	NRCCb	NIST
ME	-43.8	-29.4	-27.1	-9.7	-31.5	-30.5
σ	17.9	18.0	18.4	17.0	17.9	18.0

Figure 3-11: The effect of fire interaction and steel emissivity modelling approaches on the overall predictive quality of EC4 Annex H approach (CEN, 2005)

Effects of assumed material thermal properties

The thermal modelling of steel and concrete, requiring inputs of thermal conductivity, specific heat, and density, is a complex issue. The *Base* model assumes constant thermal properties for both steel and concrete. EC4 (CEN, 2005) presents alternative material thermal property models for steel and concrete which vary with temperature. NRCC (Lie, 1994) have also presented material properties for concrete and steel calibrated from tests involving CFSs. Six different modelling approaches are presented in Table 3-3; the *Base* model, 4 models based on variations of EC4 assumptions, and one based on data from NRCC. An attempt is made below to determine which of these combinations of assumed material properties is most appropriate on the basis of the available test data.

Table 3-3: Equations used in the thermal modelling of steel and concrete for six different modelling approaches

Model	Steel			Concrete		
	c_a	λ_a	ρ_a	c_c	λ_c	ρ_c
• *Base*	2-27	2-28	2-25	2-27	2-28	2-25
• *EC4a*	2-22	2-23		2-16	2-17 Lo.	
• *EC4b*					2-17 Up.	
• *EC4c*				2-27	2-17 Lo.	
• *EC4d*					2-17 Up.	
• *NRCCc*	2-32	2-30		2-36	2-34	

Figure 3-12 shows a comparison of the three specific heat of steel, c_a, models. The temperature dependent models, Equation 2-22 and Equation 2-32, account for the phase transition of steel at 735°C and 725°C, with peak values of 5000 J/kg°C and 1398 J/kg°C, respectively. Figure 3-13 shows the similarity of the temperature dependent EC4 (Equation 2-23) and NRCC (Equation 2-30) thermal conductivity, λ_a, models, as well as showing the slightly more conservative EC4 constant value (Equation 2-28).

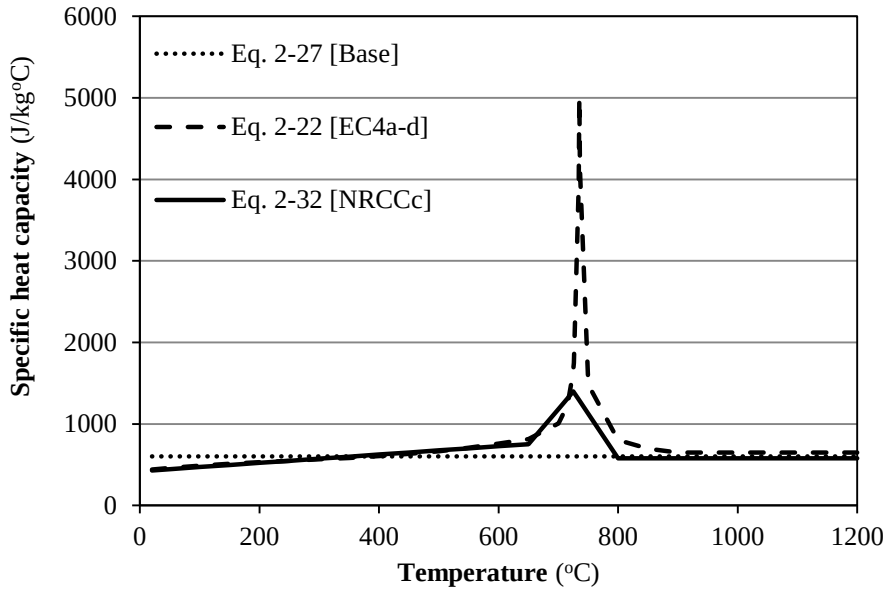

Figure 3-12: Variation of specific heat capacity of steel with respect to temperature for the EC4 (CEN, 2005) and NRCC (Lie, 1994) prescribed models

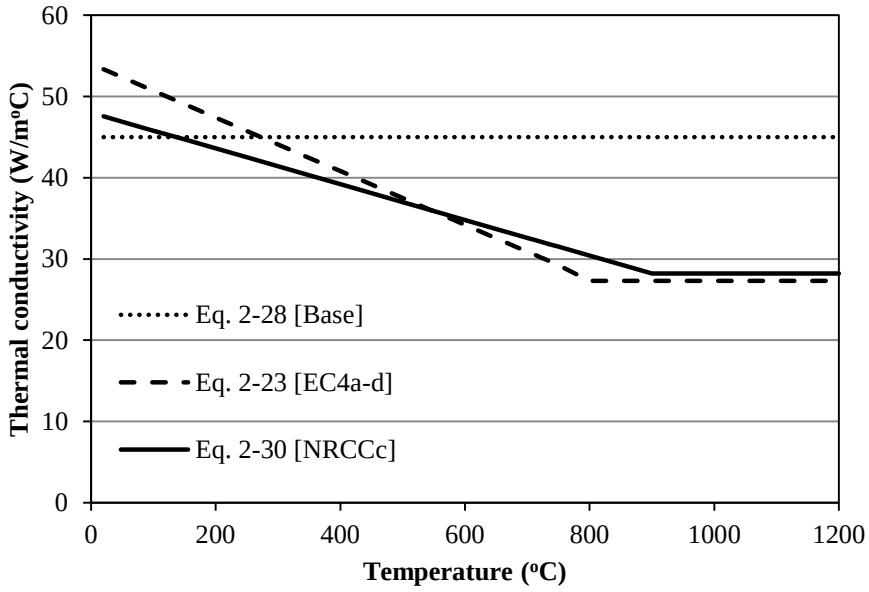

Figure 3-13: Variation of thermal conductivity of steel with respect to temperature for the EC4 (CEN, 2005) and NRCC (Lie, 1994) prescribed models

In the EC4 and NRCC models, the density of steel is assumed to be independent of the temperature of the steel at a value of 7850 kg/m^3, whilst the density of concrete is dependent on its temperature and is assumed to be the same for both the NRCC and EC4 approaches. The NRCC concrete models for thermal mass (which is the product of the density, ρ_c, and the specific heat capacity, c_c,) provides two peaks at 410^{o}C and 715^{o}C to account for chemical changes occurring within the concrete matrix, but does not explicitly account for evaporation of water. EC4 (CEN, 2005) presents two models for the specific heat capacity for concrete, c_c, a stepped method (Equation 2-16) and a temperature dependent equation (Equation 2-27) with a peak value of 5600 J/kg^{o}C at 115^{o}C; this assumes 10% moisture content by mass (suggested in EC4 as a possible situation that might occur in concrete filled hollow sections (CEN, 2005)). Figure 3-14 shows the specific heat capacity models for both approaches.

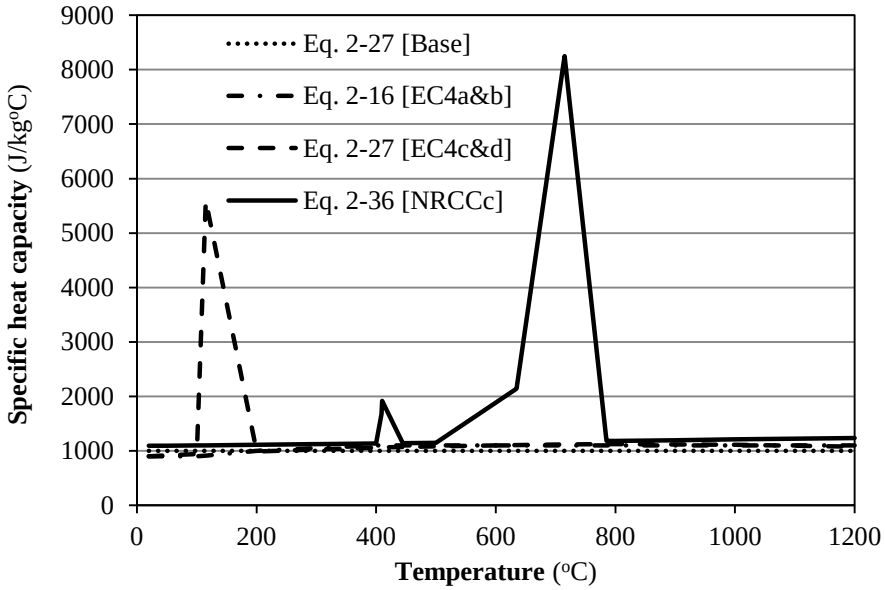

Figure 3-14: Variation of specific heat capacity of concrete with respect to temperature for the EC4 (CEN, 2005) and NRCC (Lie, 1994) prescribed models

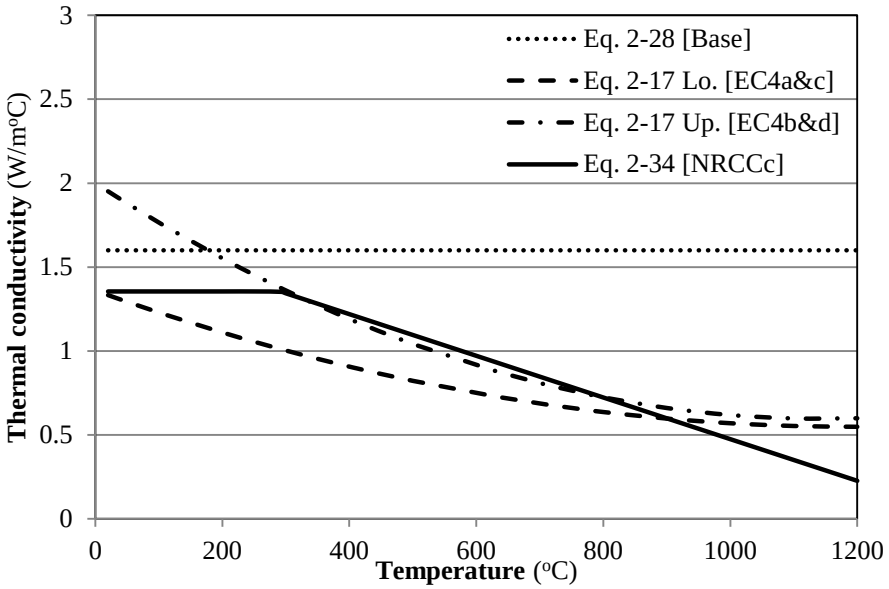

Figure 3-15: Comparison of thermal conductivity of concrete with respect to temperature for the EC4 (CEN, 2005) and NRCC (Lie, 1994) prescribed models

Figure 3-15 shows the different thermal conductivity models used in the EC4 and NRCC approaches. EC4 prescribes both upper (Equation 2-17 Up.) and lower

(Equation 2-17 Lo.) bound curves. For concrete in the NRCC model the suggested values are similar to the EC4 upper bound values.

Figure 3-16 compares the results of using the different modelling approaches compared against the furnace test database. The EC4 temperature dependent material models lead to improvements in accuracy over the *Base* model of between 6 and 19 minutes, with under-predictions varying between -33, -37, -24 and -29 minutes, for the *EC4 a, b, c,* and *d* modelling approaches, respectively. When using the *NRCC* material models the *ME* of the EC4 Annex H approach is -33 minutes, an improvement over the *Base* model of 10 minutes.

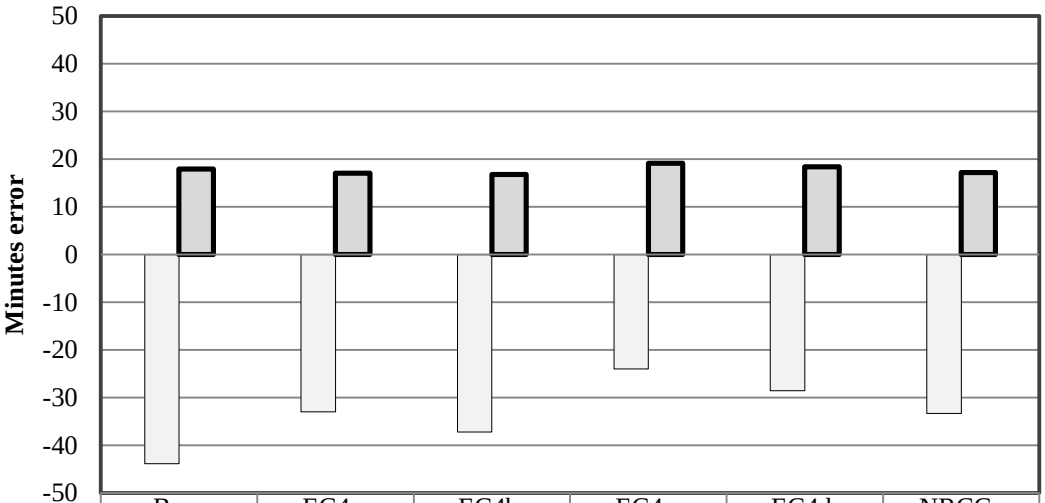

	Base	EC4a	EC4b	EC4c	EC4d	NRCCc
□ ME	-43.8	-33.0	-37.2	-24.0	-28.6	-33.3
◘ σ	17.9	17.1	16.8	19.1	18.4	17.2

Figure 3-16: The effect of six different possible thermal material property modelling approaches on the predictive abilities of the EC4 Annex H approach (CEN, 2005)

A comparison of *EC4a* and *EC4b* modelling approaches shows that having a higher conductivity in the concrete leads to a larger mean error, *ME,* of approximately 4 minutes and thus a more conservative prediction, due to the higher temperatures within the concrete. Artificially including the effect of moisture vaporization in the specific heat capacity of the concrete improves the accuracy of the predictions by approximately 9 minutes as it reduces the temperatures obtained in the concrete. This

can be seen by comparing *EC4b* and *EC4d* modelling approaches. Considering the precision of the different modelling approaches taken, only a slight change in the standard deviation is observed across all models.

Effect of explicitly accounting for gap formation

EC4 Annex H (CEN, 2005) stipulates that "in calculating the temperature distribution, the thermal resistance between the steel wall and the concrete may be neglected". This is a conservative assumption as it is well known that a thermal resistance at the interface forms due to the formation of an air gap (Ding and Wang, 2008).

Ding and Wang (2008) found that including a thermal resistance at the interface of 0.01 $K \cdot m^2/W$ (100 $W/m^2 \cdot K$ thermal conductivity at the interface) improved their thermal predictions. Ghojel (2004) proposed an interface conductance correlation as a function of temperature between 25 and 700^oC (Equation 2-8). Figure 3-17 compares the *Base* model, which assumes perfect contact between steel and concrete, against:

- Model: *D & W* - λ_{gap} = 100 $W/m^{2o}C$ (Ding and Wang, 2008); and
- Model: *Ghojel* - $\lambda_{gap} = f(\theta_a)$ (Equation 2-8) (Ghojel 2004); with $\theta_a > 700^oC$, λ_g = 98.92 $W/m^{2o}C$.

Figure 3-17 shows improvements from incorporating a thermal resistance at the steel concrete interface in the form of a gap conductance, λ_{gap}. In terms of conservatism and accuracy these are about 10 minutes for both cases, along with a slight improvement in precision.

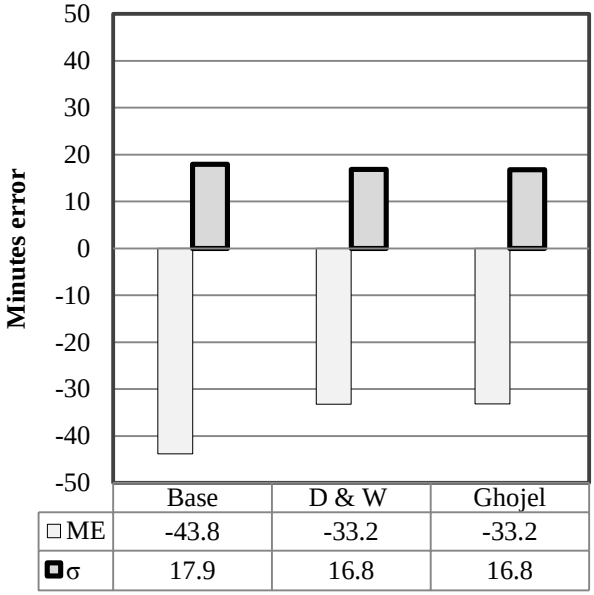

Figure 3-17: The effect of explicitly accounting for air gap formation on the predictive qualities of the EC4 Annex H approach (CEN, 2005)

Effect of mechanical model approaches for steel and concrete

The above comparisons are all based on the same mechanical property models for steel and concrete, according to EC4 (CEN, 2005) and using tables 2-6 and 2-7 along with Table 2-5 and Equation 2-13, for the mechanical properties of steel and concrete, respectively (assumed to be siliceous in the current analysis). As discussed previously in Chapter 2, Lie and Irwin (1995) also present high temperature mechanical models for both steel (Equation 2-29) and concrete (Equation 2-33) which have been specifically developed (i.e. calibrated) for concrete filled columns in a fire situation. Figure 3-18 shows a comparison of the two different mechanical modelling approaches (called *EC4 MAT* and *NRCC MAT*) using the *Base*, *EC4c*, and *NRCCc* thermal modelling approaches. The *NRCC MAT* modelling approach shows improvements of between eight and ten minutes when compared with the *EC4 MAT* modelling approach when the same thermal approach is used.

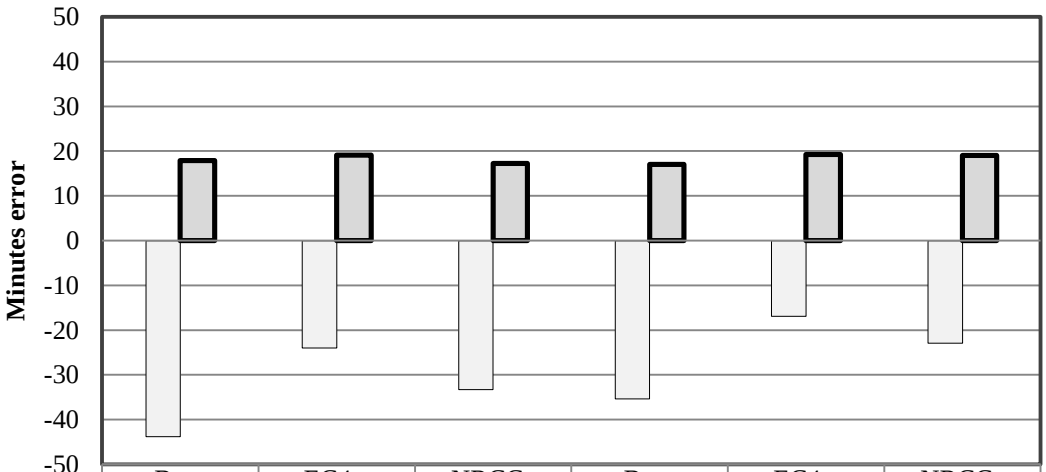

	Base	EC4c EC4 MAT	NRCCc	Base	EC4c NRCC MAT	NRCCc
□ ME	-43.8	-24.0	-33.3	-35.4	-16.9	-23.0
◘ σ	17.9	19.1	17.2	17.0	19.2	19.0

Figure 3-18: The effect of using different high temperature mechanical models, using *Base*, *EC4c*, and *NRCCc* thermal modelling approaches, on the predictions of EC4 Annex H (CEN, 2005)

When comparing the results of the *EC4c/EC4 MAT* with the *NRCCc/NRCC MAT* modelling approaches, such that the material thermal and mechanical properties were developed in conjunction with one another, the precision and accuracy are similar.

3.3.2.6 Parametric combinations results

The above analyses studied different relevant parameters individually and assessed their effects on the accuracy and precision of the Annex H approach predictions. Introducing more realistic (i.e. less conservative) thermal interactions and material models improves the predictive qualities of the Annex H approach; however the predictions remain conservative in all cases. The next set of analyses seeks to identify combinations of analysis parameters that improve the predictions of the Annex H approach, both within the guidance of the Eurocodes and using other combinations of the above parameters. The overarching goal is to provide best-practice thermal and structural modelling guidance for use by designers. EC4 (CEN, 2005) allows for combinations of the thermal material models (*EC4 a, b, c* and *d*) and net heat flux model (Equation 2-41) from EC1-1-2 (CEN, 2009c) *(Combi EC4a* to *d)*. Table 3-4 outlines the various combinations assessed in the current study.

Table 3-4: Combination of individual parametric models

	Fire interaction (Pg 118)	Steel emissivity (Pg 118)	Material thermal properties (Pg 120)	Gap interaction (Pg 125)
• *Combi EC4a*	*EC1-2*	*EC1-2*	EC4a	*N/A*
• *Combi EC4b*			EC4b	
• *Combi EC4c*			EC4c	
• *Combi EC4d*			EC4d	
• *Combi 1*	*EC1-2*	*NIST*	*EC4d*	*Ghojel*
• *Combi 2*			*EC4d**	
• *Combi 3*	*NRCCa*			
• *Combi 4*		*Drysdale*	*EC4c*	

Figure 3-19 shows that improvements can be made by combining the net heat flux fire interaction model from EC1-1-2 (CEN, 2009c) with the EC4 thermal material property models in comparison to the *Base* modelling approach (*ME* = -44, σ = 18 minutes) as well as the individual models for the EC1-1-2 (see Figure 3-11) and EC4 thermal material property models (see Figure 3-16). The precision of the models is similar to those seen in the models where the only parameters changed are the thermal material properties (see Figure 3-16) however the accuracy is improved by some 15-20 minutes. This indicates that the material properties have a more dominant effect on the precision than the fire interaction model. The most accurate of the Eurocode combinations is the *Combi EC4c* modelling approach, where the mean error of the predictions are, on average, -4 minutes, which is an improvement of about 20 minutes compared with the *EC4c* approach shown in Figure 3-16.

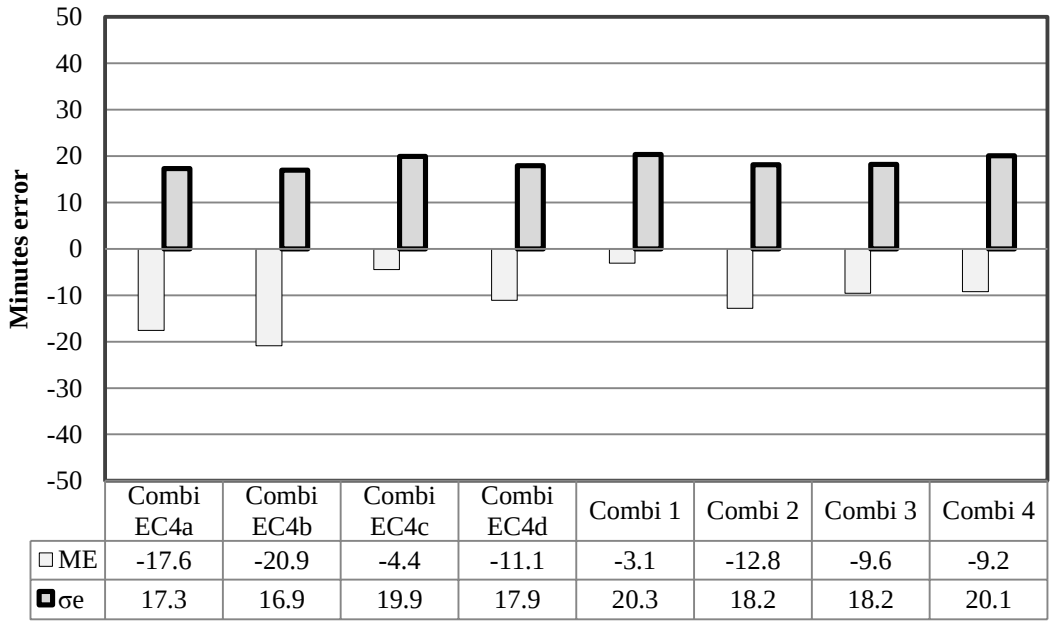

	Combi EC4a	Combi EC4b	Combi EC4c	Combi EC4d	Combi 1	Combi 2	Combi 3	Combi 4
□ME	-17.6	-20.9	-4.4	-11.1	-3.1	-12.8	-9.6	-9.2
◘σe	17.3	16.9	19.9	17.9	20.3	18.2	18.2	20.1

Figure 3-19: Comparison of *ME* and *σ* for the Eurocode restricted and non-Eurocode restricted combination modelling approaches

The *Combi EC4c* and *Combi EC4d* modelling approaches are, on average, accurate predictors of the fire resistance of CFS's; however they do not account for phenomena which are known to be observed in fire tests, specifically the formation of a gap and the variability in steel emissivity. Table 3-4 shows the combinations of individual parametric models to account for known phenomena, which produce the *Combi 1* to *Combi 4* modelling approaches. *Combi 4* combines the most accurate predictions from the individual parametric models and in the cases of *Combi 2* and *Combi 3* the specific heat capacity of concrete material model uses a lower and more realistic value of water content of 5% by mass (rather than 10% by mass).

The *Combi 1* thermal modelling approach is the most accurate of the combination models, employing the *Combi EC4d* thermal material properties and the *EC1-2* net heat flux interaction. It also employs the experimentally derived models for steel emissivity used in the *NIST* model, and the *Ghojel* model of variable gap conductivity. It is clear that it is possible to, on average, make reasonably accurate and precise predictions of the observed response using more rational and realistic approaches to the thermal modelling choices.

3.3.2.7 An improved modelling approach

The above analysis of the EC4 Annex H approach is based on 76 tested specimens and an assumption that these are evenly distributed across physical parameters: size, shape, fixity, load ratio, fill type, wall thickness, and eccentricity; this is not the case. This could cause one model to out-perform another by including a larger dataset as compared to another modelling approach. In order to understand which thermal modelling approach is the best predictor of fire resistance, each modelling approach is assessed and ranked across the different physical parameters.

When comparing the standard deviations and mean errors for the 21 different thermal modelling approaches presented in sections 3.3.2.5 and 3.3.2.6 it can be seen that the standard deviation varies between only 17 and 20 minutes (for the *Ghojel* and *Combi 1* models respectively). This suggests that the prediction method is consistent across the different thermal modelling approaches and that there is 'natural' variance in the reported test data as would be expected for furnace tests. The mean error for the modelling approaches, however, ranges from -44 to -3 minutes (for the *Base* and *Combi 1* models respectively), showing that the choices made in the modelling approaches have a considerable impact on the *ME*. The *ME* is therefore a better distinguishing qualifier for various model parameter combinations. Table 3-5 shows the best 8 modelling approaches, using *ME* as the qualifier.

Table 3-5: The best 8 modelling approaches using *ME* as the qualifier

Rank	**1**	**2**	**3**	**4**	**5**	**6**	**7**	**8**
Model	*Combi 1*	*Combi EC4c*	*Combi 4*	*Combi 3*	*Drysdale*	*Combi EC4d*	*Combi 2*	*Combi EC4a*
ME (mins)	-3	-4	-9	-10	-10	-11	-13	-18
σ (mins)	20	20	20	18	17	18	18	17

Rankings procedure

To assess whether the distribution of the physical parameters within the dataset was skewing the prediction results, a process to weight and rank the predictions was required. Each specific physical parameter was examined, separating the 76 specimen dataset with partitions; i.e. if the physical parameter was *Shape*, the data

were partitioned as circular or square. The mean error of the partitioned data set was then calculated. This was done for each of the eight best performing modelling approaches in Table 3-5, and the modelling approaches were again ranked against one another based on the mean errors, *ME,* with a ranking (*R*) of 1 given to the smallest mean error, and 8 given to the largest mean error. The rankings were then multiplied by the number of specimens (*N*) within the partitioned dataset to provide a weighted ranking, for example if the dataset had 52 square specimens (*N* = 52) and used, for instance, the *Drysdale* modelling approach ranked fifth (*R* = 5), its weighted ranking (*R.N.*) for circular sections would be 260.

This was performed for all of the partitioned datasets within the physical parameters and the weighted rankings were summed to give a total weighted ranking for that modelling approach based on an individual physical parameter, for example if the *Drysdale* modelling approach had a weighted ranking for square columns of 260 and a weighted ranking of 72 for circular columns (*N* = 24, *R* = 3), then the weighted ranking was 332 ($R.N._{tot}$). These total weighted rankings were then re-ranked to provide an aggregate ranking (R_{tot}) for that modelling choice in terms of the specific physical parameter (see Table 3-6, for example). Full results of the rankings procedure are avoided here but are given Appendix A.

Table 3-6: Total weighted ranking procedure for *Shape* physical parameter

	Circle			**Square**			**Total weighted ranks**	
	N = 24			N = 52				
	ME	R	R.N	*ME*	R	R.N	$R.N._{tot}$	$\mathbf{R_{tot}}$
Combi 1	-8.5	*1*	*24*	-0.6	*1*	*52*	76	**1**
Combi EC4 c	-10.8	*2*	*58*	-1.5	*2*	*104*	152	**2**
Combi 4	-15.0	*5*	*120*	-6.6	*3*	*156*	276	**3**
Combi 3	-14.5	*4*	*96*	-7.3	*4*	*208*	304	**4**
Drysdale	-13.0	*3*	*72*	-8.2	*5*	*260*	332	**5**
Combi EC4 d	-15.3	*6*	*144*	-9.2	*6*	*312*	456	**6**
Combi 2	-17.5	*7*	*168*	-10.6	*7*	*364*	532	**7**
Combi EC4 a	-21.3	*8*	*192*	-15.9	*8*	*416*	608	**8**

The rankings for the different physical parameters were then averaged across the different physical parameters and the lowest average was considered the best overall

modelling approach for that parameter. The dataset was partitioned based on seven different physical parameters:

- *Shape* – circular or square sections;
- *Fixity* – the idealised end restraint conditions PP, PF and FF;
- *Fill* – PC, RC and FIB;
- *Load eccentricity* – eccentric or concentric loading;
- *Size* – the minimum side length or diameter of the cross-section with the ranges of 0-200, 200-250, 250-300 and >300 mm;
- *Load ratio* – the ratio of applied test load to design capacity at ambient with the ranges of 0-0.2, 0.2-0.4, 0.4-0.6 and >0.6; and
- *Wall thickness* – thickness of the steel tube ranging from 0-4, 4-6, 6-7 or >7 mm.

Table 3-7 shows a summary of the re-ranked total weighted rankings (R_{tot}) based on *ME* across all seven physical parameters for the eight 'best' modelling approaches. Also shown are the mean and standard deviation of R_{tot} for each of the approaches showing that *Combi EC4c* and *Combi 1* are the strongest modelling approaches across all physical parameters.

Table 3-7: Summary of R_{tot} rankings; including mode, mean, and standard deviations of the rankings for *ME*

	Shape	Fixity	Fill	Load App.	Size	Load Ratio	Wall Thick.	MEAN	σ
Combi EC4 c	2	2	1	2	2	1	1	1.6	0.53
Combi 1	1	1	2	1	4	5	2	2.3	1.60
"Best" Combi	3	3	3	3	3	2	5	3.1	0.90
Drysdale	5	4	5	5	1	4	3	3.9	1.46
Combi 3	4	5	4	4	5	3	4	4.1	0.69
Combi EC4 d	6	6	6	6	6	6	6	6.0	0.00
Combi 2	7	7	7	7	7	7	7	7.0	0.00
Combi EC4 a	8	8	8	8	8	8	8	8.0	0.00

Combi EC4c uses the EC1-1-2 fire interaction method with the emissivity of the fire, $\varepsilon_{m,fi} = 1.0$, the emissivity of the steel, $\varepsilon_{m,a} = 0.7$, and assuming perfect contact between the steel tube and the concrete core. It also employs the lower bound of the concrete thermal conductivity and explicitly accounts for the specific heat of water using a

spike of 5600 J/kg^{o}C and representing 10% moisture by mass. Whilst this approach is accurate it uses approximations that do not properly account for what is observed in furnace tests. For instance observations in furnace tests at the steel tube – concrete core interface have shown the formation of an air gap and thus cannot be the perfect contact assumption made in this modelling approach.

Using *Combi EC4c* as a base model (*ME* = -4 minutes, σ = 20 minutes), modifications to the different variables, to account for interactions observed furnace tests, can be made and assessed to observe the effect on the predictive ability of the updated model and to see if a more realistic model can be produced (designated *Combi ω*). One of the most influential parameters in the predictions is the influence of the assumed specific heat capacity of concrete on the heat transfer. *Combi ω* uses the NRCC model described in Figure 3-14.

Combi ω modifies the emissivity of the steel from the EC4 value of $\varepsilon_{m,a} = 0.7$ to the variable $\varepsilon_{m,a}$ taken from the *NIST* thermal modelling approach. The emissivity of the fire is assumed to be the NRCC value of $\varepsilon_{m,fi} = 0.75$. The gap conductance is assumed as suggested by Ghojel (2004).

Figure 3-20 shows the predicted fire resistance using the *Combi EC4c* approach versus the observed fire resistance, partitioned by section shape, whilst Figure 3-21 shows the same comparison using the *Combi ω* modelling approach. By introducing the more physically realistic modifications to *Combi EC4c* to obtain *Combi ω*, similar levels of accuracy and precision are obtained and in general the predictive ability is enhanced across the physical parameters (see **Error! Reference source not found.**). The mean percentage errors, *MPE*s, are -5% and -2% with standard deviation of the percentage errors of 33% and 36% for the *Combi EC4c* and *Combi ω* models, respectively. The *ME* and the standard deviation of the errors are -4 and -2 minutes, and 20 and 22 minutes, respectively. The *Combi EC4c* and *Combi ω* are the most accurate approaches overall, and both perform well when ranked across the different physical parameters; these can be considered best-practice prediction modelling approaches when using the EC4 Annex H approach (CEN, 2005), when assessed against the full database of available (applicable) data.

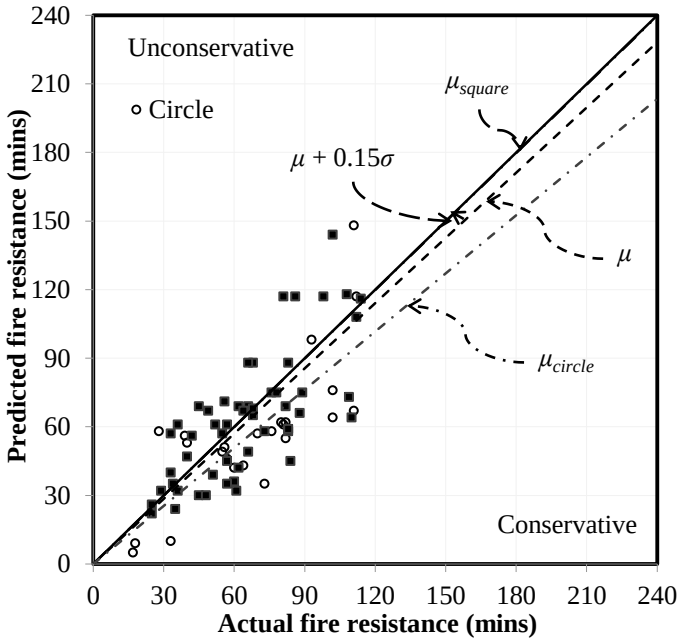

Figure 3-20: Predicted versus actual fire resistance for EC4 Annex H (CEN, 2005) approach using the *Combi EC4c* modelling assumptions with the database partitioned by shape (circular or square)

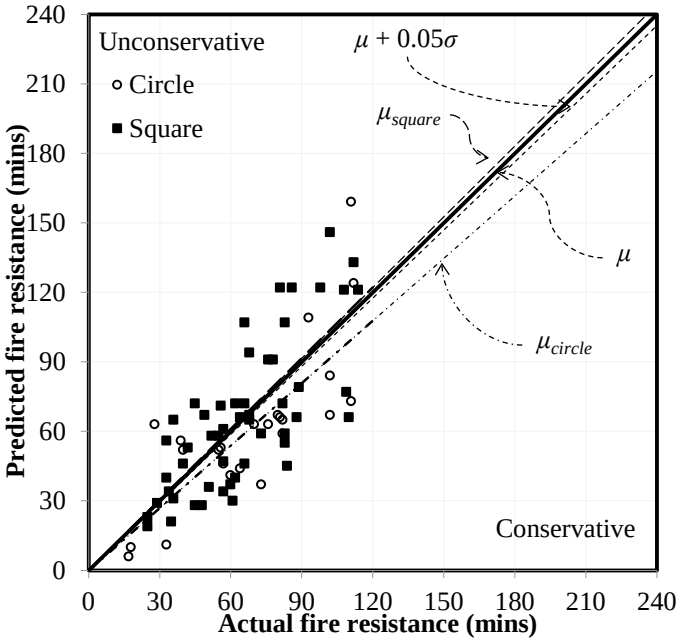

Figure 3-21: Predicted versus actual fire resistance for EC4 Annex H (CEN, 2005) approach using the *Combi ω* modelling assumptions with the database partitioned by shape (circular or square)

Table 3-8: Summary of R_{tot} rankings including *Combi ω*; and the mean and standard deviations of those rankings for the mean error, *ME*

	Shape	Fixity	Fill	Load App.	Size	Load Ratio	Wall Thick.	MEAN	σ
Combi EC4 c	3	3	1	3	3	2	1	2.3	0.95
Combi 1	1	2	2	2	5	6	2	2.9	1.86
"Best" Combi	4	4	4	4	4	3	6	4.1	0.90
Drysdale	6	5	6	6	1	5	4	4.7	1.80
Combi EC4 d	5	6	5	5	6	4	5	5.1	0.69
Combi 3	7	7	7	7	7	7	7	7.0	0.00
Combi 2	8	8	8	8	8	8	8	8.0	0.00
Combi EC4 a	9	9	9	9	9	9	9	9.0	0.00
Combi ω	***2***	***1***	***3***	***1***	***2***	***1***	***3***	***1.9***	***0.90***

To understand the respective performance of the two best modelling approaches, a study of the physical parameters is required to assess their predictive abilities.

Effect of column shape and concrete infill

It is interesting to note how the modelling approaches handle shape as shown in Figure 3-20 and Figure 3-21. Both the *Combi EC4c* and *Combi ω* modelling approaches under-predict the time to failure of circular columns, with *MEs* of -11 minutes and -7 minutes, and *MPEs* of -15% and 10%, respectively. The 24 circular sections were filled with plain concrete (PC), and 21 of the 52 square sections were filled with PC. The fire resistance predictions for the PC square sections have an *ME* of +13 and +17 minutes for the *Combi EC4c* and *Combi ω* modelling approaches, respectively. The unconservative and large mean errors for the square sections, as compared with the circular sections with the same concrete infill, show that fundamental mechanics relating to the shape (e.g. concrete confinement in circular columns, or stress concentrations and local buckling at the corners in square columns) are not being properly accounted for in the Annex H approach (CEN, 2005).

Fire resistance prediction for square cross-sections (*ME* of -2 and 0.7 minutes for the *Combi EC4c* and *Combi ω* modelling approaches, respectively) include 31 RC filled columns which are conservatively predicted by both modelling approaches, as shown in Figure 3-22. The conservatism could be due to the reinforcement; (1) halting crack propagation and increasing the flexural resistance of the column; (2) providing lateral

confinement to the concrete; or (3) the assumption that yield strength of the reinforcement equals the yield strength of the steel tube at ambient temperatures, since most reports do not specify a yield strength for the reinforcement.

Effect of fixity and eccentricity

Figure 3-22 also shows comparisons of the mean error and standard deviation of both *Combi EC4c* and *Combi ω* with regards to; (a) fixity, the idealised end rotational restraint conditions which affect the effective length of the column; and (b) load eccentricity, either concentrically or eccentrically loaded. As mentioned previously (Section 3.2.2.1), the true fixity of the tested columns is difficult to ascertain, yet both modelling approaches have reasonably consistent levels of accuracy and precision for the idealised fixity types. Both modelling approaches are conservative and reasonably precise for eccentric loads, due to the inherent design conservatisms of the EC4 Annex H approach for eccentric loads, and are more accurate for concentric loads with higher variability.

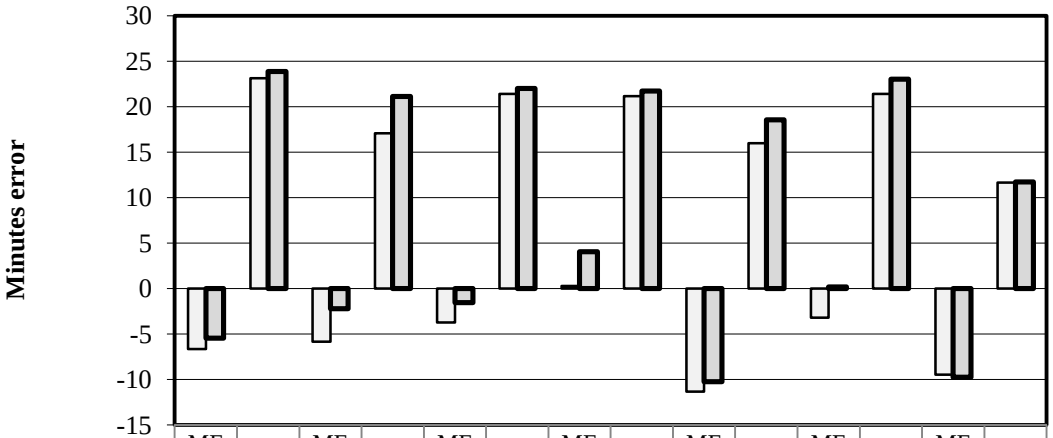

	ME	σ	ME	σ	ME	σ	ME	σ	ME	σ	ME	σ	ME	σ
	(N=9) Pin - Pin		(N=17) Pin - Fix		(N=52) Fix - Fix		(N=45) PC		(N=31) RC		(N=61) Concentric		(N=15) Eccentric	
	Fixity						Fill				Eccentrictiy			
Combi EC4c	-6.7	23.1	-5.8	17.1	-3.7	21.4	0.3	21.2	-11.3	16.0	-3.2	21.4	-9.5	11.6
Combi ω	-5.4	23.9	-2.2	21.1	-1.5	22.0	4.0	21.7	-10.2	18.6	0.2	23.0	-9.7	11.7

Figure 3-22: Comparison of *ME* and *σ* using *Combi EC4c* and *Combi ω* modelling approaches for the EC4 Annex H (CEN, 2005) approach with the database partitioned based on (a) fixity, (b) infill type, and (c) eccentricity

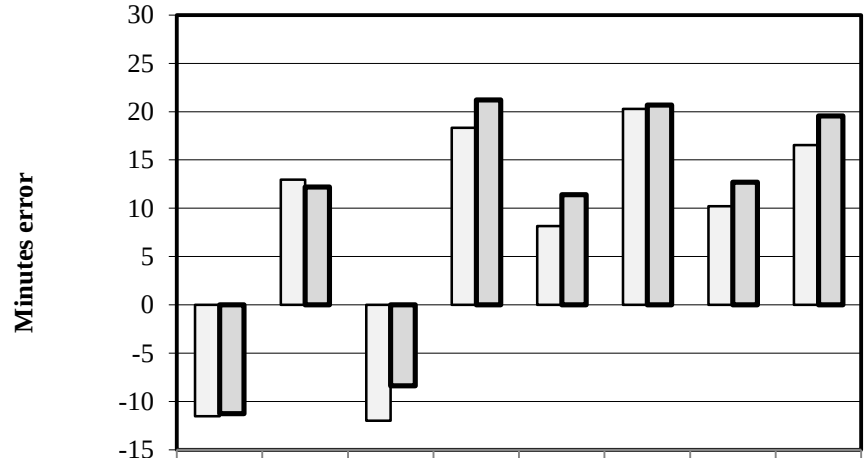

	ME	σ	ME	σ	ME	σ	ME	σ
	(N=16) 0-200mm		(N=33) 200-250mm		(N=17) 250-300mm		(N=10) 300+mm	
Combi EC4c	-11.5	13.0	-12.0	18.3	8.2	20.3	10.2	16.5
Combi ω	-11.3	12.2	-8.4	21.2	11.4	20.7	12.7	19.6

Figure 3-23: Comparison of *ME* and *σ* using *Combi EC4c* and *Combi ω* modelling approaches for the EC4 Annex H (CEN, 2005) approach with the database partitioned based on cross-sectional size

Three circular columns have predicted fire resistance rating of less than ten minutes (the three circular data points towards the origin in Figure 3-20 and Figure 3-21) with a *MPE* of about -60% for both modelling approaches. These three circular columns are filled with plain concrete, loaded eccentrically, and have pinned-pinned end restraint, a combination that the EC4 Annex H approach struggles to predict.

Effect of column size

Figure 3-23 shows a comparison of the mean error and standard deviation of both the *Combi EC4 c* and *Combi ω* with regards to cross-sectional size. As the size of the column increases, both methods fail to capture the mechanics at play. This suggests that the heat transfer across the section is not properly accounted for, with concrete temperatures under-predicted for large sections and possibly over predicted for smaller sections. This suggests that the energy absorbed into the concrete core is too great and the amount of energy being transferred through the core is too low.

Effect of wall thickness

Figure 3-24 shows a comparison of the *ME* and σ of both the *Combi EC4 c* and *Combi* ω with data partitioned based on the wall thickness of the steel tube. Both models under predict the resistance of columns with small wall thicknesses, suggesting that the modelling approaches fail to properly account for the mechanics or the heat transfer at play, whether from concrete enhancement due to confinement or to early air gap formation leading to lower concrete temperatures.

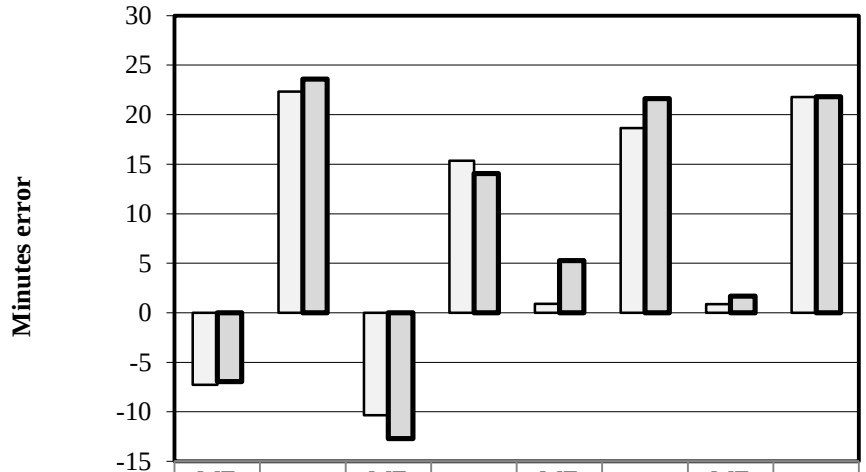

	ME	σ	ME	σ	ME	σ	ME	σ
	(N=15) 0- 4mm		(N=16) 4.01-6mm		(N=27) 6.01-7mm		(N=17) 7.01+mm	
Combi EC4c	-7.3	22.3	-10.3	15.3	0.9	18.7	0.9	21.8
Combi ω	-6.9	23.6	-12.7	14.1	5.3	21.6	1.7	21.8

Figure 3-24: Comparison of *ME* and σ using *Combi EC4c* and *Combi* ω modelling approaches for the EC4 Annex H (CEN, 2005) approach with the database partitioned based on wall thickness (t_a in mm) of the steel tube

3.3.3 Summary of the EC4 Annex H approach

This section has compared the effects of different thermal modeling approaches on the predictive qualities of the EC4 Annex H approach, and has shown that it is possible to predict the observed fire resistance of CFS columns with an average error of less than five minutes and a standard deviation of about 20 minutes. This can be accomplished using either code specified material properties and interactions, as used in the *Combi EC4c* thermal modelling approach, or the more rational material

properties and interactions that can be found in the scientific literature, as used in the *Combi ω* thermal modelling approach.

3.4 French National Annex – Annexe PCRB Approach

The French National Annex (FNA) Annexe PCRB (CEN, 2007) was developed to overcome the apparent shortcomings in the EC4 Annex H approach to the fire resistant design of CFS columns, previously described in Section 2.4.4.3. The FNA Annexe PCRB (CEN, 2007) approach uses the same two-step method as the EC4 Annex H approach for calculating a temperature distribution over the cross-section and then determining the design axial buckling/crushing capacity of the column. Unlike the EC4 Annex H approach, Annexe PCRB follows the general EC4 design method but includes thermal stress modification factors created to account for the non-uniform temperature profile within a composite section, and thus the unequal thermal stresses and strains caused by different material and sectional thermal expansions.

3.4.1 Methodology

FNA Annexe PCRB approach (CEN, 2007) sets out a method based around the general flow chart as laid out in Clause 4.3.5.1.1 of EC4 (CEN, 2005) and is as summarized as follows:

1. Determine the temperature profile within the cross-section.
2. Calculate the cross-sectional plastic resistance to crushing (Equation 2-45).
3. Calculate the relative slenderness of the column (Equation 2-46) by calculating.
   a. the effective flexural stiffness (Equation 2-48 and Table 2-12).
   b. the Euler buckling load (Equation 2-47).
4. Determine the transitional relative slenderness (Equation 2-53 or Table 2-13 and Figure 2-15).
5. Calculate the buckling curve reduction coefficient (Equation 2-54 or Equation 2-55 and Table 2-14).
6. Calculate the design axial buckling load in the fire situation (Equation 2-44).

A full description of this method was given in Section 2.4.4.3 of Chapter 2.

3.4.2 Limits of design and applicable database

To fairly assess the performance of this approach against the furnace test database, the limits (Table 2-16) given by the FNA Annexe PCRB approach (CEN, 2007) need to be applied to the full database of furnace tests results as reported in Tables 2-1 to 2-4. The approach set out in the FNA Annexe PCRB allows for a greater range of sizes as well as a stronger concrete infill than in EC4 Annex H (CEN, 2005). In applying the limits, the resulting database includes 161 tests. The data are limited in terms of end restraint conditions, effective length, and concrete type. The breakdown of applicable specimens for the Annexe PCRB approach is given in Table 3-9.

Table 3-10 shows the 73 specimens from the dataset in Table 3-9 that are able to be assessed by both the EC4 Annex H approach and the FNA Annexe PCRB approach; this is three fewer than in the previous analysis (Table 3-2) with three plain concrete columns with eccentric loading removed.

3.4.3 Application of FNA – Annexe PCRB approach

The application of this method is similar to the EC4 annex H approach described in Section 3.3.2.2. A temperature distribution over the column's cross-section is determined for every instant during fire. Once the temperature distributions in the CFS sections are obtained, the steel tube is assumed to have a uniform temperature and the concrete cross-section is divided into rings of equal thickness. This is shown schematically in Figure 3-8, where again six layers have been chosen.

Each of the concrete rings is assumed to have a uniform temperature at any given instant in time, with temperatures based on the heat transfer analysis described previously in Section 3.3.2.7. Reinforcing steel is again assumed to be at same temperature as the concrete layer in which it resides, and after the temperature of each layer is determined its mechanical properties are found by interpolation of Tables 3.1 through 3.4 of EC4 (CEN, 2005).

Table 3-9: Details of specimens used in the evaluation of the FNA Annexe PCRB approach (CEN, 2007)

Specimen details										Steel tube						Concrete							
Lengths (m)				End conditions[b]		Load ratio[c]		Eccentricity		Section shape		Section size (mm)		Wall thickness (mm)		Concrete Type[d]		28 day strength (MPa)				A_s/A_c [e]	
	Actual	Effective length[a]																					
		Design	*Furnace*																				
<2.2	5	5	45	PP	21	0-0.2	30	zero	133	C	52	<200	36	<4.1	35	PC	92	20-25	9	40-45	41	<1.5%	100
2.2-3.0	-	101	79	PF	34	0.2-0.4	74	<15%	18	S	109	200-250	61	4.1-6.1	28	RC	55	25-30	11	45-50	15	1.5-2.5%	35
3.0-3.8	77	32	15	FF	106	0.4-0.6	44	15-30%	7			250-300	30	6.1-7.0	52	FIB	14	30-35	30	50-55	8	2.5-3.5%	15
>3.8	79	23	22			0.6+	13	>30%	3			300-350	18	7.0-10	31			35-40	43	55-60	4	>3.5%	11
												350+	16	10+	15								

Table 3-10: Details of EC4 Annex H applicable specimens used in the evaluation of the FNA Annexe PCRB approach (CEN, 2007)

Specimen details										Steel tube						Concrete							
Lengths (m)				End conditions[b]		Load ratio[c]		Eccentricity		Section shape		Section size (mm)		Wall thickness (mm)		Concrete Type[d]		28 day strength (MPa)				A_s/A_c [e]	
	Actual	Effective length[a]																					
		Design	*Furnace*																				
<2.2	5	5	21	PP	6	0-0.2	19	zero	61	C	21	<200	16	<4.1	15	PC	42	20-25	8	40-45		<1.5%	45
2.2-3.0	-	45	34	PF	17	0.2-0.4	32	<15%	7	S	52	200-250	30	4.1-6.1	19	RC	31	25-30	9	45-50	-	1.5-2.5%	21
3.0-3.8	38	14	9	FF	50	0.4-0.6	21	15-30%	3			250-300	17	6.1-7.0	22	FIB		30-35	22	50-55	-	2.5-3.5%	3
>3.8	30	9	9			0.6+	1	>30%	2			300-350	7	7.0-10	16			35-40	34	55-60	-	>3.5%	4
												350+	3	10+	1								

[a] the design effective length is the code-specified effective length for the stated column end-conditions, whereas the furnace effective length is the effective length calibrated by the various testing facilities and stated in the original source references.

[b] P = pinned end condition, F = fixed end condition.

[c] the ratio of the applied load on the column during the test to the nominal strength of the column at ambient temperature.

[d] PC – plain concrete, RC – steel bar reinforced concrete, FIB – steel fibre reinforced concrete.

[e] A_s – area of steel bar reinforcement, A_c – area of concrete.

3.4.4 Results of meta-analysis

The same statistical assessment procedure was used to assess the FNA Annexe PCRB approach (CEN, 2007) as for the EC4 Annex H approach. Three representative thermal modelling approaches were adopted in the EC4 Annex H analysis to make the assessment; again these were the *Base, Combi EC4 c* and *Combi* ω modelling approaches described earlier.

Overall results

An overall assessment of the three thermal modelling approaches using FNA Annexe PCRB approach (CEN, 2007) and also partitioned into those specimens that can be analysed also by EC4 Annex H in Table 3-10. The *Base* modelling approach has an overall mean percentage error of -77% and a standard deviation of the percentage errors of 25%. With such large errors and high standard deviation it is not worthwhile to rationally assess the specific effects of any of the different physical parameters in the experimental database and so the *Base* modelling approach is not considered any further.

Figure 3-25 and Figure 3-26 show the predicted fire resistance versus the actual fire resistance found in tests using the FNA Annexe PCRB approach for the *Combi EC4c* and *Combi* ω modelling approaches, respectively. As shown in the figures both modelling approaches are conservative on average, but both have comparatively high variance with at best only 60% of the predictions being conservative. There are 15 specimens, with fire resistance predictions of less than 10 minutes (and 6 specimens have predicted fire resistances of zero). Most of these specimens are tall (quoted effective lengths greater than 3.81 m), filled with plain concrete, and failing in about 20 minutes or less in reality, however they are not eccentrically loaded. To more fully understand the performance of the FNA Annexe PCRB approach a detailed study of the physical parameters that might affect the predictive abilities is required.

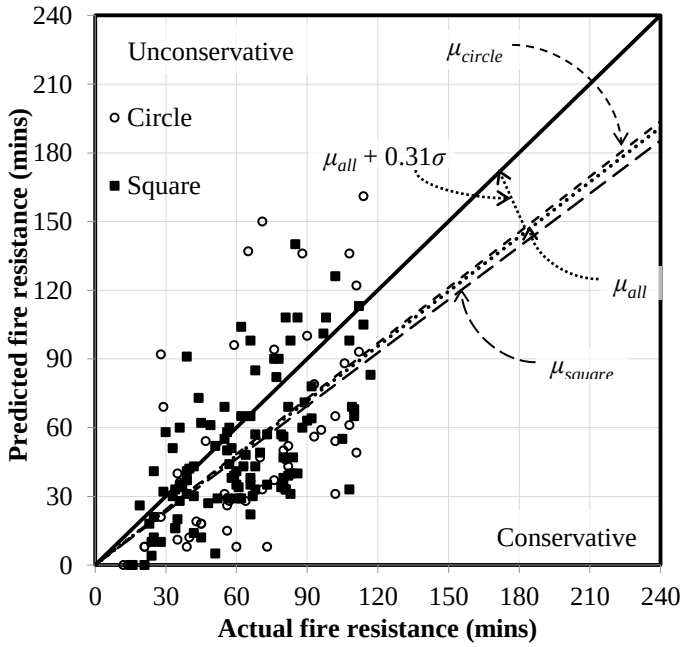

Figure 3-25: Predicted versus actual fire resistance for the FNA – Annexe PCRB approach (CEN, 2007) using the *Combi EC4c* modelling approach with the database partitioned by shape

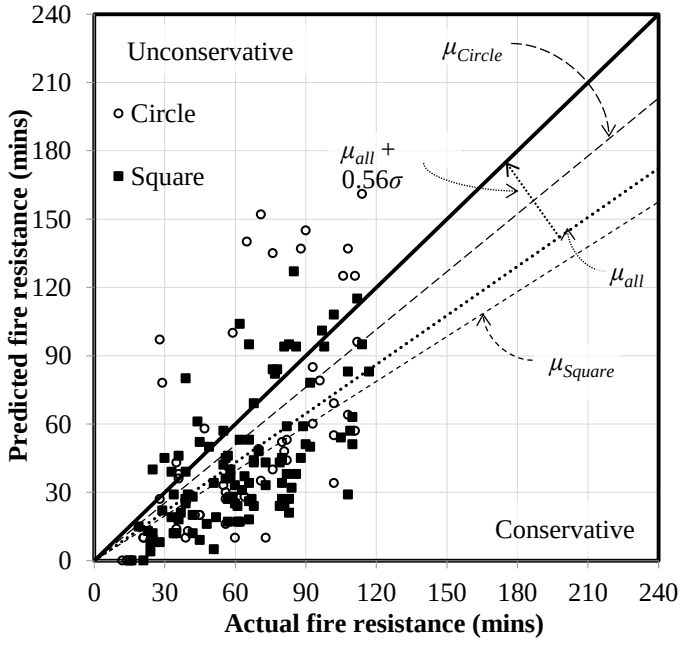

Figure 3-26: Predicted versus actual fire resistance for the FNA – Annexe PCRB approach (CEN, 2007) using the *Combi ω* modelling approach with the database partitioned by shape

Effect of size and shape

Figure 3-25 and Figure 3-26 show the predicted fire resistance times against the actual fire resistances seen in tests using the *Combi EC4c* and *Combi ω* thermal modelling approaches, respectively, partitioned by section shape. As can be seen, both thermal modelling approaches are conservative on average for square and circular sections with a greater conservatism for square sections. Both modelling approaches have large standard deviations for the circular sections of 34 and 37 minutes, for the *Combi EC4 c* and *Combi ω* modelling approaches, respectively, due in part to the number of sections above the 1:1 line. These sections are also of large diameter which is of concern as the trend in design is for large circular sections. This method certainly does not capture the response any better than the Annex H modelling approach for the same thermal and material modelling assumptions.

Figure 3-27 shows a comparison of *ME* and σ for the FNA Annexe PCRB approach (CEN, 2007) using the *Combi EC4c* and *Combi ω* modelling approaches with the database partitioned based on cross-sectional size. As the cross-sectional size increases the *ME* and σ also increase. For sections greater than 350 mm the *ME* is +29 and +26 minutes for the *Combi EC4c* and *Combi ω* modelling approaches respectively, with standard deviations of about 30 minutes. The mean of these data for these sections lies about one standard deviation away from the 1:1 line, meaning that only about 35% of the predictions are conservative.

Effect of wall thickness

The effect of the wall thickness in the FNA Annex PCRB approach is coupled to the size of the steel tube and fire resistance rating and is modified with a flexural reduction coefficient, $\varphi_{a,\theta}$, from Table 2-12, and the thickness of the wall is not explicitly account for. As seen in Figure 3-28, which shows the *ME* and σ partitioned by steel wall thickness for the *Combi EC4c* and *Combi ω* modelling approaches, the contribution of the steel wall is not properly accounted for.

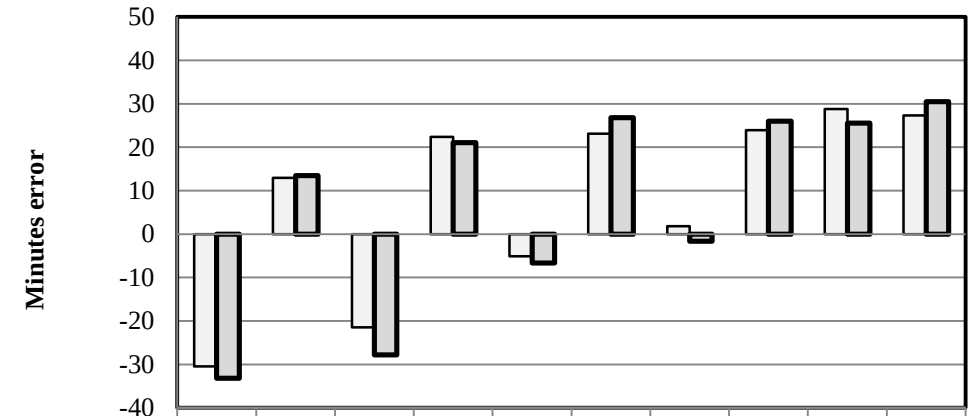

	ME	σ	ME	σ	ME	σ	ME	σ	ME	σ
	(N=36) 0-200 mm		(N=61) 200-250 mm		(N=30) 250-300 mm		(N=18) 300-350 mm		(N=16) 350+ mm	
Combi EC4c	-30.5	12.9	-21.5	22.4	-5.1	23.1	1.8	24.0	28.8	27.3
Combi ω	-33.2	13.5	-27.8	21.1	-6.7	26.8	-1.7	26.0	25.6	30.5

Figure 3-27: Comparison of ME and σ for the FNA – Annexe PCRB approach (CEN, 2007) using the *Combi EC4c* and *Combi ω* modelling approaches with the database partitioned by cross-sectional size

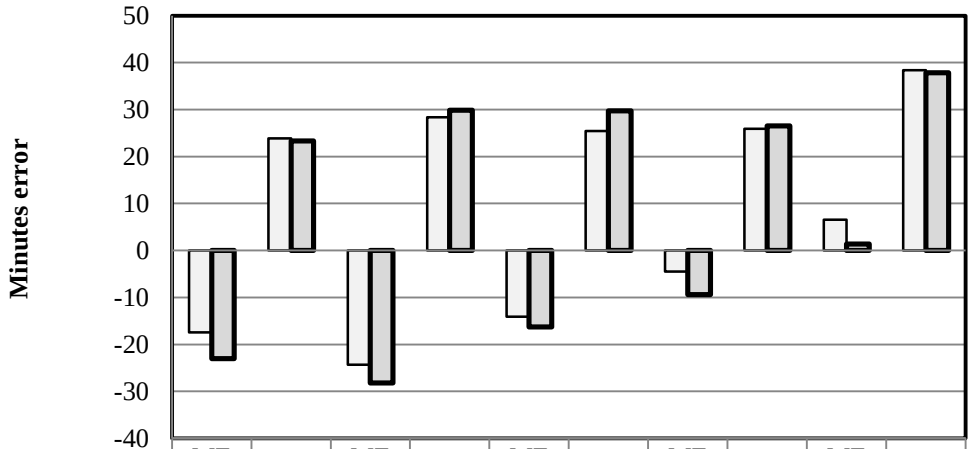

	ME	σ	ME	σ	ME	σ	ME	σ	ME	σ
	(N=35) 0-4mm		(N=28) 4.01-6mm		(N=52) 6.01-7 mm		(N=31) 7.01-10mm		(N=15) 10+ mm	
Combi EC4c	-17.5	23.9	-24.3	28.3	-14.1	25.4	-4.5	25.9	6.5	38.4
Combi ω	-23.0	23.3	-28.2	29.8	-16.3	29.8	-9.4	26.5	1.4	37.8

Figure 3-28: Comparison of *ME* and *σ* for the FNA – Annexe PCRB approach (CEN, 2007) using the *Combi EC4 c* and *Combi ω* modelling approaches with the database partitioned by the wall thickness of the steel tube

The fire resistance predictions of columns with small wall thicknesses (less than 6 mm and generally having small cross-sections) are the most conservative, and as the steel wall thickness increases, the conservatism decreases indicating that that the FNA Annex PCRB approach (CEN, 2007) underestimates the contribution of the steel wall thickness to load carrying capacity of the column in fire.

Effect of increased limitation range

Figure 3-29 shows the *ME* and σ for all 161 specimens in Table 3-9 based on the *Combi EC4c* and *Combi* ω modelling approaches and shows the data partitioned into the 73 specimens from Table 3-10 that can also be assessed using the EC4 Annex H approach and the 88 remaining specimens from Table 3-9 which can only be assessed using the FNA Annexe PCRB approach.

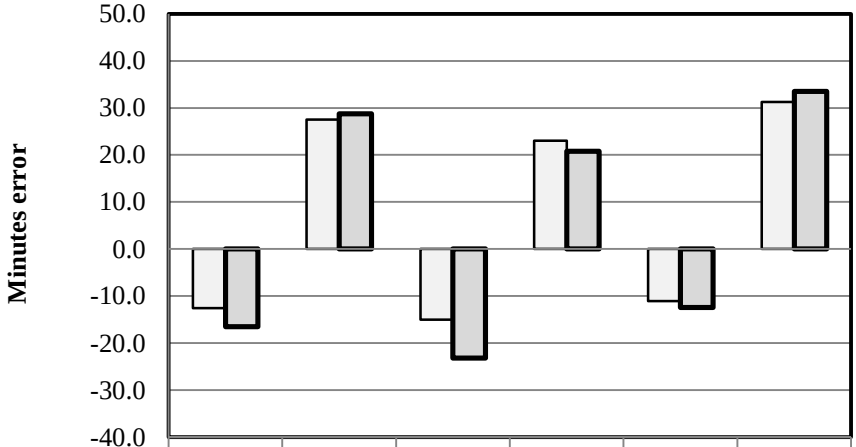

	ME (N=161) ALL	σ (N=161) ALL	ME (N=73) EC4 & FNA	σ (N=73) EC4 & FNA	ME (N=88) FNA only	σ (N=88) FNA only
Combi EC4c	-12.6	27.6	-15.0	23.0	-11.1	31.2
Combi ω	-16.5	28.7	-23.2	20.8	-12.5	33.5

Figure 3-29: Comparison of *ME* and σ for the FNA – Annexe PCRB approach (CEN, 2007) using the *Combi EC4c* and *Combi* ω modelling approaches showing overall and applicability partitioned results

Figure 3-29 shows that the specimens that can be assessed by both the FNA Annexe PCRB and EC4 Annex H approaches are the most conservative and most precise, with similar precision as found using the EC4 Annex H approach. The increased

range of application used in the FNA Annexe PCRB approach (CEN, 2007) can be seen to decrease the overall precision of the approach, with *FNA only* having twice standard deviation of the data restricted by the EC4 Annex H limits (*EC4 and FNA*). The high variance means that at most 60% of the predictions will be conservative for either approach, suggesting that either the approach does not account for the relevant mechanics or heat transfer at play or that the limits for the method are too large.

When considering the effects of fixity, load ratio, eccentricity, and fill type on the predictive qualities of the FNA Annexe PCRB approach similar trends were seen as for the EC4 Annex H approach.

3.4.5 Summary of FNA – Annexe PCRB approach

The FNA Annexe PCRB approach (CEN, 2007) proposes a method that follows the general method as prescribed in Eurocode 4, and includes specific stiffness reduction factors that had previously not been provided. The approach also includes a new concept which accounts for the transition in load capacity when instability due to concrete cracking and flexural bending occurs, and is implemented with the use of a transitional slenderness, $\lambda_{\theta,transitional}$. The analysis above, which included comparison against 161 specimens, showed that the approach fails to account for shape, section size and wall thickness properly. Using the same thermal modelling approaches, it has been shown that the EC4 Annex H approach is more accurate and more precise, and has significantly less variation across the specific physical parameters assessed. The temperature profile prediction is a key component that needs to be assessed to identify whether the thermal modelling approaches are, in a sense, artificially improving the structural models' abilities to predict the time to failure.

3.5 Critical steel tube temperature prediction

The so called "critical temperature" for steel members is a common design criterion used by engineers and is widely reported in the literature. The critical temperature is intended to be the temperature of the steel tube at which a CFS column can no longer sustain the applied fire limit state load. Furthermore, a critical temperature based on the load ratio of a CFS element is commonly used to specify the amount of fire protection required to achieve a given fire resistance. For structural steel, the

correlation between temperature and load ratio is relatively easy to determine due to the homogeneity of the material and its high thermal conductivity. When considering concrete filled sections (CFS) the ability to predict the critical steel temperature at failure is complicated because a portion of the load is carried by the concrete core.

The critical temperature of the steel tube in a CFS column is dependent on many factors. During the early stages of fire, the concrete inside the steel tube may act as a heat sink. When/if the steel expands to the point of creating an air gap, the air gap acts as an insulating layer and decreases the rate of temperature increase in the concrete. The formation of the air gap also has an effect on the load carrying capacity, of the section, as the composite actions of the confinement of the concrete and the restraint to local buckling of the steel are either reduced or lost. The time of exposure when the air gap forms also depends on the load that is being applied to the section and the manner in which the components dilate during heating. All of these interactions affect the failure time and temperatures within CFS columns. Although there is a paucity of information on these interactions at elevated temperatures and the full distribution of cross-sectional temperatures of the elements at failure, many of the tests found in the literature report the temperature of the steel tube at failure. To predict the time to failure of a column as specified in EC4 Annex H (CEN, 2005) or the FNA Annexe PCRB (CEN, 2007) approaches, a temperature profile in the section is required from which one can predict the temperature of the steel, and therefore it is possible to assess the thermal modelling approaches against the test data.

The EC4 Annex H approach (CEN, 2005) described in Section 3.3.2 led to two thermal modelling approaches that provided the most accurate predictions in terms of overall fire resistance; these were designated *Combi EC4c* and *Combi* ω and were also applied to the FNA Annexe PCRB approach (CEN, 2007) in Section 3.4. In the previous analyses in sections 3.3.2 and 3.4, the time to failure was calculated and directly relates to a temperature of the steel tube at which the column failed. This predicted steel failure temperature is compared to the observed test steel failure temperature in tests.

3.5.1 EC4 Annex H steel tube failure temperatures

Of the 76 specimens used in the analysis of the EC4 Annex H approach (CEN, 2005), nine specimens failed to report a failure temperature of the steel tube. Figure 3-30 shows the predicted steel temperature at failure using the *Combi ω* thermal modelling approach compared against the observed steel temperature in furnace tests. The overall *MPE* is -3% with a standard deviation of the errors of 18%; showing similar accuracy and precision as the structural fire resistance predictions. The *Combi EC4c* approach showed similar accuracy and precision.

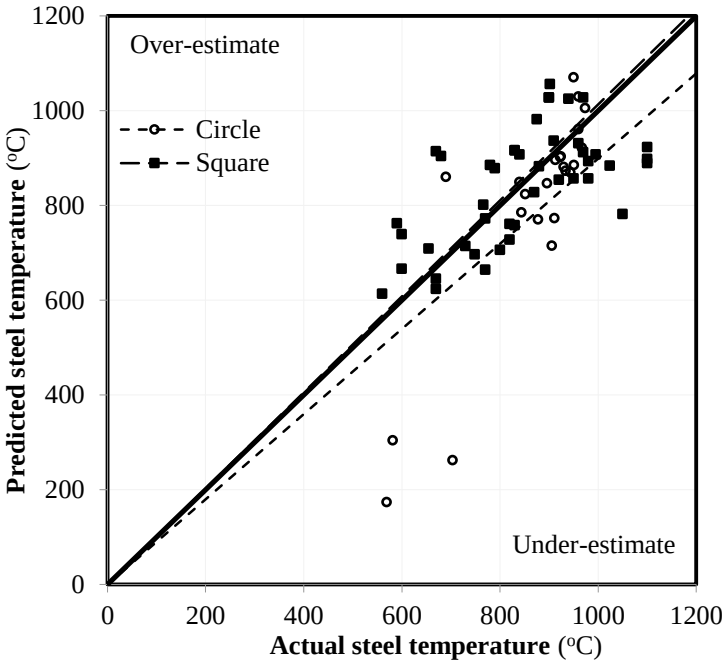

Figure 3-30: Predicted versus observed steel temperature for EC4 Annex H (CEN, 2005) using the *Combi ω* modelling approach and with the database partitioned by section shape

Figure 3-30 also shows the database partitioned by shape, and it appears that the thermal modelling approach slightly overestimates failure temperature for the square sections, with an *MPE* of +1.3%, whilst the circular column failure temperatures are underestimated with an *MPE* of -10%. The under-estimate for the circular columns is influenced by three conservative predictions which appear to be outliers. These three columns are eccentrically loaded, plain concrete filled hollow sections, which have

previously been highlighted as being poorly predicted by Annex H. If these specimens are removed the *MPE* for *circular* columns improves to -3.0%.

As for the predictions of fire resistance, the predicted failure temperatures of eccentrically loaded columns are generally underestimated, with *MPEs* of -21% and -22%, and standard deviations of 26% for the *Combi EC4 c* and *Combi ω* modelling approaches, respectively. The concentrically loaded columns are very slightly overestimated with *MPEs* of 1% and 2% and standard deviations of 12% and 12% for *Combi EC4 c* and *Combi ω*, respectively.

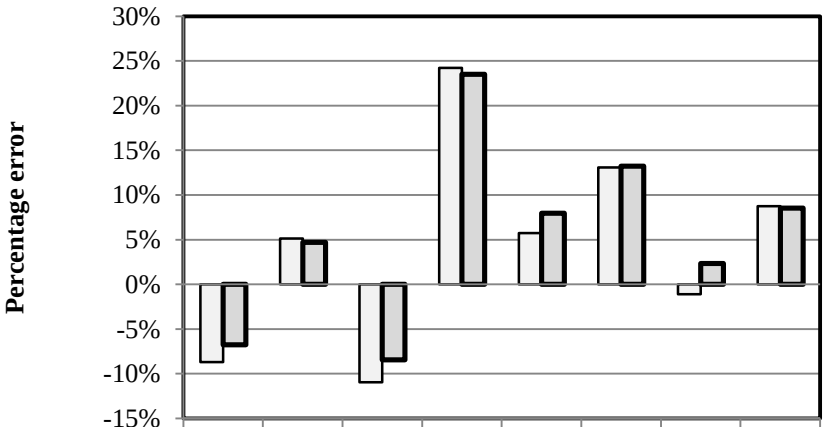

	MPE (N=15) 0-200mm	σpe (N=15) 0-200mm	MPE (N=27) 200-250mm	σpe (N=27) 200-250mm	MPE (N=17) 250-300mm	σpe (N=17) 250-300mm	MPE (N=8) 300+mm	σpe (N=8) 300+mm
Combi EC4c	-8.7%	5.1%	-11.0%	24.2%	5.8%	13.1%	-1.1%	8.7%
Combi ω	-6.7%	4.7%	-8.5%	23.5%	7.9%	13.2%	2.3%	8.5%

Figure 3-31: Comparison of steel tube failure temperature prediction *MPE* and σ_{pe} for EC4 Annex H (CEN, 2005) using the *Combi EC4c* and *Combi ω* modelling approaches with the database partitioned by cross-sectional size

Considering the effect that the cross-sectional size of the column has on the prediction of steel tube temperatures at failure, Figure 3-31 shows a slight under-prediction of steel temperatures for sections smaller than 250 mm, and an over-prediction for columns greater than 250 mm. This is similar to the trend in fire resistance time predictions in Figure 3-23. This confirms that either the mechanics

model fails to capture the true response or the heat transfer model is under-predicting the concrete temperatures, especially towards the centre of the columns.

3.5.2 FNA – Annexe PCRB steel tube failure temperatures

Of the 161 specimens used in the analysis of FNA Annexe PCRB approach (CEN, 2007) in Section 3.4, 22 specimens do not report steel tube failure temperature. Figure 3-32 shows the predicted steel temperature at failure using the *Combi ω* thermal modelling approach compared to the observed steel failure temperature.

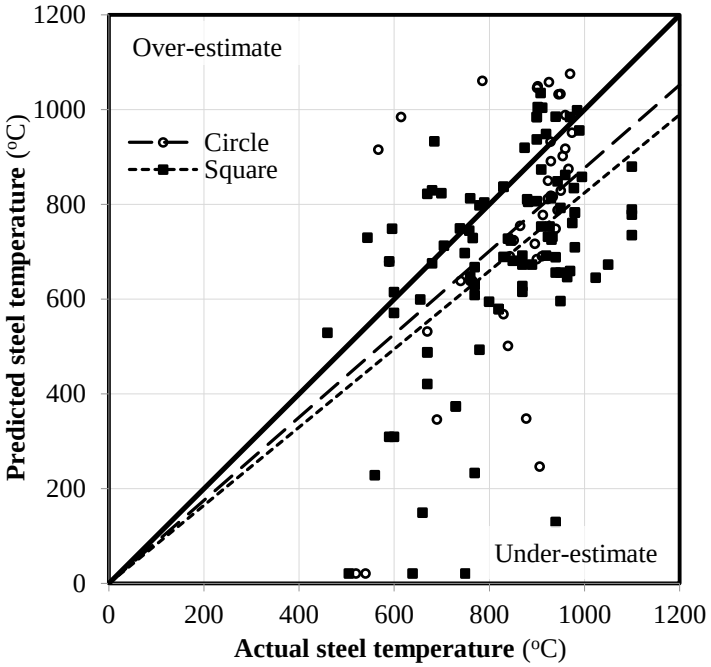

Figure 3-32: Predicted versus observed steel tube failure temperature based on the FNA – Annexe PCRB approach (CEN, 2007) design approach using the *Combi ω* modelling approach with the database partitioned by shape

Figure 3-32 shows considerable variability in failure temperature prediction; an *MPE* of -16% and σ_{pe} of 28% are evident. This is compared to the fire resistance predictions in Section 3.4.4, where the *MPE* and σ_{pe} were -28% and 50%, respectively. Due to the large variation in predicted steel tube failure temperatures, seen in Figure 3-32, further assessment of this model is not made.

3.6 Chapter summary

This chapter provides a comprehensive study of currently available code-prescribed models to predict failure of concrete filled hollow sections (CFS) subjected to fire and has assessed the statistical confidence in the approaches by comparing modelling predictions to a database of observations from furnace tests reported in the literature. The different approaches for the prediction of structural fire resistance include the NRCC approach (Kodur , 2007) which is used in the North American codes, as well as the EC4 Annex H (CEN, 2005) and FNA Annexe PCRB (CEN, 2007) approaches. The prediction of failure temperature of the steel tube have also been statistically analysed using the temperature prediction methods required for the use of the EC4 Annex H approach and the FNA Annexe PCRB approach.

3.6.1 Structural fire resistance prediction

The NRCC (Kodur , 2007) prediction method (Section 3.2) employs a single empirical equation that uses a calibrated *f* factor to predict fire resistance time. This method, whilst simple to use, was found to be unconservative on average with only 40% of the predictions being conservative. This formula also struggled to account for load ratio, wall thickness, shape, and cross-sectional size. This is problematic given the ranges of size in which these elements are likely to be employed in practice.

The tabulated approach from EC4 (CEN, 2005) was found to be very conservative and therefore not discussed in detail.

Two thermal modelling approaches were developed in Section 3.3.2.7, namely *Combi EC4c*, using EC4 (CEN, 2005) parameters, and *Combi ω*, which employed experimentally derived variables which are outside of the scope of the EC4 recommended parameters. When these two thermal models were employed in the EC4 Annex H approach, both models provided accurate predictions with average error of less than five minutes and a precision about 20 minutes. The same two models were also applied with the FNA Annexe PCRB approach (CEN, 2007) approach and their accuracy decreased to about -15 minutes with a precision decrease to about 30 minutes. Both approaches struggled to account for CFS size and

steel tube wall thickness, and particularly struggled with large circular CFS column sections.

3.6.2 Steel tube failure temperature prediction

Two modelling approaches, designated *Combi EC4c* and *Combi ω*, were used in both the EC4 Annex H and FNA Annexe PCRB approaches to predict steel tube failure temperatures, When applied to the EC4 Annex H approach, reasonable accuracy and precision for prediction of steel tube failure temperatures were obtained, with *MPEs* of -3% and -4% and associated standard deviations of 19% for the *Combi EC4c* and *Combi ω* modelling approaches, respectively. The variability of predictions for steel tube temperature is less than for fire resistance.

Accurate prediction of the failure temperature profile of the steel tube and concrete core is important for prediction of fire resistance of CFS columns, and is also required so that appropriate levels of fire protection can be applied (in cases where it is needed). The current analyses show reasonable consistency in modelling steel temperatures, with comparatively low variability in predictive performance across the different physical parameters. This is not the case for prediction of fire resistance, for which there is significant variability across size, shape and wall thickness.

Additional information is needed on the temperature profiles within CFS columns so that the thermal models that inform the structural design can be improved. This topic is treated in the following chapters.

Chapter 4: The thermal influence of an air gap

As a CFS column is heated during a fire, many thermal and mechanical phenomena occur that may affect structural response, some of which cannot currently be predicted with confidence (Wang and Orton, 2008). One area of uncertainty is the effects of the development of an air gap which is known to form at the steel-concrete interface when CFS columns are exposed to fire. During heating, the variation in thermal expansion between the steel tube and concrete core can cause separation of the steel tube from the concrete and the development and growth of an air gap. While ignoring the development of an air gap in analysis of CFS sections is widely thought to be conservative for unprotected CFS columns (Rush et al., 2010), somehow accounting for the presence of the gap considerably improves the accuracy of prediction of temperature distribution within a CFS column during fire; this has been demonstrated by both Ding and Wang (2008) and Renaud (2004), where the presence of an air gap was explicitly incorporated into computational analyses; albeit by adopting a gap of constant thickness with an assumed associated thermal resistance (so as to match thermal test data *a posteriori*). The influence of an air gap on the thermal response, and thus the structural performance (with relation to both a reduction in heat transfer to the concrete core and a loss of confinement and composite action between the steel tube and the concrete core) of CFS sections remains poorly understood, with little quantification within the literature (e.g. Ghojel, 2004).

This chapter presents a set of 15 small-scale experiments to attempt to ascertain and quantify, in a controlled fashion, the possible influence of an air gap and its size on heat transfer within a CFS column. An idealised one dimensional representation of a CFS column, comprising a flat steel plate backed by a concrete block, is subjected to heating with varying sealed air gap sizes between the steel plate and concrete backing. The results of these experiments are then used as calibration and verification data for a one-dimensional finite difference model to predict the heat transfer within the sections. The aim of the small scale testing program is *not* to assess the external factors that promote and influence the evolution of the gap, but

instead to assess the air gap's likely influence on the thermal response of the section and to provide quantitative data for future modelling.

4.1 Small-scale air gap test program

During heating of a real CFS column, differential thermal expansion will occur between the steel tube and concrete core of a composite column due to their different rates of heating and coefficients of thermal expansion, and thermal gradients arising in the section. This differential thermal expansion promotes the formation of the air gap, the size of which is dependent on several factors (such as load level, heating rate, and steel tube thickness). To date, the majority of researchers have not considered air gap formation in their analyses, instead assuming perfect thermal contact between the concrete core and steel tube, as permitted by EC4 (CEN, 2005).

To assess the effect of the air gap and its size, a set of 15 idealised one-dimensional (1-D) experiments were performed, as outlined in Table 4-1. The specimens were based on an assumed semi-infinite CFS section, where the steel tube could be considered to be flat, thus allowing a simplified 1-D heat transfer experiment, with a vertical segment of a CFS section exposed to an incident radiant heat flux. An artificial air gap was created by explicitly separating the steel and concrete elements of the specimens by a constant distance (set at 0, 1, 3 or 5 mm) using metal spacers outside of the heating zone and a record of the temperature evolution at specific depths and locations within the specimen was taken.

Table 4-1 outlines the two phase experimental program. Phase 1 consisted of four gap widths (0, 1, 3 and 5 mm) with repeat tests at each width. Phase 2 consisted of seven tests in which additional repeat tests were performed (due to equipment malfunctions in Phase 1) and the incident heat flux was varied from 50 kW/m^2 (in Phase 1) to 35 kW/m^2 (in Phase 2). The data obtained from tests 3, 4 (fan malfunction) and 13 (gas supply malfunction) all suffered some kind of testing failure and are neglected.

Table 4-1 shows that tests were repeated for a heat flux of 50 kW/m^2 using air gaps of 0 mm (to ensure the same thermal insult was experienced with both test set-ups)

and 1 mm, as well as a repeat test of the 1 mm air gap with a 35 kW/m^2 heat flux. The imposed air gap widths of 0, 1, 3, and 5 mm were chosen to cover the range of gap widths expected in full scale tests (Ding and Wang, 2008; Kodur, 2007).

Table 4-1: Testing matrix for gap size effect

Test	Heat flux (kW/m^2)	Air gap (mm)	Concrete batch
Phase 1			
1	50	0	1
2	50	0	1
3	50	1	1
4	50	1	1
5	50	3	1
6	50	3	2
7	50	5	2
8	50	5	2
Phase 2			
9	50	0	2
10	50	1	2
11	50	1	3
12	35	0	3
13	35	1	3
14	35	5	3
15	35	1	3

4.1.1 Specimen preparation

The specimens were 300 × 300 × 125 mm concrete blocks faced with 250 × 250 × 8 mm mild steel plates, as shown in Figure 4-1. The steel plates were made from mild structural steel and the concrete was a high strength, self-compacting hybrid steel (45 kg/m^3) and polypropylene fibre (2 kg/m^3) reinforced concrete mix. This mix design, the details of which are shown in Table 4-2, was selected based on the use of fibre reinforced concrete infill materials as replacement for traditional reinforcing steel cages and is similar to the mix used in the tests presented in chapters 5 and 7.

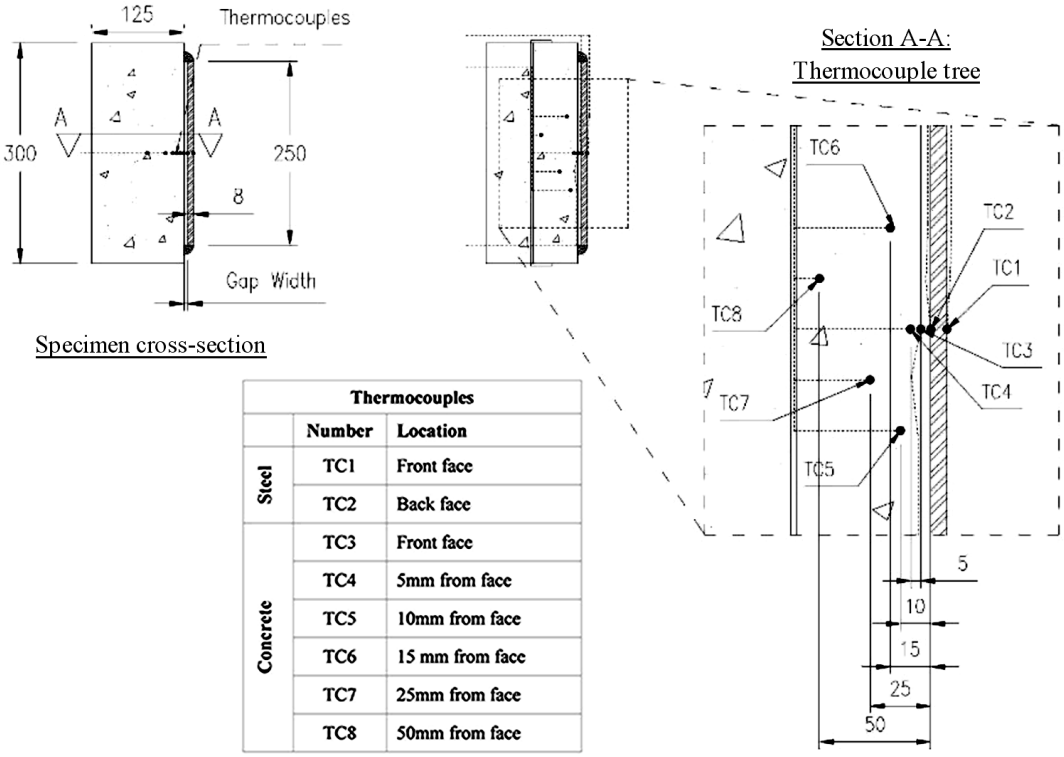

Thermocouples		
	Number	Location
Steel	TC1	Front face
	TC2	Back face
Concrete	TC3	Front face
	TC4	5mm from face
	TC5	10mm from face
	TC6	15 mm from face
	TC7	25mm from face
	TC8	50mm from face

Figure 4-1: Specimen cross-sections and thermocouple layout and locations

Eight K-type thermocouples were used in each test and were placed as shown in Figure 4-1. Two thermocouples measured the temperature of the steel, one at the front face, and one at the back face of the steel plate. The remaining six thermocouples were cast into the concrete with thermocouples at the concrete face and at depths of 5, 10, 15, 25 and 50 mm. The number and location of thermocouples was chosen to map the evolution of temperatures through the section during heating and cooling.

The thermocouples consisted of a welded tip to the two wires coiled together over 2.5 mm length. Therefore the precision of the data will be affected by the 2.5 mm length of the thermocouple, as the temperatures can be recorded anywhere along that length. The concrete face thermocouple was laid as flat as possible, parallel to the steel plate, to mitigate this effect.

The maximum aggregate size was limited to 8 mm to improve consolidation and strength, which was also improved by the use of fly ash and Portland cement with

8% silica fume. Small amounts of super-plasticiser and stabiliser were also used to improve flowability. Three concrete batches were used to cast five specimens each. Strength tests were carried out on three concrete cylinders per batch; average strengths for each batch are reported in Table 4-2. The concrete had moisture content of between 5.0 and 5.8% by mass at the time of testing and a compressive cylinder strength of about 50 MPa (Batch 3 cylinder tests failed in shear and are not considered in the averages).

Table 4-2: Concrete mix design, compressive strengths and water contents

		Percentage	Mass/m^3 of concrete (kg)	Total mass/m^3 of concrete (kg)
Cement	Portland cement and 8% silica fume	80%	488	610
	Fly ash	20%	122	
Aggregates	0-4mm	70%	1101	1582
	4-8mm	30%	481	
Fibres	Steel		45	45
	Polypropylene		2	2
Additives	Stabiliser		Trace	N/A
	Super-plasticiser		8.50	8.50
Water	Water-to-cement ratio – 0.39		190	190
			Total	2440 kg

Concrete batch	Compressive strength (MPa)	Moisture content (by mass) (%)	Comments
1	57.8	5.00	
2	49.0	5.77	
3	*28.7*	5.73	Shear Failure

The concrete was cast directly onto the steel plates to precisely match any imperfections on the steel plates and so that when the air gap was later artificially created a constant air gap was assured. The perimeter of the air gap was sealed using high temperature fire resistant cement to prevent convective heat loss from the gap and to ensure that the heat transfer was as realistic as possible (Figure 4-2).

4.1.2 Testing procedure

The heating regime consisted of 60 minutes under a well characterised constant incident heat flux value (of 50 or 35 kW/m^2) using a propane-fired radiant panel, followed by slow cooling for 60 minutes during which time temperature measurements were recorded. Prior to heating, the radiant heating panel was ignited and allowed to stabilize. A fire-insulation board was positioned to shield the 200 × 200 mm opening through which the specimens were heated (Figure 4-2). The rate of combustible gas flow supplied to the radiant heating panel was maintained constant by an automatic flow control meter. Once the front faces of the steel plate reached 35°C, the fire-insulation board was removed and 60 minutes of constant incident heat flux commenced. After 60 minutes of heating the combustible gas supply was turned off and the specimen was allowed to cool for 60 minutes.

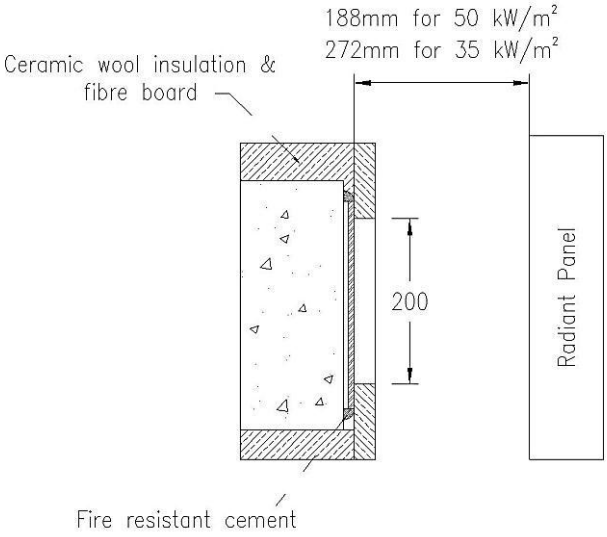

Figure 4-2: Schematic test set-up

The imposed incident heat fluxes of 50 and 35 kW/m^2 were average measured heat flux values produced by the radiant heating panel over a centralised 200 × 200 mm exposed area over which the heat flux varied by ±10%. The flow of gas and air was the same for both levels of incident heat flux; however the distance of the radiant panel from the steel surface varied between 188 mm and 272 mm for the 50 and 35

kW/m^2 fluxes, respectively. The heat fluxes were selected to represent values for heating effects on the order of those experienced in an ISO 834 furnace test (Babrauskas, 1995). The specimens were wrapped on their sides with a layer of Rockwool insulation to prevent lateral thermal losses, thus producing an idealised 1-D heat transfer regime. The data from the thermocouples were acquired at 10 Hz.

4.2 Results and observations

Figure 4-3 shows the temperature profiles of all the thermocouples for Test 9 (50 kW/m^2, 0 mm gap width) during the heating and cooling phases and is representative of all of the tests at 50 kW/m^2. Under the 50 kW/m^2 incident heat flux, the response of the steel plates (grey lines, TC1 and TC2) to heating is characterised by two phases. The first phase is a steep increase in temperature lasting for 10-15 minutes. The second phase is characterised by a shallower rate of temperature increase until the end of heating at 60 minutes. The response of the concrete (black lines, TC3 through TC8) is a gradual increase of temperatures, the onset and rate of which is delayed with depth with in the specimen. After 60 minutes heating, cooling is immediate with a sharp decrease in temperature whilst the temperatures within the concrete continue to increase, with the peak temperatures at a depth of 50 mm (TC8) occurring 15-20 minutes later.

Under the incident heat flux of 35 kW/m^2, a similar initial temperature increase occurs in the steel but only lasts for a few minutes, after which there is a gradual decrease in the rate of temperature increase, as shown in Figure 4-4. Figure 4-3 and Figure 4-4 show that the code-based design assumption of perfect thermal contact between the steel and the concrete (CEN, 2005) is incorrect. In all the tests with a 0 mm gap width, i.e. contact between the steel and the concrete, a considerable difference (>100^{o}C) is observed between the back face of steel (TC2) and the concrete front face temperature (TC3). This could however be due to imprecision in the location of the thermocouples and the measurement length of the thermocouple being 2.5mm.

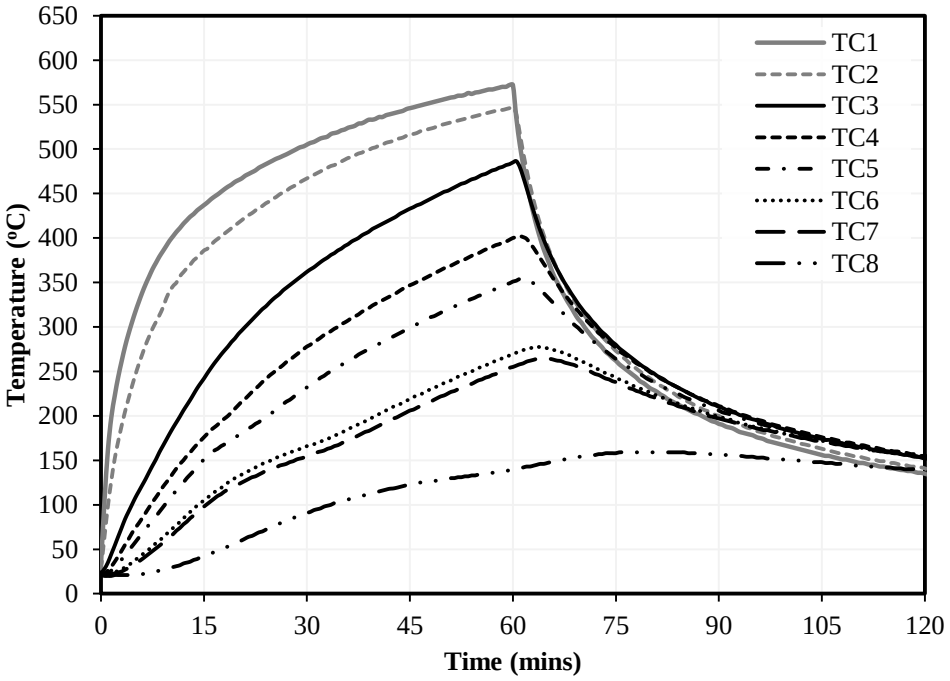

Figure 4-3: Representative thermal response of specimens exposed to a 50 kW/m^2 incident heat flux (Test 9, 50 kW/m^2, 0 mm air gap width)

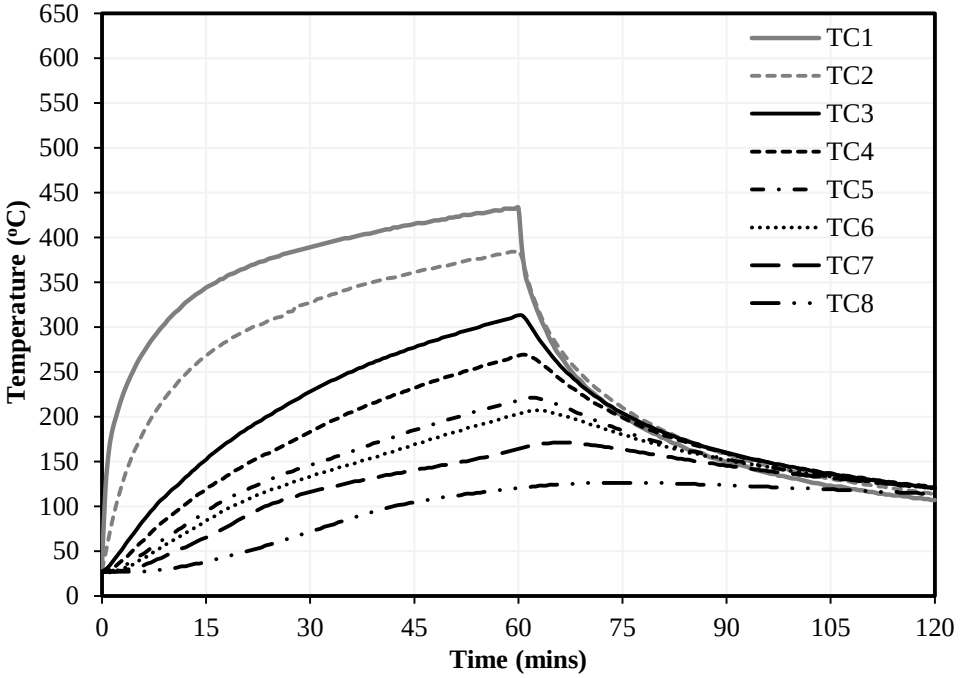

Figure 4-4: Representative thermal response of specimens exposed to a 35 kW/m^2 incident heat flux (Test 12, 35 kW/m^2, 0 mm air gap width)

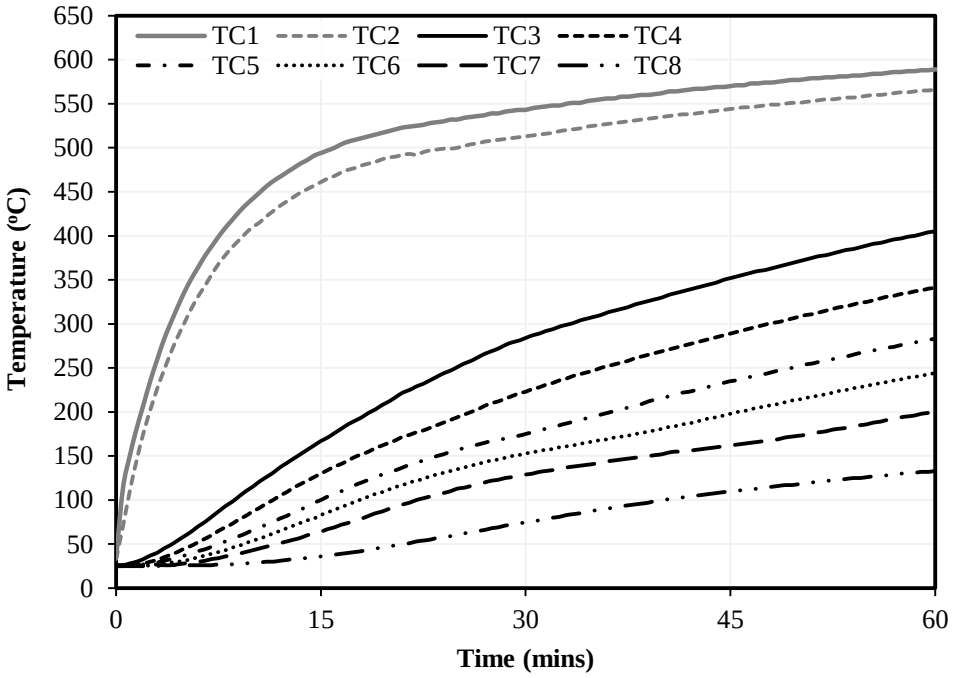

Figure 4-5: Thermal response of Test 7, exposed to a 50 kW/m^2 incident heat flux with a 5 mm air gap width

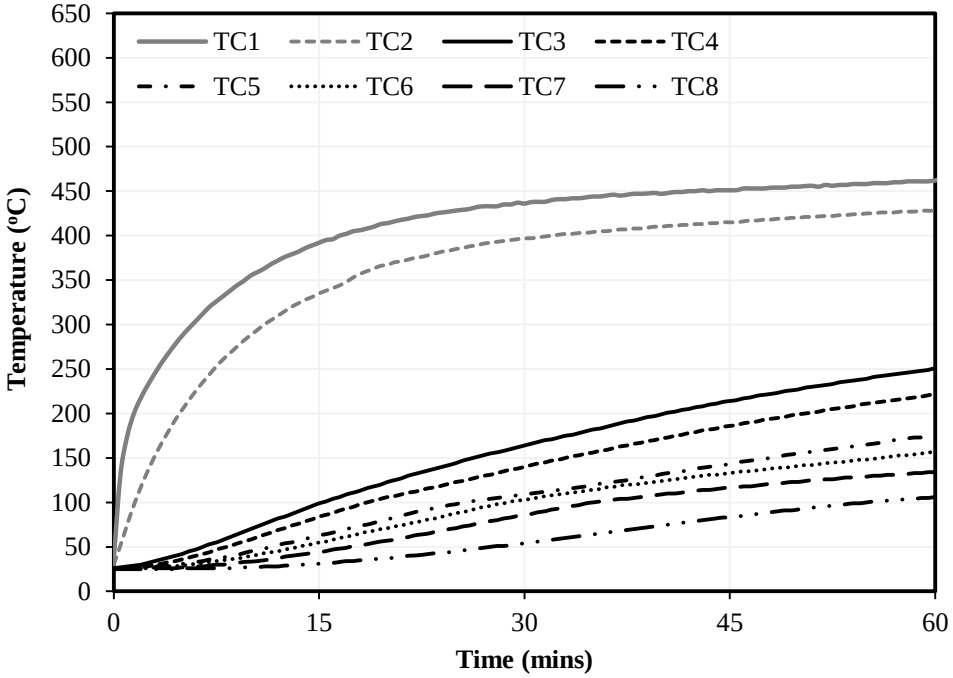

Figure 4-6: Thermal response of Test 14, exposed to a 35 kW/m^2 incident heat flux with a 5 mm air gap width

As expected, the introduction of an air gap acts as an insulator, further increasing the temperature difference between the back face of the steel plate and decreasing the concrete temperatures. Figure 4-5 and Figure 4-6 show the heating response of Test 7 and Test 14, where the gap distance was 5 mm and the specimens were exposed to the 50 and 35 kW/m^2, respectively. The figures show that temperature difference across the 5 mm gap is double (>250^{o}C) that of the 0 mm gap width at 15 minutes.

Table 4-3 shows the recorded temperatures of all the specimens at 15, 30 and 60 minutes of heating at the front and back faces of the steel (TC1 and TC2, respectively), the front face of the concrete (TC3) as well as at a depth of 10, 25 and 50 mm from the concrete face (TC5, TC7, and TC8, respectively). The table also shows the maximum temperature difference ($\Delta\theta_{gap}$) between the back face of the steel and the concrete face (TC2 and TC3) and the time after the start of the heating that the maximum difference occurs. The effect of the gap on the heat transfer is similar at both 35 and 50 kW/m^2 but the peak temperature difference across the gap is smaller (50-60^{o}C less) and occurs later (3-7 minutes) at 35 kW/m^2.

Tests 3 and 4 suffered malfunctions with the fan supplying air to the radiant panels' mixer valve, whilst Test 13 had a gas supply malfunction. These three tests are not considered in the subsequent analysis.

Table 4-3 shows that the introduction of an air gap increases the temperatures observed in the steel by approximately 60^{o}C at 15 minutes and 30^{o}C at 60 minutes for the 50 kW/m^2 heat flux, and by approximately 50^{o}C at 15 minutes and 30^{o}C at 60 minutes for the 35 kW/m^2 heat flux, confirming that the air gap effectively acts as a back face insulator for the steel plates.

Table 4-3: Temperatures recorded after 15, 30 and 60 minutes of heating at selected locations

Test	Heat flux	Air gap	Temp – 15 mins of heating (^oC)						Temp – 30 mins of heating (^oC)						Temp – 60 mins of heating (^oC)						Max $\Delta\theta_{gap}$	
			Steel		Concrete				Steel		Concrete				Steel		Concrete				(TC2-TC3)	
	(kW/m^2)	(mm)	TC1	TC2	TC3	TC5	TC7	TC8	TC1	TC2	TC3	TC5	TC7	TC8	TC1	TC2	TC3	TC5	TC7	TC8	^oC	Time
1	50	0	439	369	216	132	81	40	499	444	331	203	144	83	549	518	445	314	219	144	158	11
2	50	0	444	361	209	124	78	42	502	435	314	194	139	87	561	515	424	294	209	147	164	11
3[a]	*50*	*1*	*453*	*399*	*182*	*99*	*74*	*37*	*502*	*455*	*288*	*169*	*139*	*77*	*531*	*494*	*380*	*248*	*204*	*139*	*229*	*12*
4[b]	*50*	*1*	*460*	*291*	*168*	*95*	*72*	*37*	*511*	*381*	*277*	*165*	*139*	*79*	*185*	*192*	*184*	*167*	*156*	*126*	*207*	*11*
5[c]	50	3	507	456	164	--	60	30	551	509	283	--	123	69	590	564	407	--	196	128	295	13
6[d]	50	3	500	439	--	95	60	31	549	488	289	176	126	66	590	549	405	270	191	129	228	24
7[e]	50	5	494	461	167	100	64	36	543	513	284	175	129	75	589	566	405	283	201	133	297	13
8	50	5	497	467	164	92	67	34	547	519	278	164	131	73	590	568	400	266	206	129	305	13
9	50	0	437	386	242	151	98	42	505	467	362	232	155	91	572	547	485	351	255	140	160	10
10	50	1	471	428	188	113	71	38	526	492	309	184	131	80	578	553	433	299	208	133	244	13
11	50	1	479	446	211	127	85	40	534	511	337	213	141	87	585	569	460	332	234	132	246	11
12	35	0	344	268	152	94	65	38	389	327	228	146	116	72	433	385	313	218	164	120	116	14
13[f]	*35*	*1*	*348*	*324*	*132*	*89*	*60*	*33*	*399*	*379*	*204*	*141*	*110*	*61*	*385*	*373*	*262*	*203*	*152*	*109*	*193*	*17*
14	35	5	392	335	99	63	44	31	436	397	164	109	86	54	462	428	251	175	134	106	246	20
15	35	1	321	282	103	75	29	30	376	343	162	125	59	43	423	398	251	196	113	82	183	23

[a] fan malfunction at 40 minutes approx.; [b] fan malfunction at 30 minutes approx.; [c] TC5 malfunction throughout; [d] TC3 malfunction until 23.5 minutes approx.; [e] data logger malfunction at 60 minutes.; [f] gas supply malfunction at 25 minutes approx., and -- = malfunction failure

As the size of the gap increases the amount it insulates the concrete also increases, as shown in Figure 4-7. $\Delta\theta_{gap}$ at 35 kW/m^2 is lower than at 50 kW/m^2, although similar increases in $\Delta\theta_{gap}$ are seen between the heat flux values when the size of the air gap is increased. The maximum temperature differences at the interface, $\Delta\theta_{gap}$, occur between 10-13 minutes or 13-23 minutes for 50 kW/m^2 and 35 kW/m^2, respectively, regardless of gap size. After reaching a maximum the temperature difference slowly decreases as the rate of steel temperature increase slows. Figure 4-8 shows the magnitude of the temperature difference across the gap between TC2 and TC3.

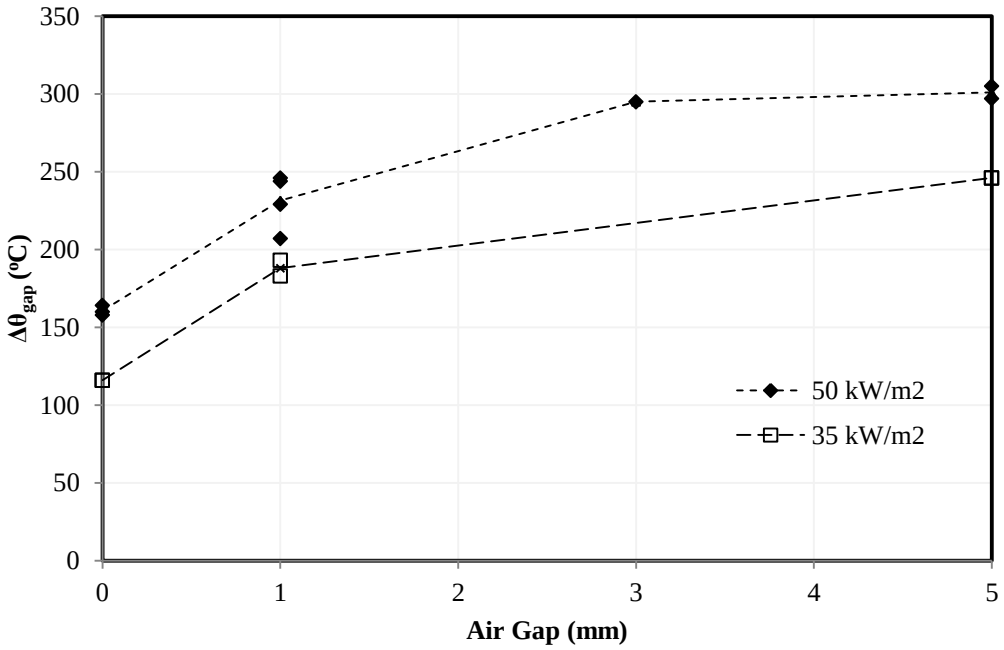

Figure 4-7: Maximum steel-concrete interface temperature difference, $\Delta\theta_{gap}$, with respect to air gap width and incident heat flux

These tests clearly show that the introduction of an air gap has a substantial influence on heat transfer within CFS sections, with temperature differences of 300^{o}C or more between the back face of the steel and the concrete face for gap widths in the range of sizes expected. Not considering air gap formation in design will lead to under-prediction of steel and over-prediction of concrete temperatures, potentially resulting in inaccurate (or unsafe) predictions of the time to failure for CFS sections in fire.

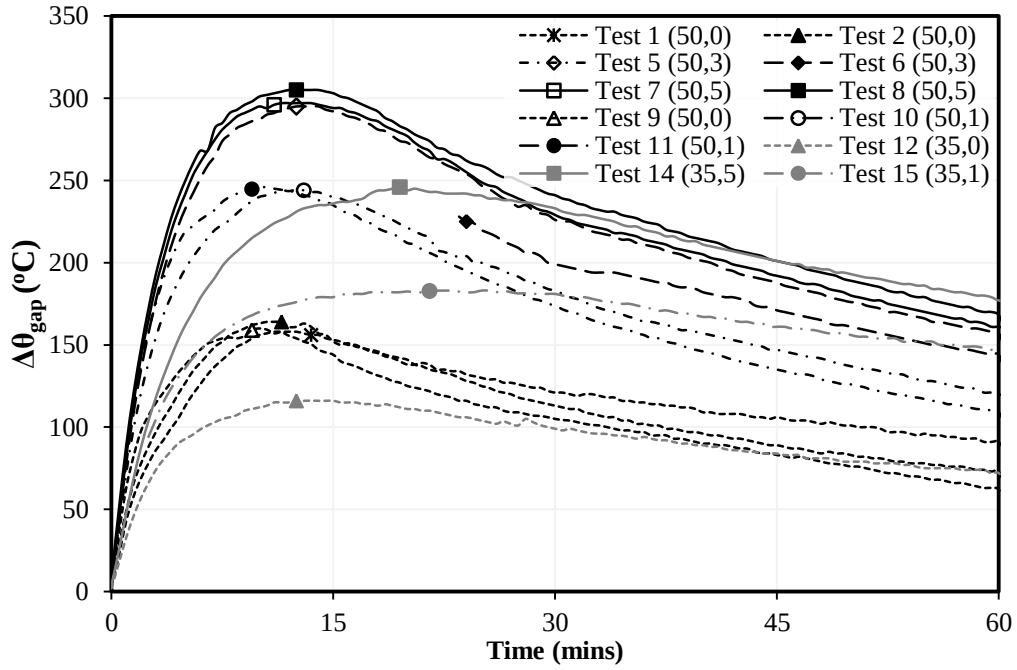

Figure 4-8: Temperature difference across the air gap, $\Delta\theta_{gap}$, for the different tests, grouped by incident heat flux and gap width [Test # (heat flux, gap)]

4.3 Computational analysis of thermal conductivity across an air gap

The meta-analyses presented in Section 3.3.2.5 assessed Ding and Wang's (2008) assumed constant interface thermal conductance (λ_{gap}) value of 100 kW/m^2 and Ghojel's (2004) empirical temperature dependent λ_{gap} (Equation 2-8); both approaches improved the predictive qualities of the EC4 Annex H approach (CEN, 2005). However, neither of the interface thermal conductances used in the meta-analysis account for the size of the air gap, which has been shown here to have an effect on the heat transfer. Ding and Wang (2008) calibrated their gap conductance against standard fire tests under load, using the standard fire heating regime described in Equation 2-37, whilst Ghojel (2004) used unloaded tests a 15 kW electric furnace and then calibrated to loaded standard fire tests.

The following computational analyses compare the Ding and Wang (2008) and Ghojel (2004) λ_{gap} relationships against the test data from the current tests to ascertain which gap size they best simulate, and an improved model where gap size

is explicitly accounted for is then presented. A gap dependent interface thermal conductance model is potentially important for rational performance-based design, where different heating regimes may affect history of gap size during heating and thus the heat transfer across the gap.

4.3.1 Meta-analysis of interface thermal relationships

To assess the interface thermal conductance, λ_{gap}, models of Ding and Wang (2008) and Ghojel (2004), appropriate material thermal properties of the concrete need to be determined. A 1-D model was created in ABAQUS to represent the concrete mass in the tests reported above. The 1-D model was created in a two dimensional space (Figure 4-9) so that surface interactions between the steel plate and the concrete mass could be modelled effectively.

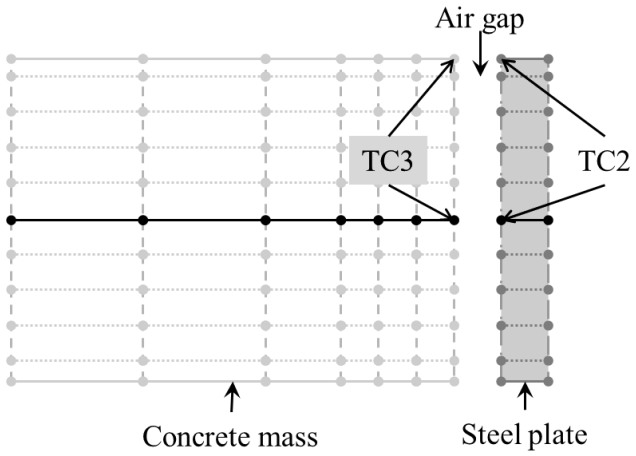

Figure 4-9: Schematic diagram of ABAQUS 1-D model

The model assumes concrete face temperatures (TC3) observed during the tests and applied to the appropriate nodes. The concrete material thermal properties are then varied and the model temperatures found compared to the observed test temperatures at three depths in the concrete. The most accurate thermal modelling approach for the concrete is then adopted in a more complex 1-D model including the concrete mass and the steel plate. The back face steel temperatures (TC2) observed during the tests are then applied to the whole of the steel mass, and a comparison of the observed and

modelled differential interface temperatures. $\Delta\theta_{gap}$, (TC2 to TC3) using the λ_{gap} models from Ding and Wang (2008) and Ghojel (2004) is made.

4.3.1.1 Determination of appropriate concrete thermal properties

The concrete thermal properties assessed using the 1-D model are those used previously in the *Combi EC4c* and *Combi ω* thermal modelling approaches discussed in Section 3.3.2.7, as well as a modelling approach developed specifically for fibre-reinforced concrete using carbonate aggregate (*FibCar*) (based on prior work by Kodur (1996)). Within the *Combi EC4c* modelling approach used previously in Section 3.3.2.7, an assumption is made that the concrete contains 10% water by mass. The concrete used in the tests was found to have a water content (W.C.) of approximately 5% by mass and the approach was adjusted accordingly. The *FibCar* thermal modelling approach employs the same specific heat capacity of concrete as *Combi ω*, and all three approaches use the same density of concrete model (Equation 2-25). The thermal conductivity of concrete in the *Combi EC4c* and *Combi ω* modelling approaches is taken as the lower bound in Equation 2-27, whilst the thermal conductivity of concrete for the *FibCar* modelling approach is taken after Kodur (1996) as:

$$\lambda_{c,\theta} = \begin{cases} 2 - 0.001775 \cdot \theta_c & 20℃ \leq \theta_c \leq 500℃ \\ 1.402 - 0.000579 \cdot \theta_c & 500℃ < \theta_c \leq 1200℃ \end{cases} \quad (4\text{-}1)$$

Figure 4-10 shows a comparison of the model temperatures, $\theta_{c,model}$, against the observed temperatures, $\theta_{c,exp}$, at concrete depths of 10 (TC5), 25 (TC7) and 50 mm (TC8) for the different modelling approaches. Normalized temperatures ($\theta_{c,model}/\theta_{c,exp}$) are shown with respect to time. All three modelling approaches over-predict the temperature at 10 mm depth by between 20 and 40% during the heating stage of the tests (0 to 60 minutes), with the smallest over-prediction being for the *Combi EC4c (5% W.C.)* approach. The *Combi EC4c (5% W.C.)* modelling approach (grey filled markers) is most accurate and, particularly averaged across the three depths (black filled circles). The *FibCar* modelling approach, developed specifically using fibre-reinforced concrete, is observed to over-predict the temperature within the concrete core at all three depths, which could be due to the model not accounting

for the effect of moisture evaporation, thus leading to higher temperatures being predicted.

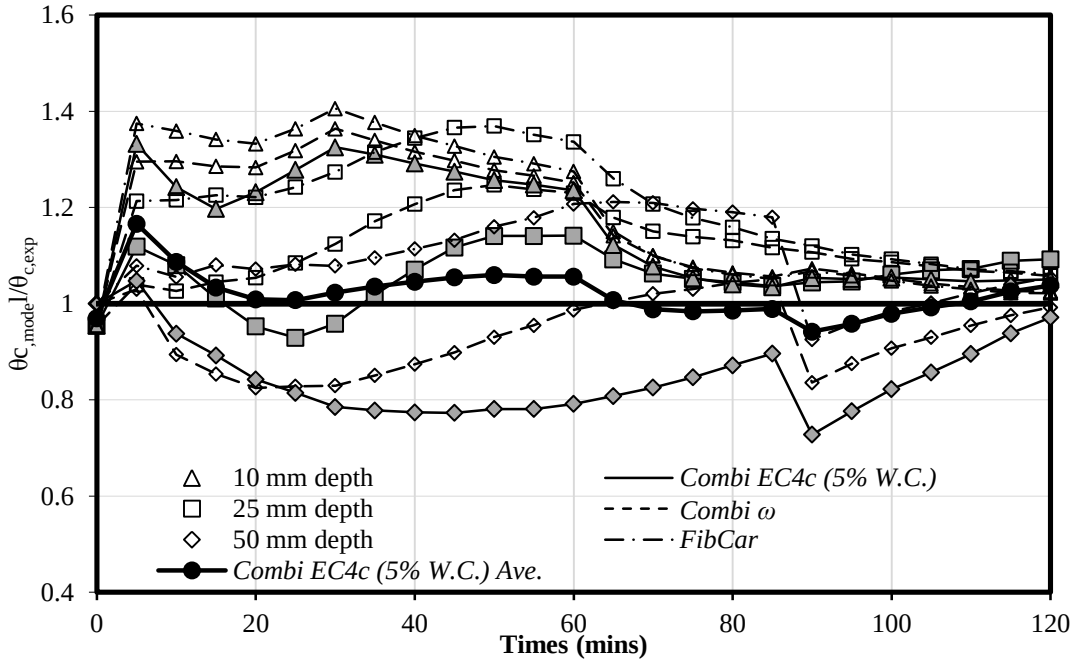

Figure 4-10: Comparison of normalised temperature ratios at different depths for different candidate thermal modelling approaches

Figure 4-11 compares the normalised temperatures predicted and observed using the *Combi EC4c (5% w/c)* modelling approach at depths of 10, 25, and 50 mm for three different tests. Test 1 and Test 10 used 50 kW/m^2 and gap widths of 0 and 1 mm, respectively. Test 14 used 35 kW/m^2 and a 5 mm gap width. These three tests were chosen to represent three different gap widths and three different concrete batches used (Table 4-1).

Figure 4-11 shows that the predictions for Test 1 and Test 10 are similar, however the predictions for Test 14 under-predict temperatures in the concrete by more than 40%. However, because lower temperatures are experienced in Test 14 due to a lower heat flux, the actual under-predictions are of the same absolute magnitude as for Test 1 and Test 10. The consistency shown across different gap widths, concrete batches, and heat fluxes indicates that the *Combi EC4c (5% W.C.)* modelling approach gives a reasonable approximation of this concrete's thermal properties.

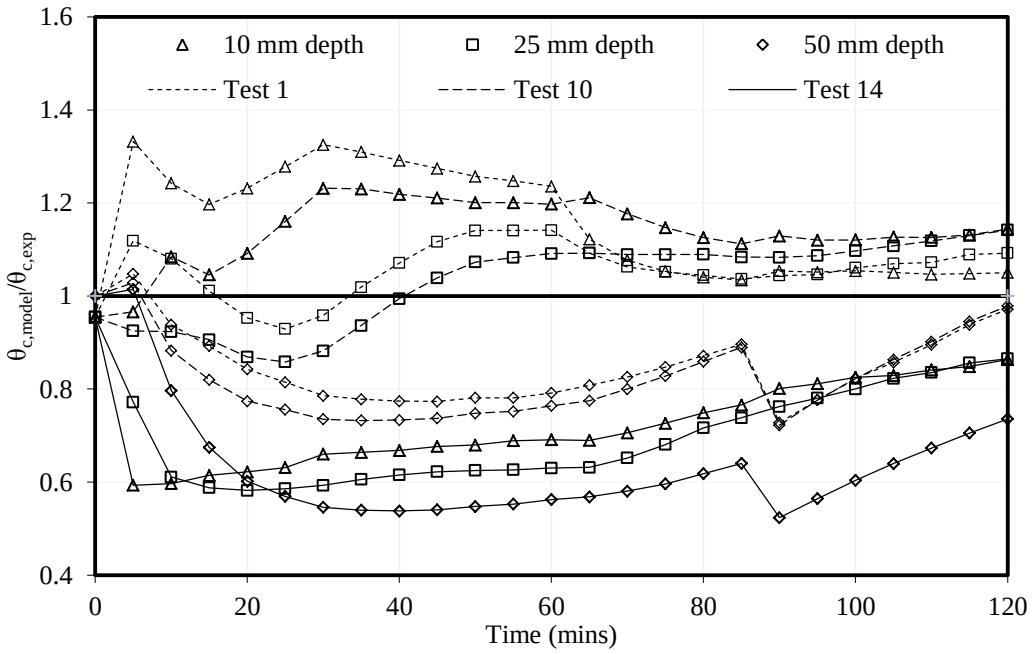

Figure 4-11: Comparison of normalised temperature ratios at various depths for different tests using the *Combi EC4c (5% W.C.)* modelling approach

4.3.1.2 Assessment of different interface thermal conductance models

Since neither the Ding and Wang (2008) or Ghojel (2004) λ_{gap} models explicitly account for the air gap size, a range of temperature-time profiles are required to properly assess the heat transfer occurring with each λ_{gap} model. Three temperature-time profiles were used for the steel plate for 50 kW/m^2 and 35 kW/m^2 heat fluxes: (1) the average back face of the steel (*BFS Ave.*) temperature from all tests under each heat flux; (2) the maximum TC2 temperature profile; and (3) the minimum TC2 temperature profile. The maximum TC2 temperature profiles were obtained from the 5 mm gap width tests (Test 8 and Test 14) with the minimum temperature profiles taken from the 0 mm gap width tests (Test 1 and Test 12) for the 50 kW/m^2 and 35 kW/m^2 heat fluxes, respectively.

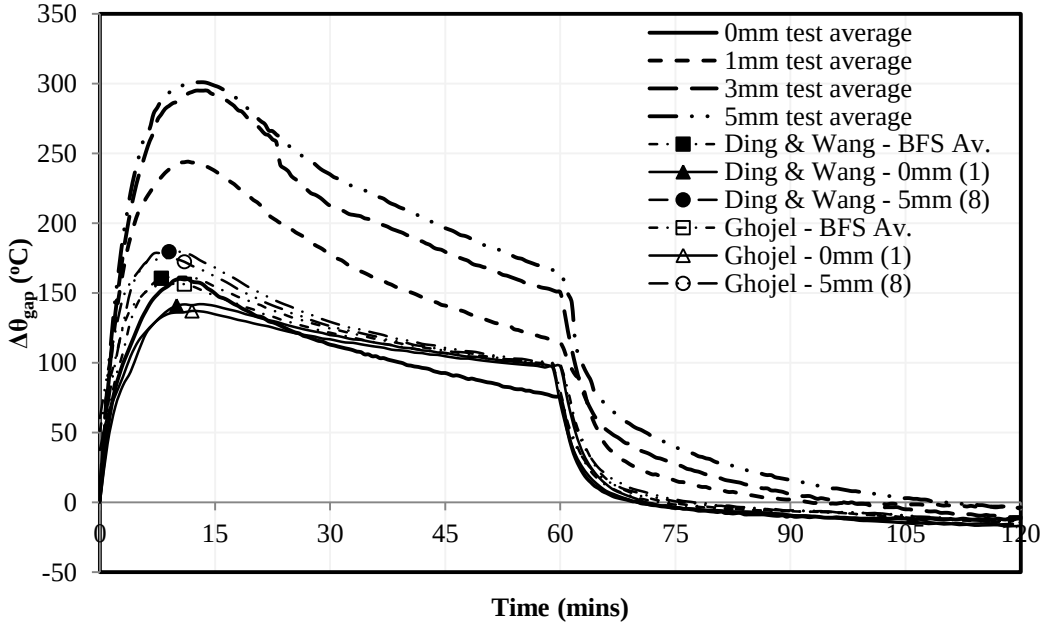

Figure 4-12: Comparison of $\Delta\theta_{gap}$, averaged for different gap widths, from the 50 kW/m^2 heat flux tests and modelled using either Ding and Wang (2008) or Ghojel (2004) λ_{gap} models

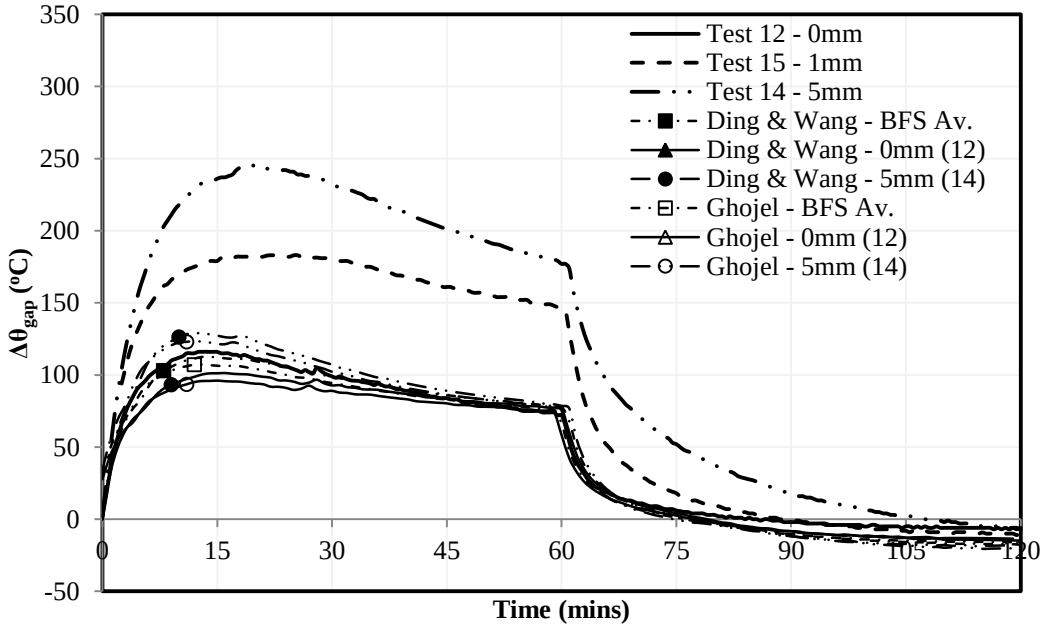

Figure 4-13: Comparison of $\Delta\theta_{gap}$, observed from the 35 kW/m^2 heat flux tests, for different gap widths and modelled using either Ding and Wang (2008) or Ghojel (2004) λ_{gap} models

Figure 4-12 shows a comparison of the temperature difference across the gap, $\Delta\theta_{gap}$, observed in tests under a 50 kW/m^2 heat flux (averaged with respect to gap width) and that determined by modelling using either Ding and Wang's (2008) constant λ_{gap} of 100 kW/m^2 or Ghojel's (2004) temperature dependent λ_{gap} (Equation 2-8). Figure 4-13 shows $\Delta\theta_{gap}$ observed in tests under the 35 kW/m^2 heat flux.

Figure 4-12 and Figure 4-13 show that neither the Ding and Wang (2008) or Ghojel (2004) interface thermal conductance model accurately accounts for the gap's influence on heat transfer within the idealised 1-D CFS cross-sections tested. However, regardless of temperature profile applied, the differential gap temperatures found from modelling show a good correlation with the differential gap temperatures observed in the 0 mm air gap width tests.

4.3.2 A gap dependent interface thermal conductance model

4.3.2.1 Simplified modelling by O'Loughlin et al. (2012)

A simplified one-dimensional spreadsheet model was created previously by the author in supervising an MSc thesis project during the course of his PhD. This resulted in a paper presented by O'Loughlin et al. (2012), in which the heat transfer from the steel plate, across an air gap and into a concrete mass was developed and modelled using an explicit finite difference approach. Analytical equations similar to those used in previous research on the structural fire performance of CFS sections (e.g. Lie and Irwin, 1995) were used.

O'Loughlin et al. (2012) describe the development of the analytical equations used in their heat transfer analysis, which are based on conservation of energy. The key equation for the heat transfer across the gap is that used for determination of the temperature in the concrete front face elements:

$$\theta_{c,0}^{i} = \theta_{c,0}^{i-1} + \frac{\Delta t}{\rho_c c_c \Delta x_c}\left[h_{gap}\left(\theta_{a,n}^{i-1} - \theta_{c,0}^{i-1}\right) + \varepsilon_{m,tot}\sigma\left(\left(\theta_{a,n}^{i-1}\right)^4 - \left(\theta_{c,0}^{i-1}\right)^4\right) - \left(\frac{\lambda_{c,0}^{i-1} + \lambda_{c,1}^{i-1}}{2}\right)\left(\frac{\theta_{c,0}^{i-1} - \theta_{c,1}^{i-1}}{\Delta x_c}\right)\right] \quad (4\text{-}2)$$

where θ is the temperature of either the steel or concrete (subscript *s* and *c*, respectively), of the element (subscript after the comma), in time step *i*, the duration

of which is Δt. The energy input to an element is determined by the conductivity of the gap, h_{gap}, the radiative heat transfer (which is determined by the total emissivity, $\varepsilon_{m,tot}$, and the Stefan Boltzmann constant, σ), and the conductivity of the concrete, λ_c. The temperature increase is determined by the energy input into the element, its density, ρ_c, specific heat capacity, c_c, and size, Δx_c.

Equation 4-2 shows that the temperatures of the concrete face elements at the current point in time, $\theta_{c,0}^{i}$, is the temperature of the element in the previous time step, $\theta_{c,0}^{i-1}$, plus the temperatures increase from the product of the inverse of the thermal conductivity of the element and the heat flux between the two surfaces; found from:

(1) radiation; $\left\{\varepsilon_{m,tot}\sigma\left(\left(\theta_{a,n}^{i-1}\right)^4 - \left(\theta_{c,0}^{i-1}\right)^4\right)\right\}$

(2) conduction into the concrete mass; and $\left\{\left(\frac{\lambda_{c,0}^{i-1} + \lambda_{c,1}^{i-1}}{2}\right)\left(\frac{\theta_{c,0}^{i-1} - \theta_{c,1}^{i-1}}{\Delta x_c}\right)\right\}$

(3) the heat transfer across the air gap through convection and conduction. $\left\{h_{gap}\left(\theta_{a,n}^{i-1} - \theta_{c,0}^{i-1}\right)\right\}$

The processes of heat transfer through radiation between two surfaces and conduction through a material (e.g. concrete) are both well understood. The net radiation between the steel back face and the concrete face, is the product of, σ (5.669×10^{-8} W/m^2·K^4), the resultant emissivity ($\varepsilon_{m,tot} = \varepsilon_{m,a} \cdot \varepsilon_{m,c}$), and the temperature difference between the two surfaces ($\theta_{s,n}^{i-1}$ and $\theta_{c,0}^{i-1}$).

The differentiation between the transfer of heat through conduction and convection within the gap is difficult due to the interactions of both processes affecting one another. De Graff and Van Der Held (1952) showed that the overall heat transfer in this scenario can be represented using a single 'conductance' term, h_{gap}, which couples the effects of conduction and convection. The h_{gap} term is based on Newton's law of convective cooling (Incropera and DeWitt, 2002), which is modified to present a relationship between the rate of heat transfer per unit area, $\dot{q}''$, and the temperature difference between the steel and concrete surfaces; given by:

$$\dot{q}'' = h_{gap}(\theta_{TC2} - \theta_{TC3}) \quad (4\text{-}3)$$

The single conductance term, h_{gap}, is obtained from the conductivity of air within the gap, λ_{air}, the gap width, w, the Nusselt number, Nu_{gap}, and an empirical parameter, n;

$$h_{gap} = n\left(\frac{\lambda_{air}}{w} Nu_{gap}\right) \quad (4\text{-}4)$$

where, for the vertical air layers in the current experiments Nu_{gap} is given by (De Graff and Van Der Held, 1952):

$$Nu_{gap} = \begin{cases} 1 & Gr_w < 7 \times 10^3 \\ 0.0384\, Gr_w^{0.37} & 10^4 < Gr_w < 8 \times 10^4 \\ 0.0317\, Gr_w^{0.37} & Gr_w > 2 \times 10^5 \end{cases} \quad (4\text{-}5)$$

The Grashof number, Gr_w, depends on the air gap width:

$$Gr_w = \frac{g\beta\rho^2(\theta_{TC2} - \theta_{TC3})w^3}{\mu^2} \quad (4\text{-}6)$$

in which g is acceleration due to gravity, β is the coefficient of thermal expansion of the air within the gap, ρ is the density of the gas, μ is the dynamic viscosity of the gas, and θ_{TC2} and θ_{TC3} are the temperatures of the steel back face and the concrete front face, respectively. For the tests presented herein the Grashof number, Gr_w, never exceeds 7×10^3 and therefore the Nusselt number, Nu_{gap}, can be taken as 1.0.

The above equations assume that the temperature of the air in the gap is equal to the average temperature of the back face of the steel and the front face of the concrete, that there is no mass transfer in terms of water vapour in the analysis; and that the gap size is constant.

O'Loughlin et al. (2012) simplified certain factors to expedite the spreadsheet analysis. The steel material properties used were those in EC4 (CEN, 2005), whilst the concrete properties used were those suggested by Kodur and Sultan (2003), with the further simplification of ignoring moisture evaporation from concrete. The steel

emissivity, $\varepsilon_{m,a}$, and concrete emissivity, $\varepsilon_{m,c}$, were taken as constant at 0.32 and 0.97, respectively, after Bejan (1993), leading to a resultant emissivity of 0.31. Thermal properties for air were taken from Incropera and DeWitt (2002). The temperatures recorded on the back face of the steel in the experiments were imposed on the steel elements in spreadsheet analysis.

As expected, the predictions produced by the spreadsheet analysis, when using the empirically calibrated parameter, *n*, shown in Table 4-4, showed reasonable correlation between theoretical and experimental results for the temperature difference across the air gap for the initial 15 minutes of heating, after which the analysis over-predicted the temperature difference across the gap. This shows that with the increase in the temperature of steel above 400^{o}C, there is not enough energy predicted as being transferred from the steel back face to the concrete face, leading to cooler concrete temperatures, and is likely due to the simplifications in emissivity of the steel and concrete faces. The spreadsheet analysis also suggests that *n* increased as the size of the air gap increased and was also dependent on the incident heat flux (Table 4-4).

Table 4-4: Parameter *n* calibrated from tests

Gap (mm)	Heat Flux (kW/m^2)	*n*
1	35	0.95
5	35	3.2
1	50	1.0
3	50	2.8
5	50	4.05

4.3.2.2 Improved modelling using finite elements

To further assess the heat transfer across the gap, a finite element model was created. The data and the empirically calibrated parameter, *n*, from the modelling presented by O'Loughlin et al. (2012) were applied to an ABAQUS heat transfer model. The size of the elements used in the ABAQUS model was the same as in the spreadsheet analysis (i.e. 5 × 5 mm) since this matches well with the test data and smaller mesh sizes were found to have no obvious impact on the accuracy of temperature

predictions, as shown in Figure 4-16. Figure 4-14 compares the predicted and measured temperatures through the cross section. The applied temperature to the steel, taken as the average back face of steel (*BFS*) temperatures for the sections with the same gap width and heat flux, obviously matches well with the observed temperature seen in Test 7. The prediction of the concrete face (*CF*) temperatures agrees with the temperature observed in tests since *n* was calibrated from the tests, and the temperatures through the concrete (at depths of 10, 25 and 50 mm) also correlate well to the observed data. This shows that the material models being used for the concrete are appropriate.

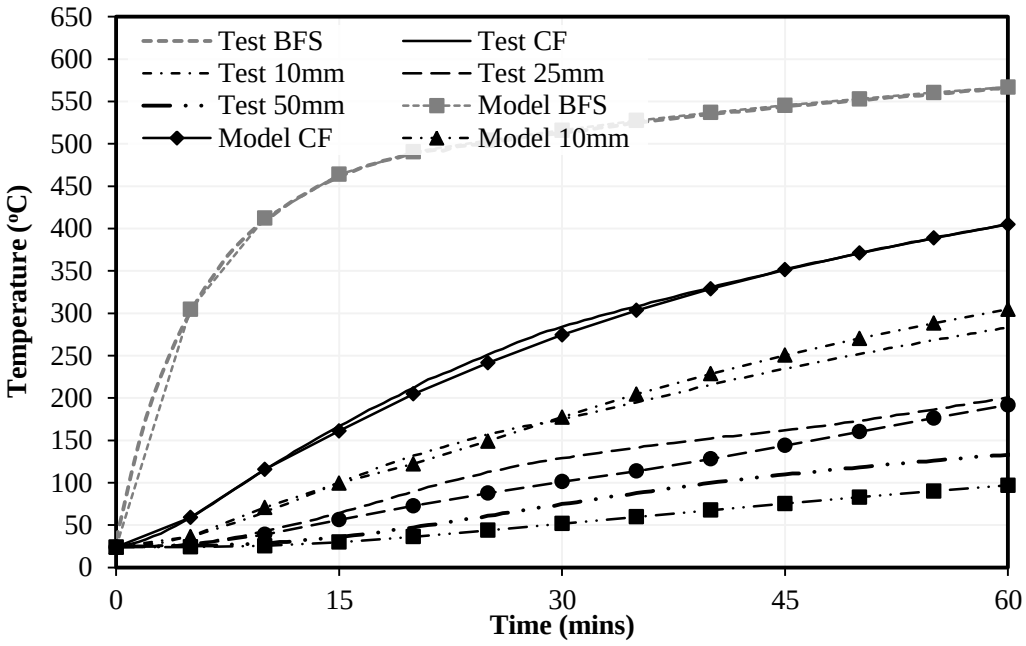

Figure 4-14: Comparison of observed (Test 7, 5 mm gap, 50 kW/m^2) and modelled temperatures (values from O'Loughlin et al., 2012)

Figure 4-15 and Figure 4-16 show the predicted temperature difference across the air gap considering the different gap widths for 50 kW/m^2 and 35 kW/m^2, respectively. The h_{gap} parameter was calculated using *n* from Table 4-4. The method proposed by O'Loughlin et al. (2012) shows good correlation with observed test data. Figure 4-16 also shows two analysis models for the 1 mm gap width which assess the effect of the mesh density on the predictions, and as it can be seen, the predictions for the finer mesh (2.5 × 2.5 mm element size) are essentially identical to the coarser mesh.

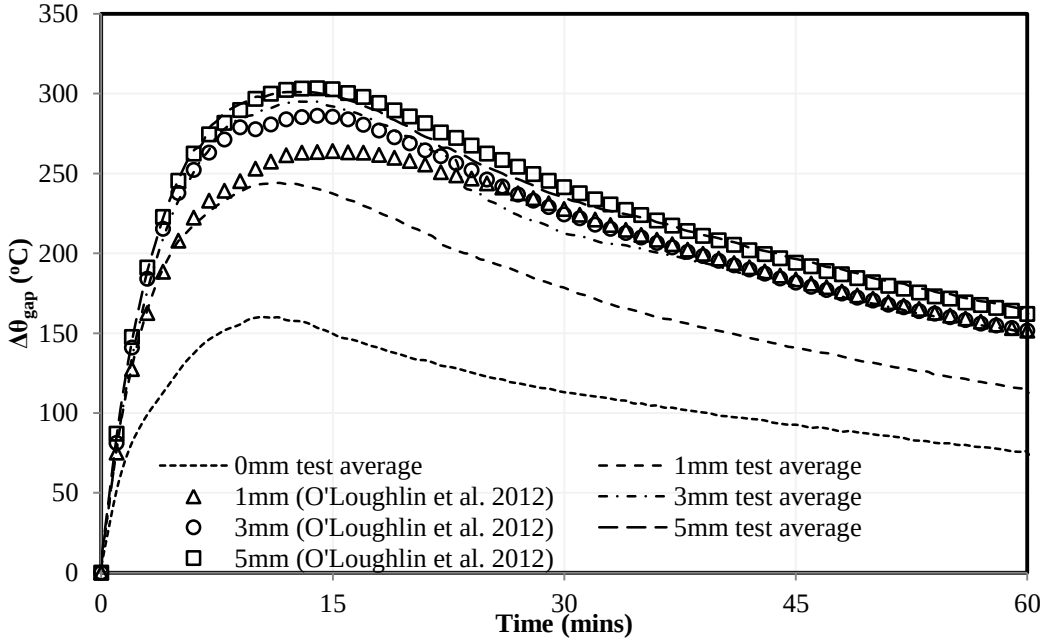

Figure 4-15: Comparison of $\Delta\theta_{gap}$ observed for 50 kW/m^2 heat flux modelled using values from O'Loughlin et al. (2012)

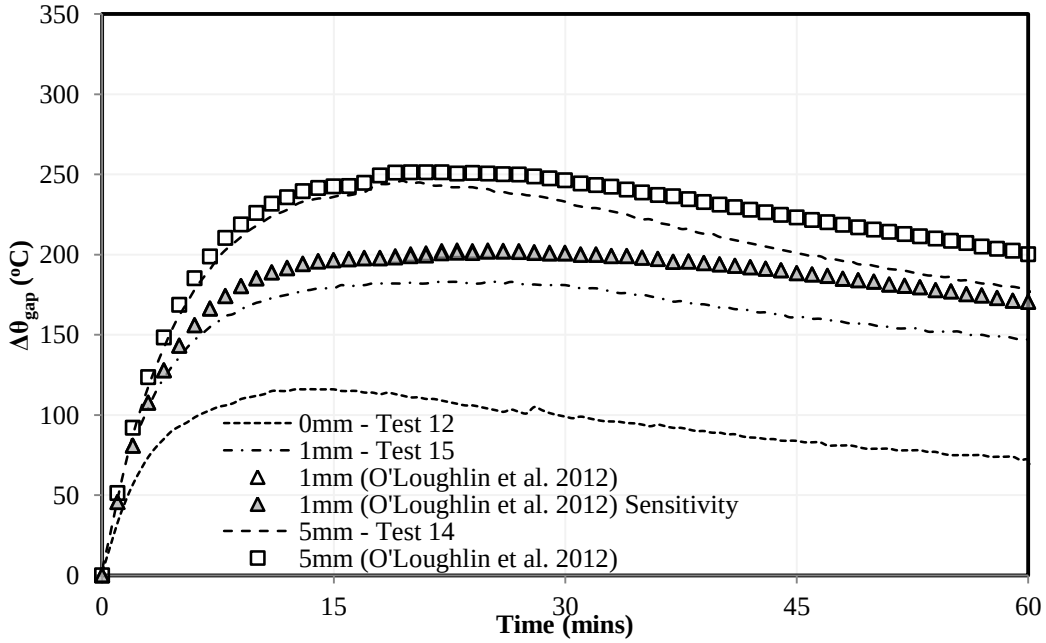

Figure 4-16: Comparison of $\Delta\theta_{gap}$ observed for 35 kW/m^2 heat flux modelled using values from O'Loughlin et al. (2012)

As previously noted, the effect of the assumed emissivity of the respective materials also effects the predictions. The analysis by O'Loughlin et al. (2012) used constant emissivity values for steel and concrete; however, as previously discussed the emissivity of steel can vary considerably with temperature (refer to Figure 2-7).

Bentz et al. (2009) showed that the emissivity of steel, $\varepsilon_{m,a}$, varied with temperature as shown in Figure 2-7, and when this relationship was used instead of the value used by O'Loughlin et al. (2012) the predicted $\Delta\theta_{gap}$ showed good correlation with tests without the need for *n* as shown in Figure 4-17 and Figure 4-18 (black markers). However, when using the temperature dependent steel emissivity (Bentz et al., 2009), the model over-predicted the heat transferred across the gap when the steel was above 400°C (i.e. after 15 minutes). This is evident when comparing the two heat fluxes. Under 35 kW/m^2 (Figure 4-18) the temperatures on the back face of the steel struggle to exceed 400°C and the predictions are considerably more accurate.

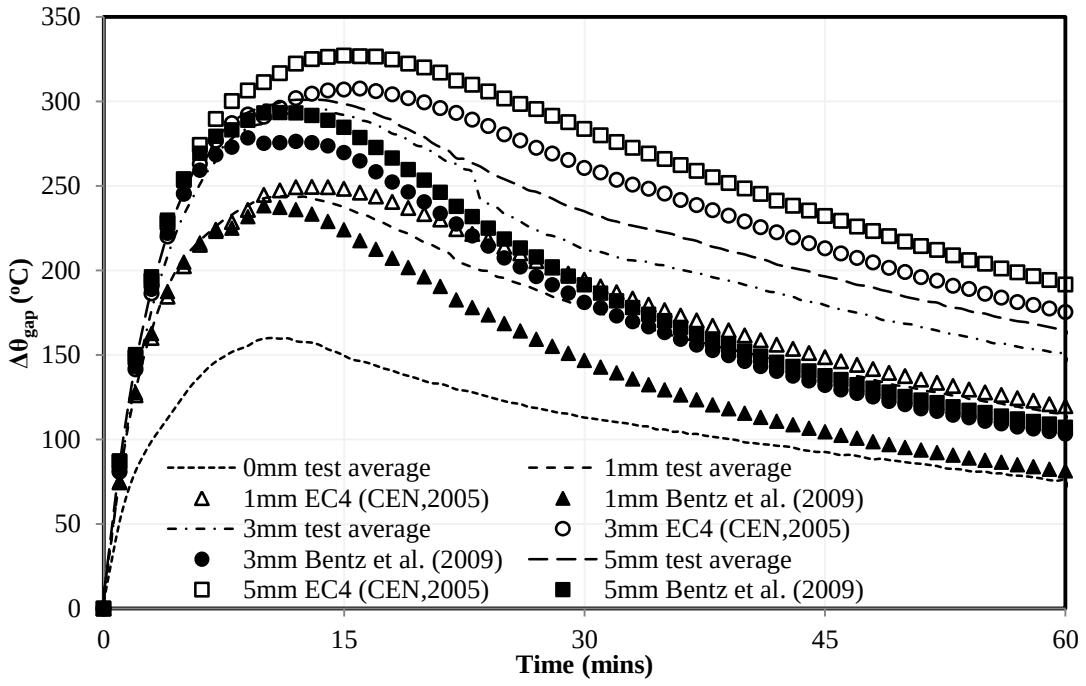

Figure 4-17: Comparison of $\Delta\theta_{gap}$ observed for 50 kW/m^2 for different gap widths modelled using EC4 (CEN, 2005) and Bentz et al. (2009) emissivities

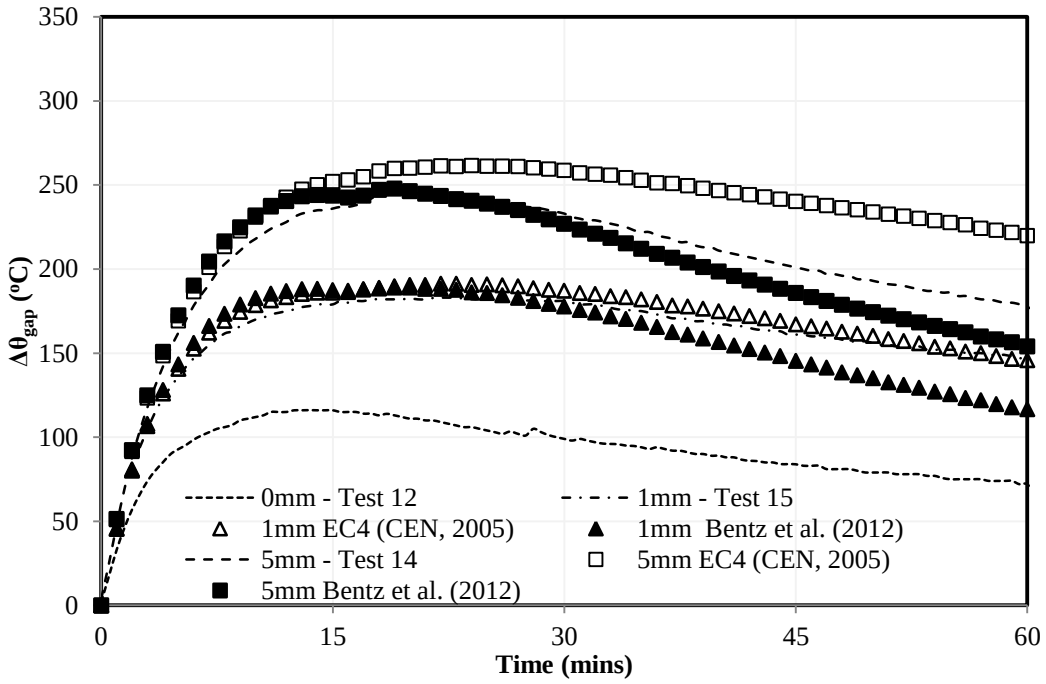

Figure 4-18: Comparison of $\Delta\theta_{gap}$ observed for 35 kW/m^2 for different gap widths modelled using EC4 (CEN, 2005) and Bentz et al. (2009) emissivities

Figure 4-17 and Figure 4-18 also show the predicted temperature difference across the gap when using the EC4 guidance of 0.7 for the emissivity of both steel and concrete leading to resultant emissivity of 0.49. Whilst a slight over-prediction in peak temperature and its timing are observed (especially for 50 kW/m^2), the gradient of the predictions closely matches those seen in the tests.

The above modelling shows that heat transfer across the gap can be predicted without the need of a calibrated parameter and that, as expected, it is highly sensitive to the assumed emissivities of the gap surfaces.

4.4 Chapter summary

This chapter has shown that the size of the air gap that is known to form in many cases between the steel tube and the concrete core due to differential expansion on heating has a direct and considerable impact on the heat transfer at the steel-concrete interface. Experiments were presented which have shown that as the size of the air gap increases the heat transfer decreases, effectively insulating the steel and leading

to lower concrete temperatures and higher steel temperatures. A 5 mm air gap can increased the temperature difference across the gap by a factor of two.

This thermal resistance for a 0 mm gap case was well predicted by the available guidance, but as the gap size increased it failed to predict the heat. A finite element heat transfer model was therefore developed and was shown to agree well with test data. The model incorporates a lumped convection and conduction heat transfer term as well as accounting for variable radiative heat transfer between the two gap surfaces. The analysis showed that the heat transfer is highly sensitive to the assumed emissivities of the two surfaces. Whilst the chapter has shown that it is possible to predict the heat transfer across the gap with reasonable accuracy, additional research is needed to understand the factors affecting the emissivities of steel and concrete. Work is also needed to assess the factors affecting the formation and size of the gap to understand the evolution of heat transfer rates at the interface as well as the potential loss of confinement due to gap formation. Until a more rational model that incorporates the evolution and formation of the air gap it is recommended that the gap conductance model from Ghojel (2004) (Equation 2-8) be adopted in heat transfer analyses for performance-based structural fire design of CFS sections.

Chapter 5: Furnace tests on unprotected and protected CFS sections

Performance-based fire resistance design calculations for CFS columns depend on accurate heat transfer modelling. Of the furnace tests on CFS columns reported in the literature, relatively few report detailed cross-sectional temperature profiles; rather the vast majority report only the steel tube temperature at 'failure.' Whilst the meta-analysis presented in Chapter 3 of this thesis showed that it is possible, on average, to predict the steel tube failure temperature and the time to failure of CFS columns in fire, considerable variability is observed in the predictions. When considered across the full database of experimental results in Chapter 3, and within the database when partitioned on the basis of different physical parameters, the failure temperature and fire resistance predictions became less accurate and more variable as section size and wall thickness increased. This indicates that the ability to predict cross-sectional temperatures is marginal and that fundamental physics may not be properly accounted for.

The ability to accurately predict the full cross-sectional thermal response of CFS sections is important in assessing the level of thermal protection required, and also to understand the effects of thermal protection on the thermal and mechanical response of CFS sections, and thus their structural capacity in fire. This chapter presents 34 medium-scale unloaded furnace tests (i.e. thermal tests) on CFS columns of various shapes and sizes in two parts: (1) 14 furnace tests on unprotected CFS sections; and (2) 20 furnace tests on CFS sections protected with intumescent paint.

5.1 Medium-scale furnace test program

5.1.1 Testing matrix

The furnace test program was carried out in ceramic lined cube and floor furnaces at International Paint Ltd, Newcastle, and involved thermal testing of a total of 34 specimens; these are detailed in Table 5-1. The influence of a number of parameters on the heat transfer within the sections was examined (as was their residual structural capacity, as described in Chapter 7). Parameters considered included the shape of the

section, the overall size of the section, the wall thickness, the type of concrete infill, the type of thermal insult (fire), and the type and amount of fire protection.

The test program included two section shapes: circular and square. More circular sections were tested than squares as there is less data in literature for circular sections despite the fact that they are more popular with architects and engineers due to their aesthetic and structural benefits (i.e. confinement of concrete core). Six main parameters were assessed and these are used to identify the individual tests using a naming scheme as outlined below. Four additional tests were also conducted, as indicated in the Table 5-1 by ".xxx" at the end of the identification string.

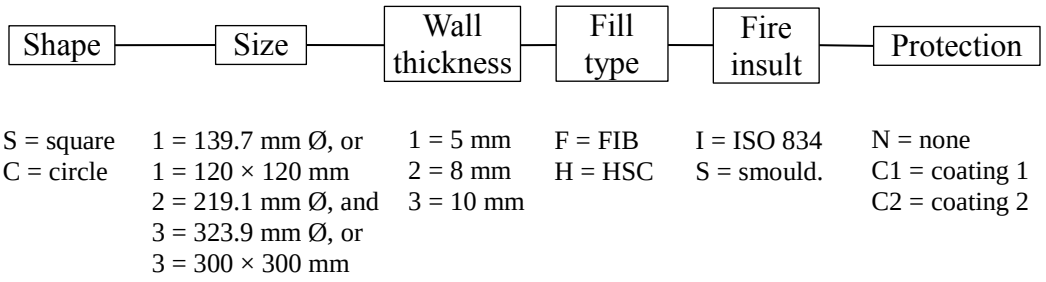

Figure 5-1: Details of six-character naming and identification scheme for the columns tested herein

Square sections included 300 × 300 mm and 120 × 120 mm columns, while circular sections included 323.9 mm ∅, 219.1 mm ∅ and 139.7 mm ∅. The largest and smallest square and circular sections had equivalent heated perimeter to total cross-sectional areas (H_p/A_{tot}) such that the effect of shape and size could be better compared, whilst the circular sections included one additional intermediate size which allowed a better understanding of the heat transfer with increasing size.

The CFS columns were prepared and tested in two phases (aside from two "concrete age" tests that took place 14 and 28 days after the first set of specimens were cast and that were used to assess the impacts of concrete age on thermal response). Two separate phases were required to accommodate storage of the large number of specimens. Phase 1 consisted of 16 circular sections as shown in Table 5-1, whereas Phase 2 consisted of a mix of square and circular sections totalling 20 specimens.

Three wall thicknesses (5, 8 and 10 mm) were used, as shown in Table 5-1, with the 139.7 mm Ø and 219.1 mm Ø circular sections including all three wall thicknesses. The 323.9 mm Ø circular sections considered only the 8 and 10 mm wall thicknesses due to sourcing difficulties (larger wall thicknesses are used in practical applications in real buildings in any case). The 323.9 mm Ø circular sections at 10 mm wall thickness included repeat tests (C33FIC1a and C33FIC1b) to assess the repeatability of the fire protection performance. The 300 × 300 mm square sections were also at 10 mm wall thickness, whereas the 120 × 120 mm squares were at 5 and 10 mm wall thicknesses.

The length of the columns for the 323.9 mm Ø circular and 300 × 300 mm square sections was limited to 1000 mm based on weight restrictions within the testing furnaces; this is the minimum permitted section length prescribed by the relevant testing standard for intumescent paint (CEN, 2010b). The remaining sections were as tall as possible given the limits of the furnaces being used, at 1400 mm. The increased height was also important for realism of the post-fire residual strength tests which are presented in Chapter 7.

The concrete infill in the majority of the specimens was a commercial, high strength, hybrid steel and polypropylene fibre reinforced mix (FIB), presented in Table 5-2, and is similar to the concrete mix used in the small scale tests described in Chapter 4. Two specimens (C11HIN and C11HIC1) were filled with high strength concrete (HSC) using the same mix design as the FIB concrete mix but without added fibres. The concrete was allowed to cure for at least 6 months after casting before testing to minimise the amount of free moisture (apart from tests C11FIC1.14d and C11FIC1.28d in which the concrete was allowed to cure for only 14 and 28 days, respectively). These two tests were used to assess the effect of concrete age, and thus free moisture in concrete, on the heat transfer within the sections so as to inform the on-going development of testing standards (CEN, 2010b) for fire protection of CFS columns

Table 5-1: Unprotected and protected CFS column section thermal test matrix partitioned by testing phase

Test no.[a]	Shape[b]	Size (b and h OR d)	Wall thickness	Length of column	Fill[c]	Fire[d]	Reactive coating	
		(mm)	(mm)	(mm)			Type[e]	F.R.[f]
Phase 1								
C11HIN	C	139.7	5	1400	HSC	ISO 834	None	N/A
C11HIC1	C	139.7	5	1400	HSC	ISO 834	C1	90
C11FIN	C	139.7	5	1400	FIB	ISO 834	None	N/A
C11FIC1	C	139.7	5	1400	FIB	ISO 834	C1	90
C13FIN	C	139.7	10	1400	FIB	ISO 834	None	N/A
C13FIC1	C	139.7	10	1400	FIB	ISO 834	C1	90
C12FIN	C	139.7	8	1400	FIB	ISO 834	None	N/A
C12FIC1	C	139.7	8	1400	FIB	ISO 834	C1	90
C11FSN	C	139.7	5	1400	FIB	Smould.	None	N/A
C11FSC1	C	139.7	5	1400	FIB	Smould.	C1	90
C11FIC1.14D	C	139.7	5	1400	FIB	ISO 834	C1	90
C11FIC1.28D	C	139.7	5	1400	FIB	ISO 834	C1	90
C11FIC1.120	C	139.7	5	1400	FIB	ISO 834	C1	120
C11FIC1.75	C	139.7	5	1400	FIB	ISO 834	C1	75
Phase 2								
S33FIN	S	300	10	1000	FIB	ISO 834	None	N/A
S33FIC1	S	300	10	1000	FIB	ISO 834	C1	90
S33FIC2	S	300	10	1000	FIB	ISO 834	C2	90
S11FIN	S	120	5	1400	FIB	ISO 834	None	N/A
S11FIC1	S	120	5	1400	FIB	ISO 834	C1	90
S13FIN	S	120	10	1400	FIB	ISO 834	None	N/A
S11FSN	S	120	5	1400	FIB	Smould.	None	N/A
S11FSC1	S	120	5	1400	FIB	Smould.	C1	90
C33FIN	C	323.9	10	1000	FIB	ISO 834	None	N/A
C33FIC1a	C	323.9	10	1000	FIB	ISO 834	C1	90
C33FIC1b	C	323.9	10	1000	FIB	ISO 834	C1	90
C33FIC2	C	323.9	10	1000	FIB	ISO 834	C2	90
C32FIN	C	323.9	8	1000	FIB	ISO 834	None	N/A
C32FIC1	C	323.9	8	1000	FIB	ISO 834	C1	90
C23FIN	C	219.1	5	1400	FIB	ISO 834	None	N/A
C23FIC1	C	219.1	5	1400	FIB	ISO 834	C1	90
C21FIN	C	219.1	10	1400	FIB	ISO 834	None	N/A
C21FIC1	C	219.1	10	1400	FIB	ISO 834	C1	90
C22FIN	C	219.1	8	1400	FIB	ISO 834	None	N/A
C22FIC1	C	219.1	8	1400	FIB	ISO 834	C1	90

[a] test numbering system *Shape – size – wall thickness- fill type – fire insult –protection type;*
[b] *C* = circle, *S* = square;
[c] *HSC* = high strength concrete, *FIB* = fibre reinforced concrete;
[d] *ISO 834* = standard fire insult (Equation 2-37) , *Smould* = slow heating curve (Equation 2-38);
[e] *None*= unprotected, *C1* = Interchar1120, *C2* = Interchar212; and
[f] *F.R.* = required fire resistance.

All specimens were heated for 120 minutes except for C31FIC1.120 which was heated for 180 minutes (reasons for this are discussed below). The application of CFS columns in industry is often in high rise buildings and these require F.R. ratings of two hours or more. Two thermal regimes were selected, the ISO 834 (ISO, 1999) standard fire (Equation 2-37) and the slow heating smouldering curve (*Smould.*) (CEN, 2009c) as prescribed in Equation 2-38. Once the two hours of heating (or three hours for C31FIC1.120) had elapsed, the gas supply was turned off and temperatures were recorded for two further hours whilst the specimens cooled. These two heating regimes were selected to advance understanding of the heat transfer in a cross-section and the performance of intumescents under different heating rates.

The thickness of protective coatings for CFS columns is conventionally based on a fire resistance time (F.R.) and a limiting steel temperature, which for most of the tests was selected as the typical value of 520^{o}C at 90 minutes under the ISO 834 fire. The limiting temperature of 520^{o}C is an industry standard based on the assumed strength of steel at this temperature being approximately 60% of its ambient strength, which is in the typical range of the ratio of the load in the fire limit state to the ultimate limit state in conventional applications. However C11FIC1.120 and C11FIC1.75 had protection thickness determined based on F.R. times of 120 and 75 minutes for a steel limiting temperature of 520^{o}C, respectively. In all cases the thickness of the protection was calculated using an equivalent steel section factor method for CFS columns described by Hicks et al. (2002) (Equation 2-10).

Fire protection on protected columns was achieved using one of two commercially available intumescent fire protection coatings at one of two thicknesses, as outlined in Table 5-1. These were coatings with the trade names ‘Interchar 1120’ and ‘Interchar 212’ which were supplied by an industry partner, International Paint, Newcastle, UK. Details of these specific coatings are available from the International Paint website at http://www.international-pc.com/products/info/Fire-Protection/Interchar-212.aspx and http://www.international-pc.com/products/info/Fire-Protection/Interchar-1120.aspx. Coating 1 (C1) was Interchar 1120; a water borne, single pack (i.e. one component), thin film intumescent coating; and Coating 2 (C2) was Interchar 212; a two pack intumescent

epoxy coating, where two components are mixed prior to application to the specimen. The different protection types allow an initial assessment of the reaction of different types of protective coatings on CFS sections.

No load was applied during heating or cooling. The tests provide comparative data on the thermal response of CFS columns exposed to different fire conditions, protection levels and physical characteristics, and help to inform the prediction of temperatures within CFS sections and improve predictions of fire resistance.

5.1.2 CFS specimen preparation

The specimens were prepared in three stages; thermocouple installation, concrete casting, and application of the fire protection coating. All thermocouples (TCs) were Inconel sheathed K-Type and were installed onto and inside the steel tubes before being filled with concrete. The steel tubes were Grade S355 (355 MPa nominal yield strength) steel and were blasted, cleaned and primed before the thermocouples were installed. Two pairs of vent holes and a pair of lifting holes were included to allow vapour pressure to escape during heating and also to enable easy handling (see Figure 5-2 and Figure 5-3).

Temperature readings were taken at two heights ($L/3$ and $2L/3$) with four thermocouples at each height measuring steel temperatures, and seven, nine and nine thermocouples measuring the concrete temperatures at each height at various depths, for the x1xxxx, x2xxxx and x3xxxx sections, respectively. The external steel wall thermocouples were placed midway through the steel wall, with the thermocouple wire placed internally so as not to interfere with the intumescent coating.

For the circular sections the external steel thermocouples were evenly spaced around the circumference, whilst for the square sections pairs of thermocouples were either placed opposite each other orthogonally or diagonally. Internally, the concrete thermocouples were attached to small stainless steel rods to form TC trees; these were placed in line with the external thermocouples and held with tie wire through the steel wall. A typical thermocouple tree is shown in Figure 5-5.

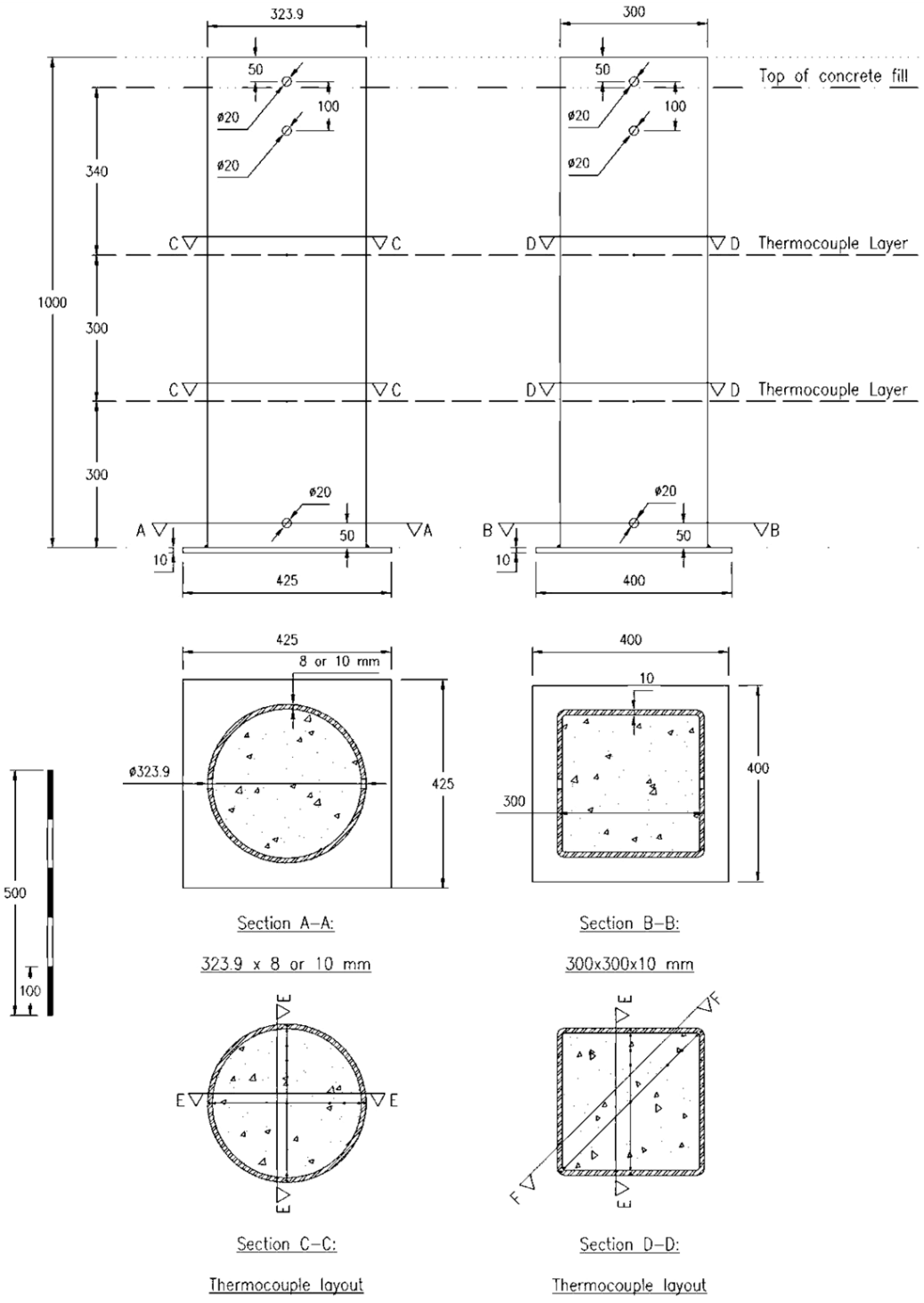

Figure 5-2: Plan, elevation and sections of S3xxxx and C3xxxx sections

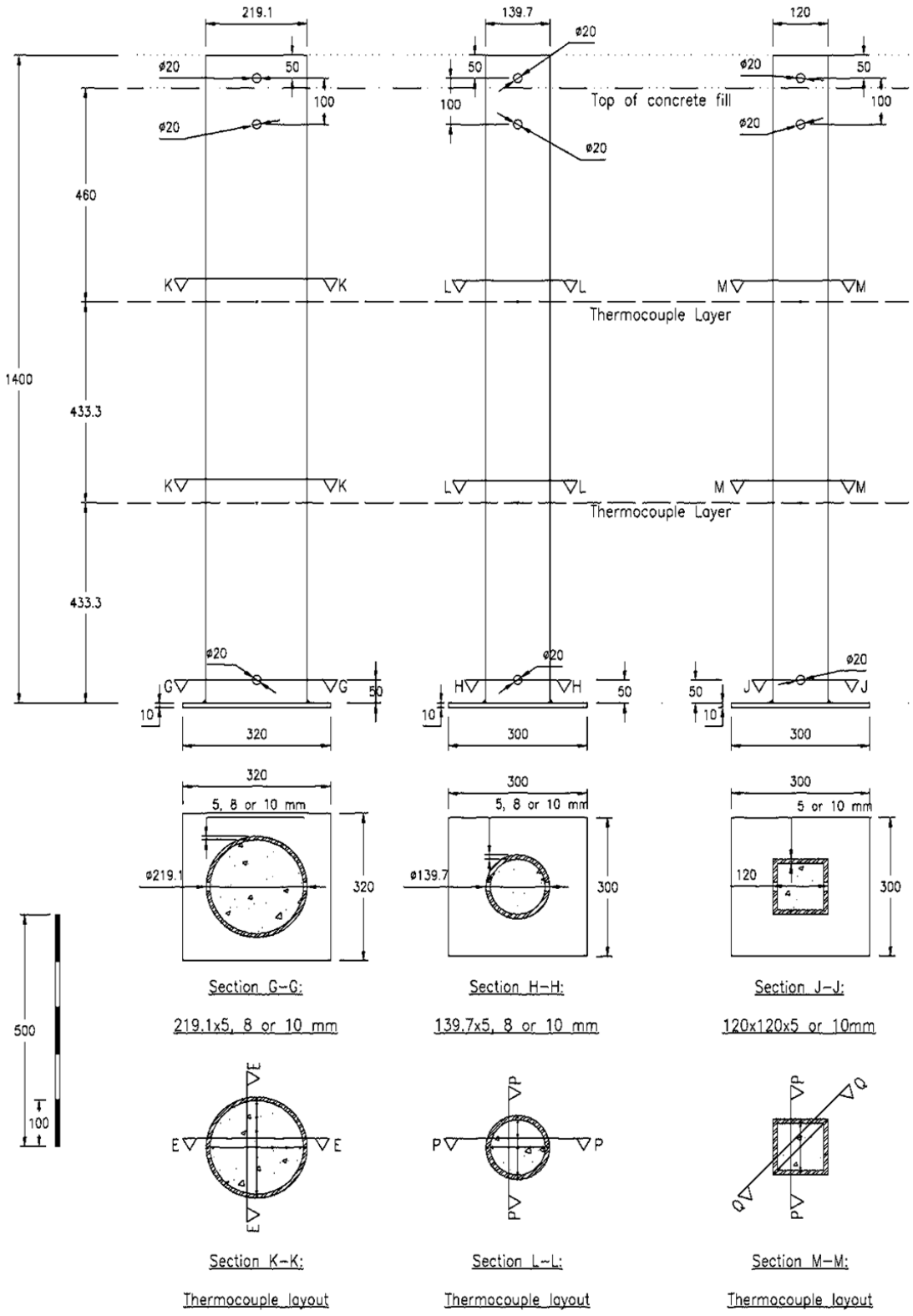

Figure 5-3: Plan, elevation and sections of C2xxxx, C3xxxx and S3xxxx sections

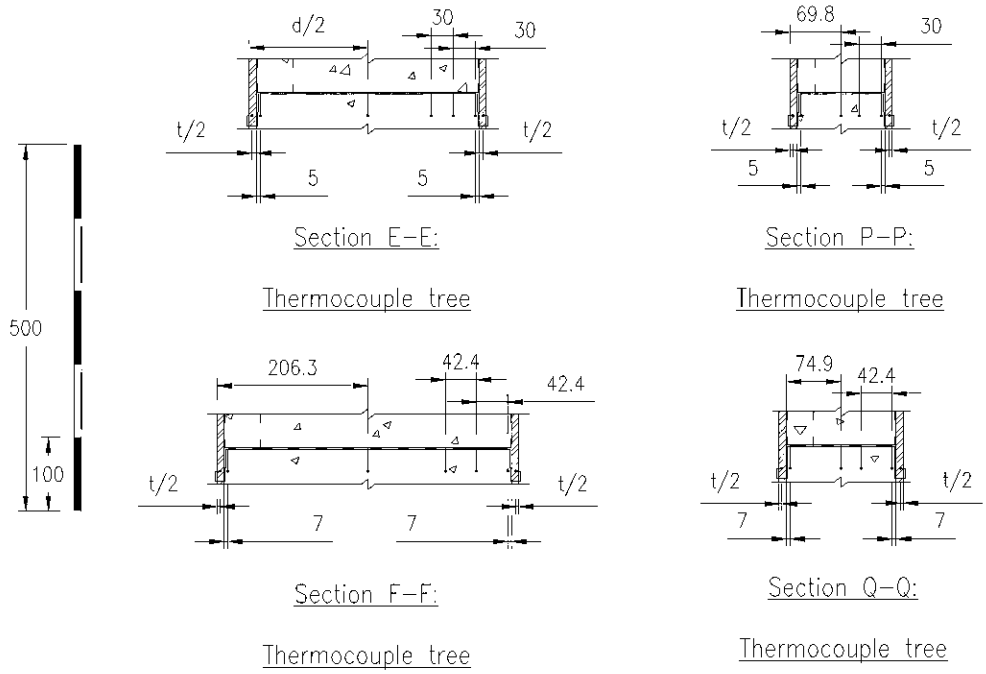

Figure 5-4: Thermocouple tree cross-sections for various CFS specimens

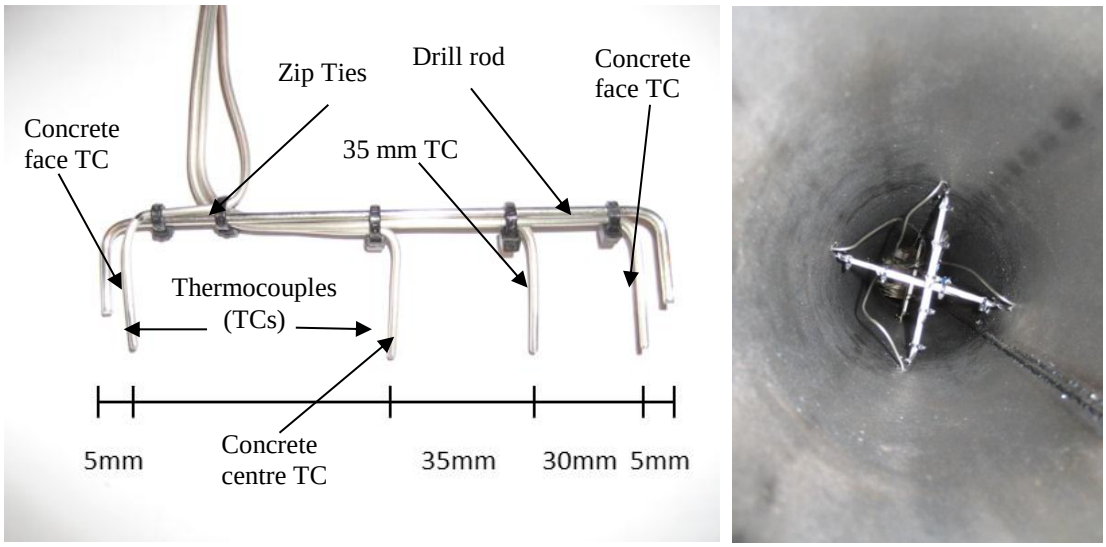

(a) (b)

Figure 5-5: (a) typical thermocouple tree for C1xxxx section (Section P-P), and (b) thermocouples in place within the tube prior to casting the concrete

Four thermocouples measured the temperature as close as possible to the steel-concrete boundary (denoted “concrete face TC”). The four thermocouples were

fabricated 5 mm from the edge of the thermocouple tree, and, when in place within the tube, were bent as close as possible to the steel tube, so that the distance between the thermocouple tip and the steel wall was as small as possible (approximately 2.5 mm from the steel). Similarly, all sections had thermocouples at the centre of the cross-section (denoted "concrete centre TC").

S1xxxx and C1xxxx sections had two additional thermocouples measuring temperatures 35 mm from the steel-concrete boundary (sections P-P and Q-Q), whilst S3xxxx, C2xxxx and C3xxxx sections had two additional thermocouples at 35 mm and 65 mm from the steel-concrete boundary (sections E-E and F-F) (denoted as "35 mm TC" and "65 mm TC", respectively).

After the thermocouples were placed specimens had steel base plates welded on and they were then filled with concrete. The casting of the C1xxxx sections was hampered by the thermocouple wires that ran internally within the tube, and the cross-hair created by the two thermocouple trees (Section L-L, Figure 5-3). The combination of these impeded the flow of the concrete to the bottom of the specimen slowing the casting process. To ensure that the specimens were full, a significant amount of rod vibration was carried out during casting, creating the potential for the thermocouple positions to have been affected. The long casting process also meant that cylinder specimens created for strength and moisture tests (very late during the cast) may be under-strength as compared to the concrete placed within the tubes.

The same concrete mix was used for both the HSC and FIB infill. The mix design and strengths at different concrete ages are given in Table 5-2. The quoted strength is the average strength of three cylinder tests. The specimens for Phase 1 were left to cure for 13 months (apart from C11FIC1.14D and C11FIC1.28D which were cured for 14 and 28 days, respectively) whilst Phase 2 specimens were cured for seven months. The specimens were allowed to cure for greater than 6 months to ensure that the concrete was representative of concrete found in real buildings. The cure time also allowed for the concrete to gain as much strength as possible before testing.

Table 5-2: Concrete mix design, compressive strength and water content of fibre reinforced (FIB) and high strength (HSC) concrete infill

		Percentage	Mass/m^3 of concrete (kg)	Total mass/m^3 of concrete (kg)
Cement	Portland cement	68.5%	315	460
	Blast furnace slag and silica fume	31.5%	145	
Aggregates	4-20 mm (Basalt)	56.9%	1035	1819
	0-4 mm	43.1%	784	
Fibres	Steel *(FIB only)*		45	45
	Polypropylene *(FIB only)*		2	2
Additives	Super-plasticiser		4	4
Water	Water-to-cement ratio – 0.39		180	180
			Total	2510 kg

Day	Phase 1							Phase 2			
	Date	Strength (MPa)[a]				Moisture content (%)[a]		Date	Strength (MPa)[a]		Moisture content (%)[a]
		FIB	*σ*	HSC	*σ*	FIB	HSC		FIB	*σ*	FIB
Cast	10.02.11	-	-	-	-	-	-	24.01.12	-	-	-
14	24.02.11	(37.3)	*3.5*	-	-	4.8	-	7.02.12	-	-	-
28	10.03.11	(48.7) *64.2*	*2.0*	(46.1) *66.7*	*4.2*	5.8	5.3	21.02.12	-	-	-
56	7.04.11	*69.3*	*10.2*	*72.4*	-	-	-	20.03.12	61.2	*6.1*	*(data lost)*
Test	19.03.12	(46.9)	*4.4*	(48.3)	*3.8*	3.4	3.0	16.08.12	59.4*	*11.9*	4.9*

recorded from cube tests, * recorded *01.03.13* as comparison to Phase 1 test age (403 days),
[a] based on three cylinder tests

Three, 100 mm Ø x 200 mm, cylinders at each age, were crushed, weighed, dried and re-weighed to determine their strength and moisture content (M.C.) by mass. The cube strengths of the concretes were provided by the ready-mix supplier and have approximately 1.3 times the measured cylinder strength, which is slightly higher than the expected ratio of 1.2 and could be due to the previously discussed casting issues. The casting issues mean that for the Phase 1 cast the cube strength data provided are more reliable, unfortunately no comparable cube strength data was provided by the ready-mix supplier for the Phase 2 cast. However, the strengths recorded for the concrete in the Phase 1 and Phase 2 casts from cubes and cylinders, respectively, show that the concrete is above the design C55/67 strengths for HSC as defined by EC2 (Table 2-5, (CEN, 2008b)). After the concrete was cast the protected CFS specimens were coated with the relevant protective coating and thickness. The thickness of the coating was based on the equivalent section factor (Hicks et al.,

2002) of a steel hollow section to account for the concrete infill and is dependent on the target fire resistance time. From the equivalent section factor, the dry film thickness of coating required to provide the F.R. for a specific limiting temperature, for the specific intumescent coatings being used, was found using tabulated data from tests on unfilled hollow steel sections.

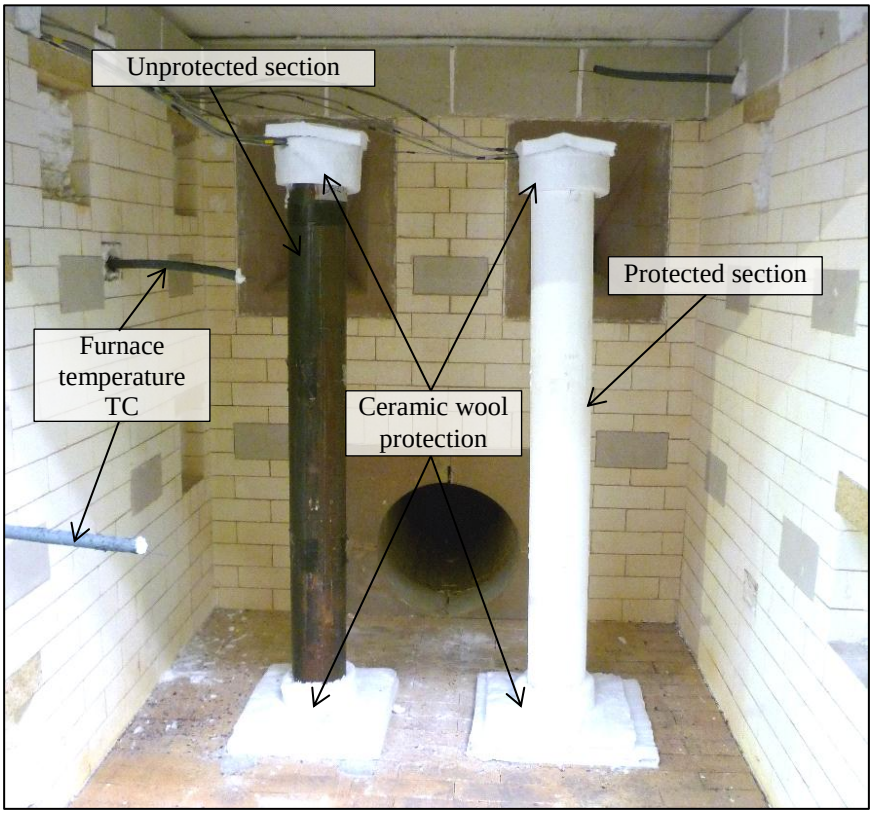

Figure 5-6: CFS sections C33FSN and C33FSC1 placed in the 'cube furnace' prior to testing

5.1.3 Test procedure

A 1.8 × 1.8 × 1.8 m cube furnace (referred to as the 'cube furnace') was used for the 14 and 28 day tests (C11FIC1.14D and C11FIC1.28D), the smouldering fire curve tests (S11FSN, S11FSC1, C11FSN and C11FSC1), and variable protected time to 520^{o}C tests (C11FIC1.120 and C11FIC1.75). A 4.0 × 3.0 × 2.0 m floor furnace (referred to as the 'floor furnace') was used for all other tests. Both furnaces are lined with ceramic tiles. When the specimens were in place in the furnaces and connected to data-loggers, ceramic wool was placed over the tops and the base plates of the

specimens to provide an idealized two dimensional heat transfer situation (see Figure 5-6).

5.2 Temperatures in unprotected specimens

Protection systems for CFS columns can be expensive and, in some situations, there is the desire to design columns without the need for protection. To safely predict the structural capacity of an unprotected column during fire (and thus its failure) accurate predictions of cross-sectional temperatures are essential. The meta-analysis presented in Chapter 3 showed that whilst it is possible to predict the temperature of the steel at failure with reasonable accuracy, the time to failure was less accurate, with the effect of size, wall thickness, and shape all influencing the accuracy and precision of the predictions. This indicates that thermal modelling of the concrete core may be marginal using available data and modelling approaches.

In this section the best-practice thermal modelling approaches suggested in Chapter 3 are used to predict the thermal response in the 14 unprotected tests outlined in Table 5-1. These are compared to temperatures observed during the tests to assess whether the suggested modelling approaches are appropriate. The tests also provide both quantitative and qualitative assessment of the heat transfer physics and phenomena at play in unprotected CFS sections exposed to fire, highlighting that the evaporation of water has considerable impacts on heat transfer.

5.2.1 Temperature predictions in unprotected specimens

To assess the cross-sectional heat transfer predictions of the two 'best' thermal modelling approaches in Chapter 3, *Combi EC4c* and *Combi* ω (summarised in Appendix B) a mesh convergence analysis was required to ensure consistency of the predictions being made. Figure 5-7 shows the mesh diagram used for the mesh convergence analysis for circular sections. The two-dimensional (2-D) mesh employed small triangular elements near centre of element to converge at a point and is divided into 4 element regions; region D represents the steel tube; region C represents the initial 5 mm of concrete; region B represents the subsequent 30 mm of concrete; and region A the remaining concrete core to the centre of the cross-section, which in this analysis is approximately 35 mm in radius.

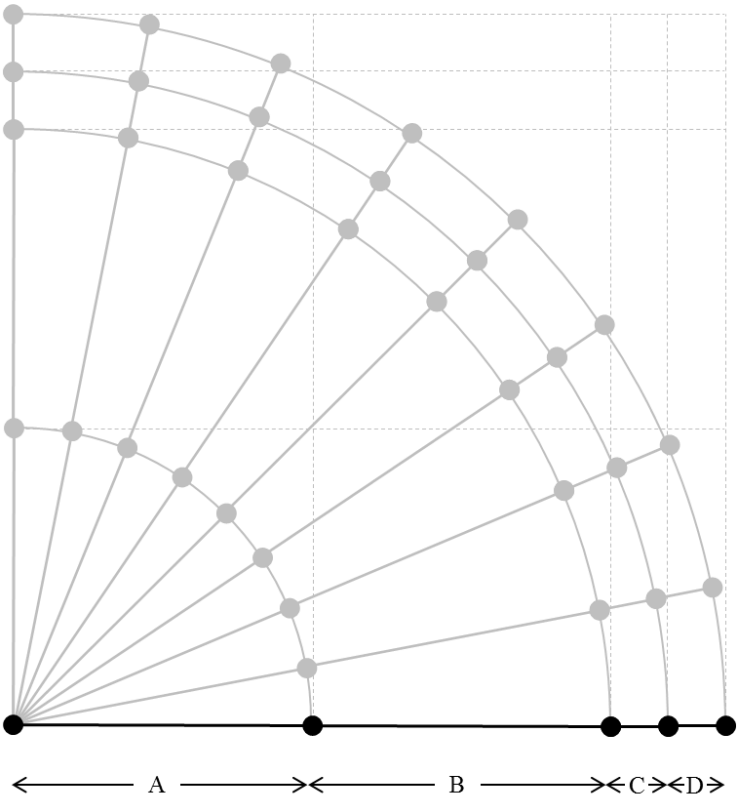

Figure 5-7: Mesh region diagram for thermal predictions made using the *Combi EC4c* and *Combi ω* thermal modelling approaches

The numbers of elements in each region (A, B, C, or D in Figure 5-6) were varied so as to produce a difference in predicted temperatures of less than 5^{o}C within ABAQUS, with plain heat transfer elements (DC2D4) adopted in the finite element analysis. Table 5-3 shows the results of the mesh convergence analysis reporting temperatures for the steel face, the concrete at a depth of 5 mm and at the centre of the cross-section at specific time intervals. Table 5-3 shows that a good level of convergence can be obtained, when using 9/8/4/4 elements in the regions A/B/C/D, respectively. This mesh density was therefore used in all subsequent 2-D predictions for the square (same mesh density as shown in Figure 5-7) and circular (i.e. x1xxxN) sections; an additional eight elements were used between regions A and B for C2xxxN and x3xxxN sections to account for the additional TC in these sections.

Table 5-3: Temperature results of the mesh convergence analysis at various locations and instances in time

	No. of elements A/B/C/D	*Time (mins)*				
		10	*20*	*30*	*60*	*120*
Steel (^{o}C)	3/1/1/1	294.4	585.9	727.7	912.3	1039.1
	4/2/2/2	310.6	595.1	727.9	910.7	1038.7
	9/4/4/4	327.3	596.6	728.1	910.3	1038.6
	16/8/4/4	330.3	597.3	728.1	910.2	1038.6
	9/8/4/4	331.6	597.8	728.2	910.2	1038.6
Concrete 5 mm (^{o}C)	3/1/1/1	147.2	446.6	603.6	835.0	1007.2
	4/2/2/2	183.5	449.0	604.3	829.6	1005.4
	9/4/4/4	216.6	454.8	603.9	828.2	1005.0
	16/8/4/4	213.7	455.9	603.5	827.8	1004.9
	9/8/4/4	215.3	456.7	603.7	827.9	1005.0
Concrete centre (^{o}C)	3/1/1/1	34.7	84.4	110.1	373.3	780.5
	4/2/2/2	30.9	74.4	104.9	372.5	780.7
	9/4/4/4	29.1	70.5	102.5	373.0	780.8
	16/8/4/4	28.9	69.5	102.0	372.7	781.0
	9/8/4/4	29.4	69.9	102.2	373.2	781.3

The predicted temperatures at 30, 60 and 120 minutes can be seen in Table 5-4 for both the *Combi EC4c* (white columns) and *Combi ω* (grey columns) thermal modelling approaches. Predicted temperatures for the cooling phase have not been made as the specific time-temperature relationships are not known during cooling and therefore cannot be modelled accurately. For the circular columns, single temperature values are given at the specific time and location due to axisymmetric heating of the cross-section, whereas for the square sections, orthogonal and diagonal temperatures are given (highlighted white and grey, respectively) since the heat transfer is truly 2-D in this case.

Table 5-4: Predicted temperatures in unprotected sections after 30, 60 and 120 minutes of heating for the steel tube, concrete face, 35 mm depth and concrete centre TC locations using the *Combi EC4c* and *Combi ω* thermal modelling approaches

Test	Size	W.T.	Steel (°C)			Concrete face (°C)			35 mm depth (°C)			Centre (°C)		
	(mm)	(mm)	30	60	120	30	60	120	30	60	120	30	60	120
Circular sections exposed ISO 834 standard fire (Equation 2-37)														
C11FIN	323.9	10	666	880	1020	523	757	936	413	632	811	132	343	589	134	310	503	22	41	101	20	34	142
C12FIN	323.9	8	684	885	1021	540	764	937	433	637	813	138	350	590	143	316	505	21	40	100	20	34	139
C21FIN	219.1	10	677	889	1027	540	778	960	429	647	838	144	384	676	148	347	564	43	101	362	32	134	378
C22FIN	219.1	8	693	892	1027	555	783	960	449	652	839	151	389	673	157	352	563	42	100	344	32	132	370
C23FIN	219.1	5	715	897	1028	577	789	960	473	658	840	162	396	669	172	360	563	40	99	318	32	129	360
C31FIN	139.7	10	697	906	1038	573	825	1009	463	680	890	162	517	877	195	456	655	104	423	828	131	391	620
C32FIN	139.7	8	707	906	1038	586	826	1007	478	683	888	167	510	866	202	455	652	104	403	809	130	383	612
C33F(/H)IN	139.7	5	726	909	1038	604	828	1005	500	687	886	176	500	851	216	455	648	102	373	781	130	372	601
Square sections exposed to ISO 834 standard fire (Equation 2-37)														
S11FIN	300	10	650	867	1013	498	727	907	391	605	777	109	268	488	117	270	453	21	41	100	20	34	137
			709	910	1037	659	881	1023	570	773	969	179	470	745	195	420	614						
S21FIN	120	10	697	907	1039	553	820	1009	440	668	870	144	546	903	192	466	657	110	505	884	161	430	642
			721	919	1042	674	895	1035	580	784	981	202	584	919	222	494	672						
S23FIN	120	5	721	908	1038	577	816	1003	471	671	864	149	512	869	204	453	647	106	447	836	156	405	623
			748	925	1043	706	902	1035	618	798	983	226	569	897	248	494	668						
Square and Circular sections exposed to smouldering curve (Equation 2-38)														
C33FSN	139.7	5	395	818	1007	288	712	966	186	598	834	95	328	778	63	326	613	75	130	696	42	235	559
S23FSN	120	5	394	815	1007	277	693	962	177	576	812	94	318	796	60	320	613	84	221	756	48	271	585
			427	842	1014	372	807	1003	258	687	941	101	392	830	71	364	636						

Table 5-5: Observed temperatures in unprotected sections after 30, 60, 90 and 120 minutes, as well as maximum temperatures, for the steel tube, concrete face, 35 mm depth and concrete centre TC locations

Test	Size	W.T.	Steel (°C)						Concrete face (°C)						35 mm depth (°C)						Centre (°C)					
	(mm)	(mm)	30	60	90	120	Max	Time	30	60	90	120	Max	Time	30	60	90	120	Max	Time	30	60	90	120	Max	Time
Circular sections exposed ISO 834 standard fire (Equation 2-37)																										
C11FIN	323.9	10	489	727	875	949	949	120	241	531	721	828	828	120	109	252	412	541	559	127	22	78	121	132	313	239
C12FIN	323.9	8	479	709	862	931	931	120	250	534	721	828	828	120	101	224	380	504	525	128	22	57	119	134	294	240
C21FIN	219.1	10	513	765	902	981	981	120	272	562	751	869	869	120	120	269	452	616	648	131	48	130	193	377	570	175
C22FIN	219.1	8	503	748	887	971	971	120	285	587	770	885	885	120	131	296	487	637	659	127	47	130	180	330	537	182
C23FIN	219.1	5	531	753	889	973	973	120	323	600	777	892	892	120	141	307	482	628	649	127	50	126	178	331	529	180
C31FIN	139.7	10	554	825	944	1005	1005	119	444	783	924	995	995	119	283	591	807	924	924	120	145	412	684	844	871	131
C32FIN	139.7	8	529	800	925	991	992	119	394	738	896	977	977	120	179	543	792	913	913	120	116	389	737	882	888	124
C33FIN	139.7	5	532	799	926	997	997	120	371	691	860	954	954	120	136	384	647	808	834	131	123	286	564	756	820	140
C33HIN	139.7	5	553	806	927	996	996	120	380	698	859	952	952	120	157	408	651	808	835	131	138	313	574	754	822	142
Square sections exposed to ISO 834 standard fire (Equation 2-37)																										
S11FIN	300	10	506	759	886	966	966	120	218	507	671	782	782	120	95	215	346	462	480	129	21	63	116	139	309	240
			506	760	893	975	975	120	291	644	823	928	928	120	139	354	556	699	713	125						
S21FIN	120	10	458	768	913	987	987	120	320	687	870	961	961	120	155	435	719	875	890	126	145	400	698	865	886	127
			479	785	922	995	995	120	356	722	891	977	977	120	169	468	741	886	897	126						
S23FIN	120	5	465	757	895	974	974	120	317	649	829	932	932	120	147	384	653	821	847	129	139	354	556	699	713	125
			513	792	912	984	985	119	305	641	822	928	928	120	161	445	696	850	864	125						
Square and Circular sections exposed to smouldering curve (Equation 2-38)																										
C33FSN	139.7	5	320	712	893	980	980	120	187	583	820	935	935	120	86	255	543	749	787	133	66	146	448	683	773	145
C23FSN	120	5	296	725	905	990	990	120	175	559	808	935	935	120	90	247	569	793	830	129	78	192	529	766	826	134
			260	714	897	987	987	120	206	661	877	978	978	120	94	268	592	807	837	128						

5.2.2 Results and observations from unprotected tests

Selected results of the unprotected tests are presented in Table 5-5, in which temperatures (averaged across all TCs at a given location) are given for the steel tube, concrete face, 35 mm depth and concrete centre TCs at 30, 60, 90 and 120 minutes, as well as the maximum temperature and the time it was reached. Again, single temperature values are given for circular columns and orthogonal and diagonal temperatures (again highlighted grey) are given for square sections.

5.2.2.1 Representative observed versus predicted response

A representative thermal response for one circular CFS column is shown in Figure 5-8 which shows the response of C22FIN to an ISO 834 fire. Figure 5-8 also shows that the applied furnace temperatures closely match the ISO 834 fire; this was the case for all tests, with the most variability (70^{o}C standard deviation in the first 20 minutes and 7^{o}C during the remaining 100 minutes) in applied temperatures during the early stages of the fire. Thermal response predictions for using the *Combi EC4c* and *Combi* ω thermal modelling approaches are also presented in Figure 5-8.

Figure 5-8 shows that the steel temperature plateaus between 700-800^{o}C which is due to the known phase change in the steel at those temperatures. The observed maximum temperature of the steel was at 120 minutes in all cases. The observed concrete face (approximately 2.5 mm deep) temperatures followed a similar trend to the steel, excluding a phase change plateauing effect and with generally lower temperatures than the steel tube, again peaking at 120 minutes. The lower temperatures observed are a result of the thermal resistance at the interface between the steel tube and the concrete infill (possibly due to gap formation), and the precise depth of the measurement as discussed below. The vaporisation of free water has a clear and considerable retarding effect on temperatures in the concrete between 120 and 180^{o}C.

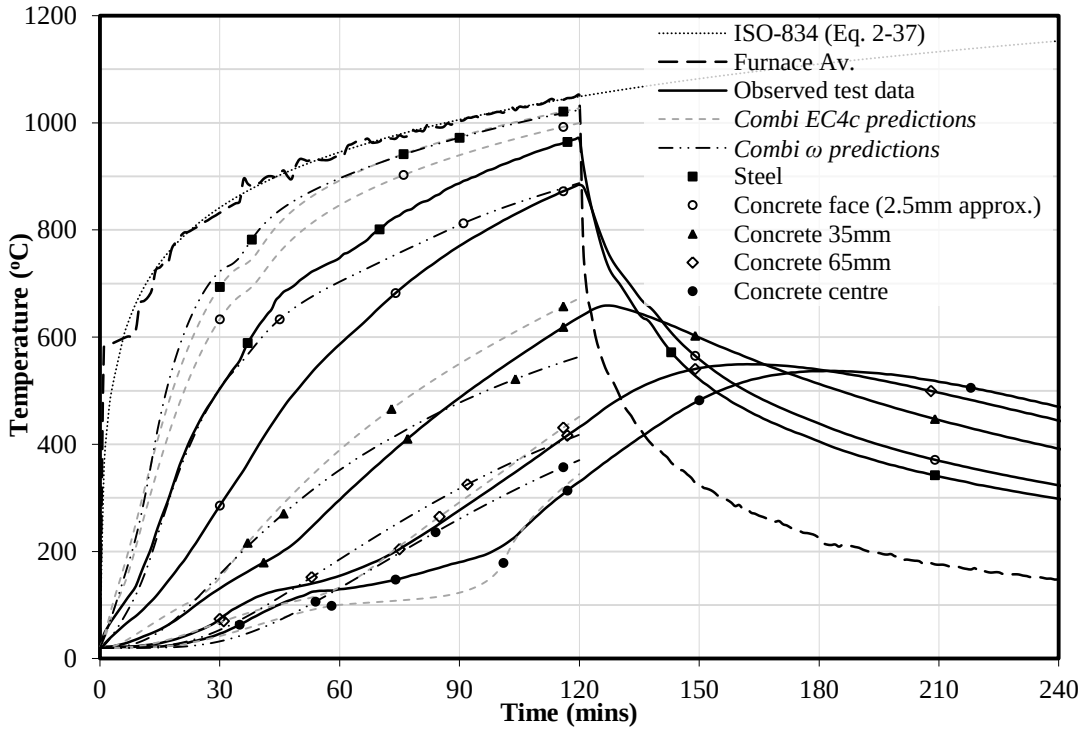

Figure 5-8: Representative predicted and observed temperatures within a C22FIN under exposure to an ISO 834 standard fire

Figure 5-8 also shows that the predictions made by both the *Combi EC4c* and *Combi ω* thermal modelling approaches fail to accurately predict observations from tests. Steel temperatures are over-predicted by 40-60^{o}C, whilst the modelling of the concrete using the *Combi EC4c* approach over-predicts the temperatures nearer the concrete steel interface and slightly under-predicts the core temperatures. The *Combi ω* approach over-predicts the temperatures at most locations. It should be noted that the error in the predictions could be caused by inaccurate thermocouple placement however given that the data sets represent averages this is not thought to be a major issue. Figure 5-9 and Figure 5-10 show, for the *Combi EC4c* and *Combi ω* thermal modelling approaches, respectively, the predictions at the assumed locations with error bars representing predictions at ±2.5 mm from these locations.

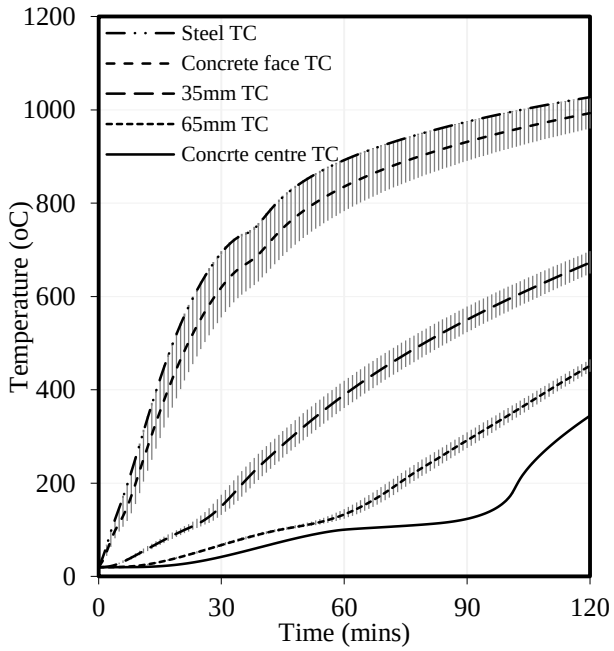

Figure 5-9: Predicted temperatures with assumed TC placement errors of ±2.5 mm for Test C22FIN using *Combi EC4c* thermal modelling approach

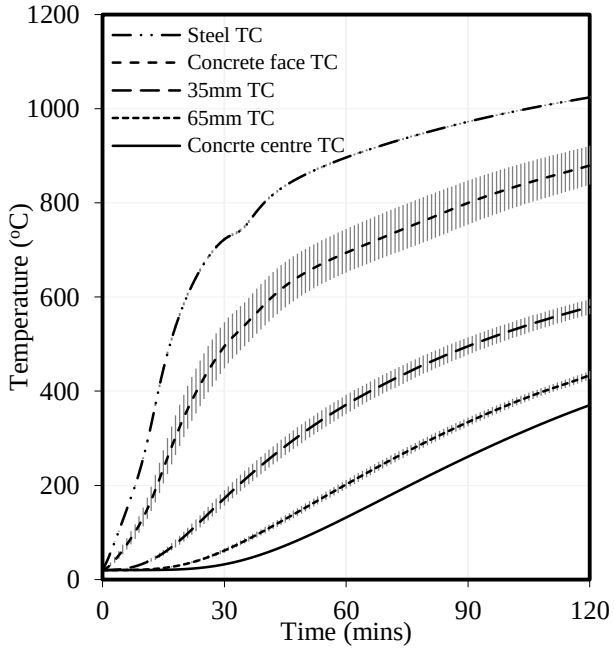

Figure 5-10: Predicted temperatures with assumed TC placement errors of ±2.5 mm for Test C22FIN using *Combi ω* thermal modelling approach

Figure 5-9 and Figure 5-10 show that the error due to thermocouple placement is not significant within the concrete apart from at the concrete face thermocouple, where errors up to 140^{o}C and 100^{o}C are possible for the *Combi EC4c* and *Combi* ω thermal modelling approaches, respectively. This should be borne in mind when drawing conclusions regarding the temperature predictions.

The trends in C22FIN section were not necessarily seen across all tests so a more detailed look at the effects of the sectional properties on the observed temperatures within the cross-section is presented next.

Steel tube temperatures

The maximum temperatures observed in the steel are influenced by the size and shape of the cross-section, as shown in Figure 5-11 and Figure 5-12 which show the temperature of the steel tube for circular and square sections, respectively. Figure 5-11 shows that as the size of the cross-section increases the temperatures in the steel decrease by approximately 80^{o}C between the C1xFIN and C3xFIN sections. The observed steel tube temperatures within each section size increase slightly as the wall thickness increase (as shown by the error bars in Figure 5-11 which represent the maximum and minimum temperatures for the cross-section size) with maximum temperatures usually being observed for the 10 mm wall thickness. The larger walled sections have slightly smaller concrete cores and the difference in temperatures could be due to lower thermal mass in the cross-section, or less moisture to absorb energy in the concrete core.

The cross-section size response was also seen for the SxxFIN sections (Figure 5-12) where in the orthogonal (O) direction a slightly lower temperature difference, between the S3xxxx and S1xxxx sections, of 40^{o}C, was observed. The diagonal (D) temperatures observed are very similar, with the temperatures in the S1xxxx sections being approximately 10^{o}C higher than those in the S3xxxx sections. The lower temperature difference diagonally, compared to orthogonally, is likely due to the increased surface area at the corners, increasing the amount of heat transferred from the fire. The difference in orthogonal and diagonal temperatures for both the S1xFIN and S33FIN sections are approximately 10^{o}C and 65^{o}C, respectively.

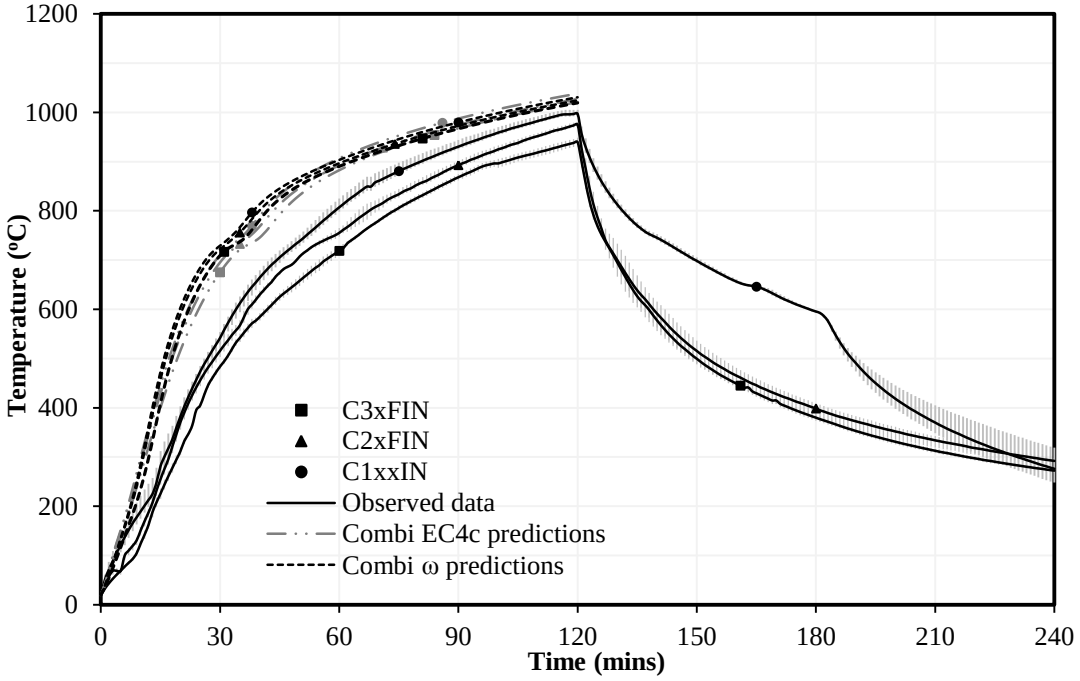

Figure 5-11: Observed and predicted temperatures of the steel tube for Cxxxxx sections

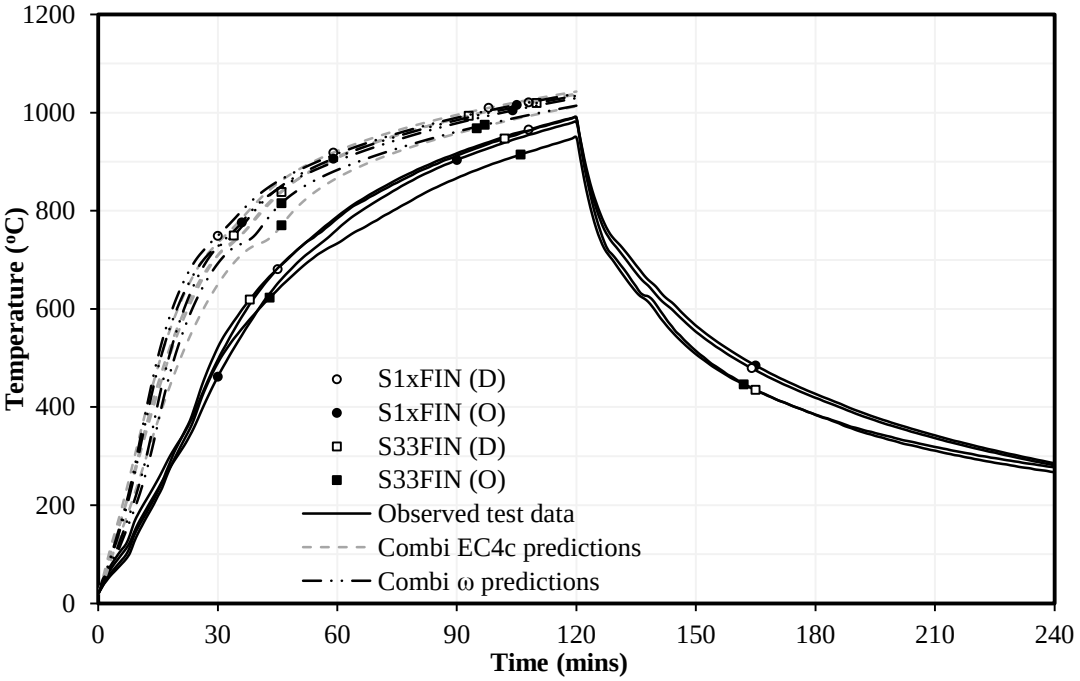

Figure 5-12: Observed and predicted temperatures of the steel tube for Sxxxxx sections

Both Figure 5-11 and Figure 5-12 show the predicted temperatures of the midpoint of the steel tube. As both figures show, the thermal modelling approaches over predict the temperatures by amounts exceeding 150^{o}C and 220^{o}C for both the *Combi EC4c* and *Combi ω* thermal modelling approaches, respectively. This is presumed to be due to inaccurate modelling of the heat transfer between the furnace environment and the steel which results in over-prediction of both concrete and steel temperatures. The modelling also shows an inverse trend to that seen in tests, with the larger walled tubes experiencing lower rather than higher temperatures than their thinner walled counterparts of the same cross-sectional size, as expected based on the discussion of test data above. The over-predictions of steel tube temperature show that there is a fundamental problem with the ability to accurately predict the heat transfer from the furnace to the unprotected steel tube. Further investigation is presented in Chapter 6.

Concrete temperatures

Figure 5-13 shows temperatures observed at the concrete face thermocouple and at 65 mm from the steel-concrete interface (or for the C1xxIN and S1xFIN sections the temperatures at their centre). The figure shows that as the tube size for circular sections (black lines) increases the temperatures observed at the concrete face decrease. Similar levels of variation as seen in the steel temperatures were observed in the concrete face temperatures for the C2xFIN and C3xFIN sections, whereas slightly greater variation was observed within the C1xxIN sections (about 70^{o}C), likely due to issues with TC placement during the concrete cast as already noted.

When considering the square sections (grey lines), S1xFIN sections show orthogonal (O) and diagonal (D) temperatures which are similar as was the case for steel tube temperatures (Figure 5-12). This was not the case for the S33FIN section tested, where the orthogonal temperatures at the concrete face were much lower than those seen for the steel wall, and with a temperature difference of approximately 150^{o}C between the orthogonal (O) and diagonal (D) temperatures. This is due the thermal conductivity of concrete being comparatively low compared to steel, thus after a gap has formed the temperature difference between the mid-point of the face to the corner is greater in the larger sections as less heat is transferred through the

conduction in the concrete as compared to the steel and so larger interface temperature differences are observed.

The diagonal temperatures in the square sections were similar between the S3xxxx and S1xxxx sections and were higher than the flat face temperatures, as expected. The temperature differences observed in the steel between the orthogonal and diagonal directions were approximately 10^{o}C and 65^{o}C for S1xFIN and S33FIN sections, respectively (Figure 5-12), whereas in the concrete, due to its low thermal conductivity, the heat is not transferred as readily and a greater disparity between the orthogonal and diagonal temperatures is observed. Temperature differences of up to 20^{o}C and 150^{o}C were observed for S1xFIN and S33FIN sections, respectively (Figure 5-13).

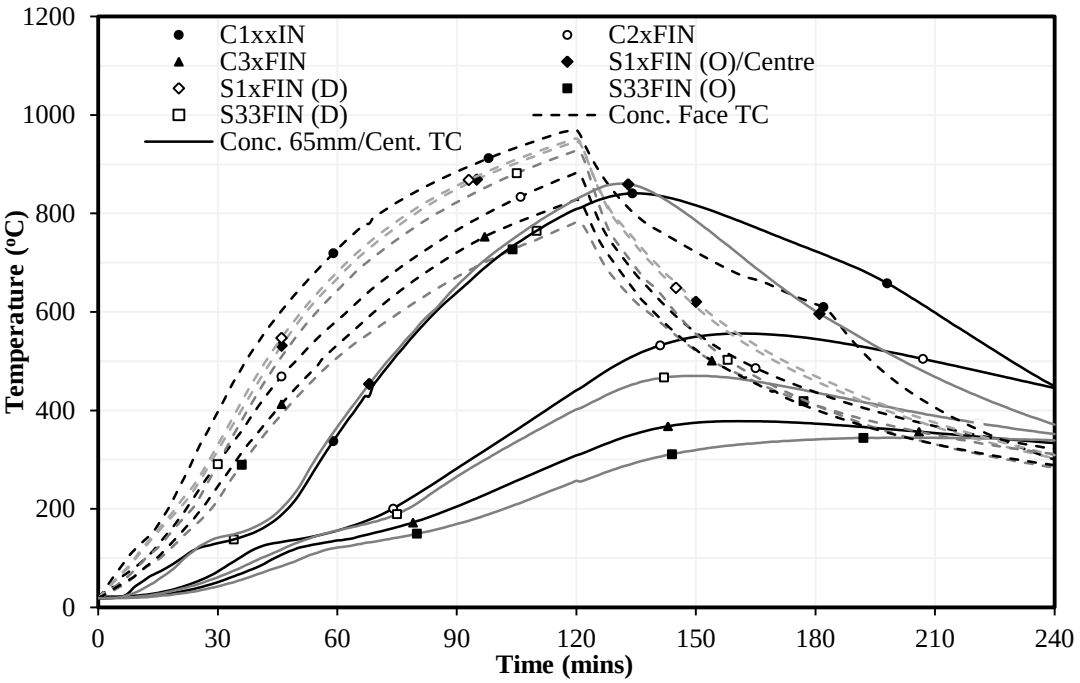

Figure 5-13: Observed temperatures at the concrete face and 65 mm depth TCs for SxxFIN and CxxxIN sections

The trends seen for both the CxxxIN and SxxFIN sections are due to both the increased thermal mass of the concrete core, as the section size increases, absorbing more energy especially in the evaporation of water, and the formation of a gap at the

steel-concrete interface (discussed later in this chapter, on Page 209), both of which reduce the temperatures observed at the concrete face.

With regard to the temperatures at the 65 mm depth TCs, it can be seen that the size of the column not only has an effect on the temperatures observed but also the time when the maximum is reached. The S1xFIN and C1xxIN sections experience their maximum temperatures 15 minutes after heating stops with magnitudes approximately 100^{o}C lower than the maximum face temperatures observed after 120 minutes. The C2xFIN, C3xFIN and S33FIN sections' maximum temperatures were lower and peaked later, and were influenced by the size of the cross-section. This is due to the thermal conductivity and specific heat capacity of concrete, and particularly the energy absorbed in the evaporation of free water between approximately 100 and 180^{o}C, which is clear in all 65 mm depth TC measurements Thus temperatures experienced during heating of a CFS column may not correlate to the weakest condition of the concrete core, and failure of a CFS column may therefore occur after a fire has been extinguished, particularly for large columns.

The evaporation of moisture has a greater effect on the temperatures observed within the C2xFIN, C3xFIN and S33FIN sections, with lower maximum temperatures due to the larger volume of free water available for evaporation. The timing of the peak temperature also depends on the free water in the concrete. If at the end of the heating phase the concrete towards the centre of the cross-section still has free water to evaporate (i.e. temperatures lower than 180^{o}C) then the energy in the surrounding concrete is absorbed in the evaporation of water rather than in increasing temperatures. Peak temperatures are therefore lower and occur earlier, as for the C3xFIN and S33FIN sections where the temperatures did not reach 180^{o}C at the end of the heating phase, both being at around 150^{o}C as seen in Figure 5-14. The C2xFIN sections on the other hand, have temperatures at the end of the heating phase at their centre of approximately 340^{o}C. This results in higher temperatures seen at 65 mm peaking later in for the C2xxxx sections compared to S3xxxx and C3xxxx sections.

The concrete centre TC temperatures seen in Figure 5-14 for the C1xxIN and S1xFIN, and the C3xFIN and S33FIN sections are very similar, due to similar heated

perimeter to total cross-sectional area ratios (H_p/A_{tot}), with values of 12.35 m^{-1} and 13.33 m^{-1} for the C3xFIN and S33FIN sections, respectively, and 28.63 m^{-1} and 33.33 m^{-1} for the C1xxIN and S1xFIN sections, respectively. The addition of fibres to the concrete mix has little obvious impact on heat transfer within the concrete, as shown in Table 5-5 where C33FIN and C33HIN experience similar temperatures.

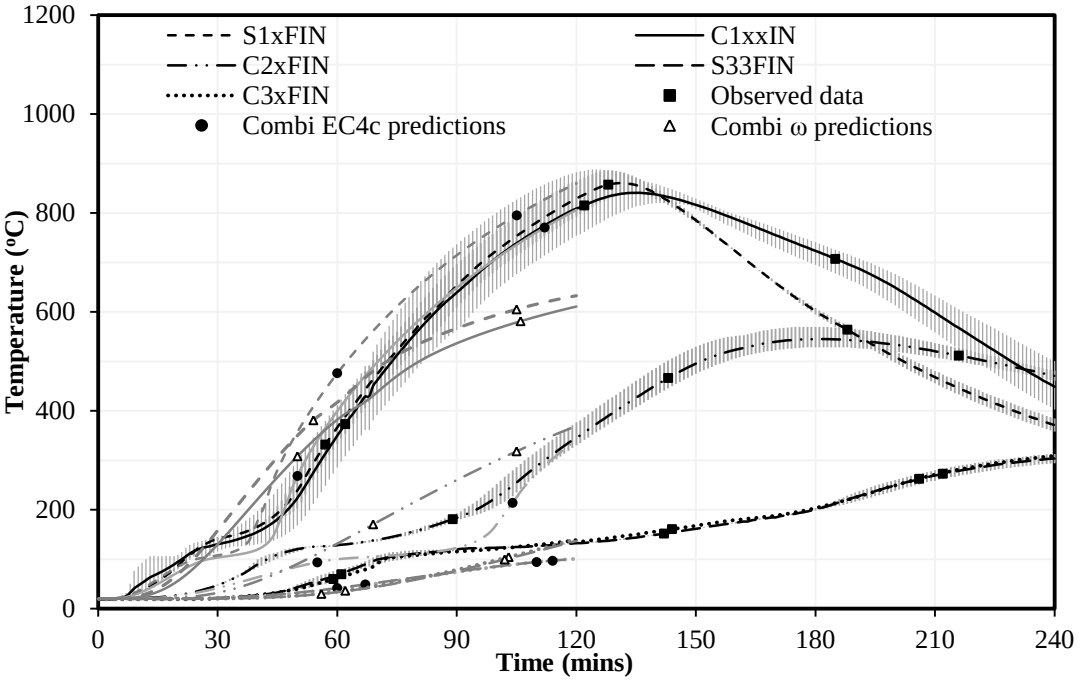

Figure 5-14: Observed and predicted temperatures at the concrete centre TC for SxxFIN and CxxxIN sections

Figure 5-14 also shows predicted temperatures at the concrete centre TC using *Combi EC4c* and *Combi ω* approaches, which demonstrate varying degrees of success. Temperatures are over-predicted for C1xxIN and S1xFIN sections whilst temperatures are generally under-predicted for C2xFIN, C3xFIN and S33FIN sections. This is surprising given that the steel temperatures are consistently over-predicted, and indicates that the thermal modelling of the concrete is not accurate.

The *Combi EC4c* thermal modelling approach explicitly accounts for the evaporation of water and, as seen in Figure 5-14, can in part model the thermal response in the concrete. Figure 5-14 shows that the temperatures at which moisture effects are predicted are lower than those observed in tests, and that there is slightly more heat

transferred in tests during the evaporation than is being modelled, as exhibited by the larger gradient (seen especially in the S1xFIN, C1xxIN and C2xFIN sections). Both thermal modelling approaches employ the lower bound of thermal conductivity (Equation 2-17) from EC4 (CEN, 2005), which appears too low to accurately predict the response in this case. The over-prediction in the S1xFIN and C1xxIN concrete temperatures is likely due to over-prediction of the steel temperatures and small concrete cores, whilst the same over-predicted steel temperatures produce concrete core under-predictions for the 300 mm × 300 mm and 323.9 mm Ø cross-sections which have the largest core sizes. This confirms that the amount of energy being transferred through conductivity is too low. Current thermal material models adopted in both the *Combi EC4c* and *Combi ω* thermal modelling approaches are therefore inaccurate; a refined thermal modelling approach is presented in Chapter 6.

Steel-concrete interface temperature differentials

Chapter 4 presented a set of tests that assessed the influence of the size of an air gap between the steel tube and concrete core on the heat transfer across an idealised one-dimensional CFS section. This showed that the as the size of the air gap increased the temperature differential across the interface also increased, and that the current state-of-the-art modelling assumptions predicted the 0 mm gap clearance with reasonable accuracy but struggled as the imposed gap size increased. It is of interest to see whether a similar response is observed in the tests conducted on real CFS sections.

Figure 5-13 showed that the observed temperatures at the concrete face are affected by the size of the cross-section and this affects the differential gap temperatures, $\Delta\theta_{gap}$, between the steel tube and the concrete face. This can be seen in Figure 5-15 which shows $\Delta\theta_{gap}$ for the CxxxIN sections along with averages for each of the diameters used. This figure shows that the peak magnitude of $\Delta\theta_{gap}$ increases as the section size increases, but the rate of increase before peak $\Delta\theta_{gap}$ is reached is similar across the different section sizes, thus affecting the time to the peak which also increases with section size. This could be due to the size of the concrete core and the amount of energy being consumed in moisture evaporation and transferred away from the concrete face by conduction; this is greater as the concrete core size increases. Alternatively, this could be due to the evolution of the gap thickness, with

the C2xFIN and C3xFIN sections experiencing larger gaps, and thus less heat transfer as suggested in Chapter 4.

Figure 5-15 also shows that for the C2xFIN and C3xFIN sections, thicker steel tube wall thickness resulted in greater temperature differences; however this was not seen for the C1xxIN sections where the thicker wall showed the lowest differential gap temperature. This could be due to inaccurate placement of the concrete face TCs which, as seen in figures 5-8 and 5-9, could cause a variation in temperature readings of approximately 100°C at the concrete face TC. The maximum difference in $\Delta\theta_{gap}$ for the C1xxIN sections was approximately 80°C.

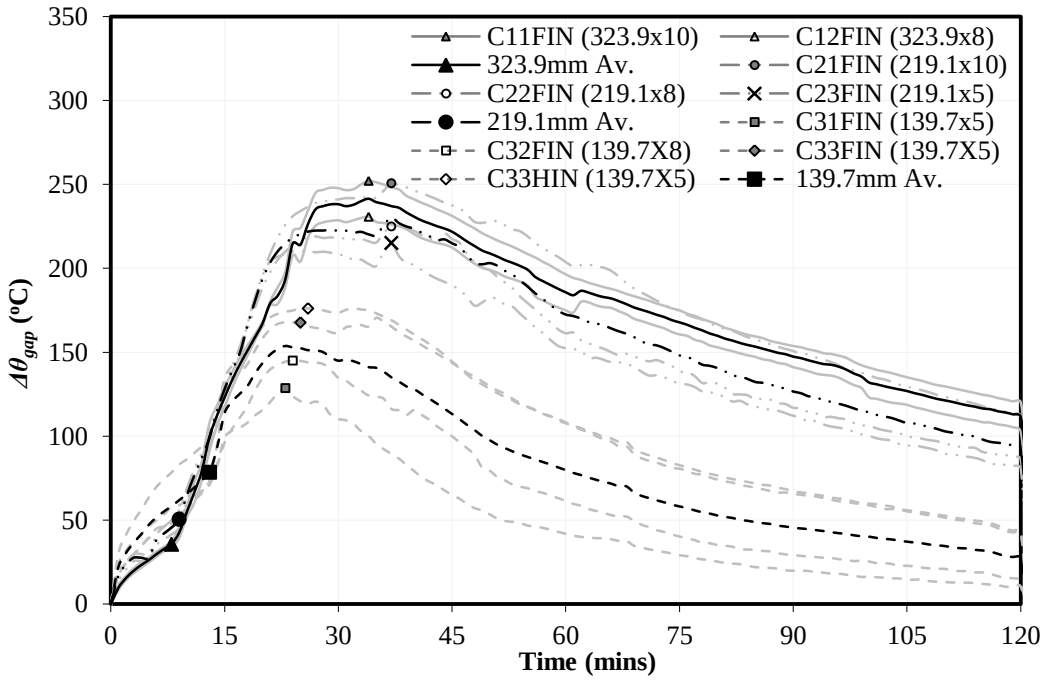

Figure 5-15: Differential interface temperatures, $\Delta\theta_{gap}$, for unprotected circular CFS sections

In terms of predicting the temperature difference between the steel and the concrete face (taken to be 2.5 mm deep in modelling), the major difference between the two modelling approaches is the inclusion of an interaction model in the *Combi ω* thermal modelling approach which empirically accounts for the air gap size and evolution, as compared to the perfect contact adopted in the *Combi EC4c* thermal modelling approach. Thus, the predicted differential gap temperatures shown in

Figure 5-16, comparing to Figure 5-15, immediately show that the perfect contact assumption used in the *Combi EC4c* approach is inaccurate for unprotected CFS sections. The inclusion of the gap interaction model proposed by Ghojel (2004) used in the *Combi ω* thermal modelling approach much better predicts the peak temperature difference for the C2xFIN and C3xFIN sections but does not predict the interface temperature difference well for the C1xxFIN sections. The inaccuracies in the predictions are likely due to over-predicted steel tube temperatures.

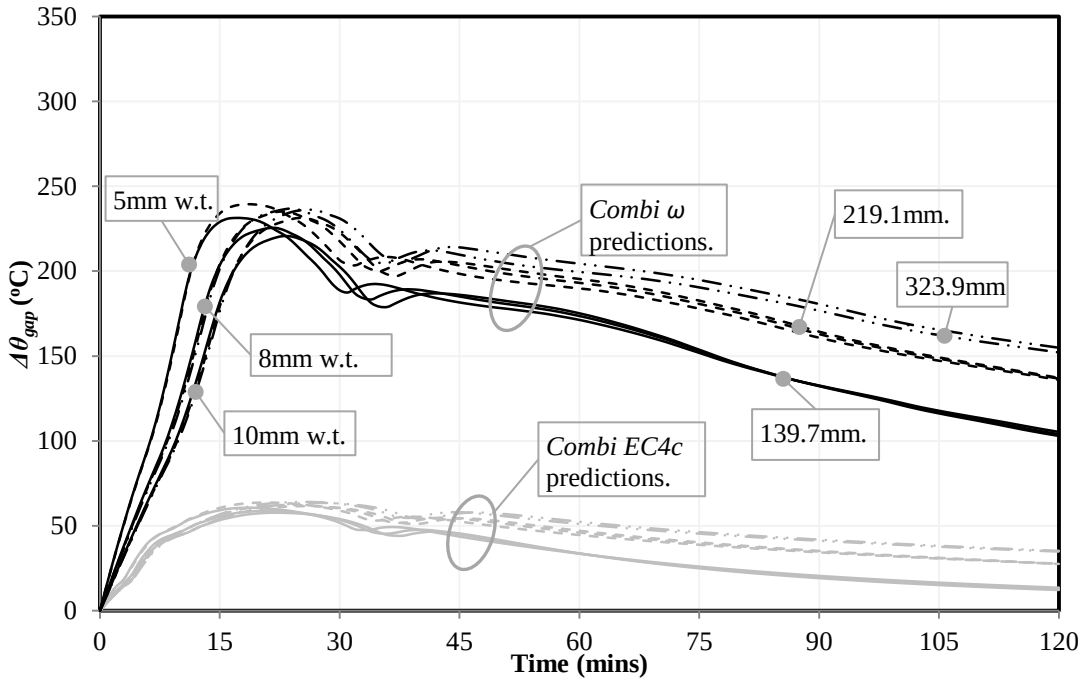

Figure 5-16: Predicted differential interface temperatures, $\Delta\theta_{gap}$, for CxxxIN sections using the *Combi EC4c* and *Combi ω* thermal modelling approaches

Figure 5-17 shows the differential gap temperatures, $\Delta\theta_{gap}$, observed during the first 16 minutes of heating. All three section sizes show similar increases in gradient for $\Delta\theta_{gap}$ at 8, 9, and 13 minutes for the C3xFIN, C2xFIN, and C1xxIN sections, respectively. This could indicate the point where the steel and concrete separate and a gap is formed due to differential thermal expansion. If this figure shows the time of gap formation, it makes sense that the C2xFIN, C3xFIN and S33FIN sections, with lower average concrete temperatures and thus a smaller degree of lateral thermal expansion, would experience an earlier separation of the steel tube and concrete core.

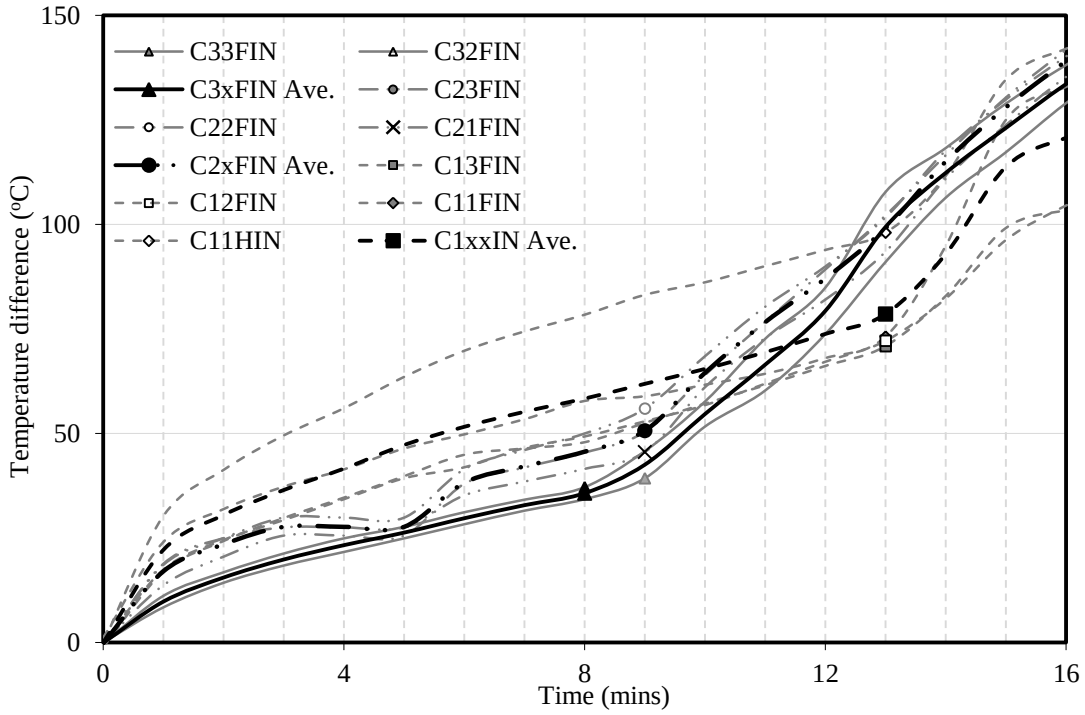

Figure 5-17: Differential interface temperatures, $\Delta\theta_{gap}$, for unprotected circular CFS sections during the first 16 minutes of heating

The effect of shape also impacts the heat transfer across the steel concrete interface. Figure 5-18 shows that for S11FIN the orthogonal (O) temperature difference was far greater than that observed on the diagonal (D). The orthogonal temperature difference was also greater than seen in the C3xFIN sections (Figure 5-15). For the S2xFIN sections, similar values to the C3xxIN sections are observed, apart from S23FIN (D) where greater temperature differences are observed most likely due to the positioning of the thermocouples. Again an increase in the rate of increase of temperature difference is observed at 7 to 8 minutes into heating, possibly indicating formation of the gap between the steel tube and concrete core. The predictions of the differential gap temperatures for the SxxFIN sections show similar levels of accuracy as for the CxxxIN sections for both the *Combi EC4c* and *Combi ω* thermal modelling approaches, and similar comments hold.

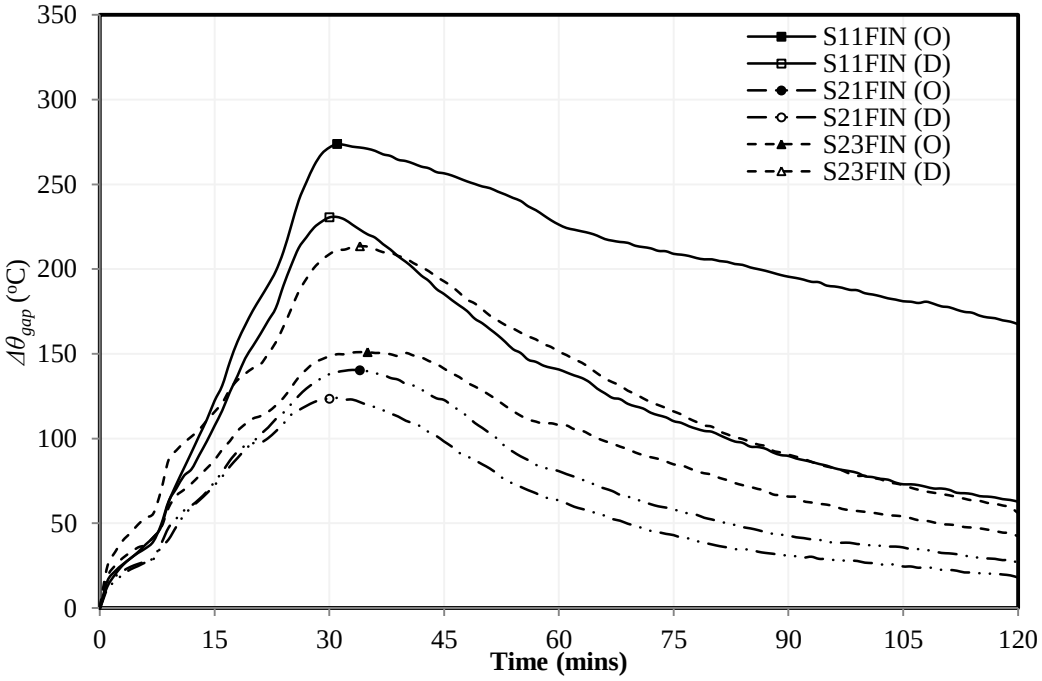

Figure 5-18: Comparison of the SxxFIN observed orthogonal (O) and diagonal (D) steel tube and concrete face differential gap temperatures, $\Delta\theta_{gap}$

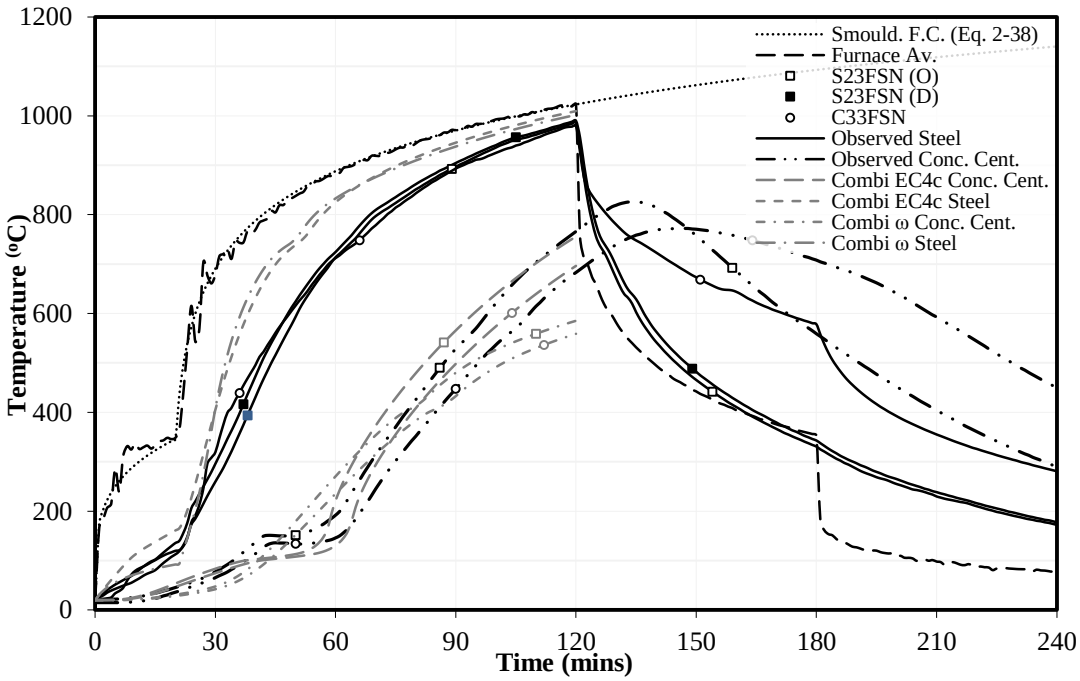

Figure 5-19: Observed and predicted temperatures of the steel tube and concrete centre for tests S11FSN and C11FSN

Influence of fire exposure

Two unprotected sections were exposed to the smouldering fire curve (Equation 2-38) for two hours, so that an assessment of the thermal modelling approaches when a different thermal insult is used could be made. C11FSN and S11FSN exhibited similar responses as previously exhibited in the sections exposed to the standard fire tests. The observed temperatures of the steel tube and at the centre of the concrete core are shown in Figure 5-19. The predictions of the steel and concrete temperatures showed similar inaccuracies as for the tests exposed to the ISO 834 standard fire.

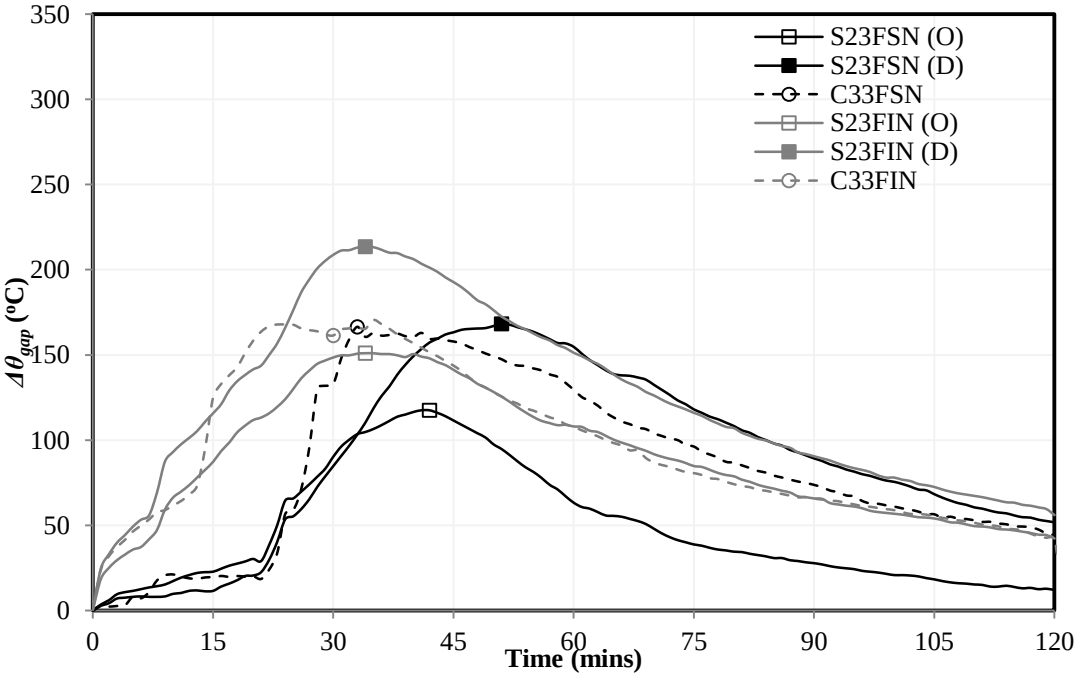

Figure 5-20: Comparison of differential gap temperatures, $\Delta\theta_{gap}$, under the smouldering and ISO 834 fire curves for S11xxN and C11xxN

When considering the temperature difference across the gap, similar post peak gradients were observed, with peak temperatures of slightly lower magnitude and occurring later as compared with ISO 834 heating due to the slow heating during the initial stages, thus reducing the thermal gradients within the cross-section and across the gap. Figure 5-20 shows that low differential temperatures were observed for the first 21 minutes of heating, coinciding with the change of heating rate in the

smouldering fire heating model (Equation 2-38). This is also likely due to delay the time to gap formation, as suggested by Figure 5-20.

5.2.2.2 Summary of the unprotected tests

The tests on unprotected CFS sections show that the size and shape of the section have impacts on the temperatures observed. As the size increases, the steel temperatures and temperatures throughout the concrete decrease, and there is an increase in the observed differential gap temperatures between the steel tube and concrete face temperatures for larger sections. The variation in measured temperatures at the different TC locations for the CxxxxN sections was within the bounds of error caused by inaccurate thermocouple placement, and the tests captured axisymmetric heating of the SxxFxN sections. Temperatures measured on the diagonals were consistently higher than those measured orthogonally due to the increases surface area exposed to the furnace temperatures near the corners of the square columns. The peak temperatures observed in the concrete were delayed due to the thermal mass of the concrete, with the C3xxxx and S3xxxx sections experiencing maximum temperatures well beyond the end of the heating phase. The addition of steel fibres had little effect on the heat transfer within the sections, and the effect of a different thermal insult reduced the temperatures observed but did not significantly alter the overall thermal response or the ability to model them.

The ability to predict the temperatures within the cross-section appears to be reasonably poor, with both of the best thermal modelling approaches from Chapter 3 not properly accounting for either the specific heat (including water vaporisation) or the thermal conductivity of the concrete. The inaccuracies in the concrete temperature predictions are influenced by the observed over-predictions of the steel temperatures found in both thermal modelling approaches, which indicates that the current furnace-to-steel tube heat transfer modelling approaches need refinement. Practically speaking, over-predictions in steel temperatures may result in design of greater thicknesses of protective coatings than is strictly necessary, unnecessarily increasing environmental and economic costs for protected CFS sections.

The introduction of a gap thermal resistance in the *Combi ω* approach improved the accuracy of the differential gap temperature predictions for the x3xxxx and C2xxxx sections, but did not predict the S1xxxx or C1xxxx nearly as well; the reasons for this remain unclear.

The current level of prediction of both concrete and steel temperatures appears to be leading to some of the inaccuracies and variability noted in the meta-analysis reported in Chapter 3. Further examination of the thermal properties of both steel and concrete, and interface interactions including the effect of gap formation and the steel tube to furnace interaction, is presented in Chapter 6 so that a statistically valid and safe thermal modelling approach can be developed to ensure accurate design of unprotected CFS columns in fire.

5.3 Temperatures in protected specimens

Intumescent paints, sometimes called reactive coatings, are the predominant form of fire protection for structural steel members in new build construction in the UK. However, there is a paucity of fire test data on CFS sections protected with intumescents. Available design guidance for the application of intumescent coatings is therefore necessarily conservative and can result in costly solutions when compared with unfilled steel sections whose thermal response and protection requirements are better characterised and supported by test data. To address this issue, 20 protected specimens were tested, as outlined in Table 5-1, where their protection thickness and type, concrete age and type, section size, shape, and wall thickness were all varied so that direct comparisons to the 14 unprotected tests could be made. The aim of these tests was to better understand the performance of intumescents when applied to CFS sections and to improve current design guidance for specifying the coating thickness and optimise its application.

5.3.1 Current guidance for specifying coating thicknesses

As described in detail in Chapter 2, the specification of thickness of intumescent fire protection coatings for CFS sections is based on defining a modified section factor for a hollow steel tube which accounts for the influence that the concrete infill has on the heat transfer within the section. The method accounts for the concrete core's

effect by artificially increasing the steel wall thickness and then calculating an "effective" section factor to account for the presence of the concrete core. Design is then based on the required fire resistance time and assumed steel tube limiting temperature, as would be the case for an unprotected or unfilled protected section. The effective section factors and dry film thicknesses (DFT) for the protected tests, based on a steel tube limiting temperature of 520°C and equivalent section factors determined in accordance with equations 2-10 and 2-11, are given in Table 5-6.

Table 5-6: Section factor determination and prescribed DFTs for the 20 protected CFS sections tested herein

Test No.	Size (b and h OR d)	Section factors (m^{-1}) (*Hp/A*)					Reactive Coating			
	(mm)	t_s (mm)	Steel tube	t_{ce} (mm)	t_{se} (mm)	CFS	Type[1]	DFT (mm)[2] Design	DFT (mm)[2] Applied	t_{FR}[3]
S33FIC1	300	10	103.45	17.17	27.17	40.47	1120	3.387	3.529	90
S33FIC2[a]	**300**	**10**	**103.45**	**17.17**	**27.17**	**40.47**	**212**	**2.94**	**3.106**	**90**
S11FIC1	120	5	208.70	16.98	21.98	55.70	1120	3.481	3.488	90
S11FSC1[b]	*120*	*5*	*208.70*	*16.98*	*21.98*	*55.70*	*1120*	*3.481*	*3.409*	*90*
C33FIC1a	323.9	10	103.19	17.63	27.63	39.57	1120	3.387	3.499	90
C33FIC1b	323.9	10	103.19	17.63	27.63	39.57	1120	3.387	3.603	90
C33FIC2[a]	**323.9**	**10**	**103.19**	**17.63**	**27.63**	**39.57**	**212**	**2.94**	**2.943**	**90**
C32FIC1	323.9	8	128.17	17.63	25.63	42.37	1120	3.434	3.480	90
C11HIC1	139.7	5	207.42	19.37	24.37	49.70	1120	3.481	3.529	90
C11FIC1	139.7	5	207.42	19.37	24.37	49.70	1120	3.481	3.509	90
C13FIC1	139.7	10	107.71	18.73	28.73	43.82	1120	3.481	3.528	90
C12FIC1	139.7	8	132.59	19.00	27.00	45.91	1120	3.481	3.515	90
C11FSC1[b]	*139.7*	*5*	*207.42*	*19.37*	*24.37*	*49.70*	*1120*	*3.481*	*3.533*	*90*
C21FIC1	219.1	5	204.67	19.48	24.48	45.99	1120	3.481	3.498	90
C23FIC1	219.1	10	104.78	19.96	29.96	38.67	1120	3.434	3.549	90
C22FIC1	219.1	8	129.74	19.78	27.78	41.22	1120	3.434	3.503	90
C11FIC1.14D[c]	139.7	5	207.42	19.37	24.37	49.70	1120	3.481	3.528	90
C11FIC1.28D[c]	139.7	5	207.42	19.37	24.37	49.70	1120	3.481	3.528	90
C11FIC1.75[d]	139.7	5	207.42	18.24	23.24	51.62	1120	2.1	2.00	75
C11FIC1.120[d]	139.7	5	207.42	20.97	25.97	47.30	1120	4	4.062	120

[1] protection type *1120*=InterChar1120, *212*=InterChar212, [2] DFT= dry film thickness, [3] t_{FR} = fire resistance time based on steel limiting temperature of 520°C,
[a] protection type tests, [b] tested under the smouldering fire curve, [c] concrete age tests of 14 and 28 days, [d] required fire resistance time tests

The DFTs specified for the CFS columns were selected so that the steel temperatures would remain below 520°C for at least 90 minutes of fire exposure to the ISO 834 (ISO, 1999) standard fire. Further temperature profile predictions for these tests are

difficult to produce. It is difficult to accurately record the temperature profile within an intumescent char due to its fragility and the way in which it forms, and published data are generally not available due to secrecy within the market and the fact that individual coating systems are unique in composition and response; general characterisation of the different available coatings is therefore not possible.

5.3.2 Results and observations for protected specimens

Table 5-7 shows selected results from tests on protected CFS sections and shows the observed temperatures at the steel tube, concrete face, 35 mm depth and concrete centre TC locations, after 30, 60, 90, and 120 minutes, as well as the observed maximum temperatures and times. These are shown for specimens protected with:

1) InterChar1120 (thin film intumescent paint coating – C1) tested under;
   a) ISO 834 fire curve (Equation 2-37); where
      i) ten circular section tests including one repeat (CxxxIC1 (a/b)),
      ii) two square section tests (SxxFIC1),
      iii) two concrete age tests (C11FIC1.xxD) (underlined sections in Table 5-7),
      iv) two tests to assess the required protection time used in DFT selection to the limiting temperature of 520^{o}C (C11FIC1.xxx) (grey sections in Table 5-7), and
   b) the Smouldering fire curve (Equation 2-38) (x11FSC1) (italic font in Table 5-7), and
2) InterChar212 (epoxy resin intumescent coating – C2, bold sections in Table 5-7) tested under the ISO 834 fire (x33FIC2).

Table 5-7 shows that only two of the protected sections reached the limiting steel temperature of 520^{o}C during the two hours of heating, in one case one because it was protected with a thinner DFT designed for only a 75 minute F.R. time, and in another case because it had a 120 minute fire rating time but was heated for 180 minutes. Table 5-7 also shows that coating C1 consistently provided fire protection, regardless of section size, up to 30 minutes (assuming the same prescribed F.R.) with steel tube temperatures being within 25^{o}C of each other for all sections heated in the same furnace. It is interesting to note that sections x11FSC1, C11FIC1.xxD, and

C11FIC1.xxx were tested in the cube furnace, whereas all other tests took place in the floor furnace, and there was a distinct difference in the thermal responses to the "same" imposed gas phase temperature-time curve; the cube furnace produced higher specimen temperatures for similar CFS sections (e.g. C11FIC1 and C11FIC1.28D).

The reasons for this difference are not known however this is a widely quoted problem with all standard furnace testing (see Harmathy and Lie (1970) for instance). Several factors are known to influence the heat transfer to a test specimen in a furnace, including: the size, shape and lining of the furnace (Torero, 2012; Welch and Rubini, 1997); the fuel used and thus the emissivity of the gas and the flame luminosity (Torero, 2012); the temperature control of the gas (Cooke, 1994; Sultan, 2006; Welch and Rubini, 1997; Wickstrom, 2011); and the thermal properties of the materials being tested. Whilst not the focus of the current project, it is recommended that additional research on heat transfer in standard fire testing furnaces is carried out so that predictions of heat transfer to specimens in a controlled furnace environment can be accurately made (e.g. Maluk et al., 2012).

The peak temperatures in the steel of the C11xxC1 sections occurred at about 180 minutes, as compared to 120 minutes in all other sections, this is due to the gas extraction in the furnace being turned off coincident with the gas supply in these tests, whereas in the other tests the hot gas extraction remained on during cooling. It was also observed that after the columns had been removed from the furnaces and allowed to cool, those with their protective char intact were warm to the touch more than 24 hours after heating had concluded; the char layer not only prevents the heating of the specimens during fire but also slows cooling. This could affect the columns' post-fire residual strength capacity, since the longer the concrete core is at hot (e.g. above 300^{o}C) the greater the damage suffered (The Concrete Society, 2008).

Table 5-7: Selected observed temperatures of protected CFS sections after 30, 60, 90, and 120 minutes of heating, for the steel tube, concrete face, 35 mm, and concrete centre thermocouples

Test	Size	W.T.	Steel (°C)						Concrete face (°C)						35 mm depth (°C)						Centre (°C)					
	(mm)	(mm)	30	60	90	120	Max	Time	30	60	90	120	Max	Time	30	60	90	120	Max	Time	30	60	90	120	Max	Time
Protected circular sections exposed ISO 834 standard fire (Equation 2-37)																										
C33FIC1a	323.9	10	122	168	204	244	244	120	94	132	166	200	200	128	58	91	124	153	160	146	22	37	60	86	145	238
C33FIC1b	323.9	10	125	168	206	246	246	120	92	128	163	196	199	127	57	89	120	149	158	143	21	36	57	80	143	239
C32FIC1	323.9	8	131	171	202	238	239	122	91	126	159	188	192	128	57	89	120	148	156	138	21	34	54	76	139	236
C33FIC2	**323.9**	**10**	**202**	**250**	**317**	**397**	**398**	**121**	**129**	**182**	**223**	**300**	**310**	**129**	**75**	**127**	**156**	**186**	**224**	**169**	**21**	**40**	**70**	**109**	**160**	**240**
C23FIC1	219.1	10	124	169	210	254	255	122	91	132	169	204	209	131	66	104	141	167	181	177	36	71	107	142	166	216
C22FIC1	219.1	8	126	168	204	275	285	128	99	139	176	235	251	135	69	109	145	207	245	150	39	76	114	136	203	239
C21FIC1	219.1	5	132	177	230	283	283	120	102	145	188	233	234	124	67	107	145	175	181	165	37	71	109	147	170	167
C33FIC1	139.7	10	133	187	247	320	375	183	116	158	206	272	358	189	88	138	147	212	350	217	79	132	140	170	349	226
C32FIC1	139.7	8	132	190	259	350	389	182	118	172	242	332	387	183	101	139	193	277	373	187	106	124	180	254	361	195
C31FIC1	139.7	5	140	197	264	366	403	181	123	174	237	333	397	183	90	130	178	259	380	191	74	118	137	169	340	228
C31HIC1	139.7	5	125	175	234	311	348	182	111	154	203	272	337	183	77	127	154	186	319	204	67	119	141	166	317	216
Protected square sections exposed to ISO 834 standard fire (Equation 2-37)																										
S33FIC1	300	10	118	160	193	230	230	123	79	110	140	173	176	132	44	71	99	130	150	218	21	35	57	82	140	238
			133	182	228	275	275	120	101	145	180	219	220	125	71	110	143	169	172	139						
S33FIC2	**300**	**10**	**207**	**256**	**317**	**398**	**398**	**120**	**126**	**174**	**225**	**289**	**299**	**129**	**67**	**115**	**151**	**179**	**220**	**190**	**20**	**40**	**82**	**109**	**159**	**239**
			226	**306**	**387**	**484**	**484**	**120**	**167**	**242**	**319**	**408**	**410**	**122**	**93**	**150**	**191**	**250**	**280**	**144**						
S11FIC1	120	5	136	194	241	316	317	121	112	166	210	267	283	179	82	138	171	191	281	211	76	133	169	180	281	216
			134	192	243	311	311	122	123	176	225	288	296	126	89	141	173	205	281	205						
Protected square and circular sections exposed to smouldering curve (Equation 2-38)																										
C11FSN	*139.7*	*5*	*125*	*178*	*250*	*352*	*380*	*163*	*110*	*160*	*227*	*326*	*375*	*179*	*100*	*144*	*204*	*302*	*368*	*182*	*100*	*139*	*202*	*300*	*366*	*180*
S11FSN	*120*	*5*	*116*	*173*	*241*	*390*	*396*	*122*	*103*	*156*	*210*	*332*	*349*	*127*	*74*	*127*	*171*	*192*	*320*	*179*	*69*	*123*	*168*	*186*	*322*	*178*
			119	*182*	*283*	*472*	*472*	*120*	*110*	*167*	*243*	*414*	*417*	*121*	*80*	*133*	*174*	*203*	*317*	*179*						
Protected circular sections exposed to ISO 834 standard fire (Equation 2-37) (age and protection thickness tests)																										
C11FIC1.14D	139.7	5	141	203	272	386	404	125	122	176	241	343	371	133	97	148	201	277	365	214	89	152	202	266	365	214
C11FIC1.28D	139.7	5	161	231	319	458	470	126	142	210	297	432	452	130	112	179	275	402	435	137	106	174	261	394	432	138
C11FIC1.75	139.7	5	184	324	461	603	608	121	150	251	381	531	542	136	106	142	251	390	509	186	90	126	179	326	514	198
C11FIC1.120	139.7	5	149	200	270	387	620	183	129	176	242	343	579	197	80	138	156	214	576	252	77	136	151	192	525	252

(a) (b) (c)

Figure 5-21: Post burn intumescent coating reaction of (a) C11FIC1, (b) C11FIC2, and (c) C22FIC1 (split)

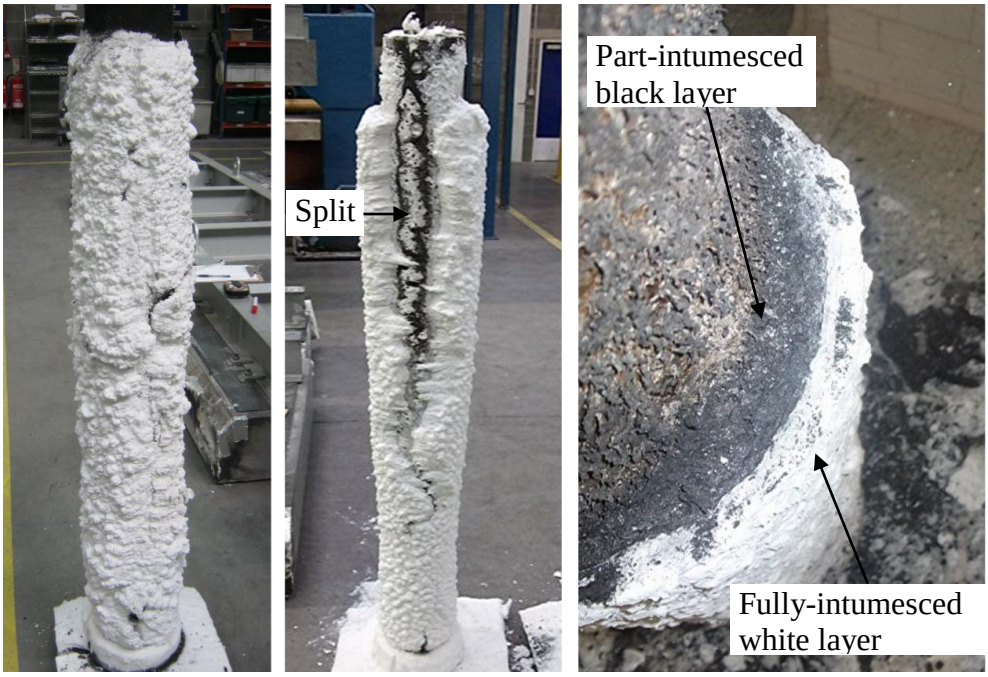

(a) (b) (c)

Figure 5-22: Post burn intumescent coating reaction of (a) C33FIC1.120, (b) S23FSC1 and (c) cut through char of C21FIC1

In comparing the temperatures observed in columns S11FIC1 and S11FSC1, the temperatures observed in smouldering fire tests were higher than in those exposed to the ISO 834 fire. This is due to longitudinal splitting of the fire protection under smouldering fire in S11FSC1 (Figure 5-22(b)). This also occurred for C22FIC1 (Figure 5-21(c)) allowing localised heating of the steel tube and thus slightly raising the overall temperatures. Figure 5-21 also shows the differences in the appearance of the two reacted coatings used on tests C22FIC1 and C22FIC2 (Figure 5-21(a) and 5-20(b), respectively).

Figure 5-22 also shows the reacted coating on test C11FIC1.120, which shows an uneven reaction as compared to the same coating on larger sized sections, and also shows a cut through the reacted coating. Two layers of char are evident, a fragile fully intumesced white layer and a part-intumesced firmer black layer. This black layer was only present in any quantity on the x3xFIC1 and C2xFIC1 sections, whereas the C1xxxC1 sections showed only the fragile white char layer with a very thin black layer. This shows that the protective coatings are not fully reacting on the x3xFIC1 and C2xFIC1 sections, and are thus not using the full potential of a reacted intumescent char. This indicates that the applied thicknesses may be too great, however the applied DFTs are based on a minimum thicknesses required to ensure char integrity, rather than maximum steel temperatures after 90 minutes. Char integrity is important for plain steel sections (on which the applied DFTs are based), where if the char were to become unstuck from the section the temperatures within the steel can rise quickly and failure can occur as the steel is resisting the entire applied load. The char integrity is less important in CFS sections as the concrete core resists a portion of the applied load and so steel temperatures are less critical.

5.3.2.1 Temperatures within protected CFS columns

The temperatures observed within the protected CFS columns were, as expected, significantly lower than those observed in the unprotected tests, clearly confirming that the protective coatings are extremely effective at limiting the amount of heat transfer into the specimens. The intumescent coating, C1, started to react at temperatures of about 100^{o}C, as shown in Figure 5-23. There was a steep initial increase in steel temperatures during the initial 10 minutes of heating followed by a

drastically reduced rate beyond 100°C. This reaction is evident in all of the specimens, as shown in Figure 5-24 where for coating C1 the lower rate of heating begins when the steel is approximately 100°C whereas for coating C2 the lower rate of heating begins at higher steel temperatures in the range of approximately 180°C. This was expected based on data provided by the paint supplier.

The observed temperatures, whilst being affected locally by splitting of the coatings in some cases, were not obviously affected overall as shown in Figure 5-23, which shows the response of specimen C22FIC1 with the steel and concrete face temperatures in the vicinity of the split shown in grey and the average temperatures at each layer (excluding the split temperatures) shown in black. The temperatures at the split exceed the 520°C limiting temperature at about 110 minutes, well beyond the 90 minute design F.R.; however the temperatures of the steel tube away from the split are only 200°C at 90 minutes, and a maximum of 285°C after 128 minutes.

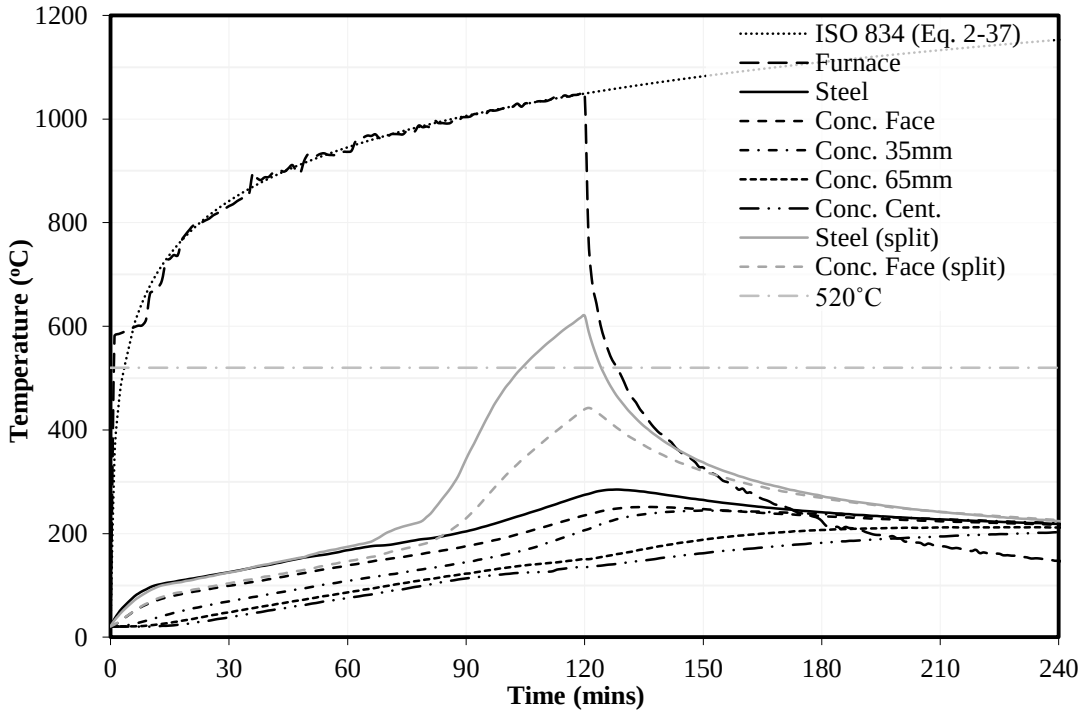

Figure 5-23: Representative temperatures within a protected CFS section under ISO 834 standard fire exposure (C22FIC1)

Steel tube temperatures

The steel tube temperatures observed for the specimens protected with coating C2 were between 170-250^{o}C higher after 120 minutes than their C1 coated counterparts, however still well below the design temperature of 520^{o}C. The steel temperature trends observed in the unprotected tests for other column parameters are also evident in the protected tests. The steel tube temperatures increased as the section size decreased, diagonal corner temperatures of square specimens were higher than those observed orthogonally, and the orthogonal square temperatures were equivalent to the temperatures observed in the steel of the circular sections with equivalent heated perimeter to total cross-sectional area ratios.

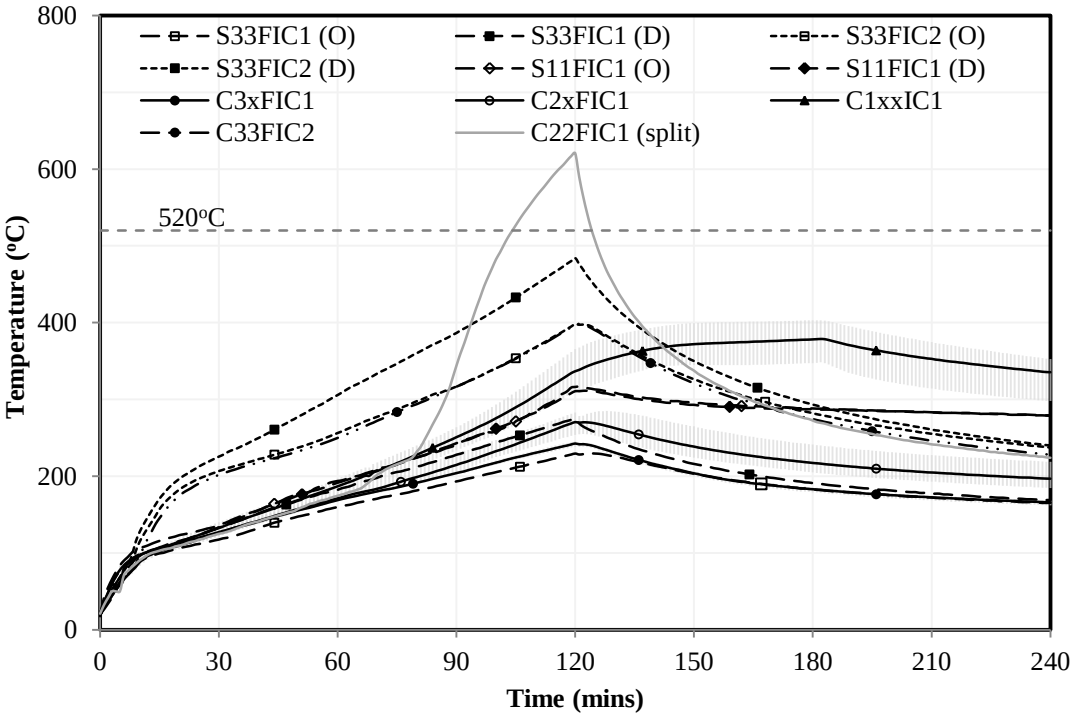

Figure 5-24: Observed protected test steel temperatures with a design F.R. of 90 minutes to 520^{o}C for both C1 and C2 coating types

Figure 5-24 shows that the steel temperatures after 90 minutes were considerably lower than the design temperature of 520^{o}C, between about 180-250^{o}C for all columns with the C1 intumescent coating; this indicates a very conservative design for the applied protection based on current guidance. The variation in temperatures for the same sized cross-sections with different wall thicknesses are shown again

with error bars for the CxxxxC1 sections. The observed temperatures show that as the steel tube thickness increases, the steel temperatures decrease, an opposite trend seen in the unprotected tests, and could be due to local variations in applied DFTs of the intumescent coating. The low temperatures observed are affected by the coarseness and conservatisms in the design tables used; and significantly by the conservative effective section factor equations 2-10 and 2-11 used to specify DFTs.

Concrete temperatures

The temperatures experienced at the concrete face TCs are very similar to those of the steel tube due to the slowed thermal response of the steel caused by the insulating effects of the protective coating. The differetial temperatures between the steel and concrete face temperatures for the protected sections are thus significantly lower (seen in Figure 5-25) than those observed in the unprotected tests (e.g. Figure 5-15). The temperature difference at the steel-concrete interface in the protected cases remains fairly constant after the intumescent reacted, with temperature differences less than 50^{o}C and 100^{o}C for the C1 and C2 coatings, repectively, apart from in the region near the split in the coating in test C22FIC1 where after the split occured the temperature differences increased dramatically to levels similar to those seen in the unprotected tests. The low temperature differences observed at the steel-concrete interface suggests gap formation did not occur at the lowered heating rate and that the differences observed are likely due solely to the approximate 2.5 mm depth of the concrete face thermocouple within the concrete core. The higher temperature differences experienced for the C2 coating are due to the higher steel temperatures experienced, caused by the higher intumecent reaction initiation temperature required for this specific reactive coating, and perhaps the formation of a small air gap. The concrete TCs showed the same overall response in the protected tests as seen in the unprotected tests, with plateaus in temperature between 100 and 180^{o}C indicating evaporation of moisture from the concrete, as shown in Figure 5-26.

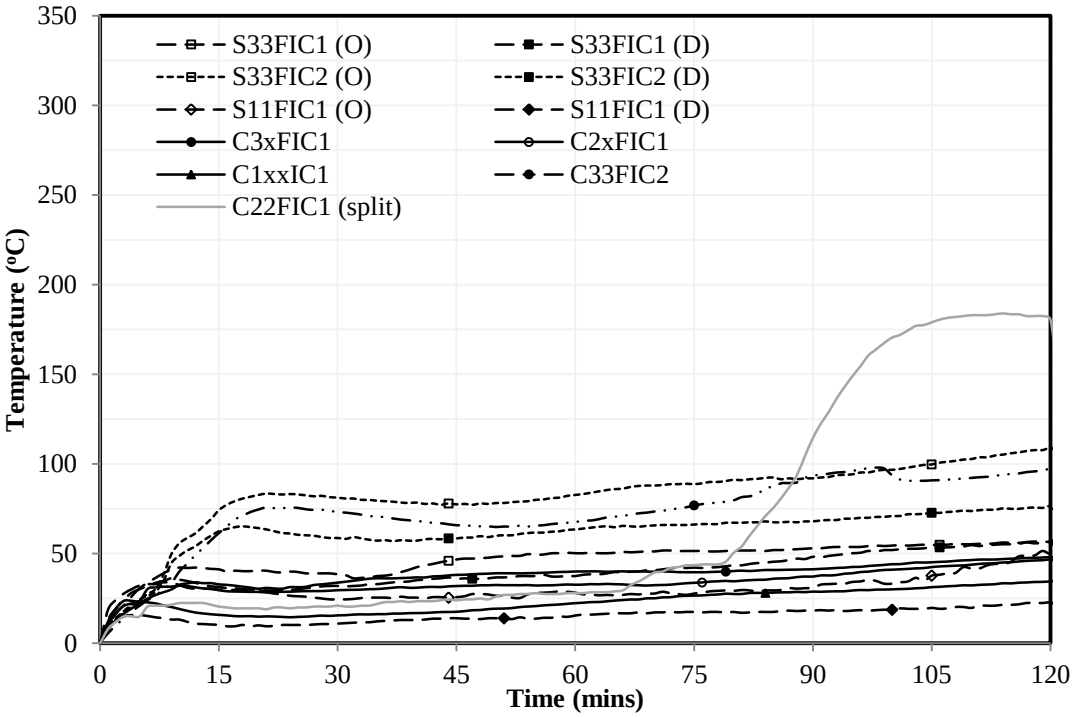

Figure 5-25: Observed differential gap temperatures for the protected tests

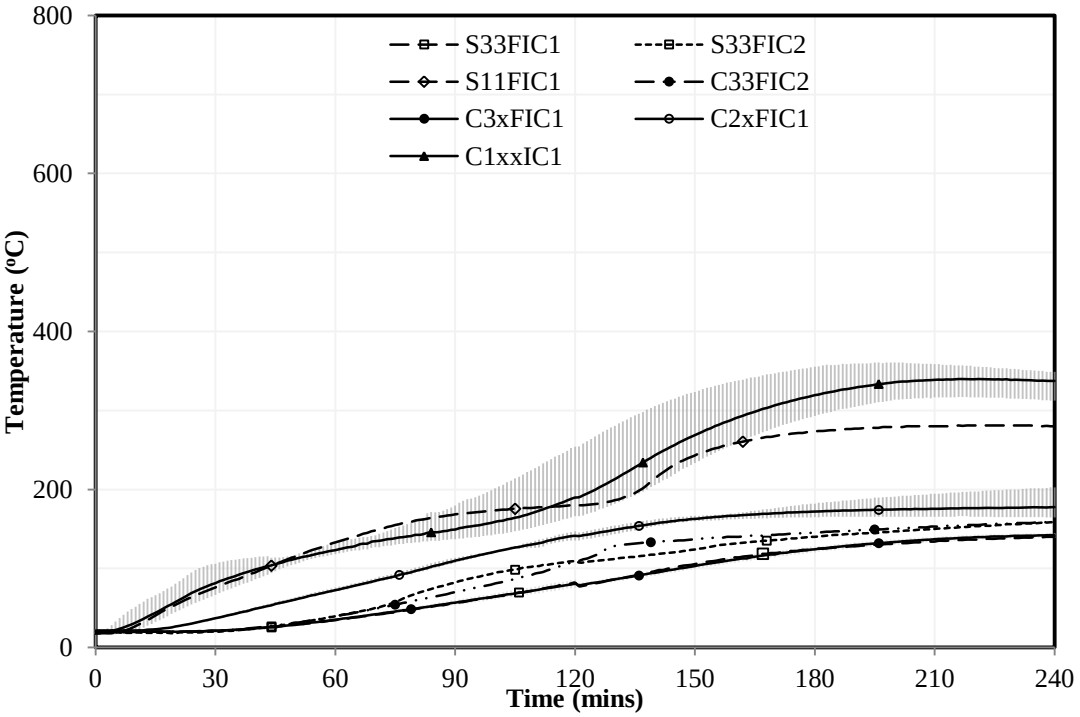

Figure 5-26: Observed average temperatures at the concrete centre TCs for the protected tests

The concrete centre temperatures in the x3xxxx sections were still increasing after 240 minutes, and similar temperatures were seen in sections with similar heated perimeter to total cross-sectional areas (i.e. S33FIC1/2 (O) and C3xFIC1/2). The data for the C1xxxC1 sections show considerable variation, similar to that seen previously in Figure 5-14 for the unprotected sections. Again, this is likely due to the difficulties experienced in the placing of the concrete and the potential for disturbance of the TCs.

Influence of fire exposure

For the safe application of the reactive coatings they need to be assessed under different possible fire exposures to ensure consistent physical evolution and hence thermal protection are observed. This is particularly important for performance-based designs where non-standard heating regimes are applied which are specific the design problem. Figure 5-27 shows the observed temperatures for the steel tube and concrete centre TCs for the two protected tests heated using the smouldering fire (Equation 2-38). It can be seen in the observed response of the square column that the temperatures increased quickly after 75 minutes, indicating a split in the intumescent coating (as seen in Figure 5-24); however the average temperature of the steel remained below 520^{o}C. The observed temperatures were similar to those recorded in tests under the ISO 834 standard fire curve (Equation 2-37) which is surprising given that the smouldering fire curve has lower temperatures at the same instance in time. This is likely due to the different furnaces used in the tests, as previously discussed.

Similar thermal response within the concrete was observed in these tests as was seen in the unprotected tests in Figure 5-19; however with markedly lower temperatures. The steep rise in concrete centre temperatures for S23FSC1 after 120 minutes was due to the splitting of the protective coating at approximately 80 minutes.

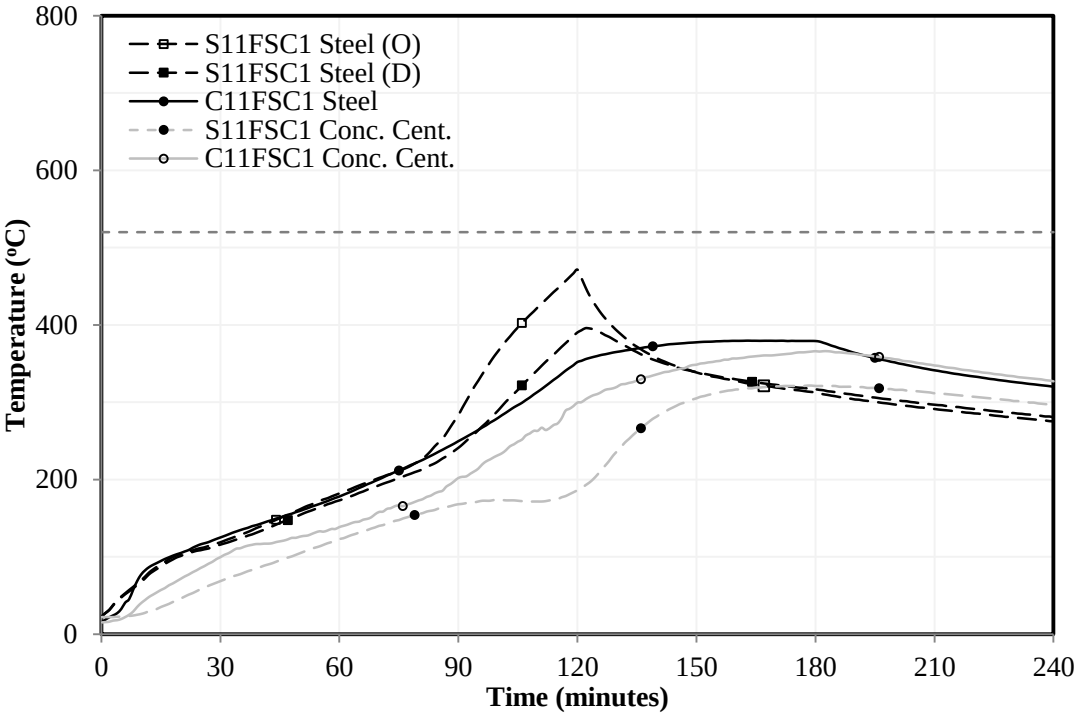

Figure 5-27: Observed average steel and concrete centre temperatures in the protected smouldering tests

Influence of concrete age and protection thickness

Intumescent paint suppliers who are wishing to demonstrate the use of their products on CFS sections require guidance on the required duration of curing to allow the concrete core to cure and fix water within the cement paste, so that a realistic thermal response can be observed within the concrete and thus for the intumescent product. Figure 5-28 shows the temperatures observed at the steel tube and concrete centre TCs for the two concrete age tests, C11FIC1.14D and C11FIC1.28D, where the concrete was allowed to cure for only 14 and 28 days, respectively.

The 14-day old concrete shows lower temperatures after 120 minutes at the steel tube and concrete centre thermocouples of 70^{o}C and 120^{o}C, respectively. This is due to the greater amount of free water available in the younger concrete which consumes a large amount of energy as it evaporates. The temperatures observed in the 28-day old concrete test are greater than those seen in the tests performed after 13 months as seen in Table 5-7, although it was expected to see slightly higher temperatures in the tests conducted after 13 months. This is again due to the different furnaces used. It is

generally known that after 28-days the majority of the free water has been fixed by the cement paste within the concrete, so 28 days should be the minimum curing time for concrete for fire testing of CFS sections; however additional testing in the same furnace is recommended to confirm that this is appropriate.

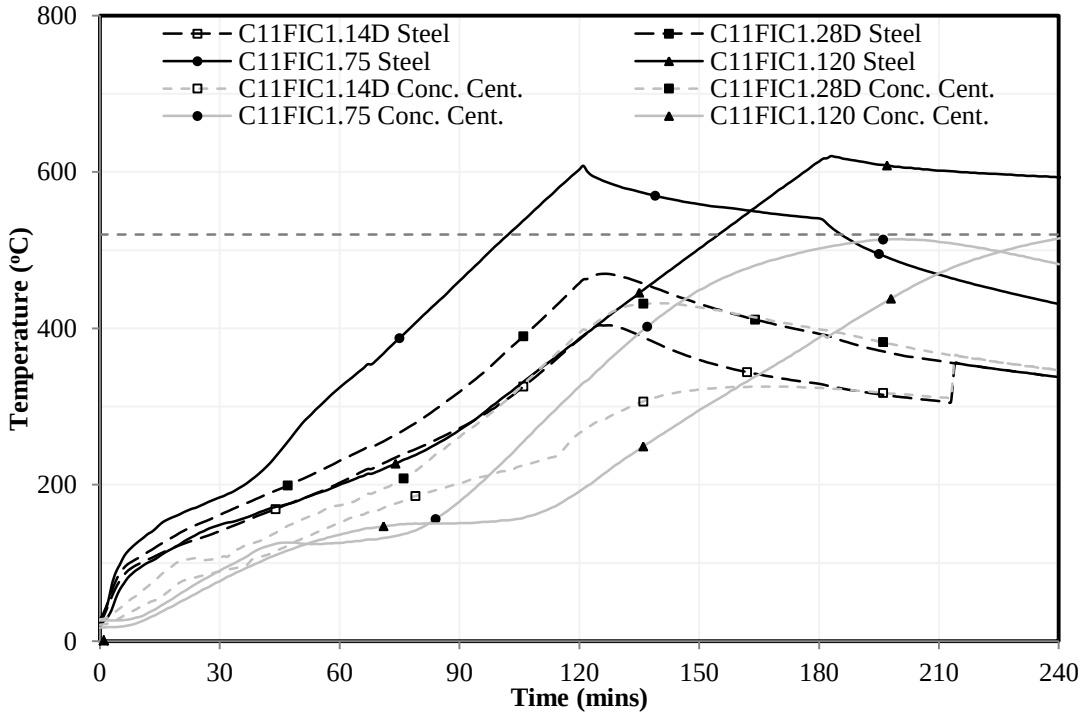

Figure 5-28: Observed average steel and concrete centre temperatures of the protected concrete age and protection thickness tests

Figure 5-28 also shows the tests used to assess the performance of different thicknesses of the protection based on the required protection time of 75 minutes (C11FIC1.75) and 120 minutes (C11FIC1.120), again with a limiting steel temperature of 520°C. These tests are useful in assessing the consistency of the protection material at different thicknesses and understanding the thermal response of the steel and concrete for different thermal response of the coating. The temperatures experienced by the steel after the required protection time in test C11FIC1.75 and C11FIC1.120 (i.e. either 75 or 120 minutes) were 388 and 387°C respectively, compared to the 90 minute fire protection time tests in which the temperatures were approximately between 200-260°C at 90 minutes (Figure 5-24). Again, and rather frustratingly, this is thought to be due partly to the different testing

furnaces used. Both fire protection thickness tests had peak temperatures just over 600^{o}C at the end of the heating phase of the tests (120 and 180 minutes respectively) and reached the design limiting temperature of 520^{o}C at 103 minutes and 155 minutes, respectively, approximately 30 minutes after the design F.R. in both cases.

5.3.2.2 Summary of the protected tests

The protected tests have shown that the intumescent coatings used are very efficient in protecting CFS columns, with the majority of tests not reaching the limiting temperature of 520^{o}C after the design F.R. of 120 minutes; 30 minutes longer even than the protection thicknesses had been designed for. Only two of the tests exceeded the limiting temperature of 520^{o}C; however at approximately 30 minutes after the designed fire resistance time. Some of the tests experienced cracking and splitting of the protective char layer, but with only localised effects on measured temperatures with the rest of the cross-sections remaining relatively unaffected on the basis of the limited temperature measurements.

The much lower than expected temperatures for the protected sections clearly indicate that either there are large conservatisms within the prescription and design of the required thickness of fire protection for these specific coatings, or alternatively that the filling of the steel tube with concrete fundamentally changes the thermal response of the coatings. An analysis of the performance of the intumescent on both filled and unfilled sections, as well as the determination of the effective section factor, is presented and discussed in Chapter 6.

5.4 Chapter summary

In this chapter 34 thermal tests have been presented, examining the effects that the sectional properties of the specimens have on the heat transfer within both unprotected and protected concrete filled hollow steel sections. Predictions for the unprotected tests showed that the two most statistically accurate thermal modelling approaches found in Chapter 3, used in the overall prediction of fire resistance time, do not accurately predict the temperature profiles observed in the cross-sections.

The tests showed that the size and shape of the section have an effect on the temperatures observed, with larger sections experiencing lower temperatures and square sections experiencing higher temperatures at their corners due to the increased heated surface area at the corners, as expected. The difference in temperature between the steel and concrete face is also affected by the size of the section, with greater temperature differences seen in the larger sections as these sections have larger concrete cores and thus a greater thermal mass that absorbs energy, reducing the concrete temperatures near the face and promoting the formation of a larger air gap. The inclusion of steel and polypropylene fibres within the concrete mix makes no obvious difference in the heat transfer within the section compared to the same concrete mix without fibres.

The ability to predict the temperatures across the cross-section needs refining in general. The steel temperatures were over-predicted whereas the heat transfer through the concrete was under-predicted, with larger sections being more severely under-predicted. The ability to predict the heat transfer at the steel concrete interface also needs refining. The assumption of perfect contact prescribed in EC4 does not predict the difference in temperatures observed whereas the interface interaction models used in Chapter 3 are able to predict the maximum differences for the x3xxxx sections but over-predict the differences for the x1xxxx sections, as well as not being able to match the profiles observed due to over-predicted steel temperatures. An improved thermal modelling approach is presented in Chapter 6.

The protected tests showed similar trends observed in the unprotected tests, with larger sections experiencing lower temperatures. The design thickness of the applied coatings were seen to be excessive, as the temperatures observed were consistently lower than expected at the specified fire resistance time, well below the design temperature of 520^{o}C, and remaining below 520^{o}C for at least 30 minutes after the required fire resistance time. An assessment of where the conservatism arises is presented in Chapter 6. Of the 20 protected tests performed, only a few experienced any cracking or splitting of the intumescent protective char, which had a local detrimental effect on the protective ability of the coating, whilst the overall temperatures remained below the limiting temperature. The age of the concrete was

also seen to be important in thermal response observed, with 14-day old CFS sections experiencing lower temperatures than those in which the concrete was at least 28-days old; this is therefore recommended to be the minimum length of time to allow the concrete to cure in certification tests and better represents the concrete seen in a real fire scenario in a real building.

Chapter 6: Design of CFS columns in fire

Chapter 5 showed that; (a) the ability to predict temperatures within unprotected CFS sections is relatively poor due to (i) poor assessment of heat transfer from the furnace to the steel tube and (ii) poor assessment of heat transfer within the concrete and (iii) poor assessment of the thermal conductance of the air gap which forms in some sections, particularly under rapid heating, and (b) that our ability to provide protection in the form of intumescent paints using current deign guidance results in protection which is overly conservative and therefore inefficient. This chapter examines available design guidance and seeks to improve the ability to predict temperatures within CFS sections during furnace tests and thus the ability to rationally design CFS columns for fire. It also provides guidance on the design of intumescent paint protection for protected CFS sections.

Predictions of temperatures within CFS sections made in Chapter 5 were executed using the *Combi EC4c* and *Combi ω* modelling approaches developed in Chapter 3. By comparison with the detailed test data presented in Chapter 5 it was found that these models over-predict the steel temperatures and under-predict the temperatures within the concrete core. These prediction errors are a likely contributor to the imprecision seen in the meta-analysis of the EC4 Annex H approach (CEN, 2005) in Chapter 3. This chapter investigates whether an improved modelling approach improves temperature predictions in CFS columns, and then applies this to the database from Chapter 3 to determine if this improves the predictive ability of the Annex H design approach. This chapter also assesses possible causes of the conservatism evident in the prescription of intumescent paint thicknesses in Chapter 5, and provides guidance for the determination of limiting temperature for the design of protected CFS sections and the fire resistance design of protected CFS sections.

6.1 Analysis and design of unprotected CFS sections

To suggest a rational modelling approach for prediction of temperatures within unprotected CFS sections, a systematic assessment of thermal properties and thermal interactions was performed, using the results from the test on unprotected CFS section C22FIN as an exemplar. This test specimen was a 219.1 mm ∅ circular tube

with 8 mm wall thickness, 1400 mm in length, filled with FIB concrete, and exposed to the ISO 834 fire (ISO, 1999) for 120 minutes.

The temperature of the steel tube in a CFS section during fire is dependent on the amount of heat transfer to the steel tube from the furnace and the amount of heat it then transfers into the concrete core through the steel-concrete interface, which is affected by the formation of an air gap and by the rate of heat transfer through the concrete. To predict the initial heat transfer from the furnace to the CFS section, accurate interface and concrete properties are required. Using a forensic assessment of the recorded temperatures presented in Chapter 5, the appropriate concrete thermal properties were first determined, followed by the appropriate steel-concrete interface thermal properties, and lastly the appropriate steel-furnace thermal interaction. The results of the forensic assessment are presented in the reverse order to how they were determined as the critical first step in the heat transfer, and thus calculation of the entire thermal profile, is to ascertain the heat transfer to the steel tube from the furnace.

6.1.1 Heat transfer to the steel tube

The heat transfer from the furnace environment to the steel tube is the first, critical step in the prediction of the temperatures within the cross-section. The tests reported in Chapter 5 showed that the observed temperatures in the steel tubes were considerably lower than those predicted using either the *Combi EC4c* or *Combi ω* modelling approaches. The *Combi EC4c* modelling approach employs the emissivities of the fire ($\varepsilon_{m,fi}$ = 1.0) and steel ($\varepsilon_{m,a}$ = 0.7) proposed in EC1 (CEN, 2009c), whilst the *Combi ω* modelling approach employs the NRCC quoted values of furnace emissivity ($\varepsilon_{m,fi}$ = 0.75), and Bentz et al.'s (2009) temperature dependent steel emissivity (given in Figure 2-5). As shown in Figure 6-1, these two modelling approaches (*Combi EC4c** and *Combi ω** employ the concrete thermal properties and steel-concrete interface properties found in sections 6.1.3 and 6.1.2, respectively) consistently over predict the temperatures observed in the steel when the measured gas phase temperatures measured during the Chapter 5 tests are applied to the model.

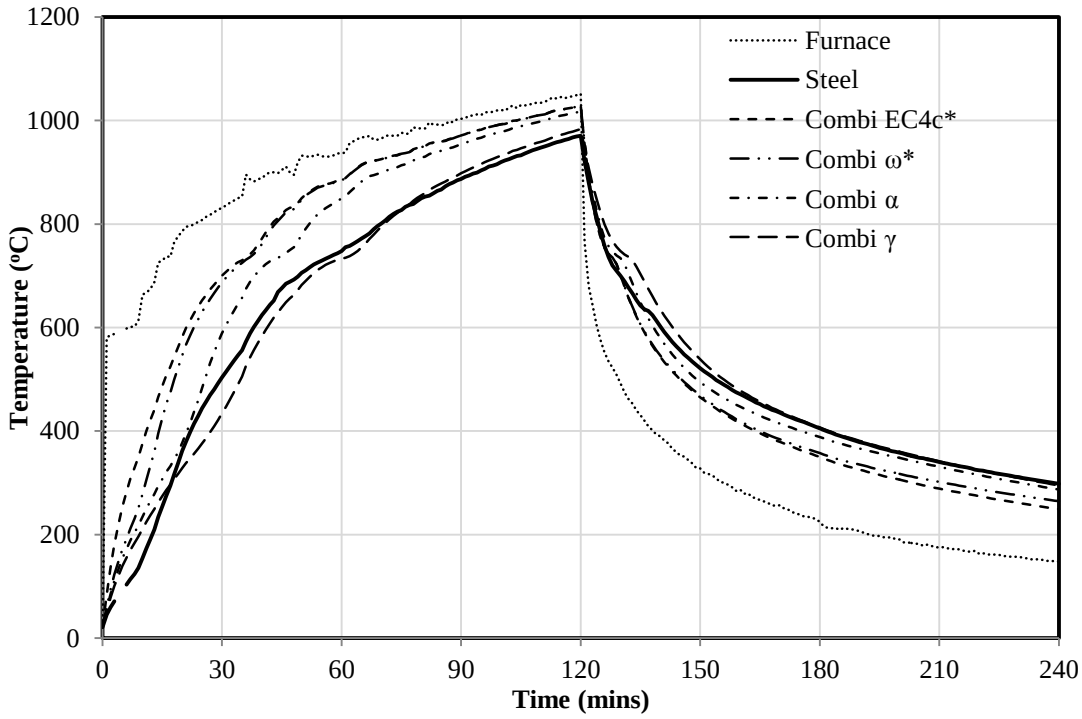

Figure 6-1: Observed and predicted steel temperatures using different modelling approaches (emissivity combinations)

Figure 2-5 also presented a temperature dependent steel emissivity suggested by Paloposki and Liedquist (2005). When this steel emissivity relationship is employed in the *Combi α* modelling approach in place of that of Bentz et al. (2009), the temperatures are still over-predicted in excess of 100^{o}C in some cases. To better match the observed temperatures, a furnace emissivity, $\varepsilon_{m,fi}$, of 0.38 was required along with Paloposki and Liedquist's (2005) temperature dependent steel emissivity, giving the *Combi γ* modelling approach shown in Figure 6-1, which very closely follows the observed response for test C22FIN. A furnace emissivity of 0.38 is slightly higher than the emissivity of a clean gas which is thought to be between 0.2-0.3 (Torero, 2012), and could be higher to account for the additional radiation from the furnace walls. This is vastly different to what can be observed in real fires where emissivities of black smoke can be 0.8 (Torero, 2012), which the Eurocodes conservatively assumes to be unity.

There is a fundamental lack of understanding in how heat is transferred differently in testing furnaces as compared to real fires, to structures, however with the use of

appropriate conservative assumptions on the heat transfer to the structures from the fire environment, safe design can be made. More work is recommended to optimise these assumptions so that optimised fire resistance designs can be produced.

6.1.2 The influence of an air gap

As mentioned in the preceding chapters, a key issue in the heat transfer within CFS sections is the effect of air gap formation and the resulting thermal conductance at the steel tube to concrete core interface. The Annex H approach of EC4 (CEN, 2005) assumes perfect contact between the steel tube and concrete core, which, as demonstrated in Figure 6-2, fails to predicted the observed temperature difference ($\Delta_{gap,\theta}$) between the steel tube and concrete face temperatures (assumed to be at a depth of 2.5 mm in the core) when the observed steel temperatures are applied to the steel elements in the cross-section heat transfer model (Region D) from Figure 5-6, and the concrete properties developed later in Section 6.1.3.

Figure 6-2 also shows the prediction of the differential gap temperatures, ($\Delta_{gap,\theta}$), when the gap conductance model proposed by Ghojel (2004) is applied at the steel-concrete interface, and there is a marked improvement in the predicted differential gap temperatures with a maximum under prediction during the heating phase of approximately 40^{o}C at 30 minutes and maximum over prediction of 30^{o}C at 120 minutes. An over prediction in $\Delta_{gap,\theta}$ means an under prediction in concrete temperatures and thus the gap's thermal conductance, whilst under predictions in $\Delta_{gap,\theta}$ represent over predictions in concrete temperatures. Ghojel's (2004) "best-fit" thermal conductance model empirically accounts for the evolution of the gap and the heat transfer across it, but was developed from tests on 140 mm Ø sections with 6 mm wall thickness heated in a modified 15 kW electric furnace.

Whilst Ghojel's (2004) "best-fit" thermal conductance model (Equation 2-8) predicts the observed differential gap temperatures in Test C22FIN, it does not necessarily reflect the interface interaction within CFS columns under all conditions. More testing is required to fully understand the formation, size, and conditions under which a gap will form, so that this highly complex interaction can be properly

characterized. Ghojel's (2004) “best-fit” thermal conductance model should be used in the interim.

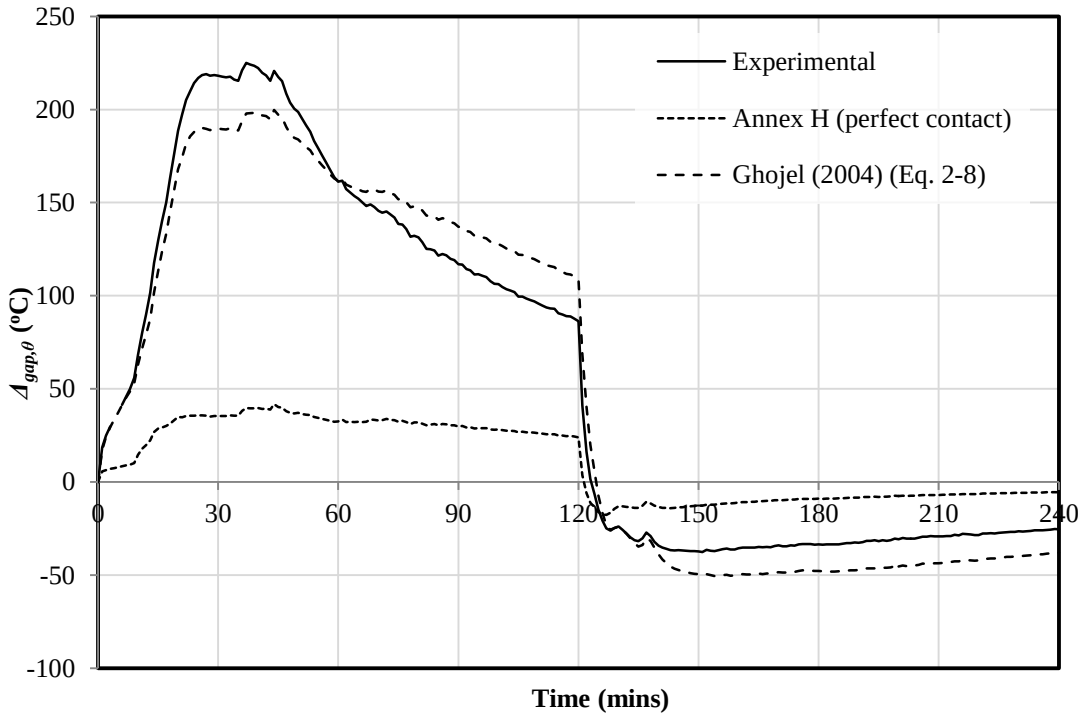

Figure 6-2: Observed and predicted differential gap temperatures for test C22FIN

6.1.3 Heat transfer in the concrete core

Determining the appropriate thermal properties for the concrete core was achieved by applying the observed concrete face temperatures to the outer ring of the concrete core (Region C in Figure 5-6). The predicted temperatures were then manually calibrated to the observed concrete temperatures by altering the specific heat capacity and thermal conductivity of the concrete using a trial and error approach. Figure 6-3 shows the observed and predicted concrete temperatures for test C22FIN, using the *Combi EC4c* modelling approach, preferred to the *Combi ω* modelling approach due to its explicit inclusion of moisture evaporation which provides a better temperature-time history curve at the various TC locations. The *Combi EC4c* modelling approach under predicts the heat transfer through the concrete, thus under predicting the temperatures through the concrete core. The predictions are outside of the range of

temperatures that would be caused by uncertainty as to the precise locations of the TCs (see Figure 5-10).

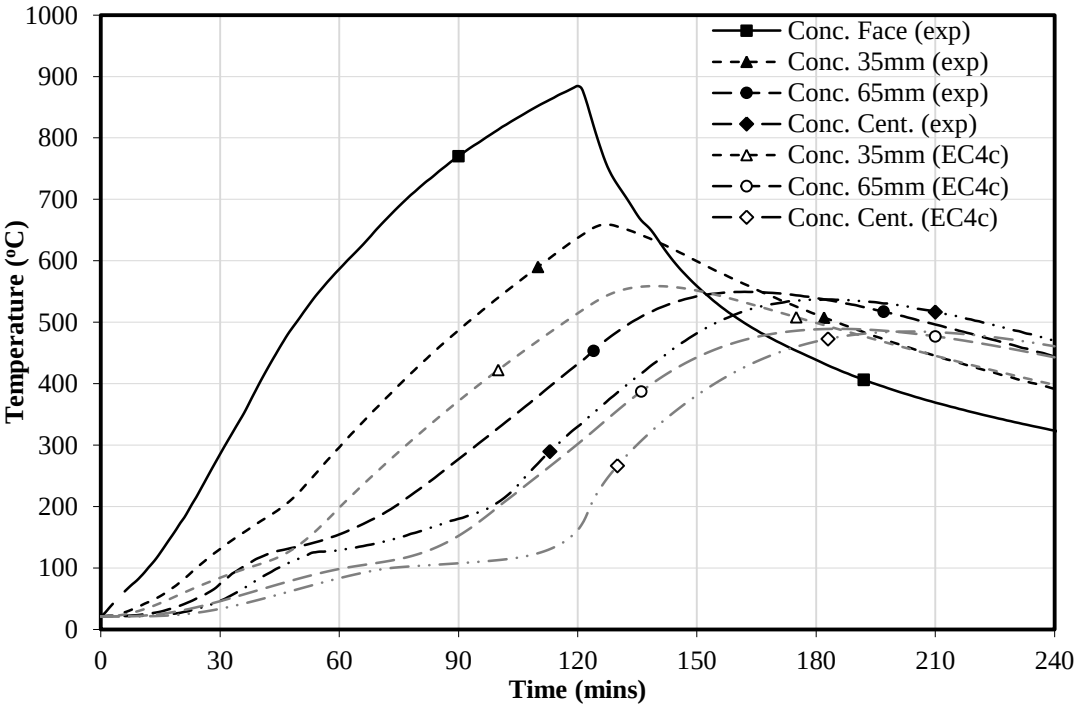

Figure 6-3: Predicted and observed temperature at various depths in the concrete core for test C22FIN using the *Combi EC4c* modelling approach with imposed experimental concrete surface temperatures

The *Combi EC4c* modelling approach employs the EC4 (CEN, 2005) lower bound of concrete thermal conductivity (Equation 2-17) and the EC4 temperature dependent model for concrete specific heat capacity (Equation 2-27) with an assumed 10% water content (W.C.). The water content for the large scale tests was determined however to be 4.9% (Batch 2 in Table 5-2) which reduces the assumed peak of the specific heat capacity from 5600 J/kg^{o}C to 2990 J/kg^{o}C, as shown in Figure 6-4; this reduced peak model is employed in the prediction of the concrete temperatures along with the upper bound of thermal conductivity (Equation 2-17) in a new model variant *EC4d (4.9% W.C.).* The actual error of the predicted temperatures compared to the observed temperatures for both the *EC4c* and the *EC4d (4.9% W.C.)* modelling approaches is shown in Figure 6-5.

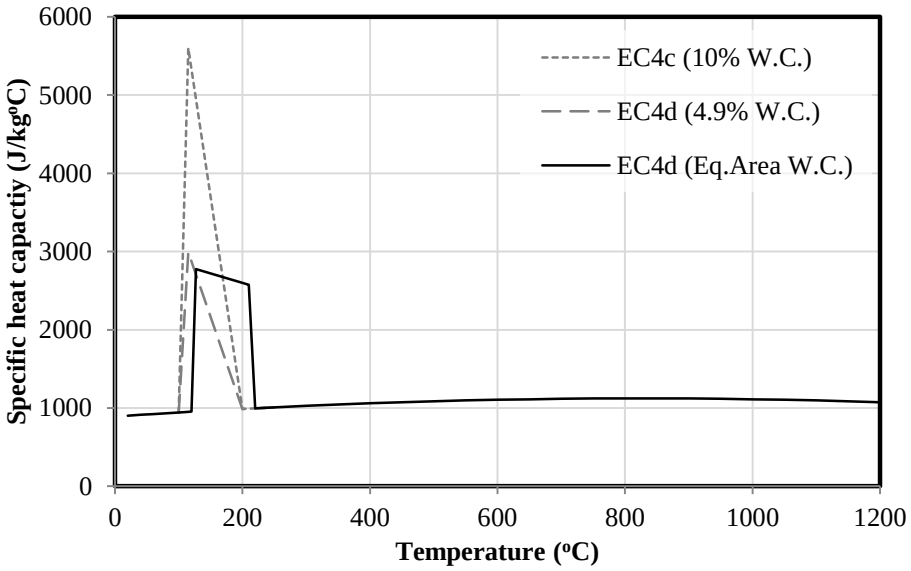

Figure 6-4: Specific heat capacity models for concrete based on the EC4 (CEN, 2005) temperature dependent model (Equation 2-27)

Figure 6-5 shows that the new *EC4d (4.9% W.C.)* modelling approach improves the prediction of temperatures within the concrete however considerable errors remain, particularly at the centre of the concrete, in excess of 150^{o}C in some cases. It was found that by introducing an equivalent area effective specific heat capacity model for concrete (*EC4d (Eq.Area W.C.)* in Figure 6-4) the predictions are improved.

The equivalent area model in Figure 6-4 attempts to capture the observed thermal response of the moisture within the concrete. A question as to where the moisture evaporates within concrete is one that research has not yet been able to properly answer. What is understood is that as a mass of concrete is heated, in addition to evaporation of moisture there is also movement of moisture away from the heated face via micro-pores in the concrete. As the moisture moves the pressure within the micro-pores increases and this increases the temperature at which the moisture will evaporate. The boiling point of water is 100^{o}C at one atmosphere of pressure and is the code-specified starting point to capture the evaporation of moisture within concrete. This effect is observed in the tests where the evaporation of moisture appears to start at around 120^{o}C based on the observed thermal profiles. The shape of the equivalent area model is rectilinear rather than triangular, as it is assumed that the

size of the pores is non-uniform and that the moisture within the pores is at different pressures at different location due to different sizes of pores. Thus the moisture is assumed to evaporate at different temperatures in different locations. The area under the rectilinear curve is equal to an area under the triangular form for the same moisture content, as shown in Figure 6-4, with water content (W.C.) of 6.5% assumed. A 6.5% W.C. is intentionally more than the measured 4.9% W.C. found from the drying of cylinders to account for the increased moisture expected given that the steel tube encases the concrete core in a CFS section.

The observed effect of the moisture within the concrete (Figure 6-3) is assumed to extend from the initial temperature of 120°C to approximately 220°C based on the experimental data from Chapter 5. The peak of the rectilinear curve is set at 2780J/kg°C at 127°C, after which the height of the curve decreases slowly to 2580J/kg°C at 210°C, based on the equal area concept and described by:

$$c_{c,\theta} = \begin{cases} 890 + 56.2(\theta_c/100) - 3.4(\theta_c/100)^2 & 20^oC \le \theta_c < 120^oC \\ 2780 & \theta_c = 127C \\ 2580 & \theta_c = 210C \\ 890 + 56.2(\theta_c/100) - 3.4(\theta_c/100)^2 & 220^oC \le \theta_a < 1200^oC \end{cases} \quad (6\text{-}1)$$

Using the new *EC4d (Eq.Area W.C.)* model along with the upper bound of concrete conductivity improves the prediction of concrete temperatures, as seen in Figure 6-5. The average error in predicted temperatures over 180 minutes at the concrete centre and the 35 mm depth thermocouples, for the EC4d *(Eq.Area W.C.)* model is +19°C and +55°C, respectively, with maximum over-predictions of 63°C and 125°C, respectively. When using the *EC4d (4.9% W.C.)* concrete thermal model the average error is +37°C and +70°C, with maximum over-predictions of 110°C and 165°C at the concrete centre and 35 mm depth thermocouples, respectively.

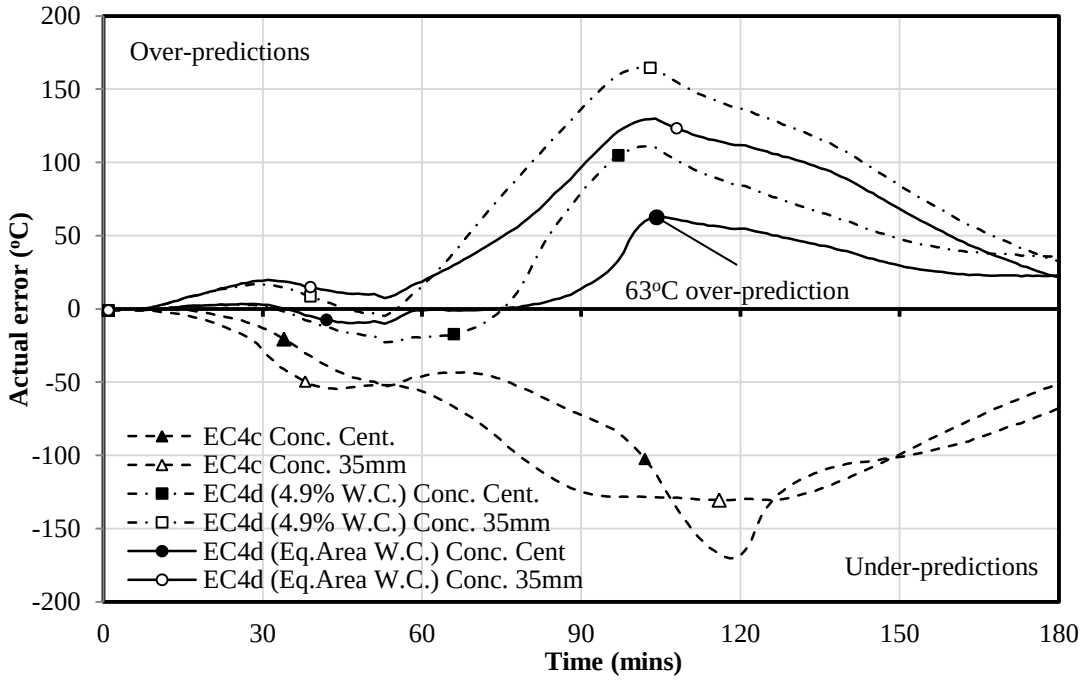

Figure 6-5: Difference between the predicted and observed concrete temperatures with three candidate concrete modelling approaches.

6.1.4 Validation of revised heat transfer model

Figure 6-6 shows the observed and predicted thermal response of test C22FIN using the *Combi γ* modelling approach with the observed furnace temperatures applied to the steel. The *Combi γ* modelling approach includes the best thermal properties and interactions from the previous three sections including: the fire emissivity of 0.38 and the temperature dependent steel emissivity as found by Paloposki and Liedquist (2005); Ghojel's (2004) thermal conductance model at the steel-concrete interface; and the *EC4d (Eq.Area W.C.)* model for concrete. Figure 6-6 shows that the predicted temperatures at most of the temperature measurement points closely match those observed in tests. The uncertainty in predicted and observed temperatures due to uncertainty in thermocouple locations is similar to that seen in Figure 5-10.

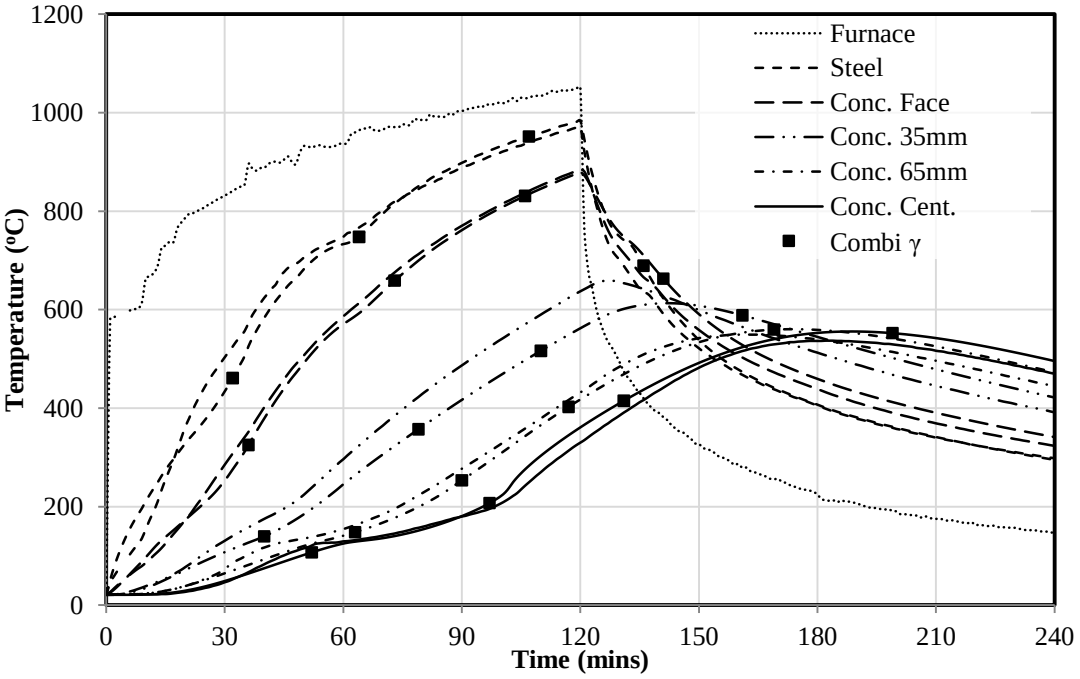

Figure 6-6: Observed and predicted temperatures for test C22FIN using the *Combi γ* modelling approach

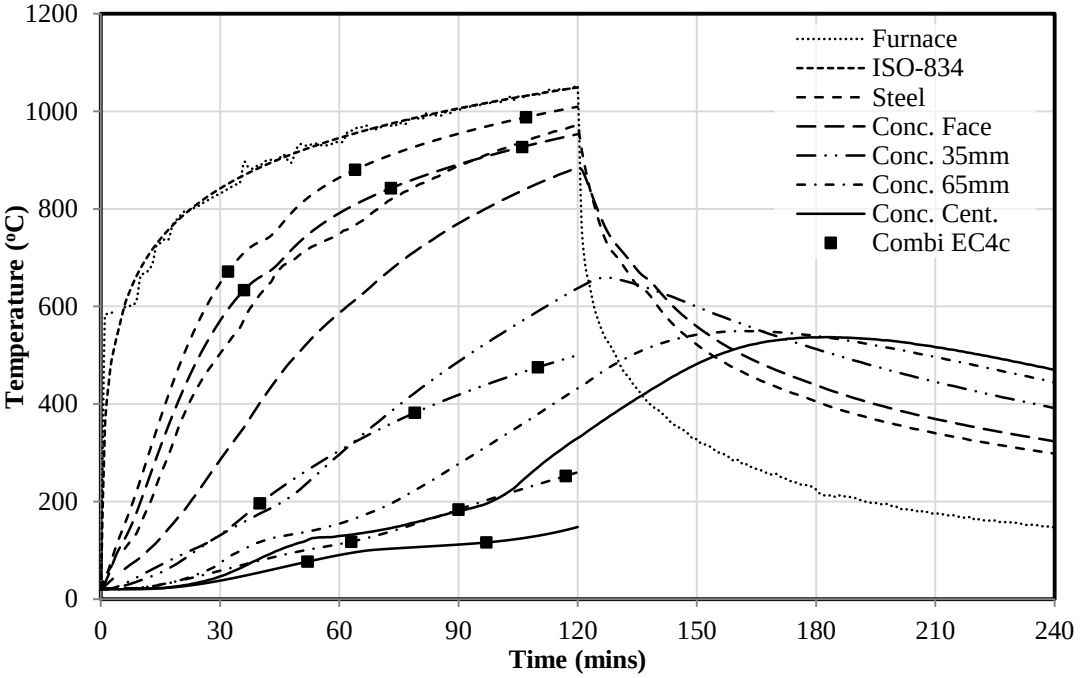

Figure 6-7: Observed and predicted temperatures for test C22FIN using the *Combi EC4c* modelling approach

As expected, the new *Combi γ* modelling approach accurately predicts the thermal response for the specific test from which its parameters were calibrated, and shows an improvement compared to the predictions made using the *Combi EC4c* modelling approach from Chapter 5, shown again in Figure 6-7. The *Combi γ* modelling approach was also used to predict the temperatures of Test C11FSN (Figure 6-8) and Test S33FIN (Figure 6-10), to see how it performs under a different heating regime (the Smouldering fire curve for test C11FSN) or shape (square section for test S33FIN). The temperature predictions using the *Combi γ* modelling approach show good agreement with the observed temperatures in these cases also. The predicted temperatures are more accurate than the predictions made using the *Combi EC4c* modelling approach, as shown in Figure 6-9 and Figure 6-11.

Table 6-1 shows the predicted temperatures using the *Combi γ* modelling approach for all the unprotected thermal tests using the observed furnace temperatures as the thermal input. Again the trend observed of thicker walled steel tubes experiencing higher temperatures than the thinner walled specimens of the same cross-section size (Table 5-6) is not predicted by the *Combi γ* modelling approach, although the observed temperatures in the steel and the concrete are reasonably accurate.

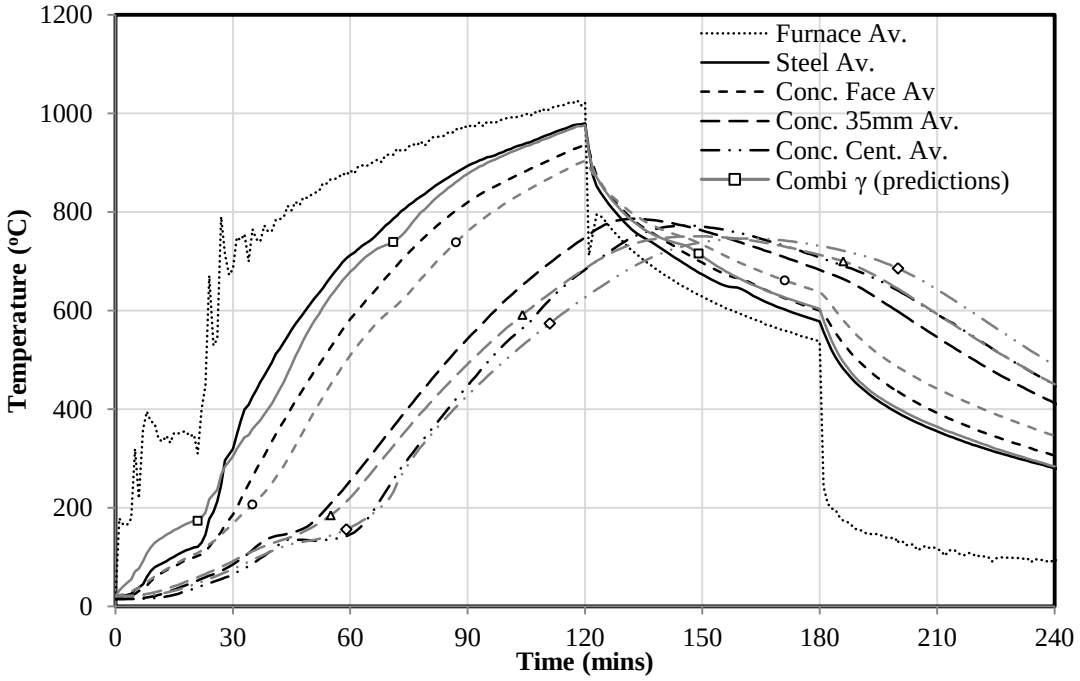

Figure 6-8: Observed and predicted thermal response of smouldering fire test C11FSN using the *Combi γ* modelling approach

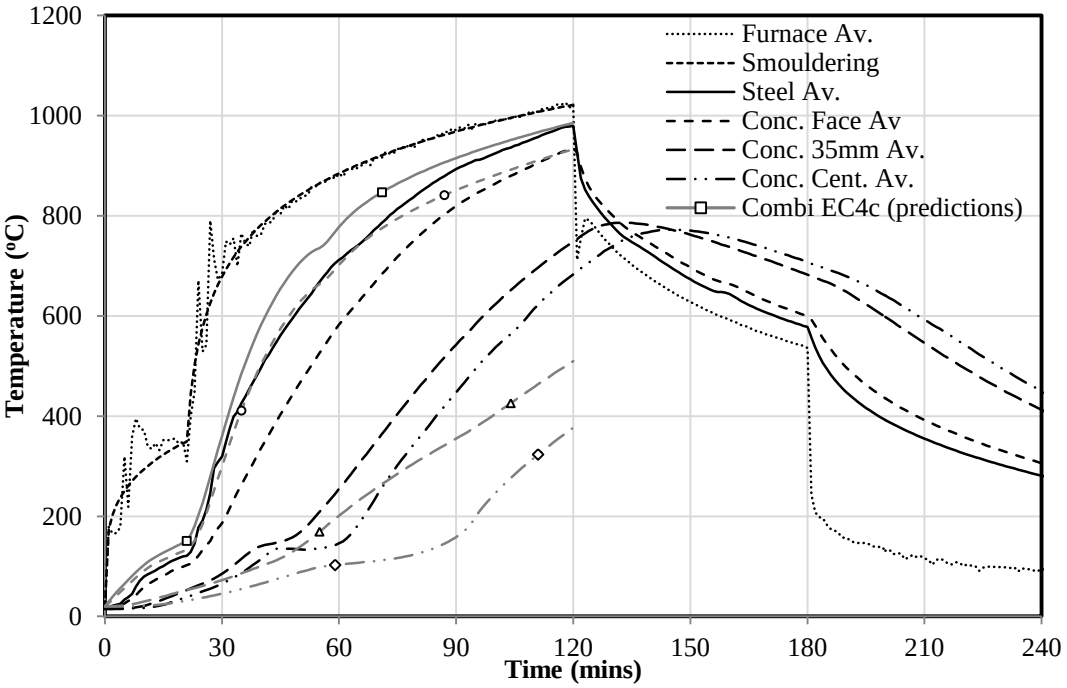

Figure 6-9: Observed and predicted thermal response of smouldering fire test C11FSN using the *Combi EC4c* modelling approach

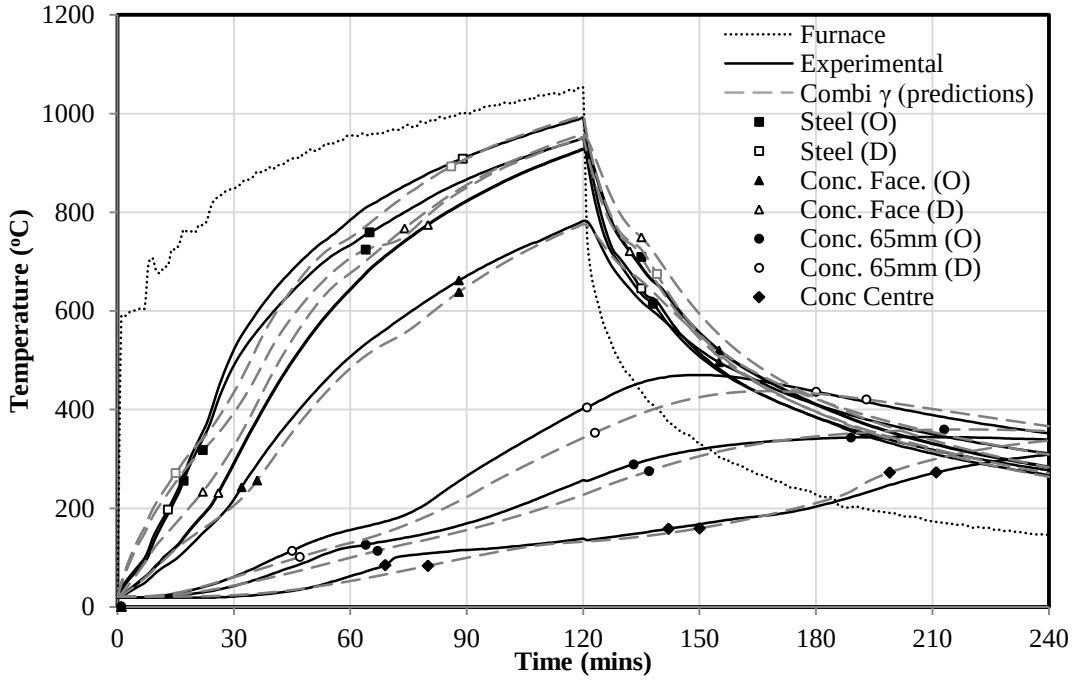

Figure 6-10: Observed and predicted thermal response of ISO 834 fire test S33FIN using the *Combi γ* modelling approach

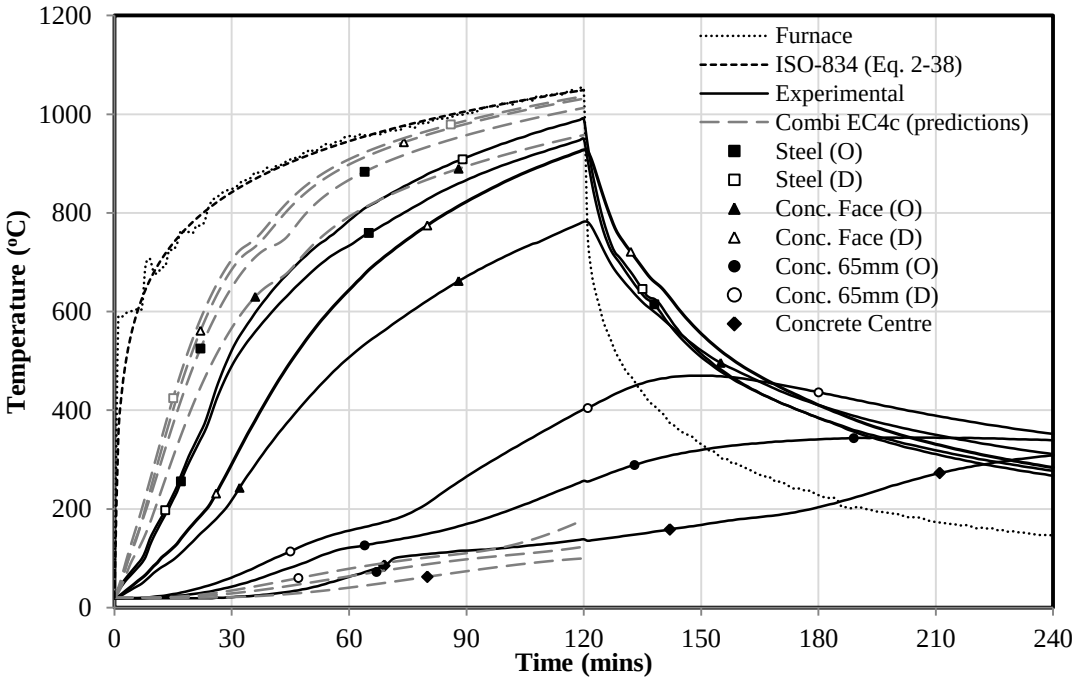

Figure 6-11: Observed and predicted thermal response of ISO 834 fire test S33FIN using the *Combi EC4c* modelling approach

Table 6-1: Observed and predicted temperatures of unprotected tests at 60 and 120 minutes, using *Combi γ* modelling approach with applied furnace temperatures

Test	Size	Wall thickness	Steel (°C)				Concrete face (°C)				Centre (°C)							
			Predicted		*Observed*		Predicted		*Observed*		Predicted				*Observed*			
	(mm)	(mm)	60	120	*60*	*120*	60	120	*60*	*120*	60	120	Max	Time	*60*	*120*	*Max*	*Time*
Circular sections exposed ISO 834 standard fire (Equation 2-27)																		
C11FIN	323.9	10	708	958	*727*	*949*	523	829	*531*	*828*	54	133	342	240	*78*	*132*	*313*	*239*
C12FIN	323.9	8	724	962	*709*	*931*	544	836	*534*	*828*	54	133	335	240	*57*	*134*	*294*	*240*
C21FIN	219.1	10	723	980	*765*	*981*	554	874	*562*	*869*	125	364	564	189	*130*	*377*	*570*	*175*
C22FIN	219.1	8	733	984	*748*	*971*	571	879	*587*	*885*	125	361	556	189	*130*	*330*	*537*	*182*
C23FIN	219.1	5	757	988	*753*	*973*	596	886	*600*	*892*	126	357	543	188	*126*	*331*	*529*	*180*
C31FIN	139.7	10	740	1012	*825*	*1005*	613	956	*783*	*995*	301	734	829	153	*412*	*844*	*871*	*131*
C32FIN	139.7	8	758	1013	*800*	*991*	628	957	*738*	*977*	301	726	822	154	*389*	*882*	*888*	*124*
C33FIN	139.7	5	805	1014	*799*	*997*	664	958	*691*	*954*	303	715	810	156	*286*	*756*	*820*	*140*
C33FHIN	139.7	5	805	1014	*806*	*996*	664	958	*698*	*952*	303	715	810	156	*313*	*754*	*822*	*142*
Square sections exposed to ISO 834 standard fire (Equation 2-27)																		
S11FIN	300	10	707	951	*734*	*950*	484	776	*507*	*782*	53	132	337	240	*63*	*139*	*309*	*240*
			749	996	*785*	*991*	677	959	*644*	*928*								
S21FIN	120	10	755	1018	*768*	*987*	604	951	*687*	*961*	369	791	854	141	*400*	*865*	*886*	*127*
			779	1024	*785*	*995*	712	1001	*722*	*977*								
S23FIN	120	5	826	1019	*757*	*974*	653	950	*649*	*932*	363	765	830	143	*354*	*699*	*713*	*125*
			851	1028	*792*	*984*	781	1006	*641*	*928*								
Square and Circular sections exposed to smouldering curve (Equation 2-28)																		
C33FSN	139.7	5	679	976	*712*	*980*	509	904	*583*	*935*	160	627	746	162	*146*	*683*	*773*	*145*
C23FSN	120	5	687	981	*725*	*990*	481	894	*559*	*935*	176	678	762	144	*192*	*766*	*826*	*134*
			712	992	*714*	*987*	622	964	*661*	*978*								

The following six figures (Figure 6-12 to Figure 6-17) show the errors between the observed and predicted temperatures, using the *Combi γ* (figures 6-12, 6-14 , and 6-16) and *Combi EC4c* (figures 6-13, 6-15 , and 6-17) modelling approaches for the unprotected tests at various times during the tests.

Figure 6-12 and Figure 6-13 show the errors in predicted temperatures compared to the temperatures observed in tests in the steel tube, for the *Combi γ* and *Combi EC4c* modelling approaches, respectively. Figure 6-12 shows that the *Combi γ* accurately predicts the steel tube temperatures in the unprotected tests with a maximum error of approximately -100^{o}C (under-prediction), but the error is generally within ±50^{o}C. This is not seen in the Figure 6-13 for *Combi EC4c* where the maximum error is approximately +275^{o}C (over-prediction), and the errors are, in general, above +50^{o}C.

Figure 6-14 shows that the *Combi γ* accurately predicts the concrete face temperatures in the unprotected tests with maximum errors of approximately ±100^{o}C, but the errors are again within ±50^{o}C, in general. Figure 6-15 shows that the *Combi EC4c* modelling approach is again less accurate, where maximum error of approximately +400^{o}C is seen, and where the errors are, in general, above +100^{o}C.

Figure 6-16 shows that the *Combi γ* also predicts accurately the concrete centre temperatures in the unprotected tests with maximum errors of approximately ±100^{o}C but the errors are within -50^{o}C (under-prediction), in general. Figure 6-17 shows similar degrees of error, as seen in Figure 6-16, between the observed and predicted concrete centre temperature when using the *Combi EC4c* modelling approach with a maximum error in excess of +100^{o}C (over-prediction), and errors, in general, within ±100^{o}C.

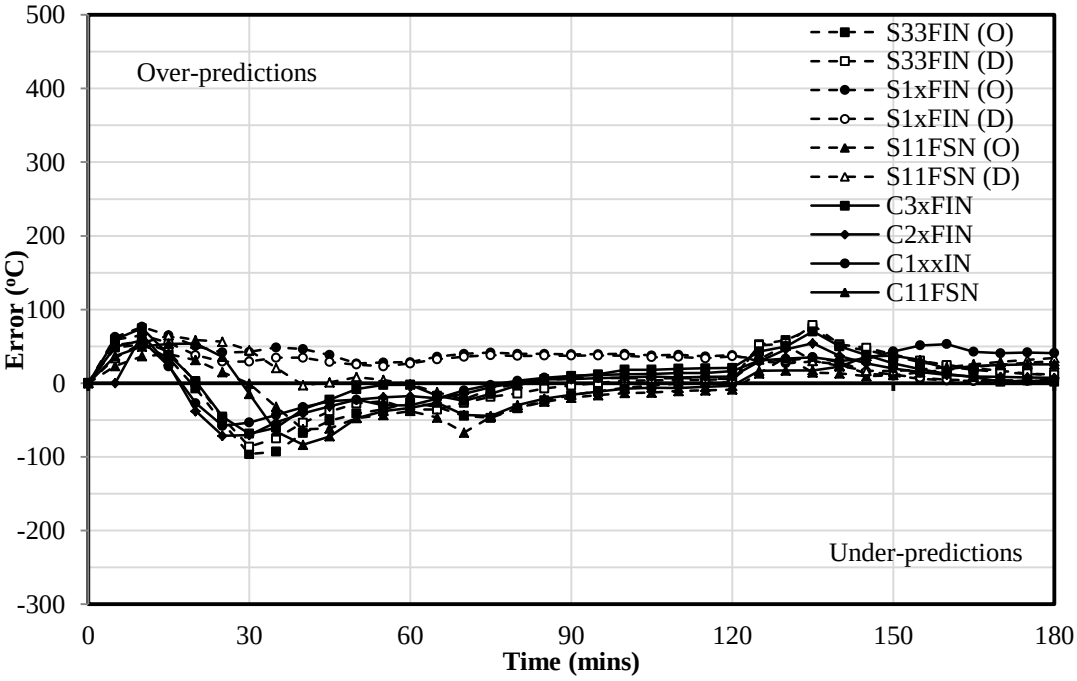

Figure 6-12: Difference between the predicted and observed steel tube temperatures for unprotected tests using the *Combi γ* modelling approach

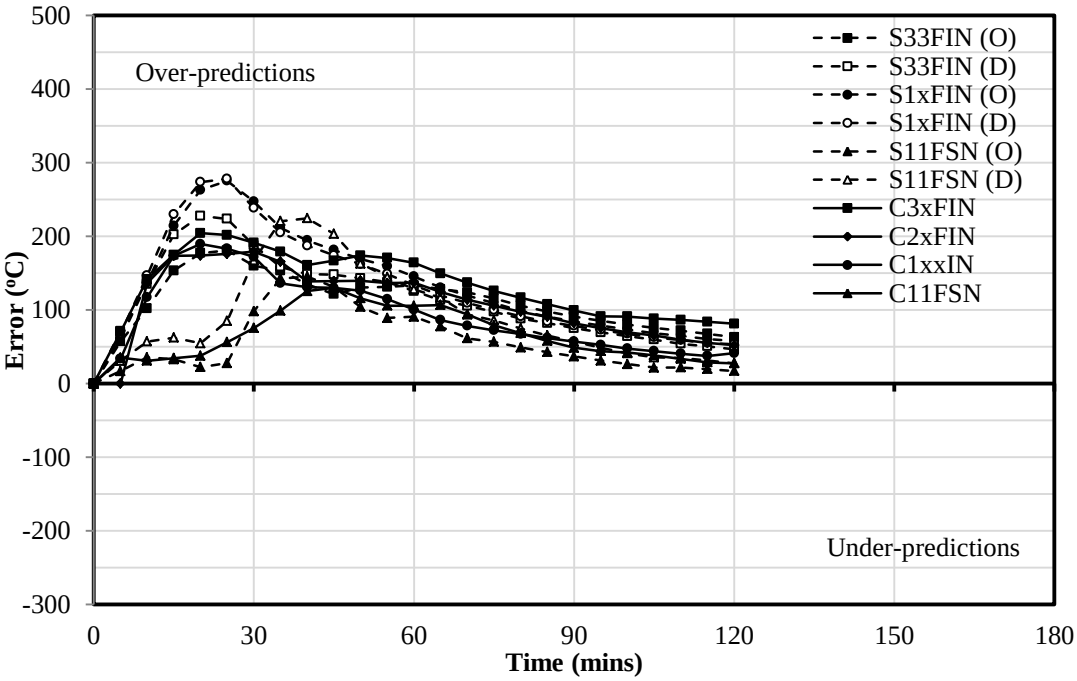

Figure 6-13: Difference between the predicted and observed steel tube temperatures for unprotected tests using the *Combi EC4c* modelling approach

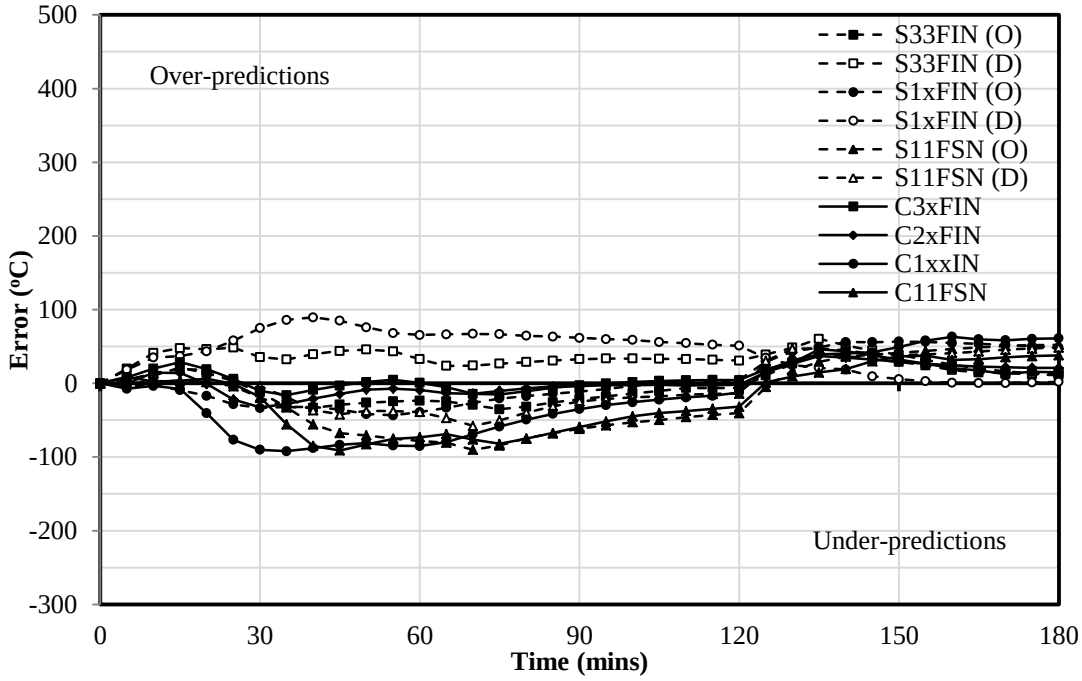

Figure 6-14: Difference between the predicted and observed concrete face temperatures for unprotected tests using the *Combi γ* modelling approach

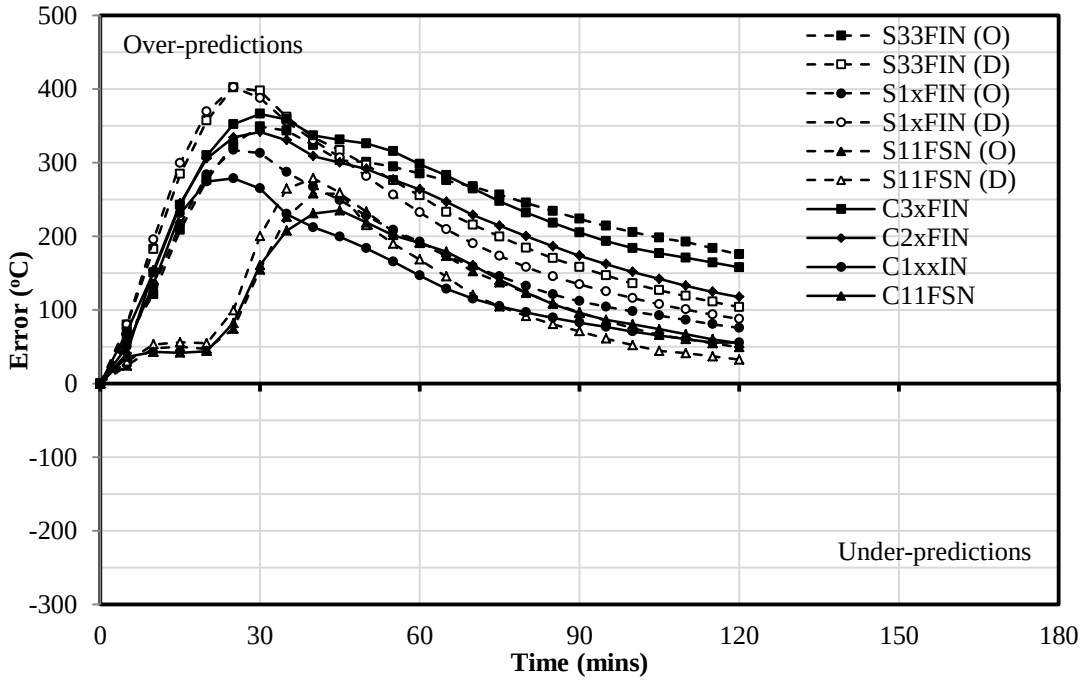

Figure 6-15: Difference between the predicted and observed concrete face temperatures for unprotected tests using the *Combi EC4c* modelling approach

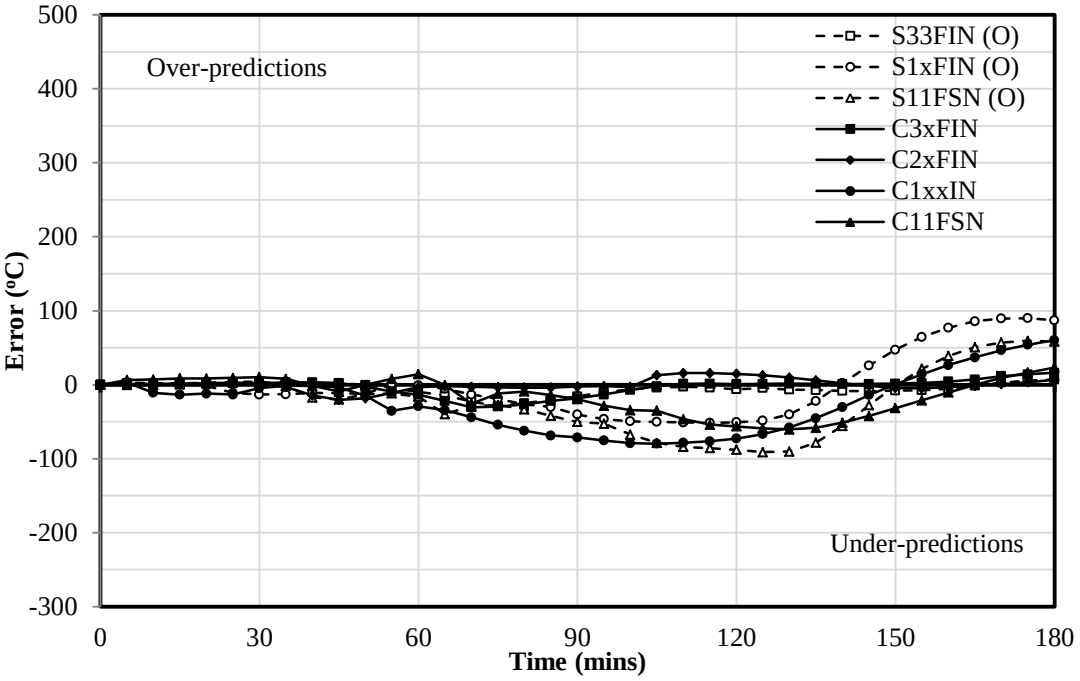

Figure 6-16: Difference between the predicted and observed concrete centre temperatures for unprotected tests using the *Combi γ* modelling approach

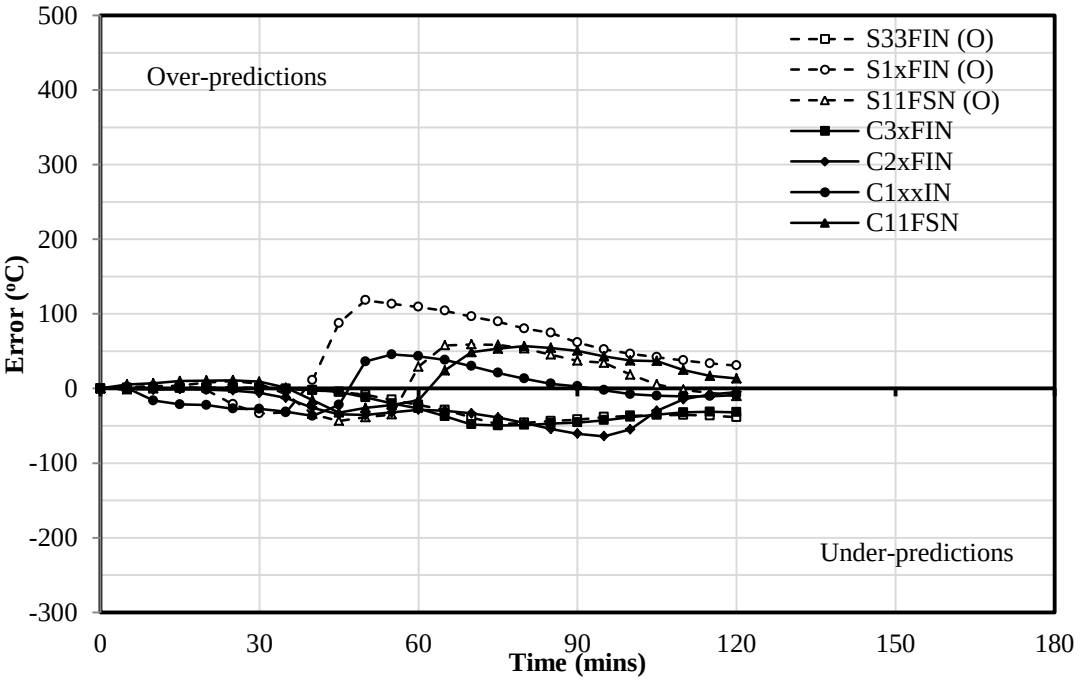

Figure 6-17: Difference between the predicted and observed concrete centre temperatures for unprotected tests using the *Combi EC4c* modelling approach

The *Combi γ* modelling approach was developed using test data from a single test but has been shown to predict the thermal response of all the unprotected CFS sections tested with accuracy generally within ±50^{o}C of the observed temperatures at all locations.

Whilst the predicted temperatures using the *Combi γ* modelling approach shows good agreement with the observed test data there are key areas of concern for appropriate modelling of heat transfer to CFS sections, is the interaction between the steel and the furnace. In order to calibrate the predicted temperatures to those observed in the thermal tests, an emissivity of the furnace ($\varepsilon_{m,fi}$) of 0.38 was required, which may be only appropriate for the specific floor furnace in which the specimens were tested and may not be realistic of other furnaces. Large scale loaded furnace tests conducted and modelled by the NRCC (e.g. Lie et al., 1992), quote emissivities of the furnaces used as 0.75; twice that required in the *Combi γ* modelling approach.

It is therefore essential to understand what influence the emissivity of different furnaces has on the predicted temperatures and the subsequent influence of the accurate prediction of fire resistance. The following section revisits the meta-analysis of furnace tests data conducted in Chapter 3 to assess the material and interaction properties proposed in the *Combi γ* modelling approach, and to ascertain which furnace emissivity is most appropriate to adopt, for the prediction of the fire resistance of loaded CFS columns in furnace tests.

6.1.5 Revisiting the meta-analysis with improved thermal modelling

The *Combi EC4c* and *Combi ω* modelling approaches, developed from the meta-analysis in Chapter 3, whilst being overall the best statistical predictors of the fire resistance of the CFS columns, using the Annex H approach of EC4 (CEN, 2005), were seen to be relatively poor predictors of the thermal profiles within the CFS sections presented in Chapter 5.

To assess the *Combi γ* modelling approach for wider use in structural fire resistance design, and to ascertain the most appropriate furnace emissivity to adopt, the meta-

analysis process in Chapter 3 was repeated applying the *Combi γ* and *Combi α* modelling approaches, in which all of the parameters are the same apart from the furnace emissivity (which is set to the NRCC value of 0.75 in *Combi α*).

Figure 6-18 shows the predicted versus actual fire resistances of the columns detailed previously in Table 3-2 partitioned with respect to shape using *Combi γ*. The predictions of fire resistance using *Combi γ* within the EC4 Annex H overall approach (CEN, 2005), is unconservative on average with a mean error (*ME*) and standard deviation (σ) of +9.6 and 19.8 minutes respectively. It is unconservative for both square and circular sections, with *ME*s of +12.0 and +4.5 minutes and σs of 19.5 and 19.9 minutes, respectively. This is due to its relatively low assumed furnace emissivity of 0.38.

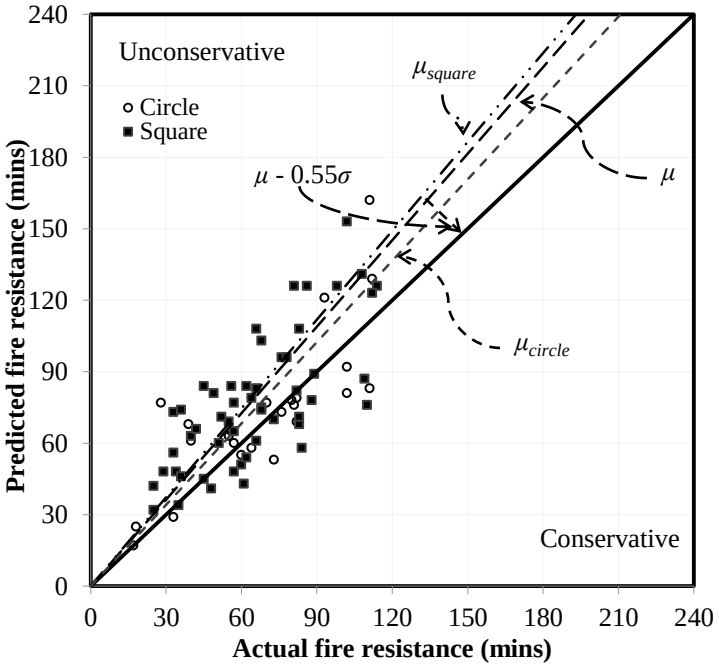

Figure 6-18: Predicted versus observed fire resistance for EC4 Annex H (CEN, 2005) using *Combi γ* with the database partitioned by shape

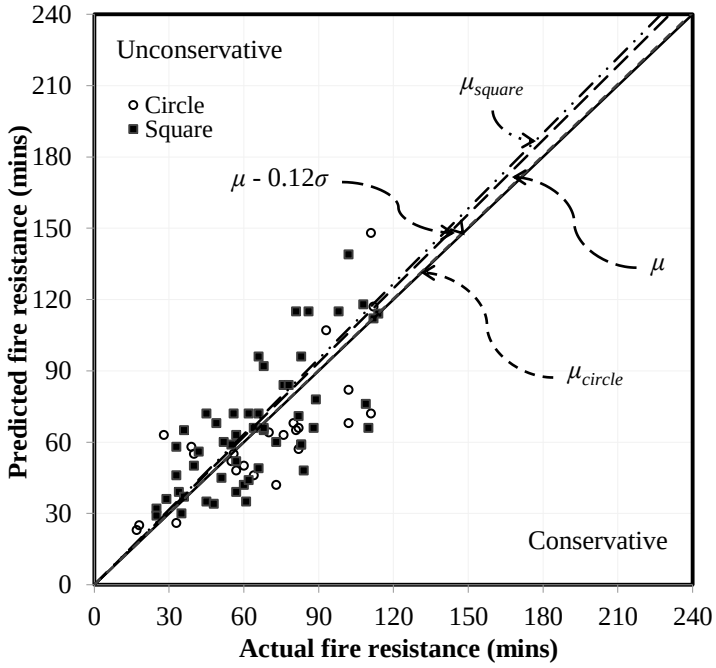

Figure 6-19: Predicted versus observed fire resistance for EC4 Annex H (CEN, 2005) using *Combi α* with the database partitioned by shape

A furnace emissivity of 0.75, quoted from the NRCC (e.g. Lie et al., 1992) is assumed in the *Combi α* modelling approach. Figure 6-19 shows the predicted versus actual fire resistances of the columns detailed in Table 3-2, and partitioned with respect to shape, using the *Combi α* modelling approach.

By using a higher furnace emissivity in the *Combi α* modelling approach, the predictions are, on average, very accurate and slightly conservative with an *ME* of -0.8 minutes with the precision of the predictions, σ, of 19.1 minutes, as seen in Figure 6-19. The overall predictive ability of the *Combi α* modelling approach has marginally better accuracy and precision than that of the *Combi ω* modelling approach developed in Chapter 3 when applied to the experimental database (a one minute improvement in *ME* and a reduction in standard deviation of two minutes).

As with the meta-analysis in Chapter 3, to ensure that the apparent improvements to the predictive abilities of the EC4 Annex H approach, when using the *Combi α* modelling approach, are not effects of the abnormally distributed dataset, the same ranking procedure presented in Section 3.3.2.7 is employed, and compares the

physical parameter partitioned results of the *Combi EC4c*, *Combi ω, Combi γ, and Combi α* modelling approaches. The results of the weighted ranking analysis are given in Table 6-2 and show that the *Combi α* modelling approach is the best predictor across the dataset when physical parameters of the sections are considered. This is demonstrated in figures 6-20 through 6-22.

Table 6-2: Summary of R_{tot} rankings; and the mean and standard deviations of those rankings for the mean error, *ME* of the predictions

	Shape	Fixity	Fill	Load App.	Size	Load Ratio	Wall Thick.	MEAN	σ
Combi α	2	1	3	1	2	1	1	1.6	0.79
Combi ω	1	2	2	2	3	2	3	2.1	0.69
Combi EC4 c	4	3	1	3	4	4	2	3.0	1.15
Combi γ	3	4	4	4	1	3	4	3.3	1.11

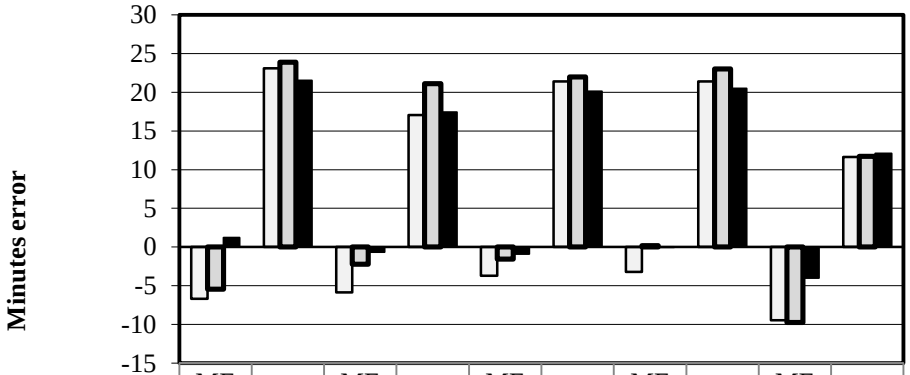

	ME	σ	ME	σ	ME	σ	ME	σ	ME	σ
	(N=9) Pin - Pin		(N=17) Pin - Fix		(N=52) Fix - Fix		(N=61) Concentric		(N=15) Eccentric	
	Fixity						Eccentrictiy			
Combi EC4c	-6.7	23.1	-5.8	17.1	-3.7	21.4	-3.2	21.4	-9.5	11.6
Combi ω	-5.4	23.9	-2.2	21.1	-1.5	22.0	0.2	23.0	-9.7	11.7
Combi α	1.2	21.5	-0.7	17.4	-0.9	20.1	0.0	20.5	-4.0	12.1

Figure 6-20: Comparison of *ME* and *σ* for the EC4 Annex H approach (CEN, 2005) using *Combi EC4c; Combi ω;* and *Combi α* modelling approaches with the database partitioned based on (a) fixity, and (b) eccentricity

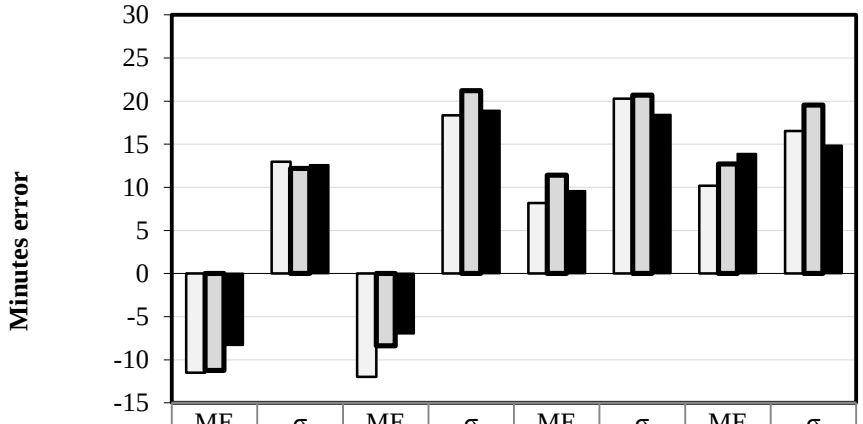

	ME (N=16) 0-200mm	σ	ME (N=33) 200-250mm	σ	ME (N=17) 250-300mm	σ	ME (N=10) 300+mm	σ
Combi EC4c	-11.5	13.0	-12.0	18.3	8.2	20.3	10.2	16.5
Combi ω	-11.3	12.2	-8.4	21.2	11.4	20.7	12.7	19.6
Combi α	-8.3	12.6	-7.0	18.9	9.6	18.4	13.9	14.9

Figure 6-21: Comparison of *ME* and *σ* for the EC4 Annex H approach (CEN, 2005) using *Combi EC4c; Combi ω;* and *Combi α* modelling approaches with the database partitioned based on size

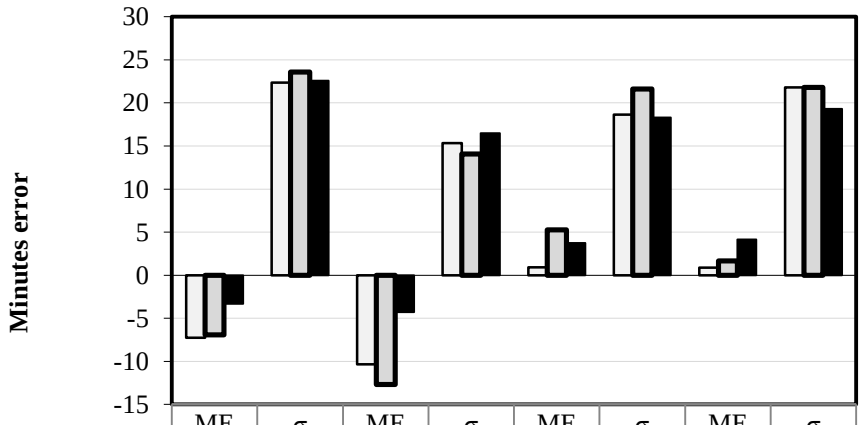

	ME (N=15) 0- 4mm	σ	ME (N=16) 4.01-6mm	σ	ME (N=27) 6.01-7mm	σ	ME (N=17) 7.01+mm	σ
Combi EC4c	-7.3	22.3	-10.3	15.3	0.9	18.7	0.9	21.8
Combi ω	-6.9	23.6	-12.7	14.1	5.3	21.6	1.7	21.8
Combi α	-3.3	22.6	-4.3	16.5	3.8	18.3	4.2	19.3

Figure 6-22: Comparison of *ME* and *σ* for the EC4 Annex H approach (CEN, 2005) using *Combi EC4c; Combi ω;* and *Combi α* modelling approaches with the database partitioned based on wall thickness

Steel tube failure temperature prediction

Figure 6-23 shows the predicted steel temperature at the point of failure using the *Combi α* modelling approach and compares them to the observed steel temperature as seen in furnace tests. The overall mean percentage error, *MPE,* for the data is -0.1%, with a standard deviation of the errors, σ_{pe}, of 13%, which shows better accuracy and precision than the *Combi ω* modelling approach (Figure 3-30). Figure 6-24 shows the small improvements as compared with the approaches of Chapter 3.

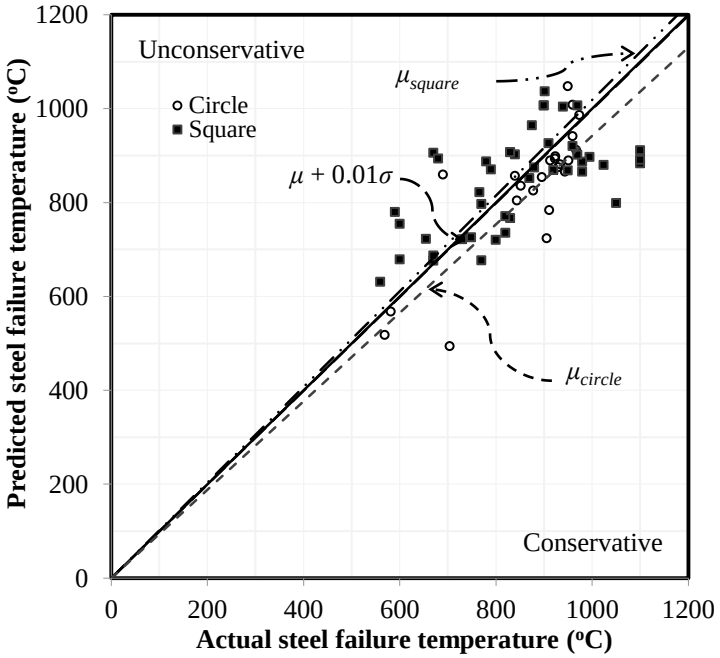

Figure 6-23: Predicted versus observed steel tube temperature for the EC4 Annex H approach (CEN, 2005) using the *Combi α* modelling approach and partitioned by section shape

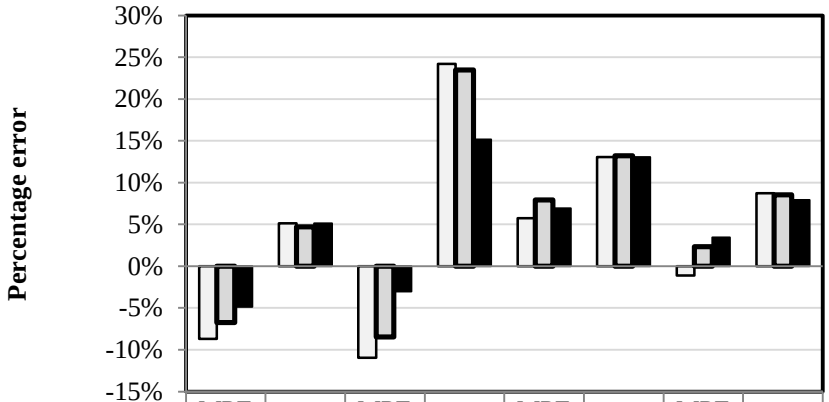

	MPE (N=15) 0-200mm	σpe (N=15) 0-200mm	MPE (N=27) 200-250mm	σpe (N=27) 200-250mm	MPE (N=17) 250-300mm	σpe (N=17) 250-300mm	MPE (N=8) 300+mm	σpe (N=8) 300+mm
Combi EC4c	-8.7%	5.1%	-11.0%	24.2%	5.8%	13.1%	-1.1%	8.7%
Combi ω	-6.7%	4.7%	-8.5%	23.5%	7.9%	13.2%	2.3%	8.5%
Combi α	-4.9%	5.1%	-3.0%	15.2%	6.9%	13.1%	3.4%	7.9%

Figure 6-24: Comparison of steel tube failure temperature *MPE* and σ_{pe} for the EC4 Annex H approach (CEN, 2005) using the *Combi EC4c*, *Combi ω*, and *Combi α* modelling approaches with the database partitioned based on cross-section size

6.1.6 Summary of thermal analysis of unprotected CFS sections

The temperature predictions made for the unprotected sections using either the *Combi EC4c* or *Combi ω* modelling approaches in Chapter 5 were inaccurate. A new modelling approach, *Combi γ*, was developed based on test C22FIN. Three major issues were assessed; (1) heat transfer to the steel tube; (2) the influence of an air gap; and (3) heat transfer within the concrete core.

The predicted temperatures of the steel tube, concrete face and concrete centre thermocouples of the unprotected tests, using the *Combi γ* modelling approach, were in general within ±50^{o}C of the observed temperatures. Whilst the temperature predictions were seen to improve using the *Combi γ* modelling approach it was noted that the emissivity for the floor furnace of 0.38, was half of the NRCC quoted value of 0.75 used in their modelling of the fire resistance of CFS sections tested within loaded column furnaces. A new modelling approach, called *Combi α*, used the

NRCC furnace emissivity of 0.75, instead of the calibrated floor furnace emissivity of 0.38, and was applied to the meta-analysis of Chapter 3. This showed that the *Combi γ* modelling approach, in general, over-predicted the fire-resistance of the CFS columns by approximately 10 minutes on average, whilst the *Combi α* modelling approach accurately predicted the fire resistance to within one minute, on average. The meta-analysis also showed that the calibrated *Combi α* thermal modelling approach was the best predictor of fire resistance when used with the EC4 Annex H (CEN, 2005). The approach is seen to have a consistency in predictions across most physical parameters, not seen in the Chapter 3 meta-analysis. It was also shown that the *Combi α* modelling approach is a very accurate and precise predictor of steel failure temperatures and should be used with the EC4 Annex H (CEN, 2005).

6.2 Analysis and design of protected CFS sections

The current method typically used for the prescription of intumescent fire protection systems (i.e. DFTs) applied to structural steel in the UK is based on three parameters:

(1) the required fire resistance, F.R., which is a pre-determined value based on building code requirements (e.g. Communities and Local Government (2007)), and is dependent on building characteristics and occupancy;

(2) a section factor defined as the ratio of the section's heated perimeter, H_p, to its cross sectional area, A; and

(3) a limiting temperature for the steel, which is intended to be the temperature at which the structural element will fail under load during a standard furnace test (typically in the region of 520°C depending on its utilisation in fire).

These parameters are used in conjunction with empirically determined, product specific, design tables to determine the required DFT for a specific intumescent coating; these are based on a large number of furnace tests of plain structural steel sections (notably not CFS sections) with various H_p/A values and at a variety of DFTs. To be able to apply existing DFT thickness design tables to CFS sections, an effective section factor, H_p/A_{eff}, must be determined; this must incorporate the effect(s) of the concrete infill on the heating rates of the steel, so that design can be

performed on the basis of a steel limiting temperature. This procedure was discussed briefly in Chapter 2, and additional detail is provided in this section. Equations 6-2 and 6-3 show the current approach which is used in the UK to determine the effective section factor (Hicks et al., 2002) based on the required fire resistance time, t_{FR}. These equations treat the problem using design guidance for unfilled sections by adding an 'equivalent' steel wall thickness, $t_{c,eff}$, to the existing steel wall thickness, t_a, to account for the effects of the concrete core, thus decreasing the effective H_p/A:

$$\frac{H_p}{A_{eff}}(Th) = \frac{1000}{t_{a,eff}} = \frac{1000}{t_a + t_{c,eff}} \tag{6-2}$$

with:

$$t_{c,eff} = \begin{cases} 0.15 b_i, & b_i < 12\sqrt{t_{FR}} \\ 1.8\sqrt{t_{FR}}, & b_i \geq 12\sqrt{t_{FR}} \end{cases} \tag{6-3}$$

where t_a is the steel wall thickness (mm), $t_{c,eff}$ is the effective increase in steel wall thickness (mm) due to the concrete, b_i is the minimum dimension of the concrete core (mm), and t_{FR} is the fire resistance time (minutes).

Equation 6-2 was used to prescribe the intumescent coating dry film thickness (DFT) for the majority of the protected CFS sections presented previously in Table 5-6 with a limiting temperature of 520^{o}C and a required t_{FR} of 90 minutes.

Figure 6-25 shows the average, maximum, and minimum observed steel tube temperatures, θ_a, for all the C1 protected tests and unprotected tests presented in Chapter 5. It is clear from this Figure 6-25 (and from Table 5-7) that use of current guidance to prescribe DFTs for CFS sections results in overly conservative steel tube temperatures.

The observed conservatism could be due to: (1) inherently conservative DFT thicknesses in the tabulated data from tests on unfilled sections; (2) changes in the expansion response and thus the effective thermal conductivity of the intumescent coatings when applied to sections with very different thermal masses; or (3) overly conservative calculation of the effective section factors for CFS sections. However, the tabulated DFTs used by reactive coating manufacturers are already highly

optimised for unfilled steel sections, and a large number of furnace tests have shown that the designed limiting temperatures, on which the DFTs are based, are actually reached at, or shortly after, the required F.R. for protected unfilled sections. Therefore inherently conservative design tables for the plain steel sections (Cause (1) above) cannot be the cause of the observed conservatism.

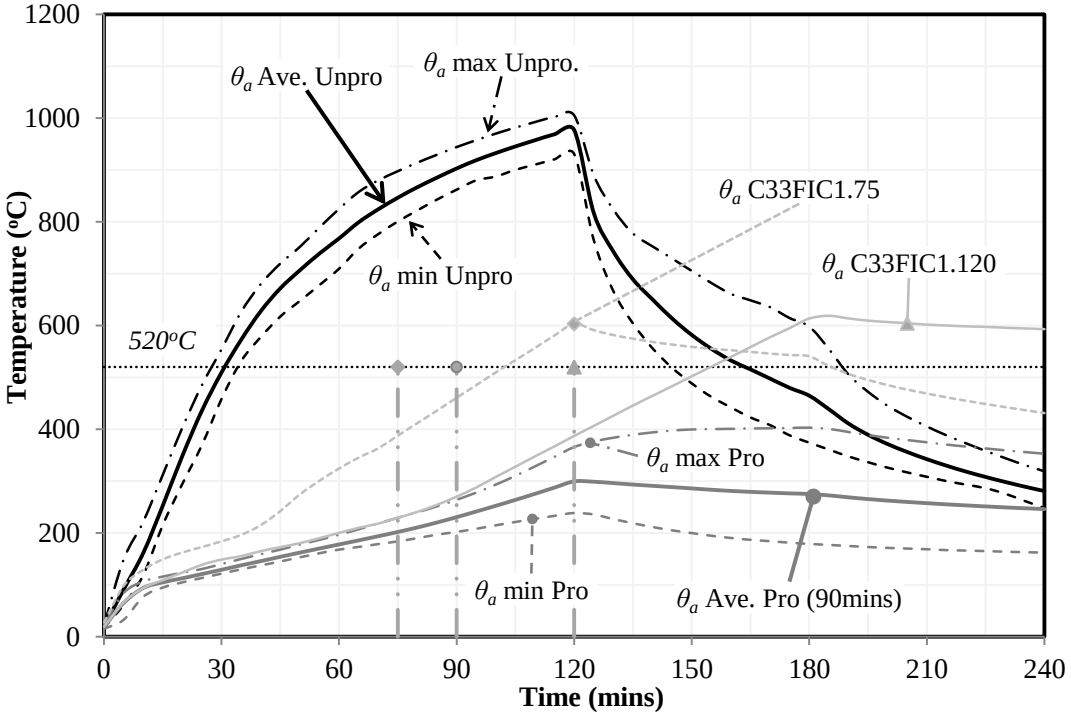

Figure 6-25: Average steel temperatures of C1 protected and unprotected square and circular sections (concrete age tests omitted)

6.2.1 Variable thermal conductivity of protection

To understand whether the conservatism seen in the observed temperatures is due to fundamental changes in the insulating performance of the intumescent coating for substrates of significantly different heating rates, an assessment of the variable effective thermal conductivity, $\lambda_{p,t}$, of the protection was made according to guidance presented in BS EN 13381-8 (CEN, 2010b). The determination of the applied dry film thickness (DFT or d_p) is based on the section factor, and the calculation of the effective variable thermal conductivity is based on both. Comparisons between the effective thermal conductivities of the protection when applied to filled and unfilled sections can thus be made, acknowledging that the effective section factors (H_p/A_{eff})

for a filled and unfilled tube of the same size, and thus initial DFTs, are not the same. The variable thermal conductivities of the protection were calculated in accordance with BS EN 13381-8 (CEN, 2010b) using Equation 6-4 (which is a rearrangement of the energy balance Equation 2-39):

$$\lambda_{p,t} = d_p \times \frac{A_{eff}}{H_p} \times c_{a,\theta} \cdot \rho_a \times \left(\frac{1}{(\theta_g - \theta_{a,t}) \times \Delta t} \right) \times \Delta\theta_{a,t} \qquad (6\text{-}4)$$

Figure 6-26 shows the calculated variable effective thermal conductivity, $\lambda_{p,t}$, for the C1 and C2 coatings applied to the CxxxCx sections, whilst Figure 6-27 shows $\lambda_{p,t}$ for the SxxxCx sections. The calculated variable thermal conductivity of the C1 coating is consistent when applied to the CxxxxC1 sections (Figure 6-26). When applied to the SxxFxC1 sections (Figure 6-27) slightly higher values and more variability are observed due to the shape effect and increased heating at the corners, as previously discussed. The general trend for the protection is a sharp drop in $\lambda_{p,t}$ in the early stages of heating before a steel temperature of 100^{o}C is reached. As the intumescent reacts, $\lambda_{p,t}$ drops to a minimum value of approximately 0.01 W/m^{o}C when the steel temperature is at about 150^{o}C. beyond this point, $\lambda_{p,t}$ slowly increases as the char layer slowly degrades due to further heating, but remaining below 0.075 W/m^{o}C.

$\lambda_{p,t}$ for the C2 coating takes longer to react to heating with the minimum $\lambda_{p,t}$ of 0.017 W/m^{o}C occurring at approximately 225^{o}C after initially higher values compared to C1. After the minimum is reached, the C2 responds in a similar manner to C1.

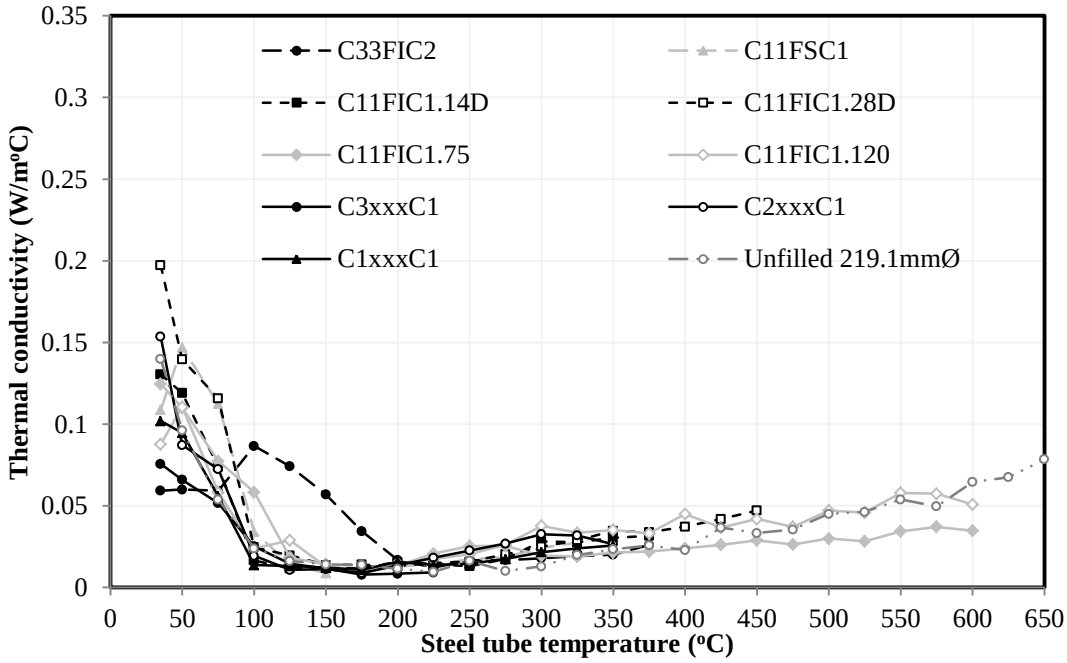

Figure 6-26: Variable effective thermal conductivity of intumescent protection coatings on circular CFS sections

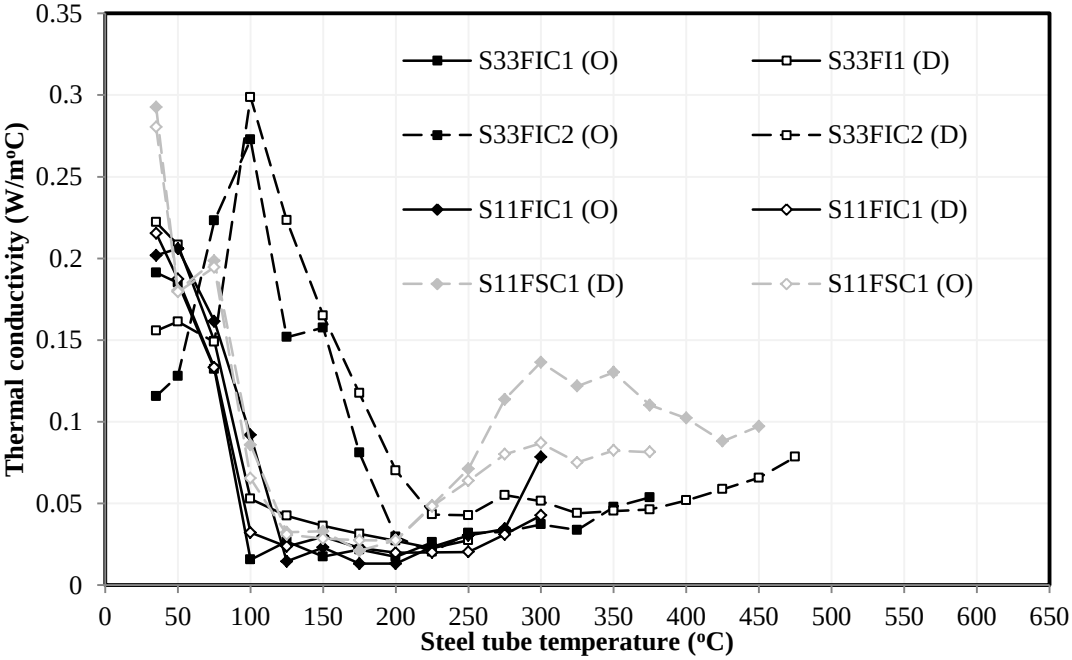

Figure 6-27: Variable effective thermal conductivity of intumescent protection coatings on square CFS sections

Figure 6-26 shows the average $\lambda_{p,t}$ response of the C1 coating on three unfilled 219.1 mm Ø hollow sections (similar to the C2xxC1 protected sections) protected for 90 and 120 minutes, respectively, with wall thicknesses of 8 mm and 16 mm and section factors of more than 60 m^{-1}. These data were provided by industry partner International Paint Ltd. The unfilled 219.1 mm Ø unfilled sections reach their limiting temperature 520^{o}C between 5 and 15 minutes after the required fire resistance time. $\lambda_{p,t}$ of the C1 intumescent coating on the unfilled hollow sections is effectively the same (within experimental accuracy) as for the protected CFS sections.

The similarities shown between the $\lambda_{p,t}$ response of the different thicknesses of C1 coating (between 2 mm DFT and 4 mm DFT) on sections with different section factors (H_p/A_{eff} varying from 38 m^{-1} to 55 m^{-1}) with different levels of fire resistance required (75, 90, 120 minutes), suggests that the relationship between the DFT and the section factor is sufficiently well understood for this product and that the thermal mass of the substrate has little obvious effect on the insulating response. This suggests that the conservatism in the prescription of DFTs is not due to Cause (2) noted in Section 6.2.

6.2.2 Effective section factors for CFS sections

The above discussion suggests that the calculation of the effective section factor for CFS columns may cause the observed conservatism in steel temperatures for protected CFS columns. To assess this hypothesis it is necessary to describe the development of the current H_p/A_{eff} guidance and to determine whether improvements can be made, both for unprotected and protected CFS sections, using data from the tests detailed in Chapter 5.

6.2.2.1 Development of the Hicks et al. (2002) guidance

The existing H_p/A_{eff} guidance given in Equation 6-2 (Hicks et al., 2002) is based on the assumptions that:

1. a CFS section can be treated as a hollow steel tube where the concrete core provides an equivalent thickness of steel wall based only on the required fire resistance of the CFS section; and
2. the effective section factor for an unprotected CFS section is the same as a protected CFS section, as would be the case (and as shown by a considerable body of testing) for protected versus unprotected unfilled hollow steel tubes.

These assumptions were used to develop current guidance by Edwards (1998), who assumed that the increase in steel temperature for an unprotected steel hollow section, or CFS section where the concrete is converted into an equivalent thickness of steel, can be calculated using a simple lumped mass energy balance taken from EN 1993-1-2 (CEN, 2009b):

$$\Delta\theta_{a,t} = \frac{\dot{h}_{net}}{c_{a,\theta} \cdot \rho_a} \cdot \frac{H_p}{A} \cdot \Delta t \qquad (6\text{-}5)$$

where the increase in steel temperatures, $\Delta\theta_{a,t}$, during time interval, Δt, is determined based on the section factor, H_p/A, and the net heat flux, $\dot{h}_{net}$, and the thermal capacity of the steel ($c_a \cdot \rho_a$). It is noteworthy that this "lumped mass" approach works in practice because steel has a relatively high thermal conductivity. Using data from six standard furnace tests on unprotected CFS columns, an instantaneous effective section factor, $H_p/A_{eff}\ (Exp)$, was suggested by Edwards (1998) at every instant in time by rearranging Equation 6-5, giving:.

$$\frac{H_p}{A_{eff}}(Exp) = \frac{\Delta\theta_{a,t}}{\Delta t} \cdot \frac{c_{a,\theta} \cdot \rho_a}{\dot{h}_{net}} \qquad (6\text{-}6)$$

The BS EN 1991-1-2 (CEN, 2009c) method for calculating $\dot{h}_{net}$ (Equation 2-41) was used by Edwards (1998), however in the determination of radiative heat flux Edwards used a resultant emissivity (i.e. the product of the fire emissivity, $\varepsilon_{m,fi}$, and steel emissivity, $\varepsilon_{m,a}$) of 0.32; his justification for using this value is not clear. It is important to note that in determining the instantaneous effective section factor from furnace experiments, low values of the resultant emissivity will calculate larger instantaneous effective section factors, which is conservative for design.

Edwards used his calculated $\dot{h}_{net}$, the EC4 (CEN, 2005) density of steel (ρ_a = 7850 kg/m^3), and the specific heat capacity of steel from Equation 6-7, up to a steel temperature of 800^{o}C after which a constant value of 877.6 J/kg was used, to calculate the effective section factor, giving:

$$c_{a,\theta} = 473 + 20.1 \cdot \left(\frac{\theta_a}{100}\right) + 3.81 \cdot \left(\frac{\theta_a}{100}\right)^2 \quad (6\text{-}7)$$

Edwards (1998) found that the effective section factor, H_p/A_{eff} *(Exp)*, and thus the effect of the concrete core, varied with time during a furnace test. This is unlike plain steel sections where the section factor remains constant for the duration of a fire test. This different response is due to thermal gradients developing with the concrete infill in a CFS section, whereas the high thermal conductivity of steel results in an almost uniform temperature profile in an unfilled CFS section. From the calculated experimental instantaneous effective section factors, Edwards calculated the apparent thickness of the steel tube, $t_{a,eff}$, at every instant in time during fire exposure, and thus determined the apparent increase in the steel tube thickness resulting from the concrete core, $t_{c,eff}$. Precisely how Edwards moves from this realization to the correlations given in Equation 6-3 is not clear and has never been presented in the literature. It is noteworthy that Equation 6-3 lies well below all of the experimentally calculated values of $t_{c,eff}$.

6.2.2.2 Calculation of H_p/A_{eff} *(Exp)* for unprotected CFS sections

Using the same process as Edwards (1998) (i.e. Equation 6-6) it is possible to calculate the instantaneous H_p/A_{eff} *(Exp)* for the unprotected CFS sections detailed in Table 5-5. To calculate H_p/A_{eff} *(Exp)* a net heat flux is required. The previous finite element heat transfer analysis (Section 6.1.1) of the tests on unprotected CFS sections found that the effective emissivity of the furnace was about 0.38 and that a temperature dependent emissivity of steel, based on tests conducted by Paloposki and Liedquist (2005), was the most appropriate modelling choice for simulation of the furnace tests presented herein. The resultant emissivity therefore varied with temperature from a value of 0.08 up to 385^{o}C, increasing up to 0.25 at 550^{o}C, after

which a constant value of 0.25 was found. The temperature dependent specific heat capacity of steel was taken from BS EN 1993-1-2 (CEN, 2009b). It is noteworthy that data were acquired every 60 seconds to a precision of ±1^{o}C during testing.

Figure 6-28 shows a representative comparison of the calculated instantaneous H_p/A_{eff} *(Exp)* using Equation 6-6 along with Edwards' theoretical H_p/A_{eff} *(Th)* (Equation 6-2) for a typical unprotected CFS section (C22FIN from Table 5-5 in this case). The obvious peak, highlighted with a data marker in the H_p/A_{eff} *(Exp)* curve, coincides with a phase change in the steel at 735^{o}C which causes a spike in the specific heat capacity of the steel. Considerable variability was observed in calculated instantaneous H_p/A_{eff} *(Exp)* values during the first 30 minutes of heating. This is due to the imperfect furnace control and large differences between the steel and furnace temperatures during the early stages of heating. This created large variations in the apparent net heat flux during each one minute time interval and thus in the calculated instantaneous H_p/A_{eff} *(Exp)*.

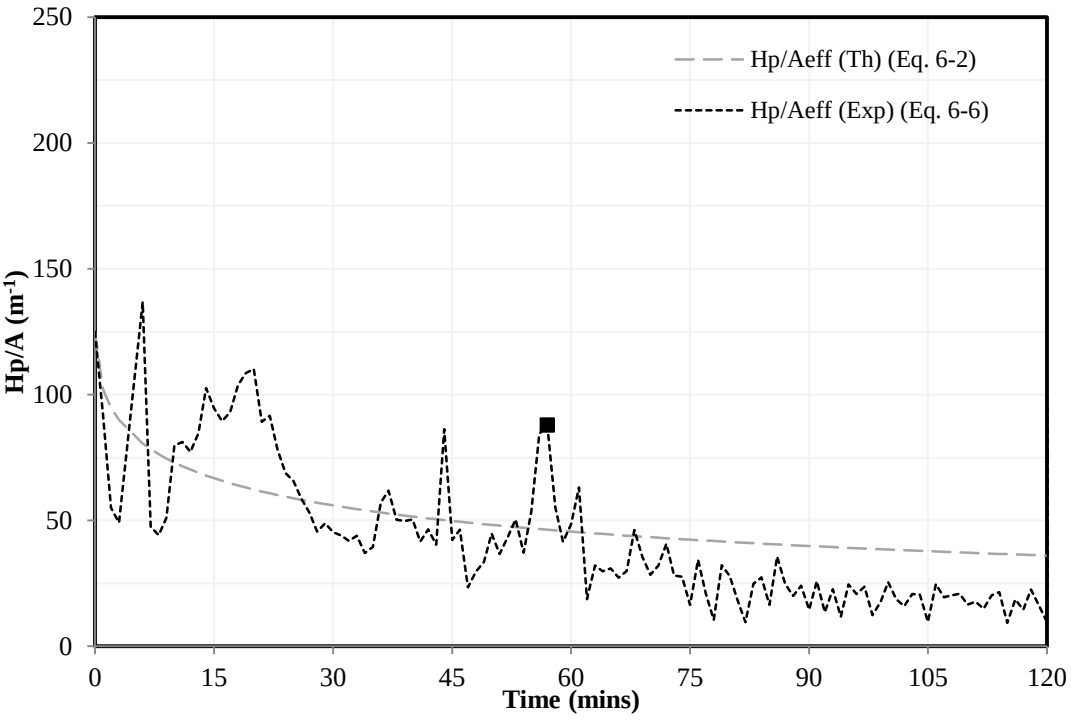

Figure 6-28: Representative theoretical (based on Equation 6-2) and calculated (based on Test C22FIN) effective section factors, H_p/A_{eff}

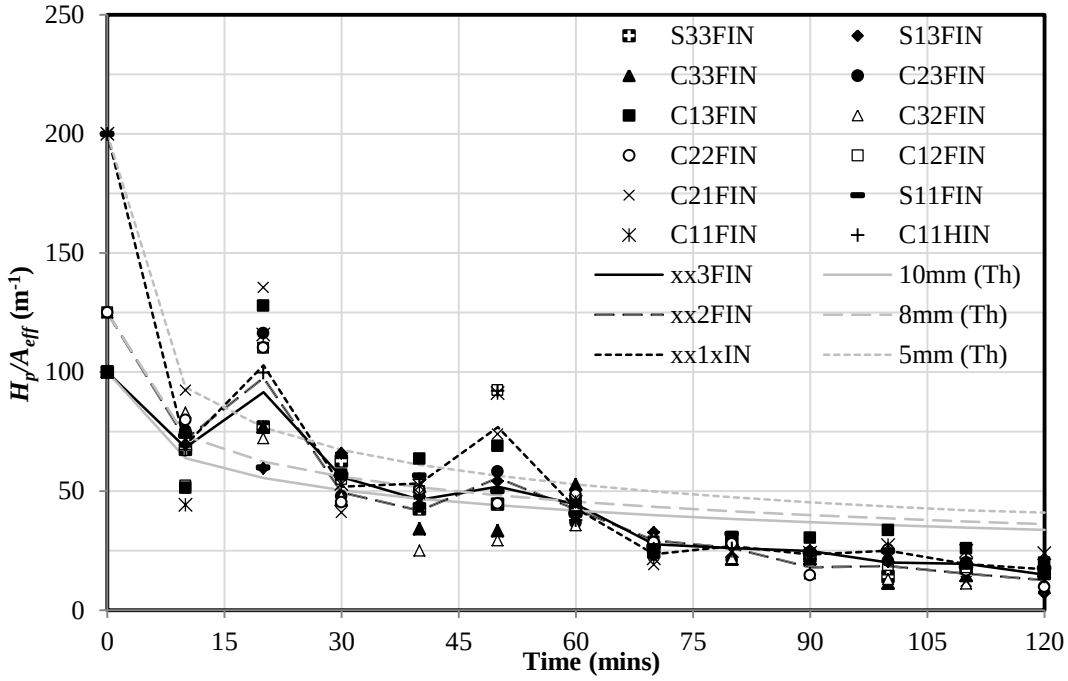

Figure 6-29: Theoretical and calculated effective section factors, H_p/A_{eff}, partitioned based on wall thickness for unprotected CFS tests

Figure 6-29 shows the instantaneous H_p/A_{eff} *(Exp)* for all unprotected sections from Chapter 5 at 10 minute intervals throughout the tests (data markers), and shows that the values of the averaged instantaneous H_p/A_{eff} *(Exp)* based on the wall thickness size are, with notable exceptions before 60 minutes of fire exposure, generally slightly less at any given time than Edwards' H_p/A_{eff} *(Th)*; however Edwards' equation does a good job of predicting the overall trends in the experimental data.

Figure 6-28 and Figure 6-29 also shows that effective contribution of the concrete core varies with time during heating, as also shown by Edwards (Edwards, 1998). This is due to the low conductivity of the concrete, resulting in thermal gradients in a CFS section that would not be present in an unfilled tube. Larger concrete cores will have larger thermal gradients, as seen in the observed temperatures in Figure 6-10, and these will persist for longer in larger sections due to the low thermal conductivity of concrete and its thermal mass. The contribution of the concrete will therefore also be dependent on the overall size of the concrete core, a factor which Edwards' guidance cannot account for.

6.2.2.3 Determining theoretical (H_p/A_{eff})' values

To make a physically realistic calculation of instantaneous H_p/A_{eff} for unprotected CFS sections the effect of the concrete core size needs to be rationally incorporated. Equation 6-8 uses a new method to calculate the instantaneous section factor, (H_p/A_{eff})' (British Standard Institute, 1994) by converting the concrete core into an equivalent *area* (rather than thickness) of steel based on the size of the core, A_c, the ratio of the respective heat capacities of concrete and steel, and an empirically determined concrete core efficiency factor, η, which is needed to account for the effect of thermal gradients in the concrete. Using the instantaneous H_p/A_{eff} *(Exp)* calculated previously on the basis of the unprotected tests from Chapter 5 as an input into Equation 6-8, the value of the concrete core efficiency factor, η, can be calculated during each one minute time interval.

$$\left(\frac{H_p}{A_{eff}}\right)' = \frac{H_p}{A_a + \eta \cdot \frac{(c_c \cdot \rho_c)}{(c_{a,\theta} \cdot \rho_a)} \cdot A_c} \qquad (6\text{-}8)$$

where η is a concrete core efficiency factor; and c_c and ρ_c, c_a and ρ_a, are the specific heat capacities and densities of concrete and steel, respectively.

Figure 6-30 shows the variation of η with time for two representative unprotected CFS sections exposed to an ISO 834 (ISO, 1999) standard fire. The relationship between η and furnace time, t_{furn}, has considerable variability. This variability occurs because the measured steel temperature changes from the tests were small and were measured with a resolution of only 1°C. The result of this is shown with three points (white circle markers) in Figure 6-30(a) where the steel temperature change between minutes 103-104-105-106 is 3^oC-1^oC-4^oC, respectively.

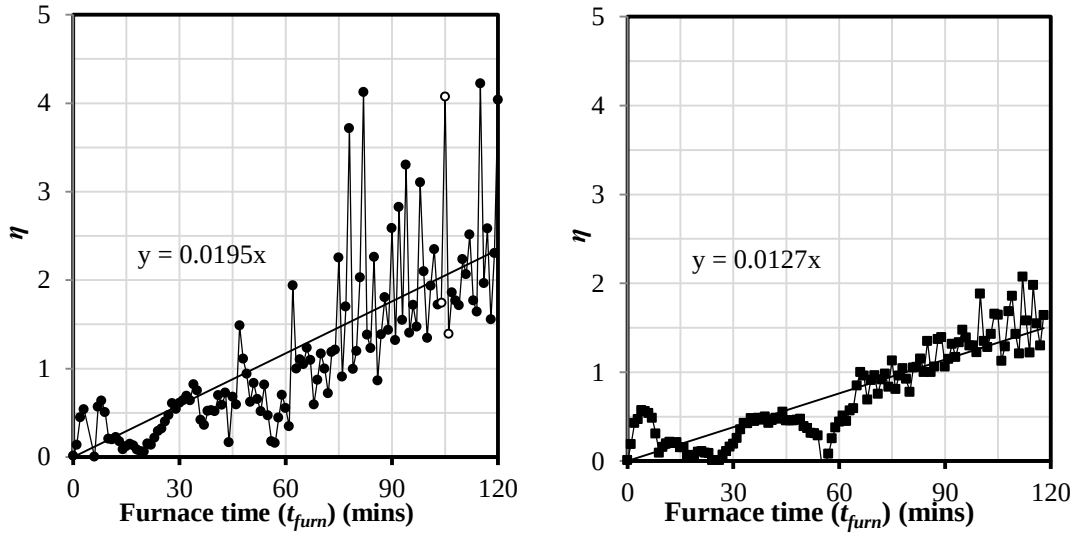

Figure 6-30: Representative η vs. t_{furn} curves for (a) Test C22FIN and (b) Tests S33FIN

As with Edwards' (1998) calibration of effective wall thickness (Equation 6-3), the apparent efficiency of the concrete core, η, varies with time of fire exposure. If the relationship between η and furnace time, t_{furn}, is assumed to be linear, then a larger gradient of η/t_{furn} is found for smaller internal breadths of concrete. Figure 6-31 shows η with respect to furnace time, t_{furn}, for all unprotected SxxFIN sections while Figure 6-32 shows η with respect to furnace time, t_{furn}, for all unprotected CxxFIN sections, presented in Chapter 5. Figure 6-31 and Figure 6-32 show that in general, as the breadth of a CFS column increases, and hence so does the size of the internal concrete core, the assumed linear gradient η/t_{furn} decreases. This is physically meaningful and confirms that the size of the concrete core has an effect on the heat transfer, and that the gradient η/t_{furn} depends on its size. Therefore the internal breadth, b_i, of a CFS section can be compared to the gradient η/t_{furn}, as shown in Figure 6-33, and a relationship for η/t_{furn} is found.

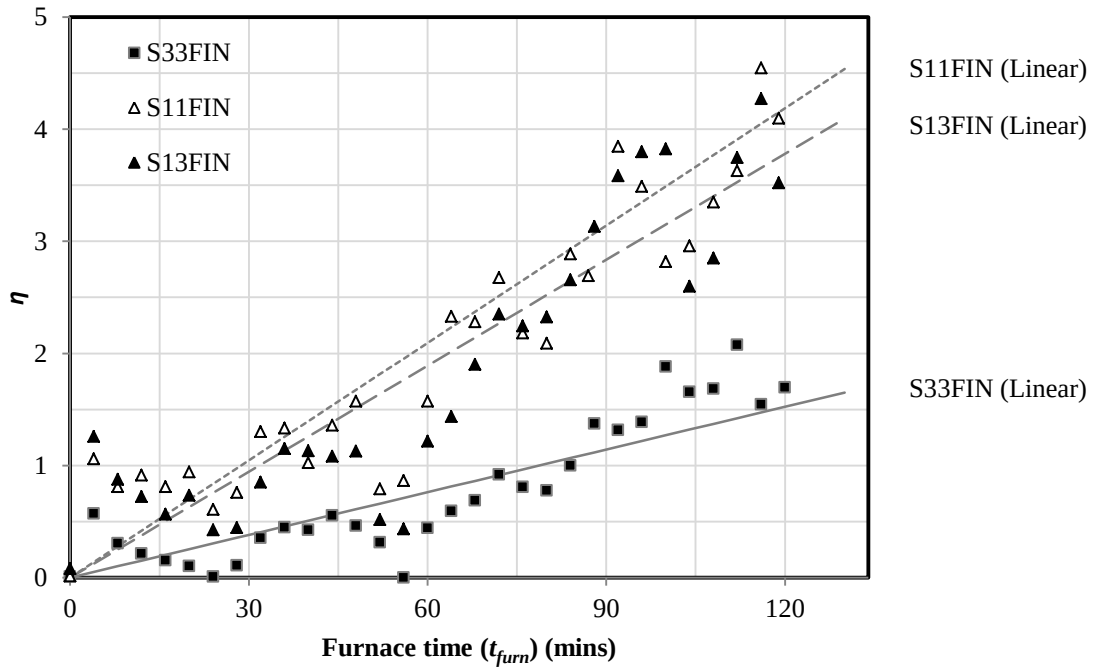

Figure 6-31: Concrete core efficiency factor, η, versus time in furnace, t_{furn}, for SxxFIN unprotected CFS tests with assumed linear relationships

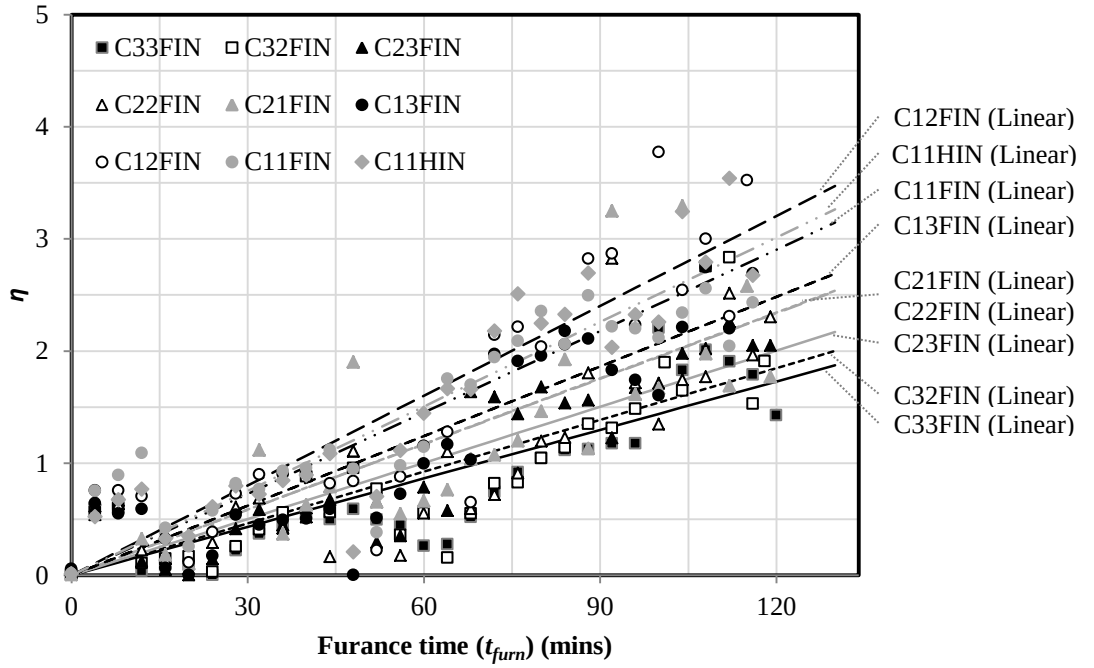

Figure 6-32: Concrete core efficiency factor, η, versus time in furnace, t_{furn}, for CxxxIN unprotected CFS tests with assumed linear relationships

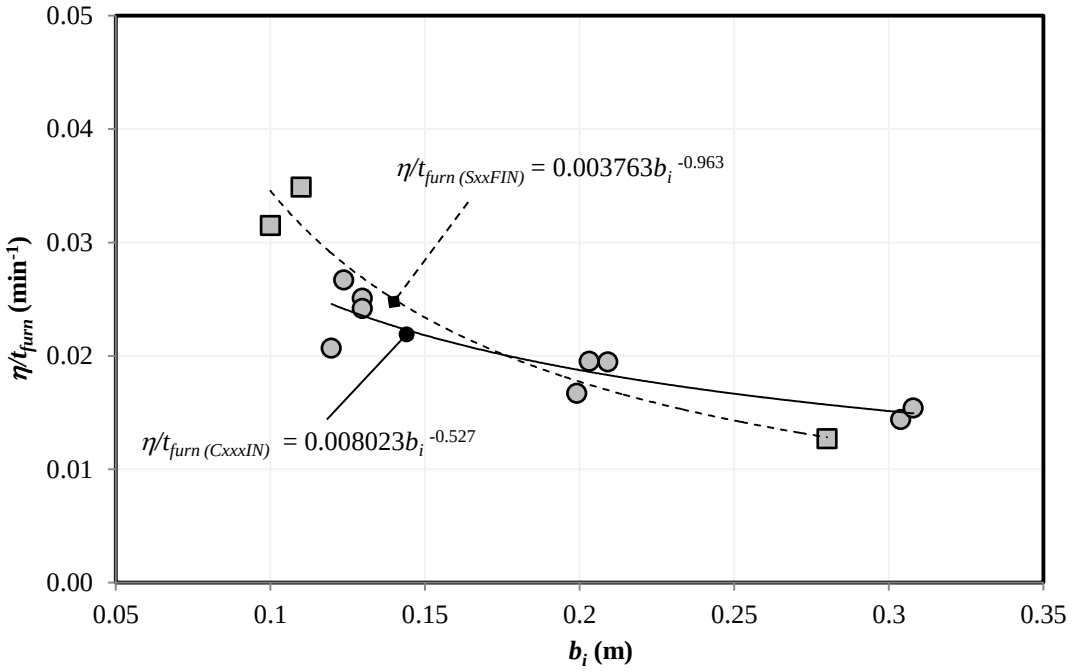

Figure 6-33: Gradient of linear η/t_{furn} relationships versus the internal breadth of the concrete core, with assumed inverse function relationships for square and circular sections

Figure 6-33 shows the relationships of the gradients of η/t_{furn} to the internal breadth of a CFS column as an inverse function. This is physically realistic since η must always remain positive and has been seen to decrease as the size of the concrete core increases. The calculation of η can be expressed in terms of the internal breadth, $b_{i,}$ and time of furnace exposure, t_{furn}:

$$\eta = \begin{cases} 0.008023 \cdot b_i^{-0.527} \cdot t_{furn} & Circular \\ 0.003763 \cdot b_i^{-0.963} \cdot t_{furn} & Square \end{cases} \quad (6\text{-}9)$$

Instantaneous theoretical (H_p/A_{eff})' values can then be calculated with respect to time using η values calculated from Equation 6-9 with an iterative process involving the calculation of the change in steel temperature using Equation 6-5. The variation of instantaneous (H_p/A_{eff})' with time is compared to the instantaneous H_p/A_{eff} *(Exp)* calculated from test data (Equation 6-6) and H_p/A_{eff} *(Th)* calculated from Edwards' current guidance (Equation 6-2) in Figure 6-34 for a representative unprotected test

(219.1 Ø × 8 mm wall thickness circular section). Figure 6-34 shows that the instantaneous (H_p/A_{eff})' is a more realistic predictor of instantaneous H_p/A_{eff} *(Exp)*.

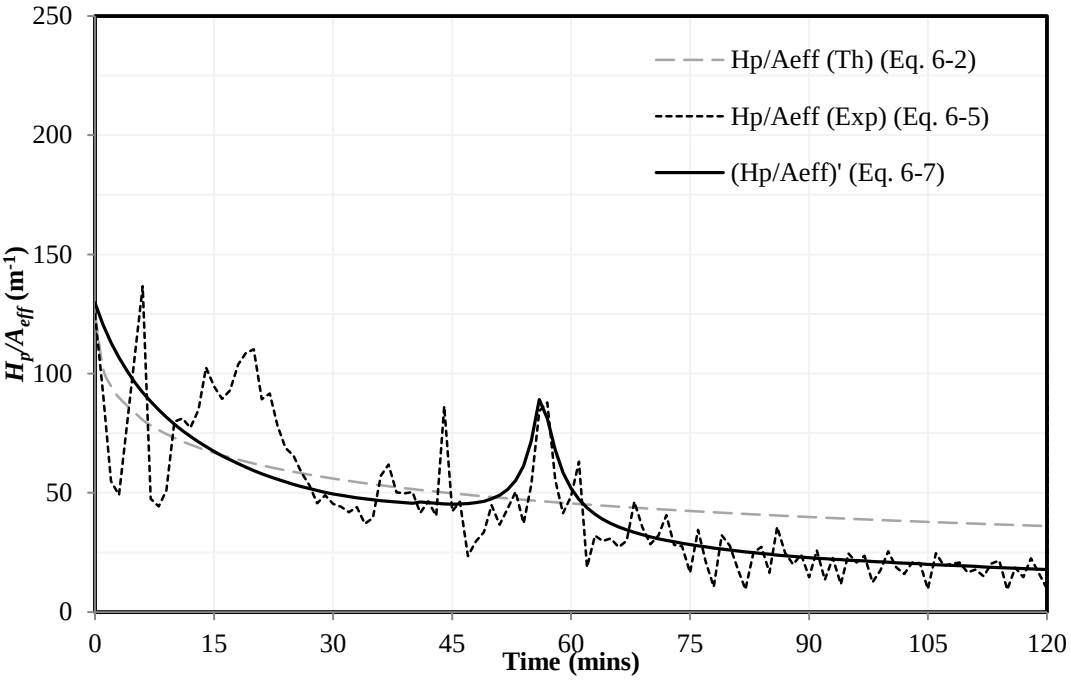

Figure 6-34: Comparison of instantaneous (H_p/A_{eff})', H_p/A_{eff} *(Exp)*, and H_p/A_{eff} *(Th)* for a representative unprotected CFS section (Test C22FIN)

6.2.2.4 Use of instantaneous (H_p/A_{eff})' in design

The instantaneous (H_p/A_{eff})' has been shown to be a better predictor of the observed *instantaneous* effective section factor for unprotected CFS sections during furnace exposure. However, (H_p/A_{eff})' only calculates the section factor for one specific one minute interval in time. The (H_p/A_{eff})' values cannot be used in determining the design DFT of an intumescent for protecting a CFS section because the theoretical steel temperatures based on a single instantaneous (H_p/A_{eff})' for a specific time of fire exposure are lower than if the steel temperatures are calculated with the time dependent variable (H_p/A_{eff})'. Figure 6-35 shows the experimental steel temperatures from the representative unprotected 219.1 Ø × 8 mm wall thickness circular section along with the steel temperatures calculated using Equation 6-5. The effective section factor is calculated at every time step using either (H_p/A_{eff})' or H_p/A_{eff} (*Th*) from Equation 6-8 or Equation 6-2, respectively. Figure 6-35 shows that the

calculation of steel temperature using either the variable (H_p/A_{eff})' or H_p/A_{eff} (Th) provides accurate predictions.

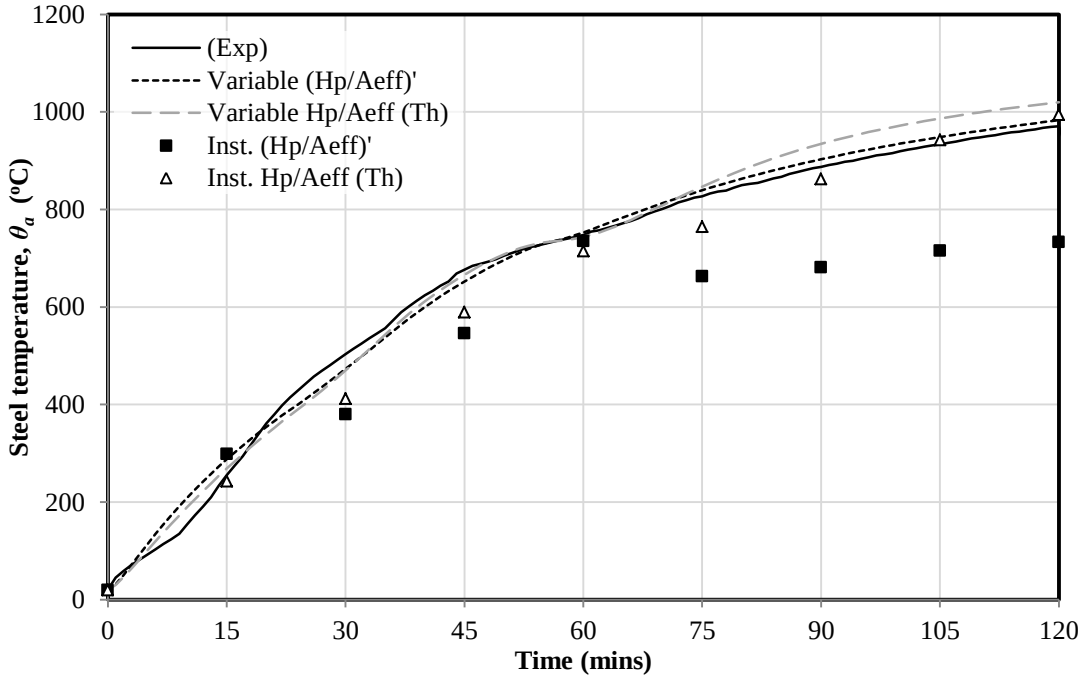

Figure 6-35: Comparison of observed and calculated steel temperatures using variable or instantaneous (Inst.) values of the effective section factor

Figure 6-35 also shows the predicted steel tube temperature at 15 minute intervals based on a single instantaneous effective section factor calculated using either (H_p/A_{eff})' or H_p/A_{eff} (Th) from Equation 6-8 or Equation 6-2, respectively. The steel temperatures are again calculated using Equation 6-5, but with a single constant value of either (H_p/A_{eff})' or H_p/A_{eff} (Th). The single constant values are given in Table 6-3. It should be noted that the instantaneous (H_p/A_{eff})' at 60 minutes is higher than the value at 45 minutes due to the peak caused by the phase change in steel at about 735^{o}C (refer to Figure 6-34). Figure 6-35 clearly shows that the use of a single instantaneous effective section factor under-predicts the observed steel temperatures, and this is unconservative for structural fire resistance calculations.

Table 6-3: Instantaneous $(H_p/A_{eff})'$ and H_p/A_{eff} (Th) effective section factors at 15 minute intervals for Test C22FIN

Time (mins)	*Inst.* $(H_p/A_{eff})'$ (Equation 6-8)	*Inst.* H_p/A_{eff} *(Th)* (Equation 6-2)
0	129.7	125.0
15	67.4	66.8
30	49.6	56.0
45	45.3	49.8
60	*51.9*	45.6
75	28.3	42.4
90	22.8	39.9
105	20.0	37.8
120	17.9	36.1

The temperatures experienced by the steel tube of an unprotected CFS cross section are due to cumulative heating where the (H_p/A_{eff})' varies with time, whereas for an unprotected plain steel section the increase in temperature (Equation 6-5) is based on a single value of H_p/A. It is therefore inappropriate and unconservative to use the instantaneous value of (H_p/A_{eff})' to calculate either the steel temperature at a specific instant in time, or the required DFT of an intumescent coating. A time-averaged (H_p/A_{eff})' that accounts for the effect of the time history of effective section factor is therefore required.

6.2.2.5 Determination of time averaged section factors, $(H_p/A_{eff})'_{t.ave}$

The preceding sections have shown that the effective section factor for a CFS column in fire varies with time due to the thermal gradients which exist within the concrete core. However, specification of intumescent coatings from tabulated DFT data requires a single initial effective section factor that can be assumed and which accounts for the cumulative heating of a CFS section caused by these time dependent (H_p/A_{eff})' values (calculated from Equation 6-8). A single time averaged effective section factor, $(H_p/A_{eff})'_{t.ave}$, that accounts for the cumulative heating history of the section factor is needed so that the theoretical steel temperatures, calculated using Equation 6-5 for a given required time of fire resistance, are the same when using either the single time averaged effective section factor, $(H_p/A_{eff})'_{t.ave}$, or the variable time dependent instantaneous (H_p/A_{eff})' values calculated from Equation 6-8.

To determine the single time averaged effective section factor, $(H_p/A_{eff})'_{t.ave}$, which, when used in Equation 6-5, predicts the same steel temperatures after the same duration of fire exposure as using the time variable $(H_p/A_{eff})'$, the $(H_p/A_{eff})'$ curve must be derived for any given section (e.g. as in Figure 6-34 for a 219.1 Ø × 8 mm wall thickness circle) and applied through Equation 6-5 to determine the increase in steel temperature with time using a stepwise approach. This results in a calculation of the steel temperature at the required fire resistance time. A similar stepwise calculation must then be performed, using a constant value of H_p/A_{eff} to arrive at the same steel temperature after the same duration of fire exposure. This procedure must then be repeated for each and every desired fire resistance time to give a trace of $(H_p/A_{eff})'_{t.ave}$ with fire exposure time.

Time averaged effective section values, $(H_p/A_{eff})'_{t.ave}$ for a representative unprotected test (219.1 Ø × 8 mm wall thickness circular section) are shown in Figure 6-36, which gives a representative comparison of the instantaneous $(H_p/A_{eff})'$ and H_p/A_{eff} *(Exp)* values with time of fire exposure, along with the current effective section factor guidance H_p/A_{eff} (*Th*) and $(H_p/A_{eff})'_{t.ave}$ values. The representative averaged areas are schematically shown for each 15 additional minutes for fire exposure. The same process was performed for all of the unprotected CFS sections in the current study, and the resulting $(H_p/A_{eff})'_{t.ave}$ values are compared to the H_p/A_{eff} (*Th*) values in Figure 6-37.

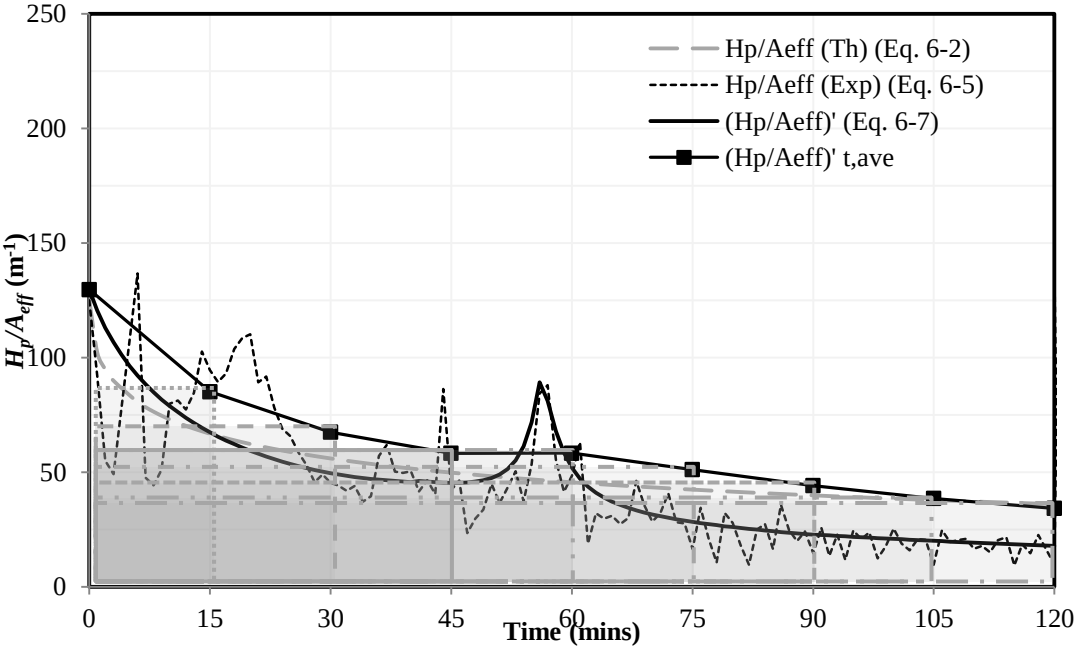

Figure 6-36: Representative comparison of time averaged $(H_p/A_{eff})'_{t.ave}$, with area blocks, to theoretical and experimentally calculated instantaneous effective section factors (Test C22FIN)

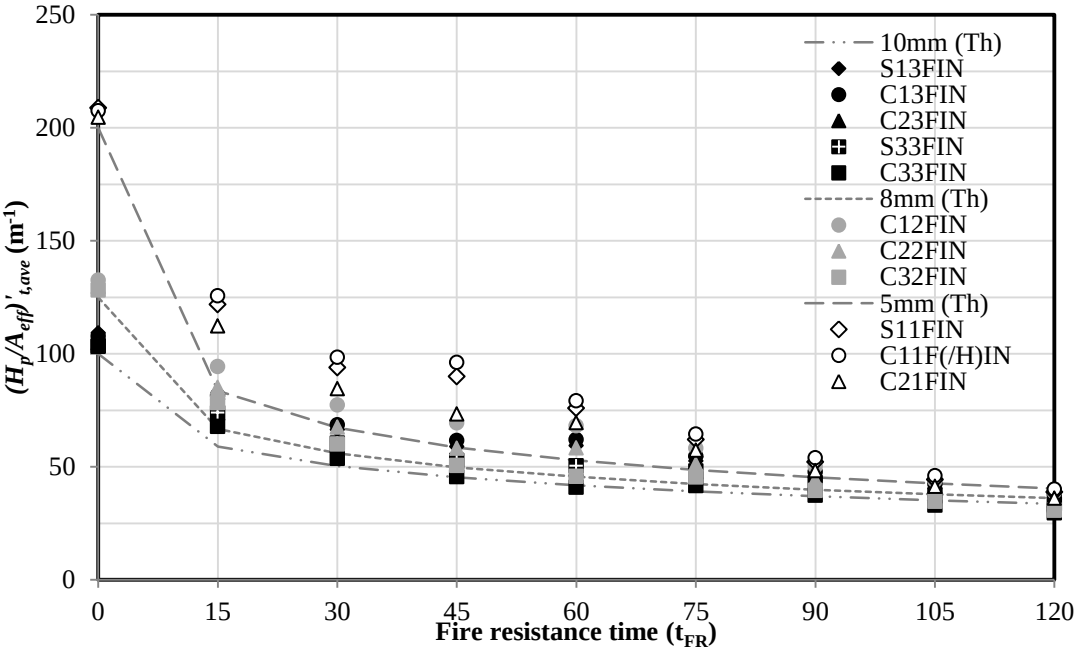

Figure 6-37: Comparison of time averaged $(H_p/A_{eff})'_{t.ave}$ for all xxxxIN unprotected tests to H_p/A_{eff} *(Th)* (Equation 6-2)

Figure 6-37 shows that the time averaged effective section factors, $(H_p/A_{eff})'_{t.ave}$, for the unprotected CFS sections presented in Chapter 5, are, in general, greater than the effective section factors calculated at the same time using the current guidance, H_p/A_{eff} (*Th*) (Equation 6-2). Therefore, if the $(H_p/A_{eff})'_{t.ave}$ values for the unprotected CFS sections were to be used in the prescription of the dry film thickness (DFT) of an intumescent paint, a *thicker* DFT would be prescribed compare to the DFT prescribed on the basis of H_p/A_{eff} (*Th*) for the same limiting temperature and required fire resistance. This would result in *even lower* steel tube temperatures for a protected CFS section than those observed in the protected tests (Figure 6-25) in which the design DFTs were based on lower effective section factors calculated from Edwards' H_p/A_{eff} (*Th*). Whilst this may be more physically realistic and thus more 'correct' than Edwards' approach, it does nothing to address the observed conservatism in furnace tests of protected CFS column.

The above discussion shows that the conservatism seen in prescription of the DFT is thus not attributable to inaccurate determination of the effective section factors for unprotected CFS sections. Instead, the conservatism must be the result of the assumption that the effective section factors for unprotected CFS sections and protected CFS sections can be treated in the same manner, and the subsequent use of unprotected CFS effective section factors to prescribe intumescent coating DFTs for protected CFS sections. This is due to the fundamental changes in the thermal gradient that is observed within a protected CFS section compared to that of an unprotected CFS section. Protected CFS sections experience a less severe thermal gradient within the concrete fill, which effectively increases the thermal effect that the concrete core has on the effective section factor of a protected section.

The thermal gradient within a protected CFS section is dependent on the heating rate that the steel experiences, which in turn is affected by:

1. the limiting temperature that the steel is protected to, since higher steel temperatures result in more severe thermal gradients in the core and lessen the effect of the concrete on the effective section factor;

2. the required fire resistance period of the CFS section, with longer fire resistances producing shallower thermal gradients and thus increasing the effect of the concrete core on the effective section factor; and
3. the performance of the intumescent coating, especially its variable effective thermal conductivity, with respect to time of heating.

If the conservatisms which appear to be inherent in the current approach for the specification of intumescent protection DFTs for CFS sections are to be avoided, additional analytical work and experimental testing of protected CFS sections is needed. A broad range of heating rates to the steel must be considered so that the effective section factor for protected CFS sections is better understood and a rational means of prescribing effective section factors can be developed. A framework to resolve this problem is presented in Section 6.2.4; however in the interim it is recommended that current guidance from Equation 6-2 and Equation 6-3 (based on Hicks et al., 2002) should be used to determine the effective section factor for CFS columns, since this has been shown to be conservative.

6.2.3 Limiting steel temperature for protected CFS sections

Designing intumescent protection systems for CFS columns requires a limiting steel temperature (i.e. the temperature of the steel at which the CFS column fails) as an input to define the required DFT. The determination of limiting steel temperature in a CFS section is complicated since the concrete core has a non-uniform temperature and carries a portion of the applied load (in large sections this can be significant).

Somewhat paradoxically, the limiting temperature also changes with the amount of protection that is applied to the CFS section. In unprotected CFS columns the thermal gradient can be steep, and at the point of column failure the steel will generally be much hotter than the concrete core. This means that the concrete core retains a greater proportion of its strength and can carry a greater proportion of the load. When fire protection is added, as seen in the tests presented in Chapter 5, the thermal gradient becomes much shallower and thus the temperature difference between the steel tube and the concrete core at the point of failure is less. At the instant of failure the temperature of the concrete core is more uniform and

comparatively higher than in a similar unprotected CFS column under the same fire exposure, whereas the steel temperatures are comparatively lower. The limiting temperature of the steel of an unprotected section is therefore higher than the limiting steel temperature of a protected section; precisely because of the thermal gradients.

The lack of widely available and reliable thermal properties for intumescent coatings means that prediction of the thermal profiles for intumescent protected CFS columns, and their resulting structural responses during fire, is very difficult to make. It also means that accurate limiting temperatures cannot be easily predicted.

In the absence of more detailed knowledge, it would be conservative to assume that a protected CFS column has a uniform temperature over its entire cross-section (i.e. no thermal gradient). The CFS columns' structural resistance could then be calculated using the EC4 Annex H approach (CEN, 2005) and a critical temperature for the section at constant temperature could be prescribed.

To illustrate this important point, Figure 6-38 shows the observed and predicted temperature profiles of an example column from the meta-analysis dataset of Chapter 3, in both unprotected and uniform thermal profile states. This column is a 219.1 Ø × 5 mm thick, unprotected circular CFS column which failed after 80 minutes at a steel tube temperature of 924^{o}C. The column had fixed-fixed end conditions and an effective length of 2 m in the fire limit state; it was filled with 31 MPa compressive strength plain siliceous aggregate concrete and the yield strength of the steel tube was 350 MPa. This results in a design strength of 1399 kN according to EC4 Annex H. The applied load during the test was 492 kN, meaning that the load ratio of the column was 0.352. The example column is similar in dimensions to C21FIN from Chapter 5.

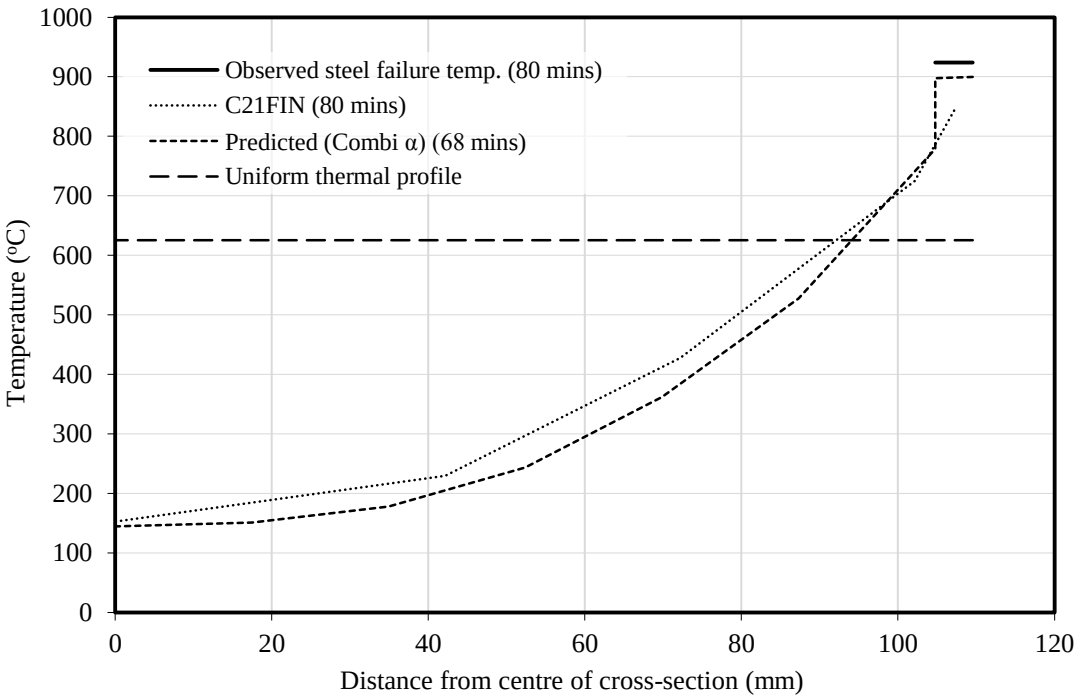

Figure 6-38: Observed and predicted temperature profiles of a 219.1 Ø × 5 mm circular column at failure

Figure 6-38 shows that the steel temperature at 80 minutes for the unloaded test, C21FIN of the current study, was 80°C lower than that observed in the example test. Using the *Combi α* modelling approach with the Annex H approach of EC4, the fire resistance time is predicted to be 68 minutes with a predicted steel failure temperature of 899°C, which is 12 minutes less and 25°C less than the observed time and temperatures in the example column. Figure 6-38 also shows the profile of the concrete temperatures seen in the C21FIN test and predicted by the *Combi α* modelling approach, and shows that the modelling approach predicts the form of the thermal profile in the concrete well. If the column were protected with an intumescent coating, based on the assumption that the column has uniform temperature, the critical temperature for the steel would be 625°C, or about 300°C less than in the unprotected case.

The limiting temperature for protected CFS sections should thus be calculated using the EC4 Annex H approach (CEN, 2005) with a uniform thermal profile assumed.

6.2.4 Recommended future development framework

The previous two sections have recommended conservative assumptions to be used in practice due to a lack of available information regarding the heating rate of the steel tube within a protected CFS column. A possible way of circumventing the paucity of information on the performance of intumescent coatings that are used to protect CFS columns is to assume a steel temperature profile. This circumvents the complex reactions that occur in the intumescent reaction and the resulting complications in predicting the heat transfer from the furnace to the steel through the insulting intumescent char layer. Instead, by assuming a rational approximate steel temperature profile, predictions of the thermal profile within the CFS section can be made, thus allowing for numerous predictions of limiting temperature and effective section factor.

Figure 6-39 shows one possible steel temperature curve for a protected CFS column. The curve is defined by two times and two temperatures; *F.R.* is the required fire resistance time and $\theta_{a,cr}$ is an assumed critical temperature for the steel tube; whilst $\theta_{int,r}$ and $T_{int,r}$ are product specific inputs defining the temperature and time at which the intumescent reacts.

For a given intumescent coating, with its independent $\theta_{int,r}$ and $T_{int,r}$, and a given CFS cross section, it is possible to calculate the thermal profile within the CFS cross-section by assuming different critical temperatures of the steel $\theta_{a,cr}$, at various fire resistance times. It is then possible to calculate the temperature dependent strength reduction factors for steel and concrete using the EC4 Annex H approach (CEN, 2005). Once the column specifications (i.e. steel and concrete strength, effective length of the column, etc.) are known, a structural capacity check can be conducted and an assessment on the fire resistance time and limiting temperature of the protected CFS section can be made.

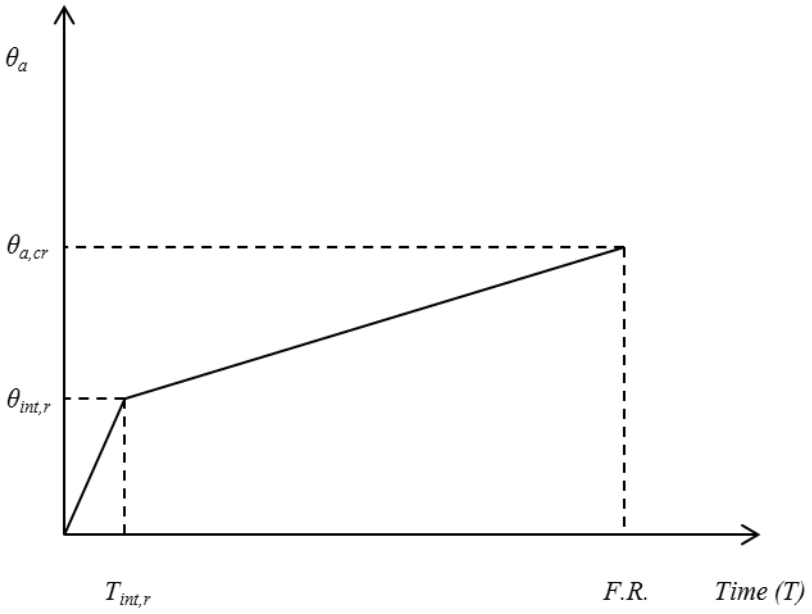

Figure 6-39: Idealised steel temperature profile for the simplified calculation of temperatures within intumescent protected CFS sections

Whilst the calculation of a limiting temperature is relatively simple, the determination of section factors (effective or otherwise) for protected CFS sections requires a far greater level of inquiry. The fundamental question that needs to be answered concerns the development and evolution of the thermal gradient within a CFS section and its effects on the effective section factor. To address this issue analytical and experimental data on protected CFS cross-sections, at various levels of fire resistance and with various limiting temperatures prescribed, are needed.

One possible approach would be to assume the idealised protected steel temperature profile from Figure 6-39. If it is then assumed that the intumescent, as well as the concrete can be transformed into an equivalent thickness of steel, then the effective section factor of a protected unfilled steel tube can be calculated using Equation 6-6. For the same steel temperature profile the effective section factor calculated using Equation 6-6 will be identical for both a protected CFS section and an unfilled hollow section. The calculated effective section factor from Equation 6-6 can then be used as an input to Equation 6-10:

$$\left(\frac{H_p}{A_{eff}}\right)' = \frac{H_p}{A_a + \eta_c \cdot \frac{(c_c \cdot \rho_c)}{(c_a \cdot \rho_a)} \cdot A_c + \eta_{int} \cdot \frac{(c_{int} \cdot \rho_{int})}{(c_a \cdot \rho_a)} \cdot A_{int}} \qquad (6\text{-}10)$$

For an unfilled steel tube A_c is zero and the effective section factor is based on the thickness of the intumescent paint. If the applicable thicknesses of paint for an intumescent product are available, for the relevant fire resistance time and limiting temperature, then the efficiency of the intumescent, η_{int}, to act as an equivalent area of steel can be calculated. Tests on filled sections are then required to compare the change in effective section factor due to the addition of the concrete core, when the same level of protection thickness is applied. From the comparison the concrete core efficiency factor, η_c, for a protected section can then be calculated. More tests are therefore required to understand how the efficiency of both the concrete and the intumescent change with respect to fire resistance time and steel limiting temperature, and how they change with respect to different products.

6.3 Chapter summary

This chapter has presented the development of a more accurate modelling approach to predict the temperatures within the CFS cross-sections tested in Chapter 5. The new *Combi γ* modelling approach employs the EC4 (CEN, 2005) steel thermal properties and the upper bound of concrete thermal conductivity. The modelling approach also employs a new equivalent area method for the specific heat capacity of concrete including the effect of water within the matrix, as well as an alternative gap conductance profile based on format presented by Ghojel (2004). The temperature dependent emissivity of the steel calculated by Paloposki and Liedquist (2005) was used in conjunction with an unrealistically low fire emissivity of 0.38 in order for the predicted heat transfer from the furnace to match that observed in the tests. The predicted temperatures were, for most instances, within 50^{o}C of the observed temperatures. The *Combi γ* modelling approach was then used in the same meta-analysis conducted with the EC4 Annex H approach (CEN, 2005) and was found to over predict the fire resistance, on average, by 10 minutes.

A more realistic fire emissivity of 0.75 was used in the *Combi α* modelling approach and again a meta-analysis was performed. The meta-analysis showed that the *Combi α* modelling approach has better predictive qualities, when used in the EC4 Annex H approach (CEN, 2005), than either of the two modelling approaches (*Combi EC4c* and *Combi ω*) developed in Chapter 3. The approach is seen to have a consistency in predictions across most physical parameters, not seen in the Chapter 3 meta-analysis, as well as an overall accuracy of less than one minute, with a standard deviation of approximately 19 minutes. It was also shown that the *Combi α* modelling approach is an accurate and precise predictor of steel failure temperatures.

The meta-analysis of the EC4 Annex H approach using the *Combi α* modelling approach, has shown improved predictive abilities compared to either the *Combi EC4c* and *Combi ω* modelling approaches, although there are areas that require further investigation. An in depth look into the mechanics models being used for both materials and the CFS column is needed so that the reasons why larger sections are consistently over-predicted when using the best-fit modelling approaches of *Combi α* and *Combi ω.* Further clarification on the heat input from the furnace is required with accurate investigation into the emissivities of both the fire and the steel, and a quantitative understanding of how the heat input varies in different furnaces.

More detailed investigations are needed into how, and under what conditions, a gap forms between the steel tube and concrete core, and what affects this varying gap size has on the overall heat transfer.

Due to the uncertainties raised and areas that still require investigation, it is recommended that, when using the Annex H approach of EC4 (CEN, 2005) for design, the emissivity of the fire be taken as 0.75, whilst the emissivity of the steel be taken as a conservative value of 0.7, and these values be employed in the EC1 (CEN, 2009c) approach to the heat transfer into an element. The thermal properties of steel should be taken from EC4, whilst for concrete the thermal conductivity should be taken as the upper bound from EC4 and the equivalent area of specific heat capacity, as described in Section 6.1.1., with the area being equivalent to the EC4 specific heat

capacity for with a peak of 6.5% water content, as presented previously. The introduction of a non-perfect contact boundary between the steel and the concrete is also recommended to improve the temperature predictions through the cross-section and should be assumed as a variable thermal conductance based on Equation 2-8.

This chapter has also discussed the difficulties in the accurate prescription of intumescent coatings for protected CFS sections. It was found that the reason for the conservative prescription of intumescent coatings was the inappropriate, if conservative, use of the effective section factor determination that is based on unprotected CFS sections. The chapter also discussed the determination of critical steel tube temperatures within CFS sections and demonstrated that the limiting temperatures of a protected and unprotected CFS section are significantly different. A framework is proposed to aid further research and development of rational guidance on the calculation of effective section factor and steel tube limiting temperature for the specification of intumescent coatings.

Due to the lack of rational guidance, it is recommended that the critical temperature, from which protection systems be prescribed, be calculated using the Annex H approach of EC4 (CEN, 2005) assuming a uniform cross-sectional temperature, and determining at what critical temperature the cross-section would fail. This is assumed to be a very conservative assumption, as in reality there would be a slight gradient. It is also recommended that the current guidance on the calculation of the effective section factor (Hicks et al., 2002) be used as it has been shown to be conservative.

Chapter 7: Residual strength of CFS columns

After a fire, where a building has not experienced a major structural failure (however that might be defined), a question remains as to how much damage may have been caused to the structure, and whether the building (possibly incorporating CFS columns) can be rehabilitated or re-used safely. Also there are questions to what level repair and strengthening may be required. Whilst there have been a large number of tests on the performance of CFS columns during fire, there has been relatively little work on the post-fire, residual strength of CFS columns.

This chapter experimentally explores the post fire residual axial compressive load bearing and deformation capacity of 19 of the 34 CFS columns presented in Chapter 5 after they had been exposed to fire and cooled back to ambient temperature, along with six unheated control columns. Predictions of the failure load are made using specific residual strength stress strain relationships based on the maximum temperatures experienced during the heating of the sections at various locations. The predictions are compared against the results of the residual strength tests.

7.1 CFS column residual strength testing program

The post fire residual testing program involved the eccentric axial compressive loading to failure of a total of 25 CFS column specimens; details are presented in Table 7-1. The 25 specimens included the 19 C1xxxx and S1xxxx thermal test specimens presented in Chapter 5, of which 15 were exposed to the ISO 834 (*I*) fire (Equation 2-37) and four were exposed to the Smouldering fire (*S*) curve (Equation 2-38). Six unheated (*N*) control specimens, cast at the same time as the thermally tested specimens (the bold xxxxNN specimens in Table 7-1), provide undamaged ambient strengths.

Table 7-1: Residual strength testing matrix and maximum temperatures experienced in the steel tube and concrete core

Test specimen[a]	Size (mm)	Wall thick. (mm)	Infill type[b]	Heating regime[c]	F.R.[d]	Temperatures (^oC)[e]			
						Steel	Conc. face	35 mm	Conc. Cent.
S13FNN	**120**	**10**	**FIB**	**N**	**N/A**	**20**	**20**	**20**	**20**
S11FNN	**120**	**5**	**FIB**	**N**	**N/A**	**20**	**20**	**20**	**20**
S13FIN	120	10	FIB	I	N/A	991	969	893	886
S11FIN	120	5	FIB	I	N/A	979	930	856	841
S11FSN	*120*	*5*	*FIB*	*S*	*N/A*	*988*	*956*	*833*	*826*
S11FIC1	120	5	FIB	I	90	314	290	281	281
S11FSC1	*120*	*5*	*FIB*	*S*	*90*	*434*	*383*	*319*	*322*
C11HNN	**139.7**	**5**	**HSC**	**N**	**N/A**	**20**	**20**	**20**	**20**
C11FNN	**139.7**	**5**	**FIB**	**N**	**N/A**	**20**	**20**	**20**	**20**
C12FNN	**139.7**	**8**	**FIB**	**N**	**N/A**	**20**	**20**	**20**	**20**
C13FNN	**139.7**	**10**	**FIB**	**N**	**N/A**	**20**	**20**	**20**	**20**
C13FIN	139.7	10	FIB	I	N	1005	995	924	871
C12FIN	139.7	8	FIB	I	N	992	977	913	888
C11HIN	139.7	5	HSC	I	N	996	952	835	822
C11FIN	139.7	5	FIB	I	N	997	954	834	820
C11FSN	*139.7*	*5*	*FIB*	*S*	*N*	*980*	*935*	*787*	*773*
C13FIC1	139.7	10	FIB	I	90	375	358	350	349
C12FIC1	139.7	8	FIB	I	90	389	387	373	361
C11HIC1	139.7	5	HSC	I	90	348	337	319	317
C11FIC1	139.7	5	FIB	I	90	403	397	380	340
C11FSC1	*139.7*	*5*	*FIB*	*S*	*90*	*380*	*375*	*368*	*366*
C11FIC1.14d	139.7	5	FIB	I	90	404	371	365	365
C11FIC1.28d	139.7	5	FIB	I	90	470	452	435	432
C11FIC1.75	139.7	5	FIB	I	75	608	542	509	514
C11FIC1.120	139.7	5	FIB	I	120	620	579	568	514

Grey highlighted sections cast from batch 2 concrete mix, [a] Specimen key – *Shape (where S = square and C = circular sections) – size – wall thickness – fill type – fire exposure – protection type (- special test)*, [b] FIB = fibre reinforced concrete, HSC = high strength concrete, [c] I = ISO 834 fire curve, S = smouldering fire curve, N = no heating, [d] F.R. = protected fire resistance design rating, [e] average maximum temperatures at thermocouple locations

The 25 specimens outlined in Table 7-1 were selected because their ambient compressive strength, according to the design procedures given by EC4 (CEN, 2004a) for composite columns, was less than the 2000 kN maximum load capacity of the testing equipment available to the author. This eliminated the possibility of testing the C2xFIx and C3xFIx specimens and imposed an upper limit on infill concrete strength of about 70 MPa. The steel grade was also limited to 355 MPa yield strength. Concrete strengths at ambient temperatures for the high strength

concrete (HSC) and fibre reinforced concrete (FIB) infills are presented in Table 5-2 on Page 193. The FIB and HSC concrete cylinder strengths for the circular sections and unheated square sections were approximately 48 MPa, whilst for the heat treated square sections (grey highlighted) it was approximately 65 MPa.

Table 7-1 also shows the maximum temperatures experienced at the four thermocouple locations within the S1xxxx and C1xxxx specimens, with the assumed maximum temperature of the unheated specimens (xxxxNN) being 20^{o}C throughout.

Since the same physical characteristics were used within the residual structural testing program as for the thermal tests presented in Chapter 5, similar comparisons can be made. The three wall thicknesses of 5, 8 and 10 mm, for the square and circular columns within the testing matrix, allows comparisons of the effect of steel tube thickness and shape on the residual strength of a fire-damaged CFS column. The FIB and HSC fill types are compared to determine if fibres within the concrete influence the residual structural response of the CFS columns.

7.1.1 Specimen preparation and test procedure

Both the unprotected and protected columns were cleaned before being tested structurally. The intumescent char was removed from protected columns as the compounds with which the intumescents were produced are known irritants. The unprotected sections required cleaning to remove a thin layer of brittle slag material that had formed on the surface of the unprotected steel tubes; this was observed to crack ad delaminate during loading if not removed, which affected the ability to measure strains and displacements during structural testing. Similar brittle slag material was also observed on the surface of the steel fibres within the infill concrete at the tops of the columns, as shown in Figure 7-1, although only in the unprotected tests.

The concrete within the fire damaged CFS sections showed differences in both colour and fragility, with the concrete within the unprotected specimens taking on a yellow tone and being more fragile to the touch, as shown in Figure 7-2 (a). The

concrete within the protected sections was less damaged and whiter in colour, as shown in Figure 7-2 (b).

(a) (b)

Figure 7-1: (a) Comparison of steel fibres pre- and post- thermal insult; and (b) surface slag on exterior steel on unprotected CFS columns

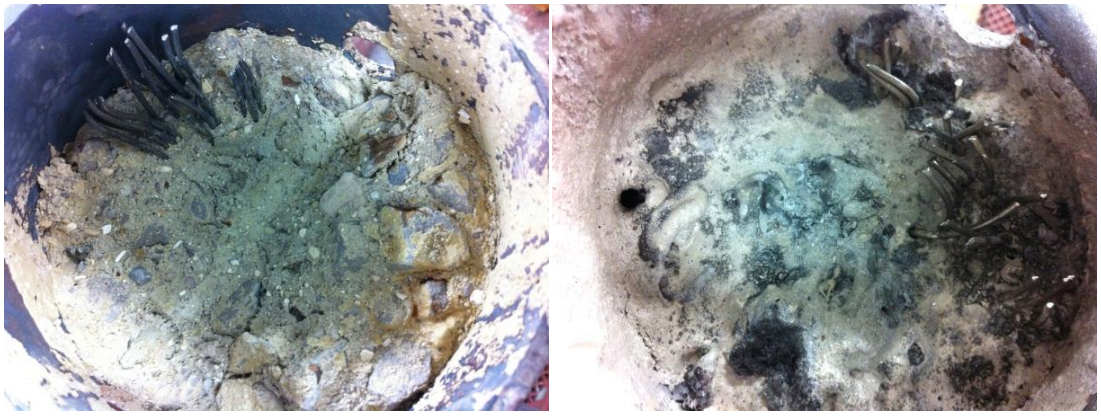

(a) C11FIN (b) C11FIC1

Figure 7-2: Representative comparison of concrete core colour and fragility for; (a) unprotected; and (b) protected CFS columns

The specimens, as shown in Figure 7-2, incorporated a void at the top to allow for easy manoeuvring of the specimens during the furnace tests presented in Chapter 5. Obviously, for structural testing, these voids need to be filled so that the applied load will be evenly distributed across the entire cross section. A high strength mortar mix was used with a designed compressive strength greater than 70 MPa to fill the voids. After the voids were filled with the high strength mortar and allowed to cure for more than 28 days, 8 mm thick grade S355 steel plates were welded to the tops of the specimens. Base plates had already been attached to the columns during casting.

The columns were attached to pin support plates at either end, which controlled the direction of lateral deflection, and thus the locations of the compressive and tensile faces, by introducing a small axial eccentricity to the load of approximately 5 mm from the columns' centreline. The columns were then inserted into a resistance frame, as shown in Figure 7-3. Four bonded foil stain gauges were installed on the steel tube evenly around the columns' perimeter at their mid-height, two placed in line with the pin supports (i.e. a 5mm offset to account for the eccentricity) so that the gauges lie on the neutral axis, and two placed perpendicular to the pin supports (shown in Figure 7-4). Three hooks were also attached at quarter heights (between the pin supports) to the steel tube to connect string pot gauges for measuring lateral deformation during loading. A linear potentiometer displacement gauge was used to measure the axial displacement relative to the 2000 kN hydraulic jack used to apply the load to the columns. A pressure gauge was attached in-line with an electronically operated hydraulic power pack capable of operating up to pressures of 10,000 psi; this was calibrated using a load cell so that the applied load from the actuator could be determined based on hydraulic pressure. The tests were manually controlled on the basis of an approximate axial displacement rate between 2.5 and 3.5 mm/min, as shown in Figure 7-5, with the exception of residual test C11FIN where applied load was used to control the test and increased at an approximate rate of 75 kN/min. Residual test C11FIN was the first test, after which it was decided that axial deflection rate was easier to control and more reliable data would therefore be captured. The addition of the steel plates and pin supports increased the length of the

columns from 1400 mm to 1480 mm (pin to pin distance) and this is taken as the effective length of the columns.

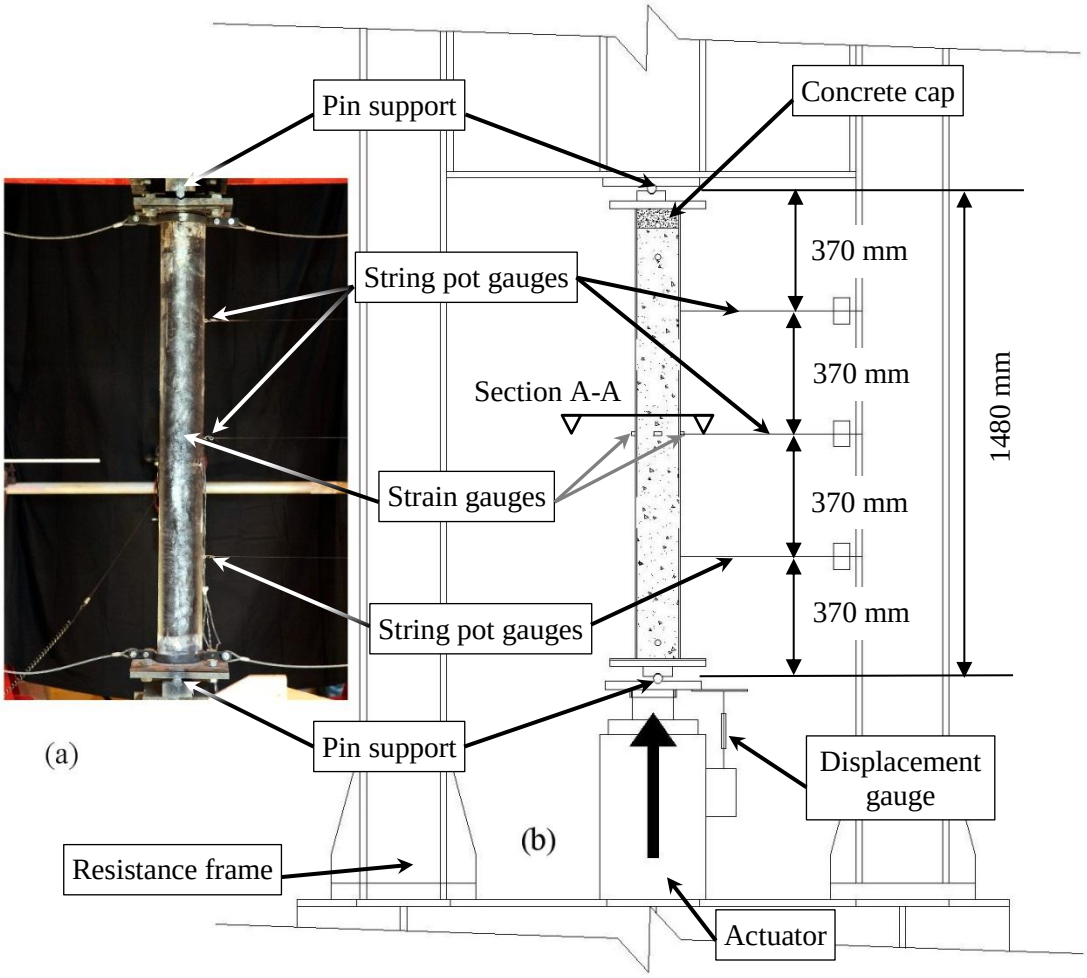

Figure 7-3: (a) Column in testing frame before loading, and (b) schematic of loading frame use in tests.

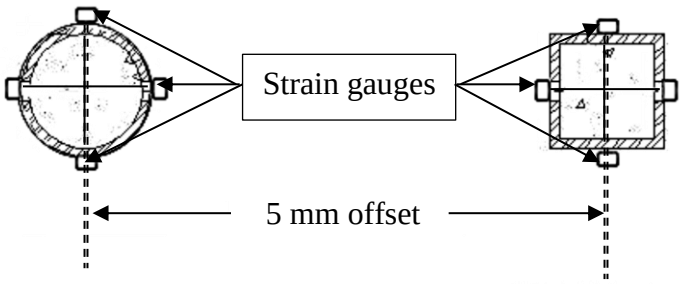

Figure 7-4: Section A-A: CFS cross-section of column showing locations of strain gauges around perimeter.

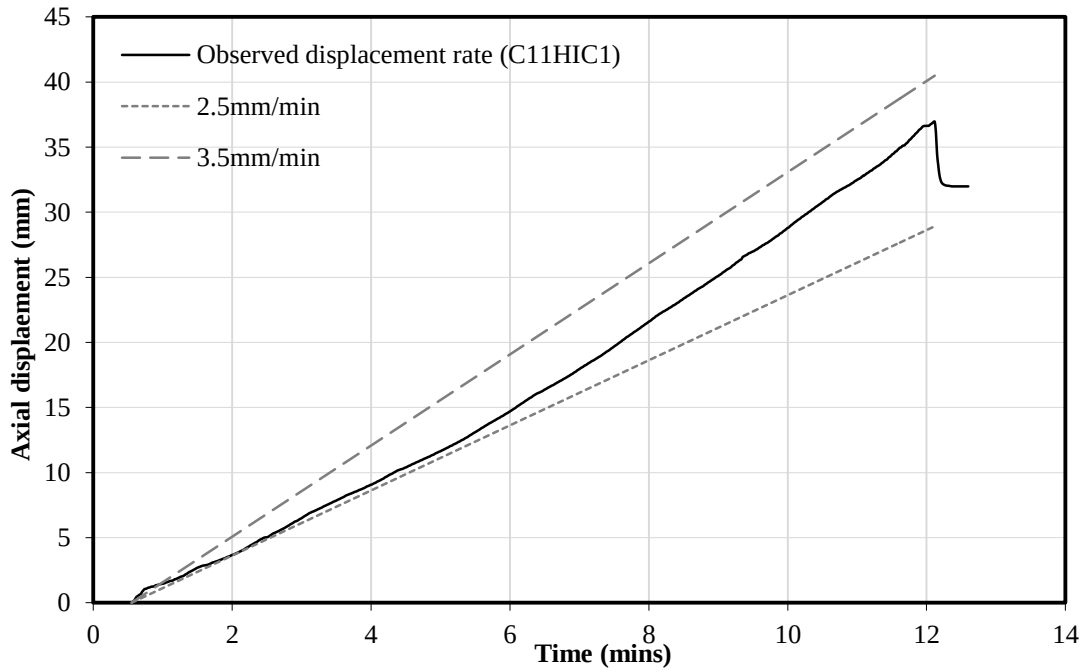

Figure 7-5: Representative axial displacement rate (residual test C11HIC1)

The tests were terminated when the rotation of either of the top or bottom plates was impeded by either of the loading plates attached to the actuator or restraint frame. All data were recorded at a frequency of 10 Hz using a Vishay Micro-Measurements System 7000 data acquisition unit and the StrainSmart software package.

7.1.2 Residual strength predictions of CFS columns

The aim of the strength predictions is to assess whether the available structural design guidance can accurately predict the load capacity of a CFS column after the cross-section has experienced different levels of peak temperature. The residual strength predictions were made using a similar process as the fire resistance predictions in Chapter 3. The CFS cross-sections were again discretised into concentric layers and each layer was prescribed a peak exposure temperature based on the observed maximum temperatures presented in Table 7-1. After the peak temperature for each layer had been determined, temperature dependent stress-strain relationships were calculated for the steel tube and each concentric layer within the concrete core. The stress-strain relationships were then used to determine the residual strength of the CFS columns using several different methods.

7.1.2.1 Determination of layer temperatures from observed thermal profiles

The CFS columns were discretised into one steel layer and six concrete layers, and each layer was prescribed a uniform temperature based on the maximum temperatures observed at that location during the fire tests presented in Chapter 5. Temperatures were measured during the fire tests at in the steel tube and at three unevenly distributed depths within the concrete (concrete face, 35 mm depth, and concrete centre). The steel tube TC temperature is assumed to be the uniform temperature within the steel tube so that no calculation of thermal profiles is required in the steel. However, for the concrete core the thermal gradient is present, therefore temperature profiles within the concrete core were obtained by fitting a parabola to the test data curve. This is shown in Figure 7-6 for tests C11FIN and C11FIC1, where the temperatures recorded at the concrete centre, the 35 mm, and the concrete face (assumed to be at a depth of 2.5 mm) TCs are plotted against their distance from the column's centre. The concrete core was then split into six equal depth layers as shown previously in Figure 3-8 and, using the best fit curve, each layer was prescribed a uniform temperature calculated at the midpoint of each layer.

7.1.2.2 Stress-strain relationship calculation for each layer

Once the temperatures of each layer have been determined, the exposure temperature dependent stress-strain relationships for the steel and each layer of the concrete were calculated by applying equations 2-57 through 2-65 on Page 91. The confinement factor was calculated to be approximately 1.5 for most specimens outlined in Table 7-1 with greater confinement factors calculated the 8 mm and 10 mm sections. Figure 7-7 shows the representative stress-strain curves for the concrete cores within the square Sxxxxx sections at 20, 350 and 900^{o}C, and circular Cxxxxx sections at 20, 350, 450, 550, and 900^{o}C, based on a confinement factor of 1.5. The temperatures represented are approximations of the maximums observed within the CFS sections (Table 7-1).

7.1.2.3 Residual strength calculations of CFS columns

Several methods can be used to calculate the residual strength of a CFS column. For instance, the EC4 Annex H approach (CEN, 2005) to fire resistance prediction of

CFS columns can be applied to the residual case. In this approach the strain is assumed to be equal across the cross-section. The strain is then increased incrementally to find the failure load (N_{ε}) which is found when the plastic resistance to crushing of the cross-section ($N_{pl,\varepsilon}$) is equal to the buckling resistance of the column ($N_{cr,\varepsilon}$). This is shown in Figure 7-8 for the C11FIN and C11FIC1 sections that were heated, as well as for the identical unheated control section, C11FNN. The significant jump in $N_{cr,\varepsilon}$ is due to the assumed bi-linear stress-strain relationship for steel shown in Figure 2-17 on Page 91, where after the yield stress of steel is reached the strain hardening modulus is 1% of the pre-yield stress Young's modulus value.

Other methods for predicting the residual strengths can be assumed from the recommended procedures for ambient temperature design of CFS columns from EC4 (CEN, 2004a). In these cases the plastic resistance of the section ($N_{pl,\,EC4}$) is calculated by summing the full resistance of the each of the layers (Equation 2-1). The sum of each layers flexural stiffness (EI) is used in calculating the Euler critical buckling load ($N_{cr,EC4}$) (Equation 2-6). The plastic resistance and Euler buckling load are used to calculate the relative slenderness (Equation 2-5) of the CFS column, which is used calculate the column's buckling resistance ($N_{br,EC4}$) (Equation 2-4).

An alternative method to calculate the residual strength of unprotected CFS sections exposed to ISO 834 standard fires is presented by Han and Huo (2003) where the ambient strength of the column is reduced by a residual strength index (RSI) factor which is dependent on the cross-sectional size of the column and the time of exposure (equations 2-66 and 2-67). As neither the thickness of the steel tube nor size of the concrete core are explicitly incorporated into the calculation the RSI of the cross-sections, the residual strengths of the C1xxIN and S1xFIN sections can also be calculated with RSI factors of 0.44 and 0.39 times the ambient strength of the specimen, respectively. These are compared to tested strengths in Section 7.2.2.

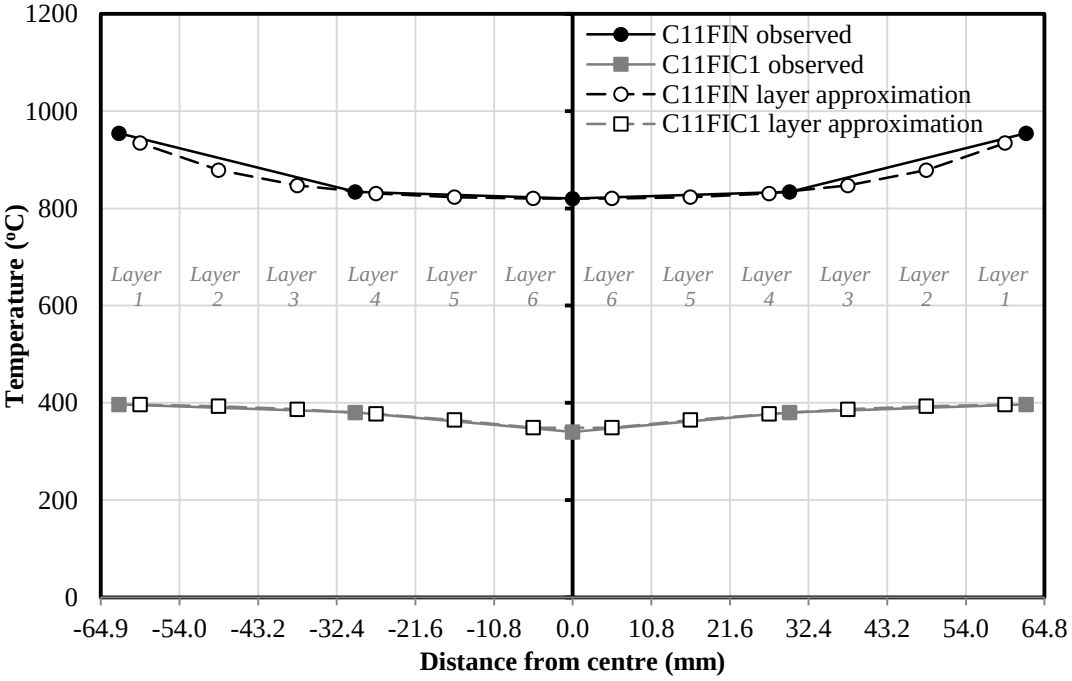

Figure 7-6: Observed and calculated temperature profiles for the C11FIN and C1FIC1 concrete cores.

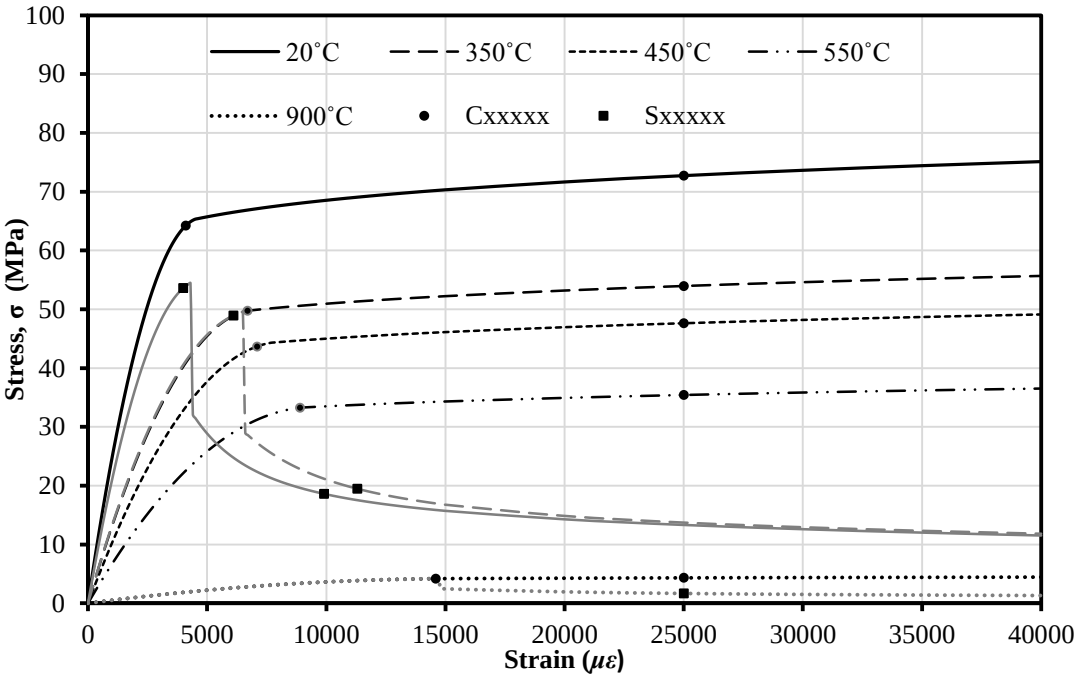

Figure 7-7: Representative stress-strain curves for the concrete core in circular (Cxxxxx) and square (Sxxxxx) CFS sections presented in Table 7-1 at approximate maximum observed temperatures

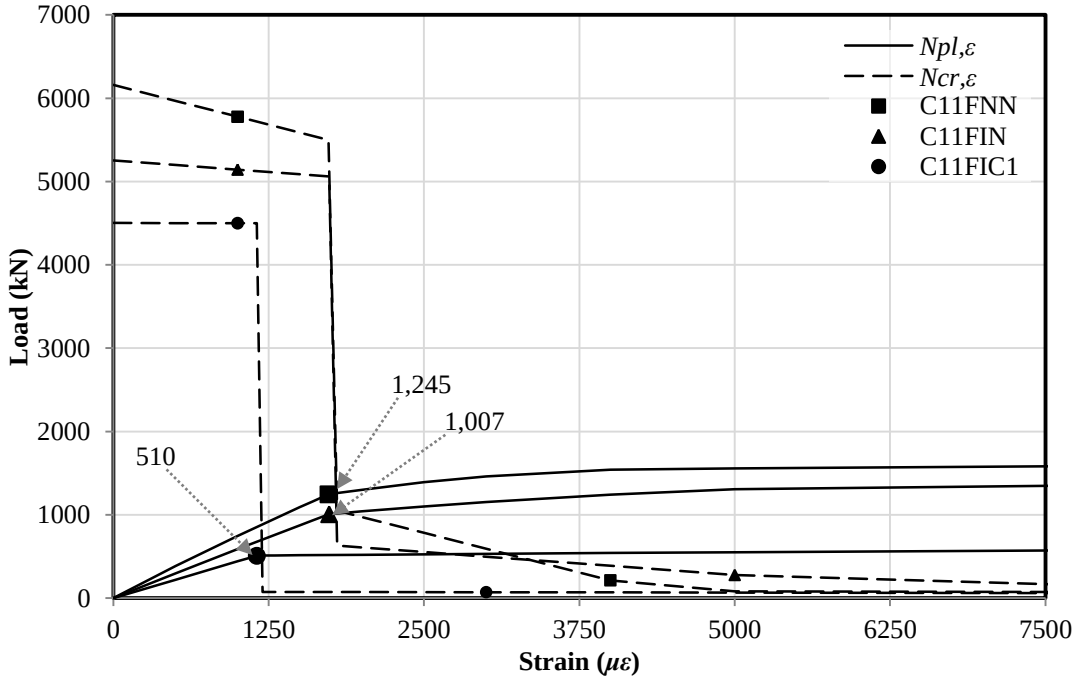

Figure 7-8: Representative $N_{pl,\varepsilon}$ and $N_{cr,\varepsilon}$ load-strain curves for the C11FNN, C11FIN, and C11FIC1 sections

7.2 Results from the residual capacity tests

Selected results and observations from the residual capacity tests are shown in Table 7-2, which gives the failure load (N_{test}); the axial deflection (δ_y) at failure; the mid-span lateral deflection (δ_{x2}) at failure; and the average axial strain at mid-height at failure. Table 7-2 also gives the observed failure mode and the pre-failure axial stiffness of the columns, measured between 200 kN and 400 kN for all tests using the average axial strain at mid-height.

7.2.1 General observed response to axial load

As expected, elevated temperature exposure affected the axial failure load (N_{test}), the axial stiffness (E_{cfs}), and axial deflections (δ_y). For instance, the axial failure loads (N_{test}) of C12FNN, C12FIC1, and C12FIN were 1372, 1285, and 813 kN, respectively. Similarly, the reduction of E_{cfs} with greater temperatures is clear when comparing C11FNN, C11FIC1, and C11FIN; these were 57.5, 33.0 and 25.0 GPa, respectively. Axial deflections at failure also decreased as the temperatures

experienced increased, as seen by comparing δ_y for C13FNN, C13FIC1, and C13FIN; these were 15.7, 11.0 and 9.7 mm, respectively.

The thickness of the steel wall affected the residual failure load (N_{test}) and the axial stiffness (E_{cfs}) insofar as thicker steel walls produced larger magnitudes (all other factors being equal). N_{test} values for C11FIN, C12FIN, and C13FIN of 583, 813 and 1061 kN, respectively, and E_{cfs} values for C11FNN, C12FNN, and C13FNN of 57.5, 73.5 and 82.4 GPa, respectively, demonstrate this.

Columns failed in either global (GB) or local buckling (LB). In most cases global buckling occurred and resulted in the formation of a local buckle close to the columns' mid height, however in some cases the local buckle formed away from the column mid height (typically near the top of the column) before global buckling occurred. Comparatively lower failure loads were observed in the columns that failed due to a local buckle compared to those that failed due to global buckling. For example the failure load of C11FIC1 was 714 kN as compared to 1192 kN for C11HIC1; the former failed by local buckling whereas the latter failed due to global buckling.

The residual strength index (RSI = N_{test}/N_{FNN}) shows that the introduction of the protective intumescent coating reduces the amount of strength lost to between 10% and 40%, an improvement of 30% compared to the unprotected strength loss, which is between 40 and 60%. The RSI is similarly dependent on the size of the steel tube. A representative selection of the various failure modes that were observed; along with post failure deflected shapes are shown in figures 7-8 and 7-9. The global buckling failure mode was similar to that reported in the literature (Han et al., 2005).

Table 7-2: Predicted residual strengths and observed loads, deflections, and strains at failure; and failure type and pre-failure axial stiffness for all of the residual strength tests

	Predictions[A]				Observed data[B]						RSI[C]	
	N_{ε} [1]	$N_{pl,EC4}$ [2]	$N_{cr,EC4}$ [3]	$N_{br,EC4}$ [4]	N_{test} [5]	δ_y [6]	δ_{x2} [7]	ε_{ave} [8]	Failure[9]	E_{cfs} (GPa)[10]	N_{FNN} [11]	N_{test}/N_{FNN}
S13FNN	**1913**	**2235**	**5084**	**1217**	**1949**	**15.7**	**-8.2**	**-2393.7**	**G**	**77.8**	**1949**	**1.00**
S11FNN	**1267**	**1607**	**3237**	**834**	**1467**	**14.4**	**-4.7**	**-2687.5**	**LB**	**49.9**	**1467**	**1.00**
S13FIN	1055	1092	4906	745	1082	10.3	-3.7	-625.2*	G	106.8*	1949	0.56
S11FIN	566	623	2792	424	617	8.0	-3.7	-4343.9	G	28.2	1467	0.42
S11FSN	*560*	*621*	*2793*	*424*	*576*	*7.7*	*-3.8*	*-1960.2*	*G*	*30.0*	*1467*	*0.39*
S11FIC1	1144	1553	3095	803	1243	12.9	-4.2	-1513.8	LB	55.1	1467	0.85
S11FSC1	*1111*	*1535*	*3059*	*794*	*1215*	*13.3*	*-4.9*	*-1587.3*	*LB*	*50.6*	*1467*	*0.83*
C13FNN	**1893**	**2204**	**8445**	**1434**	**1772**	**15.7**	**-10.0**	**-2700.4**	**G**	**82.4**	**1772**	**1.00**
C12FNN	**1647**	**1955**	**7177**	**1256**	**1664**	**14.8**	**-10.0**	**-2869.9**	**G**	**73.5**	**1664**	**1.00**
C11FNN	**1245**	**1535**	**5009**	**950**	**1372**	**13.4**	**-8.3**	**-1760.9**	**G - LB**	**57.5**	**1372**	**1.00**
C11HNN	**1245**	**1535**	**5009**	**950**	**1346**	**14.6**	**-10.2**	**-3051.2**	**G**	**36.5**	**1346**	**1.00**
C13FIN	958	990	8021	778	1061	9.7	-3.7	-991.7	G	65.5	1772	0.60
C12FIN	793	825	6704	649	813	8.6	-3.4	-1010.7	G	53.7	1664	0.49
C11FIN	510	562	4480	441	583	10.3	-4.2	-3988.2	G	25.0	1372	0.42
C11HIN	511	563	4480	441	591	7.4	-4.0	-1115.6	G	34.6	1346	0.44
C11FSN	*526*	*592*	*4483*	*459*	*601*	*7.6*	*-5.2*	*-1566.1*	*G*	*31.9*	*1346*	*0.45*
C13FIC1	1664	1962	8211	1311	1241	11.0	-4.8	-1213.6	G	64.2	1772	0.70
C12FIC1	1403	1716	6910	1133	1285	12.8	-5.8	-2105.7	G - LB	47.2	1664	0.77
C11HIC1	1039	1364	4759	862	1192	13.4	-12.5	-3378.8	G - LB	35.7	1346	0.89
C11FIC1	1007	1340	4720	850	714	9.6	-5.8	-1536.5	LB - G	33.0	1372	0.52
C11FSC1	*1014*	*1347*	*4733*	*853*	*795*	*9.6*	*-3.9*	*-2081.2*	*LB - G*	*29.1*	*1372*	*0.58*
C11FIC1.14d	1017	1349	4733	854	764	8.9	-5.3	-1359.7	LB - G	39.8	1346	0.57
C11FIC1.28d	957	1287	4684	825	741	9.2	-4.3	-1630.5	LB - G	29.3	1346	0.55
C11FIC1.75	827	1090	4586	729	833	12.5	-13.9	-3120.9	G	34.7	1346	0.62
C11FIC1.120	819	1080	4590	725	835	11.2	-8.9	-2498.7	G	33.1	1346	0.62

[A] Residual strength predictions based on [1] equal strain method, [2] plastic resistance to compression, [3] Euler buckling load, and [4] buckling resistance based on $N_{pl,EC4}$ and $N_{cr,EC4}$; [B] results at failure of ; [5] load, [6] axial deflection, [7] mid-height lateral deflection, [8] average strain, and [9] type of failure (G = global buckling, LB = local buckling); and [10] The pre-failure axial stiffness of the column; [C] RSI = residual strength index, with [11] $N_{FNN} = N_{test}$ of control section. * strain gauge failure

Observed post-fire residual failure modes for circular CFS sections

Failures of the circular sections were either: (a) global buckling failures as shown in Figure 7-10 (d), for example; (b) local buckling failures as shown in Figure 7-10 (e); or (c) global buckling failure which then resulted in a local failure of the steel tube as shown in Figure 7-10 (f). The global buckling failure modes ((a) and (c)) were seen in all tests apart from C11FIC1, C11FSC1, C11FIC1.14d, and C11FIC1.28d, all of which were protected, where local buckling failure was observed at approximately the third-height of the column. The reason for the local buckling failures could be due to small voids being present within the concrete core as a result of the problems casting the columns as mentioned previously in Chapter 5, or may simply be coincidental.

Observed failure modes within square CFS sections

Local buckling failures were observed in residual tests S11FIC1, S11FSC1, and S11FNN, around the region of the vent and lifting holes in the steel tube at the top of the columns, as seen in Figure 7-9(b) and 7-9(c). This may be due to the reduced cross-sectional area of steel at this location resulting from the lifting and vent holes and concentrating stresses locally around these holes thus locally yielding the steel. Unprotected columns S11FxN and S13FxN, however, failed in global buckling since the concrete core had a lower residual strength due to experiencing higher temperatures during fire testing and thus failed before the steel yielded around the vent holes. Failure in residual test S13FNN was not reached due to the limits of maximum load in the testing rig (2000 kN); however a global buckling failure mode with approximately 8 mm lateral deflection at mid-height was observed at the maximum load.

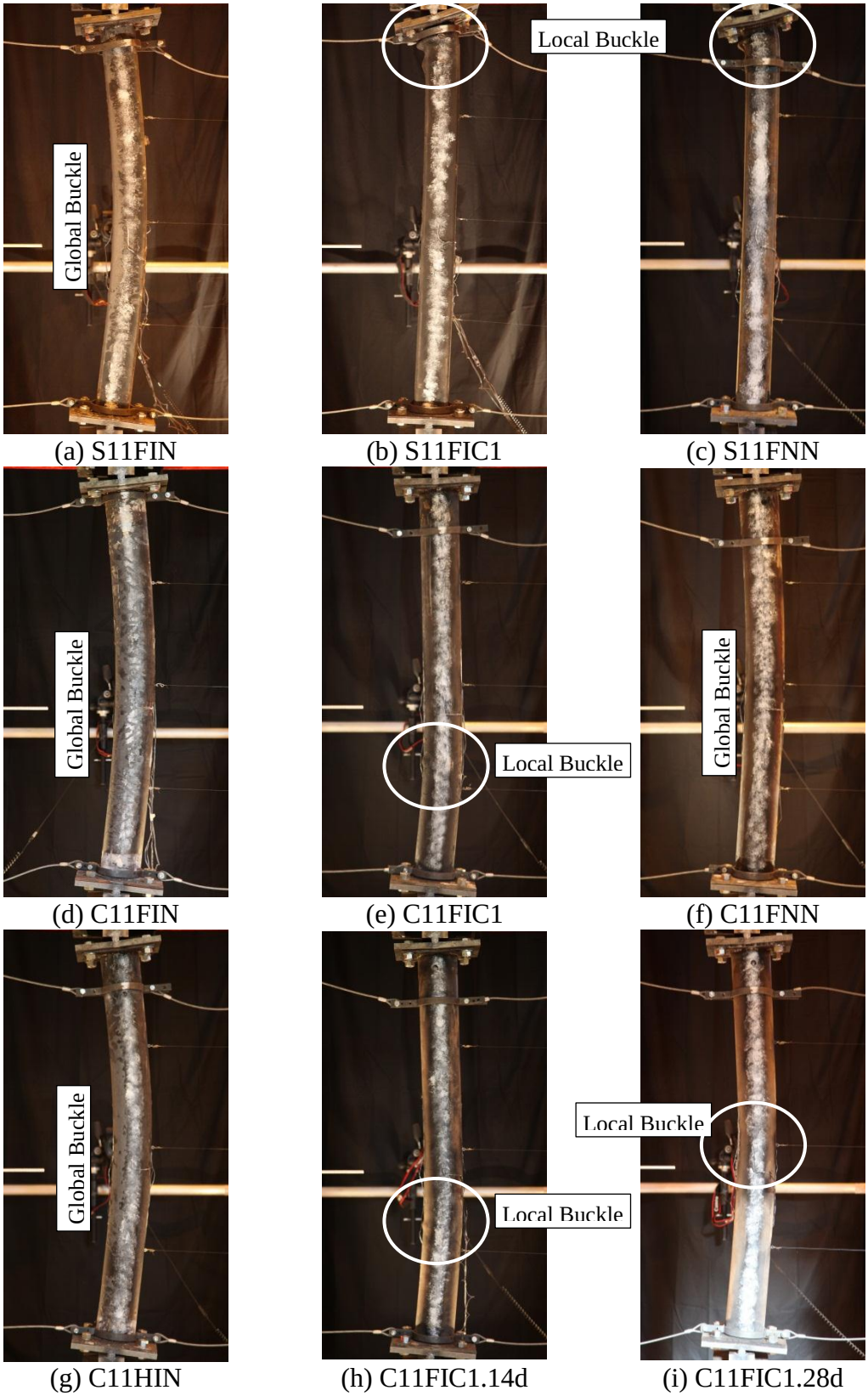

(a) S11FIN (b) S11FIC1 (c) S11FNN

(d) C11FIN (e) C11FIC1 (f) C11FNN

(g) C11HIN (h) C11FIC1.14d (i) C11FIC1.28d

Figure 7-9: Deflected shapes of representative columns after failure when the load had dropped to 75% of the maximum load

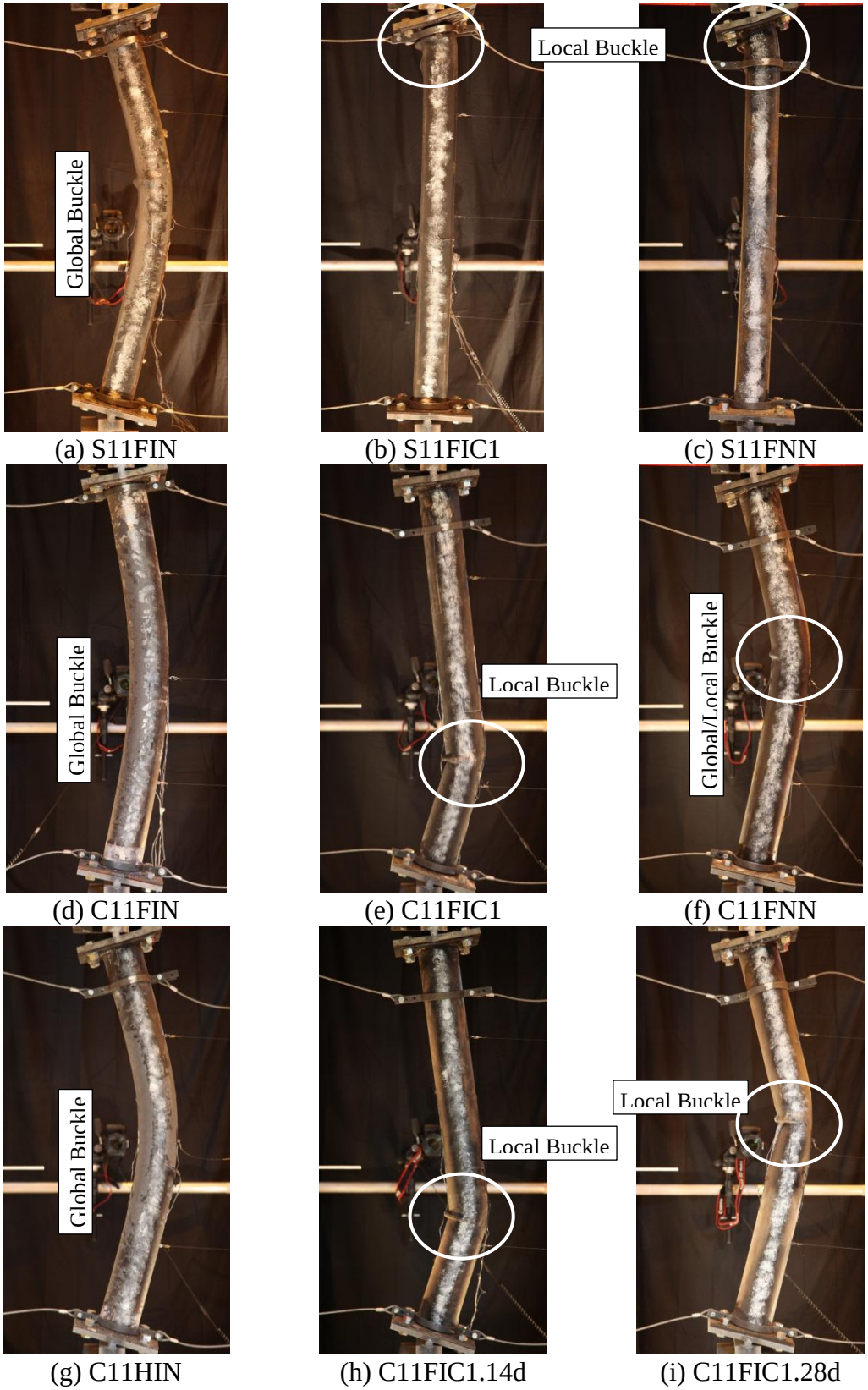

(a) S11FIN (b) S11FIC1 (c) S11FNN

(d) C11FIN (e) C11FIC1 (f) C11FNN

(g) C11HIN (h) C11FIC1.14d (i) C11FIC1.28d

Figure 7-10: Deflected shapes of representative columns at the end of testing

7.2.2 Ability to predict post-fire residual capacity

The column for the observed residual strength index (RSI = N_{test}/N_{FNN}) for the unprotected sections shown in Table 7-2 shows that in reality the residual strength of a CFS column is dependent on the size of the steel tube; this is not accounted for in the simplified prediction of RSI using Han and Huo's (2003); equations 2-66 and 2-67. As a result, the predictions of the RSI of 0.44 and 0.39 for the C1xxxN and S1xxxN columns, respectively, fail to capture the observed response and are at the lower bound of observed RSIs from the test data presented herein.

From an initial comparison of the predicted failure loads shown in Table 7-2 it can be seen that the critical buckling loads, $N_{cr,EC4}$, calculated using Equation 2-59, are significantly higher than the observed failure loads (N_{test}). The three other methods of predicting the failure load are compared to the observed failure loads in Figure 7-11 which shows the comparison for the unheated xxxxNN specimens and the unprotected heated xxxxxN specimens, whilst Figure 7-12 shows the same comparison for the protected xxxxxC1 specimens.

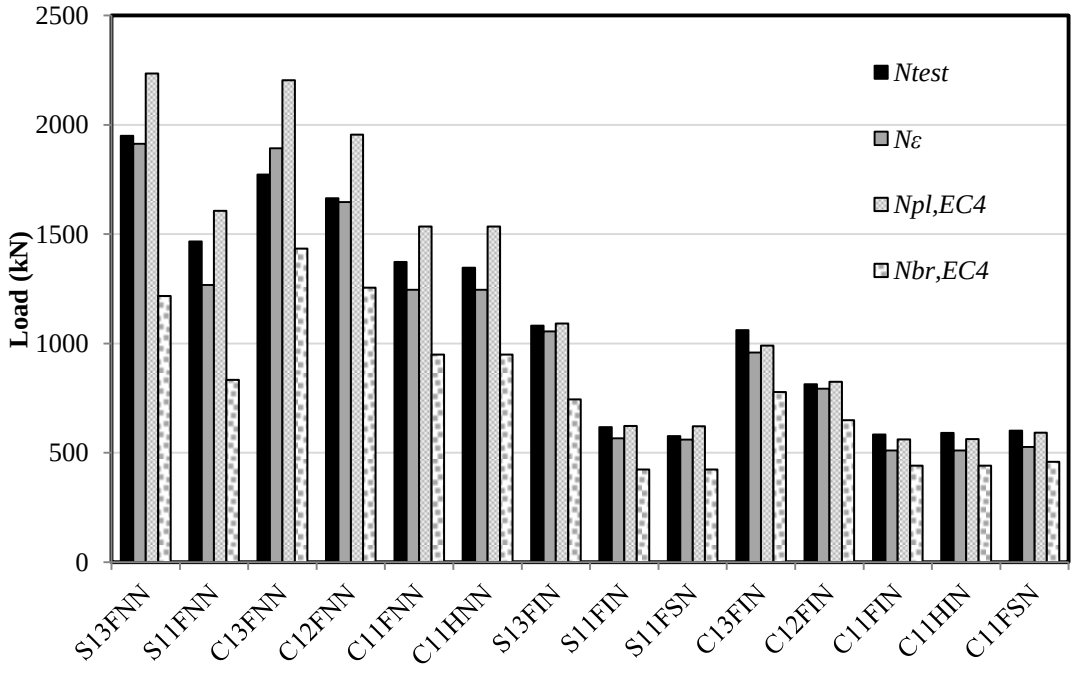

Figure 7-11: Comparison of observed and predicted failure loads for xxxxxN test specimens

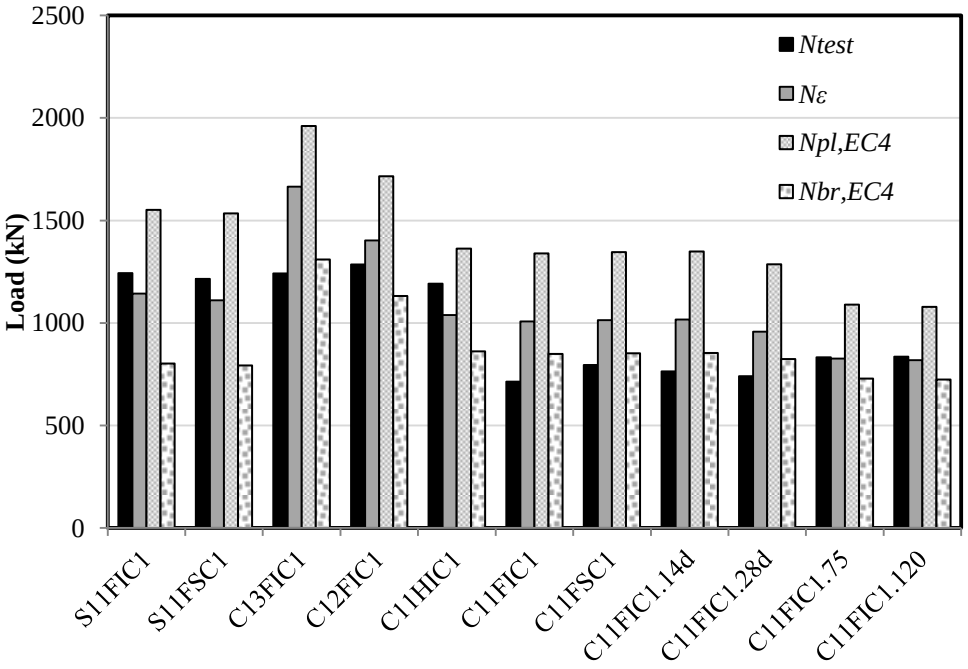

Figure 7-12: Comparison of observed and predicted failure loads for xxxxxC1 test specimens

As figures 7-11 and 7-12 show, (1) the $N_{pl,EC4}$ design calculations in general over-predict the failure load, (2) the $N_{br,EC4}$ design calculations in general under-predict the failure load, and (3) that N_{ε} is reasonably accurate. This is seen in Figure 7-13 which shows the average error in prediction (dashed lines) for the respective prediction approaches, and a solid 1:1 line representing perfect predictions. Figure 7-13 shows that, on average, the most accurate method of predicting the residual strength of CFS columns after fire is the equal strain method which is used in the EC4 Annex H approach for the calculation of fire resistance for CFS columns. The mean percentage error (*MPE*) of the predictions using this method is +2%. The standard deviation of the errors, σ_{pe}, is 17%. Four protected circular sections failed by local buckling of the column, which is not explicitly accounted for in the equal strain method; the failure loads for these columns are slightly over-predicted.

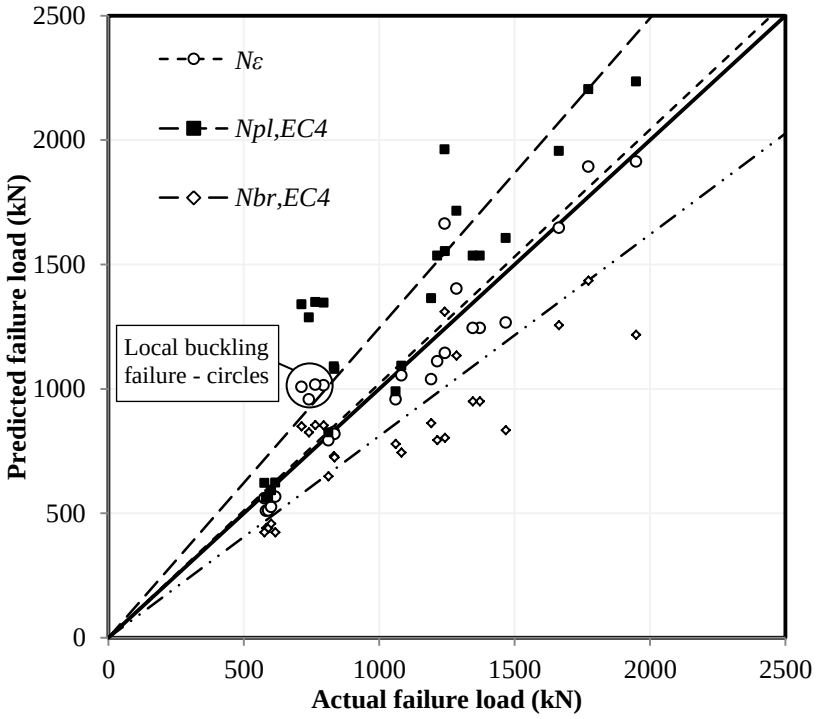

Figure 7-13: Comparison of predicted failure loads to the actual observed failure loads from tests

The use of the equal strain method to predict the failure loads of CFS columns has been shown to be accurate when based on the observed temperatures within the cross-section presented in Chapter 5. In practice these temperatures would not be known with any precision, and predictions of the temperature within the cross-section would have to be made before predictions of residual strengths of CFS columns could be made.

As previously mentioned in Chapter 6, the predictions of temperature within an unprotected, or protected, CFS cross-section can be successfully made if the heat transfer to the steel tube can be accurately modelled. However, the heat transfer to the steel is very difficult to predict due to the complexities of a real fire, from the beginning of the heating phase through the end of the cooling phase, and, in the case of protected sections the additional complexities of intumescent coatings. This results in the prediction of the residual strength of the CFS columns in practice almost impossible to make accurately.

7.2.3 Load-deflection and load-strain response

7.2.3.1 Representative responses

Figure 7-14 shows load versus the mid-height lateral deflection (left) and load versus the axial deflection (right) for the C12FIN, C12FIC1 and C12FNN residual tests. These were either not heated (xxxxNx) or exposed to 2 hours of the ISO 834 fire curve (xxxxIx), and had either no protection (xxxxxN) or were protected with intumescent coating C1 (xxxxC1). These traces are representative of the general responses seen in the tests. Figure 7-15 shows the load versus mid height average axial strain relationships for the same three columns.

Figure 7-14 shows many of the same observations made for Table 7-2; i.e. as the maximum temperatures experienced in the columns decrease the maximum loads, as well as the axial deflections, at failure increase. Figure 7-15 similarly shows that as the maximum temperatures experienced in the columns decrease, the pre-failure axial stiffness increases. C12FIN experienced the highest temperatures (approximately 950^{o}C) and as seen in Figure 7-14 this column had the lowest axial failure load, and the shallowest pre-failure load-axial strain relationship (Figure 7-15), whereas C12FNN experienced only ambient temperature and so it failed at the highest load and had the steepest load-axial strain relationship.

Figure 7-14 also shows that the pre-failure load-deflection relationships increased at similar initial rates; however as the columns neared failure the rates reduced. The initial rates indicate an elastic response in the column, after which plastic deformations start to occur. This is confirmed by Figure 7-15, where the pre-failure axial stiffness is relatively linear; however, as failure is approached the plastic deformations accelerate.

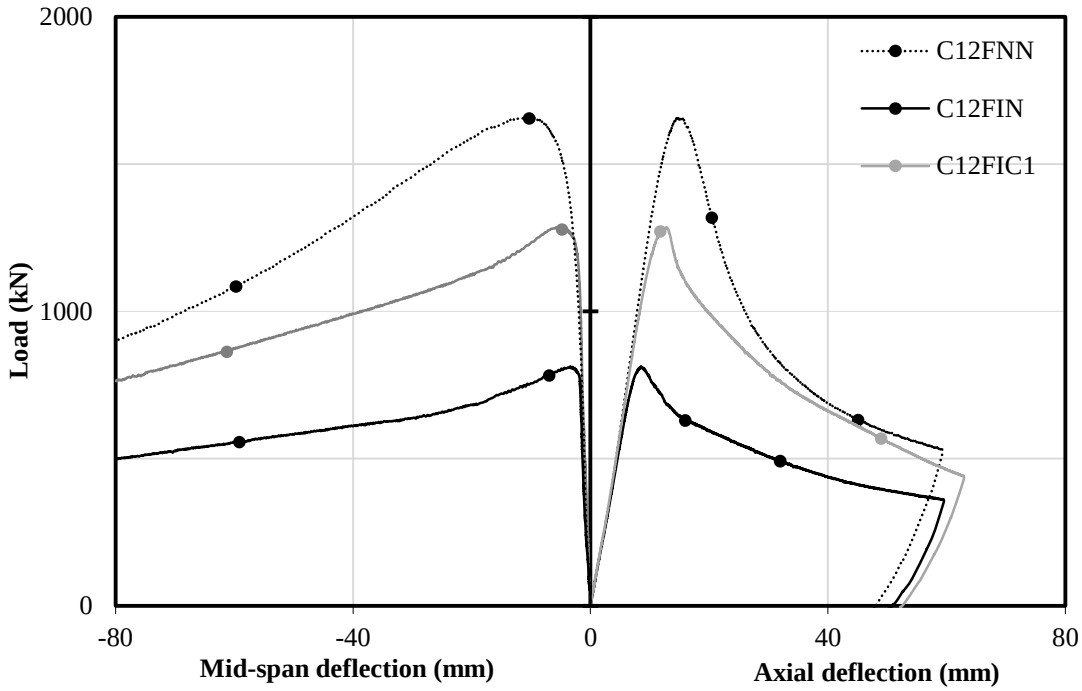

Figure 7-14: Load versus mid-height (left) and axial (right) deflection relationships for residual tests of C12Fxx sections

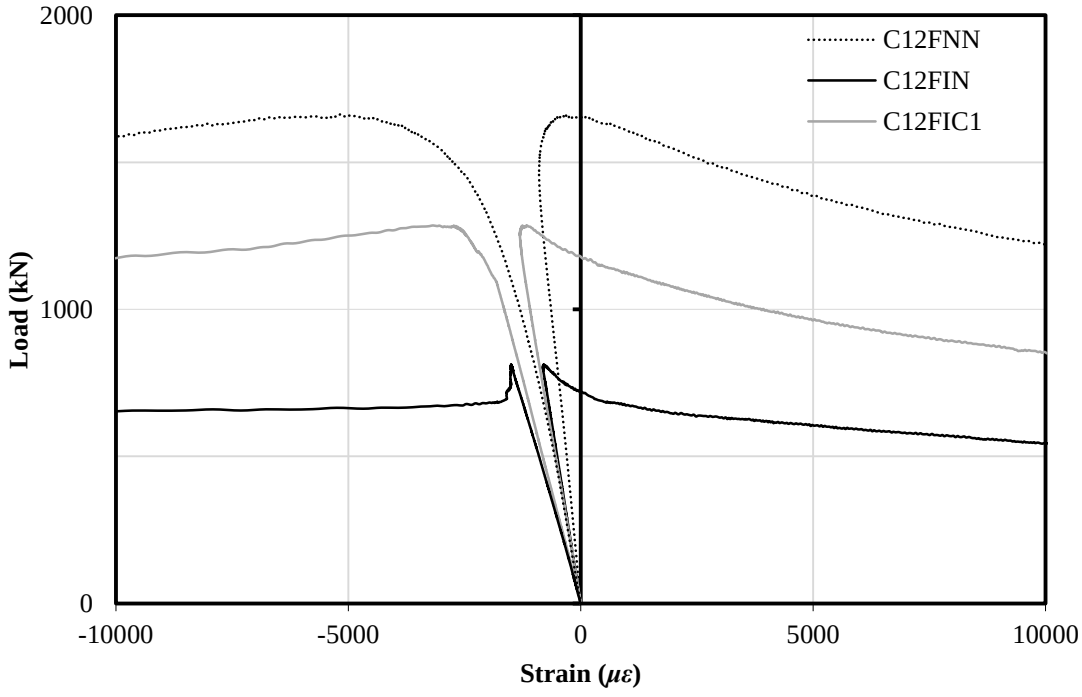

Figure 7-15: Load versus mid-height axial strain curves for residual tests on C12Fxx sections

The reduction in axial stiffness occurs at lower loads in columns that have experienced higher temperatures. The higher temperatures experienced in C12FIN resulted in the concrete core having relatively little strength (<10 MPa in all likelihood) or stiffness, and so the peak load and the form of the load-deflection and load-strain relationships were controlled by the steel tube, whereas, for C12FNN the concrete core retained its ambient strength and stiffness properties, so that the peak load and the form of the load deflection relationships were controlled by a combination of the steel tube and the concrete core.

The axial stiffness for the unheated C12FNN section varied in the same way as seen by Shanmugam and Lakshmi (2001), where the yield strain in eccentrically loaded compression tests was reached at 80-90% of the final failure load, after which tensile failure strains reached yield and the column underwent large lateral deflections. This load at which the compressive strain starts to reduce was 83% of the failure load for C12FNN. However as exposure to elevated temperature was introduced the yielding rate of the column was more rapid in C12FIC1 and not seen at all in C12FIN, where failure appeared essentially instantly.

7.2.3.2 Parameters affecting the post fire structural response

Figure 7-16 and Figure 7-17 show the load-deflection and the load-strain relationships, respectively, for all the residual column tests (apart from the C12Fxx section presented above). The effects of different column parameters are now examined.

Effect of steel tube thickness

Figure 7-16 and Figure 7-17, (a) and (b), show load-deflection and load-strain relationships for the C11FI(/N)x (5 mm wall thickness) and C13FI(/N)x (10 mm wall thickness) sections, respectively, while Figure 7-14 and Figure 7-15 show the load-deflection and load-strain relationships for the C12FI(/N)x sections.

As the wall thickness increased the observed failure load and pre-failure axial stiffness also increased. The sections failed in global buckling, apart from test C11FIC1 which failed in local buckling at the third height of the column as previously discussed. The local buckling failure causes different load-deflection and

load-strain responses compared to those recorded during a global buckling failure, as seen by comparing the previously mentioned figure.

The axial stiffness for the unheated C1xFNN sections also varied in the same way as seen by Shanmugam and Lakshmi (2001), and the loads at which the compressive strain started to reduce were 92% and 76% of the failure load for C11FNN and C13FNN, respectively. Again, as exposure to elevated temperature was introduced the yielding rate of the column was more rapid in C1xFIC1 and not seen at all in C1xFIN.

Effect of concrete infill type

The effect of the type of concrete infill had no obvious effect on the load deflection relationship for CFS columns. Figure 7-16 and Figure 7-17, (a) and (c), show load-deflection and load-strain relationships for C11xxx columns filled with either FIB concrete (xxxFxx) or HSC (xxxHxx), respectively. The only significant change in response is seen by comparing C11FIC1 and C11HIC1, where the load-deflection and load-strain relationships were markedly different; however this is thought to be due to the different failure modes experienced by C11FIC1 and C11HIC1; local buckling failure and global buckling failure, respectively.

Effect of concrete age and protection thickness

Figure 7-16(d) and Figure 7-17(d) show the load-deflection and load-strain relationships, respectively, for the two specimens that were exposed to fire after 14 days (C11FIC1.14d) and 28 days (C11FIC1.28d) after concrete casting. The load-deflection and load-strain relationships for these two columns are similar to those observed for C11FIC1 (Figure 7-16(a) and Figure 7-17(a)) since all three columns experienced local buckling failure modes at their third height. Due to the presence of local buckling of the column, other generalizations are difficult to make.

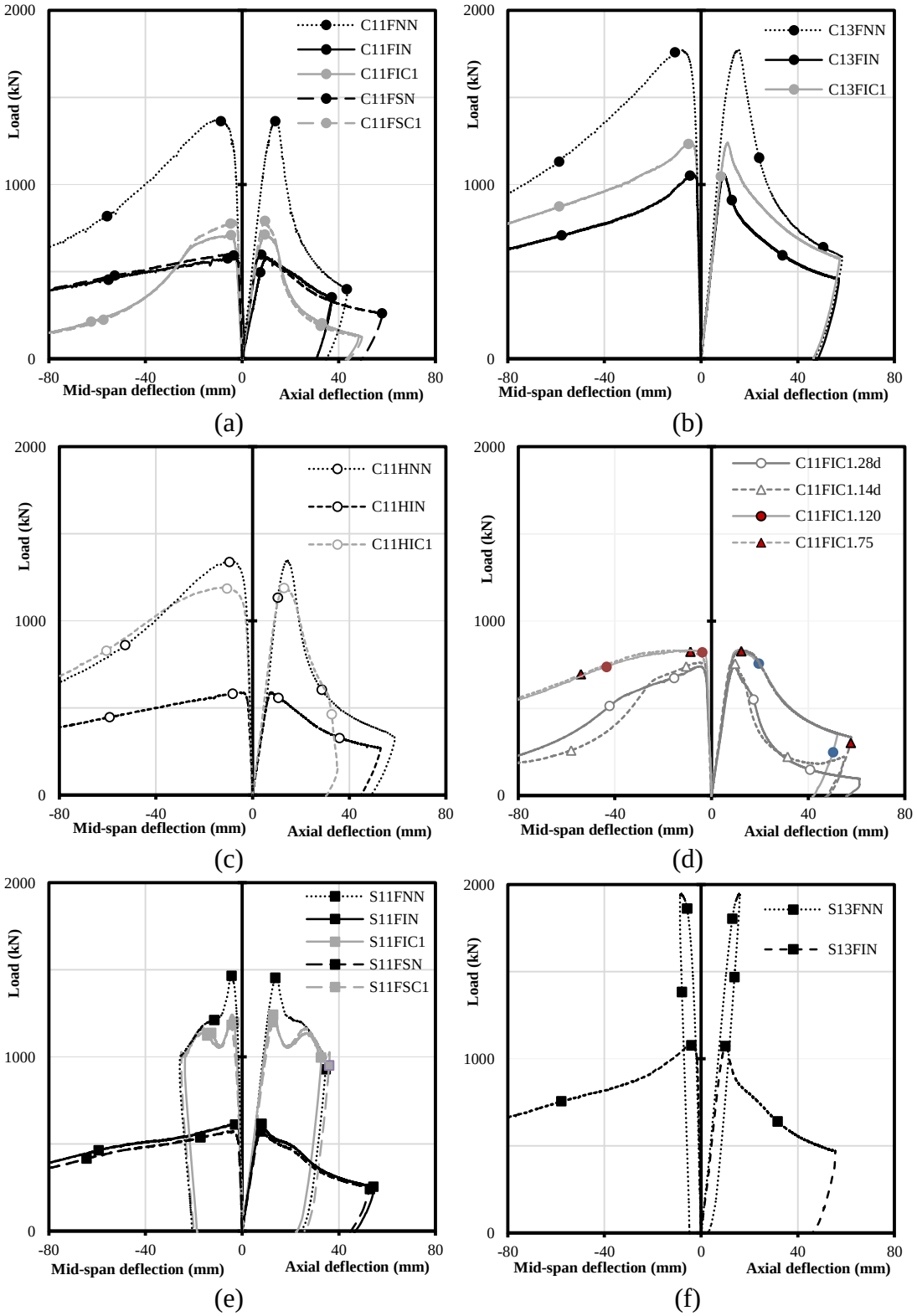

Figure 7-16: Load versus lateral deflections at mid-span (left), or axial deflections (right), for; (a) C11Fxx; (b) C13Fxx; (c) C11Hxx; (d) C11FIC1.xx; (e) S11Fxx; and (f) S13Fxx

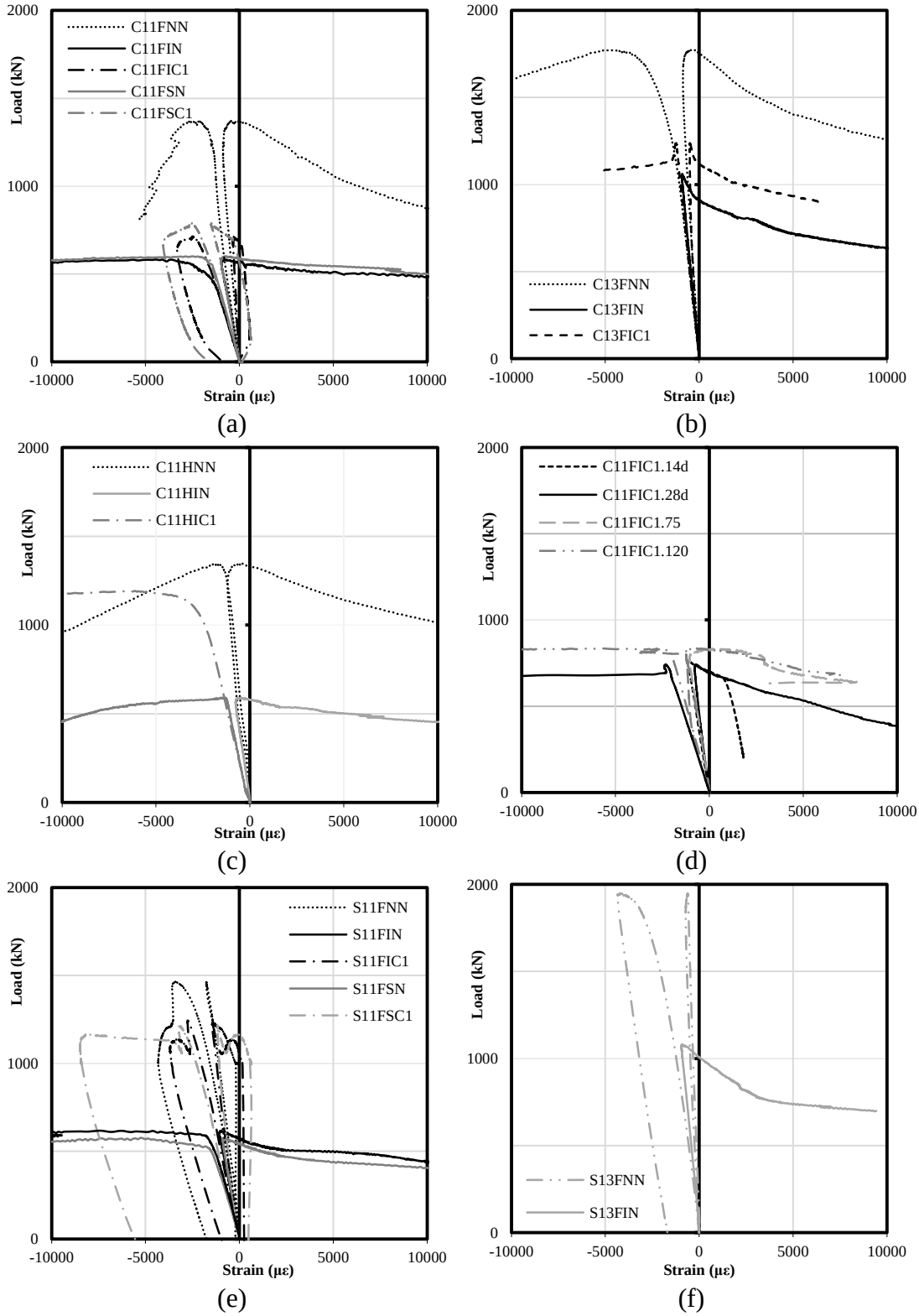

Figure 7-17: Load versus average axial strain at mid-height, for; (a) C11Fxx; (b) C13Fxx; (c) C11Hxx; (d) C11FIC1.xx; (e) S11Fxx; and (f) S13Fxx

Figure 7-16(d) and Figure 7-17(d) also show the load-deflection and load-strain relationships, respectively, for the two specimens that had dry film thicknesses (DFTs) designed and applied on the basis of F.R. times of 75 minutes (C11FIC1.75) and 120 minutes (C11FIC1.120), respectively. Both columns failed in global buckling and achieved similar maximum temperatures throughout their cross-sections. Thus, similar load-deflection and load-strain relationships were observed. A similar response was seen in Test C11HIC1 (Figure 7-16(c) and Figure 7-17(c)), which had a DFT designed for 90 minutes F.R. and also failed by global buckling, however lower temperatures were experienced in C11HIC1 and thus the column was stiffer and retained more strength.

Effect of thermal insult

Figure 7-16 and Figure 7-17, (a) and (e), show the load-deflection and load-strain relationships for the C11FSx and S11FSx sections exposed to the smouldering fire (Equation 2-38). Similar responses were seen compared to the identical sections exposed to the ISO 834 fire, with similar local buckling failure modes for the protected (xxxxxC1) sections and global buckling failure modes for the unprotected (xxxxxN) sections. No obvious differences in response were evident based on the heating curve.

Effect of cross-section shape

Figure 7-16 and Figure 7-17, (e) and (f), show the load-deflection and load-strain relationships for the S1xxxx square sections. The response of the unprotected S1xFIN sections is similar to that seen for the unprotected C1xFIN circles in Figure 7-16 and Figure 7-17, (a) and (b), with global buckling failure mode being observed.

The response of the S11FNN and S11FIC1 sections was markedly different to any of the failures observed in the other tests. The square sections failed locally at the top of the sections where the cross-sectional area was reduced due to the presence of vent holes, as mentioned previously. However after the local buckling failure and an initial loss of strength, it was observed that the CFS columns started to carry more load, as seen in Figure 7-16 (e) and Figure 7-17 (e). This indicates that the concrete core still had residual strength capacity after the initial failure, and that the load

capacity was dependent on the thickness of the steel tube rather than on the capacity of the entire cross-section.

7.3 Chapter summary

A series of 25 residual strength tests were conducted on CFS column sections that had undergone different severities of heating in furnace tests due to the type of thermal insult applied or to use of intumescent fire protection coatings. The residual tests showed that as the temperatures within the CFS sections increased, the axial failure load and axial stiffness of the CFS columns decreased. This is due to the reduction in strength and stiffness of both the steel and concrete due to elevated temperature exposure. It was also observed that protected columns, in which much lower maximum temperatures were experienced due to the protection from the intumescent coatings, retained up to 30% more of their ambient structural capacity compared to the unprotected columns, where the residual strength of the column was as low as 40% of the ambient capacity after 120 minutes of fire exposure.

Predictions of the residual load carrying capacity of the CFS sections were made using several methods. The most accurate method was a residual capacity version of the method used in EC4 Annex H for prediction of fire resistance of CFS sections. Using this method, it was found that the axial failure loads were over-predicted, on average, by only 2%.

The columns failed either by global or local buckling. For the circular sections local buckling was only observed in the sections with 5 mm wall thicknesses and where the severity of the temperatures experienced in the cross-section were reduced by the presence of intumescent coatings. For the square sections local buckling was observed when the section had not been exposed to fire. The load-deflection and load-strain relationships of different CFS columns were found to be similar, depending on the failure mode experienced.

The chapter has shown that it is possible to predict the residual axial capacity of a CFS column after exposure to fire provided that the temperatures within the cross-section are reasonably well known. A difficulty in practice is that the maximum

temperatures observed within a CFS cross-section are rarely known. It is thus recommended that future research be directed towards the qualitative assessment of damage and temperatures within CFS sections when exposed to certain degrees of fire severity, and that a framework be developed to aid in the assessment of fire damaged structures.

Chapter 8: Conclusions and recommendations

8.1 Summary

The experimental and numerical studies presented within this thesis have sought to examine the thermal response of unprotected and protected CFS columns within fire, with the specific goals of providing design guidance on predicting the structural fire resistance and post-fire residual strength of CFS columns by accounting for the requisite thermal and mechanical factors. To achieve these objectives, an exhaustive literature review was conducted; an extensive meta-analysis of furnace test data and current code-based design guidance was performed; numerical models to predict the thermal profile within unprotected CFS sections were developed and validated against small- and medium-scale thermal tests; numerical analysis of the current guidance on the prescription of intumescent protection coatings was performed to understand the inherent conservatisms within the guidance; and post-fire residual strength tests were conducted and current state-of-the-art knowledge used to predict the post fire residual failure loads.

On the basis of the numerical and experimental studies presented herein, best-practice design guidance for the structural fire resistance and post-fire residual strength of protected and unprotected CFS columns were have been presented. Thus, both the primary and secondary objectives of this thesis, as presented in Section 1.4, have been achieved.

8.2 Conclusions

A number of significant conclusions can be drawn from the experimental and numerical studies presented and discussed in this thesis. The key conclusions are:

1. Using a new thermal modelling approach that empirically accounts for the moisture within the concrete, it is possible to accurately predict within $\pm 50^{o}C$ the temperatures throughout unprotected CFS sections tested within the furnaces used, during both the heating and cooling phases of the furnace tests.
2. Using the best practice thermal modelling approaches developed in Chapter 6 (which are summarized below), a meta-analysis of historical fire resistance tests

using the EC4 Annex H fire resistance prediction approach was shown to be the most accurate predictor of fire-resistance and steel tube failure temperature, with mean percentage errors of +4% and -0.1%, respectively, and standard deviations of the errors of 32% and 13%, respectively.

3. The thermal tests and analysis of the temperatures observed within protected CFS sections showed that the current guidance on the prescription of intumescent protection coatings is overly conservative. Through forensic analysis presented within this thesis it has been shown that the conservatisms observed are due to the physically incorrect assumption that the effective section factor for an unprotected CFS section, upon which the current guidance for protected CFS sections is based, is the same as for a protected CFS section.
4. The simple single design equation developed by the NRCC (Kodur , 2007), and used in North American codes, to predict the failure time of CFS columns in fire was found to be, on average, unconservative with only 40% of the predictions being conservative when compared against a large database of experimental data from around the world, with a mean percentage error of +17% with a standard deviation of the errors of 59%. Both of these measures are considerably greater than those found for the EC4 Annex H approach. This method also appears too simple to rationally account for all of the requisite thermal and mechanical parameters which may affect the fire performance of CFS columns in fire.
5. The effects of the formation of an air gap and its size, caused by differential thermal expansion between the steel tube and the concrete, on the heat transfer within CFS columns has been shown, both numerically and experimentally, to be important in accurate prediction of CFS sections response during fire. A finite element heat transfer model was developed that incorporated a lumped convection and conduction heat transfer term, as well as accounting for radiative heat transfer between the two surfaces, to show that the heat transfer across the gap can be accurately predicted.
6. The residual post-fire strength of CFS columns can be accurately predicted by an approach based on an adaptation of the EC4 Annex H approach for fire resistance calculation, using the observed maximum temperature and state-of-the-art material and mechanical models for post fire residual properties.

A series of more specific and additional conclusions can be drawn from the individual chapters of this thesis. The following secondary conclusions can be drawn on the basis of the literature review presented in Chapter 2:

- More than 380 structural furnace tests on protected and unprotected CFS sections are available in the literature, yet a comprehensive meta-analysis of these data has apparently yet to be performed.
- The concrete infill of CFS columns in fire has received considerable attention in the literature. Research has suggested that FIB infill (whether normal strength or high strength) can provide similar fire resistance as RC infill (under concentric loading). Relatively little data is available under eccentric loading.
- CFS columns used in high rise buildings are typically larger than the maximum ever furnace tested section of 600 mm diameter and may exceed 1600 mm in practice, with steel wall thicknesses of 25 mm or more. No testing has been done (or is foreseeable) on columns of this size. The mechanics of CFS columns in fire must therefore be fully understood before accurate design can be performed.
- The emissivity of steel has been the subject of considerable research yet a wide variety of reported results are found in the literature. No clear consensus on the values to take within design seems to be available.
- Very little research is available on the use of intumescent coatings for fire protection of CFS columns. Validated models are not yet available to predict the evolution of material/thermal properties in the intumescent process; such models are needed for rational, performance-based design of these systems.
- The post fire residual strength of CFS sections has received little research attention and more information is needed, columns may not fail during a fire but during the cooling phase.

The following secondary conclusion was drawn on the basis of the meta-analysis of furnace tests data presented in Chapter 3:

- A comparison of various methods, by meta-analysis against test data available from the literature, to predict the fire resistance of CFS columns during furnace tests showed that showed that the EC4 Annex H approach was a better predictor

of fire resistance time and steel failure temperature than the French National Annex – Annexe PCRB approach, and that the extended range of columns able to be assessed under the French National Annex – Annexe PCRB approach may not be appropriate on the basis of available data.

The following secondary conclusions were drawn on the basis of the small-scale thermal tests to assess the influence of an air gap on heat transfer in CFS sections presented in Chapter 4:

- Through experimentation it was shown that as the air gap increases in size the amount of heat transferred across the gap decreases, leading to lower concrete temperatures and higher steel temperatures, as should be expected.
- Thermal modelling of the heat transfer across the air gap is highly sensitive to the assumed emissivity of the two communicating surfaces, and available data for these values shows large variability. Better data on the emissivity of concrete and steel in fire is needed.
- Current modelling techniques, whilst not explicitly account for the formation and evolution of the gap, are reasonably accurate for small air gap sizes (approximately 1 mm). Best practice modelling guidance is given below.

The following secondary conclusions were drawn on the basis of the 34 medium-scale thermal tests on unprotected and protected CFS sections presented in Chapter 5:

- The tests showed that the size and shape of a CFS section have important effects on the temperatures observed, with larger sections experiencing lower temperatures and square sections experiencing higher temperatures at their corners due to the increased heated surface area at the corners, as expected.
- The difference in temperatures between the steel tube and the concrete core face is affected by the size of the section, with greater temperature differences seen in larger sections since these sections have larger concrete cores and thus a greater thermal mass to absorb energy, thus reducing the concrete temperatures near the face and promoting the formation of a larger air gap.

- The inclusion of steel and polypropylene fibres within the concrete mix makes no obvious difference in the heat transfer within the section compared to the same concrete mix without fibres.
- Of the 20 protected tests performed herein, only a few experienced any cracking or splitting of the intumescent protective char, which had a local detrimental effect on the protective ability of the coating in these cases; the overall temperatures remained below the limiting temperature despite localised cracking.
- The age of the infill concrete was seen to affect the observed thermal response, with 14-day old CFS sections experiencing lower temperatures than those in which the concrete was at least 28-days old. Fire tests on CFS columns should therefore not be performed before CFS sections are more than 28 days old.

The following secondary conclusions were drawn on the basis of the analytical development and assessment of design of CFS section in fire presented in Chapter 6:

- The thermal tests and fire-resistance meta-analyses highlighted the historical problem of accurately modelling the highly controlled standard fire environment used in the majority of structural furnace tests.
- The critical steel failure temperature within an unprotected CFS section is considerably higher than would be observed in a protected CFS section of the same dimensions, and thus cannot be used in prescribing intumescent protection coatings for CFS sections.

The following secondary conclusions were drawn on the basis of the 25 post-fire residual strength tests presented in Chapter 7:

- Protected CFS columns retained up to 30% more of their ambient structural capacity compared to unprotected CFS columns after exposure to 120 minutes of exposure to a standard fire; the residual strength of the columns was as low as 40% of the ambient capacity in some cases.
- The CFS columns failed in one of two ways in the post fire residual condition: (1) global buckling; or (2) local buckling, which was mainly observed in the

protected sections with a 5 mm wall thickness where the severity of the temperatures experienced in the cross-section were reduced.

8.3 Best practice design recommendations

Based on the experimental and computational studies presented in this thesis, it is recommended that design and assessment of both protected and unprotected CFS columns for both fire-resistance and residual post-fire strength be based on the two step EC4 Annex H approach (CEN, 2005). This involves:

Step 1: Determination of a temperature distribution over the entire cross-section; and

Step 2: Calculation of the axial buckling/crushing capacity of the CFS column.

This approach has been shown to give the most accurate predictions of fire-resistance, and should therefore be adopted in the UK National Annex (CEN, 2008a) and in other codes available globally.

8.3.1 Design of unprotected CFS sections in fire

8.3.1.1 Step 1: Temperature distributions

Heat transfer to the steel

It is recommended to use finite element analysis and the EC1 (CEN, 2009c) heat transfer guidance to calculate the temperature distribution within CFS sections. EC1 (CEN, 2009c) guidance on modelling the net heat flux, $\dot{h}_{net}$, Equation 2-41 should be used; however

$\varepsilon_{m,a}$, the emissivity of the steel tube, should be taken as a minimum of 0.7

$\varepsilon_{m,fi}$, the emissivity of the fire, should be taken as a minimum of 0.75

The value of $\varepsilon_{m,a}$ is higher than determined herein, and is thus conservative to account for the unknowns in the heat transfer to the steel in real fires as compared with furnace tests.

Heat transfer across the gap

It is recommended that the empirically derived gap conductance relationship by Ghojel (2004) be used to model the heat transfer across the boundary between the

steel tube and the concrete core. Current EC4 Annex H guidance ignores the formation of an air gap and this may not be conservative in sections which depend to larger extents on the structural performance of the steel tube, since air gap formation will actually increase steel tube temperatures. Ghojel's relationship is given by:

$$h_j = 160.5 - 63.8 \cdot \exp(-339.9 \cdot {\theta_a}^{-1.4}) \tag{8-1}$$

Steel and concrete thermal material properties:

The thermal properties for steel (CEN, 2005) should be taken from EC4 as shown in equations 2-22 to 2-24. The thermal properties of concrete should be taken as the upper bound of thermal conductivity from EC4 in Equation 2-17 (CEN, 2005), and the density should be taken from EC4 as shown in Equation 2-18 (CEN, 2005). The specific heat capacity of concrete, $c_{c,\theta}$, developed in Chapter 6 should be assumed and is given by:

$$c_{c,\theta} = \begin{cases} 890 + 56.2(\theta_c/100) - 3.4(\theta_c/100)^2 & 20^oC \le \theta_c < 120^oC \\ 2780 & \theta_c = 127C \\ 2580 & \theta_c = 210C \\ 890 + 56.2(\theta_c/100) - 3.4(\theta_c/100)^2 & 220^oC \le \theta_a < 1200^oC \end{cases} \tag{8-2}$$

8.3.1.2 Step 2: Load capacity during fire

Once the temperature distribution is obtained, the load capacity of the CFS section should be determined by discretising the cross-section into rings of uniform temperature; a single steel tube ring; and at least 6 equal thickness rings for the concrete core; this is shown schematically in Figure 8-1, reproduced from Chapter 3.

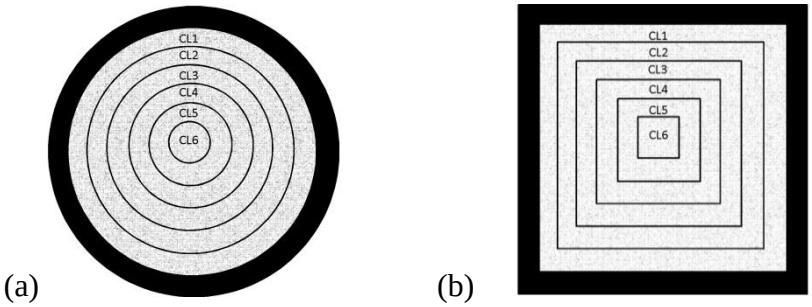

Figure 8-1: (a) Circular and (b) square segmentation used in EC4 Annex H (CEN, 2005) analysis (CL*i* = concrete layer *i*)

Once the temperatures within each ring are determined, the EC4 (CEN, 2005) temperature dependent strength reduction factors (presented in tables 2-5 to 2-7, and Equation 2-13) should be used to obtain stress-strain profiles for each layer. All materials should be assumed to experience the same strain at a given time and temperature and the strain at which the elastic critical or Euler buckling load, $N_{fi,cr,}$ is equal to the plastic (crushing) resistance to compression of the cross section, $N_{fi,pl,Rd}$ (CEN, 2005) should be determined as previously described in Section 2.4.4.2:

$$N_{fi,Rd} = N_{fi,cr} = N_{fi,pl,Rd} \quad (8\text{-}3)$$

where $N_{fi,cr}$ and $N_{fi,pl,Rd}$ are determined using equations 2-59 and 2-60, respectively. The capacity can then be determined at each instant during exposure to fire and the fire resistance checked against the fire limit state loads.

The limits of application for this method should remain as stated in EC4 Annex H (CEN, 2005).

8.3.2 Design of protected CFS sections in fire

Three inputs are required to prescribe intumescent paint protection for CFS columns: (1) the required fire resistance, F.R.; (2) the effective section factor; and (3) the limiting temperature of the steel. It is recommended on the basis of the research presented herein that:

a) the section factor be determined using the current guidance available from Hicks et al. (2002); and

b) the critical temperature should be calculated using the Annex H approach of EC4 (CEN, 2005), assuming a uniform cross-sectional temperature (i.e. the steel tube and all layers in the concrete are at a single temperature).

Until a more rational method is developed for the prescription of intumescent paints the use of these recommendations, along with the guidance presented in the previous section in terms of thermal and structural modelling, will provide conservative design.

8.3.3 Post fire residual strength design of CFS sections

If accurate maximum temperatures experienced during a fire can be assessed, the residual post-fire strength of CFS columns can be accurately predicted using the method given in EC4 Annex H (CEN, 2005) using the strength reduction models presented by Han and Huo (2003) and Yang et al. (2008); these are presented in equations 2-57 to 2-65 in Chapter 2.

8.4 Recommendations for future research

Although a number of significant conclusions have been drawn from the experimental and analytical work presented in this thesis, further research is still needed to provide more realistic design recommendations for the fire performance of CFS columns. The most important recommendations for future research into the fire-resistance and post fire residual strength of CFS columns are:

- A rational method of prescribing intumescent protection coatings is needed, since current guidance remains overly conservative. The framework presented in Chapter 6 should be followed. The assessment of the effective section factor and the critical steel limiting temperatures for protected CFS columns should incorporate a series of full-scale thermal and structural fire-resistance tests, as well as analytical studies to provide clear and simple design guidance.
- Further work is required on the assessment of the fire environment, both in real buildings and in the highly controlled furnaces used for the standard fire tests. This is required so that the optimisation of prediction methods for the heat transfer to elements in fire, which is a critical first step in the assessment of fire

resistance, can be established. Particular attention should be paid to the emissivities of the materials and fire environments used in standard testing.

- Further work is required to assess the factors affecting the formation and size of the air gap in real CFS columns in fire; likely using computational modelling.
- Loaded structural fire tests should be performed on CFS columns to simulate number of possible structural end thermal scenarios which might occur in real buildings, including: eccentric loading on FIB infill columns, one-sided heating, and vertical continuity, etc.

References

Abecassis-Empis, C., Reszka, P., Steinhaus, T., Cowlard, A., Biteau, H., Welch, S., Rein, G., et al. (2008). Characterisation of Dalmarnock fire test one. *Experimental Thermal and Fluid Science*, *32*(7), 1334–1343.

ACI. (2007). *ACI 216.1M-07: Standard method for determining fire resistance of concrete and masonry construction assemblies*. Detroit, USA.

Al-khaleefi, A. M., Terro, M. J., Alex, A. P., & Wang, Y. C. (2002). Prediction of fire resistance of concrete filled tubular steel columns using neural networks. *Fire Safety Journal*, *37*, 339–352.

Anand, N., & Arulraj, G. (2011). The effect of elevated temperature on concrete materials-A literature review. *International Journal of Civil & Structural Engineering*, *1*(4), 928–938.

ANSI/AISC. (2010). *ANSI/AISC 360-10: Specification for structural steel buildings*. Chicago, USA.

Aribert, J. M., Renaud, C., & Zhao, B. (2008). Simplified fire design for composite hollow-section columns. *Proceedings Of The Institution Of Civil Engineers - Structures and Buildings* (Vol. 161,6, pp. 325–336). doi:10.1680/stbu.2008.161.6.325

ASCE. (2005). *ASCE/SEI/SFPE 29-05: Standard calculation method for structural fire protection*. Reston, USA.

ASTM. (2007). *ASTM Standard E119: Standard test methods for fire tests of building construction and materials*. West Conshohocken, USA. doi:10.1520/E0119-12A

Babrauskas, V. (1995). Specimen heat fluxes for bench-scale heat release rate testing. *Fire and Materials*, *19*(6), 243–252.

Bazant, Z., & Kaplan, M. F. (1996). *Concrete at high temperatures - material properties and mathematical models* (p. 412). Harlow, Essex: Longman Group Limited.

Bejan, A. (1993). *Heat Transfer* (p. 675). New York: John Wiley & Sons Inc.

Bentz, D. P., Hanssen, L. M., & Wilthan, B. (2009). *NISTIR 7576: Thermal performance of fire resistive materials III. Fire test on a bare steel column*. *Fire Research* (p. 13). Massachusetts, USA: National Institute of Standards and Technology.

Beyler, C., Beitel, J., Iwankiw, N., & Lattimer, B. (2007). *Fire resistance testing needs for performance-based fire design of buildings*. Massachusetts, USA: National Institute of Standards and Technology.

British Standard Institute. (1994). *Draft DD ENV 1994-1-2: Eurocode 4: Design of composite steel and concrete structure, Part 1-2: Structural fire design, draft UK national foreward and application document*. Brussels, Belgium.

Buchanan, A. (2002). *Structural design for fire safety*. Chichester: Wiley.

CEN. (2002). *DD ENV 13381-6:2002: Test methods for determining the contribution to the fire resistance of structural members; Part 6: Applied protection to concrete filled steel columns* (Vol. 3). Brussels, Belgium.

CEN. (2004a). *BS EN 1994-1-1:2004: Eurocode 4: Design of composite steel and concrete structures; Part 1-1: general rules and rules for buildings*. *Management* (pp. 1–127). Brussels, Belgium.

CEN. (2004b). *UK National Annex to Eurocode 2: Design of concrete structures; Part 1-2: Structural fire design*. Brussels, Belgium.

CEN. (2005). *BS EN 1994-1-2: Eurocode 4: Design of composite steel and concrete structures; Part 1-2: Structural Fire Design*. Brussels, Belgium.

CEN. (2007). *NF EN 1994-1-2/NA: Eurocode 4: Calcul des structures mixtes acier-béton; Partie 1-2: calcul du comportement au feu – Annexe Nationale à la NF EN 1994-1-2*. Brussels, Belgium.

CEN. (2008a). *NA to BS EN 1994-1-2: UK National Annex to Eurocode 4: Design of composite steel and concrete structures; Part 1-2: General rules - Structural fire design*. Brussels, Belgium.

CEN. (2008b). *BS EN 1992-1-2:2004: Eurocode 2: Design of concrete stuctures; Part 1-2: General rules - Structural fire design*. Brussels, Belgium.

CEN. (2009a). *BS EN 1993-1-1:2005: Eurocode 3: Design of steel structures; Part 1-1: General rules and rules for buildings*. Brussels, Belgium.

CEN. (2009b). *BS EN 1993-1-2:2005: Eurocode 3: Design of steel stuctures; Part 1-2: General rules - Structural fire design*. Brussels, Belgium.

CEN. (2009c). *BS EN 1991-1-2: Eurocode 1: Actions on structures; Part 1-2: General Actions - Actions on structures exposed to fire*. Brussels, Belgium.

CEN. (2010a). *BS EN 1992-1-1:2010: Eurocode 2: Design of concrete structures; Part 1-1: general rules and rules for buildings*. Brussels, Belgium.

CEN. (2010b). *BS EN 13381-8:2010: Test methods for determining the contribution to the fire reistance of structural members; Part 8: Applied reactive protection to steel members*. Brussels, Belgium.

CEN. (2010c). *BS EN 13381-6:2010: Test method for determining the contribution to the structural fire resistance of structural members; Part 8: Applied reactive protection to steel memebrs*. Brussels, Belgium.

Chabot, M., & Lie, T. T. (1992). *Experimental studies on the fire resistance of hollow steel columns filled with bar- reinforced concrete - Internal Report No. 628*. Ottawa, Canada: National Research Council Canada.

Chen, B., & Liu, J. (2004). Residual strength of hybrid-fiber-reinforced high-strength concrete after exposure to high temperatures. *Cement and Concrete Research*, *34*(6), 1065–1069. doi:10.1016/j.cemconres.2003.11.010

Chung, K. S., Park, S. H., & Choi, S. M. (2008). Material effect for predicting the fire resistance of concrete-filled square steel tube column under constant axial load. *Journal of Constructional Steel Research*, *64*(12), 1505–1515. doi:10.1016/j.jcsr.2008.01.002

CIDECT. (1976). *Fire resistance of structural hollow sections: Final Report - CIDECT Programme 15 A*. Croydon, UK.

Communities and Local Government. (2007). *Approved Document B – Volume 2 – Buildings other than dwelling houses*. London, UK.

Cooke, G. (1994). Can harmonisation of fire resistance furnaces be achieved by plate thermometer control? *Fire Safety Science*, *4*, 1195–1207. doi:10.3801/IAFSS.FSS.4-1195

Cox, G. (1994). The challenge of fire modelling. *Fire Safety Journal*, *23*, 123–132.

CSA. (1994). *CAN/CSA-S16.1-M94: Limit states design of steel structures*. Toronto, Canada.

Ding, J., & Wang, Y. C. (2008). Realistic modelling of thermal and structural behaviour of unprotected concrete filled tubular columns in fire. *Journal of Constructional Steel Research*, *64*(10), 1086–1102. doi:10.1016/j.jcsr.2007.09.014

Ding, J., & Wang, Y. C. (2009). Temperatures in unprotected joints between steel beams and concrete-filled tubular columns in fire. *Fire Safety Journal*, *44*(1), 16–32. doi:10.1016/j.firesaf.2008.02.004

Drysdale, D. (2011). *An introduction to fire dynamics* (3rd Editio., p. 551). Wiley.

Duquesne, S., Magnet, S., Jama, C., & Delobel, R. (2004). Intumescent paints: fire protective coatings for metallic substrates. *Surface and Coatings Technology*, *180-181*, 302–307. doi:10.1016/j.surfcoat.2003.10.075

Edwards, M. (1998). *Reinstatment of concrete filled structural hollow section columns after short duration fires - Phase 2: Standard fire tests on full size columns.* Corby, Northants.

Edwards, M. (2000). The performance in fire of fully utilised concrete filled SHS columns with external fire protection. *Proceedings of 9th International Symposia on Tubular Structures*. Rotterdam.

Eggemann, H. (2006). Simplified design of composite columns, based on a comparative study of the development of building regulations in Germany and the United States. *Second International Congress on Construction History* (pp. 1023–1041).

Espinos, A., Hospitaler, A., & Romero, M. L. (2009). Fire resistance of axially loaded slender concrete filled steel tubular columns - Development of a three-dimensional numerical model and comparison with Eurocode 4. *Acta Polytechnica*, *49*(1), 39–43.

Fletcher, I. A., Borg, A., Hitchen, N., & Welch, S. (2006). Performance of concrete in fire: A state of the art, with a case study of the Windsor Tower fire. *4th International Workshop in Structures in Fire* (pp. 779–790).

Fletcher, I. A., Welch, S., Carvel, R., Torero, J., & Usmani, A. (2007). Behaviour of concrete structures in fire. *Thermal Science*, *11*(2), 37–52. doi:10.2298/TSCI0702037F

Ghojel, J. (2004). Experimental and analytical technique for estimating interface thermal conductance in composite structural elements under simulated fire conditions. *Experimental Thermal and Fluid Science*, *28*(4), 347–354. doi:10.1016/S0894-1777(03)00113-4

GJB. (2001). *GJB 4142-2000, Part 1: Design code for concrete filled steel tubes with square sections*. Beijing, PR China: Chinese PLA Press (in Chinese).

Goode, C. D., & Lam, D. (2008). Concrete filled steel tube columns: Tests compared with Eurocode 4. *Composite Construction in Steel and Concrete* (pp. 26–26). ASCE. doi:10.1061/41142(396)26

Grandjean, G., Grimault, J. P., & Petit, L. (1981a). *CIDECT 15B Part 1 - Determination de la duree au few des profils creux remplis de beton*. Paris, France: CIDECT.

Grandjean, G., Grimault, J. P., & Petit, L. (1981b). *CIDECT 15B Part 2 - Determination de la duree au few des profils creux remplis de beton*. Paris, France: CIDECT.

Han, L. H., & Huo, J. S. (2003). Concrete filled hollow structural steel columns after exposure to ISO-834 standard fire. *Journal of Structural Engineering*, *129*(1), 68. doi:10.1061/(ASCE)0733-9445(2003)129:1(68)

Han, L. H., Huo, J. S., & Wang, Y. C. (2005). Compressive and flexural behaviour of concrete filled steel tubes after exposure to standard fire. *Journal of Constructional Steel Research*, *61*(7), 882–901. doi:10.1016/j.jcsr.2004.12.005

Han, L. H., Xu, L., & Zhao, X. L. (2003). Tests and analysis on the temperature field within concrete filled steel tubes with or without protection subjected to a standard fire. *Advances in Structural Engineering*, *6*(2), 121–133.

Han, L. H., Yang, Y. F., & Xu, L. (2003). An experimental study and calculation on the fire resistance of concrete-filled SHS and RHS columns. *Journal of Constructional Steel Research*, *59*(4), 427–452. doi:10.1016/S0143-974X(02)00041-X

Han, L. H., Yang, Y. F., Yang, H., & Huo, J. S. (2002). Residual strength of concrete-filled RHS columns after exposure to the ISO-834 standard fire. *Thin-walled structures*, *40*(12), 991–1012.

Han, L. H., Zhao, X. L., Yang, Y. F., & Feng, J. B. (2003). Experimental Study and Calculation of Fire Resistance of Concrete-Filled Hollow Steel Columns. *Journal of Structural Engineering*, *129*(3), 346. doi:10.1061/(ASCE)0733-9445(2003)129:3(346)

Harmathy, T. Z. (1970). *Thermal properties of concrete at elevated temperatures - Research paper 426*. Ottowa, Canada.

Harmathy, T. Z., & Lie, T. T. (1970). Fire test standard in the light of fire research. *Fire Test Performance, ASTM STP 464*, 85–97.

Hass, R., Ameler, J., Zies, H., & Lorenz, H. (2000). *Fire resistance of hollow section composite columns with high strength concrete filling, final report 15P* (p. 467). Brunswick: CIDECT.

Hicks, S. J., Newman, G. M., Edwards, M., & Orton, A. (2002). *Design guide for concrete filled columns*. Corby, Northants: Corus Tubes.

Hong, S., & Varma, A. H. (2009). Analytical modelling of the standard fire behaviour of loaded CFT columns. *Journal of Constructional Steel Research*, *65*(1), 54–69. doi:10.1016/j.jcsr.2008.04.008

Huo, J. S., Huang, G., & Xiao, Y. (2009). Effects of sustained axial load and cooling phase on post-fire behaviour of concrete-filled steel tubular stub columns. *Journal of Constructional Steel Research*, *65*(8-9), 1664–1676. doi:10.1016/j.jcsr.2009.04.022

Incropera, F., & DeWitt, D. (2002). *Introduction to heat transfer* (4th Editio.). New York: John Wiley & Sons Inc.

Irwin, R. J., & Lie, T. T. (1990). *Evaluation of the Fire resistance of Reinforced Concrete Columns with Rectangular Cross-Section - Internal Report No. 601*. Ottawa, Canada: National Research Council Canada.

Irwin, R. J., & Lie, T. T. (1992). *Fire resistance of rectangular hollow steel sections filled with bar-reinforced concrete - Internal Report No. 631*. Ottowa, Canada: National Research Council Canada.

ISO. (1999). *ISO 834: Fire resistance tests-elements of building construction*. Geneva, Switzerland.

Kay, T. R., Kirby, B. R., & Preston, R. R. (1996). Calculation of the heating rate of an unprotected steel member in a standard fire resistance test. *Fire Safety Journal*, *26*(4), 327–350. doi:10.1016/S0379-7112(96)00016-1

Kim, D. K., Choi, S. M., Kim, J. H., & Chung, K. S. (2005). Experimental study on fire resistance of concrete-filled steel tube column under constant axial loads. *Journal of Steel*, *5*, 305–313.

Kimura, M., Ohta, H., Kaneko, H., & Kodaira, A. (1990). Fire resistance of concrete-filled square steel tubular columns subjected to combined loads. *Journal of Structural Constructional Engineering, AIJ*, *417*(Nov.), 372–379.

Kirby, B. R., Lapwood, D. G., & Thomson, G. (1986). *The reinstatement of fire damaged steel and iron framed structures*. London, UK.

Kirby, B. R., & Preston, R. R. (1988). High temperature properties of hot-rolled, structural steels for use in fire engineering deisgn studies. *Fire Safety Journal*, *13*, 27–37.

Klingsch, W., & Wittbecker, F. W. (1988). *CIDECT 15G - Fire resistance of hollow section composite columns of small cross sections*. Dusseldorf, Germany: CIDECT.

Kodur, V. (1996). *Factors affecting the fire resistance of square hollow steel columns filled with steel- fibre reinforced concrete - Internal Report No. 590*. Ottawa, Canada: National Research Council Canada.

Kodur, V. (1999). Performance-based fire resistance design of concrete-filled steel columns. *Journal of Constructional Steel Research*, *51*(1), 21–36.

Kodur, V. (2007). Guidelines for fire resistant design of concrete filled steel HSS columns: State-of-the-art and research needs. *International Journal of Steel Structures*, *7*(3), 173–182.

Kodur, V., Dwaikat, M., & Fike, R. (2010). High temperature properties of steel for fire resistance modeling of structures. *Journal of Materials in Civil Engineering*, *22*(5), 423. doi:10.1061/(ASCE)MT.1943-5533.0000041

Kodur, V., & Fike, R. (2009). Response of concrete filled HSS columns in real fires. *AISC Engineering Journal*, *46*(4), 243–257.

Kodur, V., & Latour, J. C. (2005). *Experimental studies on the fire resistance of hollow steel columns filled with high-strength concrete - Research Report 215*. Ottawa, Canada: National Research Council Canada.

Kodur, V., & Lie, T. T. (1995). *Experimental studies on the fire resistance of circular hollow steel columns filled with steel-fibre reinforced concrete - Internal Report No. 691*. Ottawa, Canada: National Research Council Canada.

Kodur, V., & Lie, T. T. (1996a). Fire resistance of circular steel columns filled with fibre-reinforced concrete. *Journal of Structural Engineering*, *122*(7), 776–782.

Kodur, V., & Lie, T. T. (1996b). *Experimental studies on the fire resistance of square hollow steel columns filled with steel-fibre reinforced concrete - Internal Report No. 662*. Ottawa, Canada: National Research Council Canada.

Kodur, V., & Lie, T. T. (1997). Evaluation of fire resistance of rectangular steel columns filled with fibre-reinforced concrete. *Canadian Journal of Civil Engineering*, *24*(3), 339–349.

Kodur, V., & Sultan, M. A. (2003). Effect of temperature on thermal properties of high-strength concrete. *Journal of materials in civil engineering*, *15*(2), 101–107. doi:dx.doi.org/10.1061/(ASCE)0899-1561(2003)15:2(101)

Kordina, K., & Klingsch, W. (1983). *Fire resistance of composite columns of concrete filled hollow sections, Report 15C1/C2*. Paris, France: CIDECT.

Lau, A., & Anson, M. (2006). Effect of high temperatures on high performance steel fibre reinforced concrete. *Cement and Concrete Research*, *36*(9), 1698–1707. doi:10.1016/j.cemconres.2006.03.024

Lennon, T., Moore, D. B., Wang, Y. C., & Bailey, C. G. (2007). *Designers' guides to the Eurocodes*. London, UK: Thomas Telford Publishing.

Liang, Q. Q., Uy, B., & Richard Liew, J. Y. (2006). Nonlinear analysis of concrete-filled thin-walled steel box columns with local buckling effects. *Journal of Constructional Steel Research*, *62*(6), 581–591. doi:10.1016/j.jcsr.2005.09.007

Lie, T. T. (1994). Fire resistance of circular steel columns filled with bar-reinforced concrete. *Journal of Structural Engineering*, *120*(5), 1489–1509.

Lie, T. T., & Chabot, M. (1992). *Experimental studies on the fire resistance of hollow steel columns filled with plain concrete - Internal Report No. 611*. Ottawa, Canada: National Research Council Canada.

Lie, T. T., Chabot, M., & Irwin, R. J. (1992). *Fire resistance of circular hollow steel sections filled with bar-reinforced concrete - Internal Report No. 636*. Ottawa, Canada: National Research Council Canada.

Lie, T. T., & Irwin, R. J. (1995). Fire resistance of rectangular steel columns filled with bar reinforced concrete. *Journal of Structural Engineering*, *121*(5), 797–805.

Lie, T. T., & Kodur, V. (1995a). *Mechanical properties of fibre-reinforced concrete at elevated temperatures - Internal Report No. 687*. Ottawa, Canada: National Research Council Canada.

Lie, T. T., & Kodur, V. (1995b). *Thermal properties of fibre-reinforced concrete at elevated temperatures - Internal report No. 683*. Ottawa, Canada: National Research Council Canada.

Lu, H., Zhao, X. L., & Han, L. H. (2009). Fire behaviour of high strength self-consolidating concrete filled steel tubular stub columns. *Journal of Constructional Steel Research*, *65*(10-11), 1995–2010. doi:10.1016/j.jcsr.2009.06.013

Maluk, C., Bisby, L., Terrasi, G., Krajcovic, M., & Torero, J. (2012). Novel fire testing methodology: Why, how and what now? *Proceedings of the Mini Symposium on Performance-based Fire Safety Engineering of Structures as part of the 1st International Conference on Performance Based and Life Cycle Structural Engineering, 5-7 December* (pp. 448–458). Hong Kong.

Morino, S., & Tsuda, K. (2002). Design and construction of concrete-filled steel tube column system in Japan. *Earthquake Engineering and Engineering*, *4*(1), 51–73.

Mouli, M., & Khelafi, H. (2007). Strength of short composite rectangular hollow section columns filled with lightweight aggregate concrete. *Engineering Structures*, *29*(8), 1791–1797. doi:10.1016/j.engstruct.2006.10.003

Myllymaki, J., Lie, T. T., & Chabot, M. (1994). *Fire resistance tests of square hollow steel columns filled with reinforced concrete - Internal Report No. 673*. Ottawa, Canada: National Research Council Canada.

NBCC. (2005). *National Building Code of Canada 2005*. Ottawa, Canada: National Research Council Canada.

Netinger, I., Kesegic, I., & Guljas, I. (2011). The effect of high temperatures on the mechanical properties of concrete made with different types of aggregates. *Fire Safety Journal*, *46*(7), 425–430. doi:10.1016/j.firesaf.2011.07.002

O'Loughlin, E., Rush, D., & Bisby, L. (2012). Concrete-filled stuctural hollow sections in fire: accounting for heat transfer across a gap. *15th International conference on Experimental Mechanics* (pp. 1–17). Porto, Portugal.

Paloposki, T., & Liedquist, L. (2005). *Steel emissivity at high temperatures - Research notes*. Tampere, Finland: Technical Research Centre of Finland.

Phan, L. (1996). *Fire performance of high-strength concrete: A report of the state-of-the art NISTIR 5934*. Massachusetts, USA: National Institute of Standards and Technology.

Phan, L. (2002). High-strength concrete at high temperature - An Overview. *Utilization of High Strength/High Performance Concrete, PRoceedings of 6th International Symposium, Volume 1* (pp. 501–518). Leipzig, Germany.

Pliya, P., Beaucour, A.-L., & Noumowé., A. (2011). Contribution of cocktail of polypropylene and steel fibres in improving the behaviour of high strength concrete subjected to high temperature. *Construction and Building Materials*, *25*(4), 1926–1934. doi:10.1016/j.conbuildmat.2010.11.064

Renaud, C. (2004). *Improvement and extension of the simple calculation method for fire resistance of unprotected concrete filled hollow columns, CIDET Research Report 15Q*. Paris, France: CIDECT.

Renaud, C., & Joyeux, D. (2001). *Unprotected concrete filled columns fire tests: Verification of 15Q - CIDECT Research Report 15R*. Paris, France: CIDECT.

Romero, M. L., Moliner, V., Espinos, A., Ibañez, C., & Hospitaler, A. (2011). Fire behavior of axially loaded slender high strength concrete-filled tubular columns. *Journal of Constructional Steel Research*, *67*(12), 1953–1965. doi:10.1016/j.jcsr.2011.06.012

Ruddy, J. L., Marlo, J. P., Ioannides, S. A., & Alfawakiri, F. (2003). *Steel Design Guide 19: Fire resistance of structural steel framing*. Chicago, USA.

Rush, D., Bisby, L., Lane, B., & Jowsey, A. (2010). Structural fire performance of CFS sections: State-of-the-art & knowledge gaps. *Interflam* (pp. 57–70). Nottingham, UK.

Sakumoto, Y., Okada, T., Yoshida, M., & Tasaka, S. (1994). Fire resistance of concrete-filled, fire-resistant steel-tube columns. *Journal of Materials in Civil Engineering*, *6*(2), 169.

Schaumann, P., Kodur, V., & Bahr, O. (2009). Fire behaviour of hollow structural section steel columns filled with high strength concrete. *Journal of Constructional Steel Research*, *65*(8-9), 1794–1802. doi:10.1016/j.jcsr.2009.04.013

Schneider, U. (1988). Concrete at high temperatures - A general review. *Fire Safety Journal*, *13*, 55–68.

Shanmugam, N. E., & Lakshmi, B. (2001). State of the art report on steel-concrete composite columns. *Journal of Constructional Steel Research*, *57*(10), 1041–1080.

Stanke, J. (1975). *Uuber die Auswetung von Ergrebnissen ausgefurhrter Brandversuche mit Schlussfolgerungen und Vorschlag fur ein Versuchprogramm - Report 15C1*. Berlin, Germany: CIDECT.

Stern-Gottfried, J., Law, A., Rein, G., & Torero, J. (2010). *A performance based methodology using travelling fires for structural analysis*. *8th International Conference on Performance-Based Codes & Fire Safety Design Methods* (pp. 373–384). Lund, Sweden: SFPE.

Sultan, M. a. (2006). Fire resistance furnace temperature measurements: plate thermometers vs shielded thermocouples. *Fire Technology*, *42*(3), 253–267. doi:10.1007/s10694-006-8431-7

Suzuki, T., Kimura, M., Kodaira, A., & Fushimi, M. (1985). Experimental study on fire resistance of concrete filled square steel columns: Structural behaviour under constant axial force in fire (in Japanese). (AIJ, Ed.) *Journal of Structural and Construction Engineering*, *350*(April), 77–85.

Tan, K. H., & Tang, C. Y. (2004). Interaction model for unprotected concrete filled steel columns under standard fire conditions. *Journal of Structural Engineering*, *130*(9), 1405–1413.

Tao, Z., Han, L. H., Uy, B., & Chen, X. (2011). Post-fire bond between the steel tube and concrete in concrete-filled steel tubular columns. *Journal of Constructional Steel Research*, *67*(3), 484–496. doi:10.1016/j.jcsr.2010.09.006

Tao, Z., Uy, B., Han, L. H., & Wang, Z. B. (2009). Analysis and design of concrete-filled stiffened thin-walled steel tubular columns under axial compression. *Thin-Walled Structures*, *47*(12), 1544–1556. doi:10.1016/j.tws.2009.05.006

Tao, Zhong, Han, L.-H., & Zhao, X.-L. (2004). Behaviour of concrete-filled double skin (CHS inner and CHS outer) steel tubular stub columns and beam-columns. *Journal of Constructional Steel Research*, *60*(8), 1129–1158. doi:10.1016/j.jcsr.2003.11.008

The Concrete Society. (2008). *Assessment, design and repair of fire-damaged concrete structures - Technical report no. 68*. Camberley UK: The Concrete Society.

Tide, R. (1998). Integrity of structural steel after exposure to fire. *Engineering Journal*, (1), 26–38.

Torero, J. L. (2012). Assesing the true performance of structures in fire. *First international conference of performance-based and life-cylce structral engineering* (pp. 429–440). Hong Kong.

Wang, Y. C. (2005). Performance of steel – concrete composite structures in fire. *Progressions in Structural Engineering Materials*, *7*, 86–102. doi:10.1002/pse.197

Wang, Y. C., & Davies, J. M. (2003). An experimental study of the fire performance of non-sway loaded concrete-filled steel tubular column assemblies with extended end plate connections. *Journal of Constructional Steel Research*, *59*(7), 819–838. doi:10.1016/S0143-974X(02)00092-5

Wang, Y. C., & Orton, A. (2008). Fire resistant design of concrete filled tubular steel columns. *Structural Engineer*, *7*(October), 40–45.

Welch, S., & Rubini, P. (1997). Three-dimensional simulation of a fire-resistance furnace. *Fire Safety Science*, *5*, 1009–1020. doi:10.3801/IAFSS.FSS.5-1009

Wickstrom, U. (2011). The adiabatic surface temperature and the plate thermometer. *Fire Safety Science*, *10*, 1001–1011. doi:10.3801/IAFSS.FSS.10-1001

Wickström, U., & Pålsson, J. (1999). *SP Report 1999:36 - A scheme for verification of computer codes for calculating temperature in fire exposed structures*. Lund, Sweden: SFPE.

Yang, H., Han, L. H., & Wang, Y. C. (2008). Effects of heating and loading histories on post-fire cooling behaviour of concrete-filled steel tubular columns. *Journal of Constructional Steel Research*, *64*(5), 556–570. doi:10.1016/j.jcsr.2007.09.007

Yin, J., Zha, X. X., & Li, L. Y. (2006). Fire resistance of axially loaded concrete filled steel tube columns. *Journal of Constructional Steel Research*, pp. 723–729. Elsevier. doi:10.1016/j.jcsr.2005.11.011

Zha, X. X. (2003). FE analysis of fire resistance of concrete filled CHS columns. *Journal of Constructional Steel Research*, *59*(6), 769–779. doi:10.1016/S0143-974X(02)00059-7

Zhang, Y., Wang, Y. C., Bailey, C. G., & Taylor, A. P. (2012). Global modelling of fire protection performance of intumescent coating under different cone calorimeter heating conditions. *Fire Safety Journal*, *50*, 51–62. doi:10.1016/j.firesaf.2012.02.004

Appendix A: Ranking tables from Chapter 3

Table A-1: Rankings for the Shape physical parameter

	Circle			N = 24			**Square**			N = 52			**Total weighted ranks**			
	Accuracy			Precision			Accuracy			Precision			Accuracy		Precision	
	ME	R	R.N	*σe*	R	R.N	*ME*	R	R.N	*σe*	R	R.N	*ME*	**R_{tot}**	*σe*	**R_{tot}**
Combi EC4 c	4.63	*4*	*96*	27.20	*8*	*192*	-1.50	*2*	*104*	19.25	*6*	*312*	200	**3**	504	**7**
Combi 1	-8.46	*5*	*120*	21.02	*5*	*120*	-0.58	*1*	*52*	19.73	*7*	*364*	172	**1**	484	**6**
"Best" Combi	-0.42	*1*	*24*	22.20	*6*	*144*	7.12	*3*	*156*	20.53	*8*	*416*	180	**2**	560	**8**
EC1-2,εa=0.2	1.46	*3*	*72*	20.21	*3*	*72*	-8.21	*4*	*208*	17.08	*2*	*104*	280	**4**	176	**2**
Combi EC4 d	0.46	*2*	*48*	24.32	*7*	*168*	-9.21	*6*	*312*	17.60	*5*	*260*	360	**5**	428	**5**
Combi 3	-15.79	*7*	*168*	18.74	*1*	*24*	-8.94	*5*	*260*	17.60	*4*	*208*	428	**6**	232	**4**
Combi 2	-17.50	*8*	*192*	18.83	*2*	*48*	-10.63	*7*	*364*	17.60	*3*	*156*	556	**7**	204	**3**
Combi EC4 a	-9.29	*6*	*144*	20.50	*4*	*96*	-15.87	*8*	*416*	16.91	*1*	*52*	560	**8**	148	**1**

Table A-2: Rankings for the Fixity physical parameter

	Pin-Pin			N = 9			**Pin-Fix**			N = 17			**Fix-Fix**			N = 50			**Total weighted ranks**			
	Accuracy			Precision			Accuracy			Precision			Accuracy			Precision			Accuracy		Precision	
	ME	R	R.N	*σe*	R	R.N	*ME*	R	R.N	*σe*	R	R.N	*ME*	R	R.N	*σe*	R	R.N	*ME*	**R_{tot}**	*σe*	**R_{tot}**
Combi EC4 c	-4.56	*3*	*27*	23.57	*6*	*54*	-5.12	*3*	*51*	17.27	*6*	*102*	3.32	*2*	*100*	23.84	*8*	*400*	178	**2**	556	**8**
Combi 1	-6.00	*4*	*36*	24.02	*7*	*63*	-4.62	*2*	*34*	18.62	*7*	*119*	-2.26	*1*	*50*	21.31	*6*	*300*	120	**1**	482	**7**
"Best" Combi	-4.33	*2*	*18*	26.41	*8*	*72*	3.77	*1*	*17*	22.66	*8*	*136*	5.24	*5*	*250*	20.64	*5*	*250*	285	**5**	458	**6**
EC1-2,εa=0.2	-2.56	*1*	*9*	21.56	*2*	*18*	-7.15	*4*	*68*	16.90	*3*	*51*	-4.12	*4*	*200*	19.43	*3*	*150*	277	**3**	219	**3**
Combi EC4 d	-7.89	*5*	*45*	21.75	*4*	*36*	-10.81	*5*	*85*	16.29	*2*	*34*	-3.74	*3*	*150*	21.88	*7*	*350*	280	**4**	420	**5**
Combi 3	-10.44	*6*	*54*	21.80	*5*	*45*	-10.85	*6*	*102*	17.11	*4*	*68*	-11.24	*6*	*300*	18.80	*1*	*50*	456	**6**	163	**1**
Combi 2	-12.11	*7*	*63*	21.58	*3*	*27*	-12.54	*7*	*119*	17.13	*5*	*85*	-12.94	*8*	*400*	18.83	*2*	*100*	582	**8**	212	**2**
Combi EC4 a	-13.44	*8*	*72*	20.22	*1*	*9*	-16.35	*8*	*136*	15.74	*1*	*17*	-12.46	*7*	*350*	19.44	*4*	*200*	558	**7**	226	**4**

Table A-3: Rankings for the Fill physical parameter

	Plain Concrete			N = 45			**Reinforced Concrete**			N = 31			**Total weighted ranks**			
	Accuracy			Precision			Accuracy			Precision			Accuracy		Precision	
	ME	R	R.N	*σe*	R	R.N	*ME*	R	R.N	*σe*	R	R.N	*ME*	**R_{tot}**	*σe*	**R_{tot}**
Combi EC4 c	8.53	*6*	*270*	22.17	*8*	*360*	-11.32	*3*	*93*	15.99	*2*	*62*	363	**5**	422	**6**
Combi 1	2.11	*3*	*135*	21.20	*6*	*270*	-10.58	*2*	*62*	16.63	*6*	*186*	197	**2**	456	**7**
"Best" Combi	9.71	*8*	*360*	21.41	*7*	*315*	-2.48	*1*	*31*	19.03	*8*	*248*	391	**6**	563	**8**
EC1-2,εa=0.2	0.60	*1*	*45*	17.71	*2*	*90*	-13.52	*4*	*124*	16.69	*7*	*217*	169	**1**	307	**4**
Combi EC4 d	1.76	*2*	*90*	19.41	*5*	*225*	-17.65	*6*	*186*	15.77	*1*	*31*	276	**3**	256	**2**
Combi 3	-6.82	*4*	*180*	18.20	*3*	*135*	-17.32	*5*	*155*	16.37	*4*	*124*	335	**4**	259	**3**
Combi 2	-8.56	*7*	*315*	18.25	*4*	*180*	-18.97	*7*	*217*	16.40	*5*	*155*	532	**8**	335	**5**
Combi EC4 a	-7.09	*5*	*225*	16.71	*1*	*45*	-23.52	*8*	*248*	16.05	*3*	*93*	473	**7**	138	**1**

Table A-4: Rankings for the Load Application physical parameter

	Concentric			N = 61			**Eccentric**			N = 15			**Total weighted ranks**			
	Accuracy			Precision			Accuracy			Precision			Accuracy		Precision	
	ME	R	R.N	*σe*	R	R.N	*ME*	R	R.N	*σe*	R	R.N	*ME*	**R_{tot}**	*σe*	**R_{tot}**
Combi EC4 c	2.87	*2*	*122*	23.38	*8*	*488*	-9.47	*3*	*45*	11.64	*5*	*75*	167	**2**	563	**8**
Combi 1	-1.46	*1*	*61*	21.70	*6*	*366*	-9.60	*4*	*60*	11.87	*6*	*90*	121	**1**	456	**6**
"Best" Combi	6.97	*5*	*305*	22.20	*7*	*427*	-4.33	*1*	*15*	13.74	*8*	*120*	320	**5**	547	**7**
EC1-2,εa=0.2	-4.33	*4*	*244*	19.81	*4*	*244*	-8.53	*2*	*30*	12.09	*7*	*105*	274	**4**	349	**5**
Combi EC4 d	-4.21	*3*	*183*	21.64	*5*	*305*	-14.07	*5*	*75*	10.94	*2*	*30*	258	**3**	335	**4**
Combi 3	-10.33	*6*	*366*	19.46	*1*	*61*	-14.27	*6*	*90*	11.11	*3*	*45*	456	**6**	106	**1**
Combi 2	-12.07	*7*	*427*	19.49	*2*	*122*	-15.80	*7*	*105*	11.23	*4*	*60*	532	**7**	182	**2**
Combi EC4 a	-12.51	*8*	*488*	19.49	*3*	*183*	-19.00	*8*	*120*	10.91	*1*	*15*	608	**8**	198	**3**

Table A-5: Rankings based on the Size physical parameter

	0 - 200 mm N = 16						**200 - 250 mm** N = 33						**250 - 300 mm** N = 17						**300 + mm** N = 10						**Total weighted ranks**			
	Accuracy			Precision			Accuracy			Precision			Accuracy			Precision			Accuracy			Precision			Accuracy		Precision	
	ME	R	R.N	*σe*	R	R.N	*ME*	R	R.N	*σe*	R	R.N	*ME*	R	R.N	*σe*	R	R.N	*ME*	R	R.N	*σe*	R	R.N	*ME*	$\mathbf{R_{tot}}$	*σe*	$\mathbf{R_{tot}}$
Combi EC4 c	-3.31	*2*	*32*	14.91	*8*	*128*	-8.73	*2*	*66*	17.40	*3*	*99*	11.41	*7*	*119*	22.41	*8*	*136*	18.00	*7*	*70*	28.57	*8*	*80*	287	**2**	443	**7**
Combi 1	-11.94	*5*	*80*	12.70	*3*	*48*	-9.97	*3*	*99*	18.76	*4*	*132*	9.76	*6*	*102*	20.14	*7*	*119*	12.10	*6*	*60*	18.00	*4*	*40*	341	**5**	339	**5**
"Best" Combi	-4.19	*3*	*48*	13.40	*5*	*80*	-1.00	*1*	*33*	22.22	*8*	*264*	15.65	*8*	*136*	18.78	*5*	*85*	19.40	*8*	*80*	18.51	*5*	*50*	297	**4**	479	**8**
EC1-2,εa=0.2	0.56	*1*	*16*	14.12	*6*	*96*	-12.12	*4*	*132*	19.11	*7*	*231*	-5.65	*4*	*68*	16.12	*1*	*17*	9.50	*4*	*40*	17.29	*3*	*30*	256	**1**	374	**6**
Combi EC4 d	-7.25	*4*	*64*	14.59	*7*	*112*	-14.42	*5*	*165*	17.04	*1*	*33*	1.00	*1*	*17*	19.95	*6*	*102*	10.70	*5*	*50*	26.03	*7*	*70*	296	**3**	317	**4**
Combi 3	-16.69	*7*	*112*	11.76	*1*	*16*	-16.79	*6*	*198*	18.82	*5*	*165*	-3.18	*2*	*34*	17.11	*2*	*34*	3.10	*3*	*30*	14.49	*2*	*20*	374	**6**	235	**1**
Combi 2	-18.25	*8*	*128*	11.95	*2*	*32*	-18.45	*7*	*231*	18.89	*6*	*198*	-4.82	*3*	*51*	17.28	*4*	*68*	1.00	*2*	*20*	14.38	*1*	*10*	430	**7**	308	**3**
Combi EC4 a	-13.75	*6*	*96*	13.11	*4*	*64*	-20.61	*8*	*264*	17.29	*2*	*66*	-9.06	*5*	*85*	17.21	*3*	*51*	0.60	*1*	*10*	21.32	*6*	*60*	455	**8**	241	**2**

Table A-6: Rankings for the Load Ratio physical parameter

	0.0 - 0.2 N = 18						**0.2 - 0.4** N = 33						**0.4 - 0.6** N = 22						**0.6 +** N = 3						**Total weighted ranks**			
	Accuracy			Precision			Accuracy			Precision			Accuracy			Precision			Accuracy*			Precision*			Accuracy*		Precision*	
	ME	R	R.N	*σe*	R	R.N	*ME*	R	R.N	*σe*	R	R.N	*ME*	R	R.N	*σe*	R	R.N	*ME*	R	R.N	*σe*	R	R.N	*ME*	$\mathbf{R_{tot}}$	*σe*	$\mathbf{R_{tot}}$
Combi EC4 c	9.28	*5*	*90*	18.72	*8*	*144*	-2.61	*2*	*66*	26.36	*8*	*264*	-1.91	*2*	*44*	16.97	*6*	*132*	-2.00	*2*	*6*	14.80	*6*	*18*	200	**1**	540	**8**
Combi 1	-12.28	*8*	*144*	12.66	*1*	*18*	-8.79	*3*	*99*	19.55	*1*	*33*	10.73	*7*	*154*	18.12	*7*	*154*	14.00	*8*	*24*	27.51	*8*	*24*	397	**6**	205	**2**
"Best" Combi	9.89	*7*	*126*	18.35	*7*	*126*	0.45	*1*	*33*	21.78	*6*	*198*	7.68	*5*	*110*	22.43	*8*	*176*	-0.67	*1*	*3*	21.57	*7*	*21*	269	**4**	500	**7**
EC1-2,εa=0.2	0.56	*1*	*18*	16.45	*4*	*72*	-10.76	*5*	*165*	20.48	*4*	*132*	-1.82	*1*	*22*	16.59	*5*	*110*	-2.33	*3*	*9*	7.64	*2*	*6*	205	**2**	314	**5**
Combi EC4 d	1.44	*2*	*36*	15.92	*3*	*54*	-9.58	*4*	*132*	24.68	*7*	*231*	-7.45	*4*	*88*	16.18	*4*	*88*	-4.67	*4*	*12*	9.29	*5*	*15*	256	**3**	373	**6**
Combi 3	-7.83	*3*	*54*	16.85	*5*	*90*	-16.42	*6*	*198*	19.93	*3*	*99*	-6.64	*3*	*66*	15.84	*3*	*66*	-5.00	*5*	*15*	8.89	*4*	*12*	318	**5**	255	**4**
Combi 2	-9.56	*6*	*108*	17.10	*6*	*108*	-18.21	*8*	*264*	19.90	*2*	*66*	-8.27	*6*	*132*	15.73	*1*	*22*	-6.00	*6*	*18*	7.94	*3*	*9*	504	**8**	196	**1**
Combi EC4 a	-7.94	*4*	*72*	14.31	*2*	*36*	-17.88	*7*	*231*	21.60	*5*	*165*	-13.18	*8*	*176*	15.77	*2*	*44*	-8.33	*7*	*21*	5.69	*1*	*3*	479	**7**	245	**3**

Table A-7: Rankings for the Wall Thickness physical parameter

	≤ 4.00 mm N = 15						**4.01 - 6.00 mm** N = 16						**6.01 - 7.00 mm** N = 27						**7.01 + mm** N = 17						**Total weighted ranks**			
	Accuracy			Precision			Accuracy			Precision			Accuracy			Precision			Accuracy			Precision			Accuracy		Precision	
	ME	R	R.N	*σe*	R	R.N	*ME*	R	R.N	*σe*	R	R.N	*ME*	R	R.N	*σe*	R	R.N	*ME*	R	R.N	*σe*	R	R.N	*ME*	**R_{tot}**	*σe*	**R_{tot}**
Combi EC4 c	-6.07	*3*	*45*	23.94	*7*	*105*	-3.81	*1*	*16*	20.62	*8*	*128*	4.93	*3*	*81*	22.87	*8*	*216*	2.89	*3*	*51*	20.23	*5*	*85*	193	**2**	534	**8**
Combi 1	-5.87	*2*	*30*	23.05	*5*	*75*	-13.13	*5*	*80*	14.14	*1*	*16*	1.59	*1*	*27*	19.55	*5*	*135*	1.22	*1*	*17*	21.69	*8*	*136*	154	**1**	362	**5**
"Best" Combi	-0.47	*1*	*15*	24.07	*8*	*120*	-5.44	*2*	*32*	15.01	*4*	*64*	12.67	*8*	*216*	20.55	*6*	*162*	6.22	*6*	*102*	20.97	*6*	*102*	365	**5**	448	**7**
EC1-2,εa=0.2	-8.60	*4*	*60*	22.62	*3*	*45*	-6.19	*3*	*48*	16.49	*5*	*80*	-5.07	*4*	*108*	15.90	*1*	*27*	-1.50	*2*	*34*	21.08	*7*	*119*	250	**3**	271	**3**
Combi EC4 d	-12.27	*5*	*75*	23.37	*6*	*90*	-8.63	*4*	*64*	19.51	*7*	*112*	-3.04	*2*	*54*	20.81	*7*	*189*	-3.56	*4*	*68*	17.62	*2*	*34*	261	**4**	425	**6**
Combi 3	-12.93	*6*	*90*	21.61	*2*	*30*	-20.00	*7*	*112*	14.24	*2*	*32*	-8.19	*5*	*135*	16.26	*2*	*54*	-6.06	*5*	*85*	19.06	*4*	*68*	422	**6**	184	**1**
Combi 2	-14.20	*7*	*105*	21.52	*1*	*15*	-21.56	*8*	*128*	14.24	*3*	*48*	-9.96	*6*	*162*	16.57	*3*	*81*	-8.11	*7*	*119*	19.06	*3*	*51*	514	**7**	195	**2**
Combi EC4 a	-18.40	*8*	*120*	22.67	*4*	*60*	-17.06	*6*	*96*	16.52	*6*	*96*	-11.15	*7*	*189*	17.73	*4*	*108*	-11.00	*8*	*136*	16.58	*1*	*17*	541	**8**	281	**4**

Appendix B: Summary of key thermal modelling approaches

Model	Fire Emiss.	Material properties							Gap Cond.
		Steel				Concrete			
	ε_f	ε_a	c_a	λ_a	ρ_a	c_c	λ_c	ρ_c	h_j
• *Base*	N/A	N/A	(B-3)	(B-5)	(B-7)	(B-8)	(B-12)	(B-15)	N/A
• *Combi EC4c*	1.00	0.7	(B-4)	(B-6)		(B-9)	(B-13) Lo.		N/A
• *Combi ω*	0.75	(B-1)				(B-10)	(B-14)		(B-16)
• *Combi α*	0.38	(B-2)				(B-11)	(B-13) Up.		(B-16)
• *Combi γ*	0.75	(B-2)					(B-13) Up.		(B-16)

Steel properties:

Emissivity of steel, $\varepsilon_{m,a}$

(Bentz et al., 2009)

$$\varepsilon_{m,a} = \begin{cases} 0.32, & \theta_a = 20^oC \\ 0.32, & \theta_a = 200^oC \\ 0.85, & \theta_a = 400^oC \\ 0.95, & \theta_a = 800^oC \\ 0.95, & \theta_a = 1200^oC \end{cases} \quad \text{(B-1)}$$

(Paloposki and Liedquist, 2005)

$$\varepsilon_{m,a} = \begin{cases} 0.2, & \theta_a = 20^oC \\ 0.2, & \theta_a = 385^oC \\ 0.65, & \theta_a = 550^oC \\ 0.65, & \theta_a = 1200^oC \end{cases} \quad \text{(B-2)}$$

The specific heat capacity of carbon steel, $c_a(\theta)$, in J/kg·°C is given by (CEN, 2005):

$$c_a = 600 \quad \text{(B-3)}$$

$$c_{a,\theta} = \begin{cases} 425 + 0.773\theta_a - 0.00169\theta_a^2 + 2.22 \text{ x} 10^{-6}\theta_a^3, & 20^oC \le \theta_a < 600^oC \\ 666 + \dfrac{13002}{738 - \theta_a} & 600^oC \le \theta_a < 735^oC \\ 545 + \dfrac{17820}{\theta_a - 731} & 735^oC \le \theta_a < 900^oC \\ 650 & 900^oC \le \theta_a < 1200^oC \end{cases} \quad \text{(B-4)}$$

The thermal conductivity, $\lambda_{a,\theta}$, in W/mC is defined (CEN, 2005):

$\lambda_a = 45$	(B-5)
$\lambda_{a,\theta} = \begin{cases} 54 - 0.033\theta_a & 20^oC \leq \theta_a < 800^oC \\ 27.3 & 800^oC \leq \theta_a < 1200^oC \end{cases}$	(B-6)

The density of steel is taken as (CEN, 2005):

$\rho_a = 7850\ kg/m^3$	(B-7)

Concrete properties:

The specific heat capacity of concrete, $c_{c,\theta}$, in J/kg·°C is given by:

(CEN, 2005)	$c_c = 1000$	(B-8)
(CEN, 2005)	$c_{c,\theta} = \begin{cases} 890 + 56.2(\theta_c/100) - 3.4(\theta_c/100)^2 & 20 \leq \theta_c < 100 \\ 5600 & \theta_c = 115C \\ 890 + 56.2(\theta_c/100) - 3.4(\theta_c/100)^2 & 200 \leq \theta_c < 1200 \end{cases}$	(B-9)
(Lie and Irwin, 1995)	$\rho_c c_{c,\theta} = \begin{cases} 2.566 \text{ x}10^6 & 0 < \theta_c \leq 400^oC \\ (0.1756\theta_c - 68.034) \text{ x}10^6 & 400 < \theta_c \leq 410 \\ (-0.05043\theta_c + 25.00671) \text{ x}10^6 & 410 < \theta_c \leq 445 \\ 2.566 \text{ x}10^6 & 445 < \theta_c \leq 500 \\ (0.01603\theta_c - 5.44881) \text{ x}10^6 & 500 < \theta_c \leq 635 \\ (0.16635\theta_c - 100.90225) \text{ x}10^6 & 635 < \theta_c \leq 715 \\ (-0.22103\theta_c + 176.07343) \text{ x}10^6 & 715 < \theta_c \leq 785 \\ 2.566 \text{ x}10^6 & \theta_c > 785 \end{cases}$	(B-10)
Chapter 6	$c_{c,\theta} = \begin{cases} 890 + 56.2(\theta_c/100) - 3.4(\theta_c/100)^2 & 20 \leq \theta_c < 120 \\ 2780 & \theta_c = 127 \\ 2580 & \theta_c = 210 \\ 890 + 56.2(\theta_c/100) - 3.4(\theta_c/100)^2 & 220 \leq \theta_a < 1200 \end{cases}$	(B-11)

The thermal conductivity, $\lambda_{c,\theta}$, in W/mC is defined by:

(CEN, 2005)	$\lambda_c = 1.60$	(B-12)
	$\lambda_{c,\theta} = \begin{cases} 2 - 0.2451\left(\frac{\theta_c}{100}\right) + 0.0107\left(\frac{\theta_c}{100}\right)^2 & Up. \\ 1.36 - 0.136\left(\frac{\theta_c}{100}\right) + 0.0057\left(\frac{\theta_c}{100}\right)^2 & Lo. \end{cases}$	(B-13)
(Lie and Irwin, 1995)	$\lambda_{c,\theta} = \begin{cases} 1.355 & 0 \le \theta_c \le 293 \\ -0.001241\theta_c + 1.7162 & \theta_c > 293 \end{cases}$	(B-14)

The density of concrete is taken as (CEN, 2005):

$\rho_{c,\theta} = 2354 - 23.47(\theta_c/100)\ kg/m^3$	(B-15)

Gap conductivity:

(Ghojel, 2004)	$h_j = 160.5 - 63.8 \cdot \exp(-339.9 \cdot {\theta_a}^{-1.4})$	(B-16)